JAERI-Review
99-031

NUCLEAR ENERGY SYSTEM DEPARTMENT ANNUAL REPORT
(APRIL 1, 1998-MARCH 31, 1999)

January 2000

Department of Nuclear Energy System

日本原子力研究所
Japan Atomic Energy Research Institute

本レポートは、日本原子力研究所が不定期に公刊している研究報告書です。
入手の問合わせは、日本原子力研究所研究情報部研究情報課（〒319-1195　茨城県那珂郡東海村）あて、お申し越し下さい。なお、このほかに財団法人原子力弘済会資料センター（〒319-1195　茨城県那珂郡東海村日本原子力研究所内）で複写による実費頒布を行っております。

This report is issued irregularly.
Inquiries about availability of the reports should be addressed to Research Information Division, Department of Intellectual Resources, Japan Atomic Energy Research Institute, Tokai-mura, Naka-gun, Ibaraki-ken 〒319-1195, Japan.

編集兼発行　日本原子力研究所

JAERI－Review 99－031

Nuclear Energy System Department Annual Report

(April 1, 1998 —March 31, 1999)

Department of Nuclear Energy System

Tokai Research Establishment
Japan Atomic Energy Research Institute
Tokai-mura, Naka-gun, Ibaraki-ken

(Received November 18, 1999)

This report summarizes the research and development activities in the Department of Nuclear Energy System during the fiscal year of 1998 (April 1, 1998 - March 31, 1999).

The Department has been organized from April 1998. The main research activity is aimed to build the basis of the development of future nuclear energy system. The research activities of the fiscal year cover basic nuclear and atomic & molecular data evaluation, conceptual design of reduced-moderation water reactor, development of reactor analysis code, reactor physics study on fast neutron system, control and sensing technology development for nuclear reactor, experiment and analysis of thermal-hydrodynamics, development of advanced material for reactor, lifetime reliability assessment on structural material for advanced reactor, development of advanced nuclear fuel, design of marine reactor and the research for nuclear ship system. The maintenance and operation of reactor engineering facilities belonging to the Department are undertaken.

The activities of the research committee to which the Department takes a role of secretariat are also summarized in this report.

Keywords: Nuclear Energy System Department Annual Report, Nuclear Data, Reactor Physics, Thermal Hydraulics, Advanced Material, Advanced Nuclear Fuel, Marine Reactor

JAERI－Review 99－031

平成１０年度エネルギーシステム研究部年報

日本原子力研究所東海研究所
エネルギーシステム研究部

（1999年11月18日受理）

本報告書は、平成１０年度におけるエネルギーシステム研究部の研究活動状況をとりまとめたものである。

エネルギーシステム研究部は、平成１０年度より新たに編成された部であり、将来型炉等新たなエネルギーシステムを視野に入れた基礎基盤的な研究を進めている。エネルギーシステム研究部の研究分野は、核及び原子分子データの評価や低減速スペクトル炉の概念設計研究、高速中性子体系における炉物理実験及び解析、炉特性解析コードの開発、原子炉制御及びセンシング技術の開発、伝熱流動実験及び解析、原子力用新材料の開発及び経年挙動研究、新型燃料の研究、舶用炉及び原子力船システムの研究等の研究開発に亘っている。この他、エネルギーシステム研究部の各種炉工学施設の維持・管理も行っている。

本報告では、エネルギーシステム研究部が運営を担当する研究委員会の活動報告もとりまとめられている。

東海研究所：〒319-1195　茨城県那珂郡東海村白方白根２－４

Contents

This is a blank page.

Preface

The research activities of the Department of Nuclear Energy System, Japan Atomic Energy Research Institute, during the fiscal year 1998 (April 1998 - March 1999) are presented in this report. The Department of Nuclear Energy System was newly organized in April 1998 as the course of the reorganization in Japan Atomic Energy Research Institute. The Department is expected to do the work relating to the development and utilization of advanced nuclear energy system. The research activities cover such fields as reactor physics, thermal hydraulics, material science including research for advanced fuel and R&D for nuclear ship.

The total number of permanent staff working in the department during the year was 127 including clerical service staff. The Department was funded from JAERI expenditure amounting to 1,000 million yen for FY 1998, excluding nuclear fuel cost and personnel expense. About 500 million yen was provided by the research contracts with external organization; Science and Technology Agency (STA) for non-destructive measurement technology of trans-uranic elements (TRU), for demonstration test on lifetime reliability of structural materials for advanced prototype power reactor, for demonstration of reliability of new materials used in nuclear fuel reprocessing plant and for survey on the technology for evaluating the foundation stability for offshore siting, Power Reactor and Nuclear Fuel Development Corporation (PNC) for reactor physics constants of fast breeder reactor and covariances of major actinide data.The department has served as secretariat of Japanese Nuclear Data Committee, Atomic and Molecular Data Research Committee, the Research Committee on Reactor Physics and the Research Committee on Marine Reactors.

The research activities have been conducted in thirteen laboratories with the support of two divisions.

Nuclear Data Center

This center has two main research themes; one is nuclear data and the other is atomic & molecular data. As to the nuclear data, the research activities consist of nuclear data evaluation of JENDL files (including Special Purpose Files as well as General Purpose File) for the general applications and nuclear data measurements to enrich the fundamental database. Reevaluation work for JENDL-3.3 has been continued and much effort has been made. Some progresses are also made for JENDL high-energy files. As to the atomic & molecular data, main efforts are devoted to compilation and evaluation of atomic and molecular collision data and of atomic spectrum data for JAEMDL-5. Fundamental database having been developed so far including

atomic & molecular data as well as nuclear data are available through WWW (http://wwwndc.tokai.jaeri.go.jp) of our home page.

This center has a function of the National Center that disseminates the nuclear and atomic & molecular data to Japanese customers, contacts the foreign and international centers and coordinates the international collaboration. This center also serves as a secretariat of Japanese Nuclear Data Committee and of Atomic and Molecular Data Committee.

Energy System Assessment Laboratory

In the development of analytical tools, the prototype expert system for supporting the utilization of MARKAL and the database of energy technologies were developed. In the field of analytical work, analyses were made on the roles of nuclear energy in reducing future CO2 emissions from Japan's energy systems, and also on the effect of high conversion water-cooled reactors from the viewpoint of reducing natural uranium consumption. In addition, a nuclear hydrogen production system using biomass gasification processes was designed.

Advanced Reactor Systems Laboratory

The main task of this laboratory is now to develop concepts for advanced water-cooled reactors. Design studies on the reduced-moderation water reactor (RMWR) are the major part of the current activities. Some basic thermal hydraulic investigation related to the RMWR is also in progress. Another design study on the high burn-up and long operation cycle reactors with increased moderation is simultaneously performed.

Reactor Analysis Laboratory

Major research theme of this laboratory is development and improvement of software (data/code) in reactor physics to serve for reactor design and analysis. It aims development of high speed, high accuracy Monte Carlo codes and nodal codes. Efforts are now concentrated to develop a comprehensive code system used for reactor core design including thermal hydraulics, core management and kinetics. Another theme is production of continuous energy and multi-group cross section libraries for wide applications of the developed code systems.

Reactor Physics Laboratory

Research field of this laboratory covers very wide range of reactor physics investigation and their applications to nuclear fuel cycle system. Main research area are such as study on new reactor concepts, reactor physics experiments analyses using critical assembly and the development of non-destructive measurements for TRU in radioactive waste package.

Control and AI Laboratory

In a study of sensing technology, a nuclear instrumentation based on optical sensing and a position-sensitive fission counter for ex-core measurement are investigated. In control and diagnostics research, an advanced early fault diagnosis system based on the hybrid use of neural networks and expert system is being developed. A human and mobile robot collaborative system for the inspecting patrol of nuclear power plants has also been developed.

Heat Transfer and Fluid Flow Laboratory

Three-dimensional two-phase flow analysis code has been developed and applied to the feasibility study on the passive residual heat removal system. A feasibility study on the core cooling during reflood in a PWR with a tight-lattice core was performed for the design of a reduced-moderation water reactor. Several numerical simulations of thermal-hydraulic behaviors have also performed for the accidents in a fusion reactor to establish reliable analytical tools for safety evaluation.

Material Performance and Testing Laboratory

This laboratory carries out irradiation assisted stress corrosion cracking (IASCC) study, demonstration test on lifetime reliability of structural materials for advanced prototype power reactors (STA commissioned research), research on heat resistant alloys for high temperature gas-cooled reactors, and development of material performance database.

Material Strength Laboratory

R & D on the advanced materials have been extensively carried out aiming at the establishment of new techniques for material evaluation and the development of advanced materials on the basis of the results of the material evaluation. As for the material evaluation the microindentation technique was successfully applied to the characterization of coated materials which were developed for the use as components in the IS hydrogen production process. An example of the material developments was the optimization of HIP bonding condition for tungsten/copper to be used for the divertor structure.

Interfacial Studies Laboratory

The mechanisms of SCC of metallic zirconium and local attacks of stainless steels in nitric acid environments were analyzed and modeled. Corrosion sensors and alternative materials like Nb alloys and Ni base alloys were modified by considering the practical use. On

the demonstration test of material performance for Rokkasho reprocessing plants sponsored by the STA, the acid recovery evaporator mock-up was operated and the dissolver mock-up was arranged.

Advanced Fuel Laboratory

The activities of the group focus on the R&D of advanced fuels from the viewpoint of effective utilization of plutonium in the next century. ROX like oxide fuel has been studied for burning excess plutonium by use of the present LWRs technologies coupled with the direct depository of the spent fuel because of its high chemical and geological stability. As a long term subject, nitride fuel, which has excellent thermal and neutronic properties, has been investigated as fuels/targets for the transmutation of minor actinides and also for fast reactors.

Advanced Marine Reactor Laboratory

Design of a very small-scale and highly compact marine reactor having innovative technologies has been studied, aiming use for a scientific under-sea research vessel. Main parameters such as the core size, the operational temperature and pressure and so on for the reactor with thermal output of 1.25 MW were determined. Development of the main components of the reactor is continuing.

Nuclear Ship System Laboratory

In R&D related to nuclear ship systems, advanced automatic control for nuclear ships, engineering simulation system development and safety evaluation for an offshore nuclear power plant have been studied. A prototype system of advanced automatic control has been made for normal and abnomaly situations. The engineering simulation system has almost completed for integrated marine reactor and nuclear ship database. Safety evaluation for an offshore plant were also completed as four year work under the STA program.

Reactor Engineering Facility Operation Division

This division operated two large-scale engineering facilities : FCA and Heat Transfer Fluid Flow Test Facilities in accordance with each experiment program and maintained in the monthly or the annual inspection. Consequently safety operations of these facilities were achieved and contributed sufficiently to the execution of each experimental study. Furthermore the maintenance work for VHTRC was put into practice as scheduled.

The Department is involved in the following project-oriented programs of JAERI;

(1) Design Studies of Advanced Reactors

(2) Development of High Temperature Gas-cooled Reactor

(3) Engineering Research for Fusion Reactor

The activities of the Department in FY 1998 have contributed to the essential progress in the field of reactor engineering.

Masayuki Nakagawa, Director
Department of Nuclear Energy System
November 1, 1999

1. Nuclear Data, and Atomic and Molecular Data

Evaluation for JENDL Special Purpose Files has been progressed significantly with the cooperation of JNDC (Japanese Nuclear Data Committee). As to the Intermediate Energy File, which is important for new the applications such as Accelerator Driven System in the Neutron Science Research, much effort are made for the file developments of JENDL High Energy File, JENDL PKA/KERMA File and JENDL Photonuclear Data File. The evaluation work for the neutron and proton files up to 3GeV is progressed for the first-priority 42 nuclei. Also in connection with the high-energy file development, neutron induced fission cross-sections are calculated by the method of QMD (Quantum Molecular Dynamics) + SDM (Statistical Decay Model). Also, a new version of the JENDL Dosimetry File 99 (JENDL-D/99) is produced by revising the previous version, which was published in 1991. This new version contains 67 reaction and 47 nuclides of which 33 reactions are revised. In the file, cross section and covariance data in the forms of group-wise as well as point-wise are supplied. As to the Covariance File development, estimation of covariances of neutron nuclear data important for FBR applications was made for JENDl-3.2 data. Cr and Ni covariance matrices are newly generated as well as covariances of fission neutron spectra of major actinides. Finally, evaluation for JENDL FP Decay Data File in the ENDF/B-6 format has been progressed in order to replace the previous JNDC decay data file, which was compiled in the local format other than the ENDF/B-6. In the new evaluation, decay data are re-evaluated considering the recent ESNDF evaluations.

Mass chain evaluation has been continued within the framework of the international cooperation for the ENSDF File. The evaluation of mass chain A=119 and 125 have been completed and sent to BNL for the critical review.

As to the atomic and molecular data, data developments for JAEMDL-5 have been progressed. A compilation work on wavelengths and energy level classifications for spectra of Argon (Ar I through Ar XVIII) is made. This is a series of compilations of spectra of highly ionized atoms of particular interest to the fusion energy community. To supply fundamental data for the plasma modeling, state-selected cross-sections for ion production in $H^+ + H_2$ collisions are studied. State-selected cross-sections are calculated by using a trajectory hopping method with the die-atomics-in-molecules (DIM) potential energy surfaces. Eeffects of the vibrational and rotational excited states of the molecules H_2 are studied to predict the competition mechanism between electron transfer and dissociation reactions in the collisions of this system.

1.1 Nuclear Data Evaluation and Compilation for JENDL Intermediate Energy Files in 1998

T. Fukahori and Japanese Nuclear Data Committee (High Energy Nuclear Data Evaluation WG)
(*E-mail*: fukahori@cracker.tokai.jaeri.go.jp)

The JAERI Nuclear Data Center started evaluation work in cooperation with Japanese Nuclear Data Committee (JNDC) to produce files related intermediate energy, which are JENDL High Energy File, JENDL PKA/KERMA File and JENDL Photonuclear Data File. The JENDL High Energy File includes nuclear data for proton- and neutron-induced reactions. Below 20 MeV, the data of JENDL Fusion File[1] or JENDL-3.2[2] are adopted. The compilation was being done for the neutron file for IFMIF[3] in the energy range up to 50 MeV. The evaluation work for the neutron and proton files energy range up to 3 GeV is performed for the first-priority 42 nuclei by mainly using the "quick-GNASH system"[4] and JQMD code[5]. The target isotopes included in the JENDL High Energy File are summarized in Table 1.1.1 as well as priorities. The semi-empirical formulae derived by Pearlstein[6], Wellisch[7] and NASA[8] were examined to calculate total, elastic scattering and non-elastic scattering cross sections in the intermediate energy region for the target nuclei having less experimental data (Figs.1.1.1-2). For fission cross section calculation, the systematics[9] was developed and its results are compared with experimental data in Figs.1.1.3-4.

The JENDL Photonuclear Data File is being developed for gamma-ray induced reaction data up to 140 MeV. The photon absorption cross section is evaluated with the giant dipole resonance model and quasi-deuteron model, and the decaying processes are estimated with the statistical model with preequilibrium correction by using MCPHOTO[10] and ALICE-F[11] codes. Some of evaluated results are compared with the other photonuclear data files evaluated at Los Alamos, Beijing, Moscow and Obninsk in Figs. 1.1.5-6.

The JENDL PKA/KERMA File is generated to supply primary knock-on atom (PKA) spectra, damage energy spectra, DPA (displacement per atom) cross sections and kerma factors by neutron-induced reactions in the energy region up to 50 MeV. A processing code system, ESPERANT[11] was developed to calculate above quantities from evaluated nuclear

data file by using effective single particle emission approximation (ESPEA). For light mass nuclei, SCINFUL/DDX code which considers break-up reactions with PKA spectra is used as well as EXIFON code which can calculate with correction of preequilibrium process.

References

1) Baosheng, Y., et al.: J. Nucl. Sci. Technol., **29** 677 (1992).
2) Nakagawa, T., et al.: ibid., **32** 1259 (1995).
3) Noda, K.: Proc. of 1994 Symposium on Nuclear Data, Tokai, Japan, Nov. 17-18, 1994, JAERI-Conf 95-008, p.112 (1995).
4) Chadwick, M.B. and Young, P.G.: Phys. Rev., **C47**, 2255 (1993).
5) Niita, K. and Chiba, S.: "JQMD: Quantum Molecular Dynamics and Statistical Decay Model Code", private communication.
6) Pearlstein, S.: J. Astrophys., **346**, 1049 (1989).
7) Wellisch, H.P. and Axen, D.: Phys. Rev., **C54**, 1329 (1996).
8) Tripathi, R.K., Cucinotta, F.A. and Wilson, J.W.; NASA Technical Paper 3621 (1997), NASA/TP-1998-208438 (1998).
9) Kishida, N. and Kadotani, H.: private communication.
10) Fukahori, T.: Proc. Specialists' Meeting on High Energy Nuclear Data, Tokai, Ibaraki, Oct. 3-4, 1991, JAERI-M 92-039, p.114 (1992).
11) Fukahori, T., et al.: Proc. of the Third Specialists' Meeting on Nuclear Data for Fission Reactors, Tokai, Japan, Nov. 29-30, 1995, JAERI-Conf 96-005, p.130 (1996).

Table 1.1.1 Isotopes included in neutron and proton file up to 3 GeV and their priorities.

1st priority (42 nuclides)	^{1}H, ^{12}C, ^{14}N, ^{16}O, ^{23}Na, ^{27}Al, ^{50,52,53,54}Cr, ^{54,56,57,58}Fe, ^{58,60,61,62,64}Ni, ^{63,65}Cu, ^{181}Ta, ^{180,182,183,184,186}W, ^{197}Au, ^{196,198,199,200,201,202,204}Hg, ^{204,206,207,208}Pb, ^{209}Bi, ^{235,238}U
2nd priority (42 nuclides)	^{2}H, ^{9}Be, ^{24,25,26}Mg, ^{28,29,30}Si, ^{39,41}K, ^{40,42,43,44,46,48}Ca, ^{46,47,48,49,50}Ti, ^{51}V, ^{55}Mn, ^{59}Co, ^{90,91,92,94,96}Zr, ^{93}Nb, ^{92,94,95,96,97,98,100}Mo, ^{238,239,240,241,242}Pu
3rd priority (38 nuclides)	^{6,7}Li, ^{10,11}B, ^{13}C, ^{19}F, ^{35,37}Cl, ^{35,38,40}Ar, ^{64,66,67,68,70}Zn, ^{69,71}Ga, ^{70,72,73,74,76}Ge, ^{75}As, ^{89}Y, ^{232}Th, ^{233,234,236}U, ^{237}Np, ^{241,242,242m,243}Am, ^{243,244,245,246}Cm

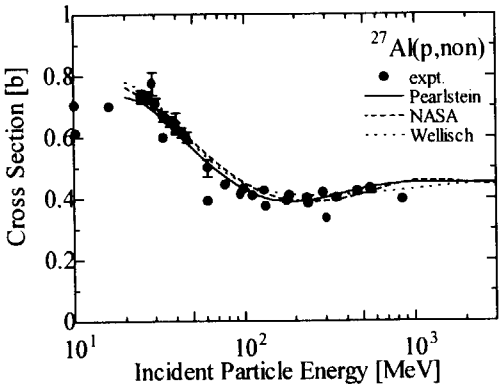

Fig. 1.1.1 Proton-induced non-elastic cross section of ^{27}Al

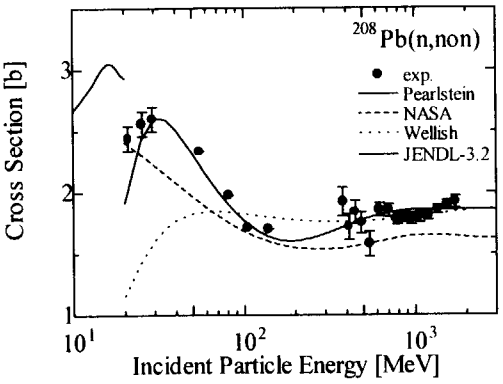

Fig. 1.1.2 Neutron-induced non-elastic cross section of ^{208}Pb

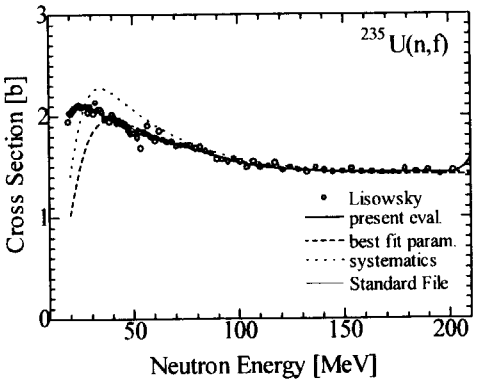

Fig. 1.1.3 Neutron-induced fission cross section of ^{235}U

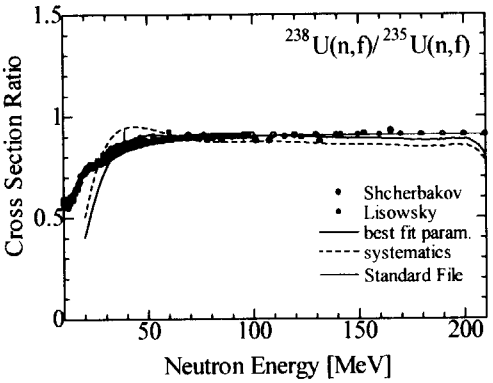

Fig. 1.1.4 Neutron-induced fission cross section ratio of ^{238}U to ^{235}U

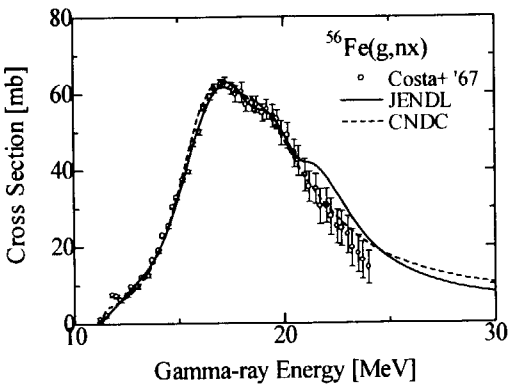

Fig. 1.1.5 Photoneutron production cross section of ^{56}Fe

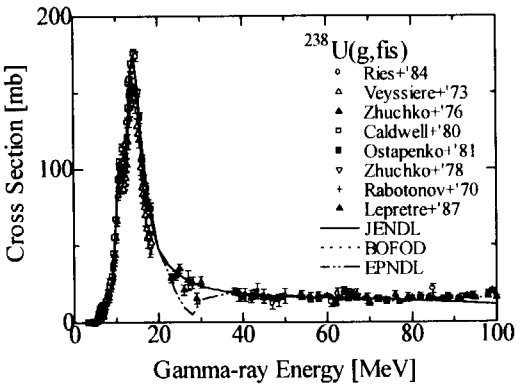

Fig. 1.1.6 Photofission cross section of ^{238}U

1.2 JENDL Dosimetry File 99

K. Kobayashi[*1], T. Iguchi[*2], S. Iwasaki[*3], T. Aoyama[*4], S. Shimakawa, Y. Ikeda, N. Odano, K. Sakurai, K. Shibata, T. Nakagawa and M. Nakazawa[*5]
(*E-mail:* shibata@ndc.tokai.jaeri.go.jp)

The Dosimetry Integral Test Working Group of the Japanese Nuclear Data Committee compiled and released the first version of the JENDL Dosimetry File[1] (JENDL/D-91) in 1991, and performed integral tests of the cross section data. The dosimetry cross sections were mainly taken from JENDL-3[2] and the covariances from IRDF-85[3].

The Working Group has re-evaluated the dosimetry cross sections and their covariances for the JENDL Dosimetry File 99 (JENDL/D-99) in order to update the data and to remove the inconsistency between the cross sections and the covariances in JENDL/D-91. JENDL/D-99 contains the data for 67 reactions and 47 nuclides in the energy region from 10^{-5} eV to 20 MeV. The group-wise and point-wise cross sections were made in the ENDF-6 format[4]. The data for 33 reactions were revised, and the others were taken from JENDL/D-91. Most of the evaluations were performed by using the least-squares fitting code GMA[5], and cross sections and covariances were generated simultaneously. Figure 1.2.1 shows the cross section for the $^{64}Zn(n,p)^{64}Cu$ reaction. In some cases, nuclear model calculation was performed on the Covariance Evaluation System[6], and uncertainties in model calculations were estimated from uncertainties in model parameters by using the law of error propagation.

In order to check the reliability of the file, several integral tests have been carried out by using measured resonance integrals and average cross sections measured in various neutron fields. We compared the evaluated data with the average cross sections measured in fast/thermal reactors, d-T and d-Li neutron spectra, and ^{252}Cf spontaneous fission spectra. Table 1.2.1 gives a comparison of the evaluated data with the average cross sections measured in the Li(d,n) neutron field.

References

1) Nakazawa, M., Kobayashi, K., Iwasaki, S., Iguchi, T., Sakurai, K., Ikeda, Y. and Nakagawa T.: "JENDL Dosimetry File", JAERI 1325 (1992).

[*1] Kyoto University
[*2] Nagoya University
[*3] Tohoku University
[*4] Japan Nuclear Cycle Development Institute
[*5] University of Tokyo

2) Shibata, K., Nakagawa, T., Asami, T., Fukahori, T., Narita, T., Chiba, S., Mizumoto, M., Hasegawa, A., Kikuchi, Y., Nakajima, Y. and Igarasi, S.: "Japanese Evaluated Nuclear Data Library, Version-3 - JENDL-3 –", JAERI 1319 (1990).

3) Cullen, D.E., Kocherov, N. and McLaughlin, P.M.: "The International Reactor Dosimetry File (IRDF-92)", IAEA-NDS-41/R, Rev.0 (1982); IRDF-85 is a modified version with additional cross section data.

4) The Cross Section Evaluation Working Group: "Data Formats and Procedures for the Evaluated Nuclear Data File ENDF-6", BNL-NCS-44945 (ENDF-102) (1995) edited by V. McLane et al., National Nuclear Data Center, Brookhaven National Laboratory.

5) Poenitz, W.P.: "Data Interpretation, Objective Evaluation Procedures and Mathematical Techniques for the Evaluation of Energy-Dependent Ratio, Shape and Cross Section Data", Proc. Conf. Nuclear Data Evaluation Methods and Procedures, BNL-NCS-51363, p.249 (1981).

6) Kawano, T. and Shibata, K.: "Covariance Evaluation System", JAERI-Data/Code 97-037 (1997) [in Japanese].

Table 1.2.1 Comparison of the evaluated data with the average cross sections measured in the Li(d,n) neutron field

Reaction	Exp. (mb)	Error (%)	JENDL/D-99 (mb) (%Error)	JENDL/D-91 (mb)
Na- 23(n,2n)Na-22	6.960E+00	9.90	6.807E+00(2.46)	6.236E+00
Mg- 24(n,p)Na-24	6.980E+01	9.70	6.964E+01(2.34)	7.042E+01
Al- 27(n,α)Na-24	4.300E+01	8.60	4.294E+01(2.23)	4.281E+01
Ti- 0(n,X)Sc-46	9.210E+00	9.10	1.062E+01(4.82)	1.081E+01
Ti- 0(n,X)Sc-48	1.480E+01	8.80	1.470E+01(6.46)	1.535E+01
Mn- 55(n,2n)Mn-54	1.600E+02	8.50	1.971E+02(5.43)	1.898E+02
Fe- 54(n,p)Mn-54	2.950E+02	8.60	2.580E+02(2.20)	2.604E+02
Co- 59(n,2n)Co-58	1.620E+02	8.60	1.809E+02(2.28)	1.821E+02
Ni- 58(n,2n)Ni-57	6.770E+00	9.80	6.712E+00(2.30)	6.623E+00
Ni- 58(n,p)Co-58	3.190E+02	8.40	3.043E+02(2.11)	2.885E+02
Ni- 60(n,p)Co-60	5.710E+01	8.90	4.992E+01(3.17)	5.367E+01
Cu- 63(n, α)Co-60	1.380E+01	8.70	1.341E+01(2.54)	1.347E+01
Nb- 93(n,2n)Nb-92	1.380E+02	8.50	1.470E+02(2.24)	1.488E+02
Au-197(n,2n)Au-196	6.680E+02	8.50	6.992E+02(2.30)	6.846E+02

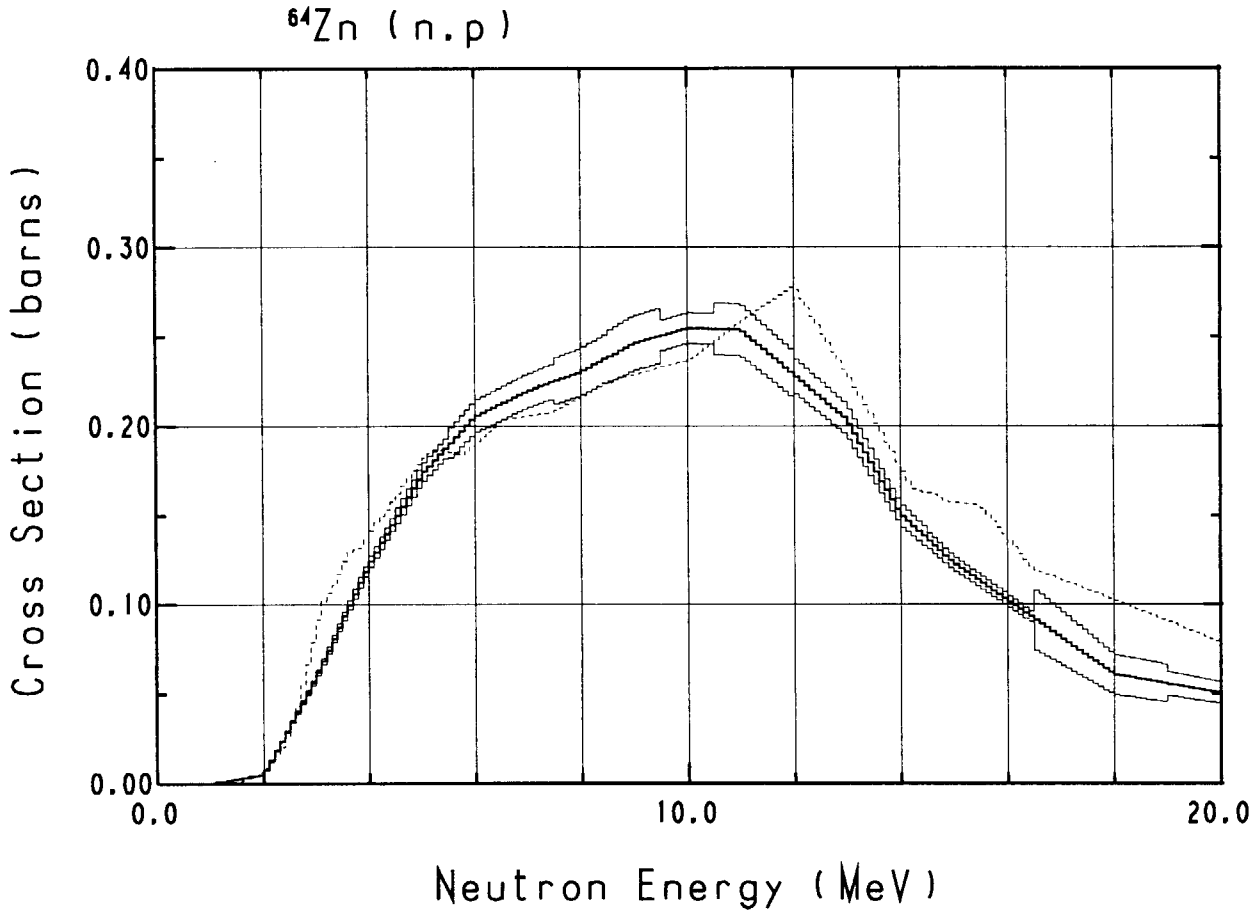

Fig. 1.2.1 $^{64}Zn(n,p)^{64}Cu$ reaction cross section
The solid lines stand for JENDL/D-99, and the dashed line IRDF-90V2.

1.3 Estimation of Covariances for Neutron Nuclear Data in JENDL-3.2

K. Shibata, S.Y. Oh[*1] and T. Kawano[*2]
(*e-mail:* shibata@ndc.tokai.jaer.go.jp)

We continued to make covariance files for JENDL-3.2[1]. In the present work, covariances were newly estimated for ^{52}Cr and ^{58,60}Ni. The covariances files for elemental Cr and Ni were generated from these isotopic data. The physical quantities for which covariances are deduced are cross sections and the first order Legendre coefficient for elastically scattered neutrons. Furthermore, covariances of fission neutron spectra were obtained for ^{233,235,238}U and ^{239,240}Pu.

As for Cr, the covariances of total and (n,2n) reaction cross sections were obtained on the basis of available experimental data by using the least-squares fitting code GMA[2]. Figure 1.3.1 shows the ^{52}Cr(n,2n) reaction cross sections and their uncertainties. The covariances of the inelastic scattering, radiative capture and other reaction cross sections and of the first order Legendre coefficient for the elastic scattering were estimated from nuclear model calculation on the Covariance Evaluation System[3].

In the case of Ni, the GMA code was applied to estimate the covariances of the total, (n,2n), and (n,p) reactions cross sections. Nuclear model calculation was carried out to obtain the covariances of the inelastic scattering, radiative capture, and other threshold reactions cross sections as well as those of the first order Legendre coefficient for the elastic scattering.

Fission neutron spectra in JENDL-3.2 were evaluated[4] by a modified Madland-Nix model. In this model, three parameters affect the calculated results. The covariances of the spectra were obtained[5] by running the model code on the Covariance Evaluation System[3]. Figure 1.3.2 shows the standard deviation of the fission neutron spectra for ^{235}U.

References

1) Nakagawa, T, Shibata, K., Chiba, S., Fukahori, T., Nakajima, Y., Kikuchi, Y., Kawano, T., Kanda, Y., Ohsawa, T., Matsunobu, H., Kawai, M., Zukeran, A., Watanabe, T., Igarasi, S., Kosako, K., and Asami, T.: "Japanese Evaluated Nuclear Data Library Version 3 Revision-2: JENDL-3.2", J. Nucl. Sci. Technol., 32, 1259 (1995).
2) Poenitz, W.P.: Proc. Conf. Nuclear Data Evaluation Methods and Procedures, BNL-NCS-

[*1] Korea Atomic Energy Research Institute
[*2] Kyushu University

51363, p.249 (1981).

3) Kawano, T. and Shibata, K.: "Covariance Evaluation System", JAERI-Data/Code 97-037 (1997) [in Japanese].

4) Ohsawa, T. and Shibata, T.: Proc. Int. Conf. Nuclear Data for Science and Technology, Gatlinburg 1994, p.639 (1994).

5) Kawano, T., Ohsawa, T., Shibata, K. and Nakashima, H.: "Evaluation of Covariance for Neutron Spectra", JAERI-Research 99-009 (1999) [in Japanese].

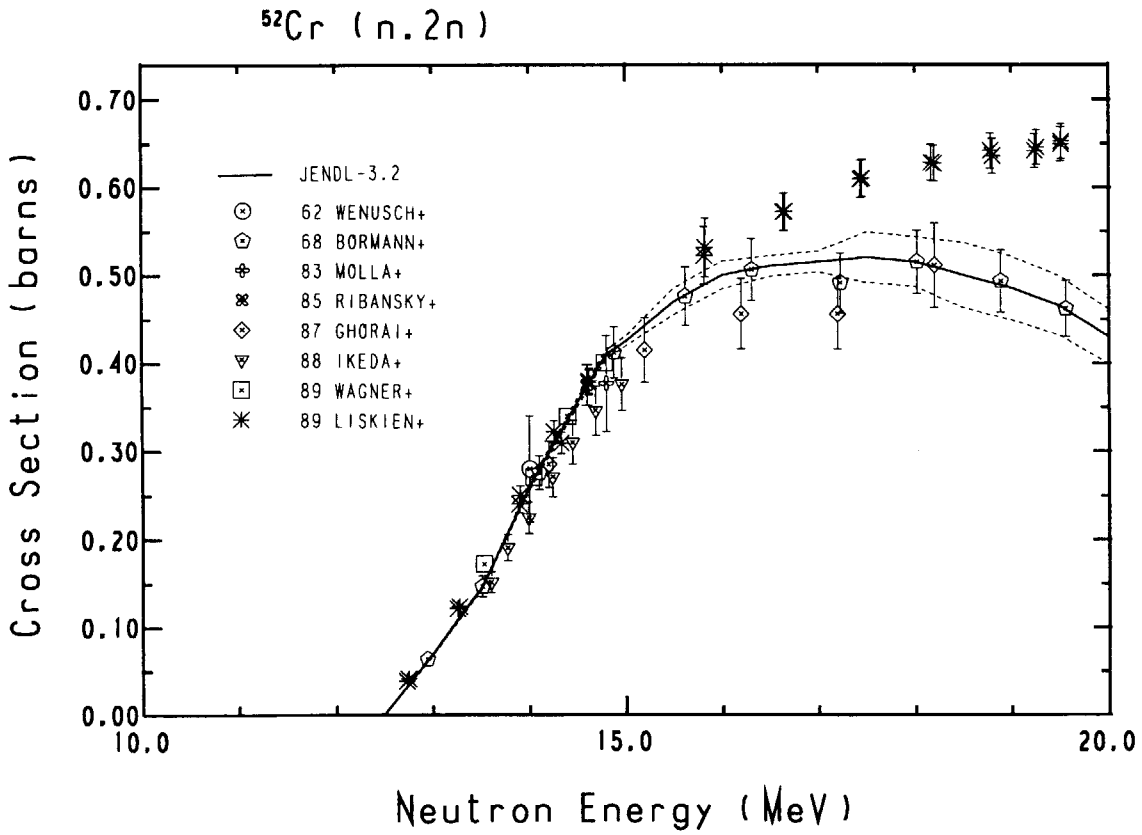

Fig. 1.3.1 Cross section and its standard deviation for the ^{52}Cr(n,2n) reaction

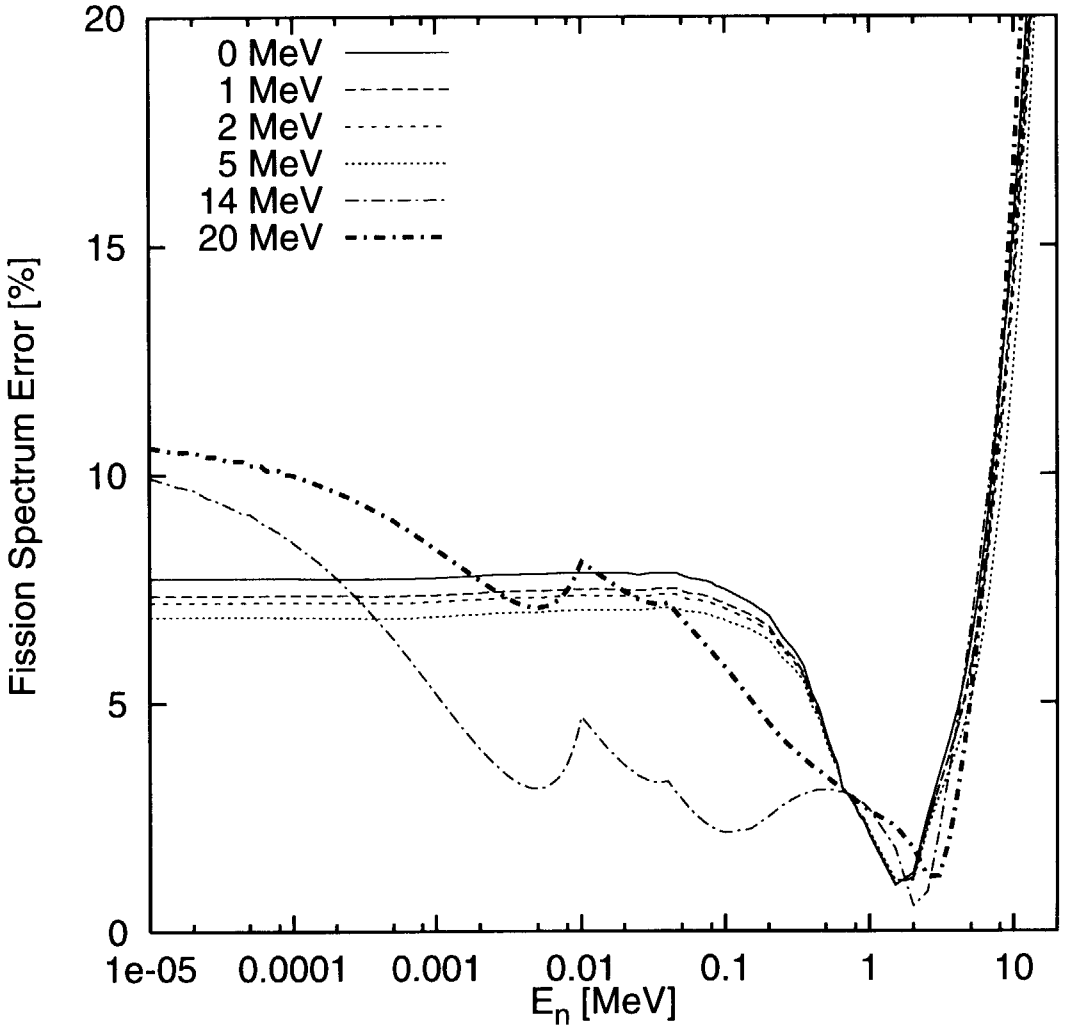

Fig. 1.3.2 Uncertainties in fission neutron spectra of ^{235}U

1.4 Calculation of High Energy Nucleon Induced Fission Cross Sections by QMD + SDM

O. Iwamoto, T. Fukahori and S. Chiba

(*E-mail:* iwamoto@cracker.tokai.jaeri.go.jp)

Nucleon induced fission cross sections were calculated in energy range from several tens MeV to 10 GeV by the Quantum Molecular Dynamics (QMD) plus Statistical Decay Model (SDM). QMD + SDM have been successfuly applied to calculations of proton induced nucleon emission and fragment production cross sections.[1),2)] QMD + SDM has the advantage of having ablity to calculate various cross sections without changing parameters and can be applied to the complex reactions occuring at high energy region. QMD simulates dynamical motions and collisions of nucleons in nucleus at early stage ($\leq$ 100 fm/c in this case) of nuclear reactions. Produced excited fragments emit light particles such as p, n, d, t, ^{3}He and α, which is calculated by SDM. Fission process is also calculated by SDM, in which fission probablity is estimasted by the model of Nakahara.[3)]

Fission cross sections were calculated for p + ^{197}Au, p + ^{209}Bi, p + ^{238}U and n + ^{238}U. Figures 1.4.1, 1.4.2, and 1.4.3 show energy dependences of proton-induced fission cross sections of ^{197}Au, ^{209}Bi and ^{238}U, respectively, and Fig. 1.4.4 shows neutron-induced one of ^{238}U. Figures show that QMD + SDM can preditct the fission cross section of these nuclei within a factor of 2 or better except for the threshold region.

References

1) Niita, K., Chiba, S., Maruyama, T., Maruyama, T., Takada, H., Fukahori, T., Nakahara, Y., Iwamoto, A.: Phys. Rev. **C52**, 2620 (1995).

2) Chiba, S., Iwamoto, O., Fukahori, T., Niita, K., Maruyama, T., Maruyama, T., Iwamoto, A.: Phys. Rev. **C54**, 285 (1996).

3) Nakahara, Y., Tsutsui, T.:JAERI-M 82-198 (1982)

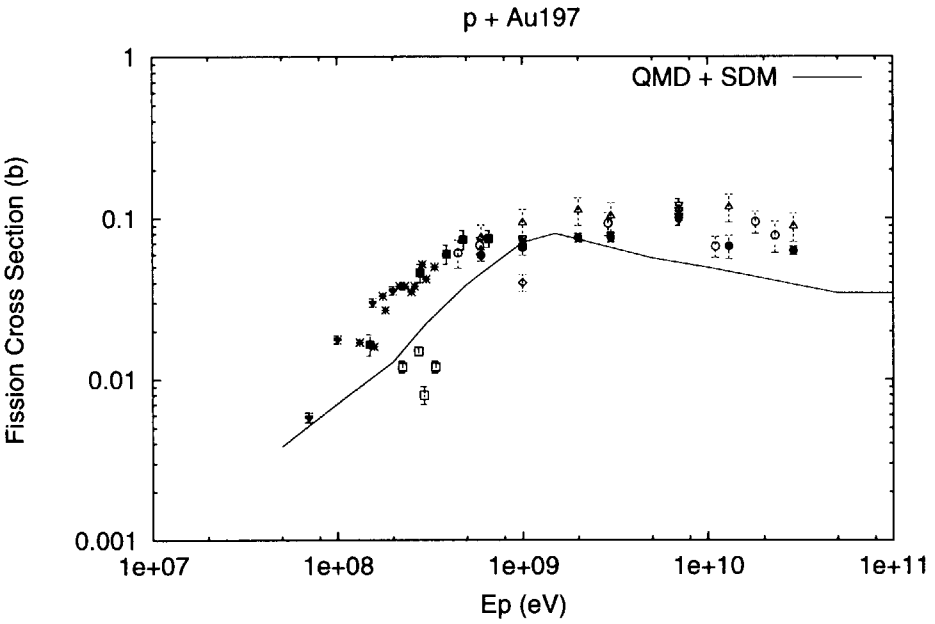

Fig. 1.4.1 Proton-induced fission cross section of ^{197}Au. Solid line shows the calculation of QMD + SDM and experimental data are shown by various symbols.

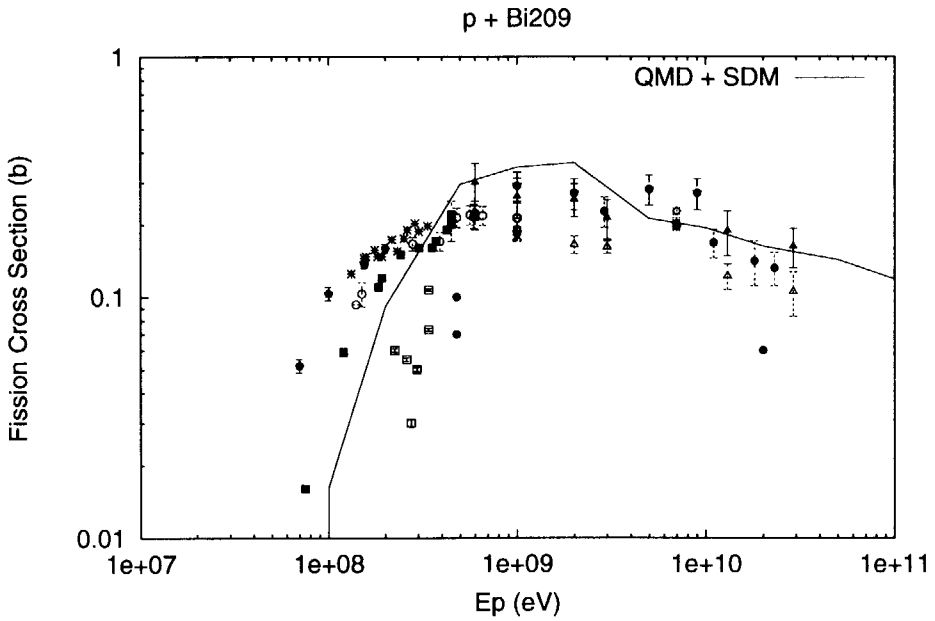

Fig. 1.4.2 Proton-induced fission cross section of ^{209}Bi. Solid line shows the calculation of QMD + SDM and experimental data are shown by various symbols.

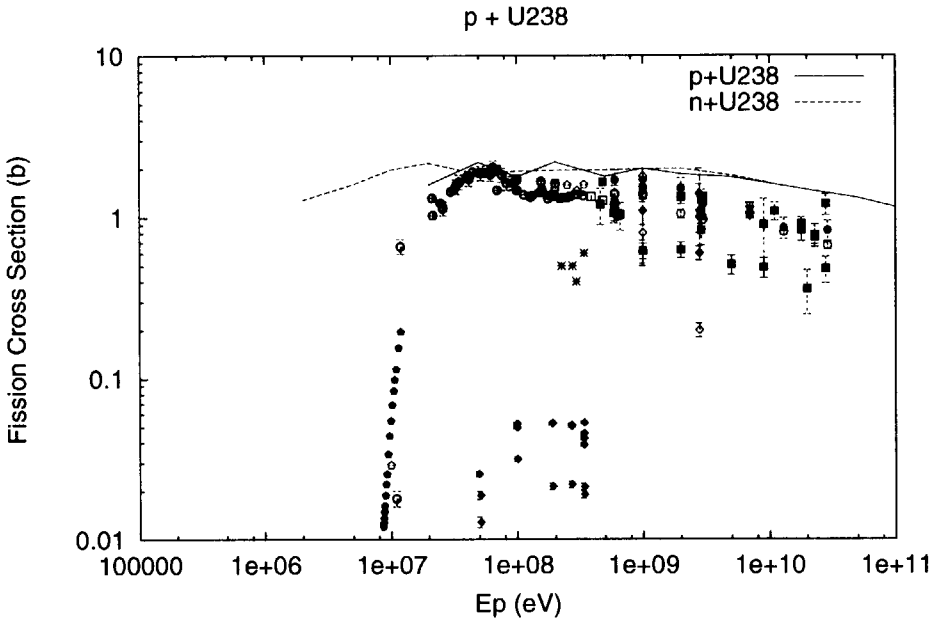

Fig. 1.4.3 Proton-induced fission cross section of ^{238}U. Solid line shows the calculation of QMD + SDM and experimental data are shown by various symbols. Calculation for n + ^{238}U is shown by broken line for comparison.

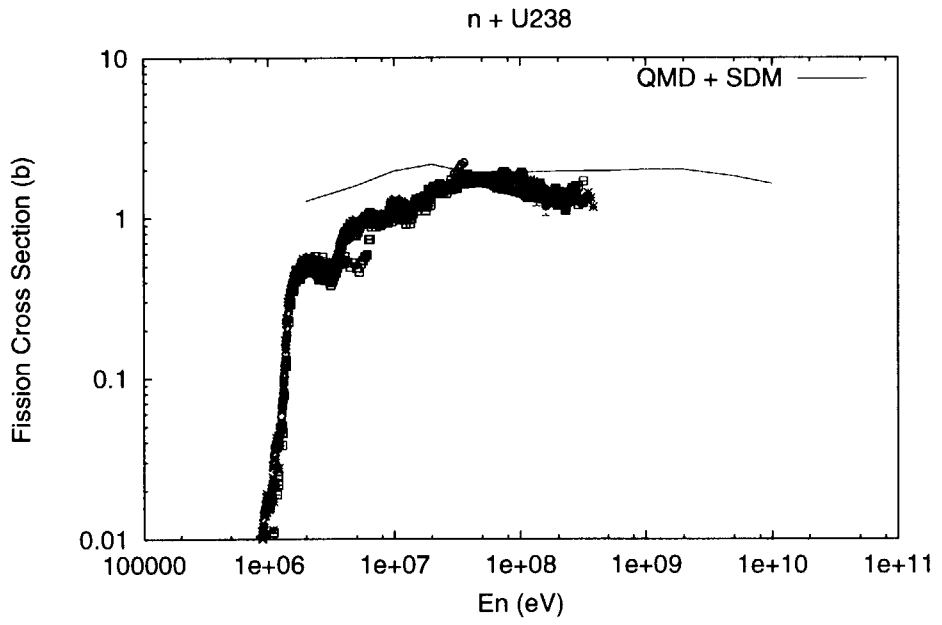

Fig. 1.4.4 Neutron-induced fission cross section of ^{238}U. Solid line shows the calculation of QMD + SDM and experimental data are shown by various symbols.

1.5 Evaluation and Compilation of Nuclear Structure and Decay Data in 1998

J. Katakura and ENSDF Group*
(*E-mail*: katakura@ndc.tokai.jaeri.go.jp)

The international network on nuclear structure and decay data evaluation aims at complete and continuous nuclear structure and decay data evaluation of all mass chains. The evaluated data are compiled as ENSDF (Evaluated Nuclear Struccture Data File) file. The data file is maintained and distributed by National Nuclear Data Center, Brookhaven National Laboratory (BNL), U.S.A. As a member of the network, Japanese group, whose data evaluation center is Nuclear Data Center, Japan Atomic Energy Research Institute, has responsibility for evaluating 12 mass chains with A=118-129.

In the fiscal year of 1998 (from April 1998 to March 1999), the evaluations of A=119 and 125 mass chains were performed and sent to BNL as a new evaluated data. The evaluation includes all experimental data available after last evaluations, 1992 for A=119 and 1993 for A=125. After critical review of the newly evaluated data, the revised data sets will be published in Nuclear Data Sheets.

In case of A=125 mass chain evaluation, the data sets in table 1.5.1 are included in the new evaluation [1].

The new data of other mass chains to which Japanese group has the responsibility are reviewed and being prepared for update of old mass chain evaluation.

References

1) Katakura, J.: Nucl. Data Sheets, *to be published*

*Members are H. Iimura, M. Oshima, S. Ohya, K. Ogawa, J. Katakura, M. Kambe, K. Kitao, T. Tamura, Y. Tendow and K. Miyano

Table 1.5.1 Updated data set of A=125

Nuclide	Data Type
^{125}Ag	Adopted Levels
^{125}Cd	Adopted Levels
^{125}In	Adopted Levels, Gammas ^{125}Cd β^- Decay (0.65 s) ^{125}Cd β^- Decay (0.48 s)
^{125}Sn	Adopted Levels, Gammas ^{125}In β^- Decay (12.2 s) ^{125}In β^- Decay (2.36 s) ^{124}Sn(n,γ) ^{124}Sn(d,p) ^{124}Sn(d,pγ) ^{124}Sn(α,^{3}He)
^{125}Sb	Adopted Levels, Gammas ^{125}Sn β^- Decay (9.52 min) ^{125}Sn β^- Decay (9.64 d) ^{124}Sn(pol p,p) IAR ^{124}Sn(^{3}He,d) ^{126}Te(d,^{3}He) ^{126}Te(t,α)
^{125}Te	Adopted Levels, Gammas ^{125}Sb β^- Decay ^{125}Te IT Decay ^{125}I ϵ Decay ^{124}Sn(α,3nγ) ^{124}Te(n,γ) E=thermal ^{124}Te(d,p) ^{124}Te(t,d) ^{125}Te(d,d′)
^{125}Te	Coulomb Excitation ^{126}Te(d,t) ^{126}Te(^{3}He,α) ^{127}I(μ^-,xnγ)
^{125}I	Adopted Levels, Gammas ^{125}Xe ϵ Decay ^{124}Te(p,p),(p,p′) IAR ^{124}Te(^{3}He,d) ^{124}Te(α,t) (HI,xnγ)
^{125}Xe	Adopted Levels, Gammas ^{125}Xe IT Decay ^{125}Cs ϵ Decay (HI,xnγ)
^{125}Cs	Adopted Levels, Gammas ^{125}Ba ϵ Decay (3.5 min) (HI,xnγ)
^{125}Ba	Adopted Levels, Gammas ^{125}La ϵ Decay (HI,xnγ)
^{125}La	Adopted Levels, Gammas ^{125}Ce ϵ Decay ^{112}Sn(^{16}O,2npγ)
^{125}Ce	Adopted Levels, Gammas ^{125}Pr ϵ Decay (HI,xnγ)
^{125}Pr	Adopted Levels

1.6 Evaluation for JENDL FP Decay Data File

J. Katakura and Decay Heat Evaluation Working Group*
(*E-mail*: katakura@ndc.tokai.jaeri.go.jp)

Decay data library of fission products with JENDL format, that is the same as ENDF format, is now being compiled as a JENDL special purpose data file. Decay data file for reactor decay heat calculation has already been available as JNDC library [1]. The summation calculation using the average decay energy data of the JNDC library shows good prediction for decay heat after fission event of various fissioning nuclides. The library, however, has a unique format different from the ENDF one and no spectral data of gamma and beta rays emitted from radioactive nuclide. And it has sometimes occurred that the JNDC library is identified as JENDL library. In order to avoid such confusion JENDL FP decay data library of fission products was planed to compile as a JENDL special purpose data file. At first the decay data of JNDC library such as half-life, average gamma and beta energies, that is, the decay energy per decay, were going to be put into the JENDL decay data file. The experimental data contained in the JNDC file, however, are based on measurement more than 10 years ago. The recent decay data compiled as ENSDF (Evaluated Nuclear Structure Data File) [2] are better than those in the JNDC library. Then the decay data of the nuclides in the ENSDF file are examined if they suffer from the so-called "Pandemonium Effect." When it is found that the data of a nuclide are deficient to derive average decay energy, theoretically calculated decay energy values are adopted. In this case the spectral data adopted from the measured data from the ENSDF file are inconsistent with the average energy calculated by the theoretical model. In order to remove the inconsistency theoretically calculated spectrum is used to compensate the gap between the spectral data and the average energy. The usefulness of the calculated spectrum is shown for the compilation of ENDF/B file. [3, 4] The isomeric states in the ENSDF file are also different from those of the JNDC file. The new data are adopted in the JENDL FP Decay Data File. As a results there are 1229 nuclides are included in the file, although 1227 nuclides are contained in the JNDC file. The number of nuclides contained in the file is listed in Table 1.6.1. The decay data in the file are now reviewed and tested if they are applicable to reactor technology such as decay heat estimation. The example of the decay heat calculation using the decay data

*Members are K. Ikeda, Y. Okawachi, I. Otake, K. Oyamatsu, K. Kaise, J. Katakura, T. Katoh, A. Zukeran, T. Tachibana, Y. Tahara, R. Nakasima, T. Murata, M. Yamada and T. Yoshida

Table 1.6.1 Number of Nuclides

Number of nuclides	1229
Stable nuclide	142
γ ray spectrum	1052
calculated	544
β ray spectrum	896
calculated	443
α ray spectrum	5

in the present JENDL FP Decay Data File is shown in Fig. 1.6.1.

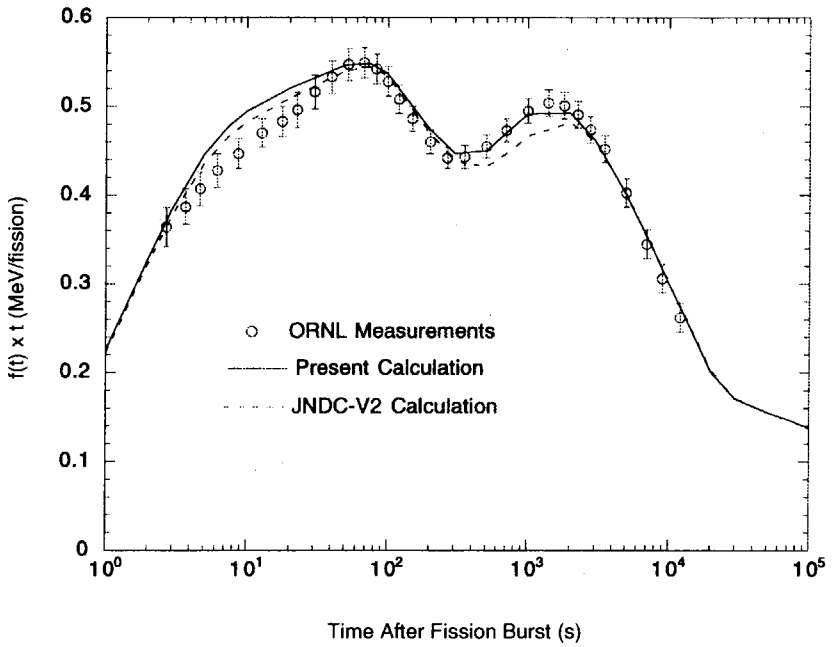

Fig.1.6.1 ^{239}Pu Thermal Neutron Fission
(Gamma Ray Component)

As seen in Fig. 1.6.1 the present calculation shows good agreement with the measured data at nearly 1000 s where the JNDC calculation shows underestimation. The new library is expected to be a consistent and complete decay data library of fission products when it is released. We are working to release the library until the end of 1999 fiscal year.

References

1) Tasaka, K., et al.: "JNDC Nuclear Data Library of Fission Products -Second Version-", JAERI 1320 (1990)

2) Evaluated Nuclear Structure Data File, maintained by National Nuclear Data Center, Brookhaven National Laboratory, U.S.A.

3) Katakura, J. and England, T. R.: "Augmentation of ENDF/B Fission Product Gamma-Ray Spectra by Calculated Spectra," LA-12125-MS, ENDF-352 (1991)

4) Katakura, J. and England, T. R.: "Introduction of Model Calculated Beta-Ray Spectrum to ENDF/B-VI Fission Products Decay Data File," Proc. Int. Conf. on the Physics of Nuclear Science and Technology, Brookhaven National Laboratory, U.S.A., pp. 438 (1998)

1.7 Wavelengths and Energy Level Classifications for the Spectra of Argon (Ar I through Ar XVIII)

J. Sugar*, A. Musgrove* and T. Shirai
(*E-mail*: shirai@ndc.tokai.jaeri.go.jp)

We have undertaken publication of a series of compilations of spectra of highly ionized atoms of particular interest to the fusion energy community. This work is part of a new series of compilations of atomic data intended to update and supplement those of Moore[1]. Our latest compilation, which is now in press, includes in a single monograph of Shirai *et al.*[2] classified wavelengths for Ti III- XXII, V IV - XXIII, Cr V - XXIV, Mn VI - XXV, Fe VII - XXVI, Co VIII - XXVII, Ni IX - XXVII, Cu X - XXIX, Kr V - XXXVI, and Mo VI - XLII.

We have compiled wavelengths, energy levels, line classifications, intensities, oscillator strengths, and transition probabilities for neutral and all stages of ionization of argon which is specifically injected into the divertor plasmas for plasma radiative cooling. These data result from critical evaluation of all the literature for argon through March 1998. In addition to our own surveys of the literature we consulted the comprehensive surveys by Kelly[3] for wavelengths Kaufman and Sugar[4] for forbidden lines arising within ground configurations of the type ns^2np^k (n=2 and 3, k=1 to 5), and an extensive review article by Fawcett.[5]

For each spectrum we give a review of the literature from which the data are taken, and include the isoelectronic sequence, ground state, ionization energy, and a list of references. This is followed by tables containing classified lines with designations of the upper and lower energy levels, intensities, oscillatior strengths, and transition probabilities, followed by tables containing energy levels with their designations, percentage compositions and g-values when available. Two finding lists are included, one for Ar I through Ar III and the other for Ar IV through Ar XVIII.

We give wavelengths in air above 2000 Å and in vacuum below. For conversion of ionization energies from cm^{-1} to eV we use $8065.5410 \pm 0.0024 cm^{-1}/eV$ given by Cohen and Taylor.[6] For the He- and H-sequences, only theoretical results are given since they are considered to be more accurate than the experimental values.

We caution that the intensity estimates quoted here are usually visual estimates of relative plate blackening. There is generally no correlation between intensity estimates by different authors, or by the same authors for widely different wavelength ranges.

---

* National Institute of Standards and Technology

We tabulate calculated values of oscillator strengths (gf) and transition probabilities(A). In cases where no observed wavelengths are given but for which calculated f-values are published, the quoted wavelengths are calculated from the known energy levels and the wavelengths are then used to calculate A-values from the f-values.

References

1) Moore C.E.: Natl. Stand. Ref. Data Ser., Natl. Bur. Stand. (U.S.), **35,** Vol. I, II, III (1971).

2) Shirai T., et al.: J. Phys. Chem. Ref. Data, monograph 8 (1999) in press.

3) Kelly R.L.: J. Phys. Chem. Ref. Data **16**, Suppl. 1 (1987).

4) Kaufman V. and Sugar J.: J. Phys. Chem. Ref. Data **15**, 321 (1986).

5) Fawcett B.C.: J. Opt. Soc. Am. B **1**, 195 (1984).

6) Cohen E.R. and Taylor B.N.: Rev. Mod. Phys. **59**, 1121 (1987).

1.8 State-Selected Cross Sections for Ion Production in the $H^+ + H_2$ Collisions

A.Ichihara, O.Iwamoto and K.Yokoyama
(*E-mail:* ichihara@cracker.tokai.jaeri.go.jp)

Cross sections for ion production occurring in the $H^+ + H_2$ collisions are fundamental to the development of a gas divertor in which the H_2 molecule is used as shock absorber. In the region near divertor, H_2 may be in the vibrationally and rotationally excited states before H^+ approaches to H_2 through collisions with other ions, atoms or molecules. Therefore, data for excited H_2 molecules are important as well as data for H_2 in the ground state. Recently, we have calculated cross sections for the reaction of H^+ with excited D_2 molecule by selecting vibrational and rotational quantum numbers v=0 to 3 and j=1, 5 and 10, and found that the electron transfer is strongly enhanced with the increase of v.[1)]

In the present work, we evaluated cross sections for the $H^+ + H_2(v, j=0)$ collisions and studied how the vibrational excited state of H_2 affects the competition between electron transfer and dissociation reactions. We selected v in the range of $0 \leqq v \leqq 15$, where the vibrational energy level in the v=15 state is only 0.04 eV below the dissociation limit in the H_2 potential curve employed. The cross sections have been calculated in the center-of-mass collision energy range of $1.0 \leqq E_{cm} \leqq 20.0$ eV by using the trajectory-surface-hopping (TSH) method[2)] with the diatomics-in-molecules (DIM) potential energy surfaces.[3)] The probability of surface hopping (nonadiabatic electronic transition) was estimated within the Landau-Zener approximation.[4)] To obtain converged cross section, more than 10000 trajectories were run for each (v, E_{cm}) combination.

Figure 1.8.1 shows cross sections for electron transfer $H^+ + H_2(v=0 \text{ to} 15, j=0) \rightarrow H_2^+ + H$. It can be seen from Fig.1.8.1 that the cross section increases as v increases up to 5, and then becomes almost constant as a function of v in the range $5 \leqq v \leqq 7$. For v above 8, the cross section decreases with the increase of v.

The enhancement of cross sections for $v \leqq 5$ can be explained from features of the DIM potential energy surfaces for the $H^+ + H_2$ and $H + H_2^+$ electronic states. Three protons in the $H^+ + H_2$ system can take the spatial configuration where the avoided crossing of two potential energy surfaces appears when H_2 is in the $v \geqq 5$ state. Then electron transfer takes place in the region near the avoided crossing point. If H_2 is in the vibrational excited state before H^+ and

H_2 approaches, further excitation into the $v \geqq 5$ state can be brought about more effectively. Therefore, electron transfer is strongly enhanced with the increase of v for $v \leqq 5$.

In contrast with the strong v dependence for $v \leqq 5$, the electron transfer cross section is insensitive to v any longer for $5 \leqq v \leqq 7$. For $v \geqq 8$, the cross section decreases with the increase of v, which is attributed to the increase of dissociation.

It should be noted that H_2^+ is produced in the $H^+ + H_2$ collisions not only from simple electron transfer but also from electron transfer accompanied with proton exchange. However, we confirmed in our TSH calculation that contribution from latter reaction is much smaller than that from former reaction for all v at energies $E_{cm} \geqq 2.0$ eV. Moreover, the H_2^+ production cross section with proton exchange decreases rapidly as E_{cm} increases. As a result, the cross section for electron transfer given in Fig.1.8.1 is a good approximation to the H_2^+ production cross section for $v \geqq 1$ and $E_{cm} \geqq 2.0$eV.

Fig.1.8.2 shows cross sections for dissociation $H^+ + H_2(v=0 \text{ to} 15, j=0) \rightarrow H^+ + H + H$. As can be seen from Fig.1.8.2, the dissociation cross section increases with the increase of v. If H_2 is in higher vibrational state, the H-H bond can be cut off more easily by the collision with H^+. It can be seen from Figs.1.8.1 and 1.8.2 that dissociation is enhanced remarkably with the increase of v at the same time electron transfer reaction is reduced for $v \geqq 8$. The dissociation is more probable than electron transfer for $v \geqq 13$.

From these results we concluded that the H_2^+ production by electron transfer is a dominant reaction in the $H^+ + H_2$ collisions in the range of $v \leqq 12$ and $E_{cm} \leqq 20$ eV. The dissociation increases with the increase of v and it becomes dominant for $v \geqq 13$. The (v, E_{cm}) dependence of cross sections for electron transfer and dissociation reactions is thought to be applicable to other collision systems with isotopic variants.

References

1)Ichihara, A. et al.: JAERI-Research 98-056(1998).

2)Ichihara, A. et al.: J.Chem.Phys.105,1857(1996).

3)Ellison, F.O.: J.Am.Chem.Soc.85, 3540 (1963).

4)Bauschlicher, C.W., et al.: J.Chem.Phys.59, 1286 (1973).

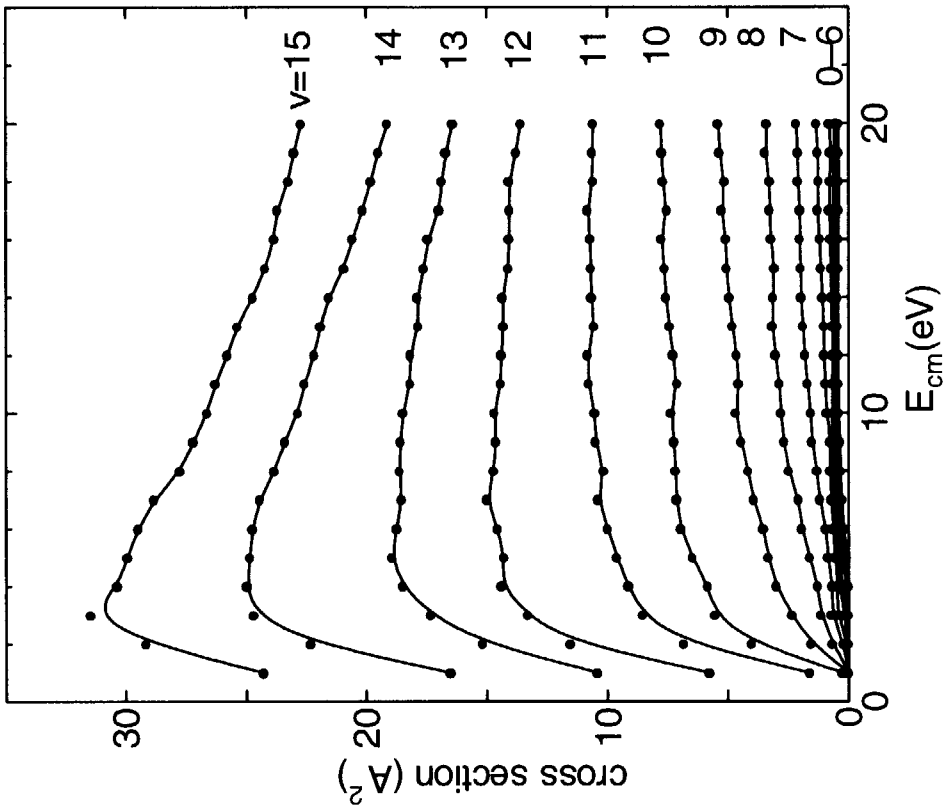

Fig.1.8.2 Cross sections for dissociation in the $H^+ + H_2(v=0\text{-}15,j=0)$ collisions

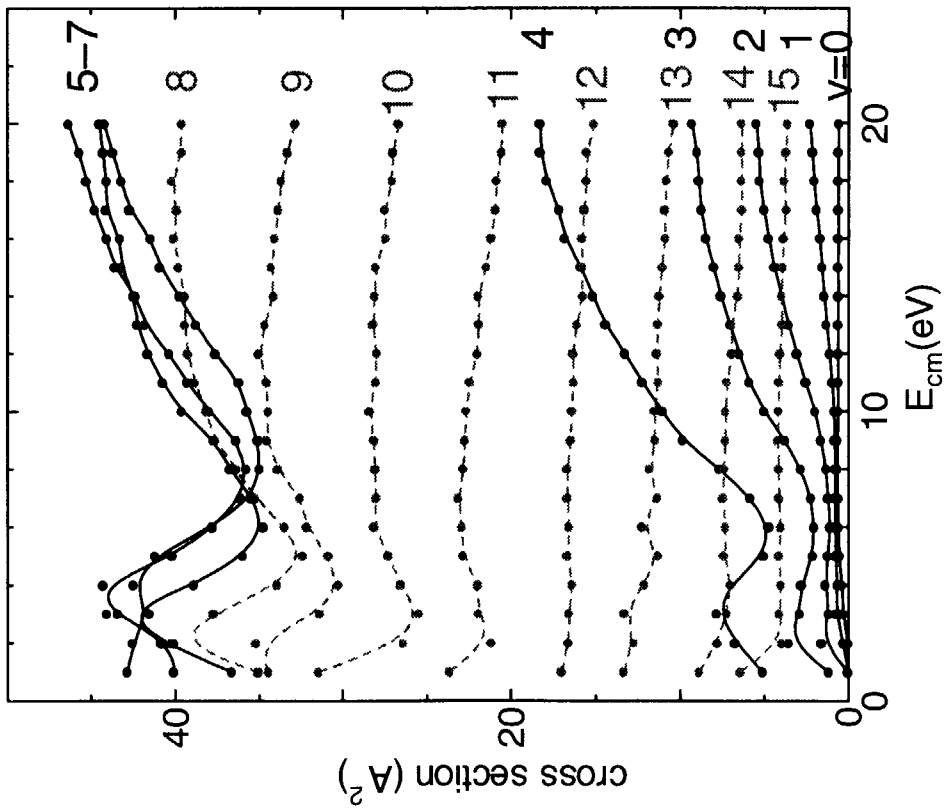

Fig.1.8.1 Cross sections for charge transfer in the $H^+ + H_2(v=0\text{-}15,j=0)$ collisions

2. Theoretical Method and Code Development

A new method based on the statistical geometry model has been developed to treat a great number of randomly distributed spherical fuels with the MVP continuous energy Monte Carlo code. A spatial distribution function used for sampling a location of a spherical fuel along a neutron flight path is calculated with the MCRDF Monte Carlo hard sphere packing simulation code or theoretically obtained. The heterogeneity effect in HTTR has been evaluated by using this model.

The physics model of MVP has been modified to analyze transport phenomena of neutrons in high and intermediate energy regions by using the evaluated nuclear data in the ENDF-B6 format. A benchmark test for the modified code and the nuclear data library LA-150 evaluated up to 150 MeV has been carried out by analyzing the JAERI/TIARA shielding experiments on iron.

For Monte Carlo perturbation calculations in eigenvalue problems, a set of equations has been derived on the basis of the differential sampling method to take into account the perturbation effect due to the change of fission source. The derived equations have been verified by simple geometry calculations.

Discontinuity factors in adjoint calculations and intra-nodal flux distribution effects in multi-dimensional problems have been studied for accurate perturbation calculations by nodal diffusion method. The consistent theory by Kobayashi has been adopted for the former problem, and a new flux reconstruction method has been developed for the latter one. The results of this study have been incorporated in the nodal diffusion code MOSRA-Light .

A convenient method has been developed to calculate spatially dependent resonance self-shielded cross sections in arbitrary heterogeneous geometry by generalization of the classical equivalent theory. The validity has been demonstrated by comparison with Stoker/Weiss's method for the benchmark problem of BWR fuel assembly with adjacent annularly divided poisoned fuel pins.

Through the course of development work of a highly accurate kinetics code applicable to various types of reactors, a prototype coupled code REFLA/TRAC/MLK3D has been developed for transient analyses of PWR-type reactors. The developed code has been verified by a benchmark calculation for a PWR core transient benchmark problem by NEACRP, in which the core transient is initiated by ejection of a central control rod at hot zero power.

2.1 Development of Statistical Geometry Model of Coated Fuel Particles for Continuous Energy Monte Carlo Code MVP

T. Mori, Y. Nagaya, H. Ando and M. Sasaki*
(*E-mail*: mori@mike.tokai.jaeri.go.jp)

A new method based on the statistical geometry model (STGM)[1)2)] has been developed to treat a great number of randomly distributed spherical fuels (coated fuel particles, CFPs) with the MVP continuous energy Monte Carlo code. In a random walk process by the STGM, location of a spherical fuel is sampled probabilistically along a neutron flight path from the spatial distribution of spherical fuels which is called the nearest neighbor distribution, NND. By using the STGM, the heterogeneity effect of CFPs can be taken into account without any loss of the advantage of the continuous energy method.

The STGM has been implemented in MVP as an extension of lattice capability. The spatial region represented by the STGM (STGM region) is assumed to consist of 2 unit cells; one is a spherical fuel cell and the other is a matrix cell. When a neutron enters a spherical fuel, the spatial coordinates of the neutron are transformed into those in the spherical fuel cell and the neutron is tracked in the cell. Neutrons outside the cell are tracked in the matrix cell. The STGM of MVP allows the arrangement of a spherical fuel cell interfering with the boundary surface of the STGM region and treats the subspace in the cell and outside the STGM region as the outside of the cell.

The accurate NND is calculated with the Monte Carlo hard sphere packing simulation code MCRDF[3)]. In addition to the NND by MCRDF, the MVP code can use the theoretical NND based on the assumption of statistical uniformity[1)] :

$$\frac{dNND(r)}{dr} = \frac{3}{2}\cdot\frac{f_p}{1-f_p}\cdot\exp\left(-\frac{3}{2}\cdot\frac{f_p}{1-f_p}\cdot r\right) ,$$

where f_p and r are the packing fraction and the distance from the reference position in unit of spherical fuel diameter, respectively.

In order to evaluate the heterogeneity effect of CFPs in the fuel compacts, fuel rod cells of HTTR, which are infinite hexagonal cells consisting of a fuel compact, a graphite sleeve of

---

* Japan Research Institute, ltd., Tokyo.

fuel rod, helium coolant and graphite moderator, were analyzed with and without the present STGM. The JENDL-3.2 cross section library was used in the analysis. The total number of neutron histories for each calculation was about 1,000,000. The results are shown in Table 2.1.1, which are summarized as follows.

(1) The heterogeneity effects evaluated with the NND by the MCRDF code and the theoretical one show good agreement with each other, though the latter NND is quite different from the former at a small distance in case of low packing fraction[1].

(2) The heterogeneity effect strongly depends on fuel rod pitch and U-235 enrichment. This fact means that whole core calculations are necessary to evaluate accurately the heterogeneity effect in such a complicated core as HTTR.

The whole core of HTTR with 30 fuel assemblies loaded were analyzed on the basis of the geometry model used in the preliminary analysis[4]. All control rods except for the outermost R3 rods are inserted to 1740 mm level from the core bottom. In the present calculation, the packing fraction of CFPs is assumed to be 30% and atomic number densities in the CFPs are adjusted to keep total amounts in the fuel compact, though actual packing fractions slightly deviate from 30%. The calculations were performed with the JENDL-3.2 library. The results are summarized in Table 2.1.2. No significant discrepancy is observed between the results with 2 kinds of NNDs. The heterogeneity effect is evaluated to be about 1.1 $\%\Delta k / kk'$ from the present calculations, while the cell calculations with the conventional SRAC95 code has predicted that the effect is 1.2 $\%\Delta k / kk'$ for an effective fuel rod cell[4].

The present study has shown that the STGM of the MVP code can predict the heterogeneity effect of CFPs and that the theoretical NND is available in analyses of heterogeneity with comparable accuracy to those by the high cost MCRDF calculation.

References

1) Murata I., Mori T. and Nakagawa M.: Nucl. Sci. Eng., 123, 96 (1996).

2) Murata I., et al.: J. Nucl. Sci. Technol., 34, 734 (1997).

3) Murata I., Mori T., Nakagawa M., et al.: JAERI-Data/Code 96-016 (1996).

4) Nojiri T., et al.: JAERI-Tech 98-032 (1998).

Table 2.1.1 Heterogeneity effect of coated fuel particles in HTTR fuel rod cell*

Fuel rod Pitch	U-235 enrichment	k-infinity (heterogeneity effect ($\%\Delta k/kk'$))		
		Smeared density in fuel compact	STGM with NND by MCRDF	STGM with theoretical NND
5.16 cm**	3 w/o	1.21928±0.043%	1.25142±0.045% (2.106±0.050)	1.25318±0.045% (2.219±0.050)
	10 w/o	1.36986±0.042%	1.40173±0.043% (1.660±0.043)	1.40181±0.042% (1.664±0.043)
6.27 cm***	3 w/o	1.37032±0.035%	1.39238±0.041% (1.156±0.039)	1.39293±0.035% (1.185±0.036)

* fuel compact: outer diameter=2.6 cm, inner diameter=1.0 cm, packing fraction=30%,
** nominal fuel rod pitch, *** fuel rod pitch averaged over fuel assembly

Table 2.1.2 Heterogeneity effect of coated fuel particles in HTTR fully loaded core with 30 fuel assemblies*

	Smeared density in fuel compact	STGM with NND by MCRDF	STGM with theoretical NND
k-effective	0.98975±0.09%	1.00092±0.12%	0.99923±0.14%
Heterogeneity effect ($\%\Delta k/kk'$)	------	1.13±0.14	1.12±0.17
Total histories	10,000×93	10,000×47	10,000×47
Skipped batches	5	5	5
CPU time (h)**	10.0	11.6	11.6

* Geometry model is taken from Ref. 4).
** on Fujitsu VPP-500

2.2 Benchmark Calculation of TIARA Shielding Experiment on Iron with MVP for Intermediate Energy Neutrons

T. Mori

(*E-mail*: mori@mike.tokai.jaeri.go.jp)

The physics model of a continuous energy Monte Carlo code MVP has been modified to analyze transport phenomena of neutrons in high and intermediate energy regions by using the evaluated nuclear data in the ENDF-6 format. A benchmark test for the modified MVP code and the nuclear data library LA-150 evaluated up to 150 MeV[1] has been carried out by analyzing the JAERI/TIARA shielding experiments on iron[2].

The arrangement of TIARA shielding experiments is shown in Fig.2.2.1. Transmission of quasi-monoenergetic neutrons generated by 43 MeV and 68 MeV protons on lithium was measured on the beam axis and with offset distance of 20 cm and 40 cm behind the test shield. In the present work, neutron energy spectra behind the iron test shield by 68 MeV protons have been calculated with the modified MVP code using the track length estimator. The continuous energy cross section library for MVP was prepared by changing the format of the MCNP library, which was produced from the LA-150 library with the NJOY code. The angle-energy distribution of quasi-monoenergetic neutrons was taken from Ref. 2.

Table 2.2.1 shows the summary of calculations. The total number of neutron histories in each case was 4,000,000. No special variance reduction technique was used except for the case of 100 cm thick iron shield, in which the Russian-roulette kill and splitting based on the importance was employed to enhance deep penetration of neutrons. The calculation results are compared with the measured ones in Figs. 2.2.2 and 2.2.3. General agreements are obtained between the calculation and the measurement, though the calculation gives slightly larger fluxes in several ten MeV region in case of 100 cm thick iron shield. The present benchmark test has confirmed the validity of the modified physics model in the MVP code.

References

1) Young P.G. and Chadwick M.B.: "Neutron- and Proton-Induced Nuclear Data Libraries to 150 MeV for Accelerator-Driven Applications", Proc. Int. Conf. on Nucl. Data for Sci. and Technol., 19-24 May, 1997, Trieste, Italy, pp.1440-1442 (1998).

2) Nakane Y., et al.: "Neutron Transmission Benchmark Problems for Iron and Concrete Shields in Low, Intermediate and High Energy Proton Accelerator Facilities", JAERI-Data/Code 96-029 (1996).

Table 2.1.1 Summary of benchmark calculations

Thickness of test shield(cm)	Measured position	Total histories	Variance reduction	CPU time (s)*
20	On beam axis	4,000,000	None	158
	off axis	4,000,000	None	192
40	On beam axis	4,000,000	None	195
	off axis	4,000,000	None	224
100	On beam axis	4,000,000	Importance	307

* on Fujitsu VPP-500

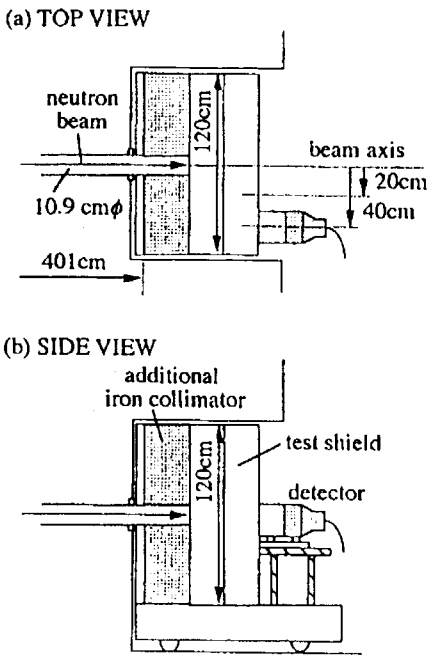

Fig.2.2.1 Top view and side view of the experimental arrangement for the iron test concrete shield with additional iron collimator

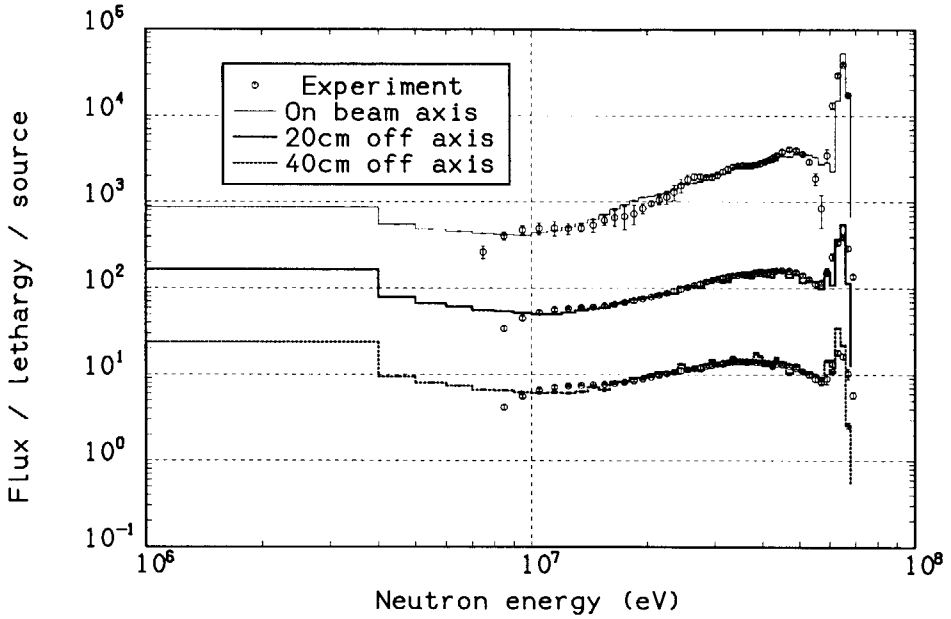

Fig.2.2.2 Comparison of neutron spectra between experiment and MVP calculation for 68 MeV p-Li neutrons on 20 cm thick iron shield

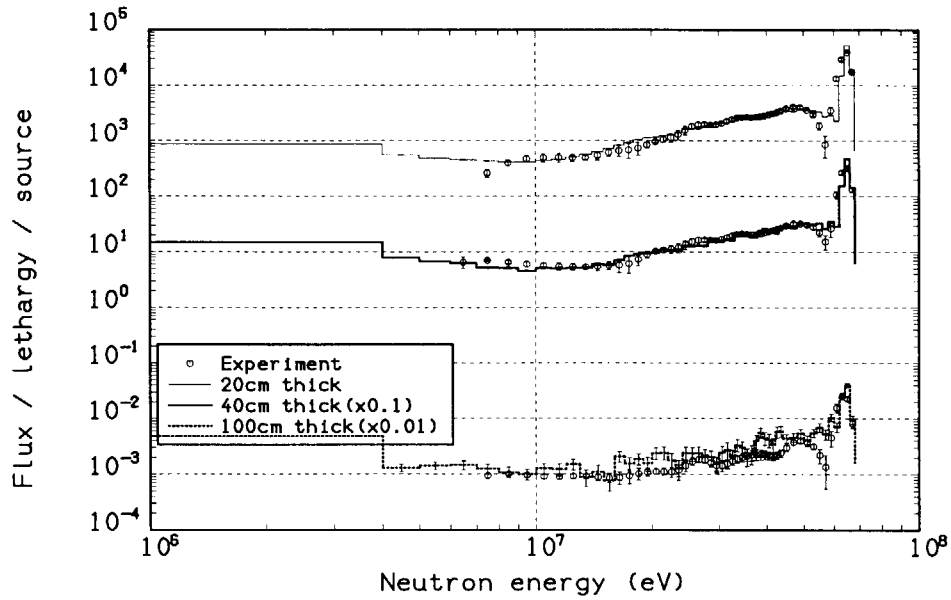

Fig.2.2.3 Comparison of neutron spectra on the beam line between experiment and MVP calculation for 68 MeV p-Li neutrons
(20, 40, 100cm thick iron shields)

2.3 Estimation of Perturbation due to Fission-Source Change for Simple Geometry by Monte Carlo Methods

Y. Nagaya and T. Mori
(*E-mail* : nagaya@mike.tokai.jaeri.go.jp)

It is very difficult to estimate small perturbations for neutronic parameters by multiple Monte Carlo calculations. Thus some special techniques such as the correlated sampling method or the differential operator sampling method have been employed for perturbation calculations. Particularly, it is quite difficult to estimate a change in an effective multiplication factor in eigenvalue problems because the fission source distribution is changed by some introduced perturbation and it is, therefore, required to estimate the perturbation due to the fission-source change. Nakagawa et. al. proposed a method to estimate the perturbation due to the fission-source change in the correlated sampling method and demonstrated that estimation of changes in effective multiplication factors was improved[1]. In the present work, we have derived a set of equations to estimate the perturbation due to the fission-source change by the differential operator sampling method and have verified it by a simple geometry.

A change in an effective multiplication factor is expressed by an equation expanded by the Taylor series;

$$\Delta k = \frac{\partial k}{\partial a}\Delta a + \frac{1}{2}\frac{\partial^2 k}{\partial a^2}(\Delta a)^2 + \cdots + \frac{1}{n!}\frac{\partial^n k}{\partial a^n}(\Delta a)^n + \cdots \tag{1}$$

where k is an effective multiplication factor, Δk its change and a a perturbation parameter. In the differential operator sampling method, each differential term is estimated separately and the first-order or second-order approximation is usually employed for an estimate of the change. For simplicity, we represent the equation for the first-order differential operator sampling as follows;

$$\begin{aligned}\frac{\partial k}{\partial a} = \frac{1}{\int S_f dP_0}\sum_m \int dP_m \cdots \int dP_0 \Bigg[& \frac{1}{C_{f,m}}\frac{\partial C_{f,m}}{\partial a} + \frac{1}{T_m}\frac{\partial T_m}{\partial a} \\ & + \frac{1}{C_{s,m-1}}\frac{\partial C_{s,m-1}}{\partial a} + \frac{1}{T_{m-1}}\frac{\partial T_{m-1}}{\partial a} + \cdots + \frac{1}{T_1}\frac{\partial T_1}{\partial a} + \frac{1}{S_f}\frac{\partial S_f}{\partial a}\Bigg] \\ & \times C_{f,m}T_m C_{s,m-1}T_{m-1}\cdots C_{s,1}T_1 S_f\end{aligned} \tag{2}$$

where T is a transport kernel, C a collision kernel, S_f a fission source and P a six-dimensional

phase space. The last term in the blacket represents the perturbation effect due to the fission-source change. We estimate it by the following formula;

$$\frac{\partial}{\partial a}S_{f,i}(P)=\frac{\int S_{f,i-1}dP'}{\int dP\int dP'\tilde{K}_F S_{f,i-1}}\left(\int dP'\frac{\partial}{\partial a}\left[\tilde{K}_F S_{f,i-1}\right]\right.$$
$$\left.-\int dP\int dP'\frac{\partial}{\partial a}\left[\tilde{K}_F S_{f,i-1}\right]\frac{\int dP'\tilde{K}_F S_{f,i-1}}{\int dP\int dP'\tilde{K}_F S_{f,i-1}}\right) \quad (3)$$

where $\tilde{K}_F$ is a kernel to represent a random walk from particle birth until a fission point and the subscript i means i-th particle generation.

In order to verify the above formulation, benchmark calculations were performed for a simple one-dimensional slab geometry. It consists of 3 homogeneous regions (0.5, 2, 0.5cm in thickness) and all regions have the same composition that total, absorption and production cross sections are 1.0, 0.2 and 0.36cm^{-1}, respectively. The multiplication factor is almost unity in the unperturbed system. Perturbations were introduced by changing the density in the central region.

Tables 2.3.1 and 2.3.2 show comparison of the change in the effective multiplication factor between 3 Monte Carlo schemes for the density decrease by 0.1% and 10%, respectively. The deterministic result obtained by the ANISN[2] code is also shown below the tables. All the Monte Carlo calculations were done for 2.2 million histories with the collision estimator. In the case of the small perturbation (-0.1%), the result obtained by 2 Monte Carlo runs is unreliable but the other results obtained by the correlated and differential operator sampling methods are in very good agreement with the ANISN result. As found from these results, the perturbation effect due to the fission-source change is 20% of the total change in the effective multiplication factor and the fission-source change must be taken into account. On the other hand, the result of 2 independent Monte Carlo calculations is obtained with good accuracy for the relatively large perturbation (-10%) and is in very good agreement with the ANISN result. The result obtained by the correlated sampling method agrees with the ANISN one within 1 standard deviation but the variance is relatively large. The result by the differential operator sampling method is in fairly good agreement and the variance is comparable with that of the direct method.

In this work, it has been shown that the perturbation effect due to the fission-source change can be estimated by the formula proposed for the differential operator sampling

method and the estimate of the change in the effective multiplication factor is improved by this procedure. Incorporation of the procedure into the MVP/GMVP[3] code is in progress for the general-purpose use.

References

1) Nakagawa, M., et. al. : J. Nucl. Sci. Technol, 15, 400 (1978).

2) Engle, W. W. Jr. : "A User Manual for ANISN, A One Dimensional Discrete Ordinates Transport Code with Anisotropic Scattering", K-1693 (1967).

3) Mori, T. and Nakagwa, M. : JAERI-Data/Code 94-007 (1994) [in Japanese].

Table 2.3.1 Change in the effective multiplication factor for the one-dimensional slab geometry in the case of density change of -0.1%

	Direct	Correlated sampling (without approximation)			Differential operator sampling (2nd order)	
		Without source perturbation	Source perturbation only	Total	Without source perturbation	With source perturbation
Δk	-4.430E-4	-3.344E-4	-0.717E-4	-4.061E-4	-3.344E-4	-4.059E-4
1σ	4.458E-4	0.007E-4	0.045E-4	0.046E-4	0.007E-4	0.046E-4

*ANISN Δk = -4.05E-4 (error criterion = 1.0E-6)

**collision estimator, 2,200,000histories, batch size=20,000

Table 2.3.2 Change in the effective multiplication factor for the one-dimensional slab geometry in the case of density change of -10%

	Direct	Correlated sampling (without approximation)			Differential operator sampling (2nd order)	
		Without source perturbation	Source perturbation only	Total	Without source perturbation	With source perturbation
Δk	-4.209E-2	-3.478E-2	-0.778E-2	-4.255E-2	-3.474E-2	-4.132E-2
1σ	0.043E-2	0.007E-2	0.081E-2	0.082E-2	0.007E-2	0.047E-2

*ANISN Δk= -4.204E-2 (error criterion = 1.0E-6)

**collision estimator, 2,200,000histories, batch size=20,000

2.4 Accurate Perturbation Calculation for Nodal Diffusion Method

K. Okumura
(*E-mail* : okumura@mike.tokai.jaeri.go.jp)

Nodal diffusion methods[1] have widely been used in reactor physics analyses. However, two problems remain for the methods in relation to adjoint calculations. The first one is the treatment of a discontinuity factor[2] in an adjoint problem. Conventional treatment[1), 2)] of the discontinuity factor for a forward problem can not be applied to the adjoint one; meaningful adjoint fluxes can not be obtained and eigenvalues for both problems don't coincide. To overcome this problem, Kobayashi presented a consistent theory[3] for the treatment of the discontinuity factor in adjoint problems, and he demonstrated analytically that an accurate perturbation calculation could be done in a simple one-group and one-dimensional problem by introducing his theory. On the other hand, the second problem appears in multi-dimensional problems. In conventional nodal methods, a three-dimensional flux distribution in a node is not directly calculated, while a one-dimensional transverse integrated flux in each direction is obtained. In the case of an exact perturbation calculation, the following two terms appear;

$$\begin{aligned}\left\langle \phi_g^{\dagger} \cdot \phi_g^{*} \right\rangle &\equiv \int_{Node} \left\{ \phi_g^{\dagger}(\boldsymbol{r}) \cdot \phi_g^{*}(\boldsymbol{r}) \right\} d\boldsymbol{r} \\ &\approx \int_{Node} \phi_g^{\dagger}(\boldsymbol{r}) d\boldsymbol{r} \cdot \int_{Node} \phi_g^{*}(\boldsymbol{r}) d\boldsymbol{r} \; / \; \int_{Node} d\boldsymbol{r} ,\end{aligned} \tag{1}$$

$$\begin{aligned}\left\langle \nabla \phi_g^{\dagger} \cdot \nabla \phi_g^{*} \right\rangle &\equiv \int_{Node} \left\{ \nabla \phi_g^{\dagger}(\boldsymbol{r}) \cdot \nabla \phi_g^{*}(\boldsymbol{r}) \right\} d\boldsymbol{r} \\ &\approx \int_{Node} \nabla \phi_g^{\dagger}(\boldsymbol{r}) d\boldsymbol{r} \cdot \int_{Node} \nabla \phi_g^{*}(\boldsymbol{r}) d\boldsymbol{r} \; / \; \int_{Node} d\boldsymbol{r} ,\end{aligned} \tag{2}$$

where, $\phi_g^{\dagger}(\boldsymbol{r})$ and $\phi_g^{*}(\boldsymbol{r})$ is an adjoint flux and a perturbed forward flux in a node, respectively. The approximations in Eqs. (1) and (2) are appropriate in the finite difference method, but not always valid in the nodal methods that use coarse meshes. This problem doesn't appear in a one-dimensional problem, because an intra-nodal flux distribution can be given explicitly by analytical or polynomial functions.

To overcome the second problem, a kind of flux reconstruction technique[4] was introduced. In the case of the 4th order polynomial nodal expansion method (NEM)[1], a three-dimensional flux distribution in each node is approximated as

$$\phi_g(\boldsymbol{r}) \approx \phi_{g,0} + \sum_{u=x,y,z} \left\{ C_{1u,g} u + C_{2u,g} u^2 + C_{2u,g} u^3 + C_{2u,g} u^4 \right\}, \tag{3}$$

where $\phi_{g,0}$ is the node averaged flux, and $C_{1u,g} \sim C_{4u,g}$ are expansion coefficients of a transverse integrated flux in each direction. This function is consistent with all nodal parameters like volume or surface averaged fluxes and surface averaged currents obtained in a core calculation by NEM. In addition, no additional computation cost is necessary, because all of the coefficients are obtained in the consequence of core calculation. It was confirmed that Eq. (3) always give sufficient accuracy for the integrated parameters in Eqs. (1) and (2), in spite of the simple reconstruction as compared with that used in a pin power reconstruction[4].

In order to complete the perturbation calculation by the nodal method, Kobayashi's theory and the presented method were incorporated in our nodal diffusion code MOSRA-Light[5], which was based on the 4th order NEM. The method was verified in the two-dimensional and two-group DVP-BWR benchmark problem[2] shown in Fig.2.4.1. Six kinds of discontinuity factors are considered in the problem for the surfaces with wide or narrow gap of fuel assemblies with three types. As an extension of the original benchmark problem, a perturbation by withdrawal of all control rods was considered as shown in Fig.2.4.1. The perturbed reactivities were calculated on the basis of the exact perturbation theory by using the unperturbed adjoint flux and the perturbed forward one obtained with MOSRA-Light. In the core calculation, one node per fuel assembly was taken as a coarse mesh. The following three cases of calculations were performed.

Case 1: without Kobayashi's theory in the adjoint core calculation and no flux reconstruction in perturbation calculation (by Eqs. (1) and (2)),

Case 2: with Kobayashi's theory and no flux reconstruction,

Case 3: with Kobayashi's theory and the flux reconstruction by Eq. (3).

The perturbed reactivities obtained for the above three conditions were compared with the reference solution that was directly obtained from two forward solutions of eigenvalues for the unperturbed and perturbed cores. As shown in Table 2.4.1, a very accurate reactivity was

obtained by the condition of the Case 3. Thus, Kobayashi's theory was validated in a multi-dimensional and multi-group problem. The contribution of the flux reconstruction by Eq. (3) was relatively small in this problem. However, it should not be neglected when smaller perturbation reactivity (~20 pcm) is evaluated.

The presented method is easily applicable to the calculations of one-point kinetics parameters or space dependent kinetics analyses by the improved quasi-static method, which is based on the exact perturbation theory.

References

1) Lawrence R. D. : Prog. Nucl. Energy, 17, 271 (1986).

2) Smith K. S. : Prog. Nucl. Energy, 17, 303 (1986).

3) Kobayashi K. : J. Nucl. Sci. Technol., 35, 20 (1998).

4) Koebke K. and Hetzelt L. : Nucl. Sci. Eng. 91, 123 (1985).

5) Okumura K. : JAERI-Data/Code 98-025 (1998) [in Japanese].

Table 2.4.1 Comparison of perturbed reactivities ($\Delta k / kk'$) in DVP-BWR benchmark

Case 1	Case 2	Case 3	Reference
2.58E-2	2.31E-2	2.30E-2	2.30E-2

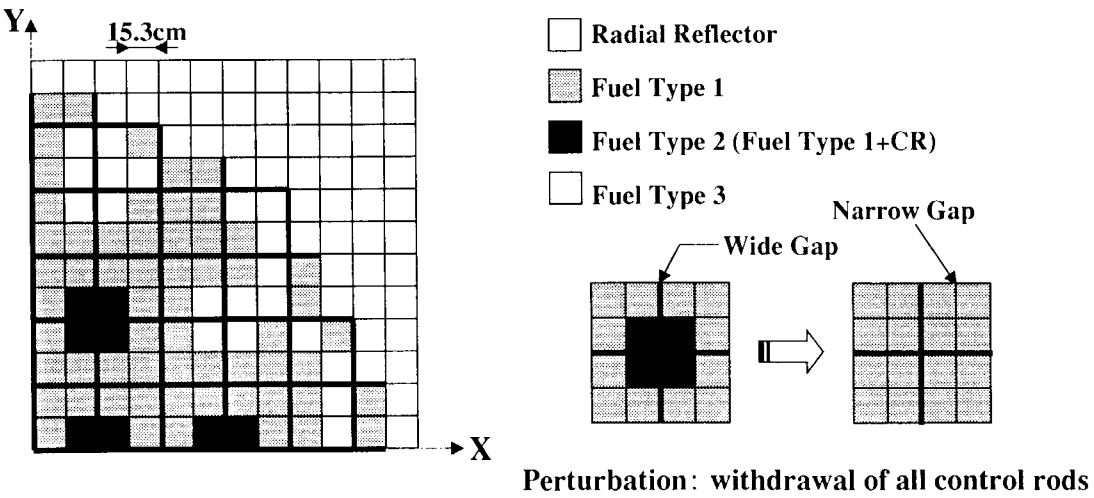

Fig. 2.4.1 Extended DVP-BWR benchmark problem for perturbation investigation

2.5 Spatially Dependent Resonance Self-Shielding Calculation Method Based on the Equivalence Theory

T. Kugo and K. Kaneko*

(*E-mail* : kugo@mike.tokai.jaeri.go.jp)

We propose a convenient calculation method of a spatially dependent resonance self-shielded cross sections in arbitrary heterogeneous systems. The proposed method is established by the generalization of the classical equivalence theory to arbitrary heterogeneous systems and can be applied to any geometry in which the collision probability can be calculated. The validity of the proposed method is demonstrated by the comparison with Stoker/Weiss's method[1] in application to the benchmark problem of a BWR fuel assembly with adjacent annularly divided poisoned fuel rods.

From a comparison between an expression of neutron spectrum obtained from the neutron balance equation and a general expression based on the narrow resonance (NR) approximation, we obtain an exact heterogeneity term except for the NR approximation as

$$\gamma = \frac{X_i(u)}{N_i\, l_i} \cdot \frac{1 - \sum_{j\in R} P_{ij}(u)\, \dfrac{N_j / \Sigma_j(u)}{N_i / \Sigma_i(u)}}{\sum_{j\in R} P_{ij}(u)\, \dfrac{N_j / \Sigma_j(u)}{N_i / \Sigma_i(u)}} \sim \frac{X_i^g}{N_i\, l_i} \cdot \frac{1 - \sum_{j\in R} P_{ij}^g\, \dfrac{N_j / \Sigma_j^g}{N_i / \Sigma_i^g}}{\sum_{j\in R} P_{ij}^g\, \dfrac{N_j / \Sigma_j^g}{N_i / \Sigma_i^g}} , \qquad (2.5.1)$$

where $X_i(u)$ is defined by $X_i(u) = \Sigma_i(u)\, l_i$, N_i a number density of an resonant isotope and l_i the mean chord length of the region i. This heterogeneity term is consistent with the conventional equivalence theory in the two-region system, with use of the suitable X value corresponding to the conventional Bell factor value. Assuming that the consistency in the two-region system is applicable to arbitrary heterogeneous systems, instead of the point-wise expression, we use a group-wise one where we only change the lethargy u into the suffix for the neutron energy group g. The key of success of the present method is to define appropriately the microscopic total cross sections of a resonant isotope used in Eq. (2.5.1). In this study, we refer the conventional Bell factor values and introduce the energy dependency to improve the applicability. We classified the

* Integrated Technical Information Research Organization (ITIRO), Tokyo

microscopic total cross section used in evaluating the heterogeneity term by Eq. (2.5.1) into three definitions according to the strength of the resonance. These definitions are classified by the infinite dilution total cross section value stored in the f-table library of SRAC[2] as shown in Table 2.5.1.

Table 2.5.1 Classification of microscopic total cross section used in evaluating the heterogeneity term

Range of infinite dilution microscopic total cross section :σ_∞ (barn)	Corresponding σ_t value (barn)
$\sigma_\infty < 150$	$\sigma_t = 300$
$150 < \sigma_\infty < 500$	$\sigma_t = 2 \times \sigma_\infty$
$500 < \sigma_\infty$	$\sigma_t = 3 \times \sigma_\infty$

The present method is applied to the numerical benchmark problem[3] which was proposed to investigate the calculation accuracy of burn-up characteristics for the BWR fuel assembly with adjacent poisoned fuel rods. A simplified BWR lattice geometry was employed as shown in Fig. 2.5.1. This problem is appropriate to verify the applicability of the method to the fuel assembly with strong heterogeneity and the one to the fuel with burnable poison nuclides. A poisoned fuel pellet was divided into eight annular depleting zones to consider the change of spatial shielding effect of resonant isotopes during burn-up time, while other fuel pellets were not divided.

The present method has been implemented into SRAC which employs the collision probability method. Stoker/Weiss's method has also been implemented into it and was used to calculate appropriately the spatially dependent resonance cross sections in the annularly divided fuel pin by applying the two-term rational expressions. Both methods are executed with the 107-group library based on JENDL-3.2 and compared with MVP[4].

We compare the capture reaction rates at 0 GWd/t between the present and Stoker/Weiss's methods for U-238 in Table 2.5.2. The present method overestimates the U-238 capture rate by 1.7% compared with MVP in non-poisoned rods, Stoker/Weiss's method does by 3% and 2.4% in poisoned and non-poisoned rods, respectively. Thus, the present method improves the spatially dependent U-238 capture cross

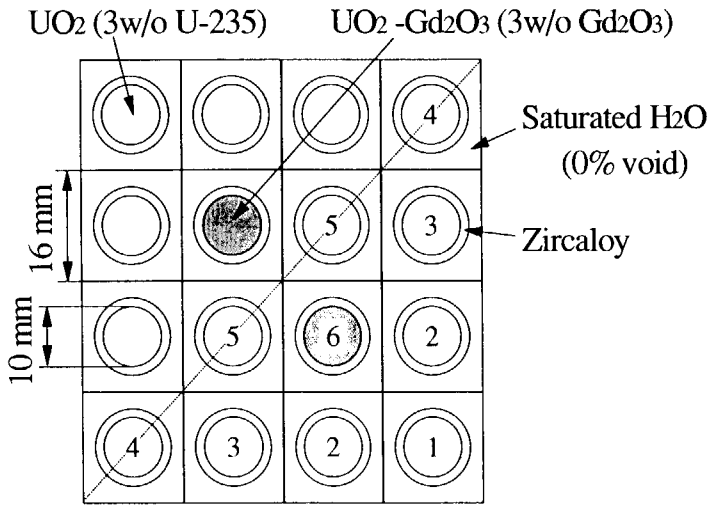

Fig. 2.5.1 Lattice geometry of the benchmark problem on BWR lattice with adjacent gadolinium pins

sections compared with Stoker/Weiss's method. The conventional Bell factor was selected for the usual condition in thermal reactors where the X value is around 6 or 7. On the other hand, the two-term rational expression proposed by Carlvik overestimates the escape probability (e.g., Fig.2 in Chap. IX of the Ref. 5)) and also self-shielded cross sections for larger X values greater than 5. Therefore, Wigner's rational expression with the conventional Bell factor is more accurate than the two-term rational expression by Carlvik for U-238 and, therefore, Stoker/Weiss's method overestimates the capture rate of U-238 compared with the present method. From the above discussions, it is concluded that the present method is useful for the design-oriented transport codes. For further improvement of the present method, the algorithms for the resonance interference are under investigation.

Table 2.5.2 Ratio of U-238 capture rates of the present method and Stoker/Weiss's method to those of MVP

Zone no. / Pin no.	Radius (cm)	Present	Stoker/ Weiss
1	0.184	0.955	1.080
2	0.260	0.962	1.080
3	0.303	0.956	1.061
4	0.340	0.974	1.064
5	0.393	1.003	1.072
6	0.440	1.063	1.068
7	0.471	1.128	1.051
8	0.500	0.935	0.909
sum.		0.996	1.030
1		1.016	1.023
2		1.020	1.027
3		1.020	1.027
4		1.008	1.016
5		1.017	1.024
average		1.017	1.024

References

1) Stoker, C. C. and Weiss, Z. J.: "Spatially Dependent Resonance Cross Sections in a Fuel Rod", Ann. Nucl. Energy, 23, 9, 765 (1996).

2) Okumura, K., Kaneko, K. and Tsuchihashi, K.: "SRAC95; General Purpose Neutronics Code System", JAERI-Data/Code 96-015 (1996) [in Japanese].

3) Maeder, C. and Wydler, P.: "International Comparison Calculations for a BWR Lattice with Adjacent Gadolinium Pins", NEACRP-L-271 (1984).

4) Mori, T., Nakagawa, M. and Sasaki, M.: "Vectorization of Continuous Energy Monte Carlo Method for Neutron Transport Calculation", *J. Nucl. Sci. Technol.*, 29, 325 (1992).

5) Stamm'ler, R. J. J. and Abbate, M. J.: "Methods of Steady-State Reactor Physics in Nuclear Design", Academic Press, London (1983).

2.6 Benchmark Calculation for 3-D PWR Core Transient by using REFLA/TRAC/MLK3D

Y. Nagaya and H. Inoue*

(*E-mail:* nagaya@mike.tokai.jaeri.go.jp)

Recently, it has been getting more important to use a reactor kinetics code coupled with neutronics and thermohydraulics for a detailed reactor safety analysis. We have been developing the coupled kinetics code applicable to various types of reactors. In this fiscal year, we have developed a prototype coupled code REFLA/TRAC/MLK3D for transient analyses of PWR-type reactors. The code consists of the REFLA/TRAC thermohydraulics module and the MLK3D kinetics module[1]. The kinetics module includes the MOSRA-Light neutronics module[2] and solves the time-dependent multigroup diffusion equation. Therefore, all schemes equipped in the code are available (the point kinetics method, fully implicit method or improved quasi-static method[3]).

In order to verify the code, a benchmark calculation were performed for a PWR core transient benchmark problem A1[4] organized by NEACRP. The PWR core geometry is derived from a real PWR. Only the core region is modeled and the primary and secondary loops are omitted in the benchmark problem. The core is comprised of 157 fuel assemblies with 196 fuel rods and 64 radial reflector elements. The core transient is initiated by the central rod ejection at hot zero power. The control rod is fully inserted at the critical state and the time for control rod ejection is 100 msec.

The critical boron concentration and the control rod worth are listed in Table 2.6.1 and compared with the reference results obtained by the PANTHER code[5]. The present results are obtained by a calculation model where spatial spacings are 2x2 nodes per an assembly with 16 layers and a time step size of 2.5 msec is fixed in the fully implicit method. These are in good agreement with the PANTHER results. Fig. 2.6.1 shows the reactor power obtained by the present code and the peak powers by the PANTHER code. Discrepancies of the power and time

* S&E Inc.

are found at the peak. Some reasons can be considered such as axial node spacings, time step

sizes and so on, but dominant causes have not been revealed yet.

In this work, we verified the prototype reactor kinetics code coupled with neutronics and thermohydraulics for PWRs. Further calculations are being performed for the above benchmark problem to refine the solutions obtained by the present code. Moreover, we are developing the coupled reactor kinetics code with a BWR-type thermohydraulics module TRAC-BF1.

References

1) Nagaya, Y. and Inoue, H. : JAERI-Review 98-022, p56 (1998).
2) Okumura, K. : JAERI-Data/Code 98-025 (1998) [in Japanese].
3) Ott K. O., et. al. : Nucl. Sci. and Eng., 36, 402 (1969).
4) Finnemann, H. and Galati, A. : "NEACRP 3-D LWR Core Transient Benchmark Final Specifications", NEACRP-L-335 (Revision 1) (1991).
5) Knight, M. P. and Bryce, P. : "Derivation of a Refined PANTHER Solution to the NEACRP PWR Rod-Ejection Transients", Proc. of the Joint Int. Conf. Math. Methods and Supercomputing for Nuclear Applications, Vol. 1, p302 (1997).

Table 2.6.1 Comparison of results for NEACRP PWR Transient A1 problem

Code	REFLA/TRAC/MLK3D	PANTHER	
Node	2x2 nodes/assembly 16 layers	2x2 nodes/assembly 18 layers	4x4nodes/assembly 36 layers
Critical boron concentration (ppm)	563.00	567.61	567.70
Control rod worth (pcm)	821	819.77	821.20

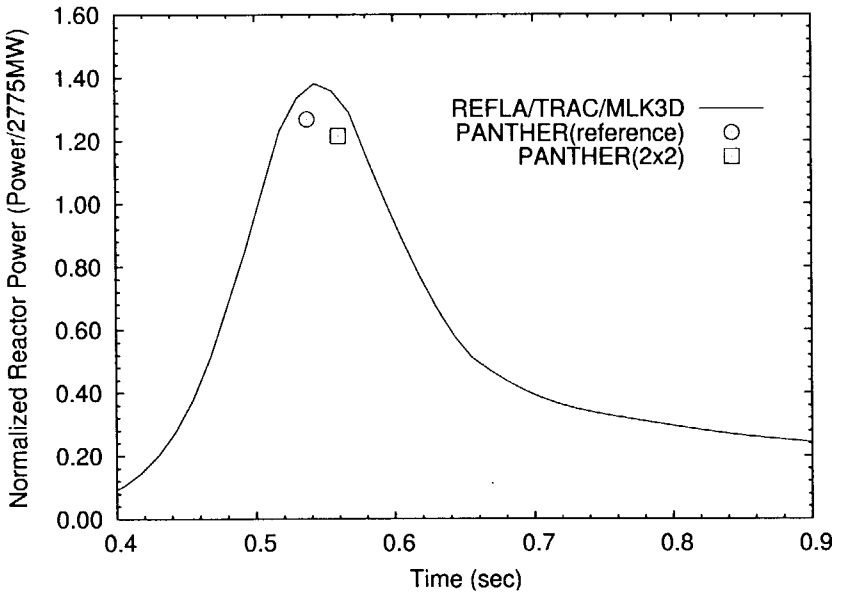

Fig. 2.6.1 Normailzed reactor power for NEACRP PWR A1 problem

3. Reactor Physics Experiment and Analysis

In order to validate the calculation accuracy by experiment for Pu burning fast reactor, a unique core without uranium fuel was constructed at the FCA assembly. Excellent agreements were observed between the measured and calculated sample worths for Pu and B_4C. Concerning the sodium reactivity worth, the calculation underestimates the measured one by about 30% at the core center, whereas this underestimation tends to be eliminated at the core axial edge.

Finalization of the measured data was carried out for the international β_{eff} benchmark experiments at FCA with three different core configurations; XIX-1 (U-core), XIX-2 (Pu/NU core) and XIX-3 (Pu core) by six research organizations from five countries. The final β_{eff} value of each core was obtained by taking the mean value of the β_{eff} values measured by participants using their own measurement techniques. The resulted mean values satisfied the target accuracy of 3%. The calculated and measured β_{eff} values were in good agreement for cores of XIX-1 and XIX-2, however, the calculated value for XIX-3 core was 2-3% smaller than the measured one.

The calculation accuracy was examined for External-GEM reactivity worth measured at the FCA-XX-1 core using sodium blocks to simulate the GEM equipment. It was found that the calculation overestimated the measured reactivity effects more than 10%, and that the degree of overestimation increased with enlarging the voided volume of GEM. It was also found that there was no significant dependency of C/E values on the sodium level in the simulated GEM.

The HTTR achieved the first criticality of annular core with 19 fuel columns, then that of full core with 30 columns. The calculated excess reactivity for the annular core with 18 fuel columns and for the full core were obtained as about 4 % and 13 %Δk/k, respectively. The difference of the calculated and the measured values for the first criticality is considered that impurity in dummy fuel blocks may be underestimated and the neutron absorption of air in pore of graphite blocks is neglected in the calculation. For the excess reactivity of full core, the calculated value was overestimated about 10% to preliminary measured one.

A new high-sensitive non-destructive method for measuring fissionable materials in concrete-solidified TRU radioactive waste has been developed using active neutron assay. This method utilizes the neutrons moderated within the waste matrix itself. It was shown by experiments that the new method could overcome the problems associated with a conventional active neutron assay, such as low sensitivity or position-dependent sensitivity of the fissionable materials in the waste drum.

3.1 Experimental Study on Uranium-Free Fast Reactor at FCA

H. Oigawa, S. Iijima and M. Andoh
(*E-mail :* oigawa@omega.tokai.jaeri.go.jp)

Fast reactors have a potential to flexibly cope with the demand and supply of plutonium because of their good neutron economy. Recently, fast reactors for burning plutonium, instead of breeding, have been actively studied[1,2]. For plutonium burning, fast reactors using highly enriched plutonium or uranium-free fuel are considered preferable to enhance the fission reaction of plutonium and to reduce the capture reaction of uranium. In order to experimentally validate the calculation accuracy for such plutonium burning fast reactors, a unique core without uranium was constructed at the FCA assembly XIX-3B, and sample reactivity worth of plutonium and B_4C and sodium void reactivity worth were measured.

The core consisted of a test region (49 cm in diameter and 61 cm in length), a driver region and a blanket region. All the measurements were performed in the test region that consisted of plutonium, sodium and stainless steel. In Table 3.1.1, atomic number densities of the test region are compared with those of a reference MOX core, XVII-1[3], which simulated the prototype LMFBR core. The XIX-3B core contained twice of plutonium and steel in comparison with the XVII-1 core, while neither uranium nor oxygen was included in XIX-3B. The resultant normal and adjoint neutron spectra in the test region are compared with those of the XVII-1 core in Fig. 3.1.1. It is clearly observed that the neutron spectrum of XIX-3B core shifts to high energy and that the adjoint neutron spectrum decreases with neutron energy between 20 and 500 keV where that of the XVII-1 core shows opposite slope.

The measured items were the axial distribution of plutonium sample worth, the B_4C sample worth for various ^{10}B enrichments, and the axial distribution of sodium void reactivity worth.

As for the calculation, the 70-group library, JFS-3-J3.2, based on JENDL-3.2 was used. For the cell calculation , the SLAROM code was used. The reactivity worth was calculated by the 70-group diffusion approximation in an RZ-geometry. The transport correction was performed for the non-leakage term and the leakage term separately in the

calculation of the sodium void reactivity worth.

The measured and the calculated sample worths are compared in Fig. 3.1.2 and Fig. 3.1.3 for plutonium and B_4C, respectively. A very good agreement was observed for both plutonium and B_4C sample worths. This implies that the axial flux distribution and neutron spectrum were well calculated by the present cross section library and calculation method.

On the other hand, the measured and the calculated sodium void reactivity worths are compared in Fig. 3.1.4, where the calculated values are decomposed into the non-leakage and leakage terms. It should be noted that the sodium void reactivity worth shows a negative value even at the core center, since the adjoint neutron spectrum decreases with the neutron energy below 500 keV as shown in Fig. 3.1.1. The calculation underestimates the absolute value of the sodium void reactivity worth by about 30 % at the core center, whereas this underestimation tends to be reduced at the core axial edge. This tendency suggests that the non-leakage term, which is dominant at the core center, is underestimated and the leakage term, which increases with the distance from the core center, is fairly well predicted. Further study on the non-leakage term is, therefore, necessary to explain this underestimation.

References

1) Languille, A., et al. : "CAPRA core studies － The Oxide Reference Option", Proc. Int. Conf. Evaluation of Emerging Nuclear Fuel Cycle Systems, GLOBAL '95, Versailles, France, September 11-14, 1995, Vol. I, p. 874 (1995).
2) Wakabayashi, T., et al. : Nucl. Technol., 118, 14 (1997).
3) Oigawa, H. and Iijima, S. : J. Nucl. Sci. Technol., 35, 264 (1998).

Table 3.1.1 Atomic number densities (10^{22}atoms/cm^3)

	Core name	
	XIX-3B	XVII-1
Nuclide	U-free fast reactor	Prototype LMFBR
^{239}Pu	0.21	0.11
^{238}U	------	0.69
O	------	1.70
Na	0.96	0.77
Fe	2.67	1.22

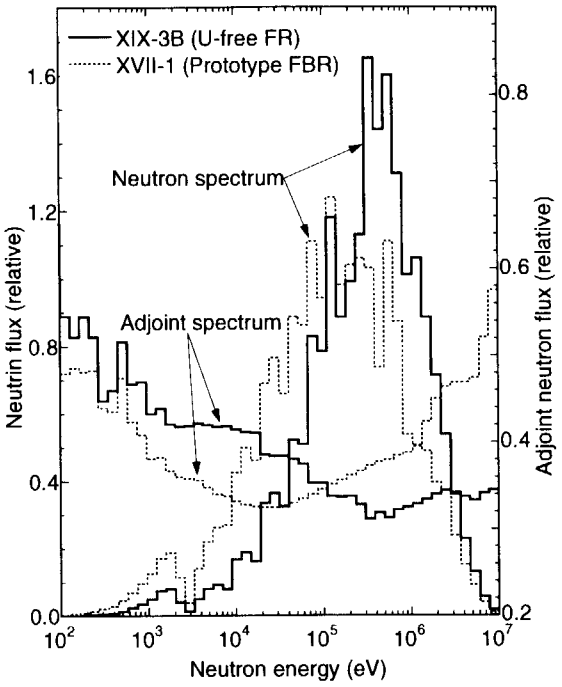

Fig. 3.1.1 Normal and adjoint neutron spectra in the test regions of FCA cores

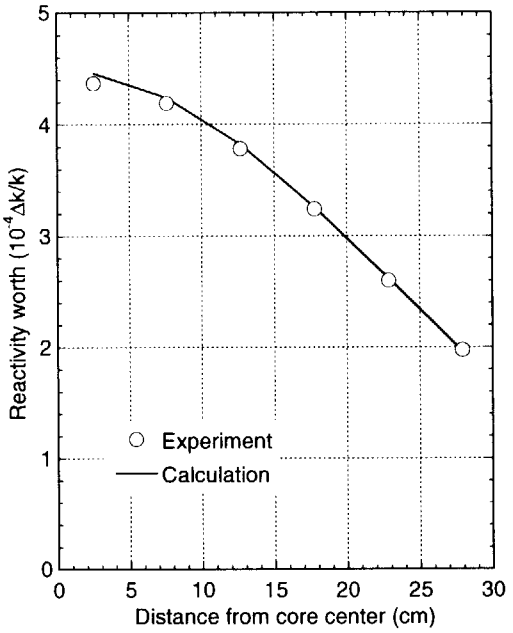

Fig.3.1.2 Results of plutonium sample worth

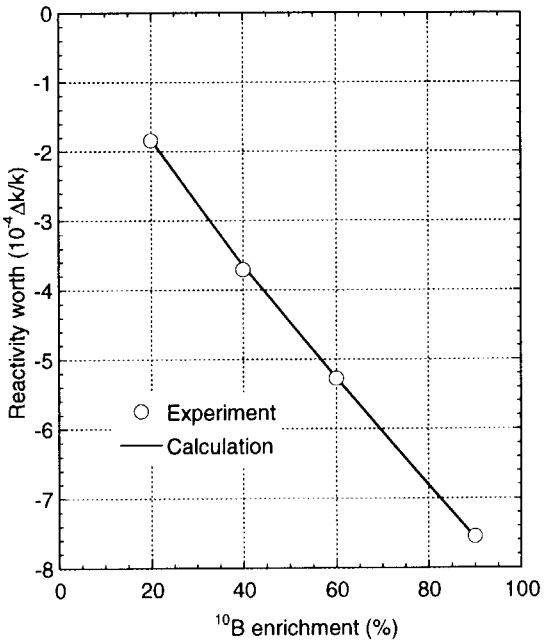

Fig. 3.1.3 Results of B_4C sample worth

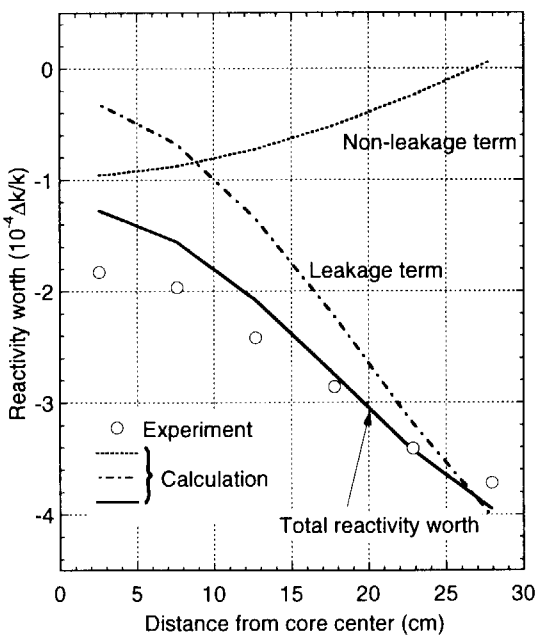

Fig. 3.1.4 Results of sodium void reactivity worth

3.2 International β_{eff} Benchmark Experiments in FCA

T. Sakurai, S. Okajima, H. Sodeyama, M. Andoh and T. Osugi
(*E-mail* : sakurai@tru.tokai.jaeri.go.jp)

Benchmark experiments of the effective delayed neutron fraction β_{eff} were performed at FCA between 1995 and 1998 to improve prediction accuracy of the β_{eff}[1,2]. The experiments were carried out in three cores which were built to provide a systematic change in ^{235}U, ^{238}U and ^{239}Pu contributions to the β_{eff}: XIX-1 core(U fuel), XIX-2 core(Pu/U fuel) and XIX-3 core(Pu fuel). Table 3.2.1 summarizes main characteristics of these cores. Six organizations from five countries(CEA/France, IPPE/Russia, KAERI/Korea, LANL/USA, Nagoya-University/Japan and JAERI/Japan) participated in the experiments with their measurement methods and have reported their β_{eff} values so far.

The final value of experimental β_{eff} was derived by comparing the β_{eff}'s between the measurement methods to improve reliability of the final value. The analysis of experiments was made using the JENDL-3.2 nuclear data file[3] and JAERI's calculation system for fast reactor neutronics to check the prediction accuracy of β_{eff}[4].

Table 3.2.1 Main characteristics of FCA cores

Core name	XIX-1	XIX-2	XIX-3
- Fuel	Enriched uranium	Plutonium /Natural uranium	Plutonium
- Fuel enrichment	93%	23%	(92% fissile Pu)
- Core dimensions Radius x Height(cm)	33.0 x 50.8	35.7 x 61.0	35.1 x 61.0
- β_{eff} (pcm)	742	364	251
- Nuclide contributions to β_{eff}			
^{235}U	94%	10%	9%
^{238}U	6%	47%	11%
^{239}Pu	—	41%	77%
^{240}Pu, ^{241}Pu, ^{241}Am	—	2%	3%

Finalization of Experimental β_{eff}

Table 3.2.2 shows the β_{eff}'s that were measured by the individual method. The final value of β_{eff} in each core was obtained by taking the mean value of these individual β_{eff}'s. Correlations of β_{eff}'s between different methods were taken into account in this procedure because several common parameters such as fission rate were used to determine the β_{eff} in the different methods. The mean value m of the β_{eff} was determined by

$$m = (\mathbf{u} \cdot \mathbf{C}^{-1} \cdot \mathbf{u}^{T})^{-1} \cdot \mathbf{u} \cdot \mathbf{C}^{-1} \cdot \mathbf{p} . \qquad (3.2.1)$$

where $\mathbf{p}$ is a column vector whose elements are the β_{eff}'s by the individual method, $\mathbf{C}$ is a covariance matrix of β_{eff}'s, $\mathbf{u}$ is a row vector with all elements equal to unity and T means a

transpose of vector. The internal uncertainty δ_{int} of the $\bar{m}$ was estimated by the error propagation law :

$$\delta_{int} = \sqrt{(u \cdot C^{-1} \cdot u^{T})^{-1}} . \quad (3.2.2)$$

The external uncertainty δ_{ext} was estimated by

$$\delta_{ext} = \sqrt{\chi^2/f} \cdot \delta_{int} . \quad (3.2.3)$$

where f is the degrees of freedom, χ^2 the statistical parameter calculated from the residuals of individual β_{eff}'s around the $\bar{m}$. The δ_{ext} reflects the scattering of the individual data around the $\bar{m}$. Table 3.2.3 presents the results for the $\bar{m}$, δ_{int} and δ_{ext}. The δ_{ext} was larger than the δ_{int} in the XIX-1 and XIX-2 cores where the δ_{ext} was adopted as the uncertainty of the final value. The δ_{int} was adopted in the XIX-3 core. These results satisfied the target accuracy of 3% required for the experimental β_{eff}[5].

Table 3.2.2 β_{eff} values obtained by different experimental methods

Unit : pcm

	Core name	XIX-1	XIX-2	XIX-3
(1)	Covariance-to-mean method (JAERI)	724±13(2%)*	—	252±5(2%)
(2)	Modified Bennett method (Nagoya-University)	782±16(2%)	368±6(2%)	256±4(2%)
(3)	Noise method (CEA)	743±19(3%)	—	250±6(2%)
(4)	Rossi-α method (IPPE)	771±23(3%)	—	—
(5)	Nelson-number method (LANL)	737±20(3%)	—	—
(6)	Cf source method			
	JAERI/KAERI	735±20	358±10	249±7
	IPPE	706±30	351±10	244±7
	Mean of two participants	727±20(3%)	355±10(3%)	247±7(3%)

* Values in parentheses : relative uncertainty

Table 3.2.3 Final value and uncertainty of β_{eff}

Unit : pcm

Core name	XIX-1	XIX-2	XIX-3
Mean value of $\beta_{eff}(\bar{m})$	742	364	251
δ_{int}	±11(2%)	±7(2%)	±4(2%)
δ_{ext}	±24(3%)	±9(3%)	±4(2%)

Analysis of the measured β_{eff}

Cell calculations were made for each region in the reactor to prepare cell averaged effective cross sections in seventy energy groups. We used the SLAROM code[6] which is based

on the collision probability method, a group constants set JFS3-J3.2 with a seventy energy group structure[7] and a one-dimensional infinite slab model of the cell.

Core calculations were made by a diffusion theory code POPLARS[8] in a three-dimensional X-Y-Z model. The β_{eff} was calculated by using the delayed neutron(D.N.) yields and the D.N. spectra of the JENDL-3.2. The incident neutron energy dependence of D.N. yields was taken accout of in this calculation. To see the effect of changing the D.N. spectra on the β_{eff} calculation, the D.N. spectra of ENDF/B-VI[9] were also used for the calculation with the D.N. yields of JENDL-3.2. A correction of about 1% for transport effect was applied to these results. This correction factor was estimated with a two-dimensional transport theory code TWOTRAN-II[10].

Table 3.2.4 presents the ratios of calculation to experiment(C/E's) of the β_{eff}. The effect of changing the D.N. spectra on the β_{eff} calculation was found to be small(at most 0.6%). Good agreement was found in the XIX-1 and XIX-2 cores between experiment and calculation. On the other hand, the calculation underpredicted the β_{eff} of XIX-3 core by 2~3%. The present values of β_{eff} and the C/E's will be used in future for evaluation of the D.N. yields.

Table 3.2.4 Ratios of calculation to experiment(C/E's) of β_{eff}

Core name			XIX-1	XIX-2	XIX-3
	D.N. yield	D.N. spectra			
(a)	JENDL-3.2	JENDL-3.2	1.004	1.005	0.972
(b)	JENDL-3.2	ENDF/B-VI	1.003	1.009	0.978

References

1) Sakurai, T., et al.: Proc. of International Conference on the Nuclear Science and Technology, Long Island, USA, 182 (1998).
2) Sakurai, T. and Okajima, S.: Proc. of the Specialists' Meeting on Delayed Neutron Nuclear Data, JAERI-Conf, 99-007, 29 (1999).
3) Nakagawa, T., et al.: J. Nucl. Sci. Technol., 32, 1259 (1995).
4) Sakurai, T. and Okajima, S.: Proc. of the Specialists' Meeting on Delayed Neutron Nuclear Data, JAERI-Conf, 99-007, 85 (1999).
5) Blachot, J., et al.: OECD Nuclear Energy Agency, Committee on Reactor Physics and Nuclear Data Committee., NEACRP-L-323, NEANDC-299"U" (1990).
6) Nakagawa, M. and Tsuchihashi, K.: JAERI 1294 (1984).
7) Takano, H., Akie, H. and Kaneko, K.: Proc. of International Conference on Nuclear Data for Science and Technology, Gatlinburg, USA, 809 (1994).
8) Iijima, S.: Private communication, Japan Atomic Energy Research Institute (1999).
9) Rose, P.F. (Ed.): BNL-NCS-17541, 4th Edition (1991).
10) Lathrop, K.D. and Brinkley, F.W.: LA-4848-MS (1973).

3.3 Measurement of GEM Reactivity Worth at FCA

M. Andoh, H. Oigawa and S. Iijima
(*E-mail:* andoh@fca001.tokai.jaeri.go.jp)

The Gas Expansion Module (GEM) was designed[1] to add negative feedback to sodium cooled fast reactors in case of a loss-of-flow accident. Reactivity worth of the GEM external to the core (Ex-core GEM) had been measured using a small FBR mockup core (XIX-2G core) at Fast Critical Assembly (FCA) to estimate calculation accuracy for the GEM reactivity worth.[2] In this study, Ex-core GEM reactivity worth was measured in a FBR mockup core (FCA XX-1 core) using sodium blocks which newly prepared to simulate GEM.

Experiment

The XX-1 core is a large size FBR mockup core constructed at the FCA (the volume of the core region is 883 ℓ). The core region consists of a mixed nitride (MN) fuel region and MOX and enriched uranium (EU) driver regions. The core region is surrounded by a soft blanket (SB) and depleted uranium blanket (DUB) regions. The Ex-core GEMs are located in the SB region adjacent to the EU-driver in horizontally symmetric positions. The horizontal cross section of the core is shown in Fig. 3.3.1(a).

The GEM is simulated by the use of the sodium blocks covered with stainless steel. GEM reactivity worths were measured as the reactivity change caused by replacing the sodium blocks with empty cans. The sodium blocks were replaced step by step (-20.3cm, -66.0cm, -111.8cm and -132.1cm from the top of the GEM) to simulate the decrease of the sodium level in the GEM. To investigate dependence of the calculation accuracy on the volume of the voided area, sodium voided area in the GEM was varied as follows: 6cm×17cm, 11cm×17cm and 17cm×17cm (see Fig. 3.3.1(b)). Measured GEM reactivity worths are shown in Fig. 3.3.2.

Analysis

The experiment was analyzed using the standard analysis method[3] for FBR cores at FCA and the JFS-3-J3.2 group constant set generated from the JENDL-3.2 library[4]. A set of 70-group constants for the GEM was calculated using the Tone's method[5] considering the effect of the neighboring core region. The GEM reactivity worth was calculated by the exact perturbation theory with 25-group energy structure in XYZ geometry. The transport effect was considered for leakage and non-leakage term separately in R-Z geometry.

The result of the calculation is shown in Table 3.3.1. The leakage term is dominant for all the cases; a ratio of the non-leakage to leakage term is -0.06. It is pointed out from Table 3.3.1 that the transport effect on the leakage term is significant. The C/E values are

also shown in Table 3.3.1. The calculations overestimated the experiments more than 10%. It was found that there was no significant dependence of C/E values on the sodium level, while the degree of the overestimation increased with enlarging voided area.

References

1) Slovic, G. C., et al. : "Assessment of PRISM response to loss of flow events", Proc. Int. Conf. on Design and Safety of Advanced Nuclear Power Plants (ANP'92), Tokyo, Oct. 25～29, 1992, AESJ, Vol.III, pp.26.5-1～26.5-7(1992).
2) Oigawa, H., et al. : "Measurement of External GEM Reactivity Worth at FCA", JAERI-Review 98-022, p. 78(1998).
3) Iijima, S. : private communication.
4) Nakagawa, T., et al. : J. Nucl. Sci. and Technol., 32, 1259 (1995).
5) Tone, T. : "A Numerical Study of Heterogeneity Effects in Fast Reactor Critical Assemblies", J. Nucl. Sci. and Technol., 12(8), 467(1975).

Table 3.3.1 Result of the analysis on the GEM reactivity worth

Void area & sodium level (cm)	Transport effect NL[a)]	Transport effect L[b)]	Calcualted GEM reactivity worth ($\times 10^{-4}\Delta k/k$)	C/E
6cm×17cm				
-20.3	1.07	0.494	-0.51	1.12±3.7%[c)]
-66.0	0.887	0.683	-5.03	1.07±0.6%
11cm×17cm				
-20.3	1.10	0.582	-0.97	1.16±2.0%
-66.0	0.897	0.722	-9.26	1.12±0.5%
-111.8	0.878	0.765	-17.2	1.12±0.5%
-132.1	0.897	0.736	-18.3	1.12±0.5%
17cm×17cm				
-20.3	1.12	0.608	-1.27	1.28±1.7%
-66.0	0.926	0.738	-12.2	1.16±0.5%
-111.8	0.905	0.782	-22.6	1.16±0.5%
-132.1	0.929	0.754	-24.0	1.17±0.5%

a) Non-leakage term, b) Leakage term, c) Experimental error

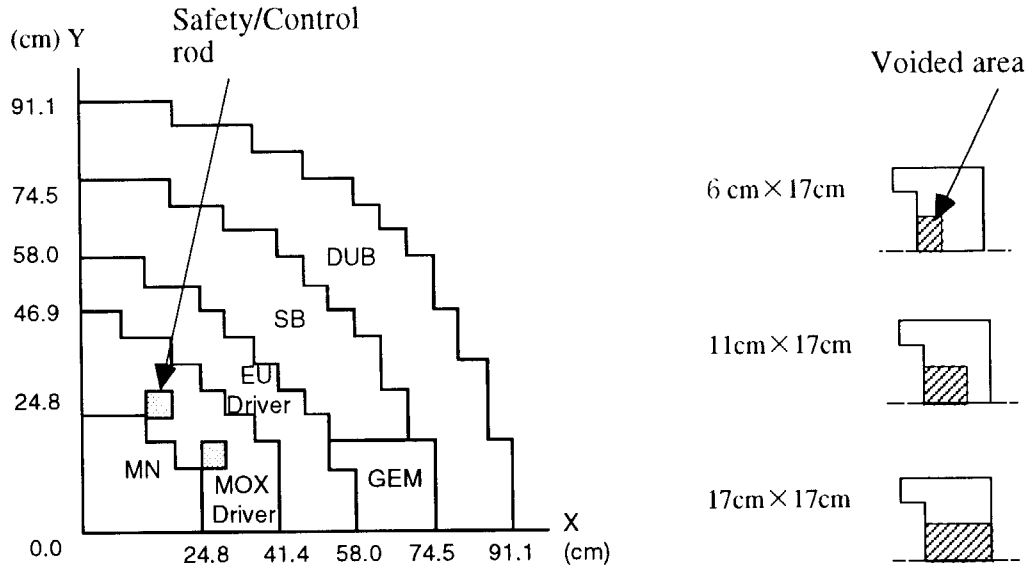

(a) XX-1 core　　(b) Voided area in the GEM

Fig. 3.3.1 Horizontal cross section of the XX-1 core and voided area

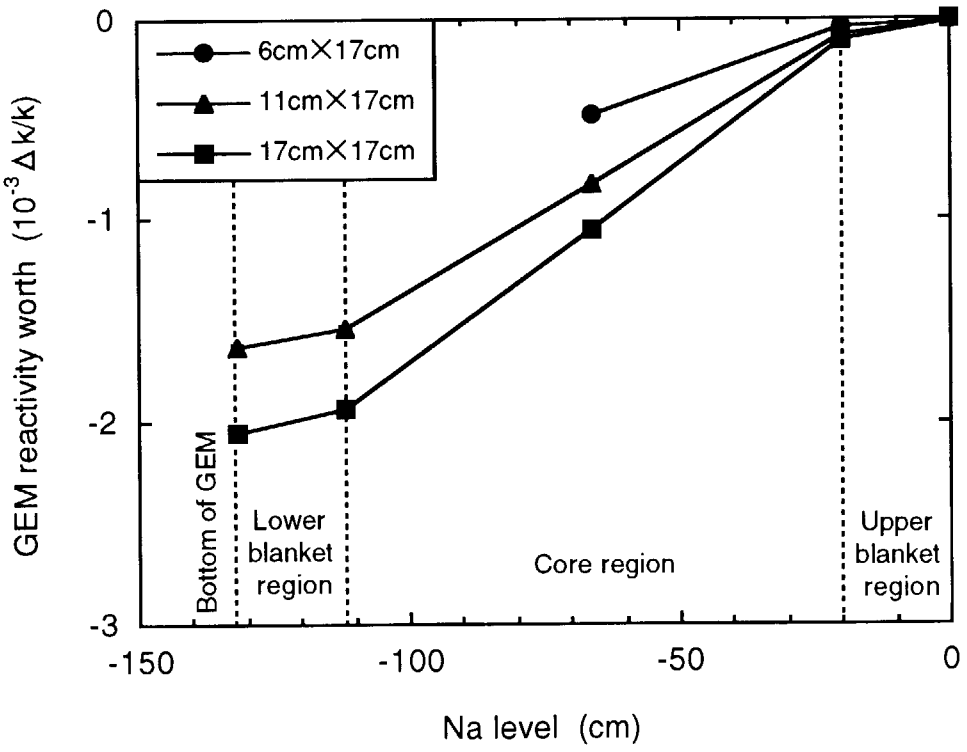

Fig. 3.3.2 Experimental results of the Ex-core GEM reactivity worth

3.4 Analysis of Benchmark Problems of Start-up Core Physics of HTTR Using the Diffusion Approximation

F.Akino and T.Yamane
(*E-mail* : akino@sensing.tokai.jaeri.go.jp)

The HTTR under construction in JAERI has a graphite moderated and low-enriched uranium fueled core of pin-in-block type[1]. The approach to the first criticality was planned by an annular core type fuel loading, because the experimental data of an annular core are strongly expected for validation of computer codes and models for the design of large scale annular core. The calculational benchmark problem of start-up core physics of HTTR was proposed by JAERI in the first meeting of IAEA-CRP-5 on the 24-28th Aug., 1998. Then, the analysis of critical masses and excess reactivities of annular core (18 fuel columns) and full core (30 columns) was carried out by the diffusion approximation. The first criticality[2] of HTTR was achieved with 19 fuel columns in an annular core on the10th of Nov., 1998.

The calculation was carried out by using the SRAC code[3] with the ENDF/B-IV nuclear data library. The calculational flow of effective multiplication factor, k_{eff}, for HTTR core is shown in Fig. 3.4.1. The following conditions were adopted in the cell calculation :

1) As the scattering law of thermal neutrons, the Young-Koppel's and the free gas models were used for graphite and the other materials, respectively.
2) Resonance absorption in the energy region from 1.1254 eV to 130.07 eV was calculated by PEACO routine to execute an ultra fine-group and multi-region cell calculation by the collision probability method.
3) The isotropic reflective condition was used at the outer boundary of the unit cell.
4) The core temperature was 300 K.

In the calculation of the effective cross section of the fuel block, the double heterogeneity due to the structure of fuel rods and the coated particles were considered by the collision probability method. The fuel block containing 33 fuel rods and 2 burnable poison (BP) rods was taken as a unit cell in the first and second fuel regions. For the third and fourth fuel regions, 31 fuel rods and 2 BP rods was taken as a unit cell.

In the calculation of the effective cross sections of the control rod block with three void holes, the collision probability method was also employed. The directional diffusion coefficients were calculated by the Benoist's formula. The void holes were filled with only helium gas at an atmospheric pressure. The thermal neutrons in the energy region from 10^{-5} eV to 1.1254 eV were divided into 39 groups and the fast neutrons in the energy region from 1.1254 eV to 10 MeV were divided into 22 groups in the cell calculation. Using the neutron spectra obtained by the cell calculation, the 61 group cross sections were collapsed into the 16 group ones (thermal: 8 groups , fast: 8 groups) for the core calculation. On the other hand, the

group constants for the permanent reflector region were calculated using the asymptotic spectrum in SRAC consisting of fission, 1/E and Maxwellian spectra. The core calculation was performed in a triangular-Z geometry with use of the modified 3-dimensional diffusion code CITATION which permits to use the directional diffusion coefficients. A cross section of the fuel block was divided into 6 triangular meshes, and in the axial direction, the core including the top and the bottom reflectors of 507 cm long was divided into 55 meshes.

The calculated values of k_{eff} during approach to the critical state are shown in Fig. 3.4.2. As the calculated result, the first criticality of annular core of HTTR was estimated to be achieved at 14 fuel columns. The cause of difference of calculated and measured values of critical mass is considered that impurity contents in dummy fuel blocks may be underestimated and the neutron absorption of air in pores of graphite is neglected in the calculation. The calculated excess reactivities of an annular core with 18 fuel columns and a full core were obtained to be about 4 % and 13.4 % Δ k/k. For the excess reactivity of full core, the calculated value was overestimated about 10 % in comparison with a preliminary measured one. In the calculation, the central control rod and three control rod rings of HTTR core were full out from core including the reflector.

Therefore, this calculational method which was established by analyses of VHTRC experiments[4] satisfies the accuracy required for the fundamental nuclear design of HTTR.

References

1) Saito,S., et al.: JAERI 1332,"Design of High Temperature Engineering Test Reactor (HTTR)" (1994).
2) Yamashita, K., et al. :Annual Meeting of the Atomic Energy Society of Japan, F7 (1999) [in Japanese].
3) Tsuchihashi,K., et al.: JAERI 1302, " Revised SRAC Code System" (1987).
4) Akino,F., et al. :J. At. Energy Soc. Japan, 31,682 (1989) [in Japanese].

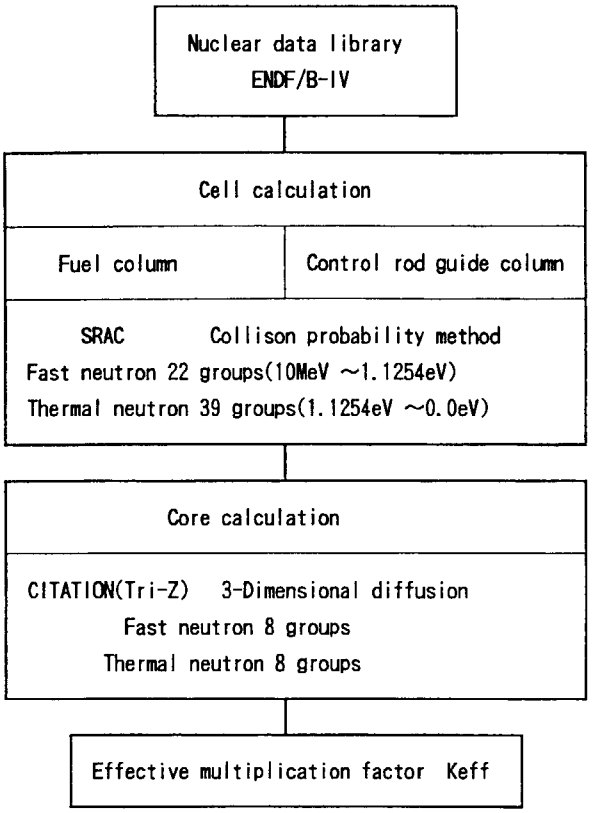

Fig. 3.4.1 Calculational flow for effective multiplication factor

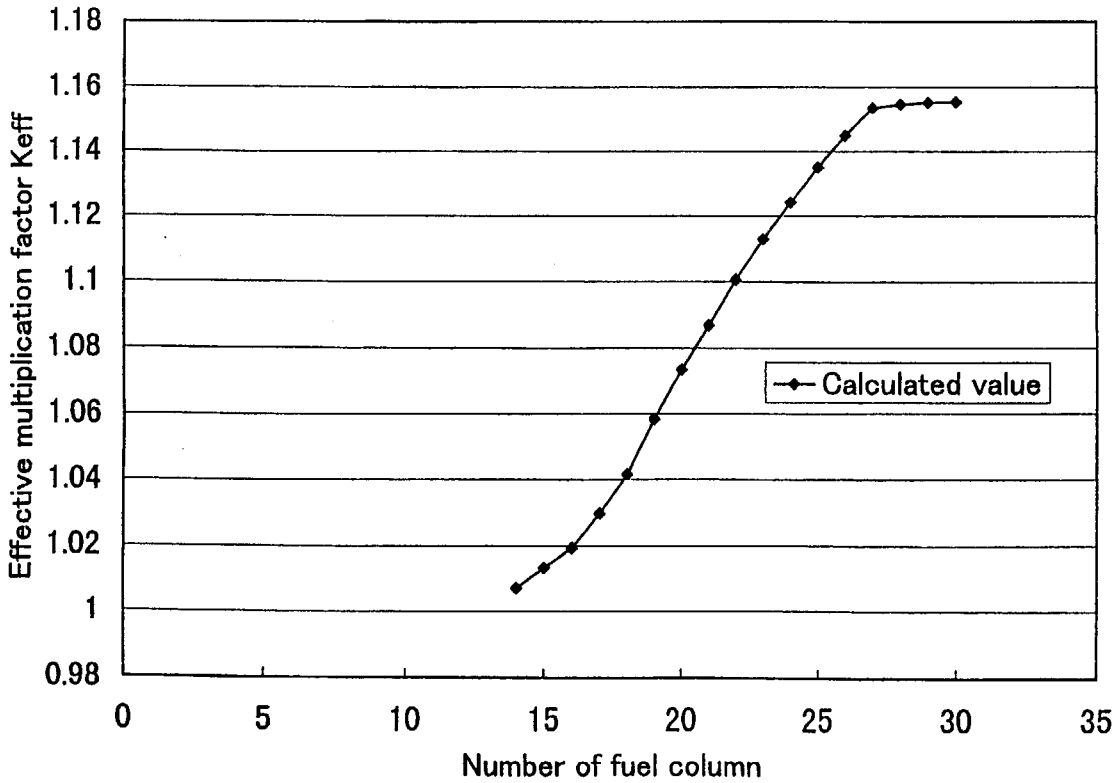

Fig. 3.4.2 Effective multiplication factor versus number of fuel columns

3.5 R&D of New Detection Method for Trace Amount of Fissionable Material in Waste

M. Haruyama, Y. Sugimoto, M. Takase, T. Osugi and K. Ara
(E-mail: haruyama@tru.tokai.jaeri.go.jp*)*

The authors have developed a new high–sensitivity method of non–destructive measurement for the fissionable materials contained in the concrete–solidified TRU (transuranic). The method of an active neutron assay has been invented to solve a problem in the conventional method in which the detection sensitivity varies widely depending on the location of the fissionable material in the solidified waste.

In the case of determination of fissile material quantities by active neutron assay, the influence of lopsided distribution and existing position of fissile material in which the composition of waste matrix have largely obstructed infallibility. This has been a great problem in the conventional active neutron assay and the detection sensitivity has usually differ more than 100 times for the fissionable material locations between in the surface and the center of the solidified concrete waste. In order to solve these problem, we have developed a new detection method that employs the neutrons moderated by the waste matrix itself.

Active Neutron Measurement Experiment

In experiments, a Pu sample was installed at one of the sample position with 2.5cm intervals in the radial direction of the concrete drum which weighs of 450kg, then the sample position was moved to the next position for following measurement. The interrogation neutron are of a 14MeV pulsed neutron with emission rate of 1×10^8 n/sec generated by a transformer type accelerator. The measurement time was 400 seconds at a generator pulse repetition rate of 100 pulses per second. The total number of neutrons generated was about 4.0×10^{10}.

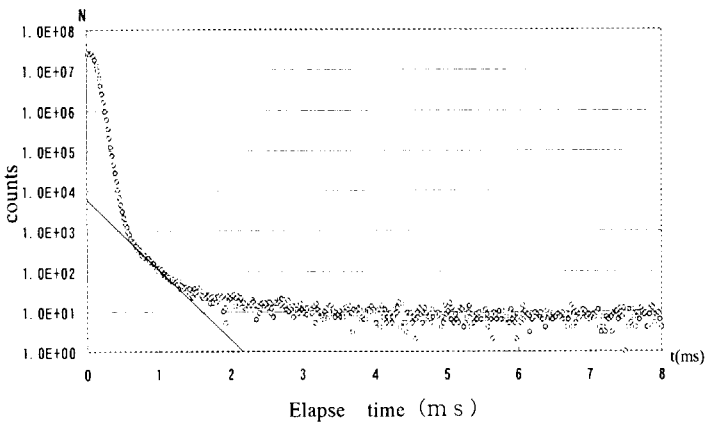

Fig. 3.5.1 Raw data obtained by active assay

Figure 3.5.1 shows raw data of active neutron measurements, which were obtained by a 1.0g Pu sample at the center of concrete drum. These are

time dependent data composed of the sum of three exponential functions. One of three exponential functions is a counting component that is treated in the new detecting method. This counting was educed and separated from the raw data by a computer analysis, as shown by a solid straight line in Fig. 3.5.1.

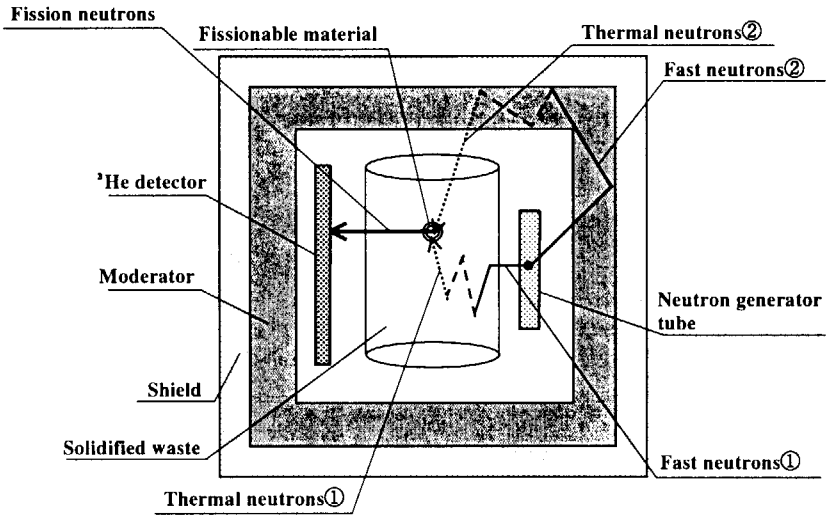

Fig. 3.5.2 Detecting process of conventional method and new method

In the conventional detection method, fast neutrons emitted from the neutron generator lose their energy in the moderator and become thermal neutrons as shown by ② line in Fig. 3.5.2. These thermalized neutrons are getting absorption by the concrete matrix and stainless steel blocks after penetrating inside the waste drum. The absorption tends to become greater at close with the center of concrete drum and it brings about baneful influence. Consequently, the detection sensitivity tends to deteriorate at closing center.

Contrariwise, the new detection method can well avoid the obstructive effect in the conventional detection method. The fast neutrons from accelerator are moderated to the thermal neutrons by repeating collisions with nuclide of matrix after penetrating directly to the waste drum as shown by ① line in Fig. 3.5.2. Then, those neutrons moderated by the concrete matrix itself increases a chance of reaction with close-in fissile nuclide. As a result, the probability of induced fission reaction increases at every location inside the concrete drum notably. Particularly, it is conspicuous by the center of concrete drum.

Result

Figure 3.5.3 shows the variation of detection sensitivity with the position of fissile (Pu) sample, obtained with the measurements by the new method and conventional one for comparison. The ^{3}He counters in the detector bank (see Fig. 3.5.2) detects fast neutrons emitted from the 1.0g-Pu sample located at each sample position of 2.5cm interval in the radial direction of the concrete drum.

It was confirmed that there is a great difference between the response of the new method and the conventional one. The improvement by the new method is conspicuous as

the sample position become close to the center of the concrete drum.

New detection method presented the great result. It well applied the self-moderation effect by concrete matrix of waste drum. A deterioration of fission-neutrons detection efficiency for the center position is 1/6.5 times as compared with that for the surface position in the concrete drum. Inversely, the fission rate for the central position is 5.7 times higher than that for the surface position. Accordingly, a difference of detection sensitivity between those for the center point and the surface point is counterbalanced only 1/1.14 times as shown by ① line in Fig. 3.5.3.

As a result, deviation of sensitivity in the new detection method from average line, which sensitivity depends on radial position, is within only±25%. On the other hand, the difference of detection sensitivity between the center and the surface point in the conventional method is 1/120 times as shown ② line in Fig. 5.3.3.

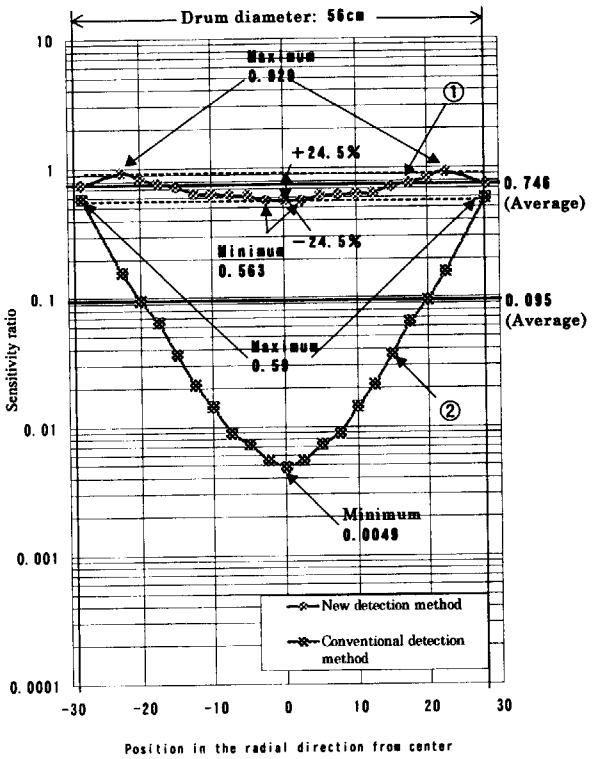

Fig. 3.5.3 Variation of detection sensitivity with Pu sample position in the radial direction

The new detection method can avoid an occurrence of extreme sensitivity difference to be biased by the distribution and different location of fissionable materials. Namely, it could be said that there is no necessity to correct that difference by the determination of fissionable material distribution and location in the solidified waste if the measurement with reliability of 1± 0.25 is acceptable.

In conclusion, the new detection method can improve greatly the fission response. Accordingly, detection limit is improved extremely by center of drum. If optimization of apparatus for new detection method is performed, one can expect to more decrease the position-dependent sensitivity difference; namely less than 25%.

Reference

1) Haruyama, M., et al.: JAERI-Review 96-012, p144 (1996).
2) Haruyama, M., et al.: JAERI-Review 97-011, p170 (1997).

4. Advanced Reactor System Design Studies

The Reduced-Moderation Water Reactor (RMWR) is an advanced water-cooled reactor which aims at effective utilization of uranium resource, high burn-up and long operation cycle and plutonium multi-recycle. Four types of RMWR core concepts were developed. 1) The BWR type core without blankets: Reduction of water to fuel volume ratio (Vm/Vf) of the bundles was realized by introducing hollow tubes in flow channels and adding follower on control rods. Instantaneous conversion ratio of 1.1 and negative void coefficient were achieved. 2) BWR type double-flat-core with an upper, lower and inner blankets: A discharge burn-up of 45GWd/t and the conversion ratio of 1.1 were attained. 3) Long operation cycle BWR type core: The proposed core has void tube subassemblies to reduce the void reactivity coefficient. A discharge burn-up of 60GWd/t and the conversion ratio of 1.01 were attained. 4) The PWR type RMWR core that has axial and radial blanket inside the core and absorber in the reflector: The burn-up of 45GWd/t, the conversion ratio of 1.04 and nearly zero void reactivity coefficient were obtained.

For the sake of investigating the thermal-hydraulic feasibility of RMWR, CHF experiment and analysis were conducted. The experiment was performed to obtain the CHF data for the narrow rod gap width of 1mm and 1.5mm. Subchannel analyses with COBRA-Ⅳ- I code were performed to evaluate the applicability of an existing prediction method.

For the MOX fuel critical experiment in TCA simulating the RMWR cores, a required number of MOX and UO_2 fuels was evaluated in terms of multiplication factor considering the effect of void fraction.

Aiming to improve the fuel utilization, a high burn-up full MOX PWR core with increasing Vm/Vf of 3.0 was investigated. In comparison to the previous result of Vm/Vf of 2.6, the core characteristics were significantly improved. As a thermal hydraulic designing of the high burn-up full MOX PWR, an effect of rod diameter was investigated to prevent the reduction of DNBR. Analyses of small break LOCA and control rod cluster ejection accident were preformed for the high burn-up full MOX PWR. Together with the previous analyses results, feasibility of the designed system was demonstrated.

4.1 Conceptual Designing of Reduced-Moderation Water Reactor (1) － Study on High Conversion BWR Type Core without Blanket －

T. Shirakawa, T. Okubo and M. Ochiai
(*E-mail :* shira@jprews1.tokai.jaeri.go.jp)

Our design goals are a blanketless simple core configuration, a conversion ratio more than 1.0 and negative void coefficient with keeping current ABWR fuel bundle configuration. Since fissile Pu increases in discharged fuel by this design, new fuel can be fabricated with the material obtained by the simply reprocessed discharged fuel only adding depleted UO_2 . Therefore, there is no need to separate U or Pu from spent fuels. This is expected to result in the simplification of the reprocessing process, and hence, the reduction of fuel cycle cost.

Base fuel bundle configuration is the same as ABWR 9X9 square lattice bundle. This fuel bundle has axial distribution in PuO_2 content to reduce axial power peaking and to improve conversion ratio. Investigation to reduce water to fuel volume ratio (Vm/Vf) of the bundle has been carried out by increasing fuel pin diameter, introducing hollow tubes in flow channels and adding follower on control rods. The fuel bundle geometry is shown in Fig .4.1.1.

Neutronics calculations for 2-dimensional XY fuel assembly lattice and 3-dimensional XYZ core burn-up were performed by using JAERI's general purpose neutronics code system SRAC95.

Table 4.1.1 gives core neutronics specifications. The low burn-up is due to keeping void coefficient negative. Figure 4.1.2 shows that normal core reactivity is higher than that for 100% void at the beginning of cycle and both core reactivities become almost equal at the end of cycle. Eigenvalues at 100% instantaneous steam void are considered to be reference value, because large break LOCA (Loss-Of-Coolant Accident) is not expected to occur in ABWR. An instantaneous conversion ratio of 1.1 and negative void coefficients are realized by the blanketless design concept with 1/3 core height comparing to ABWR.

Figure 4.1.3 shows radial power distribution without control rods. Maximum linear power density at the beginning of equilibrium cycle is 610W/cm and at the end of cycle is 561 W/cm. We can decrease the maximum linear power density at the beginning of the cycle by control rod. Therefore, the maximum linear power density is 561 W/cm of the end of cycle. This value is almost the same as for BWR/4 7x7 fuel bundle.

Table 4.1.1 Neutronics specifications

item		
fuel rod configuration	9X9 square lattice	
discharged fuel cumulative conversion ratio	~1.11	
fuel length(m)	1.56	
clad outer diameter(mm)	15.17	
clad thickness(mm)	0.5	
PuO_2 content(wt%)	10.5 and 9.0 (axialy distributed)	
total thermal power(MW)	2355.6	
cycle length(EFPD)	328	
discharged fuel burnup(MWd/t)	13.5	
equilibrium core time	BOC	EOC
keff(historical average void 45%. rated power)	1.007	1
keff(instantaneous steam void 100%. rated power)	0.997	1
maximum linear power density	610(W/cm)	561(W/cm)

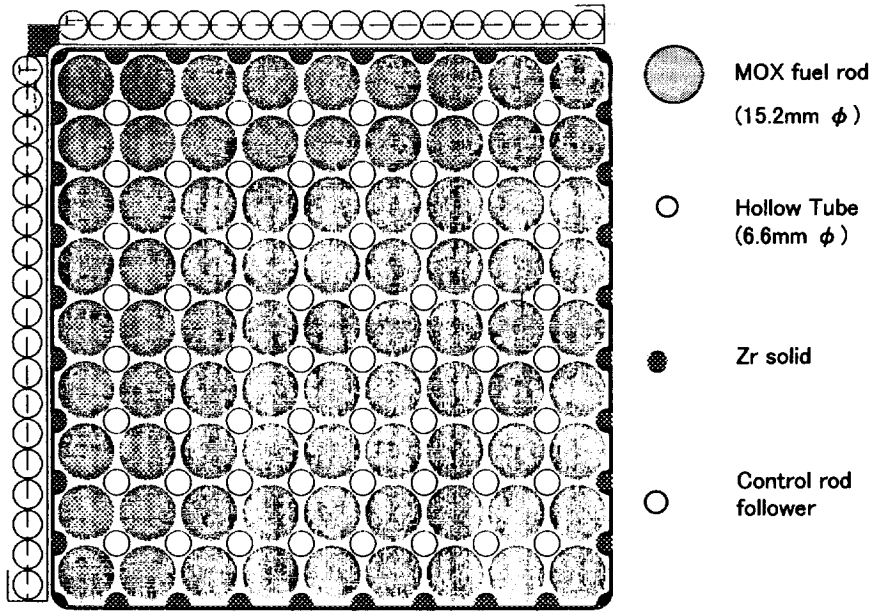

Fig.4.1.1 Fuel bundle sectional view

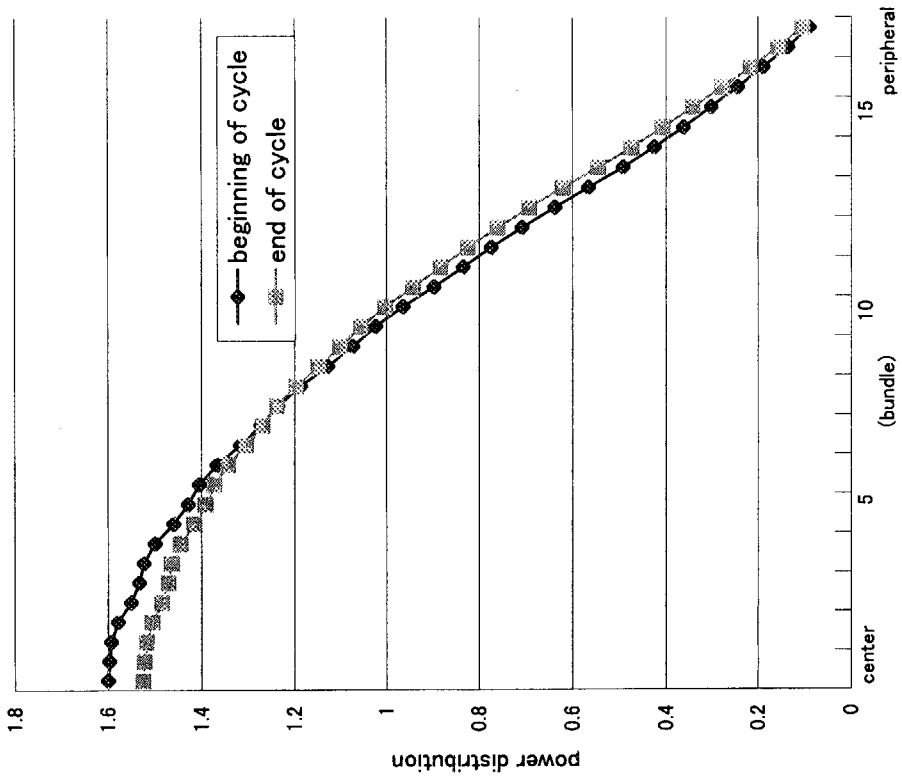

Fig.4.1.3 Equilibrium core radial power distribution

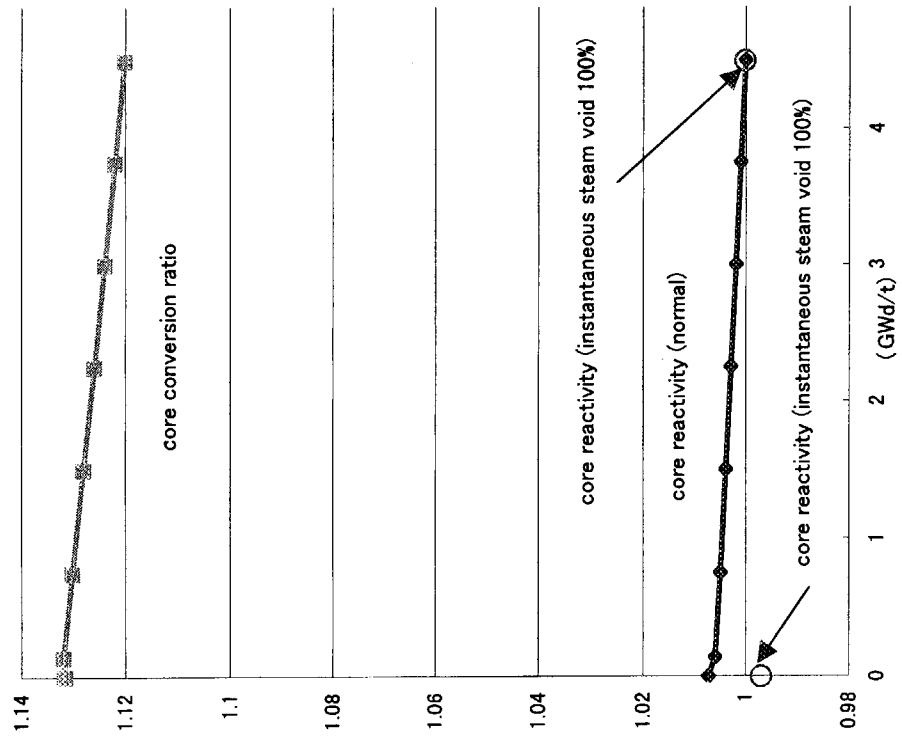

Fig.4.1.2 Core reactivity and conversion ratio

4.2 Conceptual Designing of Reduced-Moderation Water Reactor (2)
－ Study on High Conversion BWR Type Core －

T.Okubo, M.Ochiai, R.Takeda*[1] and S.Wada*[2]
(*E-mail:* okubo@jpsrews1.tokai.jaeri.go.jp)

A BWR type reduced-moderation water reactor aiming at the conversion ratio of 1.1 has been studied in order to investigate the attainable upper limit for the conversion ratio. The reactor with such a high conversion ratio is mainly expected to be beneficial to the long-term energy supply with the uranium resource. In order to attain the conversion ratio of 1.1, the effective moderator to fuel volume ratio (Vm/Vf) is set about 0.17 by using fuel rods with a large diameter of 14.5 mm arranged in the triangular lattice with the gap width of 1.3 mm between rods, as well as the core average void fraction is increased to 70%. The cross section of the fuel assembly is shown in Fig. 4.2.1. The fuel assembly and the channel box are hexagonal. Control rods are Y-shaped and with the follower for water removal.

In order to keep the void reactivity coefficient negative, the core is designed very short of about 20 cm high. As shown in Fig. 4.2.2, the core is the double-flat-core type one with the upper, lower and inner blankets. As a result of this core design, the void reactivity coefficient is evaluated to be negative of $-1.0\times10^{-4}\,\Delta k/k/\%void$. However, the diameter of the core must be increased by this short core design and it is evaluated to be about 7.2 m for 1,100 MWe output.

Major characteristics of the core are summarized in Table 4.2.1 compared to values for ABWR. The average content of fissile plutonium in each MOX part of the core is 18 w/o. Although the maximum linear power density is 17 kW/ft, this value is lower than the limit of 18.5 for the previously used 7×7 type BWR fuel assembly with the same large fuel rod diameter. The local peaking factor in the assembly is designed to be less than 1.05 by introducing plutonium contents distribution. The core water mass flow rate is set at about 1/4 of that in ABWR to establish the high core void fraction, and hence, the core outlet steam quality is about 4 times high of that in ABWR. The minimum critical power ratio is evaluated to be 1.3 with the modified CISE correlation[1].

*1 Hitachi, Ltd., *2 The Japan Atomic Power Company

The average core discharge burn-up is 45 GWd/t including the inner blanket. The cycle length is 14 effective full power months. The cladding material is assumed to be the Zyrcaloy as in ABWR. The gap width of 1.3 mm between rods is the evaluated minimum value considering structural effects such as bowing as well as the thermal hydraulic effects.

Reference

1) Matsumoto, T. *et al.*: "Development of Critical Power Correlation for Tight Lattice Fuel Assembly", *1987 Annual Mtg. Atomic Engy. Sco. Jpn.*, E40 (1987).

Table 4.2.1 Major core parameters of high conversion BWR type RMWR

Item		RMWR	ABWR
Electric output	MWe	1,100	1,356
Thermal output	MWt	3,188	3,926
Pressure	MPa	7.2	7.2
Core outer diameter	m	3.60	2.69
No. of fuel assembly		924	872
Discharge burn-up	GWd/t	45	38
Core height*	m	0.68	3.71
Core water flow rate	10^4t/h	1.3	5.2
Core outlet quality	%	55	14.5
Core void fraction	%	70	38
Average Pu content	%	10.2	3.6^+
Pu amount	t	12.1	—
Pu conversion ratio		1.06	—
Conversion ratio		1.10	—
Max. linear power	kW/ft	17	12.5
MCPR		1.3	1.30
Void coefficient	$10^{-4}\Delta$k/k/%void	-1.0	-7.0
Operation length	EFPM	14	13
Axial Pu content Distribution	w/o cm	18	18.5
	DU cm	0	29.5
	w/o cm	18	20.0

Pu : Fissile Pu, ＋ : U enrichment, ＊ : Including inner blanket of 29.5 cm high

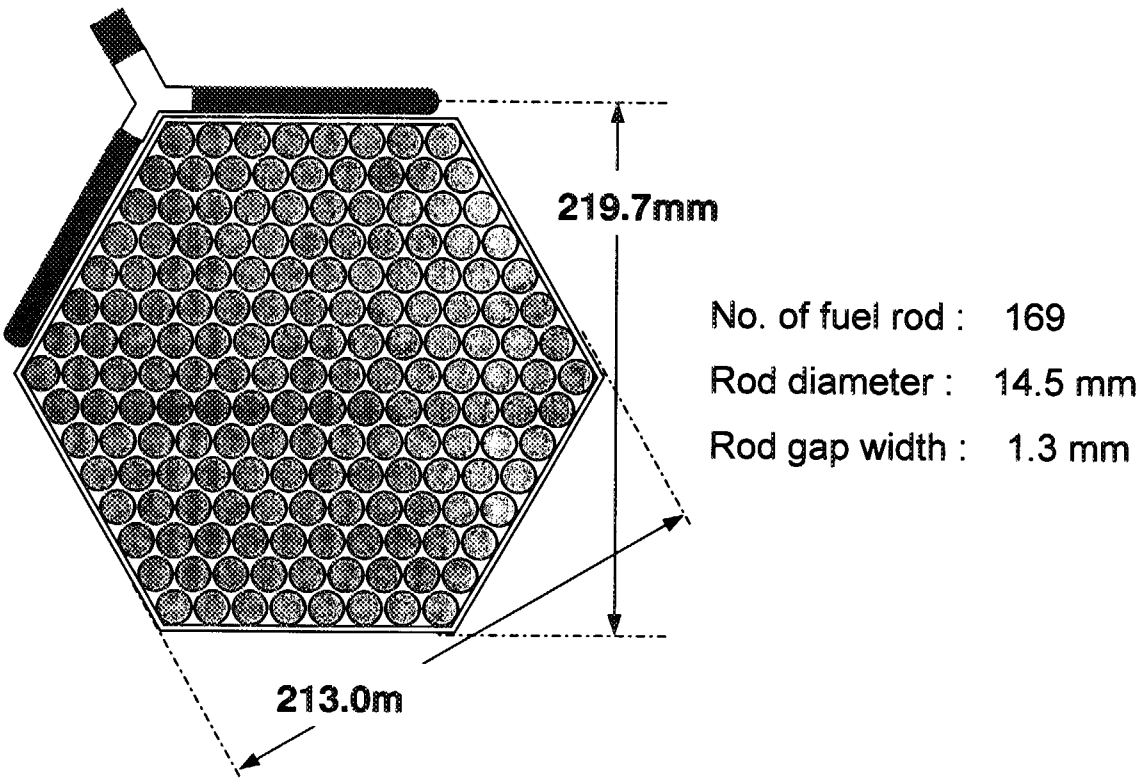

Fig. 4.2.1 Configuration of fuel rod assembly

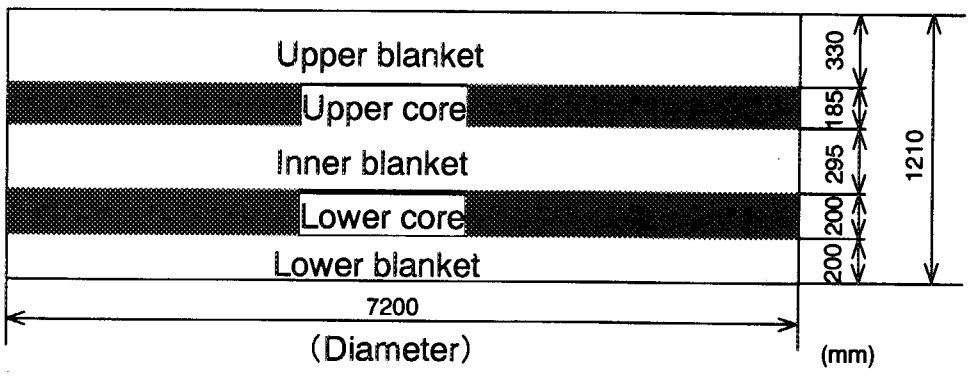

Fig. 4.2.2 Core vertical configuration

4.3 Conceptual Designing of Reduced-Moderation Water Reactor (3)
－ Study on Long Operation Cycle BWR Type Core －

T. Shirakawa, T. Okubo, M.Ochiai, T.Yokoyama[*1] and S.Wada[*2]
(*E-mail:* shira@jprews1.tokai.jaeri.go.jp)

A feasibility study on a BWR core whose operational cycle length is longer than 2 years, conversion ratio is larger than 1.0 and void reactivity coefficient is negative was performed.

We performed the parametric survey with 2 dimensional diffusion burn-up code for a core with an electric output of 1350MWe. The results of the survey is as follows:

① The conversion ratio decreases 1.5% per 10GWd/t of discharge burnup increase.

② The conversion ratio increases 5.5% per 0.1 of water to fuel volume ratio (V_m/V_f) decrease.

③ The conversion ratio increases 3.0% per 10% of core void increase.

④ The influence of axial blanket thickness saturates at 30cm for 1.6m height core.

Based on the parameter survey results the core concept is constructed. Figure 4.3.1 shows the core configuration. A triangular tight lattice configuration of fuel pins with hexagonal wrapper tube and this large size subassembly whose arrangement pitch is 304mm are applied. Figure 4.3.2 gives fuel subassembly specification. Void tube subassemblies are introduced among fuel subassemblies in order to reduce the void reactivity coefficient. The void tube subassembly is a device for decreasing void reactivity coefficient by a neutron-streaming effect under the increase in void in the void tube subassembly. The void tube subassemblies are arranged in the core by about 20% of fuel subassemblies. Figure 4.3.3 shows void tube subassembly specification.

The main core characteristics such as discharge burn-up, conversion ratio and void reactivity coefficient under 2-year operational cycle length and 4 batch fuel exchange were estimated. The results are as follows: the discharge burn-up is 60GWd/t, the conversion ratio is 1.01 and the void reactivity coefficient is nearly $-2\times10^{-4}\triangle k/k/\%$.

Thermodynamic survey was also performed. When the radial peaking factor is larger, the core pressure drop becomes larger due to larger water flow rate required. The results showed that the radial peaking factor should be reduced to 1.2 in order to keep core pressure drop as much as the conventional BWR and to attain the critical power ratio about 1.35.

We will perform further detailed study on transient behavior of void tube subassembly core.

---

*1 Toshiba Co. *2 The Japan Atomic Power Co.

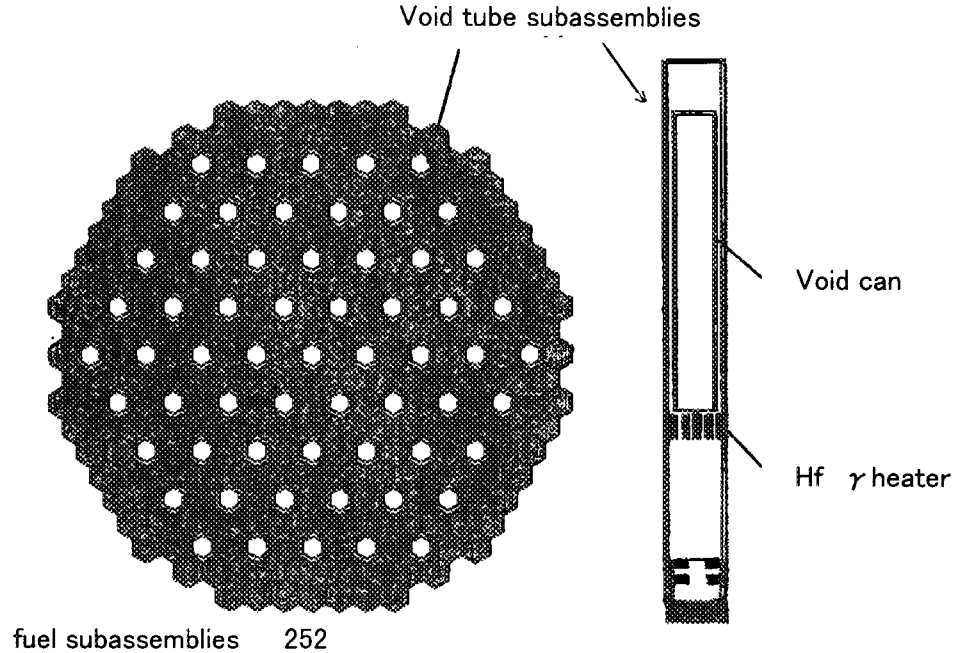

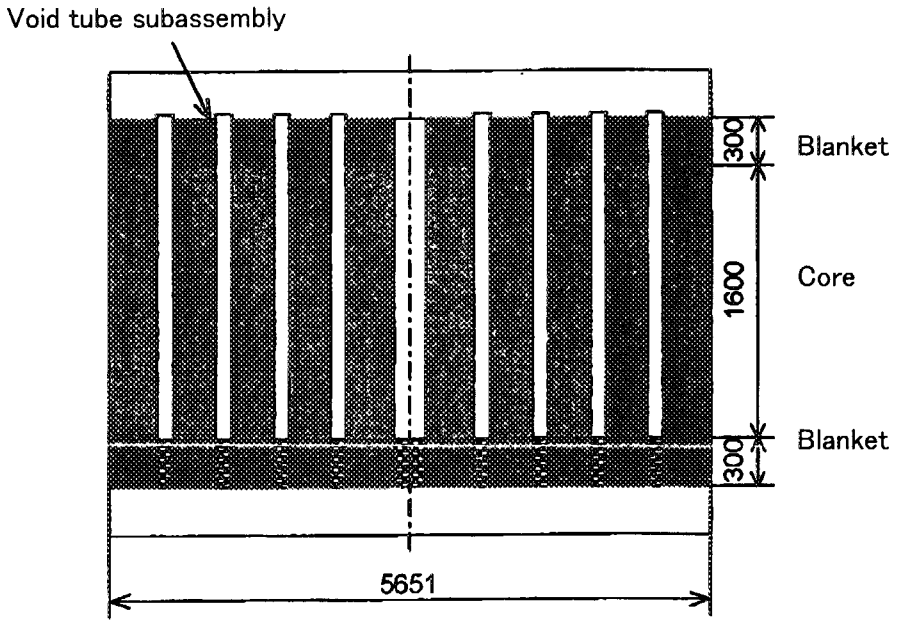

Fig.4.3.1 Core configuration

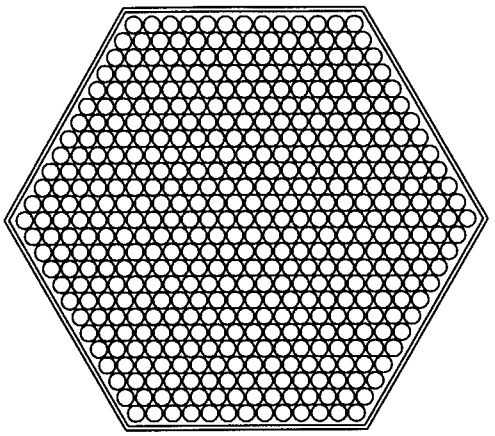

item	specification
fuel pin outer diameter	11.91mm
fuel pin inner diameter	11.11mm
fuel pin pitch	13.21mm
fuel pin number/bundle	469
fuel smeared density	93%
channel box inner pitch	289mm
channel box outer pitch	299mm
subassembly pitch	304.2mm

Fig.4.3.2 Fuel subassembly dimension

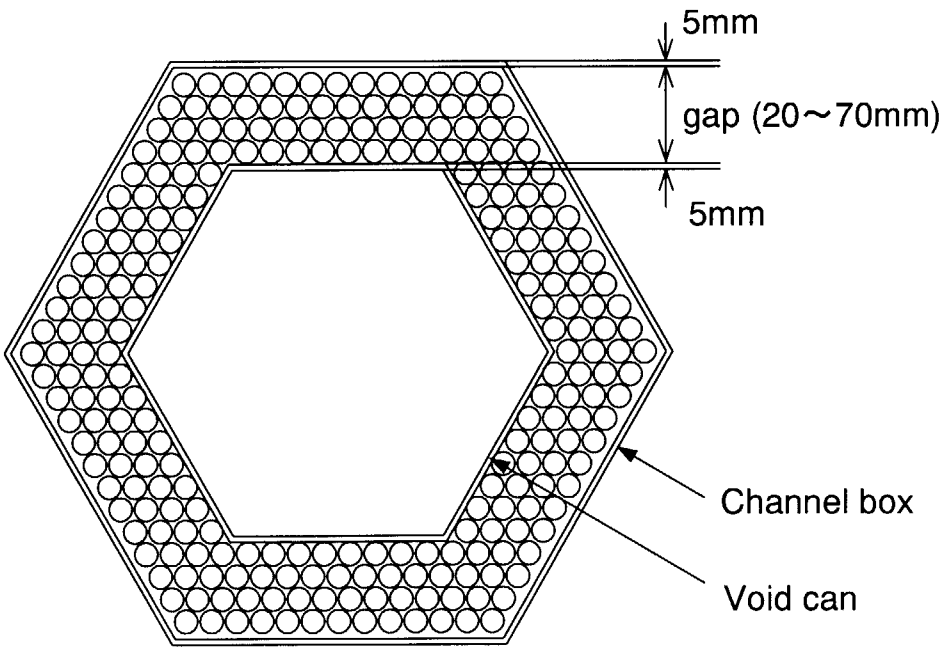

Fig.4.3.3 Void tube subassembly horizontal view

4.4 Conceptual Designing of Reduced-Moderation Water Reactor (4) – Study on High Conversion PWR Type Core –

S. Shimada, T. Kugo, T. Okubo, M. Ochiai, M. Ishida*1, S. Wada*2

(*E-mail* : shimada@jpsrews1.tokai.jaeri.go.jp)

Studies on high conversion PWR type core using the light water or the heavy water as the coolant have been performed[1), 2)]. To improve the design, the efforts to evaluate the effects of fuel lattice spacing and moderator material on nuclear characteristics were started[3)]. Void reactivity coefficients were positive as in the sodium cooled fast reactor, if any special measures were not taken. To make the void reactivity coefficients negative was the most important efforts in this design study. Several methods were evaluated to make void reactivity coefficients negative. One core concept was constructed combining these methods to improve void reactivity coefficients.

Parametric studies Parametric studies were performed for the conversion ratio and void reactivity coefficients by changing rod diameter, distance between fuel rod surfaces and moderator material. The conversion ratio and void reactivity coefficients depend on only the water to fuel volume ratio, but not rod diameter or rod gap. Although the heavy water gives more positive void reactivity coefficients, comparing the light water, it can give the higher conversion ratio as expected.

Void reactivity coefficients of the tight lattice core are positive for the infinite situation. Neutron leakage plays very important role to make void reactivity coefficients negative. Reducing the core height, blankets located in radial or axial direction in the core reduce the void reactivity coefficients. Placing absorber in the reflector to absorb neutrons from the core is also effective to reduce the void reactivity coefficients. The distance of about 30cm from the core periphery was optimal. The void reactivity coefficients should be negative when these methods are applied simultaneously.

Core concept Axial and radial blanket are located in heterogeneous configuration and absorber is placed in the reflector as shown in Fig. 4.4.1. MOX fuel rod configuration is the

---

*1 MHI and Current affiliation : Comision National de Energia Atomica Ar. Libertador 8250 (1429), Buenos Aires, Argentina

*2 The Japan Atomic Power Company

same as for UO_2 rod of the 17×17 type fuel assembly, but the cladding material is selected SUS-316 instead of zircaloy. The cladding thickness is determined as 2/3 of zircaloy. Number of fuel rods in an assembly is 504. The rod size of blanket is a little bit lager than MOX rod to obtain higher conversion ratio. The plutonium composition used in evaluation is shown in Table 4.4.1. The plutonium fissile weight percent is 15 to obtain the burn-up of about 45GWd/t and attainable power is 1000MWe. The main parameters of this core are shown in Table 4.4.1. Nearly zero void reactivity coefficients and the conversion ratio more than 1.0 are obtained.

A cluster type control rod with 6 pins is employed. Enriched boron of 90% B-10 is used as the material of control rod. 6 rods per a cluster are required in the design. The number of control rod clusters is 84. Shutdown margin of 2.8 to 3.0 %Δk/k is obtained by this control rod configuration . The more detailed evaluation will be continued.

References

1) Shimada, S., *et al.* : "Pressurized Heavy Water Moderated Tight Lattice", *Annual Meeting of the Atomic Energy Society of Japan,* F51 (1998)

2) Ishida, M., *et al.* : "Conceptual Design of recycle type PWR" *1998 Fall Meeting of the Atomic Energy Society of Japan,* E10 (1998)

3) Ishida, M., *et al.* : "Study on High Conversion PWR Core" *1999 Annual Meeting of the Atomic Energy Society of Japan,* F38 (1998)

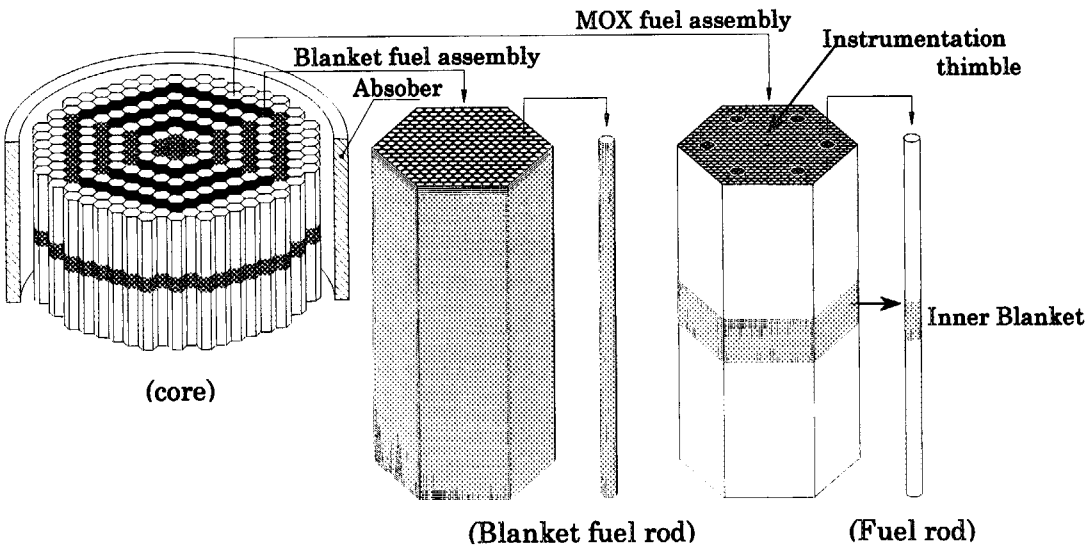

Fig. 4.4.1 Core Configuration

Table 4.4.1 Core summary data

Core thermal power		2900 MWt
Electric power		1000 MWe
Core effective diameter		5 m
Core effective height		2 m
Operating pressure		157 kg/cm^2
Inlet temperature		290℃
Outlet temperature		325℃
Number of fuel assemblies		379
Number of MOX fuel assemblies		210
Number of blanket assemblies		169
Number of fuel rods/assembly		504
Fuel diameter		9.5 mm
Pellet diameter		8.6 mm
Pitch		10.5 mm
Cladding material		SUS-316
Axial blanket length		40 cm
Water to pellet volume ratio		0.5
Fissile Pu enrichment		15.0 wt%
Pu composition(wt%)		^{238}Pu, ^{239}Pu, ^{249}Pu, ^{241}Pu, ^{242}Pu, ^{241}Am 1.9, 57.5, 23.3, 10.0, 5.4, 1.9
Number of blanket/assembly		271
Diameter		13.5 mm
Pellet diameter		12.5 mm
Pitch		14.7 mm
Cladding material		SUS-316
Number of control rods		84
Number of pins/cluster		6
Absorbing material		90% Enriched B-10(B_4C pellet)
Pin diameter		21.5 mm
Peeking factor	Fxy	2.5 (Seed fuel average)
	Fz	1.4
	Fq	3.5
Linear heat rate (average)	MOX fuel	11.4 kW/m
	Blanket	3.5 kW/m
Void reactivity coefficient		～0 Δk/k/%Void
Conversion ratio		1.04
Burn-up		45 GWd/t
Shut-down margin		2.8% Δk/k(@BOL), 3.0% Δk/k(@EOL)

4.5 CHF Experiments for Reduced-Moderation Water Reactor

H. Yoshida, F. Araya, T. Okubo, T. Yoritsune, H. Watanabe, T. Satoh and M. Ochiai
(*E-mail:* yoshida@jpsrews1.tokai.jaeri.go.jp)

In the reduced-moderation water reactor (RMWR) concept, the gap spacing between the fuel rods is remarkably narrower than in a reactor currently operated. Therefore, an evaluation of the core thermal margin becomes very important in the design of the RMWR. The gap between the fuel rods is about 1 mm, and no experimental data are available from the past the critical heat flux (CHF) experiments. Then, we have performed CHF experiments to obtain basic data for studying the RMWR concepts and check the accuracy of CHF correlation.

The steady state CHF experiments were performed with a high-pressure water loop. The test section consists of seven heater rods arranged in a triangular lattice, whose cross section is shown in Fig. 4.5.1(a). The outer diameter of the heater rod is 9.5mm. Two types of test sections with different rod gap widths (1mm and 1.5mm, respectively) have been used in the experiment.

Thermocouples are embedded in the cladding of the heater rod to detect the onset of CHF. The heating power of the central rod is about 1.2 times higher than that of the peripheral one to ensure the first CHF occurrence at the center rod, because effects of the unheated flow shroud in the center rod are relatively small in comparison to the peripheral rods. The heated length of heater rods is 1.8m and the axial power distribution is a chopped cosine shape with the peaking factor of 1.35. The heater rods are supported by seven grid spacers shown in Fig. 4.5.1(b).

An example of experimental results of critical heat flux (inlet water temperature and pressure are 320°C and 15.5MPa, respectively) is shown in Fig. 4.5.2. As the mass velocity increases, CHF also increases. At the mass velocity smaller than 2000 $kg/s \cdot m^2$, the differences between results for rod gap 1.0mm and for 1.5mm are small. However, in the cases of mass velocity larger than 2000 $kg/s \cdot m^2$, the differences become large, and CHFs for rod gap 1.0mm are about 10% smaller than for 1.5mm. Comparisons between these experimental results and numerical simulations are shown in next section (sec. 4.4).

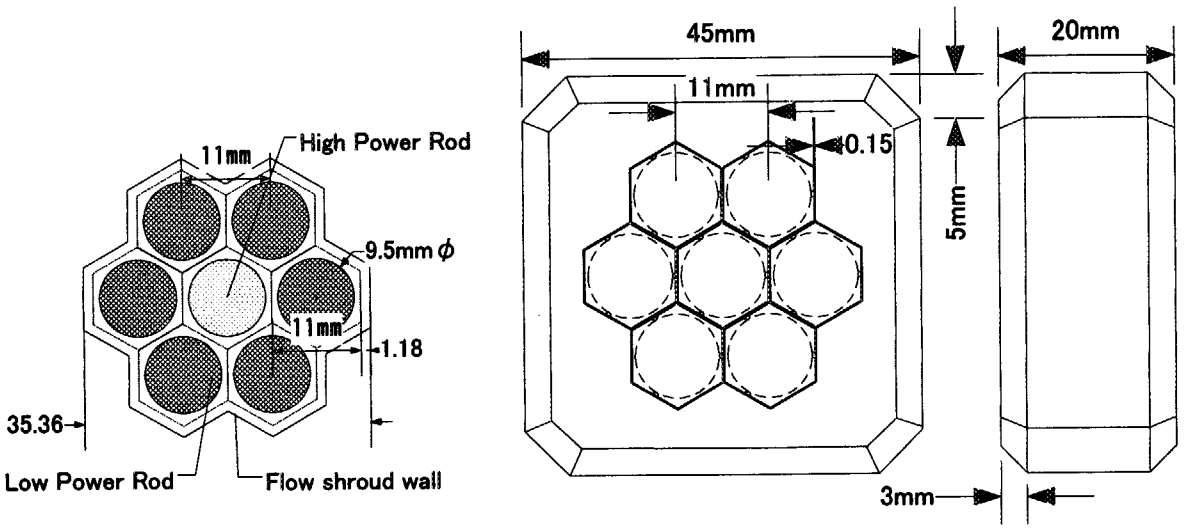

(a) Cross section　　(b) Grid Spacer

Fig. 4.5.1 Cross Section of test section and grid spacer

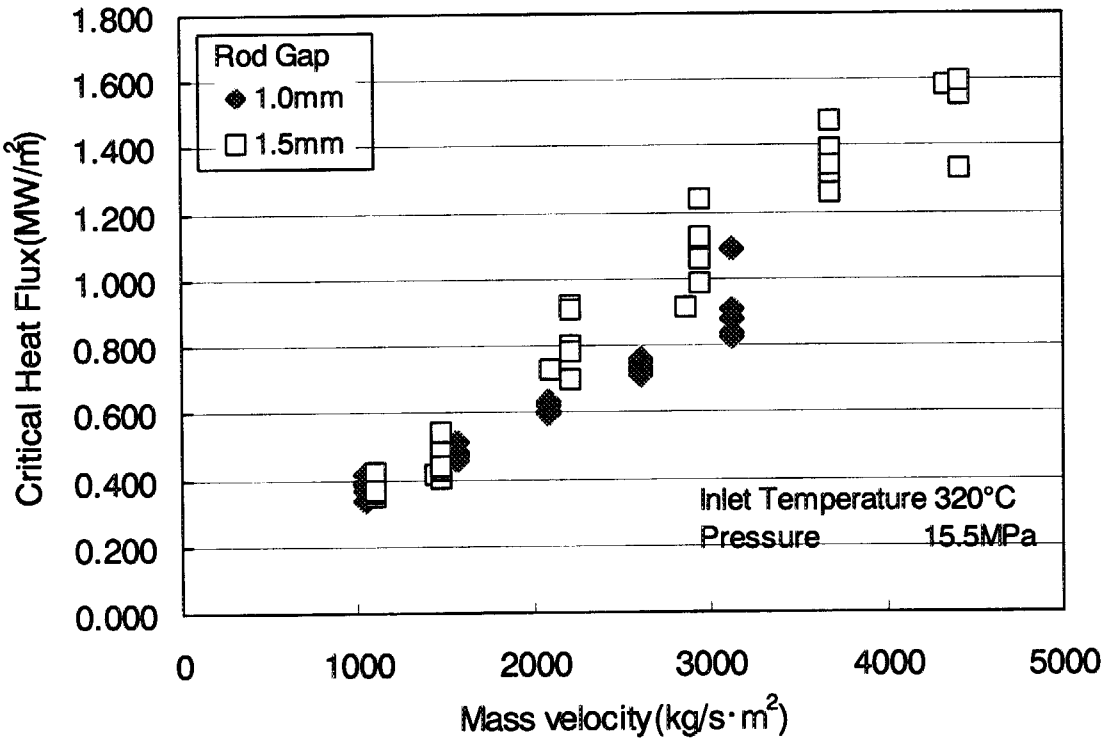

Fig. 4.5.2 Example of rod gap effects on critical heat flux

4.6 Subchannel Analysis on CHF Experiments for Reduced-Moderation Water Reactor

T. Yoritsune, H. Yoshida, F. Araya, T. Okubo, H. Watanabe, T. Satoh and M. Ochiai
(*E-mail :* tyori@koala.tokai.jaeri.go.jp)

In the present study, subchannel analyses were performed on the steady-state CHF experiments for the tight lattice core (See section 4.5), with an objective to evaluate applicability of an existing evaluation method to the reduced-moderation water reactor core. The analyses were performed by using the COBRA-IV-I subchannel analysis code[1] coupled with the KfK critical heat flux correlation[2] which was developed for triangular tight lattice core. In the analyses, the subchannel noding shown in Fig. 4.6.1 is used for the cross section and 30 axial division is applied for the flow direction. The major thermal-hydraulic correlations, parameters and factors adopted in the analyses are as follows:

Subcool void model:		Levy's subcool void model
Bulk void model:		EPRI bulk void correlation
Spacer loss coefficient:		1.0
Turbulent mixing coefficient:	Single phase:	0.003
	Two-phase:	Same as single phase
Solution algorithm:		Implicit solution

Where, the above turbulent mixing coefficient was determined based on an experiment[3] for single phase flow mixing in four and seven-rod bundles with rod pitch spacing of 11.4mm and 10.7mm. For the two-phase turbulent mixing coefficient, it is expected that the mixing is promoted more than in the single phase flow. But, it was set the same value as the single phase mixing coefficient in the present analyses intending to be the severe condition, because sufficient knowledge on it for the tight lattice core has not accumulated.

The analytical results in the case of heater rod pitch of 11mm (gap width of 1.5mm) are shown in Fig. 4.6.2. ECHFR is defined as a ratio of calculated CHF to measured CHF. As shown in the figure, the ECHERs are in the range of 0.6～1.0. This means that the calculation gives conservative evaluation. Furthermore, the figure shows a tendency that as inlet temperature increases, ECHFR becomes high, and ECHFR decreases as local mass velocity becomes high.

The analysis on the experimental data for the rod pitch of 10.5mm (gap width of

1.0mm) is being continued. The applicability of the CHF evaluation method for the RMWR core will be concluded based on all results from analyses.

References

1) Wheeler, C. L., *et al.*: "COBRA-IV-I: An Interim Version of COBRA for Thermal-Hydraulic Analysis of Rod Bundle Nuclear Fuel Elements and Cores", BWL-1962 (1976).

2) Dalle Donne, M., *et al.*: "Critical Heat Flux Correlation for Triangular Arrays of Rod Bundles with Tight Lattices, Including the Spiral Spacer Effect", Nuclear Technology, 71, 111 (1985).

3) Murao, Y., *et al.*: "Thermal-Hydraulic Study of a High Conversion Light Water Reactor", JAERI-M 91-055 (1991).

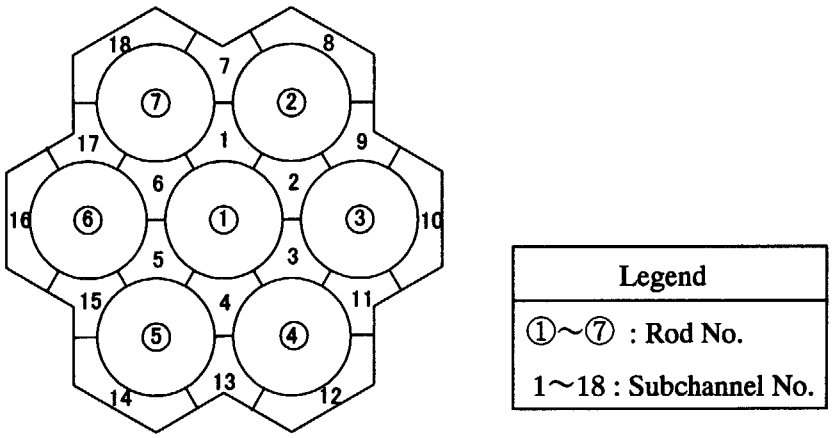

Fig. 4.6.1 COBRA-Ⅳ- I subchannel noding model

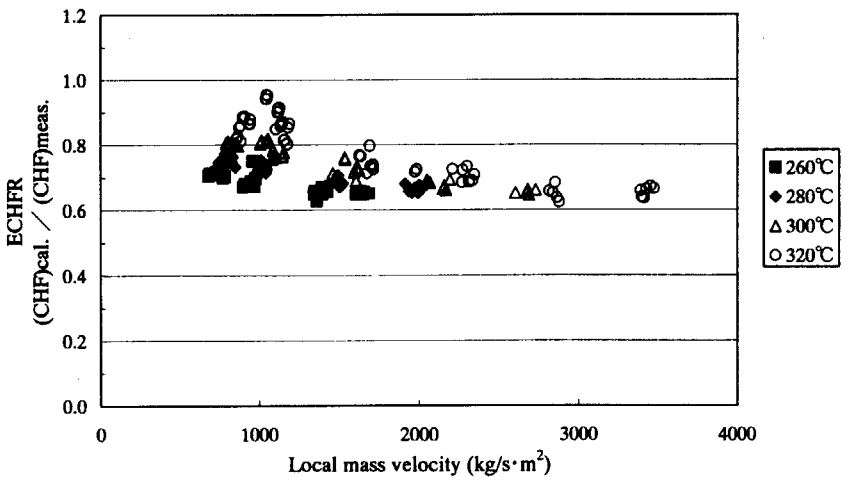

Fig. 4.6.2 Comparisons of analytical CHF values to experimental values for rod pitch 11mm

4.7 Preliminary Calculations for MOX Fuel Critical Experiments in TCA

S. Shimada and M. Ochiai

(*E-mail :* shimada@jpsrews1.tokai.jaeri.go,jp)

Preliminary Calculations for MOX fuel critical experiments in TCA were performed to obtain an approximate number of MOX fuel rods, blanket fuel rods, UO_2 fuel rods and burnable poison rods used in the critical experiments.

Calculation Method The configuration of the critical experiments is assumed as shown in Fig. 4.7.1. The MOX fuel rods are located in the center surrounded by blanket fuel rods. The buffer region is introduced between the center region and driver region. The MOX fuel specification is shown in Table 4.7.1 and the driver fuel specification is in Table 4.7.2. Depleted uranium is used as blanket and buffer fuel. Critical experiments will be performed for the water to fuel volume ratio ranging from 0.25 to 1.0. In this calculation, however, the volume ratio of 0.5 was selected for the center region as a reference case. The volume ratio of 2.0 was assumed for the driver region. MOX enrichment and uranium enrichment were assumed to be 9.0 wt% and 4.1 wt%, respectively. Group constants with 10 energy groups were obtained by the SRAC code and reactivity calculations were performed by the CITATION code with RZ model.

Calculation results Calculated results are shown in Table 4.7.3. The effective multiplication factors (k_{eff}) as a function of void fraction are shown in Fig. 4.7.2. As shown in Table 4.7.4, the infinite multiplication factor (k_∞) increases with void fraction for the MOX and blanket region, while decreases for the driver region. As shown in Fig.4.7.2, the total void reactivity effect seems to be negative for case 101 to 103, but positive for case 201 and 202, because void is produced in the whole region for case 101 to 103 and only in the center region for case 201 and 202.

Conclusions Following results were obtained by the preliminary calculations :

Number of MOX fuel rods: 1500

Number of UO_2 fuel rods for driver region: 4000

Number of the blanket fuel rods: 2000

Diameter of the center region: 40 to 45 cm

More detailed calculations will be performed to determine the final numbers.

Reference

1) Okumura, K., et al. : "SRAC95 : General Purpose Neutronics Code System", JAERI Data / Code 96-015 (1996)

Table 4.7.1 MOX fuel rod specification for test region

Moderator to pellet volume ratio	0.50
Fuel rod diameter (cm)	0.95
Cladding material	SUS-316
Fuel	MOX
Enrichment ($Pu^{fis.}$)	9.0 %
Moderator	D_2O

Table 4.7.2 UO_2 fuel specification for driver region

Moderator to pellet volume ratio	2.0
Fuel rod diameter (cm)	0.95
Cladding material	Zry-4
Fuel	UO2
Enrichment	4.1 %
Moderator	H_2O

Table 4.7.3 TCA calculation cases (Refer Fig. 4.7.1)

Case No.	a(cm)	b(cm)	c(cm)	d(cm)	Voided region
101	10	10	15	72	Whole region
102	10	10	25	82	Whole region
103	5	5	25	72	Whole region
201	10	10	25	82	Center region
202	2(ZrH_2)	18	25	82	Center region

Table 4.7.4 k_∞ as a function of void fraction

Void (%)	MOX fuel	Driver fuel	Blanket Driver fuel
0	1.10312	0.22982	1.35411
10	1.10921	0.23325	1.34620
40	1.13441	0.24325	1.29771
99	1.28621	0.35346	0.87857

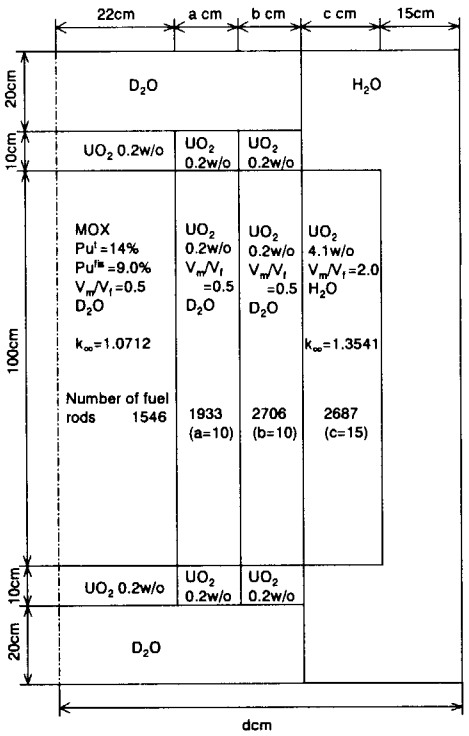

Fig.4.7.1 TCA calculation model

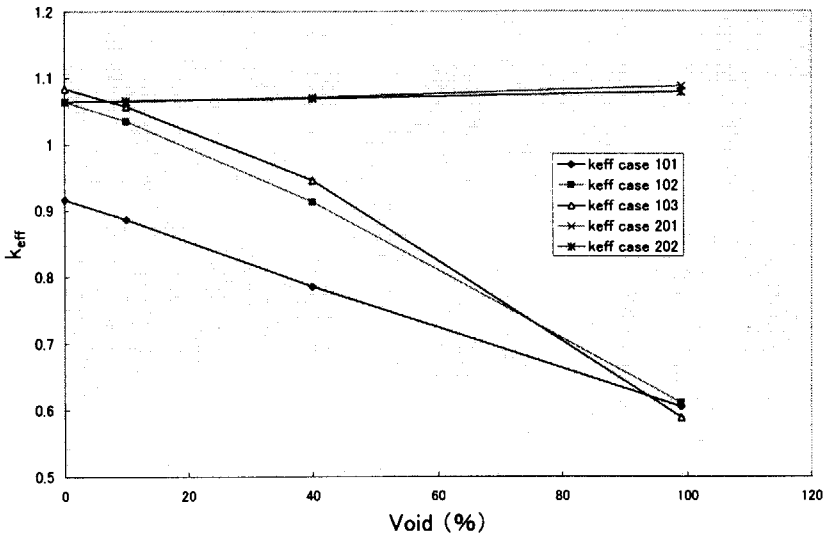

Fig.4.7.2 Relation between k_{eff} and void fraction

4.8 Core Physics Characteristics of High Burn-up Full MOX PWR Core with Thin Fuel Rods

T. Kugo, T. Okubo, S.Shimada* and M.Ochiai
(*E-mail:* kugo@mike.tokai.jaeri.go.jp)

As one of options for future light water reactors, we have been studying a high burn-up full MOX PWR core based on existing light water reactor technology to ensure a discharged burn-up of 100GWd/t and a 3-year operation cycle. We have already confirmed the feasibility of the core, in which a moderator to fuel volume ratio(Vm/Vf) is increased to 2.6 with the same fuel pin diameter of 9.5mm as in the current PWR but with the enlarged fuel pin pitch of 13.8mm[1]. In this report, to improve the neutronics and thermal hydraulics performance of the high burn-up core, we propose a 600MWe core ensuring discharge burn-up of 100GWd/t by increasing Vm/Vf to 3.0 with the same fuel pin pitch of 12.6mm as in the current PWR but with the smaller fuel pin diameter of 8.3mm instead of 9.5mm.

It has been found in the previous study[1] that the appropriate range of Vm/Vf is around 2.5 ～ 3 to effectively extend the burn-up, although the larger is the Vm/Vf value, the better is the nuclear characteristics of the core. First, in the previous study, we increased Vm/Vf to 2.6 by enlarging the lattice pitch so as to increase the cycle length as much as possible. In this study, we increase Vm/Vf to 3.0 namely to improve the fuel utilization. The departure from nucleate boiling ratio(DNBR) becomes worse with increasing Vm/Vf by enlarging the lattice pitch. Therefore, we adopt to reduce the fuel pin diameter in order to improve the DNBR, although it sacrifices the cycle length to some extent.

Proposed core specification for Vm/Vf=3.0 is shown in Table 4.8.1 in comparison with that for Vm/Vf=2.6. The lattice pitch is 12.6mm and is the same as in the current PWR. The average linear heat rate is 13.1kW/m which corresponds the same power density as the previous core of Vm/Vf=2.6.

We investigate the neutronics characteristics of the proposed core and compare them between Vm/Vf=2.6 and 3.0 in Table 4.8.2. This table includes the results for 60GWd/t discharge

---

* Engineering Development Co., Ltd.

burn-up cases. From the comparison, it is found that the proposed core with Vm/Vf=3.0 has more promising characteristics except for the cycle length shortened by 9% than withVm/Vf=2.6 as follows.

1) A fissile plutonium content ant its inventory are reduced.

2) The critical boron concentration is reduced by more than 10%.

3) The moderator temperature coefficient and moderator void coefficient at BOC become more negative, because the critical boron concentration is reduced.

4) The plutonium transmutation and minor actinide production properties are a little bit improved.

Reference

1) Kugo T., *et al.*: "Study on Nuclear Physics of High Burnup Full MOX PWR Core",JAERI-Research 98-059 (1998) [in Japanese].

Table 4.8.1 Core specification

Vm/Vf	2.6	3.0
Number of batch	3	3
Thermal output (MWt)	1685	1685
Electric power (MWe)	573	573
Number of fuel assemblies	109	133
Effective core diameter(cm)	277	279
Effective core height(cm)	366(12ft.)	366(12ft.)
Average linear heat rate (kW/m)	16.0	13.1
Average power density (kW/l)	76.5	75.6
Lattice pitch (mm)	13.8	12.6
Rod diameter (mm)	9.5	8.3

Table 4.8.2 Core characteristics of equilibrium cycle

Vm/Vf	2.6		3.0	
Average discharge burn-up (GWd/t)	60	100	60	100
Cycle length (EFPM)	20.2	33.5	18.3	30.6
Plutonium-fissile content (wt%)	7.0	12.1	6.6	11.8
Plutonium-fissile inventory loaded for equilibrium cycle (kg)	1140	1990	980	1750
Net plutonium transmutation (kg/GWe/year)	580	679	596	693
Net plutonium transmutation percentage (%)	32.0	35.8	34.6	37.8
Net minor actinide production (kg/GWe/year)	71.7	87.0	65.5	81.7
Net minor actinide production percentage (%)	3.9	4.5	3.7	4.4
Peaking factor				
Fxy (BOC-HFP)	1.33	1.45	1.34	1.39
Fxy*Fz (BOC-HFP)	1.69	1.94	1.74	1.85
Flocal (BOC-HFP)	1.11	1.11	1.11	1.11
Burnup reactivity(%dk/kk')	9.8	10.6	10.2	10.9
Boron efficiency (pcm/ppm) (BOC/EOC)	-3.5/-4.1	-2.5/-2.9	-4.2/-5.0	-2.9/-3.5
Critical boron concentration (ppm) (BOC)	2800	4200	2400	3800
Moderator temperature coefficient at critical boron concentration (pcm/℃) (BOC)	-26	-11	-28	-14
Moderator temperature coefficient at no boron (pcm/℃) (BOC/EOC)	-61/-65	-49/-54	-61/-65	-51/-58
Doppler coefficient (pcm/℃) (BOC/EOC)	-2.7/-2.8	-2.5/-2.6	-2.7/-2.9	-2.5/-2.6
Moderator void coefficient at critical boron concentration (pcm/%void) (BOC) 0～10/ 0～40/ 0～99%void	-99/-147 /-318	-43/-69 /-19	-109/- 166 /-466	-55/-83 /-98

4.9 Thermal Hydraulic Designing of High Burn-up Full MOX PWR Core with Thin Fuel Rods

T. Okubo, T. Kugo and M. Ochiai
(*E-mail:* okubo@jpsrews1.tokai.jaeri.go.jp)

As described in the previous study 4.8, high burn-up and long operation cycle full MOX PWR core design is under investigation at JAERI. From the results[1] of the reactor physics study, the appropriate range for the moderator to fuel volume ratio (*Vm/Vf*) has been found to be between 2.5 and 3.0. Although the larger volume ratio is better from the reactor physics point of view, the smaller volume ratio is better from the thermal design point of view. That is, when the rod pitch is expanded to get the larger volume ratio, both the core power density and the core coolant velocity become smaller. The latter results in reduction of the departure from nucleate boiling ratio (DNBR). Also, to compensate decrease in the core power density, core diameter should be increased and/or the rod linear power density should be increased. However, reactor vessel diameter has the maximum limit for fabrication and increase in the rod linear power density results in reduction of DNBR as well as reduction of operation cycle length. From the DNBR point of view, to reduce the fuel rod diameter is another possible way to increase *Vm/Vf*

Therefore, in order to investigate the effect of volume ratio on DNBR, some parametric calculations were performed. The calculated results are shown in Fig. 4.9.1. This presents ΔMDNBR, *i.e.* reduction in minimum DNBR value from the value for the existing 17×17 type fuel assembly of *Vm/Vf*=1.9 with the linear power density of 17.9 kW/m, against the volume ratio. The calculations were performed by using COBRA-IV-I subchannel analysis code[2] and the modified W-3 correlation[3] for the case of 600 MWe class core. The maximum power peaking (*Fq*) in the hot assembly was assumed to be 2.4. The figure indicates that the effect of *Vm/Vf* on DNBR is not significant when the rod diameter is reduced, although the effect is significant when the rod pitch is increased keeping the rod diameter constant. However, the core power density becomes very small, when the rod diameter is reduced. Therefore, the linear power density is increased up to give the same heat flux from the rod surface as the reference case for *Vm/Vf*=1.9. The results in Fig. 4.9.1

indicate reduction in DNBR is about 0.5 even for *Vm/Vf*=3.0 when the rod diameter is reduced to 8.3 mm from 9.5 mm under the fixed heat flux condition.

The average linear power density was determined to 13.1 kW/m, which gives almost the same core power density of 75.6 kW/l as for previously proposed case with *Vm/Vf*=2.6[1]. Effective core diameter is also the same. Based on these determined key values, reactor physics calculation was performed and values presented in the previous study, *i.e.* 4.8, have been obtained. The calculated power peaking factor in the radial direction Fxy was 1.39.

Based on the reactor physics calculation results, MDNBR values were evaluated with the COBRA-IV-I code and the modified W-3 correlation. Some safety assumptions normally considered in this type of safety evaluation were also adopted. Evaluated MDNBR values along the core elevation are presented in Fig. 4.9.2 under the normal operation conditions compared with values for *Vm/Vf*=2.6. For the modified W-3 correlation, the MDNBR value for the safety criterion is widely known to be 1.3. Therefore, it has been confirmed that there is enough safety margin on DNB under the normal operation condition for the present core design. This figure also indicates MDNBR is 10% higher in the present case than in the previous case for *Vm/Vf*=2.6.

References

1) Kugo, T., *et al.*: "Study on Nuclear Physics of High Burn-up Full MOX PWR Core", JAERI-Research 98-059 (1998).
2) Wheeler, C.L., *et al.*: "COBRA-IV-I: An interim version of COBRA for thermal-hydraulic analysis of rod bundle nuclear fuel elements and cores", BNWL-1962 (1976).
3) Tong, L.S. and Weisman, J.: "Thermal Analysis of Pressurized Water Reactors, Third Ed.", ANS (1996).

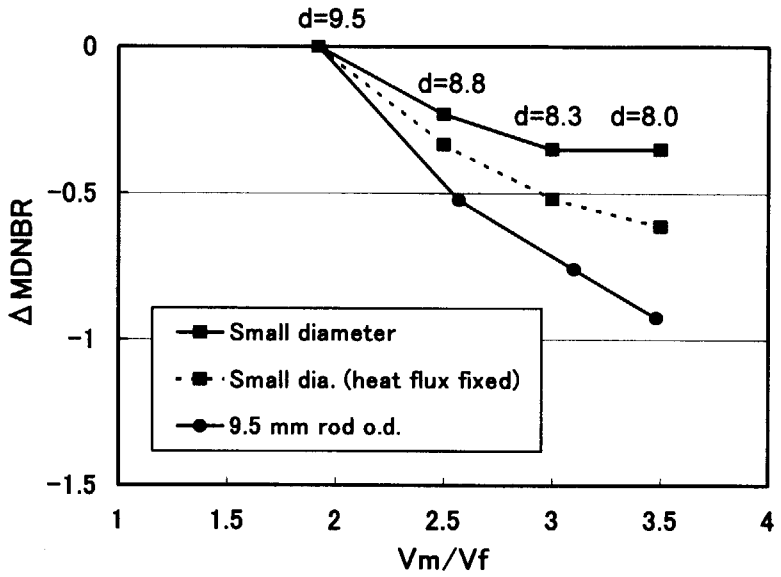

Fig. 4.9.1 Reduction in minimum DNBR value from value for the existing 17×17 type fuel assembly (*i.e. Vm/ Vf*=1.9) against volume ratio

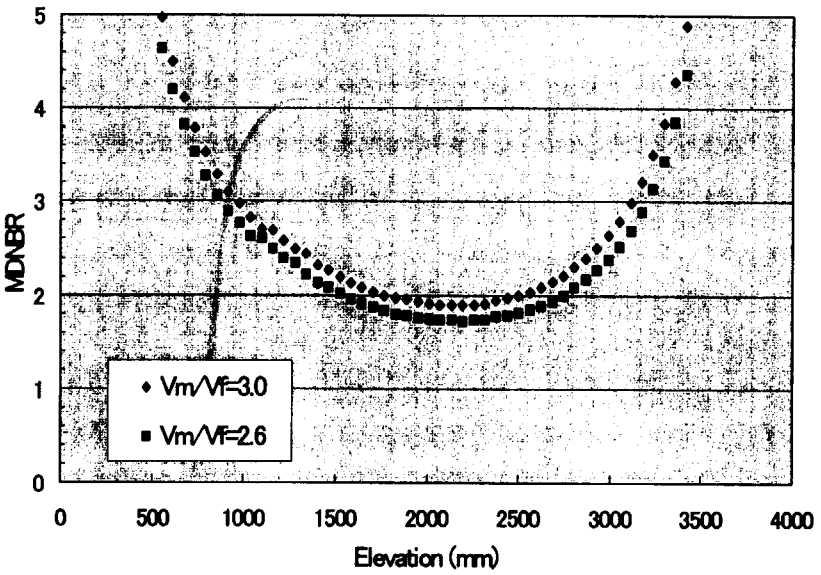

Fig. 4.9.2 Predicted minimum DNBR values along core axial position for *Vm/Vf*=3.0 compared with *Vm/Vf*=2.6

4.10 Accident Analyses for Design of Primary Coolant and Safety Systems in High Burn-up Full MOX PWR

F. Araya, H. Yoshida and T. Teramae*

(*E-mail:* araya@jpsrews1.tokai.jaeri.go.jp)

A design study has been carried out on a high burn- up full MOX PWR performing accident analyses for confirming adequacy of design features. The primary coolant and safety systems have been designed based on the nuclear design of the full MOX core[1], the design of typical two- loop PWR and the passive safety reactor JPSR[2]. Overview of the design features is outlined in the previous report[3]. In order to confirm adequacy of the design, accident analyses were performed on representative accidents, i.e., loss of heat sink, main steam line break and large break loss- of- coolant accident (LOCA), and no safety problem was found, as presented in the previous report[3]. In the present paper, analyses of control rod cluster ejection accident and small break LOCA are presented.

A preliminary analysis on the rod cluster ejection accident was performed with the RETRAN- 02 code. Although multidimensional neutron behaviors are important in this accident, a point kinetics model was used. Therefore, some assumptions were made based on the safety analysis on a current PWR[4]. The present analysis is focusing on the end of cycle conditions in view of the control rod worth. Since only a rod worth due to position change from full in to full out conditions was presented by the nuclear design, 30% of the worth, 1.22 $ was assumed to be inserted in 1 second. The calculated core power transient is shown in Fig. 4.10.1. The increase in the power is very steep. The maximum power of 773 % of the design power is attained at 0.12 seconds. After reaching the maximum value, the core power is decreased steeply due to the Doppler effect. The adiabatic fuel enthalpy was evaluated for the time period of 0.22 seconds after the accident initiation. The adiabatic enthalpy of the fuel was evaluated assuming a power peaking factor of 7.23 which was derived by multiplying a factor of 3, which was determined based on the safety analysis results of the current PWR[4], to the peaking factor at the EOC design condition, 2.41. The evaluated value is 146

* Mitsubishi Heavy Industries, Ltd.

cal/g.MOX and is quite lower than the safety limit for the UO_2 fuel of 230 cal/g. Since it has been found that the fuel defect threshold energy of the MOX fuel is larger than that of the UO_2 fuel[5], the result shows the safety will be kept in the present accident.

In the previous report, analysis results on large break LOCA were shown for the break areas ranging from 200% to 50% of the cold leg flow area with use of the thermal equilibrium code RETRAN- 02. Due to limitation of applicability of RETRAN- 02 to LOCA analyses, the thermal non- equilibrium code REFLA/TRAC was applied to small break LOCA (SBLOCA) analyses with break areas ranging from 1 to 20 %. The input data set developed for REFLA/TRAC models most of safety systems. The accident is assumed to initiate at the nominal operating conditions. Only one unit in each safety system was assumed to work. The reactor scram, main coolant pump and steam generator isolation were tripped with the low pressure signal generated using the pressurizer pressure at 12.8 MPa. The calculated mass flow rates of the accumulator (ACC) and the gravity coolant injection system (GDCIS) in the 1 % beak case are shown in Fig. 4.10.2 together with actuation timings of these systems in the other cases. In all cases, it is shown that the safety injection systems are properly actuated. As a result, the heat- up of the core was not experienced. The calculated results show that the present full MOX core does not have any problems in the small break LOCAs.

As shown above and in the previous report, any problems were not found in all calculation cases performed for the representative accidents. Based on the results, it can be concluded that the plant system with the passive safety feature loading the high burn- up full MOX core is feasible.

References

1) Kugo, T., et al.: JAERI-Research 98-059 (Oct. 1998).

2) Murao, Y., et al.: J. Nucl. Sci. Technol., Vol. 32, No. 9, pp.855-867 (1995).

3) Araya, F., et al.: JAERI-Review 98-022, pp. 103-105 (Nov. 1998).

4) Kyushu Electric Power Co.: "License Application Report, Genkai Units 3, 4" (Oct. 1982), [in Japanese].

5) Roepenach, H., et al.: Nucl. Technol., Vol. 77,pp. 175-186 (May 1987).

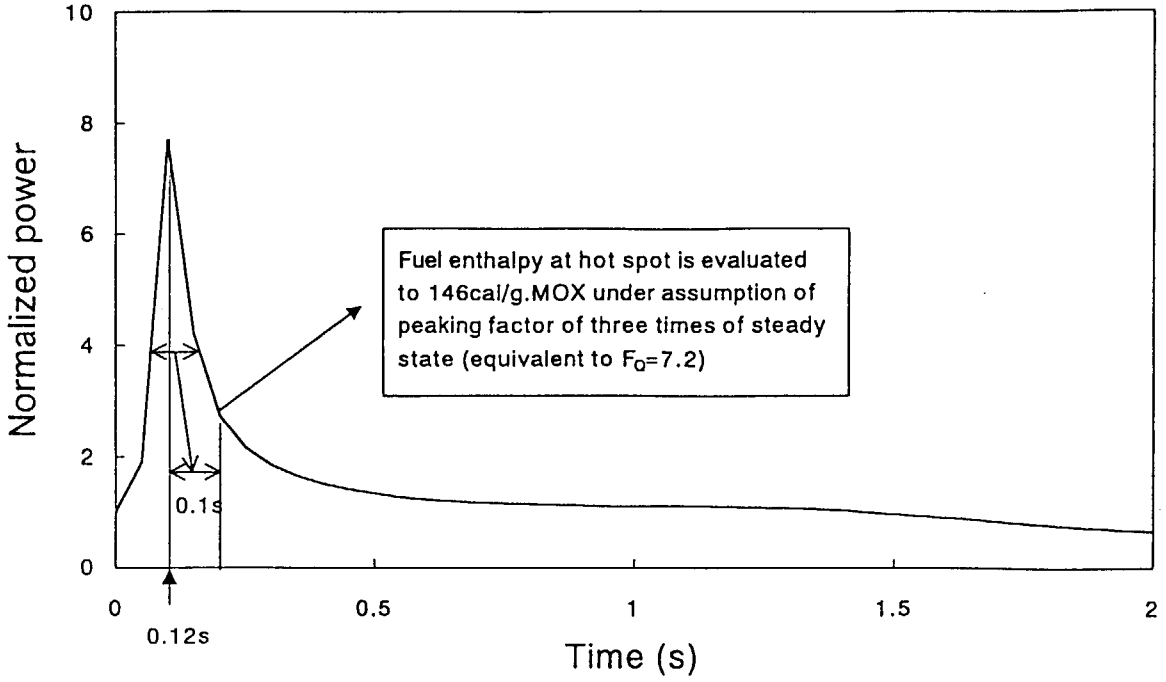

Fig. 4.10.1 Core power in control rod cluster ejection accident.

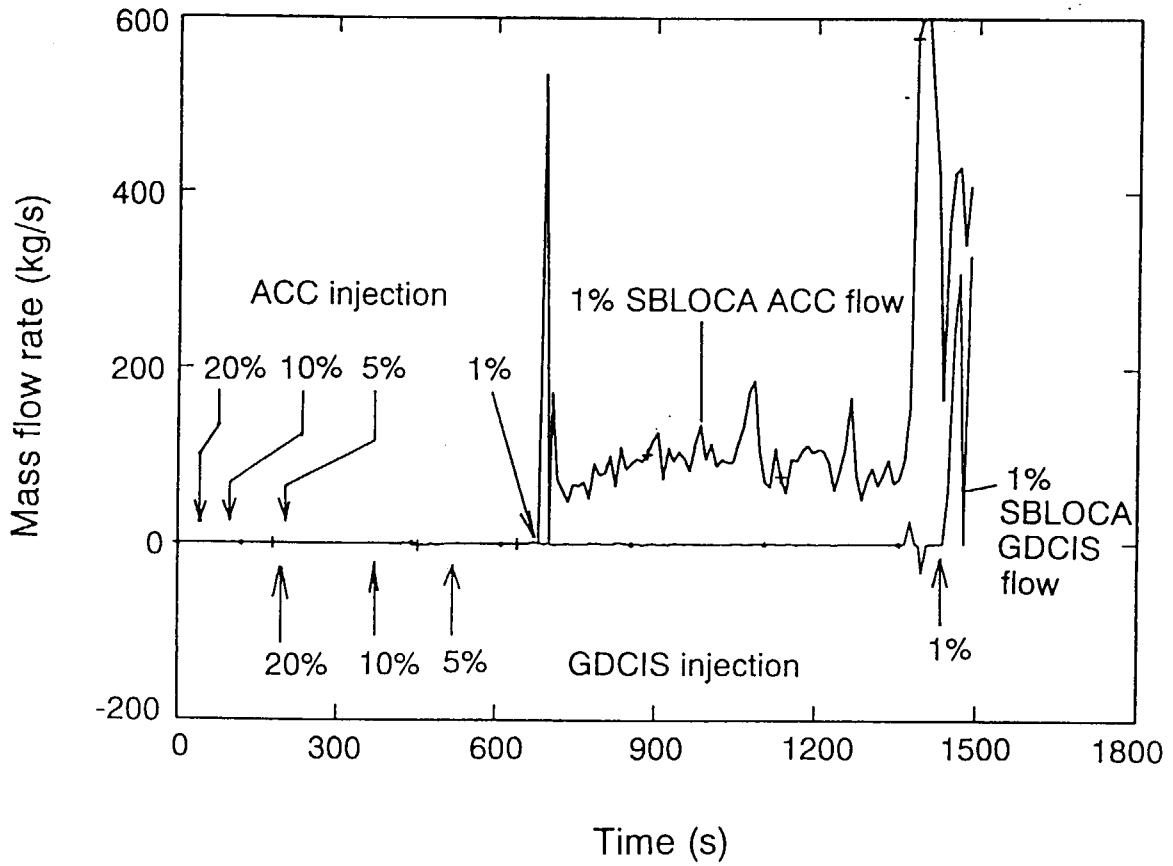

Fig. 4.10.2 Effects of break area on actuation timing of coolant injection systems in SBLOCA and injection flow rates in 1% break case.

5. Reactor Instrumentation, Control and Diagnostics

For the development of new optical reactor instrumentation system such as in-core radiation and temperature monitors in nuclear power reactors, two types of heat and radiation resistant optical fibers were developed and their optical phenomena were examined in the Japan Materials Testing Reactor (JMTR) in JAERI. The experimental result shows that a gamma-ray dose rate and a temperature in the reactor core can be monitored by measuring intensities of radio-luminescence and thermo-luminescence in optical fibers.

The auto-associative recurrent neural network (RNN) with back propagation learning algorithm was applied to the plant wide monitoring system for the High Temperature Engineering Test Reactor (HTTR) in JAERI. The RNN was selected because of its capability of modeling for slower dynamic behavior. The monitoring system has been tested by using a simulation code of HTTR. The results indicate that small anomalies can be detected successfully by the RNN.

OECD/NEA FORSMARK 1&2 BWR stability benchmark has been conducted. This focuses on the analysis of time series data by means of noise analysis technique in the time domain. The first goal is to elucidate the possibility of determining the main stability parameters from neutronic signals. As a new stability parameter, the Slope of Correlation Integral (SOCI) was proposed for evaluating the stability. From the shape of the SOCI curve, the time series data can be classified into stable, quasi-unstable and unstable states.

For inspecting patrol of nuclear power plants, a "human collaborative mobile robot system" was developed, in which human assistance is incorporated to improve rapidity and reliability of task performance. The feasibility of the system has been demonstrated under the mock-up environment. Through the demonstration it was clarified that this system serves for effective human-machine interface for human collaborative task performance.

5.1 Development of New Reactor Instrumentation System Using Optical Techniques

T. Kakuta, K. Suzuki, H. Yamagishi and H. Itoh

(*e-mail :* kakuta@stsp2a0.tokai.jaeri.go.jp)

For the development of new optical reactor instrumentation system such as that in-core radiation monitor and temperature monitor in advanced nuclear power reactors under development in JAERI, two types of heat and radiation resistant optical fibers were developed and their dynamic optical phenomena were examined with a JMTR fission reactor[1].

Measuring procedure for examination is illustrated in Fig. 5.1.1. The developed heat and radiation resistant optical fibers, SiO_2 with Fluorine contained core fiber whose diameter is 0.2 mm and SiO_2 with 800ppm OH contained core fiber whose diameter is 0.8 mm, were used for detection of radio-luminescence itself and transmission of thermo-luminescence from sensing material. The sapphire crystal as a black body, whose purity is 99.99%, was used for sensing the thermo-luminescence due to the gamma-ray heating at the high reactor power. The intensity of radio- and themo-luminescence of fibers was measured by optical spectrum analyzer, whose wavelength range from 350 nm to 1800 nm. A special capsule in the core region of JMTR fission reactor was used for examination of dynamic optical phenomena of optical fibers. The fast (E>1MeV) and the thermal (E<0.678eV) neutron fluxes are 1.5×10^{18} n/m^2·s and 3.6×10^{18} n/m^2·s, respectively, and the gamma-ray dose rate is 5.0×10^3 Gy/s (heat rate:5.0 W/g) at the reactor power of 50 MW. The developed heat and radiation resistant optical fibers kept good optical transmission characteristic during heavy irradiation up to a neutron fluence of 10^{24} n/m^2 and a gamma-ray doses of larger than 10^9 Gy under temperature of 1100 K.

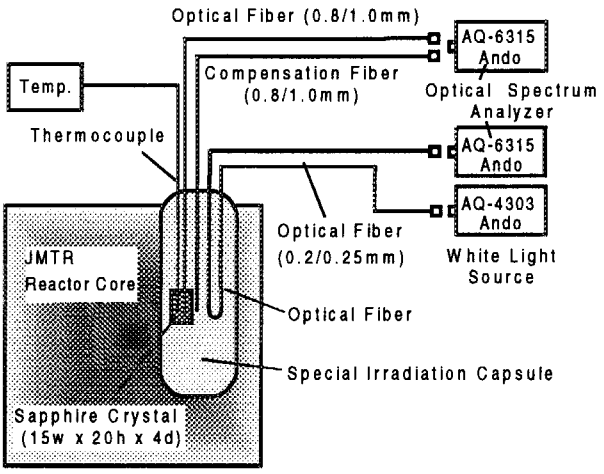

Fig.5.1.1 Measuring procedure for dynamic optical phenomena of optical fibers

During heavy neutron irradiation in the core region of JMTR, strong radio-luminescence with some of peaks and thermo-luminescence in infrared region were observed.

Intensities of observed radio-luminescence peaks such as that at 450 nm and 1270 nm in SiO_2 core of optical fibers, and Cerenkov radiation, were found to directly proportional to the reactor power (See Fig. 5.1.2). Also, temperatures could be estimated by measuring the thermo-luminescence from sapphire crystal as a black body (See Fig. 5.1.3).

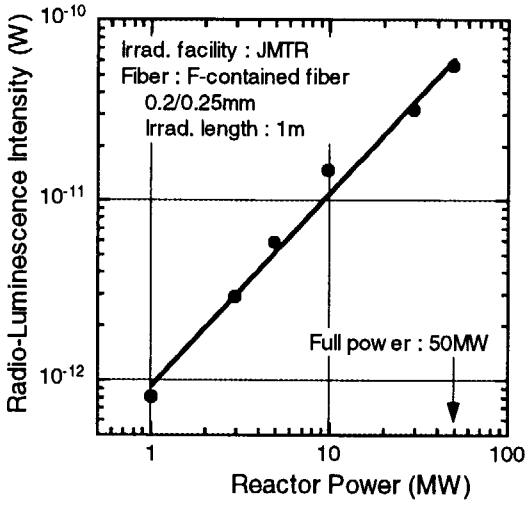

Fig. 5.1.2 Relation of reactor power and Radio-luminescence peak at 1270nm

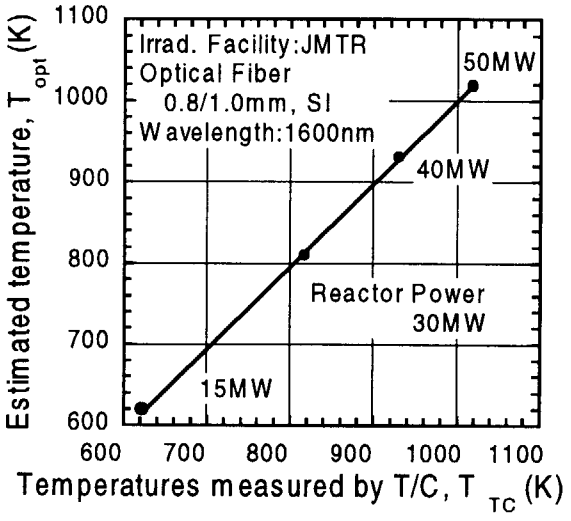

Fig. 5.1.3 Estimated temperature as a function of temperatures measured by a conventional thermocouple

The results demonstrate that a gamma-ray dose rate and a temperature of in the core region of fission reactor can be monitored by measurements of the radio-luminescence and thermo-luminescence in infrared signals under heavy irradiation.

Reference

1) Kakuta, T., Yamagishi, H., Itoh, H., Shikama, T. and Urakami, M.:"Application of Optical Fibers to Instrumentation System in Advanced Nuclear Power Reactors", 7th Int. Conf. on Nuclear Engneering, Tokyo, Japan, April 19-23, ICONE-7128(1999).

5.2 HTTR Monitoring System with Recurrent Neural Network

K. Nabeshima, K. Inoue*, K. Kudo* and K. Suzuki
(*E-mail:* nabe@clsu3a0.tokai.jaeri.go.jp)

The auto-associative recurrent neural network (RNN) with back propagation learning algorithm was applied to the plant wide monitoring system for the High Temperature Engineering Test Reactor (HTTR) in Japan[1]. The RNN is selected to take account of the high capability of modeling for slower dynamic behavior. The monitoring system has been tested by using a simulation code of a HTTR.

The safety demonstration test of the HTTR will be carried out for the safety features of a next generation HTGR. The HTTR has 30 MW thermal power, and consists of core, main cooling system, auxiliary cooling system, vessel cooling system. Figure 5.2.1 shows the plant configuration and its components with the location of 56 plant parameters. The reactor core is a graphite moderated gas cooled reactor with prismatic fuel elements and hexagonal blocks. Three main cooling systems are active at the HTTR, namely primary cooling system, secondary helium cooling system and the pressurized water cooling system. The primary cooling system has two heat exchangers of a helium-helium intermediate heat exchanger (IHX) and a primary pressurized water cooler (PPWC). The HTTR is planned to be operated in two loading modes; one is parallel-loaded operation in which the IHX and the PPWC are operating simultaneously, and the other one is single-loaded operation using PPWC only.

Plant dynamical analysis code ACCORD[2] is used to simulate the plant operation in wide power range and also will be used in safety demonstration tests. The ACCORD code is designed based on a modular structure: reactivity control module, heat transfer calculation module, He-loop calculation module, pressurized water module, safety protection module and control module. To make a RNN dynamic model of HTTR, we selected 22 plant parameters given in Table 5.2.1. In this table the first number in the first column indicates the identification number of the parameters in Fig. 5.2.1, the second (in italic) number is corresponding to the selected channels of RNN inputs, in the second column are the names of the parameters and in the third column physical units are given.

---

* Engineering Department, Kyushu University

The RNN monitors the current and past system inputs and outputs and is trained, so that it can predict the next outputs of the system, which is equivalent to one-step-ahead prediction. This has been effectively implemented with RNN and proposed for dynamic tracking. The basic principle of this methodology is to detect the anomaly from the deviation between process signals measured from the actual plant and the corresponding values predicted by the plant model which is developed using three-layered RNN.

The RNN consists of a set of 22 input nodes, a set of 22 output nodes and one layer with 22 hidden nodes. Output signals are the same as input signals at the next time step. Here the feedback connection from output node to hidden node is a concern with time delay. The RNN is trained with the data covering from 50% power to 100% in increasing and to 30% in decreasing (1 to 660 patterns). The learning is enhanced until the satisfactory results are obtained. The whole data from pattern 1 to 1182 including different power rates of operation and small perturbation are tested.

After 1062 patterns a perturbation of increasing 10% rotational speed is introduced at the primary gas circulator. Figure 5.2.2 shows the secondary coolant pressures simulated by ACCORD, predicted by the RNN and the deviations between them. Deviations are extremely small even under power change operation. The RNN detects the anomaly condition at 1066 points because the deviations exceeds the fault severity levels which depend on the plant states and are defined by expert system.

The results obtained from this suggests that the RNN makes very good prediction for the plant conditions under any operation states. We are developing the hybrid monitoring system which combines recurrent neural network and real-time expert system for HTTR. In order to consider additional operational information from human operators, an expert system is introduced primarily as a supervisor for the RNN agent, and secondarily as an interface between the system and human operators. One of the goal of plant monitoring is to infer the current states of the operational plant using observed signals.

References

1) Saito, S., et al.: "Design of High Temperature Engineering Test Reactor (HTTR)", JAERI -1332 (1994).
2) Takeda, T., et al.: "Development of Analytical Code 'ACCORD' for Incore and Plant Dynamics of High Temperature Gas-cooled Reactor", JAERI –Data/Code 96-032 (1996).

Table 5.2.1 Plant parameters for RNN inputs

No.	Parameter	Unit
1 -*1*	Reactor Power	MW
4-*2*	Primary Coolant Pressure	kgf/cm²a
5-*3*	Secondary Coolant Pressure	kgf/cm²a
6-*4*	Pressurized Water System Pressure	kgf/cm²a
8-*5*	Primary Coolant Reactor Outlet Temperature	°C
10-*6*	Primary Coolant Reactor Outlet Temperature	°C
14-*7*	Primary Coolant Temperature at Inlet of Core Side Area (low-temp.-side)	°C
15-*8*	Reactor Vessel Temperature	°C
16-*9*	Primary Coolant Temp. at Outlet of Core Side Area (high-temp.-side)	°C
18-*10*	Core Inlet Temperature	°C
19-*11*	Core Outlet Temperature	°C
21-*12*	20MW PWC Primary Coolant Inlet Temperature	°C
23-*13*	20MW PWC Primary Coolant Temperature at Outlet of Body	°C
24-*14*	20MW PWC Pressurized Water Inlet Temperature	°C
26-*15*	20MW PWC Pressurized Water Outlet Temperature	°C
27-*16*	IHX Primary Coolant Inlet Temperature	°C
32-*17*	IHX Secondary Coolant Outlet Temperature	°C
33-*18*	10MW PWC Primary Coolant Inlet Temperature	°C
35-*19*	10MW PWC Coolant Temperature at Outlet of Body	°C
38-*20*	10MW PWC Pressurized Water Outlet Temperature	°C
40-*21*	Auxiliary Cooler Primary Coolant Flow Rate	kg/sec
47-*22*	Pressurized Water temperature at Air Cooler Outlet	°C

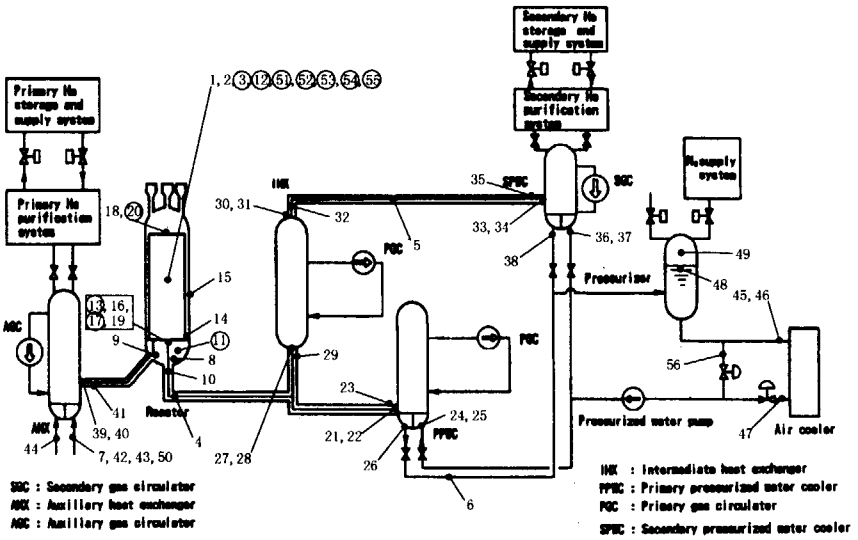

Fig. 5.2.1 Schematic representation of HTTR

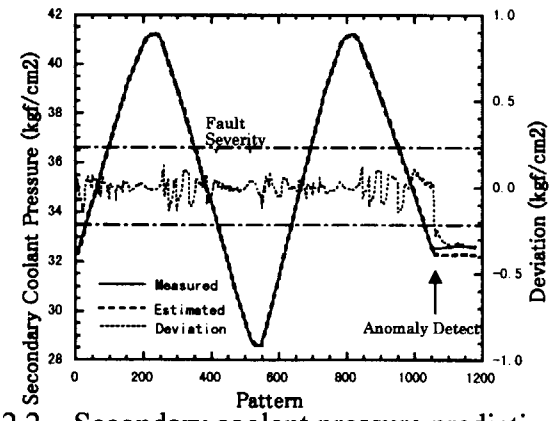

Fig. 5.2.2 Secondary coolant pressure prediction

5.3 OECD/NEA FORSMARK 1&2 BWR Stability Benchmark of Time Series Analysis Method

T. Suzudo

(*E-mail:* suzudo@clsu3a0.tokai.jaeri.go.jp)

The purpose of this benchmark is the intercomparison of the different time series analysis methods that can be applied to the study of BWR stability. The benchmark is being organized under the auspices of the Nuclear Science Committee (NSC) of the OECD/NEA, as a follow-up activity of the Ringhals 1 Stability Benchmark organized by the NSC during 1996. While the Ringhals 1 Stability Benchmark included both time domain and frequency domain calculation models to predict stability parameters, the new activity concerns the analysis of time series data by means of noise analysis techniques in the time domain. The first goal is to elucidate if it is possible to determine the main stability parameters from the neutronic signals time series with enough reliability and accuracy. Typically, the main stability parameters are assumed to be the decay ratio (DR) and the frequency of the oscillation. However, there are other parameters that provide valuable information, such as the Haussdorff dimension.

The data given in this benchmark were obtained during several stability tests performed at the Swedish BWR reactors Forsmarks 1 and 2, in the period 1989 to 1997.

I have participated the benchmark test submitting the estimated DRs, and proposed the usage of the Slope of Correlation Integral, SOCI[1)] which the estimation of the Hausdorff dimension bases on. The methodology adopted for the evaluation of DR with oscillation frequency and proposed usage of the SOCI are described in the following.

Decay Ratio

1) The direct current (DC) component (the best fit linear trend) from the time series was

removed.

2) The time series data was fitted by autoregressive (AR) model. The order of the model was determined by the Akaike Information Criteria (AIC). For the fitting, the Yule-Walker Method was adopted.

3) The impulse response of the identified AR model was calculated.

4) The impulse response was fitted by the function $y(t) = \lambda_1 e^{-\lambda_2 t}\cos(\lambda_3 t + \lambda_4)$, where $y(t)$ is an impulse response at time t; λ_1- λ_4 are fitting parameters. The Gauss-Newton method of the nonlinear optimization technique was used. The fitting region of impulse response was ~10 sec. from the beginning, but the first 1 second of time series were discarded.

5) DR and the oscillation frequency f are evaluated by:

$$DR = e^{-(2\pi\lambda_2/\lambda_3)},\ f = \frac{2\pi}{\lambda_3}.$$

SOCI[1)]

When the time-series data is caused by dumping oscillation with stochastic noise, its trajectory given by the dynamics-reconstruction moves around the equilibrium. On the other hand, sustained or limit-cycle oscillation cause the trajectory to be a closed orbit and the trajectory can then be characterized by the diameter of the orbit, say r_0. The SOCI given by such time-series data has a peak at its right edge because the correlation integral soars at $r=r_0$. In other words, SOCI shows the spatial correlation of the trajectory. One can easily deduce the position of the peak r_0 corresponding to the peak-to-peak amplitude of the oscillation. In this way SOCI can discriminate dumping oscillations from persistent oscillations in a noisy environment and consequently can present the signals in another way.

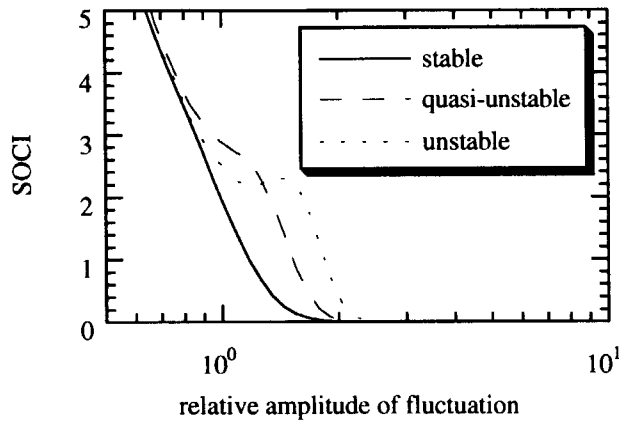

Fig. 5.3.1 SOCI's change according to the stability change

In actual cases, we see three kinds of SOCI's shapes all of which are depicted in the above figure. The graph of solid line is simply decreasing curve and the corresponding oscillation presumed to be stable. The dashed and dotted lines have a small bump and a peak, respectively. The bump is recognized by checking that the second-order derivative of the curve has positive value. The peak is recognized by checking that the first-order derivative of the curve has positive value. From the numerical study it is found that the peak appears only when the oscillation becomes limit-cycle, i.e. unstable. The existence of the small bump accordingly understood as a sign of quasi-unstable state. In summary it is possible to classify the time-series data into the above three states, stable, quasi-unstable and unstable.

The results from all the paticipants were collected, and will be presented at Physor 2000 conference. Finally, the draft article will be published at Nuclear Science and Engineering or Nuclear Technology.

Reference

1) Suzudo, T., et al.: J. Nucl. Sci. Technol. 30[8], 727 (1993).

5.4 Development of a Human Collaborative Mobile Robot System

N. Ishikawa, Y. Furukawa* and K. Suzuki
(*E-mail:* ishikawa@clsu3a0.tokai.jaeri.go.jp)

Autonomous mobile robot is widely studied in the robotics research field to realize a self-consistent system for performing given tasks in the unstructured environment. Autonomous mobile robot recognizes the environment by external sensors to correct the pre-assigned action if the environmental change is occurred. In order to correct the action dynamically based on the sensory information, however, sophisticated AI techniques such as environment recognition and action planning have to be adopted. In nuclear facilities, we have to especially place careful consideration on safety, reliability and ability of taking urgent action in emergency. Considering these points, we have developed a "human collaborative robot system" in which human assistance is incorporated to improve rapidity and reliability of task performance[1]. The system is constructed by adding interfacing functions for human assistance to ordinary autonomous robotic system. The configuration of the system is shown in Fig.5.4.1.

We demonstrate the feasibility of the system for inspecting patrol of nuclear power plants under the mock-up environment as shown in Fig.5.4.2. Figure 5.4.3 depicts the path for the demonstration of inspecting patrol. In this demonstration human assists the robot navigation when the obstacle avoidance is necessitated and a closer approach to the plant component is required to get more detailed TV image for inspection. Demonstration scenario and execution results are as follows:

1) Prior to the patrol we generate the sequence of the navigation commands by assigning the path on the map. (Fig.5.4.4).
2) Sending the navigation command sequence to the interpreter the robot starts to run autonomously.
3) The robot stops at the inspection point and gets the image for inspection by TV camera (Fig.5.4.5). These images are transferred to the host computer and indicated on its display (Fig.5.4.6).

---

* KCS Corporation

4) In case obstacles are detected on the path the robot stops (Fig.5.4.7), and indicates some message on the display to get necessary assistance (Fig.5.4.8). The operator navigates the robot for obstacle avoidance to the place where the robot can take autonomous action of returning to the nominal path and continue the inspecting patrol.

Through this demonstration we show that this system serves for effective human-machine interface for human collaborative task performance.

Reference

1) Ishikawa, N. and Suzuki, K.: "Development of Human and Robot Collaborative System for Inspecting Patrol of Nuclear Power Plants", Proceedings of 6th International Workshop on Robot and Human Communication RO-MAN '97, pp.118-123 (1997).

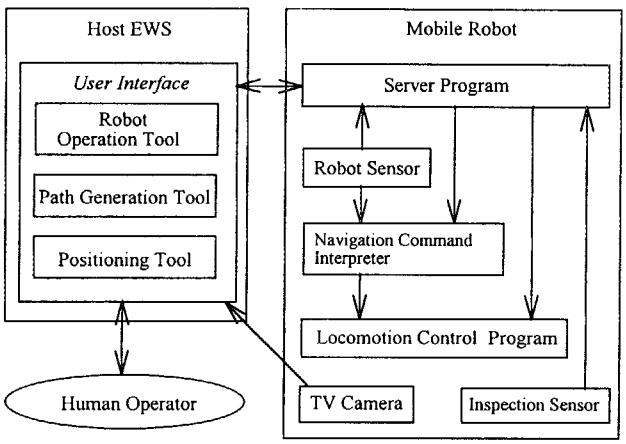

Fig. 5.4.1 System configuration.

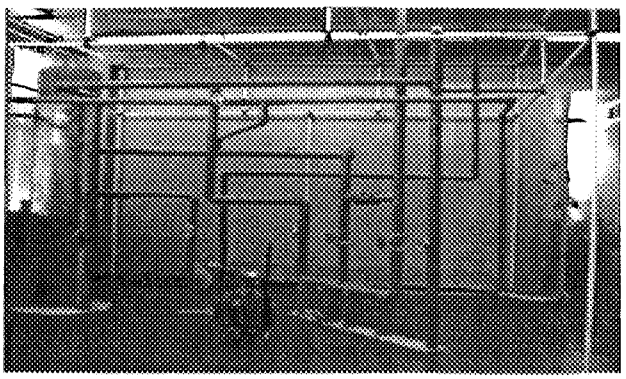

Fig. 5.4.2 Mock-up environment.

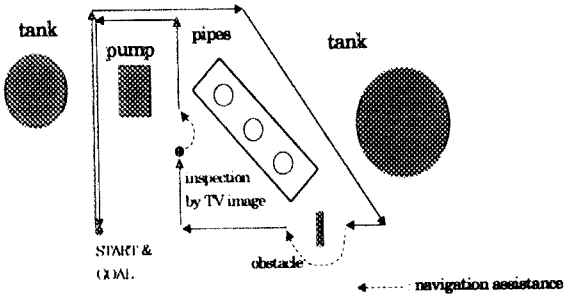

Fig. 5.4.3 Path for the demonstration.

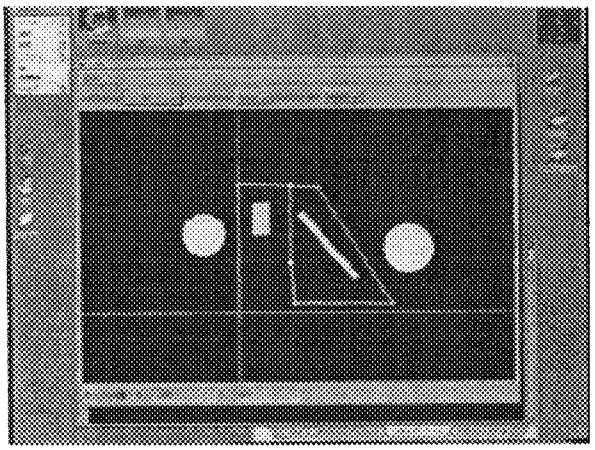

Fig. 5.4.4 Path assignment on the map.

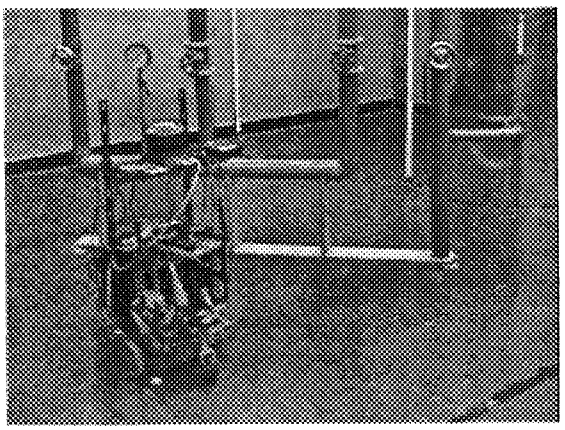

Fig. 5.4.5 Stopping at the inspection point.

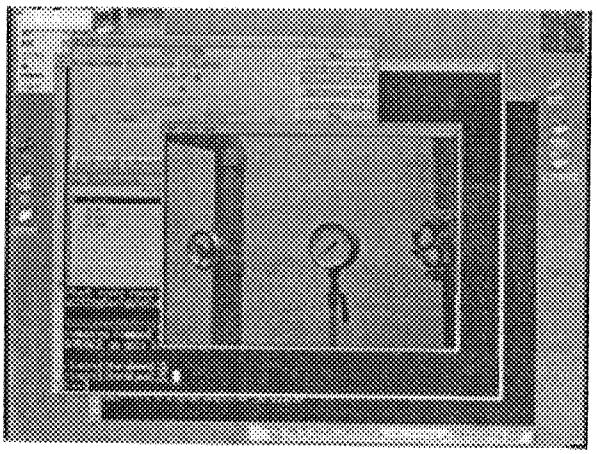

Fig. 5.4.6 Displaying the TV image.

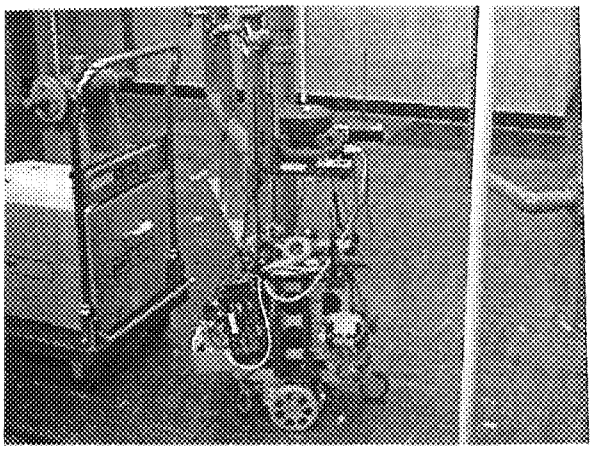

Fig. 5.4.7 Stopping by obstacle detection.

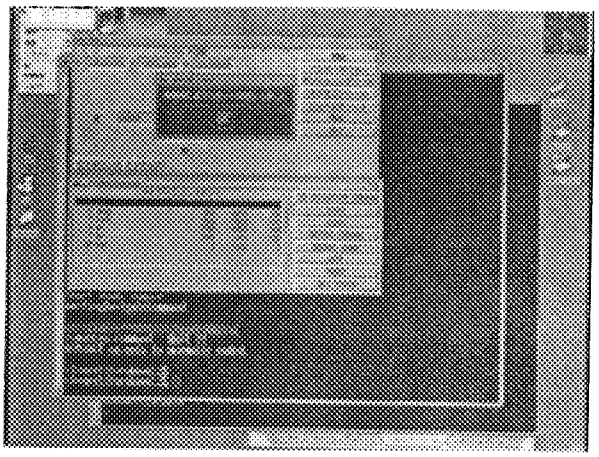

Fig.5.4.8 Indication of obstacle detection

6. Thermal and Fluid Engineering

Advanced computer programs have been developed and verified for thermal-hydraulic analyses of next-generation nuclear systems such as future light water reactors (LWRs), fusion reactor, a target of an intense neutron source, etc.

In Fy 1998, a multidimensional two-phase flow analysis code, named ACE-3D, has been improved by adding the turbulent heat transfer model and the heat structure model in order to establish an analytical tool based on multidimensional two-phase flow model for design of next-generation reactors. The improved code was applied to the design study of the water pool of the JAERI Passive Safety Reactor (JPSR) to check the capability of the residual heat removal system. A system code for accident analyses in light water reactors, named REFLA/TRAC, was applied to a feasibility study on core cooling performance during the reflood phase of the hypothetical large break loss-of coolant accident (LBLOCA) in a high conversion type PWR with tight lattice core. Coupling of REFLA/TRAC and TRAC-BF1 codes with three-dimensional neutronics code was also performed as a cooperative work with the reactor physics research group.

A series of experiments on thermal-hydraulic safety in a fusion reactor was performed to get validation data for safety analysis codes of fusion reactors as one of International Thermonuclear Experimental Reactors (ITER) subtasks. In Fy 1998, design of a new test facility for the simulation of the ingress of the coolant event (ICE) in the ITER was completed. The ICE simulation test is planned to start in November 1999. Numerical simulation study was also performed to support the design of the facility using the TRAC code focusing on the parameter effect on the pressure transient during the ICE. A new code was developed to evaluate the dust transport phenomena during the loss-of coolant accident (LOVA) in the ITER and assessed using the test data of the preliminary LOVA experiments.

A model experiment of critical heat flux was also performed to understand the burnout under subcooled conditions with extremely high heat flux. A measuring technique of void fraction changes in a subcooled flow was developed using the thermal neutron radiography.

Major results obtained in FY 1998 are described in the following sections.

6.1 A Feasibility Study on Core Cooling of Pressurized Heavy Water Moderated Reactor with Tight Lattice Core

A. Ohnuki, T. Okubo and H. Akimoto
(*E-mail*: ohnuki@hflwing.tokai.jaeri.go.jp)

A design study of a pressurized heavy water moderated reactor with tight lattice core is being carried out at the Japan Atomic Energy Research Institute (JAERI) as one candidate for future reactors.[1] The concept is developed to achieve a conversion ratio greater than unity using the tight lattice core (volume ratio of moderator to fuel is around 0.5) and heavy water as the moderator. The high conversion is attractive for the fuel cycle, but the possibility for such tight lattice core is governed by the safety margin during the reflood phase in a Large Break loss-of-coolant accident (LOCA) which is one of the most important issues to be evaluated. In this study, feasibility analyses on the core cooling were carried out by two-dimensional numerical simulations using the REFLA/TRAC code[2], which is a multidimensional two-fluid model code in JAERI.

The present design adopts multi-layer inner blankets which are arranged at concentric positions and seed assemblies (MOX fuel) are located in between the blankets as shown in Fig. 6.1.1. In the current design, the core cooling is considered to be governed by multidimensional thermal-hydraulic behaviors in the pressure vessel. Thus, we adopted the two-dimensional input nodalization shown in Fig. 6.1.2 and the corresponding region in the current design is indicated in Fig. 6.1.1. The analyses were performed only for the pressure vessel, where the bottom of the downcomer was blocked. As a base case, bottom flooding analyses using FILL (REFLA/TRAC component to inject ECC water) at the lower plenum were performed but a combined injection using FILL at the upper plenum was also investigated in this study because a good core cooling was supposed to be difficult only by the bottom flooding. In the combined case, the ECC water was injected into the upper plenum just above the region 10 or the region 1 together with the lower plenum injection.

In the bottom flooding case with the lower plenum injection, several flow circulations in the core below quench front enhanced the heat transfer in the seed assemblies but the heat transfer in the peripheral region, Region 10, where no cross flow is expected from outer region, was degraded. The peak clad temperature (PCT) was calculated in Region 10 and was higher than 2000K as shown in Fig. 6.1.3. The PCT is much higher than that in the current safety criteria under cold leg ECC injection (1500K). On the other hand, the PCT is

significantly reduced under the combined injection cases. This reduction was attained by changing the two-dimensional thermal-hydraulic behaviors in the pressure vessel due to the upper plenum injection. A high downward liquid flow was realized through the central blankets, Regions 1 and 3. The downward flow suppressed the cross flow from the seed assemblies below the quench front and increased the upward liquid flow rate especially for Region 10. In the case with the upper plenum injection above Region 1, the downward flow rate was higher than that in the case above Region 10. The higher downward flow rate gave a higher upward liquid flow rate in Region 10 and attained the better core cooling. It is found from this study that the multidimensional thermal-hydraulic behaviors in the pressure vessel is very important to judge the feasibility of this reactor and a combined injection of ECC water is effective as one of the safety system.

References

1) Shimada, S., et al.: JAERI-Review 98-022, 4.7 (1998).
2) Akimoto, H., et al.: Fifth Int. Topical Meeting on Reactor Thermal Hydraulics (NURETH-5), Salt Lake City, U.S.A., Vol. VI, 1797 (1992).

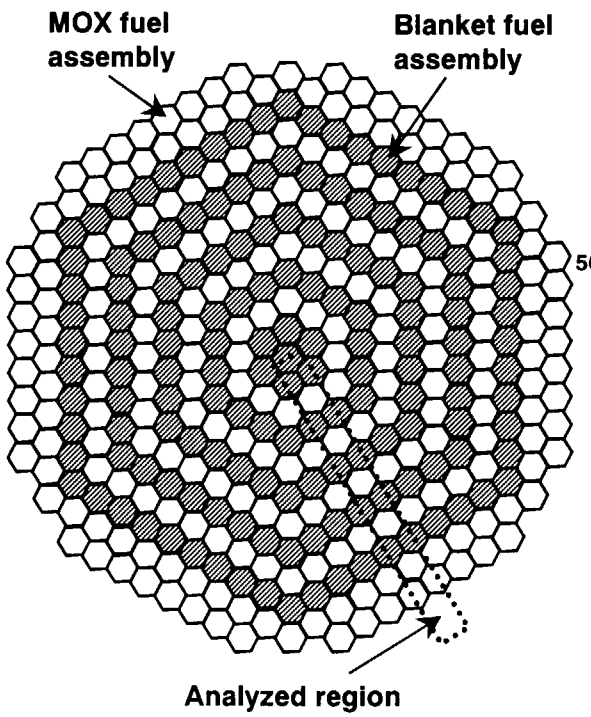

Fig. 6.1.1 Schematic of radial core arrangement

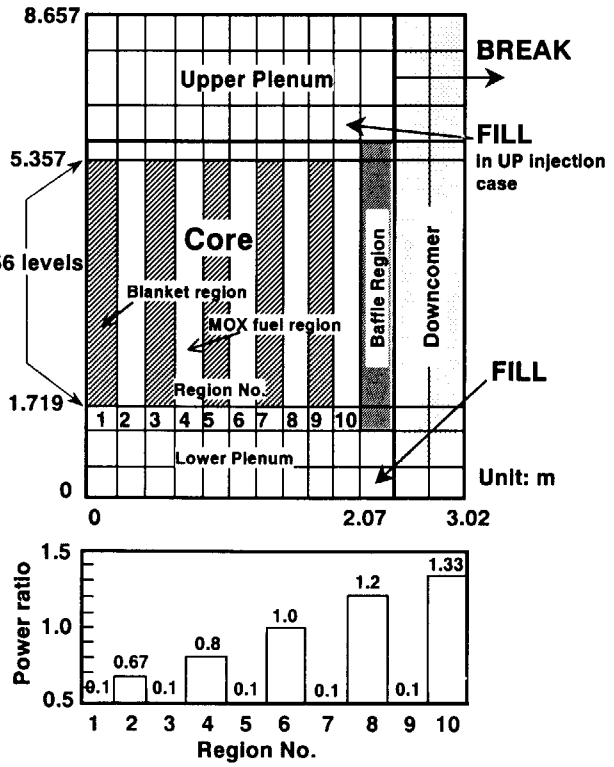

Fig. 6.1.2 Nodalization of pressure vessel

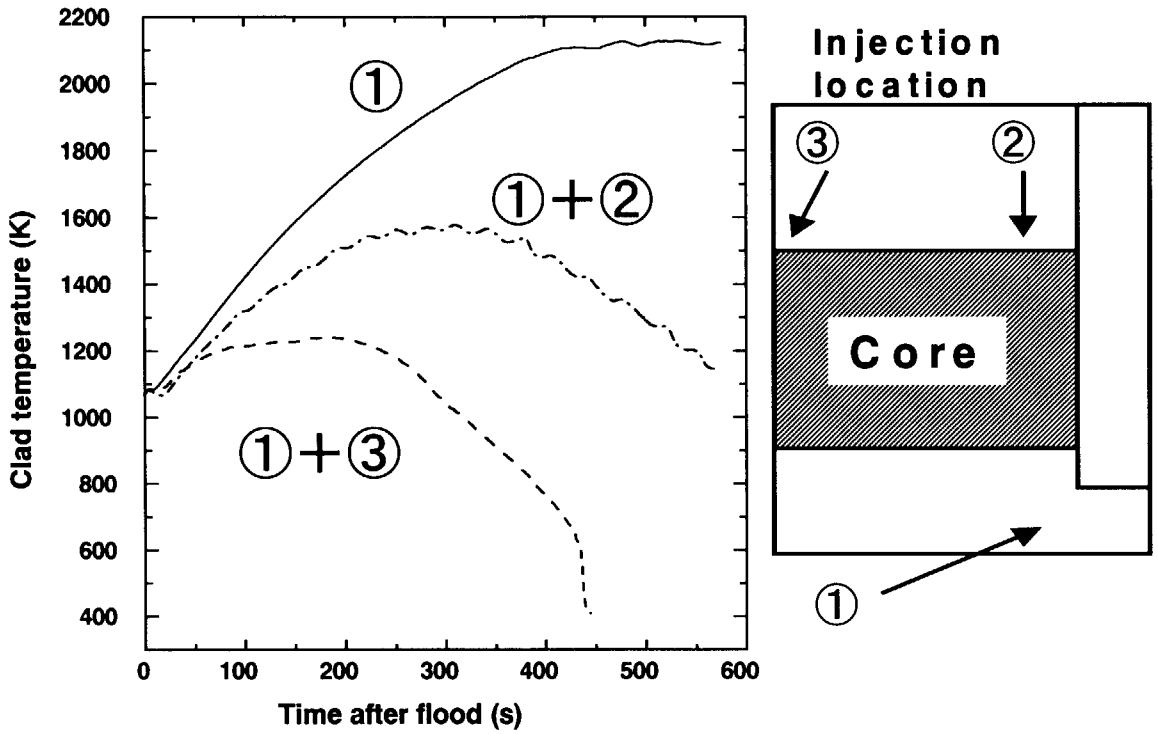

Fig. 6.1.3 Effect of upper plenum injection on PCT

6.2 Improvement of Multi-dimensional Two-Fluid Model Code ACE-3D and Application to Thermal-Hydraulic Analysis of Water Pool for Passive Residual Heat Removal

A. Ohnuki, H. Kamo and H. Akimoto
(*E-mail*: ohnuki@hflwing.tokai.jaeri.go.jp)

In order to develop a detailed analytical tool for gas-liquid two-phase natural circulation taking place in passive safety equipment, we improved ACE-3D code[1] which is based on multi-dimensional two-fluid model. In this section, the improved functions and the verification of the functions using experimental data are described. Then, the performance of passive residual heat removal of water pool in JPSR[2], which is a passive safety reactor designed in JAERI, is evaluated by this code.

The improved ACE-3D code can analyze effects of turbulent heat flux and execute coupled analyses with heat conduction structures. In the evaluation of turbulent heat flux, the turbulent Prandtl number is assumed to be constant. The heat conduction module can be coupled as a one-dimensional module or a three-dimensional one. The applicability of the improved functions were verified using data from steam jet experiments in water pool which were obtained in this study. The water pool is a rectangular shape and the horizontal dimension is 500x700 mm. The steam was injected through an orifice nozzle (3 mmϕ) at the bottom center of the pool under 1200 mm water depth. Two heat exchangers are equipped at both sides to adjust the pool water temperature. The jet flow pattern was recorded by a digital still camera and a high speed video recorder. The distribution of fluid temperature was measured and the water velocity distribution was also estimated by PIV method using small polymer particles with the high speed video system. Through the verification analyses, the introduction of the turbulent heat flux model was found to be indispensable. Figure 6.2.1 shows the effect of the turbulent heat flux. The analyses were performed for one section of water pool divided into four sections under symmetric property. The steam is injected at one corner of right side. Under the laminar model, no significant steam condensation is occurred and the injected steam reaches to the top surface. On the other hand, the steam is totally condensed under the turbulent model and the tendency was consistent with the observed flow pattern. The distributions of water velocity and the fluid temperature were also predicted well by the improved ACE-3D code.

The ACE-3D code was then applied to the analysis of water pool for passive residual

heat removal of JPSR in order to evaluate the performance of the heat removal. Figure 6.2.2 shows the input nodalization which models a half of one unit out of four active units in real system. The steam was injected uniformly through 5 mm slit opening along Y direction of sparger. Several initial and boundary conditions were set from a design requirement. Figure 6.2.3 indicates the distributions of water velocity and water temperature when the injected residual heat is removed sufficiently. From this application, it was found that the capability of residual heat removal of water pool in JPSR is high and it is possible to remove the amount of heat which is required from a design criterion.

References

1) Ohnuki, A. et al.: JAERI-Data/Code 96-033 (1996) in Japanese.

2) Murao, Y. et al.: J. Nucl. Sci. Technol., 32, 885 (1995).

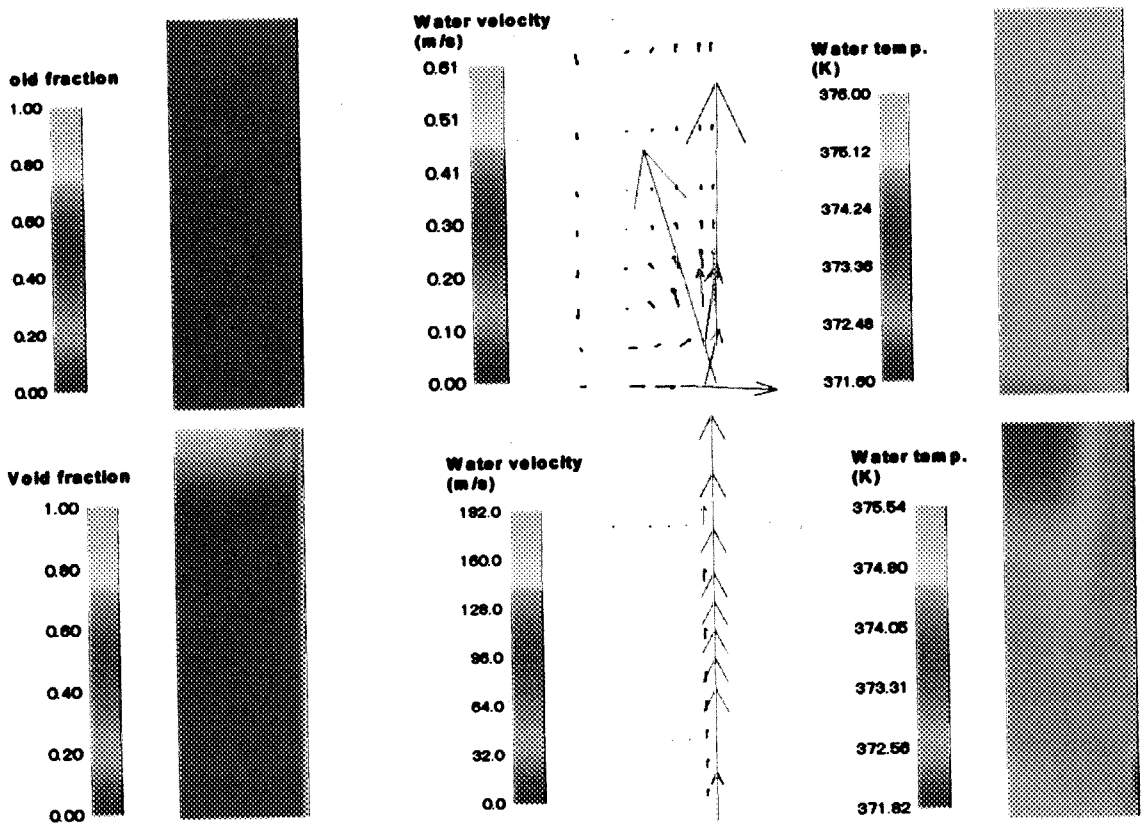

Fig. 6.2.1 Effect of turbulent heat flux (Upper three figures by turbulent model and lower figures by laminar model)

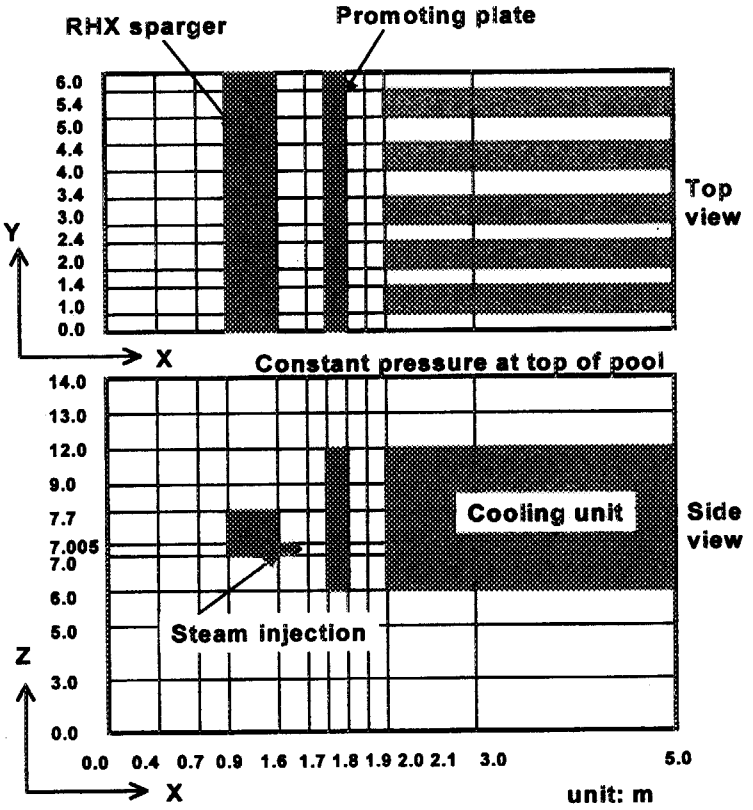

Fig. 6.2.2 Nodalization of JPSR water pool

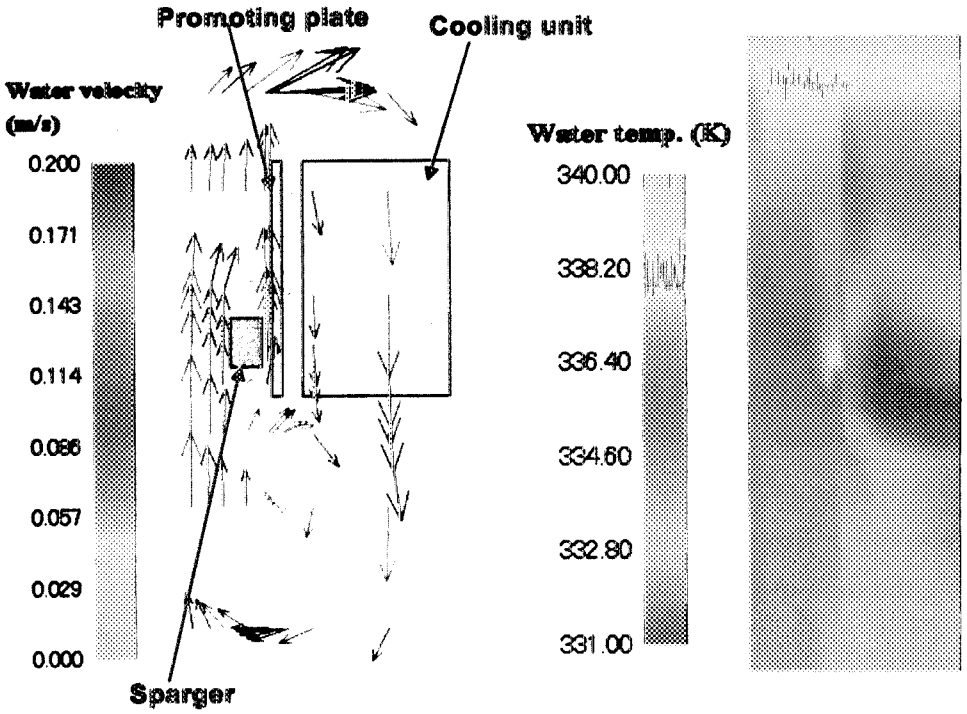

Fig. 6.2.3 Distribution of water velocity and water temperature in water pool

6.3 Void Fraction Measurement of Subcooled Flow Boiling by Neutron Radiography

M. Kureta and H. Akimoto
(*E-mail*: kureta@hflwing.tokai.jaeri.go.jp)

The high-frame-rate neutron radiography system that can visualize and measure the void fraction distribution of subcooled flow boiling has been developed. In this report, we focus on (1) an instantaneous void fraction measurement, (2) a time-averaged void fraction measurement, (3) effects of system parameters on void fraction and (4) the discussion about void fraction in the critical heat flux (CHF) model.

The test channels used in the experiment were rectangular channels heated from one side with gap thickness of 3 mm and 5 mm, channel width of 30 mm, heated width of 20 mm and heated length of 100 mm as shown in Fig. 6.3.1. The test channel was installed at the thermal neutron radiography port of the JRR-3M of Japan Atomic Energy Research Institute. Purified water flowed through the channel upwardly to be heated and boiled in the heated section. The pressure at the exit of the heated section was kept near the atmospheric pressure. Figure 6.3.2 shows the schematic diagram of high-frame-rate neutron radiography imaging system used in the present experiment. The method of void fraction measurement is based on the Σ-scaling method proposed by Mishima et al [1].

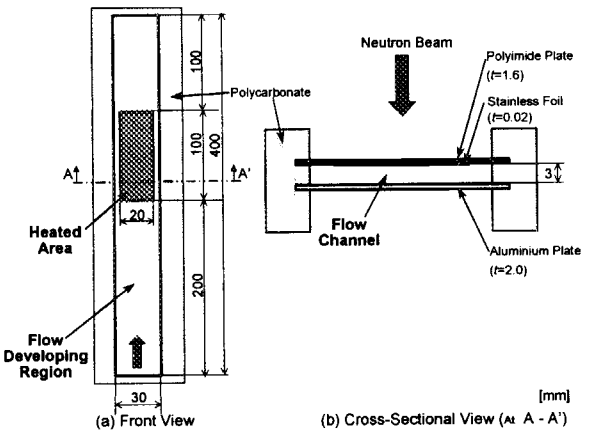

Fig. 6.3.1 Schematic view of the test section

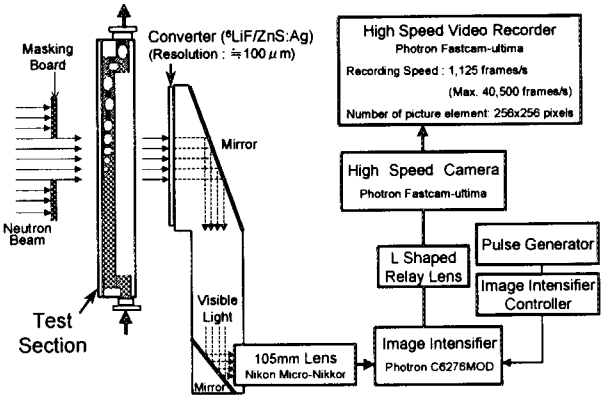

Fig. 6.3.2 Schematic diagram of high-frame-rate neutron radiography imaging system

Because the flow pattern of the forced convection subcooled flow boiling had not become clear, we had to visualize the instantaneous void fraction distribution of subcooled flow boiling before measuring the time-averaged void fraction. Figure 6.3.3 shows instantaneous void distribution images of subcooled flow

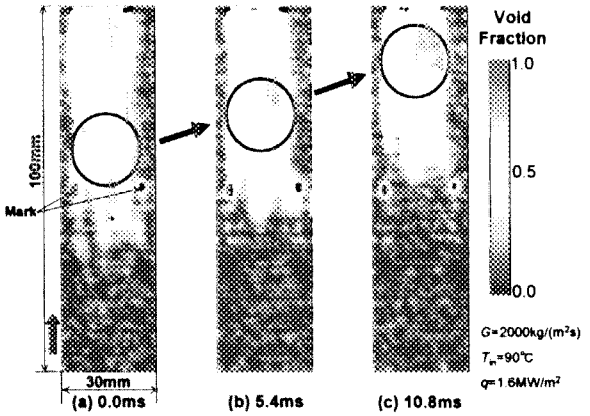

Fig. 6.3.3 Instantaneous images of subcooled boiling taken at 1125frames/s

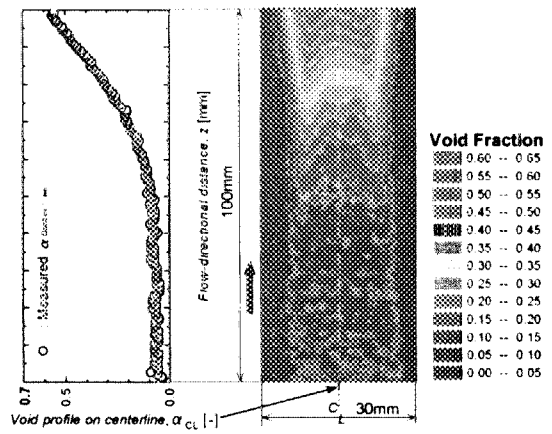

Fig. 6.3.4 Time-averaged void distribution (s=3mm, G=400kg/m^{2}s, T_{in}=90℃, and q=0.65MW/^{2})

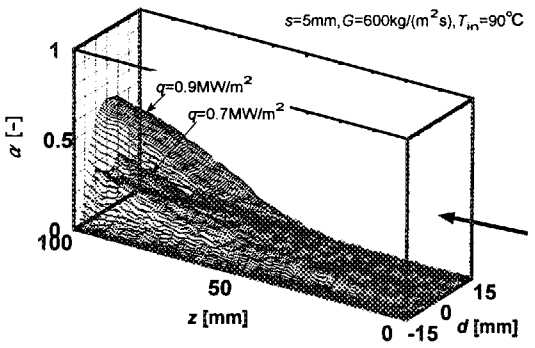

Fig. 6.3.5 (a) Void distribution in the channel

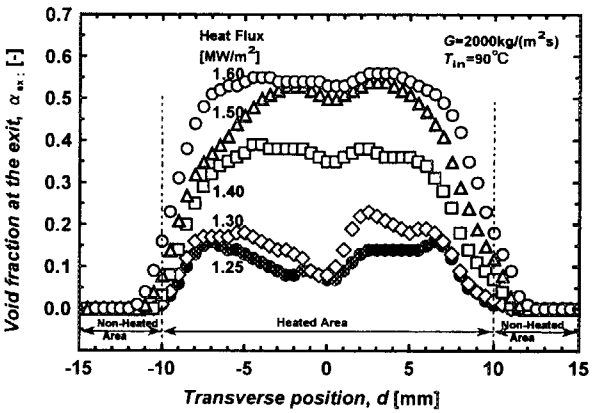

Fig. 6.3.5 (b) Transverse profiles of void fraction

boiling. The behavior of generated bubbles was successfully visualized. Detailed observation suggested that periodical flow oscillations were induced spontaneously. The period of oscillation was found to be about 10 ms for this condition. A burnout was observed at the exit of the heated section when a slug bubble expanded to its maximum length covering a wide area of the flow channel.

Figure 6.3.4 indicates an example of two-dimensional time-averaged void fraction distribution as well as void profile along the channel centerline. This image was obtained by integrating 2250 instantaneous images: about 200 times longer than the oscillation period. More boiling bubbles are generated near both sides of the heater than along the center.

Void distribution with the heat flux as a parameter is shown in Fig. 6.3.5. Figure 6.3.5 (a) shows 3D image of void fraction distribution. Figure 6.3.5 (b) shows the transverse profile of void fraction at the exit. The saddle-shaped profile was obtained when the heat

flux is lower. Vapor bubbles that were generated near both side of the heater coalesce each other when heat flux increases, and the transverse profile changes to the center-peak shape. This may be due to the secondary flow in the narrow rectangular channel. It was found that the inlet subcooling affects the void fraction significantly, and that the significant increase of void fraction was measured under the conditions of low mass velocity.

At the present time, it is difficult to predict the CHF for narrow and short rectangular channels. The Katto CHF model, which is originally proposed for a tube, tends to over estimate the CHF for present conditions. Main issue is that the void fraction distribution at the burnout was calculated higher than the applicable range of the model. So we tried to replace the calculated void fraction and the thermal quality at the net vapor generation point x_d with measured values. Then, the predicted CHF by the model tends to close the measured CHF value, e.g., C/E changes from 21 of original to 6.6 under the conditions of mass velocity G=2000 kg/(m^{2}s). We also tried to replace the forced convection heat transfer coefficient with experimental one and vapor velocity coefficient from 5.4 to 1.0. C/E becomes 1.4 for the above case. From the trial, it was found that the Katto model could calculate more suitable CHF if the void fraction distribution and heat transfer coefficient were calculated with high accuracy. Some x_d correlations and void fraction models were compared with the measured data.[2] Since existing x_d correlations did not agree with the measured x_d, we need to investigate incipient point of boiling and propose the x_d correlation for the present condition.

The instantaneous and time-averaged void fraction distributions were measured by high-frame-rate neutron radiography. System parameter effects on void distribution were made clear. If the void fraction etc. in the Katto CHF model were replaced with the measured values, C/E value would be better.

References

1) Mishima, K. and Hibiki, T. : Nucl. Sci. Eng., 124, 327, 1996.

2) Kureta, M. and Akimoto, H. : "Proc. of 2nd Int. Symp. on Two-Phase Flow Modelling and Experimentation", Edizioni ETS, 3, 1509 (1999).

6.4 ICE/LOVA Experiments

K. Takase, M. Shibata, T. Takahashi and H. Akimoto

(E-mail: takase@popsvr.tokai.jaeri.go.jp)

For the thermofluid safety study for fusion reactors, two experimental studies on the ingress-of-coolant event (ICE) and loss-of-vacuum event (LOVA) have been carried out as International Thermonuclear Experimental Reactor (ITER) safety R&D subtasks in order to validate the fusion safety analysis codes.

A scenario of the ICE and LOVA in a fusion reactor is shown in Fig. 6.4.1. If cooling tubes installed into plasma-facing components (PFCs) in the vacuum vessel (VV) of a fusion reactor are broken, water under high temperature and pressure in the cooling tubes will be discharged into the VV, and the discharged water will impinge on the surface of the PFCs and evaporate. As a result, the pressure in the VV will increase rapidly. This is called the ICE.

On the other hand, if the VV or some penetrations are broken by pressurization in the VV after the ICE, buoyancy-driven exchange flows caused by the temperature difference between the inside and outside of the VV will take place through breaches. In addition, the activated dust accumulated inside the VV and the tritium retained in the PFCs will be entrained by the exchange flows from the inside of the VV through the breaches to the outside. This is called the LOVA.

The ICE experiments were carried out using the preliminary ICE apparatus[1] with a small-scale VV and a boiler. In the ICE experiments, the hot and pressurized water from the boiler was injected through a water nozzle into the VV, and the pressure and temperature transients in the VV were measured.

Figure 6.4.2 shows the measured pressure transient in the VV. The initial conditions are: the wall temperature inside the VV of 250°C; the injected water temperatures of 200°C; the injection time of 10 s; and the water nozzle diameter of 2 mm. The pressure increased rapidly during the water injection and reached about 0.45 MPa at 10 s, and then increased gradually to 0.7 MPa. The initial first rise is believed to result from flashing evaporation of the injected water and evaporation of the water jet impinging onto the hot wall in the VV. The slower rise is thought to be due to boiling of the water which accumulates on the floor of the hot VV.

The LOVA experiments were performed using the preliminary LOVA apparatus[2], which consisted of a toroidally-shaped VV with simulated breaches. In the LOVA experiments, pressure and temperature transients in the VV during the LOVA were measured for various breach sizes and locations.

Figure 6.4.3 shows the relationship between d_B and Δt. Here, d_B denotes the breach diameter and Δt represents the saturation time from vacuum to atmospheric pressure in the VV after the breach located on the roof of the VV was opened. In Fig. 6.4.3, d_B and Δt are correlated as almost linear on a logarithmic scale. The volume of the VV in ITER is approximately 10,000 times larger than that of the present LOVA apparatus. Therefore, it can be estimated that, if the LOVA occurred in ITER and its breach size was very small, Δt would be very long and determination of the breach position might be very difficult.

Thermal-hydraulic characteristics during the ICE and LOVA in a fusion reactor were clarified by the present ICE/LOVA experiments. These results will be very useful for the themofluid safety design in ITER.

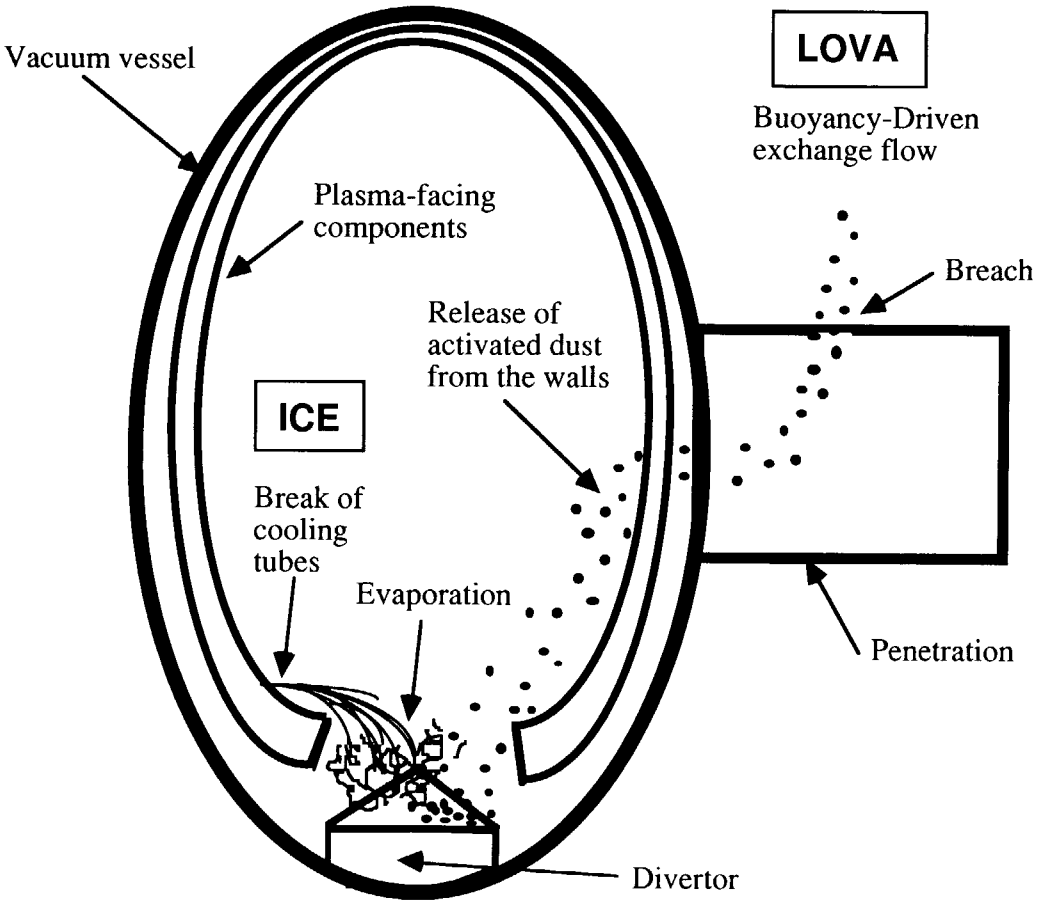

Fig. 6.4.1 Scenario of the ICE and LOVA events in the fusion reactor

References

1) Takase, K., et al.,:"A Fundamental Study on a Water Jet Injected into a Vacuum Vessel of Fusion Reactor under the Ingress of Coolant Event," Fusion Technology, 30, 3, pp.1453-1458 (1996).

2) Takase, K., et al.,:"Experimental Study on Buoyancy-Driven Exchange Flow Though Breaches of a Tokamak Vacuum Vessel in a Fusion Reactor Under the LOVA Condition," Nuclear Science and Engineering, 125, 3, pp.223-231 (1996).

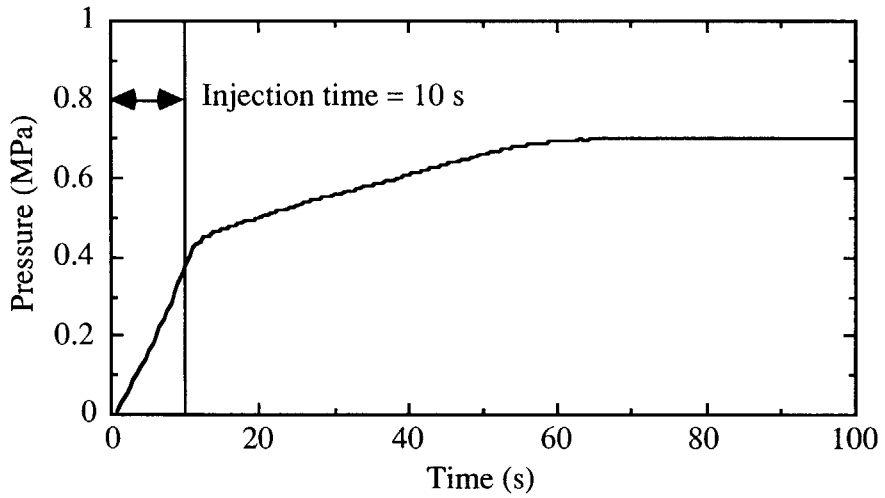

Fig. 6.4.2 Pressure transient in the VV measured during the ICE

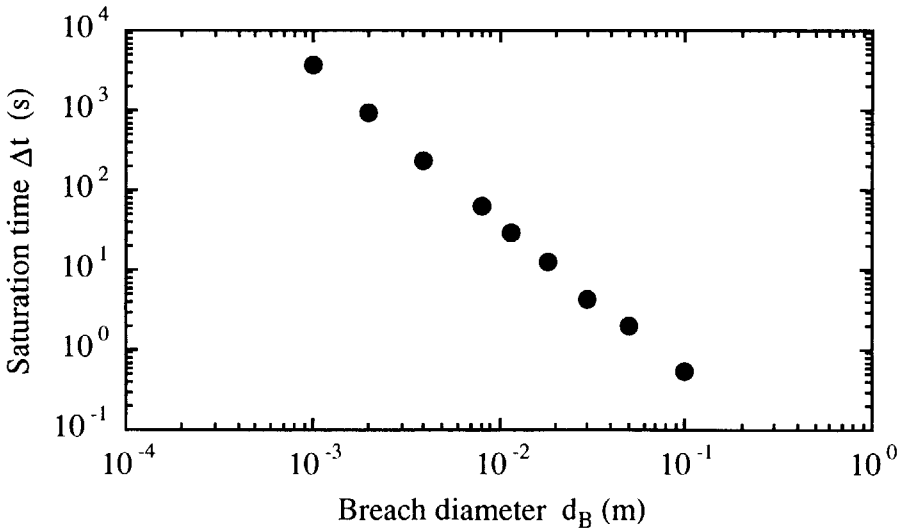

Fig. 6.4.3 Relationship between d_B and Δt measured during the LOVA experiments

6.5 Numerical Predictions on Pressure Rise Characteristics in Fusion Reactors During Ingress-of-Coolant Events

K. Takase, Y. Ose and H. Akimoto

(E-mail: takase@popsvr.tokai.jaeri.go.jp)

When cooling tubes installed in plasma-facing components (PFCs) of a fusion reactor are damaged by some accidents, water may be discharged into a vacuum vessel (VV) of the fusion reactor. In such a case, the discharged water will impinge on a surface of PFCs at high temperature and be evaporated. The generated steam can cause a rapid pressurization, and consequently, the VV may be broken by that. This event is called the ingress-of-coolant event (ICE). The ICE is one of the most severe scenarios in the safety of the fusion reactors.

An analytical study was performed to understand the controlling mechanism of the pressure transient during the ICE. Using the TRAC code[1], which was originally developed for accident analyses in light water reactors, numerical simulations were carried out.

The present numerical analyses were performed based on this preliminary ICE apparatus[2]. It mainly consists of the VV, boiler, water injector and vacuum pump.

A nodalization diagram of the TRAC-PF1 input model is shown in Fig. 6.5.1. The ICE apparatus was simulated by one-dimensional components of the vessel, pipe and valve models. Here, the boiler, inlet piping, VV, outlet piping and blowdown tank consist of 6, 20, 24, 10 and 6 nodes, respectively. The valve model was adapted to the node between the inlet piping and the VV, and then, the water injector was simulated using this valve model. In the calculations, the valve model was opened at time zero and closed at 10 s.

The inlet piping is connected to near the center position of the VV and the outlet piping is connected to the lower position of the VV. The VV is simulated by using 24 nodes for horizontally and one node for vertically. The wall of the VV consists of two heat structures: the copper is set to the inside wall and the stainless steel is set to its outside. Here, the heat conduction was considered for vertically and ignored for horizontally.

An additional valve model was used in the outlet piping. This valve was opened when the inside pressure of the VV reached 0.19 MPa during the ICE. After the valve was opened, the VV and blowdown tank are connected with the outlet piping. The blowdown tank was provided to decrease the inside pressure of the VV during the ICE.

Figure 6.5.2 shows a comparison among three pressure transients obtained by the experiment and numerical analyses. Here, the initial wall temperature (T_v)=250°C and initial

water temperature (T_w)=100℃. The solid line indicates the experimental results and dashed and three-pointed lines indicate the numerical analysis results. Here, the dashed line is the case that the surface heat flux from the wall of the VV is not zero, and then, the three-pointed line is the case that it is zero and the wall boundary condition is adiabatic. Namely, the three-pointed line shows the pressure rise due to only the flashing without the effect of the heat transfer from the wall.

The dashed line was in good agreement with the experimental result although it overestimated in a time range of less than 30 s. The three-pointed line showed about 0.04 MPa after 10 s and its value was very small in comparison with the dashed line. Therefore, it was found that the pressure rise during the ICE receives strongly the effect of the heat transfer from the heated wall.

From the present numerical study, it was confirmed that the TRAC-PF1 code could predict the major trend of the pressure transient in the VV during the ICE events and the pressure transients were mainly affected by the water temperature in the early period and by the wall temperature in the later period.

The injected water flashed and reached the thermal equilibrium after the water injection. Then, the remained water at saturation temperature was accumulated on the bottom of the VV after the impingement to the target plate and evaporated by the heat transferred from the heated wall.

The predicted maximum pressure increased with the wall temperature resulting from the increase in the steam generation on the heated wall, and also, it increased with the water temperature due to increase in the steam generation by the flashing. It was clarified quantitatively from the present numerical study that the main control factors on the pressure rise in the VV during the ICE events were the flashing and the boiling heat transfer inside the VV.

References

1) Liles, D. R.: "TRAC-PF1/MOD1: An Advanced Best-Estimate Computer Program for Pressurized Water Reactor Thermal-Hydraulic Analysis", NUREG/CR-3858 (LA-10157-MS), (1986).

2) Takase, K., Kunugi, T. and Seki, Y.: "Thermal-Hydraulic Characteristics in Tokamak Vacuum Vessels under Transient Events, " Proc. of the 8th International Topical Meeting on Nuclear Reactor Thermal-Hydraulics (NURETH-8), 3, pp.1321-1327 (1997).

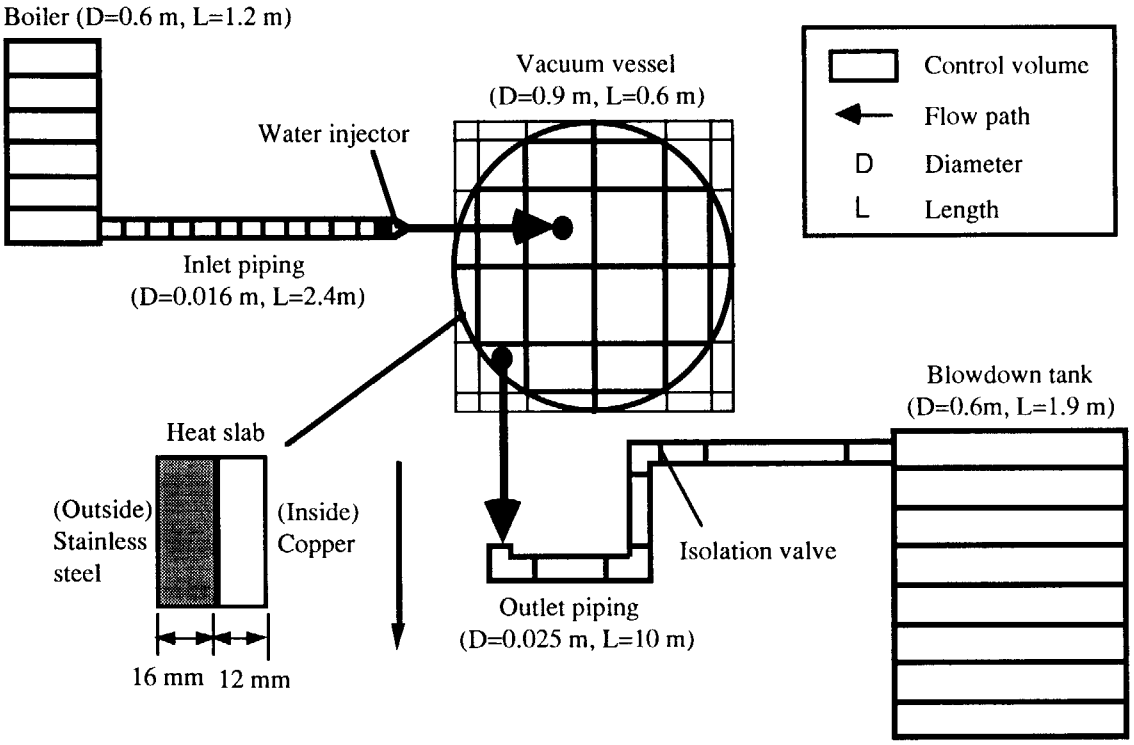

Fig. 6.5.1 Nodalization diagram of input model for the TRAC-PF1 code

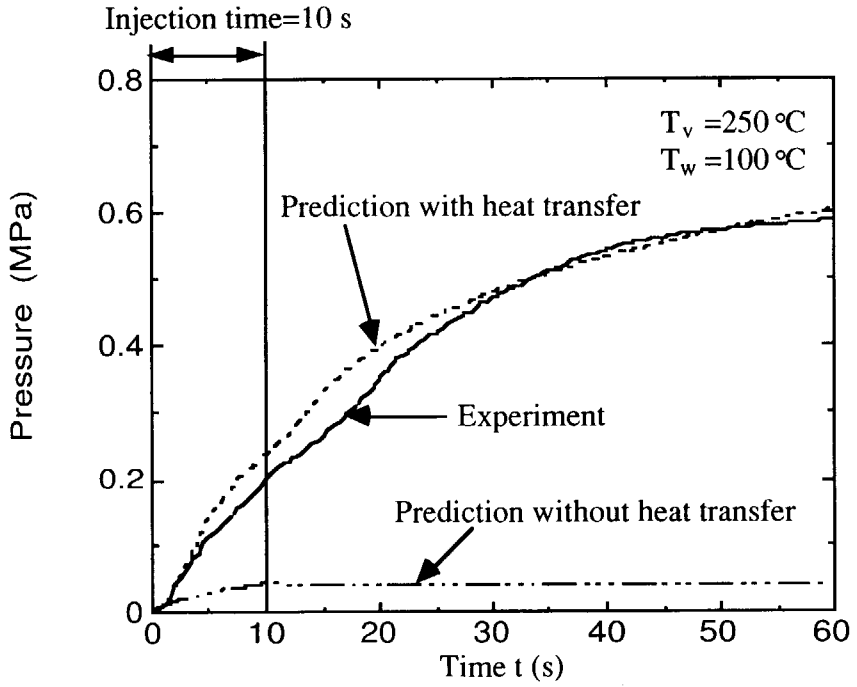

Fig. 6.5.2 Comparison between the experimental and numerical analysis results

6.6 Development of 3-Dimensional Thermal-Hydraulic Analysis Code for Fusion Reactors Under Loss-of-Vacuum Events

K. Takase and H. Akimoto

(E-mail: takase@popsvr.tokai.jaeri.go.jp)

In the International Thermonuclear Experimental Reactor (ITER) design, it is estimated that a mean diameter of the dust particle will be around 10 μm and the total mobilized dust within 1st confinement barrier as the environmental release limit will be 100 kg in beryllium, 200 kg in carbon and 100 kg in tungsten. Therefore, as a conservative estimate, it can be presumed that all the dust may be transported from the breaches to the outside of a vacuum vessel (VV) in a fusion reactor during an loss-of-vacuum-accident (LOVA) event.

The exchange flow characteristics were investigated using the preliminary LOVA apparatus[1], and it was clarified that since the exchange flow receives the large flow resistance according to the breach diameter and length, its velocity becomes very low. Thus, it can be expected that the transported dust from the walls in the VV during the LOVA event may drop on the floor if the dust is heavy and may be conveyed with the exchange flows if that is not heavy. Therefore, it is very important to investigate the dust transport characteristics during the LOVA event from the viewpoint of the thermofluid safety design of ITER.

However, it is not easy to investigate experimentally the dust transport behavior in the VV because measuring procedures of the dust particles with micron diameters are still not established enough. Thus, a three-dimensional thermal-hydraulic analysis code for fusion reactors has been developed to estimate the dust transport behavior under the LOVA conditions.

The three-dimensional continuity, momentum and energy equations in a compressible with a cylindrical coordinate were used for the present numerical study.

Main assumptions on the dust transport calculations are as follows: The dust particle has a spherical shape; All the dust have the same size and the same specific heat; The motion of the dust particle is expressed using the drag coefficient; The phase transformation dose not occur; and the dust particle has no temperature gradients in the radial direction.

The drag coefficient of the dust particle, C_D, is calculated using the following equations[2] as a function of particle Reynolds number, Re_p:

$$C_D = \frac{24}{Re_p}\left(1+0.125 Re_p^{0.72}\right) \quad , \quad Re_p \ 1000;$$

$$C_D = 0.44\ ,\ 0<\mathrm{Re_p}<1000.$$

The analytical region and boundary conditions are shown in Fig. 6.6.1. The analytical region is a cylinder with a diameter of 2500 mm and a height of 2500 m, and it is enclosed with the walls. The no-slip and adiabatic boundary conditions were adopted for the side and bottom walls, and the free-slip boundary condition was set to the top wall. At the top wall of the analytical region, the temperature gradient and pressure were set to zero and 1 bar, respectively. The VV is put in the center of the analytical region. The no-slip and adiabatic boundary conditions were set to all the walls of the VV. The breach is positioned at the top of the VV and its cross-sectional area is almost equal to the experimental condition. The breach configuration for the experiment is round with a diameter of 100 mm, however, that for the present analysis is not round in relation to the computational grid formation.

Figure 6.6.2 shows the comparison between the experimental and analytical results. Here, the solid line shows the pressure transients in the VV during the LOVA event and these data were measured by the preliminary LOVA apparatus. The solid symbols represent the predicted average pressures in the VV and those were calculated from the present analysis results. The predicted average pressure reached a saturation value (i.e., atmospheric pressure) until about 0.5 s and it was found that the predicted numerical analysis results were in good agreement with the experimental results.

Figure 6.6.3 shows the numerical analysis results after 1 s from the start of the calculation. Here, Figs. 6.6.3(a)-(d) represent the predicted axial velocity, pressure, fluid temperature and dust transport distributions in the vertical direction, respectively.

From the results of the present numerical analysis, it was found that the predicted average pressure in the VV agreed well with the experimental results and the present numerical approach was effective to estimate the thermal-hydraulic and dust transport characteristics in fusion reactors during the LOVA events.

References

1) Takase, K., Kunugi, T., Ogawa, M. and Seki, Y.: Nuclear Science and Engineering, 125, pp. 223-231 (1997).

2) Schlichting, H.: "Boundary layer Theory", McGrow-Hill, New York, p. 17. (1979).

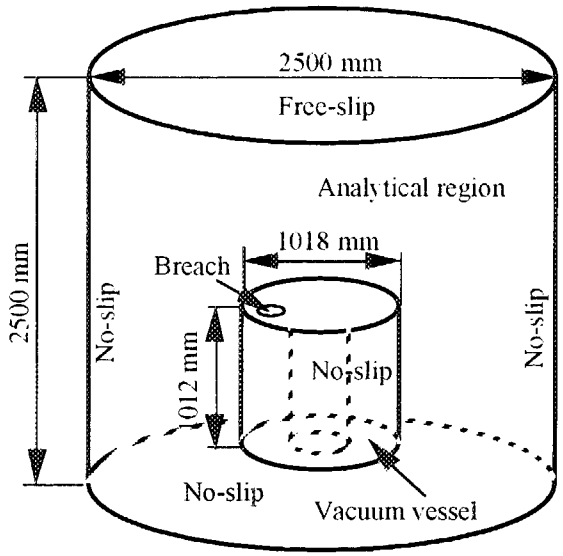

Fig. 6.6.1 Analytical model and boundary conditions

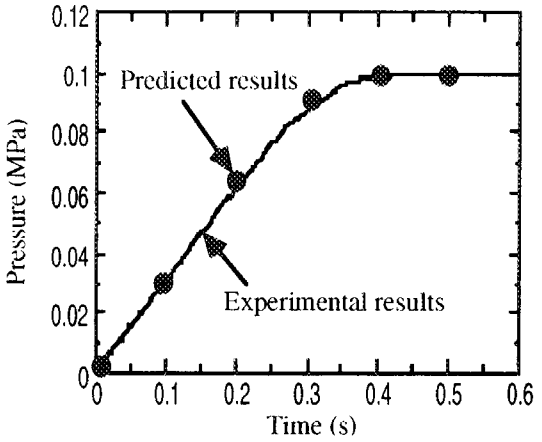

Fig. 6.6.2 Comparison between experimental and predicted pressures

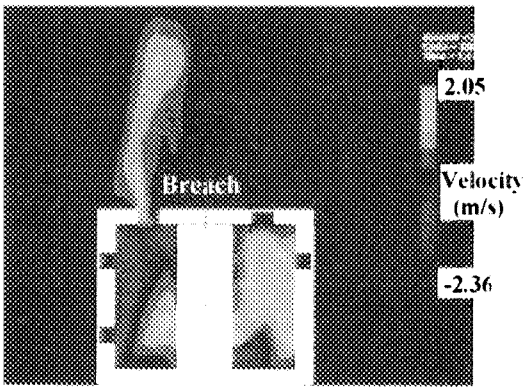

(a) Axial velocity distribution

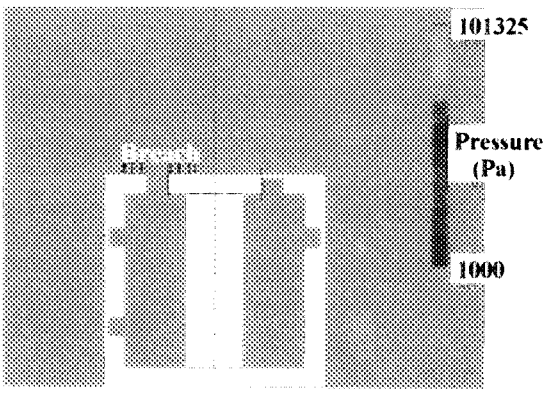

(b) Pressure distribution

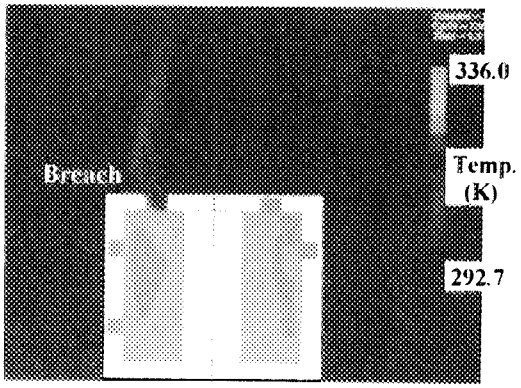

(c) Fluid temperature distribution

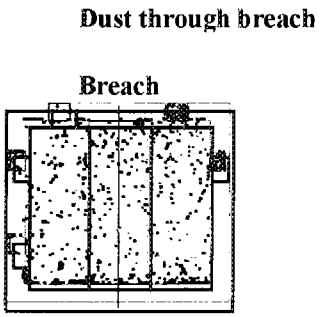

(d) Dust mobilization behavior

Fig. 6.6.3 Numerical analysis results after 1 s from the start of the LOVA calculation

7. Energy System Analysis and Assessment

In order to assess the roles of nuclear energy and its relevant technologies in future energy systems, the development of analytical tools and application studies have been made so far. Among the development and studies made in the fiscal year 1998, five topics are presented in the following.

The roles of nuclear energy in Japan's long-term energy systems have been analyzed from the viewpoint of securing future energy supply and reducing CO_2 emissions. By analyzing the energy scenarios with different assumptions on the availability of future options, it has been concluded that, without increasing the utilization of nuclear energy, the CO_2 emissions can hardly be reduced below the 1990 emission levels even if the utilization of natural gas and renewable energy is increased as much as possible.

In order to establish the foundation of energy systems analysis, a model has been developed on the evolution of Japan's long-term energy systems. A reference energy system has been defined by incorporating all important energy sources, energy carriers, and energy technologies that are currently used or to be possibly used in the future. Then, characteristic data are compiled for each of energy technologies in the system.

Income and price elasticity of final energy consumption in Japan has been analyzed by using statistical data and a method of regression analysis. The results have indicated that the consumption in raw material production industries has significant price elastcity. However, the consumption in other sectors has shown little or no correlation with prices, although income elasticity is large in these sectors.

The roles of high-conversion water-cooled reactors (HCWRs) have been analyzed from the viewpoint of reducing the long-term consumption of natural uranium. According to the results, HCWRs should have high conversion ratios and/or low plutonium inventory in order to reduce the consumption at significantly low levels such as to be achieved by using fast breeder reactors.

Nuclear energy is expected to meet non-electric energy demand in the future by using high temperature gas-cooled reactors. The conceptual study has been made so far on the combined system of HTGRs and a UT-3 thermochemical process. In addition, the potential of reducing CO_2 emissions by introducing this system has been analyzed within the framework of Japan's long-term energy systems.

7.1 CO_2 Emission Reduction Strategy and Roles of Nuclear Energy in Japan

O. Sato, M. Shimoda, K. Tatematsu and Y. Tadokoro

(*E-mail*: sato@ruby.tokai.jaeri.go.jp)

The roles of nuclear energy in Japan's future energy systems were analyzed from the viewpoint of enhancing the stability in energy supply and reducing the emissions of CO_2. The MARKAL model developed in the Energy Technology Systems Analysis Programme (ETSAP) of International Energy Agency (IEA) was used for analyzing energy scenarios with a time horizon of 1990 - 2050.

The analytical procedures are as follows: 1)Future demand for energy services was estimated by assuming GDP growth rates and other indicators as listed in Table 7.1.1. 2)A reference energy system was built by incorporating all energy sources and technologies that might be available by 2050. 3)The assumptions were made on the prices and availability of imported fuels. The availability of energy technologies was also assumed.

Then, future energy scenarios and cases were defined as indicated in Table 7.1.2. For each of these analytical cases, the utilization of energy sources and technologies was determined by minimizing discounted system costs. In all cases except for A1, the penalty to CO_2 emissions was included in the costs. After optimizing the structure of energy demand and supply, the CO_2 emissions and system costs were compared between the cases.

As shown in Fig. 7.1.1, the CO_2 emissions increase much in the case A1 (no nuclear energy and no CO_2 penalty) due to the utilization of coal. In the case B1 (A1 plus CO_2 penalty), the emissions can be substantially reduced by energy conservation, renewable energy, and natural gas. However, the emission levels exceed 1.5 billion ton(CO_2) after 2040. In the case C1 (B1 plus nuclear power), the emission levels can be reduced below the 1990 levels after 2025. In the case D1 (C1 plus nuclear process heat), the emissions are further reduced.

The CO_2 disposal option is effective to the drastic reduction. In the case B2 (B1 plus CO_2 disposal), the emission in 2050 is lowered to the level of the case D1 by disposing CO_2 of more than 1.0 billion ton(CO_2). In the case D2 (D1 plus CO_2 disposal), the emission in 2050 is lowest of all cases. On the other hand, the expansion of natural gas utilization alone is not effective enough. In the case B1G (B1 plus natural gas expansion), the future emissions are not lowered below the 1990 emission levels.

The average costs necessary to reduce one ton of CO_2 as measured from the case A1 are shown in Fig. 7.1.2. It is evident that the costs in C1, D1, and D2 with nuclear energy are lowest. While the costs in non nuclear cases are more than double of those in C1 or D1.

The above results are summarized as follows. Without nuclear energy, the CO_2 emissions will hardly be reduced due to the increases of coal utilization. CO_2 disposal will be effective in reducing the emissions, however, at much higher costs than the case with nuclear energy. Increases of natural gas imports alone will not reduce the emissions at enough low levels.

Table 7.1.1 Socio-economic indicators

	1990	2000	2010	2020	2030	2050
Population (Million)	123.6	127.4	130.4	128.3	123.0	111.5
Household (Million)	40.7	44.7	48.3	49.4	49.2	48.5
GDP Growth Rate (%)		*2.21*	*2.50*	*2.00*	*1.50*	*1.20*
Industry Production (%)						
Primary Industry	2.3	1.9	1.5	1.3	1.1	0.9
Manufacturing	42.7	42.6	42.9	42.6	42.4	42.2
Construction	9.2	8.5	7.9	7.5	7.2	6.7
Services	45.8	47.0	47.7	48.7	49.3	50.2

Table 7.1.2 Scenarios and cases

Scenario	Case	CO_2 Penalty (1)	Nuclear (2)	CO_2 Disposal	LNG Import
Base	A1	No	No	No	Normal
	B1	Yes	No	No	Normal
Nuclear	C1	Yes	Electricity	No	Normal
	D1	Yes	Electricity + Heat	No	Normal
CO_2 Disposal	B2	Yes	No	Yes	Normal
	D2	Yes	Electricity + Heat	Yes	Normal
Natural Gas	B1G	Yes	No	No	Expanded
	B2G	Yes	No	Yes	Expanded

(1) CO_2 Penalty

Year	2005	2010	2030	2050
Penalty (Yen/ton CO_2)	5000	10000	25000	50000

(2) Nuclear Energy

No : No Nuclear Investment after 2000

Electricity : LWR & FBR Capacity 100GWe in 2030, 125GWe in 2050

Electricity + Heat : In addition to the above, HTGR Capacity 80GWe in 2050

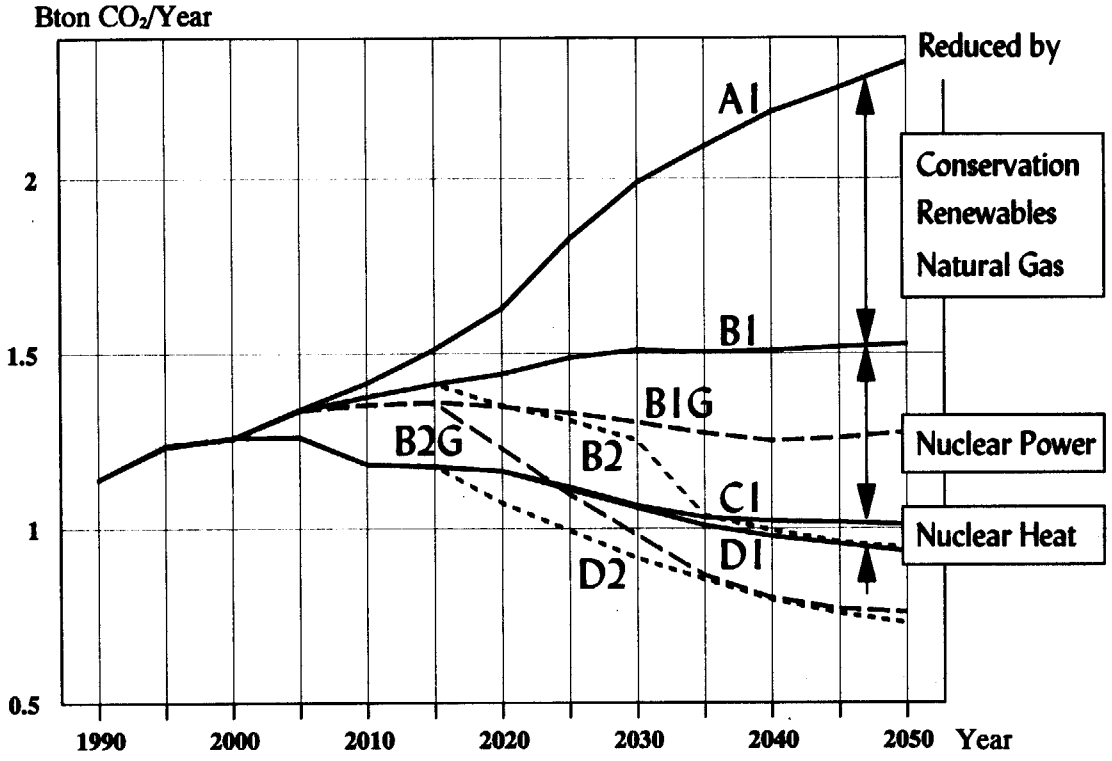

Fig. 7.1.1 Annual CO_2 emissions in analytical cases

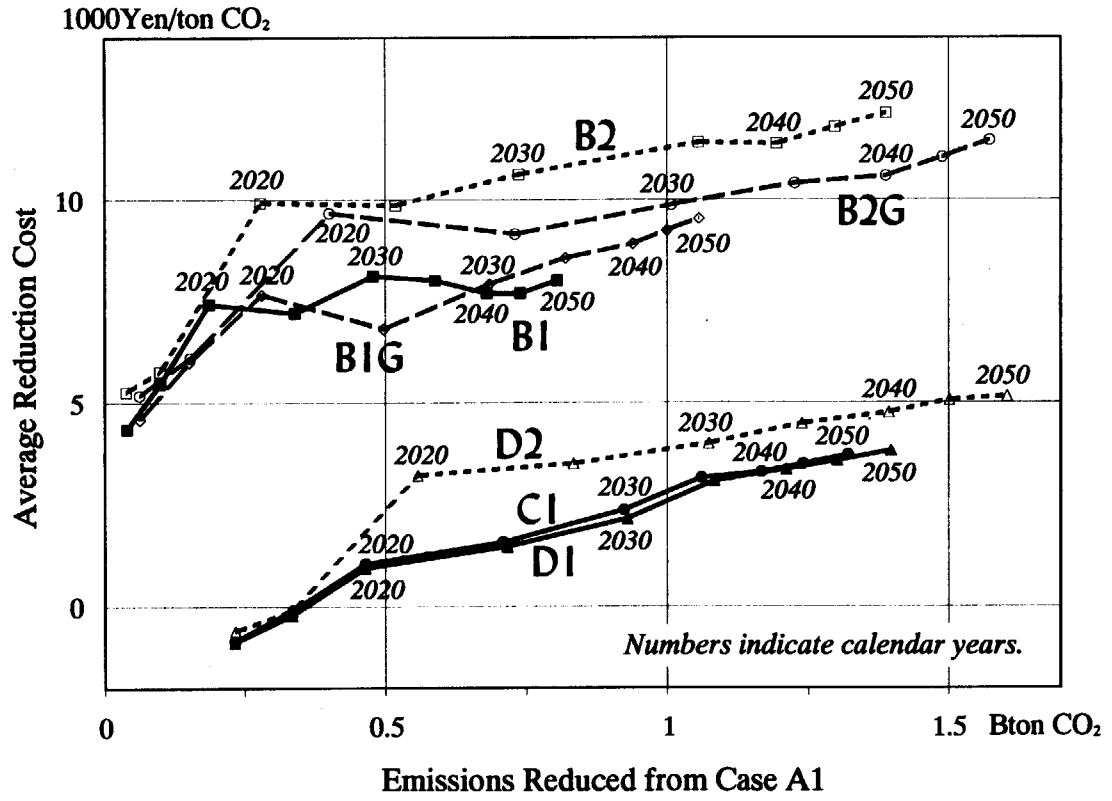

Fig. 7.1.2 CO_2 reduction vs average reduction cost

7.2 Modeling of Long-Term Energy System of Japan

Y. Gotoh, O. Sato, Y. Tadokoro
(*E-mail:* gotohy@ruby.tokai.jaeri.go.jp)

In order to analyze the future potential of reducing carbon dioxide emissions[1], a long-term energy system of Japan was modeled following the framework of the MARKAL model, and the database of energy-technology characteristics was developed[2].

A reference energy system (RES) was built by incorporating all important energy sources and technologies that will be available by the year 2050. The RES consists of 25 primary energy sources, 33 technologies for electric power generation and/or low temperature heat production, 97 technologies for energy transformation, storage, or distribution, and 171 end-use technologies (Table 7.2.1). As shown in Fig. 7.2.1, the energy supply system, comprising electric power generation, low temperature heat production, transformation, storage, and distribution technologies, was divided into nine subsystems; i) coal conversion processes, ii) oil refinery processes, iii) town gas processes, iv) fuel processing for power generation, v) power generation & district heating, vi) CO_2-separation & disposal, vii) nuclear heat applications, viii) nuclear power generation & nuclear fuel cycle systems, and ix) energy distribution technologies. Input energy carriers to the RES from 25 energy sources are transformed into 24 types of energy carriers that are delivered to the end-use system by the energy distribution technologies. The end-use system is comprising 3 sectors; industry, residential & commercial, and transportation sector.

The energy-technology characteristic data consist of input and output of energy carriers, efficiency, availability, lifetime, investment cost, operation and maintenance cost, CO_2 emission coefficient, and others. For the existing technologies, data were extracted from the available statistics, while for the future technologies still under development, data were estimated from the technological data found in literatures. In the fiscal year 1998, the database for 130 technologies in the energy supply system was developed. The database for 171 technologies included in the end-use system is now under development.

References

1) Sato, O., Shimoda, M., Tatematsu, K. and Tadokoro, Y. : JAERI-Res. 99-015 (1999).
2) Gotoh, Y., Sato, O. and Tadokoro, Y. : JAERI-Res. 99-046 (1999).

Table 7.2.1 Main specifications for the modelling of the long-term energy system of Japan

Analytical model	MARKAL
Time period	1990 - 2050
Number of primary energy sources defined	25
Number of energy carriers defined	24
Number of energy conversion & delivery technologies	130
(Electric power- and heat-generation technologies)	(33)
(Energy conversion, storage and delivery technologies)	(97)
Number of end-use technologies	171

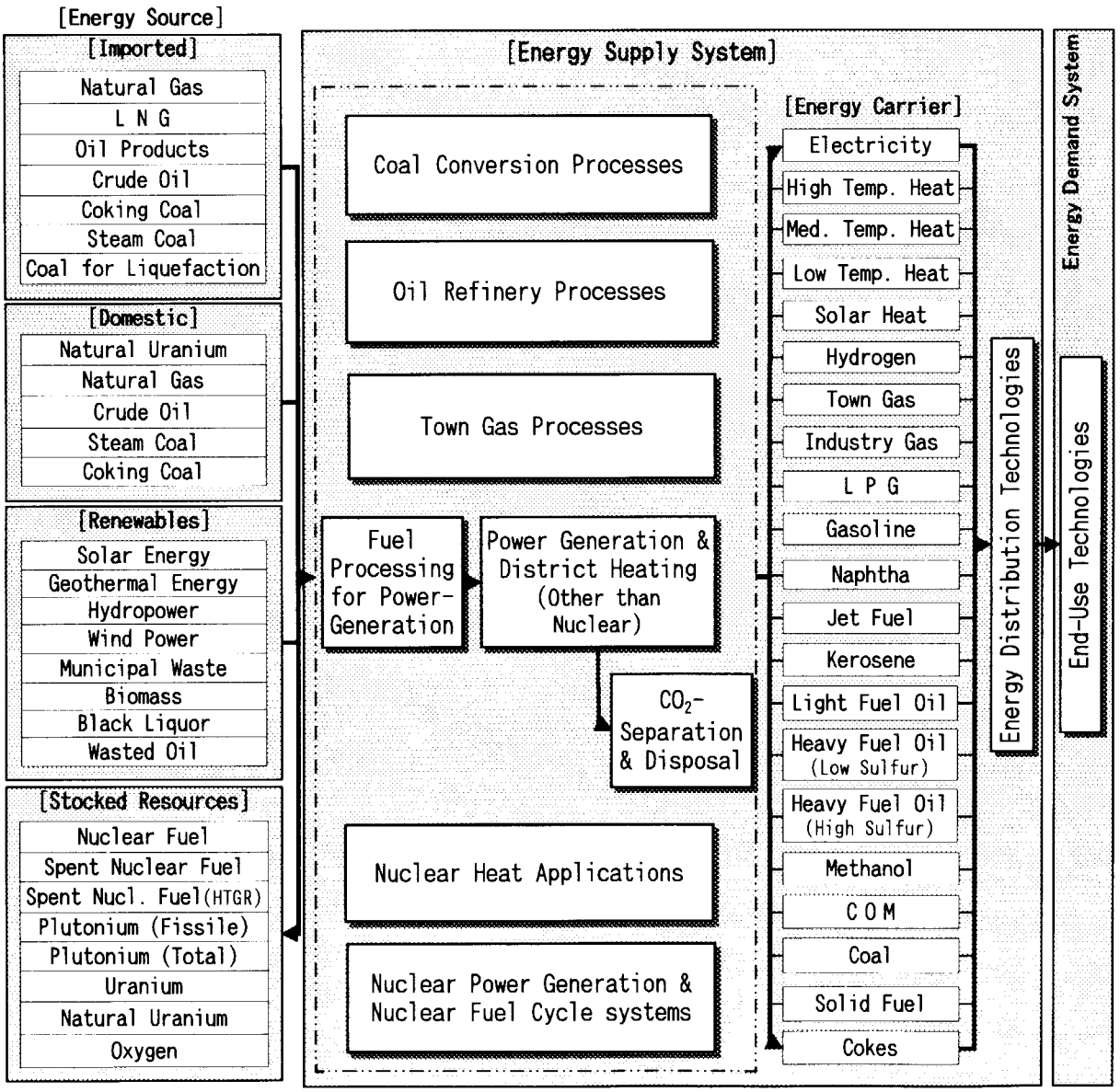

Fig. 7.2.1 Outline of the reference energy system for Japan.

7.3 Income and Price Elasticities of Final Energy Consumption

K. Kunii and T. Sato
(*E-mail*: kunii@jpsrews1.tokai.jaeri.go.jp)

In analyzing the interaction of energy and economy, it is very important to know how energy consumption will respond to the changes in income and energy prices. We analyzed income and price elasticities of final energy consumption in Japan in order to derive the information for estimating future energy demand and to develop the input data necessary for energy-economy interaction models.

Framework and Method

(1) Classification of energy consumption sectors :

- Industry : 5 sectors (Iron & Steel, Chemicals, Cement & Glass, Pulp & Paper, Others).
- Residential & Commercial : 2 Sectors (Commercial and Residential).
- Transportation : 2 Sectors (Passenger and Freight) .

(2) Time period :

- 1969-1996 (Analysis was made both for the entire time period and for short time intervals arbitrary chosen).

(3)Sources of statistical data :

- Final energy consumption : Energy Balances in Japan (1997).
- Real GDP, GDP deflator, energy prices : EDMC-Handbook of Energy and Economic Statistics in Japan (1998).
- Real domestic production by industries : Annual Report on National Accounts (1998).
- Domestic transportation of passenger and freight : EDMC-Handbook of Energy and Economic Statistics in Japan (1998).

(4)Analytical method :

Final energy consumption was expressed as a function of income (GDP or other indices) and average energy price. The above function was identified by regression analysis with the statistical data, and income elasticity and price elasticity were estimated. Following equations were used for the regression analysis of each demand sector ;

$E = c \cdot Y^{b1} \cdot P^{b2}$ or ,

$\ln E = a + b1 \cdot \ln Y + b2 \cdot \ln P$

where, E : final energy consumption, Y : income (real GDP or domestic production by industries) or amounts of domestic transportation (ton·km, passenger·km) for transportation sector, P : real energy price, b1 : income elasticity, b2 : price elasticity, a,c : constant .

A commercial software, TSP(Time Series Processor)[1] was applied to carry out computations of the regression analysis. Most of analytical results were significant from the viewpoint of statistical analysis theory.

Results and Findings

Income and price elasticities (I.E., P.I.) for each sector are shown in Table 7.3.1. The findings and remarks important to evaluate the correlation between energy consumption and income or energy prices are summarized as follows:

(1) Income elasticity of final energy consumption

- Strong correlation with income was observed in the residential & commercial sector, the transportation sector and others in the industry sector.
- Negative elasticities were derived for iron & steel, cement & glass industries, i.e., decreases of the energy consumption in spite of increases of production in monetary amount.

(2) Price elasticity of final energy consumption

- Contrary to income effect, almost no correlation with prices was observed in the residential & commercial sector, the transportation sector and others in the industry sector. Elasticities were very small even for short-term changes of energy prices.
- A significant correlation with prices was observed in the raw material production industries.

Reference

1) Wago, H. and Pan, K.: "Analyzing econometric data by TSP (2nd Edition)" , Tokyo-Univ. Publishing (1996) (in Japanese).

Table 7.3.1 Income and price elasticities of energy consumption
(Time period : 1969 - 1996)

Sector		Income Elasticity (I. E.) and Price Elasticity (P. E.)
Industry	Iron & Steel	I. E. : Inverse correlation (about -0.2) with GDP and production. P. E. : Small in long-term. Around -0.4 in short-term.
	Chemicals	I. E. : Very small in long-term. Around 0.5 after 1986. P. E. : About - 0.3 in long-term. -0.4 or higher in short-term.
	Cement, etc	I. E. : Inverse correlation with GDP and production (- 0.1) P. E. : Very small in long-term. Less than -0.4 in short-term.
	Pulp, Paper	I. E. : About 0.3 in long-term. Unstable in short-term. P. E. : About - 0.3 in long-term. -0.5 or higher in short-term.
	Others	I. E. : About 0.5 in long-term. Unstable in short-term. P. E. : Very small both in long-term and in short-term.
	Total	I. E. : About 0.2 in long-term. Larger in short-term (unstable). P. E. : - 0.15 in long-term. A little higher in short-term.
Resid. & Commer.	Commercial	I. E. : About 1.0 in long-term. Possibly larger in short-term. P. E. : - 0.1 in long-term. Unstable in short-term.
	Residential	I. E. : About 1.0 in long-term. Similar results in short-term. P. E. : No correlation observed.
Transport	Passenger	I. E. : 1.6 (pas.*km), 1.2 (GDP) in long-term. P. E. : No correlation observed.
	Freight	I. E. : 1.0 (ton*km), 0.6 (GDP) in long-term. Both 0.6 after 1986. P. E. : No correlation observed.
Total Final Energy		I. E. : About 0.5 in long-term. About 0.9 after 1986. P. E. : Very small (- 0.1) in long-term. A little higher in short-term.

7.4 An Analysis on the Roles of High Conversion Water-Cooled Reactors

K. Tatematsu and O. Sato
(*E-mail* : ktate@ruby.tokai.jaeri.go.jp)

As an alternative to the current FBR concept, water-cooled reactors with a high conversion ratio (HCWRs) is being developed. Last year we analyzed the roles of HCWRs in reducing the consumption of natural uranium (NU), and found that it was necessary to expand the time horizon in order to estimate the ultimate consumption of NU. In this study, the time horizon has been expanded by 200 years, and the cumulative NU consumption by three types of HCWRs with different conversion ratios (CRs) has been evaluated.

The PC version of JALTES-II has been used for the analysis with the assumptions listed in Table 7.4.1. The time horizon has been set as 1970 - 2300. Six analytical cases have been defined with different combinations of seven reactor types including three types of HCWRs that have different CRs. The installed capacity of individual reactor types in each analytical case has been determined by minimizing NU consumption with the assumption of total nuclear power capacity over the time horizon.

The cumulative NU consumption is shown in Fig. 7.4.1. At the year 2100 the NU consumption does not differ much between the cases, however the differences become larger thereafter. In the case C1, the consumption increases very rapidly with time. While, in the case C2 with FBRs, the cumulative consumption becomes constant after 2100 at the level of 1.3 million ton, the lowest of all analytical cases. This result can be attributed to the high breeding ratio and low plutonium inventory of FBRs.

The NU consumption in the case C3, C4, and C5, all with HCWRs, falls between the levels in the case C1 and C2. Among the three cases, the consumption in C5 remains at 1.5 million ton. In other two cases, the consumption increases much after 2100. Relatively higher NU consumption in these cases is due also to higher plutonium inventory of HCWRs as compared with FBRs. These results indicate that HCWRs with a current design can be regarded as an alternative to FBRs only if such high CRs as 1.1 can be realized.

Considering that it is difficult to realize CRs as high as 1.1 in the near future, and also it is not realistic to assume constant CRs over a very long time period, a more realistic scenario has been investigated. In the case C6, the CR of HCWRs is assumed to become higher with future technical progresses, i.e. from 0.98 in 2015, to 1.13 in 2050. It is shown in Fig. 7.4.1, that the NU consumption in this case can be reduced to the same level as in the case C5. This result indicates that HCWRs can be an alternative to FBRs by introducing in the near future with a modest CR and by improving their performance gradually.

Table 7.4.1 Major Assumptions for Analysis

1. Total Nuclear Power Capacity (GWe)

Year	～2004	2005	2010	2030	2050	2075	2100 ～
Capacity	Actual or Planned	50	70	100	120	134	140

2. Reactor Types

Enriched Uranium LWR (EU-LWR)	: fixed capacity until 2004, high burnup fuel after 1993
Partially MOX Fueled LWR (P-MOX)	: 12.1GWe (fixed capacity)
Fully MOX Fueled LWR (F-MOX)	: after 2006, with max. annual new capacity 1.35GWe
Fast Breeder Reactor (FBR-BR1.21)	: after 2050, with max. annual new capacity 1 GWe for initial 15 years, and 2 GWe for the next 15 years
High Conver. Water Reactor (HCWR-CR0.98)	: after 2015, without annual new capacity constraint
High Conver. Water Reactor (HCWR-CR1.03)	: after 2020 in C3, after 2030 in C6, without annual new capacity constraint
High Conver. Water Reactor (HCWR-CR1.13)	: after 2030 in C4, after 2050 in C6, without annual new capacity constraint

3. Analytical Cases

Case	EU-LWR	P-MOX	F-MOX	FBR-BR1.21	HCWR-CR0.98	HCWR-CR1.03	HCWR-CR1.13
C1	X	X	X_{2006}				
C2	X	X		X_{2050}			
C3	X	X			X_{2015}		
C4	X	X				X_{2020}	
C5	X	X					X_{2030}
C6	X	X			X_{2015}	X_{2030}	X_{2050}

A subscript shows the year when the use of each reactors become possible.

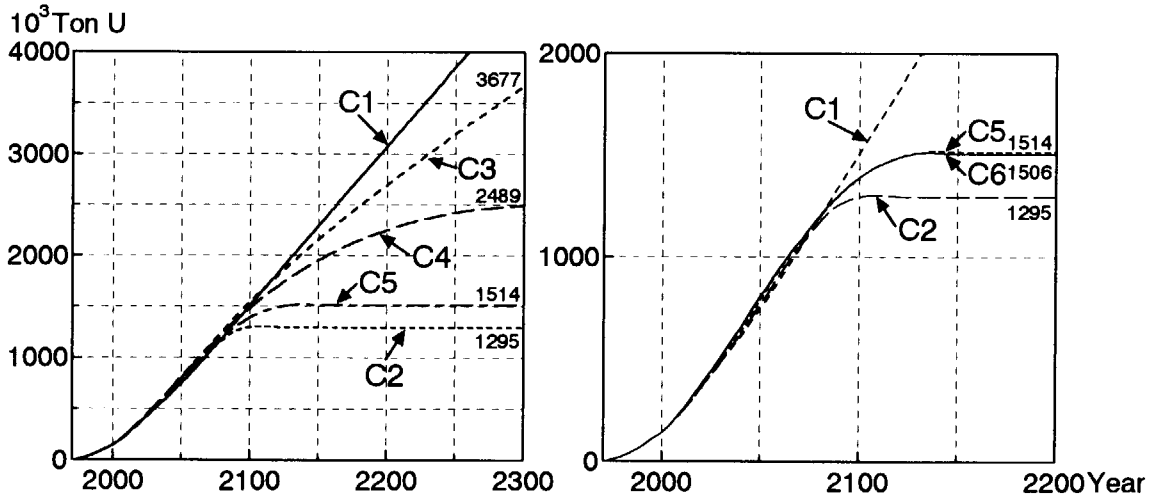

Fig. 7.4.1 Cumulative Consumption of Natural Uranium

7. 5 Future Potential of Nuclear Hydrogen Process on CO_2 Emission Reduction

Y. Tadokoro and O. Sato

(*E-mail:* tadokoro@ruby.tokai.jaeri.go.jp)

Environmental potential of nuclear hydrogen HTGR-UT3 process has been studied together with the roles from the viewpoint of energy and economy by utilizing the MARKAL model. This process is based on a cycle of the following four reactions to form chemical decomposition of water.

$$CaO + Br_2 = CaBr_2 + 1/2O_2 \quad (1)$$

$$CaBr_2 + H_2O = CaO + 2HBr \quad (2)$$

$$Fe_3O_4 + 8HBr = 3FeBr_2 + 4H_2O + Br_2 \quad (3)$$

$$3FeBr_2 + 4H_2O = Fe_3O_4 + 6HBr + H_2 \quad (4)$$

All the reactions of the UT-3 cycle are performed continuously in reactors by circurating only the gaseous reactants. Thus, the solid reactants are fixed in the reactants and exposed alternately to two reactions of both hydrolysis and bromination. As reaction (2) and (4) are endothermic, heat must be supplied from an external heat source which is assumed to be from the high temperature gas cooled reactor HTGR.[1)]

The commercial size UT-3 hydrogen plant producing 30,000 Nm^3/h has been designed at a fundamental conceptual level. Figure 7.5.1 shows the flowsheet of the UT-3 hydrogen plant having membrane gas separator. The UT-3 process mainly consists of Ca reactor units, Fe reactor units, hydrogen separation units, oxygen separation units, gas circulation units, membrane separation units and heat recovery units. Helium gas is assumed to be introduced to the UT-3 hydrogen plant at 875℃ and supplies the necessary heat for the reaction.

The analyses have been made through comparison of results between two cases, i.e. with and without HTGR-UT3 process. HTGR is assumed to be available from the year 2015 with the maximum installed capacity 72GWt in the year 2030. The growth of installed capacity assumed here can be regarded as feasible incomparison with the historical growth of LWR capacity. The optimization of systems has been performed from the

viewpoint of system cost and environmental emissions. CO_2 emission taxes are assumed 4 cases which are 0$, 5$, 10$, and 30$ respectively to reduce CO_2 emissions.

The comparison of the results with and without HTGR-UT3 process is given in Fig.7.5.2(a) and Fig.7.5.2(b) for emission taxes. From the viewpoint of environmental emission, HTGR-UT3 process contributes largely to the reduction future CO_2 emissions. The reason for this is that the high temperature nuclear heat from HTGR can be utilized not only for electlric power generation but also for hydrogen production from water, and is able to contribute to the substitution of conventional liquid fuels in final demand sectors.

As the result analyzed by the MARKAL model, it was found that HTGR-UT3 process has the potential of contributing to reduce future CO_2 emissions on environment, throgh providing high temperature nuclear heat for thermochemical hydrogen production.

Reference

1) Tadokoro, Y., et al. : Int. J. Hydrogen Energy, Vol.22, No.1, pp.49-56 (1997).

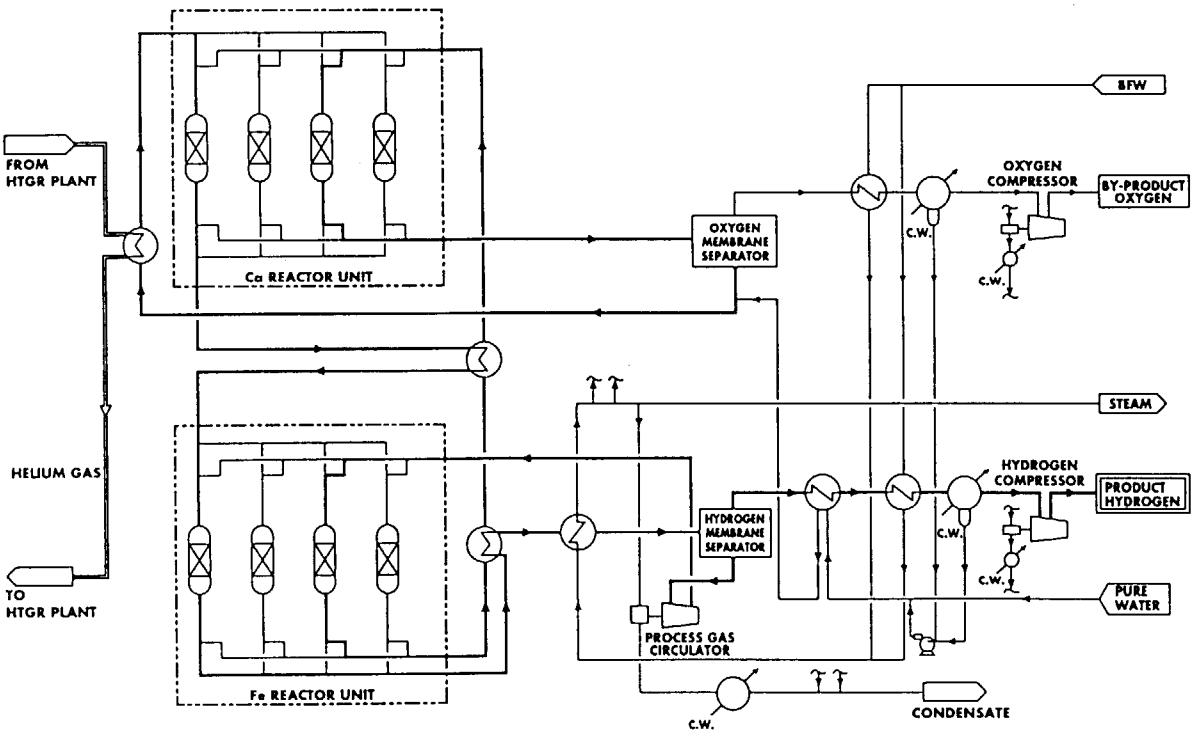

Fig. 7.5.1 Flowsheet of UT-3 Hydrogen Plant

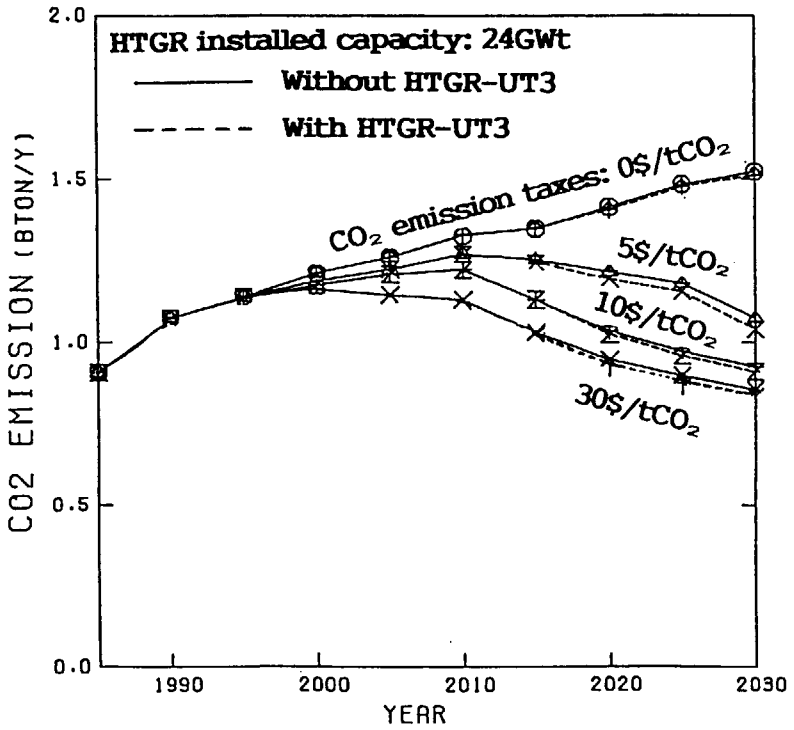

Fig. 7.5.2(a) Effect of nuclear hydrogen process on CO_2 emission reduction [HTGR installed capacity : 24GWt]

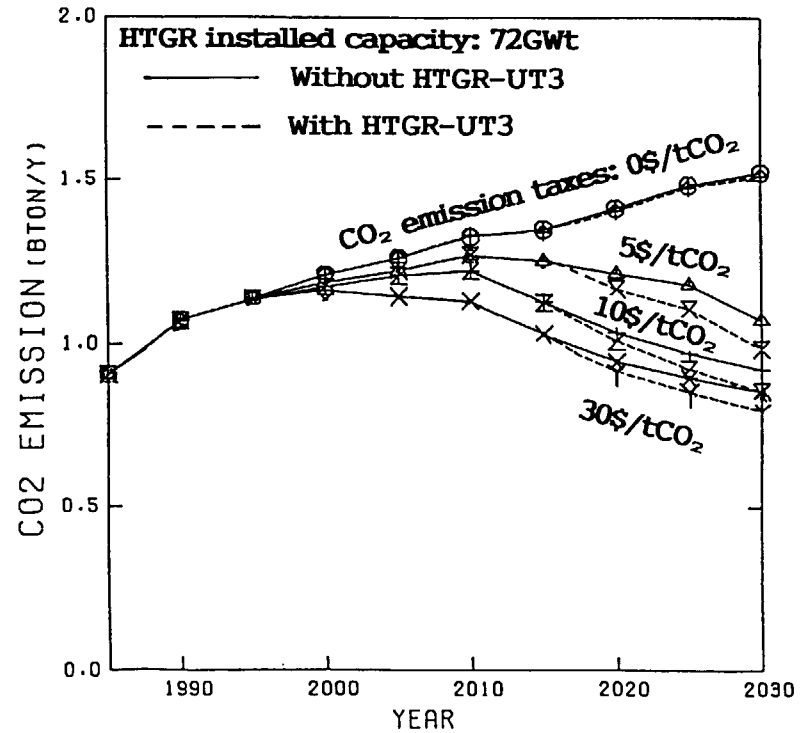

Fig. 7.5.2(b) Effect of nuclear hydrogen process on CO_2 emission reduction [HTGR installed capacity : 72GWt]

8. Reactor Structural Materials

Research items carried out were classified into four different categories,. i.e., irradiation assisted stress corrosion cracking (IASCC) study, demonstration test on lifetime reliability of structural materials for advanced prototype power reactors (STA commissioned research), research on heat resistant alloys for high temperature gas-cooled reactors, and development of material performance database.

In the field of IASCC study, effects of minor elements on IASCC behavior of model austenitic stainless steels were investigated. It was revealed that addition of Mo entirely suppressed IASCC susceptibility, and that addition of S is very injurious. As the result of microstructural analyses of neutron-irradiated model stainless steels, the following conclusions were derived. Addition of Mo or Si decreased the average diameter and the number of density of Frank loops, and addition of C increased the number of density of Frank loops though the average diameter of Frank loops were decreased by addition of C. In the field of IASCC study, in-pile strain measurement techniques also have been tried to be developed.

In the demonstration test on lifetime reliability of structural materials for advanced prototype power reactors, a series of mechanical tests was performed on the pre- and post-irradiation type 304 stainless steel which is used as the structural material of Japanese prototype fast breeder reactor "Monju". Mechanical properties of neutron irradiated materials are affected by both the displacement damage level and the amount of gaseous ingredient such as H and He produced by nuclear transmutation. Three types of neutron irradiation capsules, therefore, were specially designed, namely thermal neutron shielding, normal, and thermal neutron trapping types, in order to examine the effect of He production level on mechanical properties of type 304 stainless steel using JMTR. As for creep properties, in-pile tests were also carried out.

In the research on heat resistant alloys, the filler metal for Ni-Cr-W superalloy, which was developed as a structural material for process heating high-temperature gas-cooled reactors with coolant outlet temperature of around 1000℃ by our laboratory, was developed.

In the field of material performance database, JAERI material performance database (JMPD) and the distributed database named "Data-Free-Way" have been developed. Based on the experience of development of JMPD, Data-Free-Way was constructed under the collaboration of JAERI, the National Research Institute for Metals, the Japan Nuclear Cycle Development Institute and the Japan Science and Technology Corporation in order to share fresh and stimulating information as well as accumulated information for the development of advanced materials, for the design of structural components, etc.

8.1 Effects of Minor Elements on IASCC Behavior of Model Austenitic Stainless Steels Irradiated at JRR-3M.

T. Tsukada, Y. Miwa, H. Tsuji, M. Shindo, H. Mimura, I. Goto, T. Hoshiya and H. Nakajima
(*E-mail:* ttsukada@popsvr.tokai.jaeri.go.jp)

High-purity type 304/316 model stainless steels and alloys doped with minor elements (C, Si, P, S and Ti) into the high-purity base alloys were irradiated at JRR-3M. Susceptibilities to stress corrosion cracking (SCC) of the irradiated specimens were evaluated by the slow strain rate testing (SSRT) in high-purity water. Objective of this study is to separate effects of additions of various elements on the irradiation assisted stress corrosion cracking (IASCC). [1-4)]

Chemical compositions of specimen materials are shown in Table 8.1.1. Two high-purity base alloys, HP304 and HP316 have similar concentrations of major alloying elements except for Mo. Other twelve alloys were doped with minor elements, i.e., C, Si, P, S and Ti, into both base alloys to separate the effect of those elements on IASCC. The alloys were solution annealed and machined to round bar type specimens with the dimensions shown in Fig. 8.1.1. Neutron irradiation of the specimens was carried out in an irradiation capsule loaded into JRR-3M. A neutron fluence of specimens was 6.7×10^{24} n/m^2 (E>1MeV) and an irradiation temperature was 513K. Susceptibility to SCC in high temperature water of the irradiated specimen was evaluated by SSRT method with a test machine installed in a hot cell at the JMTR hot laboratory. SSRTs were carried out in the oxygen-saturated high-temperature water at 573 K in 9.3 MPa and at an initial strain rate of 1.7×10^{-7} s^{-1}. Fracture morphologies of the SSRT specimens were examined with a scanning electron microscope (SEM) and fractions of SCC area on the whole fracture surfaces were evaluated as IASCC susceptibility.

Fast neutron fluence (6.7×10^{24} n/m^2) of the tested materials was slightly higher than the threshold fluence (5×10^{24} n/m^2) of IASCC[5)]. However, some of the materials showed relatively high susceptibility to IASCC. Two types of fracture morphologies by IASCC were observed which were intergranular (IG) cracking and transgranular (TG) cracking. In Fig. 8.1.2, IASCC susceptibilities of the model stainless steels are summarized where ratios of IG or TG cracking area to whole fracture area are illustrated as %IASCC. It is known from the field experience that IASCC in power plants appears as IG cracking, therefore, a comparison

of susceptibilities to IG type IASCC is more important. In case of SCC test by SSRT, frequently an appearance of TGSCC has been reported, and it is probably due to the severe loading condition by SSRT method to maintain a constant strain rate.

Effects of C, Mo and S additions on IASCC behavior can be derived from the results shown in Fig. 8.1.2. In a series of type 304 alloys, an effect of C addition can be seen obviously on fracture morphology. A dominant fracture mode of alloys without C addition was IGSCC and C addition of about 0.1 wt% changed it to TGSCC. Comparing HP304 with HP316, or HP304/C with HP316/C, one can conclude that addition of Mo entirely suppressed IASCC susceptibility. Among the type 316 alloys, only two alloys, i.e., HP316/C/Ti/S and HP316/All, showed susceptibilities to TGSCC and IGSCC. The element commonly doped for both alloys is S (0.037 wt%). In addition, type 304 alloy doped with S, i.e., HP304/S, showed the highest susceptibility to IASCC in 513 K pure water. It implies that addition of S to about 0.04 wt% is very injurious to IASCC. On the other hand, effects of Si, P and Ti on IASCC susceptibility are not clear from Fig. 8.1.2, though it seems that an addition of P reduced IASCC susceptibility in HP304/P.

References

1) Tsukada, T., Miwa, Y. and Nakajima, H.: "Stress Corrosion Cracking of Neutron Irradiated Type 304 Stainless Steels", Proc. 7th Int. Symp. on Environmental Degradation of Materials in Nuclear Power Systems - Water Reactors, pp.1009-1018 (1995).
2) Tsukada, T., Miwa, Y. and Shindo, M.: "Stress Corrosion Cracking of Model Austenitic Stainless Steels Irradiated in JRR-3M", Proc. 4th Japan/China Symp. on Materials for Advanced Energy Systems and Fission and Fusion Engineering, pp.223-227 (1996).
3) Tsukada, T., Miwa, Y., Nakajima, H. and Kondo, T.: "Effects of Minor Elements on IASCC of Type 316 Model Stainless Steels", Proc. 8th Int. Symp. on Environmental Degradation of Materials in Nuclear Power Systems - Water Reactors, pp.795-802 (1997).
4) Tsukada, T.: "Irradiation Assisted Stress Corrosion Cracking of Austenitic Stainless Steels," JAERI-Research Report 98-007 (1998). [in Japanese]
5) Andresen, P.L.: "Irradiation-Assisted Stress Corrosion Cracking", *Stress-Corrosion Cracking*, edited by R.H. Jones, Chapter 6, pp.181-210 (1992).

Table 8.1.1 Chemical compositions of model stainless steels (wt%)

Alloy-ID	C	Si	P	S	Mn	Cr	Ni	Mo	Ti	Fe
HP304	**0.003**	**0.01**	**0.001**	**0.001**	**1.36**	**18.17**	**12.27**	**-**	**0.01**	**bal.**
HP304/Si	0.003	0.69	0.001	0.001	1.36	18.01	12.24	-	0.01	bal.
HP304/P	0.006	0.03	0.017	0.001	1.40	18.60	12.56	-	0.01	bal.
HP304/S	0.002	0.03	0.001	0.032	1.41	18.32	12.47	-	0.01	bal.
HP304/C	0.098	0.03	0.001	0.002	1.39	18.30	12.50	-	0.01	bal.
HP304/C/Ti	0.099	0.03	0.001	0.002	1.39	18.50	12.47	-	0.31	bal.
HP304/All	0.107	0.72	0.019	0.036	1.41	18.66	12.68	-	0.29	bal.
HP316	**0.004**	**0.02**	**0.001**	**0.001**	**1.40**	**17.21**	**13.50**	**2.50**	**0.01**	**bal.**
HP316/C	0.061	0.03	0.001	0.001	1.40	17.28	13.50	2.49	0.01	bal.
HP316/C/Ti	0.062	0.04	0.001	0.001	1.39	17.05	13.47	2.48	0.29	bal.
HP316/C/Ti/Si	0.065	0.70	0.001	0.001	1.39	17.16	13.53	2.44	0.30	bal.
HP316/C/Ti/P	0.061	0.05	0.019	0.002	1.40	16.95	13.53	2.48	0.29	bal.
HP316/C/Ti/S	0.061	0.03	0.001	0.037	1.41	17.82	13.60	2.47	0.30	bal.
HP316/All	0.063	0.76	0.018	0.037	1.42	17.32	13.56	2.43	0.30	bal.

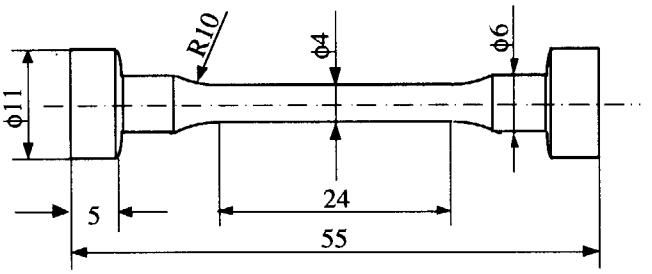

Fig. 8.1.1 SSRT specimen (mm)

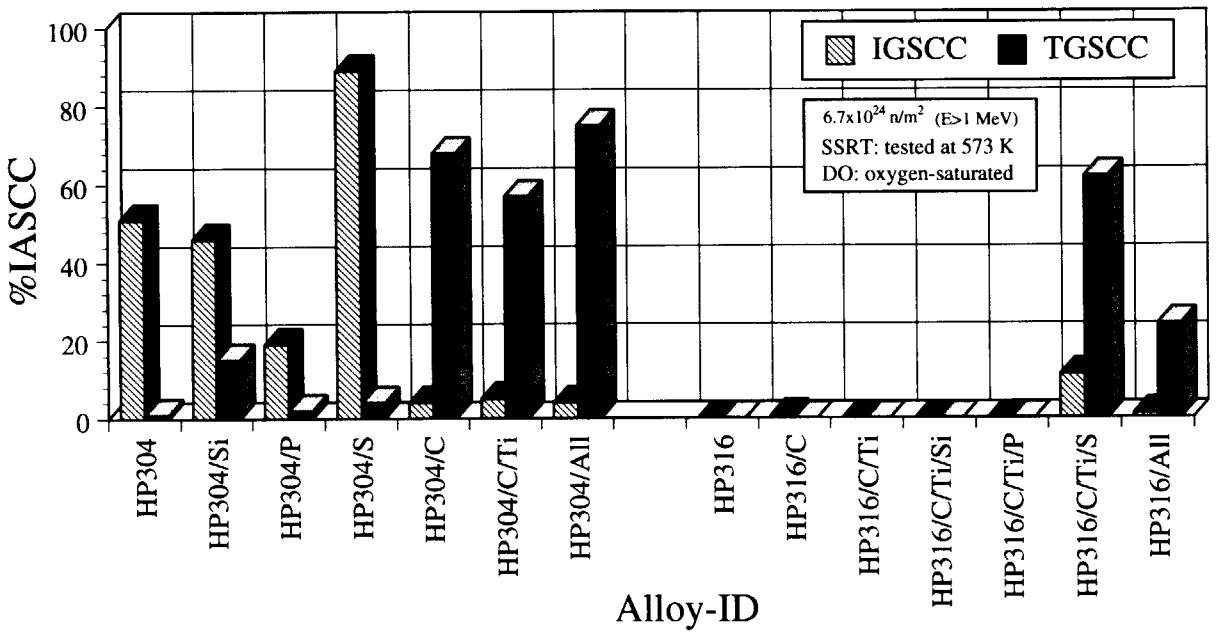

Fig. 8.1.2 IASCC susceptibility of the alloys irradiated up to 6.7×10^{24} n/m^2 at 513 K

8.2 Microstructural Analyses of Neutron-irradiated Model Stainless Steels for IASCC Study.

Y. Miwa, T. Tsukada, S. Kita, H. Tsuji and H. Nakajima
(*E-mail:* ttsukada@popsvr.tokai.jaeri.go.jp)

The irradiation assisted stress corrosion cracking (IASCC) is caused by the irradiation-induced changes of microstructure and microchemistry in the materials and water chemistry. Recently much attention has been focused on the changes of grain boundary microchemistry and microstructure. The change of grain boundary microchemistry is due to radiation-induced segregation (RIS) which then degrades the corrosion resistance of grain boundaries. The RIS, especially Cr depletion at grain boundaries, is considered to be one of the important mechanisms for IASCC. Therefore, solution-annealed, high-purity type 316 stainless steel and its heats doped with C, Ti, Si, P and S alone or together were irradiated at JRR-3M, and after the irradiation, transmission electron microscopy was carried out. In this study, the effects of minor elements on microstructure in the neutron-irradiated type 316 model alloys were investigated. [1,2)]

A high-purity Fe-17Cr-13Ni-2.5Mo and its heats doped with C, C/Ti, C/Ti/Si, C/Ti/P, C/Ti/S and C/Ti/Si/P/S were used for this study. The chemical compositions and notations are shown in Table 8.2.1. A high-purity Fe-18Cr-12Ni was also used in order to compare the effect of Mo addition. These alloys were solution-annealed at 1273 and 1398 K for 0.5 h. The specimens irradiated in this study were disks of 3 mm diameter and about 0.25 mm thickness. Neutron irradiation was performed at about 513 K to a dose level of about 1 dpa in JRR-3M. After the irradiation, transmission electron microscopy was carried out using a HF-2000 microscope.

In all alloys, Frank loops and small defect clusters were the dominant microstructural features, while neither precipitates nor cavities were observed. Development of defect-free zone along grain boundaries was also not observed. Fig. 8.2.1 shows the size distributions of Frank loops in all alloys. The densities and diameters were influenced by either alloying elements or impurities. As seen in Fig. 8.2.1, two high-purity alloys, both HP304 and HP316, had relatively larger Frank loops which reached a diameter up to 25 nm. The number density and the average diameter in HP316 were smaller than those in HP304. Chemical compositions between these alloys were slightly different except for Mo content, so that an addition of Mo

decreased the average diameter and the number density of Frank loops (NFL). The number density of small defect clusters in HP316 seemed to be lower than that in HP304. By addition of C in HP316, NFL drastically increased and the average diameter decreased. The diameter of the largest Frank loop was reduced to about 15 nm. By further addition of Ti in HP316/C, NFL decreased and average diameter increased slightly. The diameter of the largest Frank loop in HP316/C/Ti was almost equivalent to that in HP316/C. No TiC-like precipitate was detected in diffraction patterns of HP316/C/Ti. Addition of P in HP316/C/Ti made NFL increase and the average diameter decrease, but the changes of NFL and the average diameter were not remarkable. Larger Frank loops up to about 15 nm were observed in this P-doped alloy as well as in HP316/C. An addition of S in HP316/C/Ti did not change NFL, the average diameter, or the size distribution. Decreases of NFL and the average diameter were observed in HP316/C/TJSi. The largest diameter of Frank loops reduced to about 10 nm. Similar size distributions and number density of Frank loops were observed in all the elements doped alloy, HP3 1 6/C/Ti/Si/P/S.

Effects of minor elements on microstrucutres are summarized as follows;

1. Addition of Mo decreased the average diameter and the number density of Frank loops.
2. Addition of C decreased the average diameter of Frank loops but increased the number density of Frank loops.
3. Addition of Si decreased the average diameter and the number density of Frank loops.
4. Other alloying elements and impurities such as Ti P and S had a weaker influence on the development of Frank loops than either C or Si.

References

1) Miwa, Y., et al.: "Effect of Minor Elements on Irradiation Assisted Stress Corrosion Cracking of Model Austenitic Stainless Steel", J. Nuclear Materials, 233-237, pp.1393-1396 (1996).

2) Miwa, Y., Tsukada, T., Tsuji, H. and Nakajima, H.: "Microstructures of Type 316 Model Alloys Neutron-Irradiated at 513 K to 1 dpa," J. Nuclear Materials. 271-272, pp.316-320 (1999).

Table 8.2.1 Chemical compositions of irradiated stainless steels (wt%)

Alloy-ID	C	Si	P	S	Mn	Cr	Ni	Mo	Ti	Fe
HP316	**0.004**	**0.02**	**0.001**	**0.001**	**1.40**	**17.21**	**13.50**	**2.50**	**0.01**	**bal.**
HP316/C	0.061	0.03	0.001	0.001	1.40	17.28	13.50	2.49	0.01	bal.
HP316/C/Ti	0.062	0.04	0.001	0.001	1.39	17.05	13.47	2.48	0.29	bal.
HP316/C/Ti/Si	0.065	0.70	0.001	0.001	1.39	17.16	13.53	2.44	0.30	bal.
HP316/C/Ti/P	0.061	0.05	0.019	0.002	1.40	16.95	13.53	2.48	0.29	bal.
HP316/C/Ti/S	0.061	0.03	0.001	0.037	1.41	17.82	13.60	2.47	0.30	bal.
HP316/C/Ti/Si/P/S	0.063	0.76	0.018	0.037	1.42	17.32	13.56	2.43	0.30	bal.
HP304	**0.003**	**0.01**	**0.001**	**0.001**	**1.36**	**18.17**	**12.27**	**-**	**0.01**	**bal.**

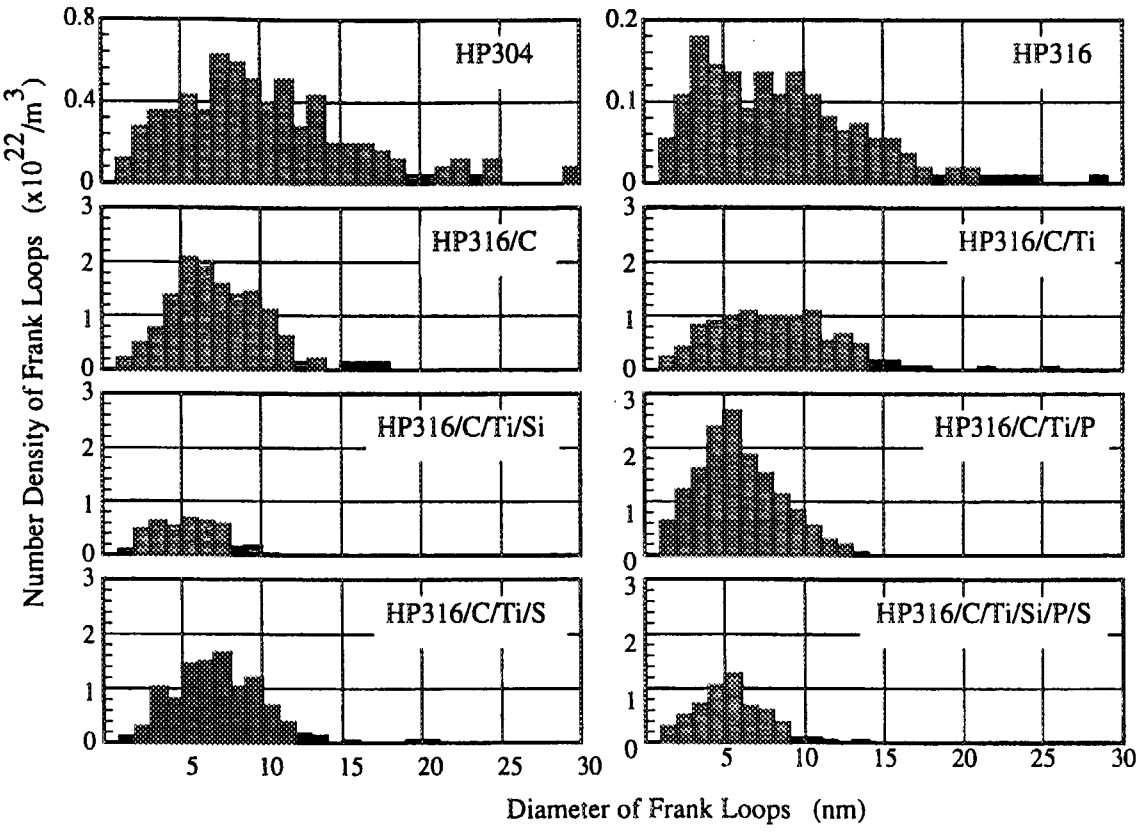

Fig. 8.2.1 Frank loop size distributions in grain interior

8.3 Development of Strain Measurement Techniques under Irradiation - Capsule Type Strain Gage and Fiber Optic Grating Strain Sensor –

Y. Kaji, Y. Matsui*, S. Kita, T. Tsukada and H. Tsuji
(E-mail: kaji@popsvr.tokai.jaeri.go.jp)

In JAERI, in-pile strain measurement techniques have been developed by using JMTR. In order to evaluate the performance of capsule type strain gage and fiber optic grating sensor under irradiation environment, the heat-up tests in electric heater before irradiation and in-pile tests were performed.

As for the heat-up tests in electric heater before irradiation results, Fig. 8.3.1 shows relationship between strain and temperature for capsule type strain gage. Though the same tests were cyclically carried out four times, it is found that the scatter of data is small and strain increases with increasing temperature. The strain for strain gage with base is larger than that without base of strain gage.

The example of change of Bragg reflected wave with increase of temperature for

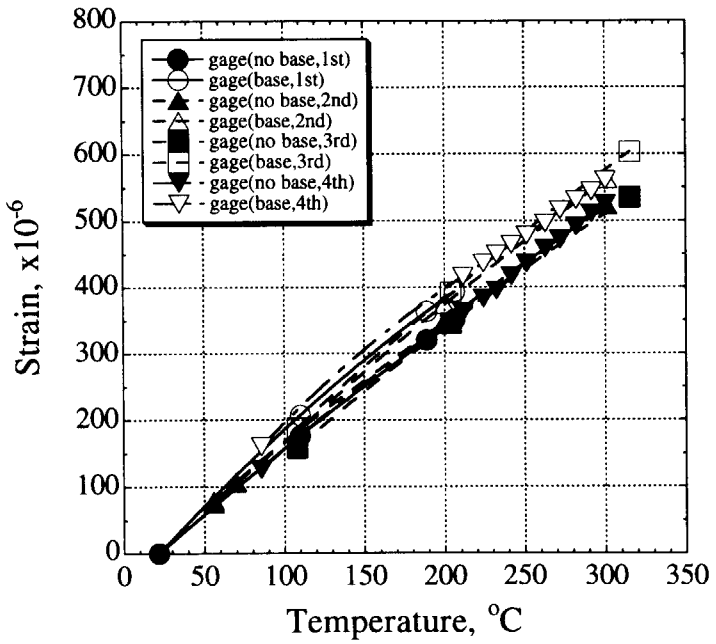

Fig. 8.3.1 Relationship between strain and temperature for capsule gage in heat-up tests before irradiation

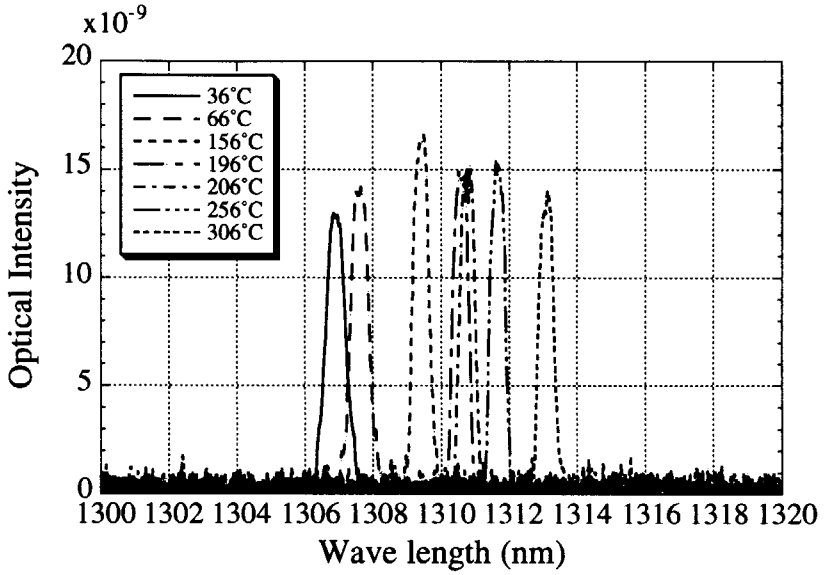

Fig. 8.3.2 Change of Bragg reflected wave with increase of temperature

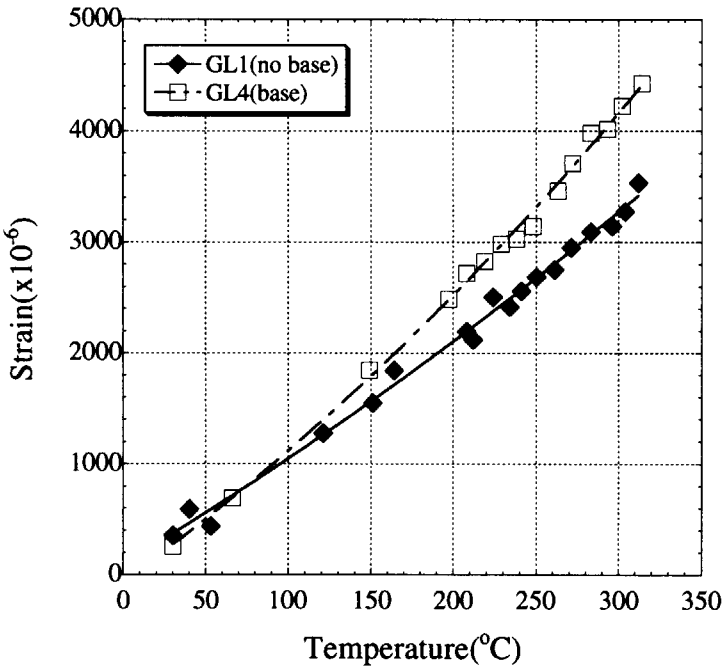

Fig. 8.3.3 Relationship between strain and temperature for fiber optic grating strain sensor in heat-up tests

fiber optic grating strain sensor in the heat-up tests in electric heater before irradiation is shown in Fig. 8.3.2. Though peak values are scattered in each temperature, peak wave length of Bragg reflected wave are transferred to direction of large wave length with increasing temperature.

The response of fiber optic grating sensor, that is, the change of peak wave length is given as function of axial strain of grating sensor and temperature as follows:

$$\frac{\Delta\lambda}{\lambda_0} = GF \times \varepsilon + \beta \times \Delta T \qquad (8.3.1)$$

where $\Delta\lambda=\lambda-\lambda_{init}$: change of peak wave length, λ_0: characteristic initial wave length of fiber optic grating strain sensor, GF: gage factor, ε: axial strain, β: temperature factor and ΔT: change of temperature.

Relationship between strain which is calculated from peak wave length and temperature by using eq.(8.3.1) and temperature is shown in Fig. 8.3.3. Strain increases with increasing temperature and the value of strain is about 4000×10^{-6} at around 300°C. Though strain of strain gage without base is larger than that with base of gage at room temperature, strain with base is larger than that without base of gage with increasing temperature.

As the in-pile test results for capsule type strain gage, history of capsule gage output for 1 cycle of JMTR is shown in Fig. 8.3.4. The strain moves strangely without change of temperature as shown in Fig. 8.3.4. The cause is under investigation from viewpoint of resistance of gage. As for fiber optic grating strain sensor, peak of Bragg reflected wave disappeared because heat-up tests were cyclically carried out and characteristics of the grating sensor was changed.

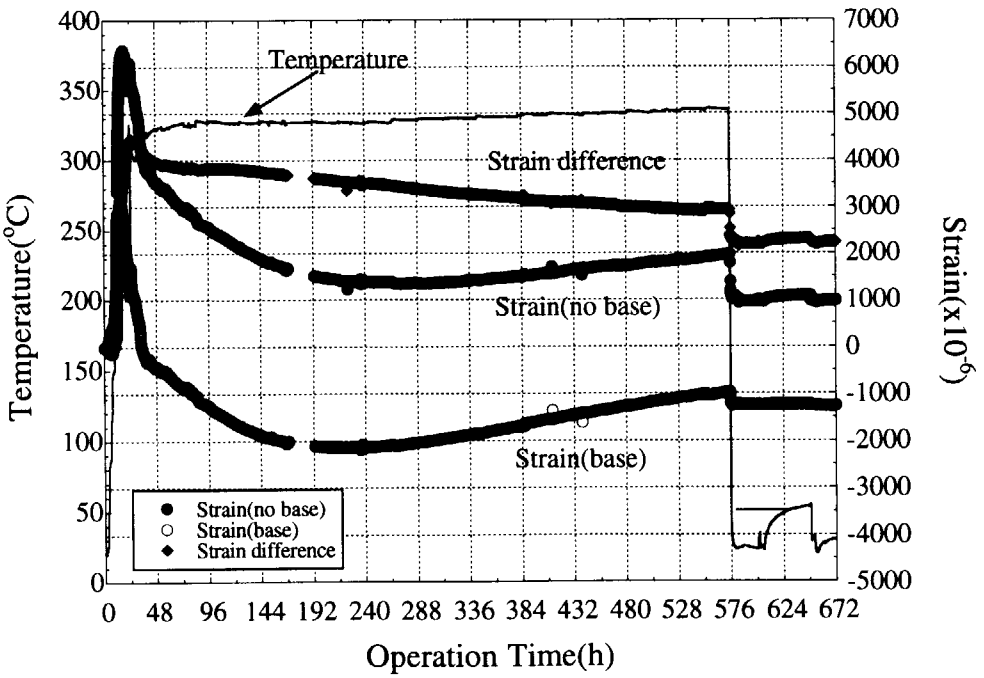

Fig. 8.3.4 History of capsule gage output for 1 cycle of JMTR

8.4 JAERI Material Performance Database (JMPD) – Present Status and Examples of Utilization –

Y. Kaji, T. Sakino, T. Tsukada and H. Tsuji
(*E-mail:* kaji@popsvr.tokai.jaeri.go.jp)

Fundamental studies of structural materials have been performed at JAERI regarding practical applications for nuclear plants. For the evaluation of reliability and safety of structural materials, various material tests have been conducted. The JMPD was designed for mechanical properties data such as fatigue crack growth, creep, tensile, low-cycle fatigue, SSRT, etc.

Referring to more than ten materials databases which have been already developed in Japan and foreign countries[1)-3)], the data structure for metallic materials in the JMPD was originally determined in a three-level hierarchy. Six categories such as data source, material, specimen, test method & data reduction, test condition, and test result, were classified into the primary level. Twenty-five tables were considered to be in the secondary level. More than 420 data items were prepared for the final level.

The JMPD is implemented with Oracle, which is a relational database system on a workstation. A data entry supporting system is implemented with spreadsheet-type software on a personal computer and is connected with the JMPD by middle software through Ethernet.

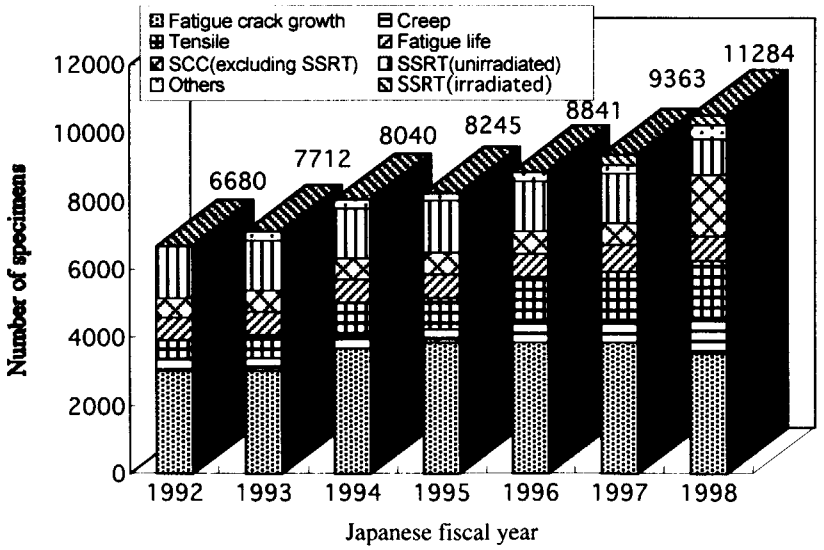

Fig. 8.4.1 Transition of data stored in JMPD

The main feature of this system is (a) to design the input sheet by extracting the data item from the data dictionary of the JMPD, (b) to enter the data by using the guide function. Users can access the Internet through their own computers in the WWW browser, retrieve the required data from JMPD and output the graph.

The data stored in the JMPD by the end of March 1999 are listed in Fig.8.4.1, in which the data from around 11,000 test pieces are prepared for data evaluation. The data stored were checked through the author's review in order to prevent the unexpected miss-input within the range of possibility. Only the data of the materials whose origin such as chemical compositions and heat treatment conditions as well as experimental methods are clear have been stored.

Both nickel-base and iron-base heat resistant alloys, which are important for advanced power engineering, have been widely studied. Data from such research activities have been collected and stored in the JMPD. Figure 8.4.2 shows example of data handling, that is, the comparison in the creep rupture strength between Hastelloy XR, whose boron content level is less than 10 mass ppm, and Alloy 800H (nominally Fe-33Ni-21Cr-Ti-AL alloy in mass%). In this figure, the data for Hastelloy XR were obtained in the inert (helium

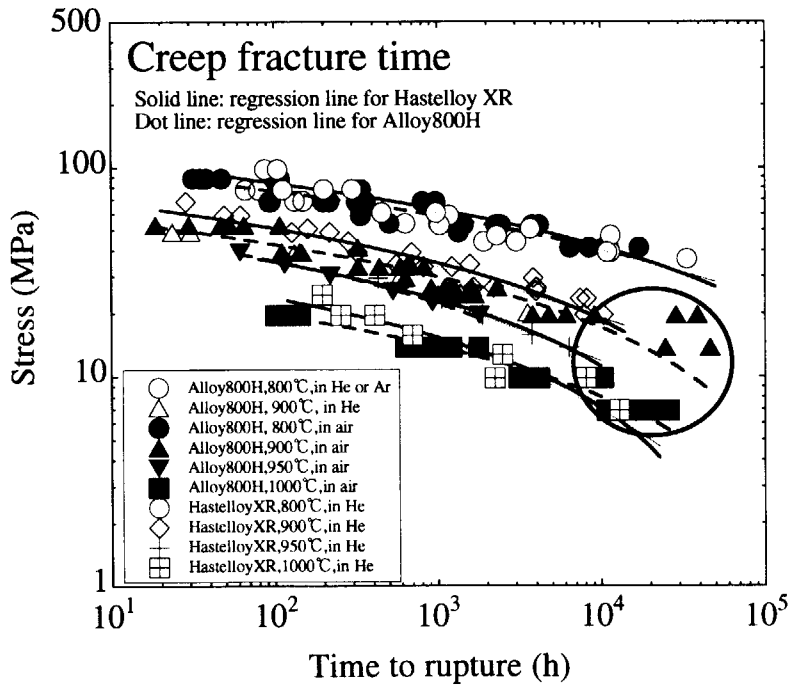

Fig. 8.4.2 Comparison in the creep rupture strength between Hastelloy XR and Alloy 800H

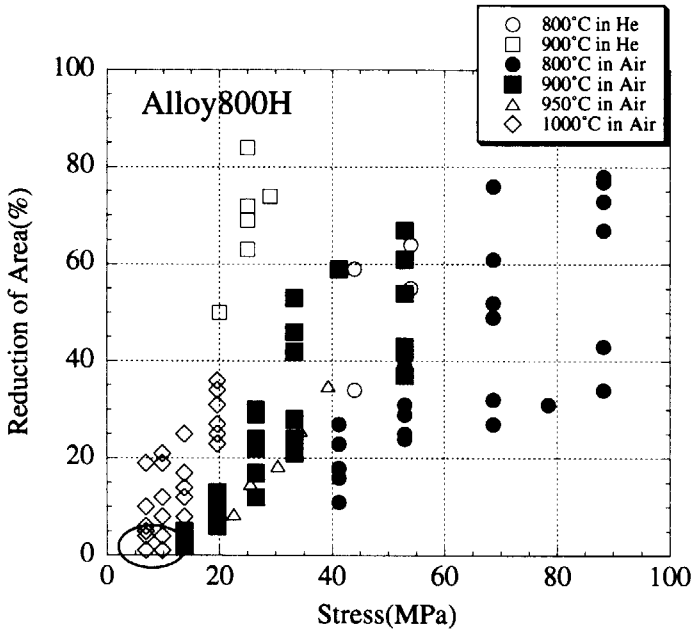

Fig. 8.4.3 Reduction of area after creep rupture tests for Alloy 800H

gas), and those for Alloy 800H were obtained in the inert (argon and helium gases) and in the air environments. Generally the creep strength of nickel-base alloy Hastelloy XR is higher than that of iron-base alloy Alloy 800H. Some exceptional cases, however, are observed in this figure, especially in the long creep rupture time region. Those exceptional data for Alloy 800H were obtained in the air environment. It is considered that the extremely long creep rupture lives observed for Alloy 800H are derived from the so-called abnormal creep phenomenon where nitride is formed. Because the data search from the JMPD revealed that the reduction of area after creep rupture tests are very small for the Alloy 800H specimens which showed extremely long creep rupture lives as shown in Fig. 8.4.3.

In summary, this paper describes the present status of the JMPD. As example of utilization of the system, the creep rupture strengths are compared between Hastelloy XR and Alloy 800H.

References

1)Yokoyama, N., Tsukada, T. and Nakajima, H., JAERI-M90-237, (in Japanese) (1987).

2)Tsuji, H., Yokoyama, N., Tsukada, T. and Nakajima, H., J. Nucl. Sci. Technol., Vol. 30, No. 12, pp. 1234-1242 (1993).

3)Yokoyama, N., Tsuji, H., Tsukada, T. and Shindo, M., ASTM STP 1311, pp.261-272 (1997).

8.5 Analysis of IASCC Behavior of Austenitic Stainless Steels using The Nuclear Materials Database, JMPD.

T. Tsukada, Y. Kaji, T. Sakino and H. Tsuji
(*E-mail:* ttsukada@popsvr.tokai.jaeri.go.jp)

Experimental data obtained through the post irradiation examinations (PIEs) for study of the irradiation assisted stress corrosion carcking (IASCC) at JAERI were stored in the JAERI Material Performance Database (JMPD) together with literature data on IASCC. Analysis of IASCC data in JMPD was performed to confirm dependence of IASCC susceptibility on alloy composition and test environment.

A comprehensive material performance database, which was named JAERI Material Performance Database (JMPD), has been developed since 1986 at JAERI.[1] It was designed for effective utilization of material data focused on the environmentally assisted degradation, e.g., fatigue or stress corrosion carcking (SCC) behavior in the aqueous or gaseous environment, and at present the data corresponding to about ten thousands test specimens are stored in JMPD. As for the part of IASCC database, about 300 data from the post irradiation slow strain rate testing (SSRT) were stored. IASCC data in JMPD consist of those from type 304 and 316 stainless steels tested at irradiation temperatures between 333 K and 573 K. Fast neutron fluences of the materials are in a range of $1x10^{22}$ n/m^2 to $8x10^{26}$ n/m^2. Data analyses were performed based on the knowledge about the factors controlling IASCC that were derived from results of the post irradiation SSRT carried out at JAERI[2-4].

In Fig. 8.5.1, all data of IASCC susceptibilities compiled into JMPD are plotted against fast neutron fluence. Susceptibility was evaluated in terms of a ratio of intergranular (IG) cracking area and whole fracture area observed on fracture surface of specimen tested by SSRT. Data shown in Fig. 8.5.1 scattered over a wide range of susceptibility through the neutron fluence and it is difficult to deduce any relation between the susceptibility and the fluence level. Since the dissolved oxygen (DO) content in high temperature water is known as an essential factor for SCC phenomenon, in Fig. 8.5.2 the data are classified into two groups by levels of DO content during SSRT. In Fig. 8.5.2, a tendency is observed that IASCC susceptibilities of alloys tested in lower DO environment are smaller. According to the results from post irradiation SSRT at JAERI, an addition of Mo caused a drastic suppression of IASCC.[4] In Fig. 8.5.3, therefore, the data from the higher DO environment are plotted

separately for type 304 and 316 alloys to confirm the effect of Mo. As seen in Fig. 8.5.3, at a lower fluence level around $1x10^{25}$ n/m^2, type 316 alloys show smaller susceptibility compared with type 304 alloys and it can be attributed to Mo addition. However, at higher fluence level, susceptibilities of type 316 alloys are increasing with the fluence and the effect of Mo addition seems to be diminished with increasing neutron fluence. In Fig. 8.5.4, the data from type 304 alloys in Fig. 8.5.3 are plotted into two ranges of C content of alloys because it was known that an addition of C affected remarkably susceptibility to IASCC[2]. At a lower fluence level, an effect of C addition to suppress IASCC appeared, but at higher fluence levels the effect seems to be lost as seen in two boxes shown in Fig. 8.5.4.

From analyses of IASCC data in JMPD, the following conclusions were obtained[5,6];

(1) By means of a combination of the post irradiation SSRT and database analysis, the dependence of IASCC susceptibilities on alloy composition, neutron fluence and dissolved oxygen could be drawn.

(2) At fluence levels below about $1x10^{25}$ n/m^2 (E>1 MeV), an addition of C into type 304 alloys reduced a susceptibility to IG cracking.

(3) Addition of Mo remarkably suppressed susceptibility to IASCC at the lower fluence levels.

(4) At higher neutron fluence levels, the above effect of C became obscure and effect of Mo gradually diminished.

References

1) Tsuji, H., Yokoyama, N., Tsukada, T. and Nakajima, H. "Development of Comprehensive Material Performance Database for Nuclear Applications", J. Nucl. Sci. and Tech., 30, pp.1234-1242 (1993).

2) Tsukada, T., Miwa, Y. and Nakajima, H.: "Stress Corrosion Cracking of Neutron Irradiated Type 304 Stainless Steels", Proc. 7th Int. Symp. on Environmental Degradation of Materials in Nuclear Power Systems - Water Reactors, pp.1009-1018 (1995).

3) Tsukada, T., Miwa, Y. and Shindo, M.: "Stress Corrosion Cracking of Model Austenitic Stainless Steels Irradiated in JRR-3M", Proc. 4th Japan/China Symp. on Materials for Advanced Energy Systems and Fission and Fusion Engineering, pp.223-227 (1996).

4) Tsukada, T., Miwa, Y., Nakajima, H. and Kondo, T.: "Effects of Minor Elements on IASCC of Type 316 Model Stainless Steels", Proc. 8th Int. Symp. on Environmental

Degradation of Materials in Nuclear Power Systems - Water Reactors, pp.795-802 (1997).

5) Tsukada, T., Miwa, Y., Yokoyama, N. and Tsuji, H.: "Irradiation Assisted Stress Corrosion Cracking Study based on the Post-Irradiation Examination and Database Retrieval", Proc. 75th JSME Spring Annual Meeting, pp.582-583 (1998) [in Japanese].

6) Tsukada, T., et al., "Stress Corrosion Cracking Susceptibility of Neutron Irradiated Stainless Steels in Aqueous Environment," Proc. 7th Int. Conf. on Nuclear Engineering (ICONE-7), pp. (1999).

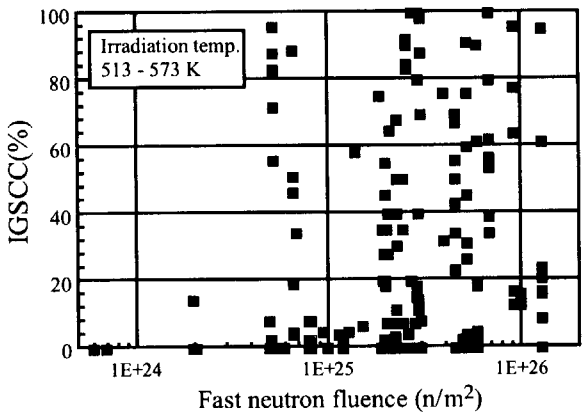

Fig. 8.5.1 IASCC data stored in JMPD

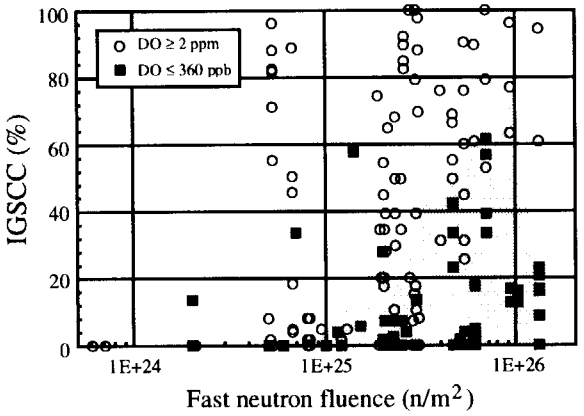

Fig. 8.5.2 Effect of dissolved oxygen

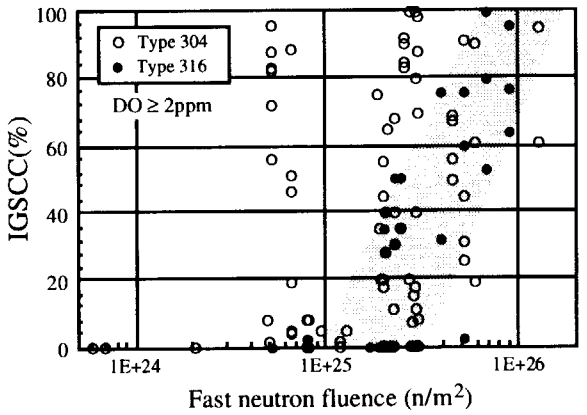

Fig. 8.5.3 Effect of Mo addition

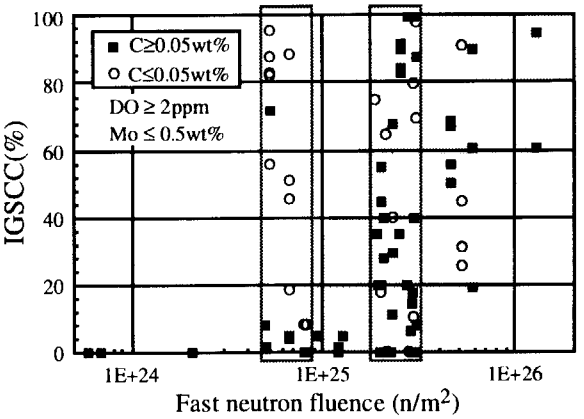

Fig. 8.5.4 Effect of C content

8.6 Distributed Database System for Advanced Nuclear Materials (Data-Free-Way)

H. Tsuji, T. Sakino, Y. Kaji and T. Tsukada
(*E-mail:* tsuji@jmpdsun.tokai.jaeri.go.jp)

Introduction

Material behavior under the service conditions in the nuclear field can be little understood without practical examination. An easily accessible material information system with a huge material database using effective computers is, therefore, necessary for the design of new materials and the analyses or the simulations of the phenomena occurring in the materials of the nuclear plants under the service conditions, especially neutron irradiation relevant phenomena.

Hence, the pilot system on the distributed database for advanced materials named "Data-Free-Way" was constructed under the collaboration of the National Research Institute for Metals (NRIM), the Japan Atomic Energy Research Institute (JAERI) and the Japan Nuclear Cycle Development Institute (JNC)[1)-3)] in order to share fresh and stimulating information as well as accumulated information for the development of advanced materials, for the design of structural components, etc. In the original pilot system, material information was mutually utilized through the local circuit. Now the system has been made more substantial through the advanced network with high data processing speed and multi-functions by taking advantage of current excellent data communication techniques like the Internet.

System overview and present status

Development of the system has progressed and is scheduled as follows. Design of the pilot system was initiated in 1990. In 1991, the organizations, NRIM, JAERI and PNC, participating in the cooperation prepared their own computer programs and computers with their peripheral machines based on the same technical specifications. These computers were connected by a network through a "digital data exchange packet (DDX-P)" line. In 1993 three other organizations, the Japan Information Center of Science and Technology (JICST), the National Research Laboratory of Metrology (NRLM) and the Ship Research Institute (SRI), joined the cooperations as observers and their computers were connected with the Data-Free-Way. Then JICST began to develop its own database. In order to make the system more substantial, the second stage collaborative research activity in which the main objective was to develop the utilization techniques for the Data-Free-Way was initiated in 1995 among NRIM,

JAERI, PNC and JICST, whose name was changed to be the Japan Science and Technology Corporation (JST) after that.

Figure 8.6.1 shows the present status of the system construction of the Data-Free-Way. The computer network consists of six organizations. These computer systems were introduced in each organization and connected to each other formerly through the DDX-P communication line and now through the Internet. Accordingly these databases and user interface can be mutually utilized through the computer network.

The system consists of a common database and a generic database. Evaluated, selected and edited data in each in-house database, which has been developed by each organization, are stored in the common database. For easy comparison of the relevant data sets from one organization with those of the others, a common data model is adopted.

Contents of the common database have already been shown in the previous reports [1),4)-9)]. NRIM prepares physical properties and ion irradiation data, JAERI prepares corrosion data, thermal neutron irradiation data and mixed spectrum neutron irradiation data, JNC prepares high temperature data and fast neutron irradiation data, and JST prepares public fact data. At present, the data of more than 35,000 specimens in various kinds of materials are stored in the common database. The generic database contains meta data, a data dictionary and sets of generic materials data for smooth communication. Both the common database and the generic database can be exchanged mutually among the participating organizations through the network. The user interface of the system plays an important role in developing a useful system, especially to extract information from the complex mixture of material data. Concepts of the user interface including a graphic analytical model and application programs for analysis and evaluation of data are adopted to the system. The system can be easily accessed by engineers and scientists in the advanced power engineering field.

The world wide web (WWW) home page and the WWW server have been prepared. The URLs of NRIM, JAERI and JST sites are "http://inaba.nrim.go.jp/," "http://jmpdsun.tokai.jaeri.go.jp/dfw-e/dfw-e.html" and "http://dfw.jst.go.jp/," respectively. As the data input-output supporting system, the additional functions have been prepared to reinforce the linkage function between the database and the WWW, such as the retrieval-layout function of image data, the simple graph preparation function, the linkage function between numerical data and image data, the preparation function of a fixed retrieval screen, the saving-reproducing function of retrieval conditions, etc. The dictionary on data items and unit conversion function have been prepared as a users' supporting system.

References

1) Nakajima H. et al.: J. Nucl. Mater. 191-194, 1046 (1992).

2) Nakajima H. et al.: J. Nucl. Mater. 212-215, 1711 (1994).

3) Fujita M. et al.: "Computerization and Networking of Materials Databases V, ASTM-STP 1311", American Society for Testing and Materials, Philadelphia, USA, 249 (1997).

4) Fujita M. et al.: "Computer Aided Innovation of New Materials", Elsevier Science Publishers B.V., Amsterdam, Netherlands, 25 (1991).

5) Fujita M. et al.: "Computer Aided Innovation of New Materials II", Elsevier Science Publishers B.V., Amsterdam, Netherlands, 81 (1993).

6) Ueno F. et al.: J. Nucl. Sci. Technol. 31,1314 (1994).

7) Tsuji H. et al.: "Materials for Advanced Power Engineering 1998, Part III", Forschungszentrum Jülich, Jülich, Germany, 1739 (1998).

8) Tsuji H. et al.: "Innovative Materials in Advanced Energy Technologies", TECHNA Srl, Faenza, Italy, 417 (1999).

9) Tsuji H. et al.: J. Nucl. Mater. 271&272, 486 (1999).

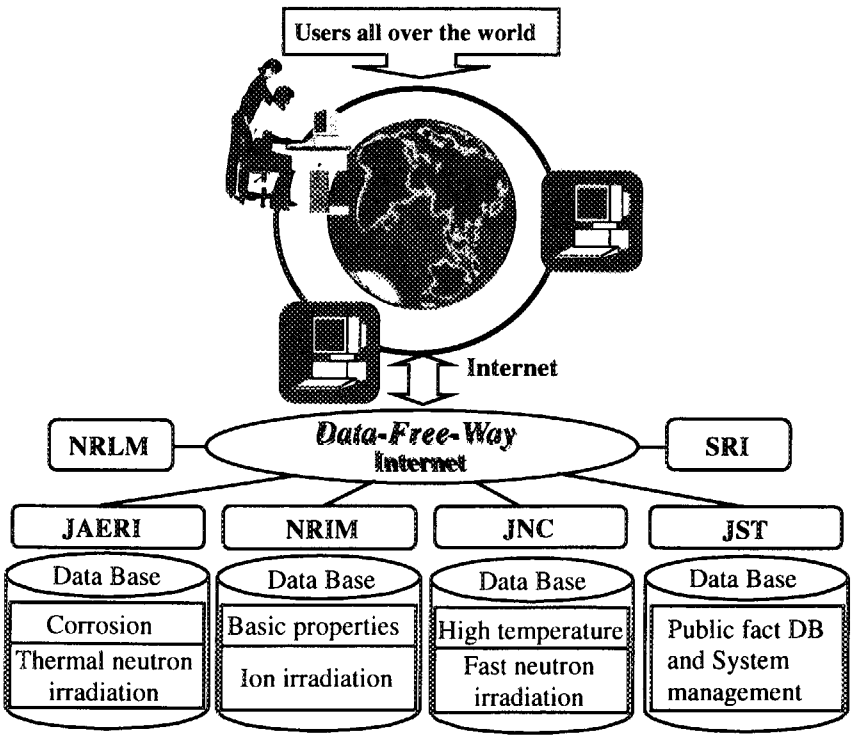

Fig. 8.6.1 Networking overview of Data-Free-Way system

8.7 Effect of Helium to dpa Ratio on Tensile Properties of Austenitic Stainless Steel Irradiated to 2dpa

I.Ioka, M.Yonekawa, Y.Miwa, H.Mimura, H.Tsuji and Y.Hoshiya

E-mail: ioka@popsvr.tokai.jaeri.go.jp

The tensile properties of 304SS irradiated in the Japan Material Test Reactor (JMTR) spectrally tailored experiment have been measured in order to evaluate the effect of a helium to dpa (displacement per atom) ratio on the tensile properties of 304SS. Three experiments normal, thermal shield and thermal trap irradiation) are designed for irradiation in the fuel or beryllium reflector region of the JMTR. The helium in the irradiated austenitic stainless steel was produced mainly by the two-stage Ni reaction[1]: $^{58}Ni(n,\gamma)^{59}Ni(n,\alpha)^{56}Fe$. Changing the thermal neutron flux in the specimen can control the helium to dpa ratio. In the thermal shield irradiation, a cadmium shield surrounds the specimens in order to reduce the thermal neutron flux and achieves lower helium to dpa ratio. A graphite shield surrounds the specimens to enhance the thermal neutron flux and achieves higher helium to dpa ratio. The normal irradiation in the JMTR was performed with a peak thermal neutron fluence of approximately $2x10^{21}$ n/cm^2 (E<0.683eV) and a fast neutron fluence of $1x10^{21}$ n/cm^2 (E>1MeV) to give a damage level of 1.7dpa with helium concentration of 3 appm at temperature of 823K. This irradiation resulted in the helium to dpa ratio of 1.8 appmHe/dpa. Details of the normal, thermal shield and thermal trap irradiation conditions can be found in Table 8.7.1.

The chemical composition of 304SS is given in Table 8.7.2. The tensile specimens were cut from 40mm thick hot rolled plate. The specimens were in the form of flat plate specimens with an overall length of 25.4mm. The gauge section of the specimen is 7.6mm long by 1.5mm wide by 0.76mm thick. Tensile tests were conducted at 823K in a vacuum of approximately $1x10^{-3}$ Pa at a strain rate of approximately $1x10^{-3}$ s^{-1} using an Instron universal-testing machine. Some normal irradiated specimens were tested at strain rate of to examine

the influence of strain rate. Recorded load versus cross head displacement curves were converted to engineering stress-elongation curves for all the specimens tested. Yield stress (YS), which is defined here as the 0.2% proof stress, ultimate tensile stress (UTS), uniform elongation (Eu) and total elongation (Et) were calculated form the engineering stress-elongation curves.

The influence of helium to dpa ratio level and strain rate on tensile properties (YS, UTS, Eu, Et) after irradiation to an exposure of 2dpa at an irradiation and test temperature of 823K is shown in Fig. 1, together with values for the unirradiated specimens. The irradiation causes an increase in YS and UTS, and a decrease in Eu and Et. There is no significant difference between the levels of YS and UTS in spite of the different helium to dpa ratio. This is also true for Eu and Et. The similar tendency of YS was reported: no strong effect of helium on YS level of 316SS irradiated at the temperature ranging between 200 to 330C up to 7dpa was seen[3]. Irradiated stainless steels are prone to high temperature embrittlement due to the weakening of the grain boundaries by helium form (n,α) reaction. An indication of the phenomenon was observed in the experiment with specimens irradiated at a low strain rate[2]. The specimens failed in a brittle intergranular way. In this experiment, there is no influence of low strain rate ($1x10^{-4}$ s^{-1}) on tensile properties of irradiated 304SS as shown in Fig. 8.7.1.

References

1) Ketema, D.J. and Voorbraak: Neutron Metrology Report ECN-I-90-040(1990).

2) Horsten, M.G. and de Vries, M.I.: J. Nucl. Mater., 212-215, 514(1994).

3) Shiba, K. et al.: Effects of Radiation on Materials: 18th International Symposium, ASTM STP 1325, 659(1999).

Table 8.7.1 Normal, thermal shield and thermal trap irradiation conditions in the experiment.

Irradiation type	Fluence(n/cm^2)		Dose(dpa)	Helium(appm)
	Fast(E>1MeV)	Thermal(E<0.683eV)		
Normal	$1x10^{21}$	$2x10^{21}$	1.7	3
Thermal shield	$1x10^{21}$	$2x10^{19}$	2	16
Thermal trap	$1x10^{21}$	$4x10^{21}$	2	1

Table 8.7.2 Chemical composition of 304SS (mass%).

C	Si	Mn	P	S	Cu	Ni	Cr	Nb	V
0.047	0.54	0.78	0.024	0.003	0.09	9.08	18.52	0.02	0.08
N	Co	B	Fe						
0.034	0.05	0.0002	Bal.						

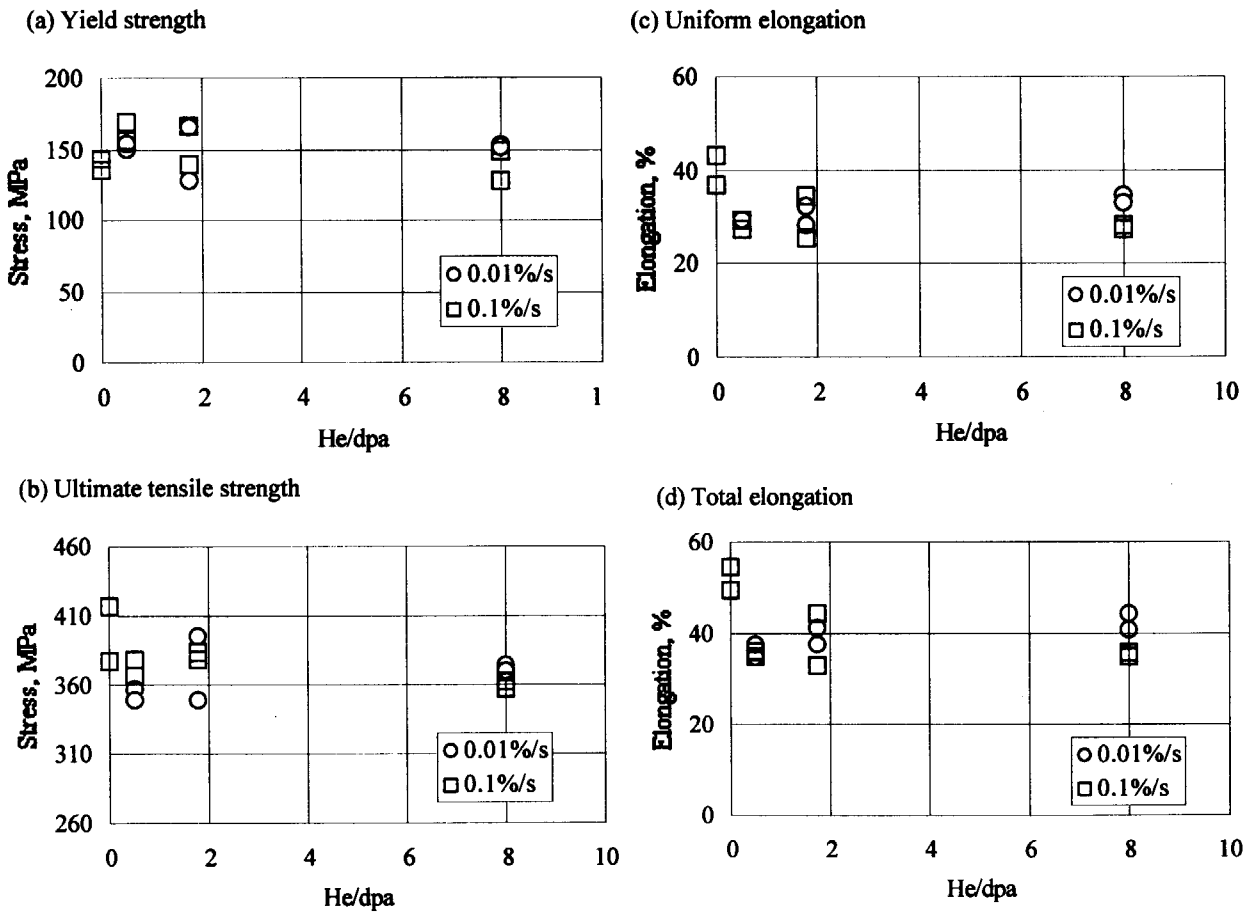

Fig.8.7.1 Tensile properties of 304SS irradiated to 2dpa at 823K as a function of helium to dpa ratio (a) yield stress, (b) ultimate tensile stress, (c) uniform elongation and (d) total elongation.

8.8 In-pile and Post-irradiation Creep of Type 304 Stainless Steel

Y. Kurata, Y. Itabashi, H. Mimura, T. Kikuchi, H. Amezawa,
S. Shimakawa, H. Tsuji and M. Shindo
(*E-mail:* ykurata@popsvr.tokai.jaeri.go.jp)

Effects of irradiation should be taken into consideration to use materials under neutron irradiation. In order to study irradiation effects on creep properties, many irradiation creep tests of stainless steels using a pressurized tube technique have been performed at high temperatures above 600℃ or temperatures below 400℃. The former was mainly for study on fuel cladding tubes of fast breeder reactors[1] and the latter was for that on materials of nuclear fusion reactors[2]. In this study, we made a plan shown in Fig.8.8.1 to clarify effects of a neutron spectrum on creep properties at 550℃. The aims of this study are to develop irradiation creep capsules under different neutron spectra and to investigate effects of neutron irradiation on creep properties. We present results of in-pile uni-axial creep under different neutron spectra and of post-irradiation creep after normal irradiation for type 304 stainless steel in this paper.[3]

The tested material is type 304 stainless steel for reactor internals of fast breeder reactors. Table 8.8.1 shows aim condition of irradiation. The condition of (3)94M-3A in this table is a simulated neutron spectrum which reactor internals of fast breeder reactor are exposed to. Figure 8.8.2 shows schematic diagram of an irradiation creep capsule, 94M-2A. Different levels of stress can be loaded on two creep specimens in terms of bellows pressured by helium gas. The temperature of the specimen was normally controlled at 550±1℃.

The following conclusions were drawn from this study.

(1)The irradiation creep capsule with in-situ measurement of elongation under a high thermal neutron flux condition or thermal neutron shield condition was developed.

(2)Creep rupture time of in-pile creep under a high thermal neutron flux condition is the shortest. The order of rupture time following the above is post-irradiation creep, in-pile creep under a thermal neutron shield condition and the unirradiated material in increasing order.(Fig. 8.8.3)

(3)The steady-state creep rate of in-pile creep under a thermal neutron shield condition is a little larger than that of the unirradiated material. The steady-state creep rate of in-pile creep under a high thermal neutron flux condition and of post-irradiation creep increases compared with that of the unirradiated material.

References

1) Gilbert E.R. and Chin B.A.: Nucl. Technol., 52, 273 (1981).
2) Grossbeck M.L., Ehrlich K. and Wassilew C. : J. Nucl. Mater., 174, 264 (1990).

3) Kurata Y., Itabashi Y., Mimura H., Kikuchi T., Amezawa H., Shimakawa S., Tsuji H. and Shindo M. : Proc. of the Sixth Asian Symposium on Research Reactors, March 29-31,1999, Mito, Japan , p.175(1999).

Table 8.8.1 Aim condition of irradiation

Capsule name	Fluence(n/cm^2)		Damage (dpa)	Helium production (appm)
	Fast neutron (>1MeV)	Thermal neutron (<0.683eV)		
(1)93M-33A, Post-irradiation creep (Normal irradiation)	1x10^{21}	2x10^{21}	1.7	3
(2)94M-2A, In-pile creep (8cycles) (High thermal neutron flux)	1x10^{21}	4x10^{21}	2	16
(3)94M-3A, In-pile creep (8cycles) (Thermal neutron shield)	1x10^{21}	2x10^{19}	2	1

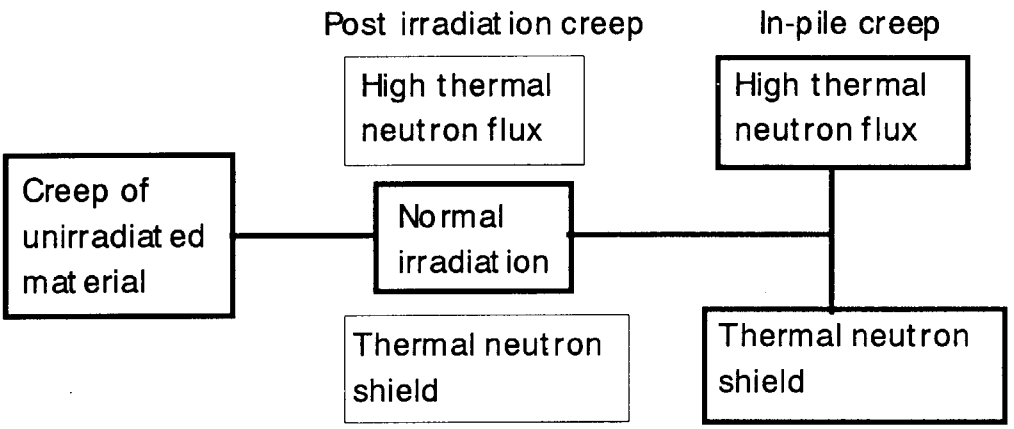

Fig. 8.8.1 Total plan of study on in-pile and post-irradiation creep.

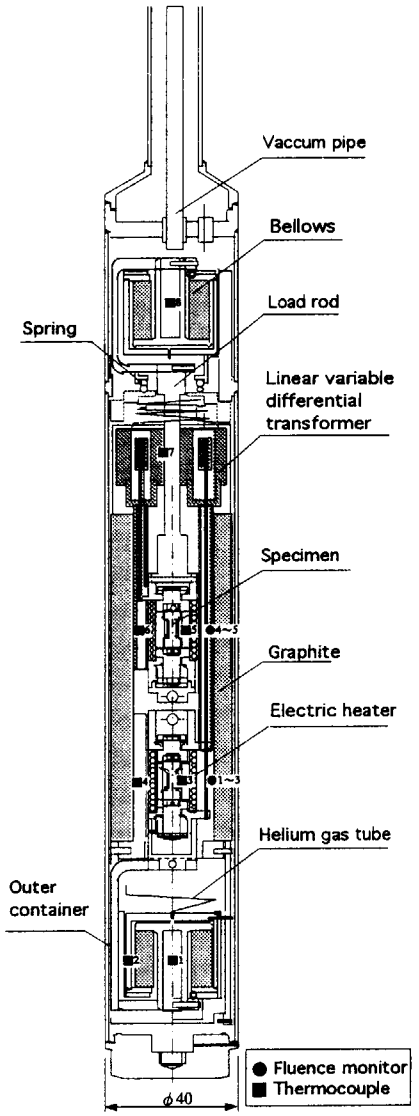

Fig. 8.8.2 Schematic diagram of irradiation creep capsule, 94M-2A under a high thermal neutron flux condition.

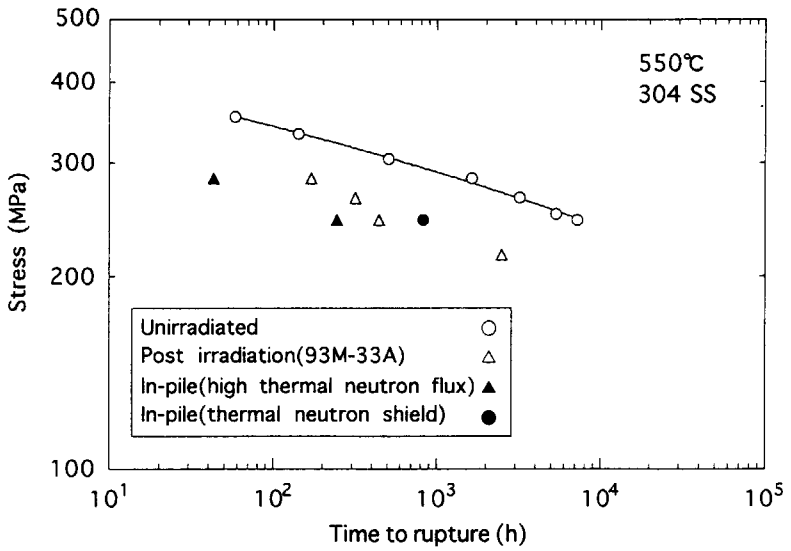

Fig. 8.8.3 Effect of neutron irradiation on rupture time of type 304 stainless steel.

8.9 Development of Filler Metal for Ni-Cr-W Superalloy

Y. Kurata, T. Saito*, H. Tsuji, T. Takatsu*, M. Shindo and H. Nakajima
(*E-mail:* ykurata@popsvr.tokai.jaeri.go.jp)

Development of filler metal is the important item to be solved in study on development of Ni-Cr-W superalloy for high temperature gas-cooled reactors with coolant outlet temperatures around 1000℃. Effects of minor alloying elements on weldability were studied for the alloy with basic composition of Ni-18.5Cr-21W proposed as an optimum chemical composition for the base metal. On this basis the filler metal for the Ni-Cr-W superalloy was developed. The main results obtained were as follows[1]:

(1)Minor alloying elements and condition of heat-treatment had large effects on susceptibility to cracking in the weldments of Ni-Cr-W alloy. For this reason, good weldability could not be obtained constantly using alloys within optimum range of chemical composition for the base metal.

(2)Improvement effect to reduce susceptibility to cracking in the weldments was little obtained by means of increase in contents of elements which had deoxidizing or desulfurizing effect. Addition of optimum contents of Ti or Mg reduced the susceptibility to cracking in the weldments slightly.

(3)It was found that elements such as Zr, Y and B, which were added to the base metal of Ni-Cr-W alloy to maintain high temperature properties, made susceptibility to cracking high significantly as shown in Figs. 8.9.1 and 8.9.2. Contents of these minor alloying elements were adjusted in the lower ranges than those of the base metal. The filler metal with good weldability for Ni-Cr-W alloy was developed through the investigation of effect on weldability.

Creep properties of weldments produced using the filler metal developed here were estimated. Figure 8.9.3 shows comparison of time to rupture between weld metal(P3) and base metal(Heat C). As shown in this figure, creep rupture strength of the weld metal is almost equal to that of the base metal. As a result of a series of study, the filler metal with excellent weldability, creep properties, corrosion resistance and hot workability was developed.

References

1) Saito T., Kurata Y., Takatsu T., Tsuji H., Shindo M. and Nakajima H. : "Study on Development of Filler Metal for Ni-Cr-W Superalloy", JAERI-Research 99-036 (1999).

---

* Nippon Welding Rod. Co.Ltd

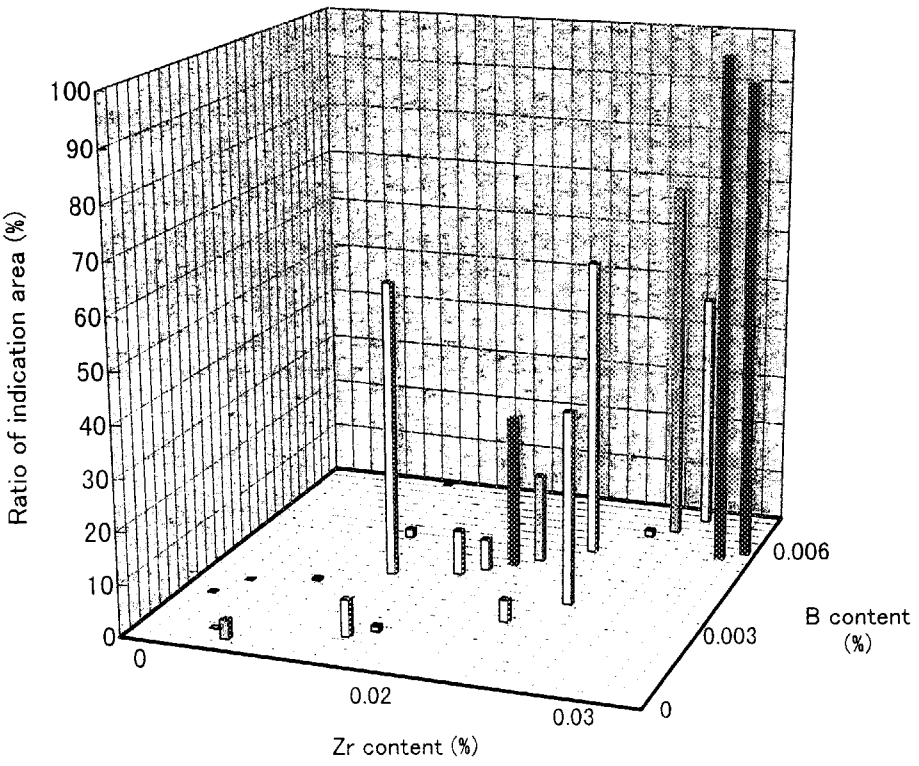

Fig. 8.9.1 Effect of Zr and B contents on weld crack susceptibility of Ni-Cr-W superalloy.

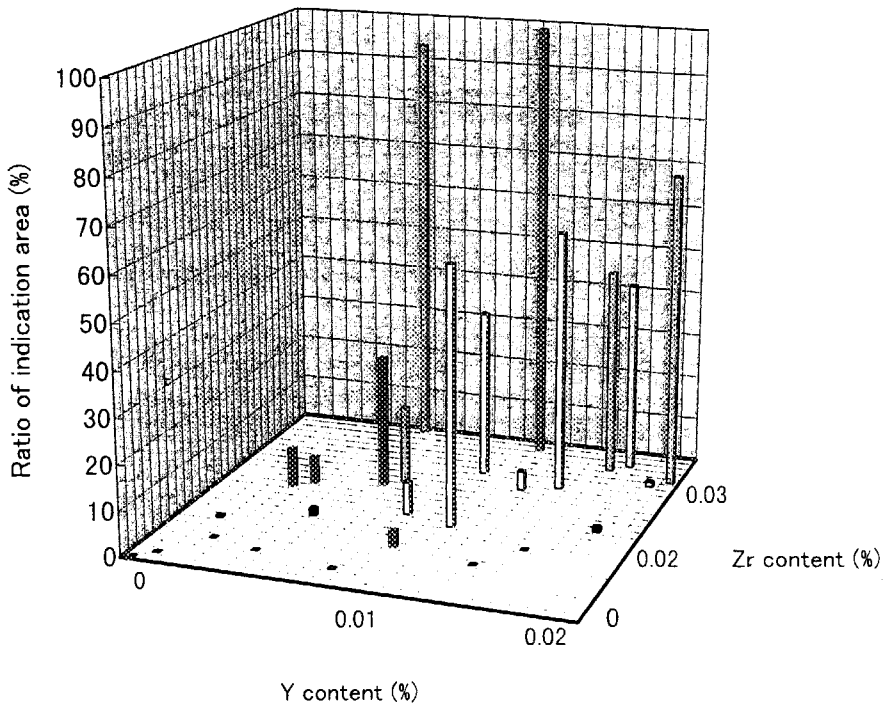

Fig. 8.9.2 Effect of Y and Zr contents on weld crack susceptibility of Ni-Cr-W superalloy.

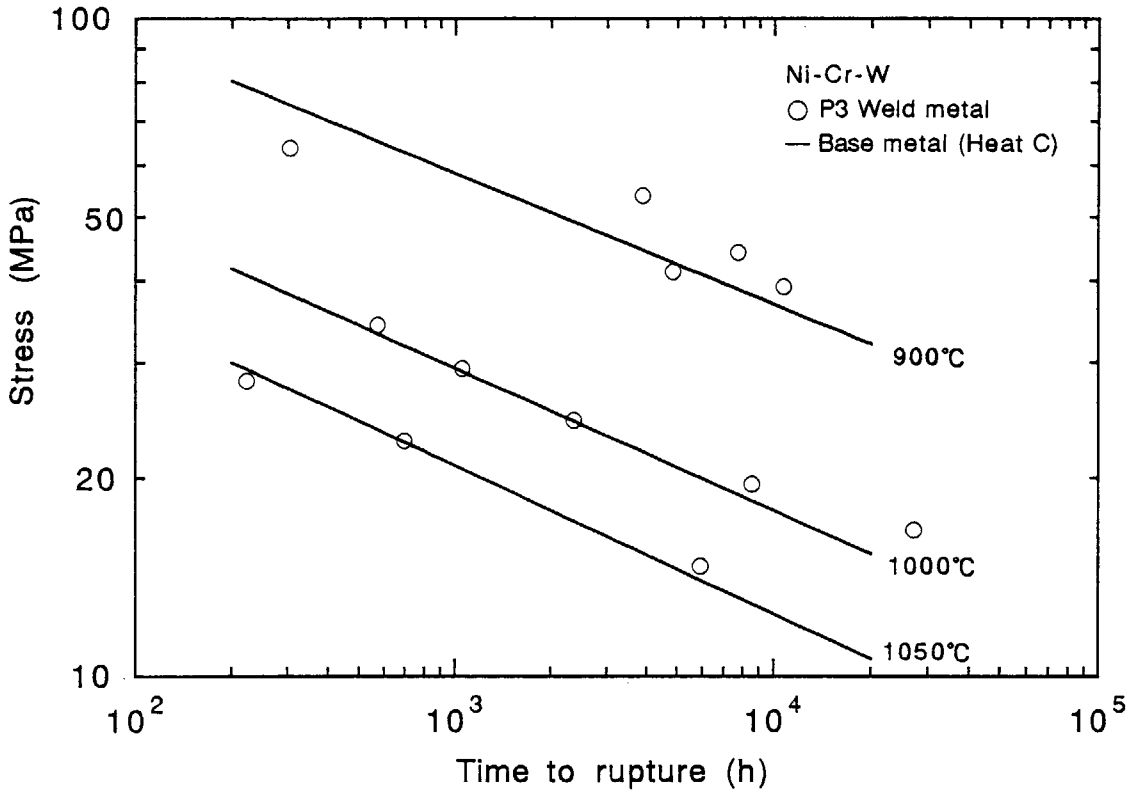

Fig. 8.9.3 Comparison of time to rupture between weld metal(P3) and base metal(Heat C) of Ni-Cr-W superalloy.

9. Advanced Materials for Nuclear Applications

The research was mainly carried out in the three fields: (1) corrosion-resistant materials for IS(Iodine-Sulfur) hydrogen production process, (2) bonding techniques for the fusion reactor components and evaluation of the vacuum vessel welding structure of ITER, and (3) advanced alloys and carbon materials for HTGR. Since in most cases the advanced materials cannot be fully evaluated on the basis of the conventional techniques only, the above research subjects naturally include the development of advanced techniques for material evaluation.

As for the research on IS Process materials, the corrosion behavior of several ceramics were examined in boiling 95% sulfuric acid. The behavior was divided into 3 types; (1) the formation of protective film(Si-SiC and SiC), (2) decrease in the strength due to corroded layers(Si3N4 and Al2O3), and (3) pronounced loss of strength due to weight loss(ZrO2). Information about promising candidates was obtained on the basis of the above results. As for metallic alloys the behavior of Fe-Si was clarified in the sulfuric acid, indicating that the microstructure of the passive film on the alloy differs corresponding to the concentration of the acid. In these experiments the microindentation technique was assessed from the aspect of its applicability to the evaluation of mechanical properties and film structure. With the aide of FEM approach it was demonstrated that the technique was effective to characterize the corrosion resistant materials as well as ion-irradiated ones.

An optimum HIP condition for bonding W and Cu alloys was determined on the basis of mechanical strength tests and microscopic observations, aiming at its application to the plasma facing components of fusion reactor. For the first wall components it was found that the diffusion bonding can be applicable to the bonding of alumina dispersion-strengthened copper and stainless steel if a sheet of Au, Cu or Ni is inserted between the two materials. As for the welding structure of the vacuum vessel of ITER, the partly welded joints were characterized for several welding methods.

Modified creep constitutive equations were proposed on the basis of the shape of the creep curves for Ni-18.5%Cr alloy, indicating that the equations were more widely, accurately and conservatively applicable to the estimation of rupture and rupture life. Carbon/carbon composite materials as well as the method for fabricating components were investigated, giving rise to a prospect for the future application to the control rod of HTTR.

9.1 Corrosion Resistance of Ceramics in Boiling Sulfuric Acid

M. Futakawa, T. Wakui*, I. Ioka, M. Eto, K. Onuki and S. Shimizu

(*E-mail* : futakawa@popsvr.tokai.jaeri.go.jp)

Thermochemical hydrogen production system, IS (Iodine- Sulfur) process investigated by Japan Atomic Energy Institute[1], consists of chemically active environments, i.e., boiling sulfuric acid, halogen gasses, in which most of the conventional structural materials are attacked by corrosion[2]. It is a key issue to find appropriate corrosion-resistant materials for proceeding to a next stage, the scaled-up IS process. Some brittle materials, ceramics, high silicon iron are expected to be usable as corrosion-resistance structural materials for very severe corrosive environments. The strength of such brittle materials is very sensitive against the corroded surface properties including roughness, thickness of corroded layer, existence of flaw, etc., as causing chaotic fracture. An instrumented depth-sensitive micro-indentation technique was applied to evaluate mechanical properties on the thin corroded layer of some ceramics which were immersed in boiling high condense sulfuric acid up to 1000 hr. This corrosive environment simulates the sulfuric acid decomposition step in the IS process.

First the corrosion behaviors of ceramics (Si-SiC, SiC, Si_3N_4, Al_2O_3, ZrO_2) were examined in boiling 95wt% sulfuric acid by measuring weight change, concentration of dissolved ions in the sulfuric acid, 4-point bending strength and apparent hardness calculated from load-depth curve obtained by the micro-indentation technique. The corroded surface and the fracture surface of the specimens were analyzed by SEM and EPMA. As a result, the corrosion behaviors of these ceramics were divided into 3 types; (1)Si-SiC and SiC showed excellent corrosion resistance because of protective oxide films which developed during immersion, (2)the bending strength, apparent hardness of Si_3N_4 and Al_2O_3 decreased with increasing immersion time because of corroded layers produced during immersion, and (3)the bending strength of ZrO_2 decreased with remarkable weight loss.

An inverse analysis on the load-depth relationship obtained from the micro-indentation technique was carried out by using an FEM code to qualitatively determine the properties of the corroded surface layer, associated more strongly with the strength degradation in the ceramics rather than the mass change which was conventionally used to evaluate corrosion resistance in the metals. Figure 1 shows the comparison on Load/Depth-Depth curves between experimental and analytical results in the case of Si_3N_4. The curve is influenced by corrosion: the surface condition of Si_3N_4 changed due to the formation of corroded layer consisting of film and porous layers.

---

*Niigata University

Through the combination between analytical and experimental results on the indentation curves, the mechanical properties of both the oxide films on Si-SiC and SiC and the corroded layers on Si_3N_4 and Al_2O_3 were evaluated. Additionally, it was found that the thickness (T) of the oxide films and the corroded layers were obtainable by using the depths (d) which were determined by the slope change on the indentation depth-load/depth curve. The relationship between T and d was found to be described as $T \approx 10d$.

The corroded depth and the film thickness may be used to quantify the corrosion damage. In the cases of Al_2O_3 and Si_3N_4, the relationships between the slope change depth d and the fracture strength for each immersion time were plotted in Fig. 2. Assuming that the corroded layer is the surface flaw which causes crack propagation to fracture, the equivalent crack length a_e to the surface flaw is given by

$$a_e \approx T_c \approx 10d . \qquad (1)$$

We tried to evaluate the strength degradation of Si_3N_4 and Al_2O_3 using the relationship between the equivalent crack length a_e and an intrinsic fracture toughness K_{IC}, given by;

$$a_e = (K_{IC}/1.12\_)^2/\pi \quad , \qquad (2)$$

assuming a surface edge crack[3]. The relationship between the equivalent crack length and the fracture strength was described as a line drawn in Fig. 2. Except for Si_3N_4 in 1000 hr immersion, it is found that the strength degradation was adequately evaluated by using Eq (2) and the relationship between a_e, T_c and d is describable by Eq(1) and the strength degradation due to corrosion is nondestructively evaluated by using the micro-indentation technique. The strength of Si_3N_4 after 1000 hr immersion, at $a_e \approx 20$ μm, is higher than the line given by Eq (2). This seems to be because the film formation above the porous layer in Si_3N_4 has a function to strengthen: the thickness of the film after 1000 hr immersion reaches to about a third of the corroded layer. It was confirmed that the strength degradation of Si_3N_4 and Al_2O_3 due to boiling sulfuric acid corrosion can be evaluated with both the K_{IC} and the d value obtained by the micro-indentation technique.

References

1) Onuki, K., Nakajima, H., Ioka, I., Futakawa, M., and Shimizu, S. : "IS-process for thermochemical hydrogen production", JAERI-Review 94-006 (1994).

2) Onuki, K., Nakajima, H., Ioka, I., Futakawa, M., Nakajima, H., Shimizu, S. and Tayama, I. : "Screening tests on materials of construction for the thermochemical IS process, Corrosion engineering", Vol.46, pp.141-149(1997).

3) Koiter, T.W., Trans. ASME, Ser. E, 32, 237 (1965).

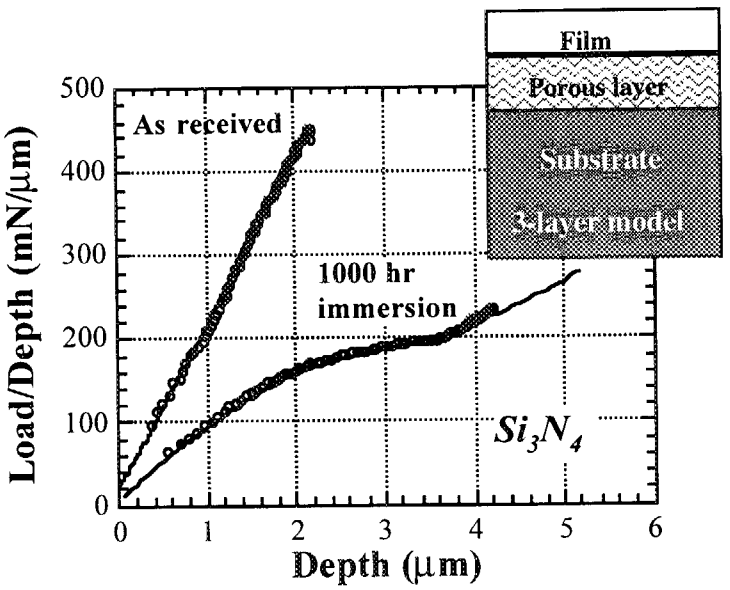

Fig.9.1.1 Comparison on Load/Depth-Depth curve between experimental and analytical results in the case of Si_3N_4

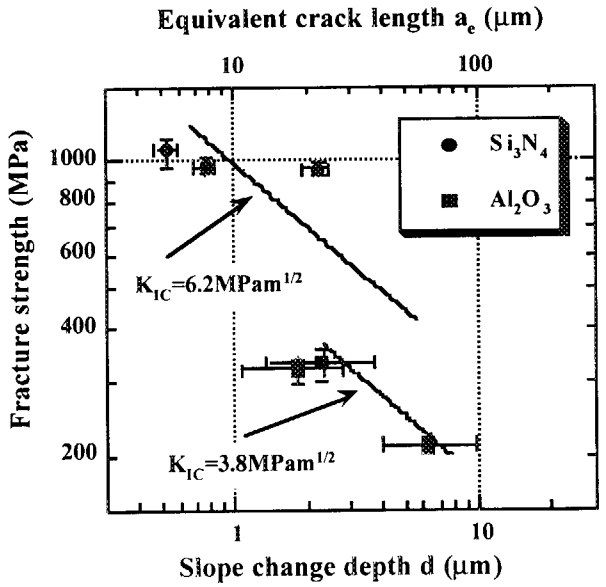

Figure 9.1.2 Fracture strength of Si_3N_4 and Al_2O_3 as a function of equivalent crack length calculated from depth of slope change d

9.2 Characterization of Passive Films on Fe-Si Alloy in Boiling Sulfuric Acid

I.Ioka, J.Mori, C.Kato, M.Futakawa and K.Onuki
(*E-mail*: ioka@popsvr.tokai.jaeri.go.jp)

The thermochemical hydrogen generation process, which makes use of a solar or nuclear power heat source, is considered as a promising basic technology for hydrogen energy systems that are under development. The IS process has a severely corrosive environment, involving sulfuric and hydrogen iodide acids. In our previous study[1], a Fe-12%Si alloy was dissolved by boiling 50% sulfuric acid, though the alloy showed good resistance in boiling 95% sulfuric acid by the passive film. The Fe-12%Si alloy with the passive film, which was produced by pre-immersion in boiling 95% sulfuric acid, was dissolved in boiling 50% sulfuric acid. The passive film formed in boiling 95% sulfuric acid was not effective in boiling 50% sulfuric acid. So, the difference between the passive films of Fe-20%Si alloy formed in boiling 95% and 50% sulfuric acids is studied in this work.

The Fe-20%Si alloy was prepared by arc melting of iron(99.9%) and silicon(99.99%). Specimens of approximately 6x1.5x25mm were ground to a 600-grit finish and rinsed in distilled water and acetone. The specimens were placed in a glass cradle and held in a glass container of 1000ml capacity equipped with a circulation cooling tube and immersed in 50% or 95% sulfuric acids at the boiling temperature (140℃ or 320℃). The specimens were weighed to yield a corrosion rate. The passive films on the specimens were evaluated in terms of X-ray Photoelectron Spectroscopy(XPS) analysis.

The corrosion rates of the specimens immersed in boiling 50% sulfuric acid (50% acid specimen) and in boiling 95% sulfuric acid (95% acid specimen) were 2.0×10^{-3} and 2.2×10^{-3} g/m^2/h, respectively. The Fe-20%Si alloy showed good resistance in boiling 50% and 95% sulfuric acids. The 50% acid specimen acquired a yellow tint with a gloss of metal. The 95% acid specimen changed color to black without a gloss of metal.

The chemical bonding of Si and O in the passive films were characterized by XPS analysis using Mg Kα radiation from X-ray source operating at 10kV and 30mA. The binding energy was referenced to the C 1s peak at 284.6eV from the carbon contamination on surface and then the passive films were sputtered by the Ar ion beam to remove the surface contamination. The XPS spectra from the passive films of the 50% and 95% acid specimens

are shown in Fig.1. For comparison, the XPS spectra from SiO powder are also shown in Fig.1. Sulfur has S 2p bands in the 160-170.6eV range[2]. No peak corresponding to sulfur, however, was detected in the 95% acid specimen because the S/N ratio of the XPS is low. The Si 2p and O 1s spectra of the 50% acid specimen are symmetric and showed the peak of 103.5eV and 534.2eV. According to the literature, the binding energies of Si 2p and O 1s in SiO_2 are 103.2-104.7eV[3] and 532.6-534.7eV[4], respectively. The peaks in the 50% acid specimen are in good agreement with that in SiO_2. Therefore, the passive film on the 50% acid specimen can be described as SiO_2. On the other hand, the Si 2p and O 1s spectra of the 95% acid specimen are slightly asymmetric on the low binding energy side compared with that in the 50% acid specimen. This is, the spectra are asymmetric, indicating the presence of more than one chemical state. The Si 2p spectrum of SiO powder is also asymmetric. The behavior is probably due to the presence of Si-metal that is made by reduction under in situ cleaning by the Ar ion beam. In order to obtain the SiO peak, we have decomposed the Si 2p spectrum into two different components by the binding energy (99.7eV) of Si-metal[2]. The obtained data are best fitted with a Gaussian-Lorentzian curve with a peak at 102.3eV(SiO) as shown in Fig.2(a). Other authors have reported that the prominent peak shifts towards the lower binding energy when the O/Si ratio of the SiOx ($X<2$) film decreases[3,4]. The Si 2p spectra of the 95% acid specimen could be decomposed into constituent peaks at 103.8eV and 102.3eV assigned to SiO as shown in Fig.2(b). It is considered that the peak at 103.8eV is assigned to SiO_2. The passive film on the 95% acid specimen can be described as a composite between SiO_2 and SiO.

Jana et al.[5] have shown that the O/Si ratio of a SiO_X film produced by a photo-chemical vapor deposition technique increased with increasing the wave number for the stretching vibration of Si-O-Si band(ν) which was measured using infrared spectroscopy. Exposure of the SiO_X film to a dry forming gas at 800℃ leads to densification and an increase in the value of ν[6]. It seems that the density of the 50% acid specimen film is higher than that of the 95% acid specimen film, since the O/Si ratio of the 50% acid specimen film is higher than that of the 95% acid specimen film. Generally, the diffusion of elements through the film becomes difficult due to the densification of the film. So, it is considered that the faster growth rate of the 95% acid specimen film is attributed to the low density of the film.

References

1) Ioka, I. et al. : J. of the Soci. of Mater. Sci. Japan, 46,1041(1997).[in Japanese]

2) Stypula, B. and Stoch, J., Corro. Sci., 36,2159(1994).

3) Alfonsetti, R., et al. : Appl. Surf. Sci., 70/71,222(1993).

4) Finster, J., Schulze, D. and Meisel, A.: Surf. Sci., 162,671(1985).

5) Jana, T., Ghosh, S. and RAy, S.: Mater. Sci., 32,4895(1997).

6) Krongelb, S.: Electrochem. Techno., 6,251(1968).

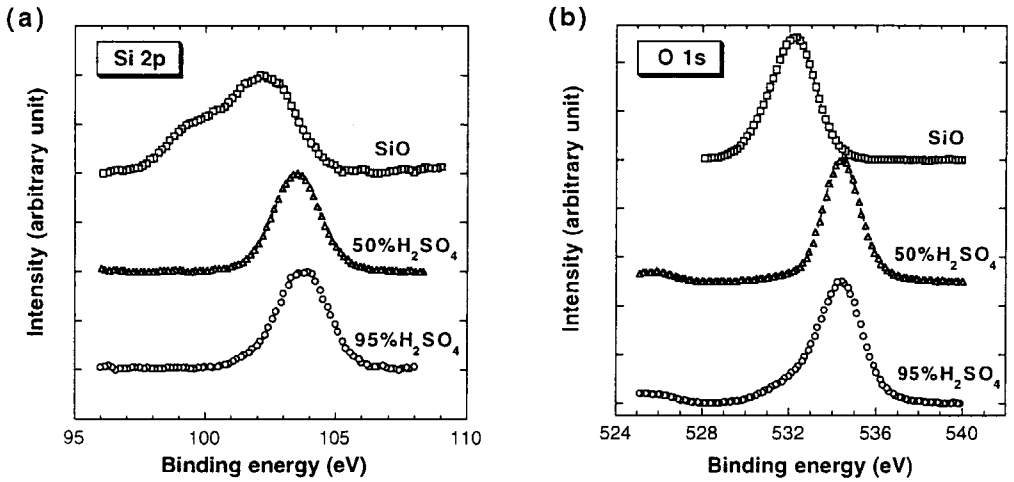

Fig.9.2.1 Si 2p and O 1s spectra from the 50% acid, 95% acid specimens and SiO powder

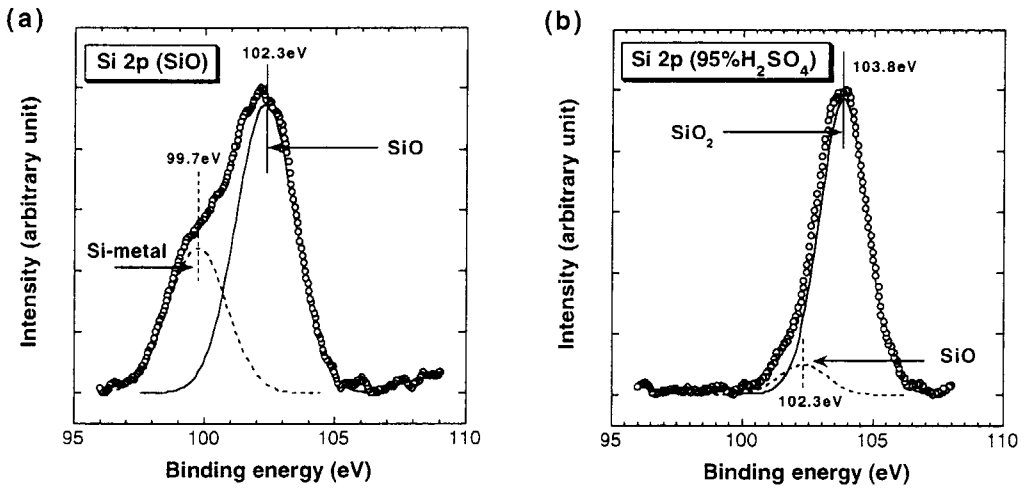

Fig.9.2.2 Decomposition of the Si 2p spectra from (a) SiO powder and (b) 95% acid specimen

9.3 Development of HIP Bonding Techniques of W and Cu-alloys for Plasma Facing Components of Fusion Reactor in 1998

S. Saito, K. Fukaya, S. Ishiyama, M. Eto and M. Akiba
(*E-mail* : sai@popsvr.tokai.jaeri.go.jp)

Plasma facing components(PFC) of fusion reactor are designed as the duplex structure where W armor tiles are bonded with Cu alloy heat sink. Therefore, it is necessary to develop a reliable bonding techniques in order to fabricate PFC with enough integrity. We have applied the hot isostatic pressing (HIP) method to bond W with Cu-alloys. Bonding tests of W and OFHC-Cu were performed [1, 2]. From four point bending test we obtained an optimum HIP bonding condition as 1273K×2hours×98-147MPa. Tensile tests were also performed for specimens bonded in this condition. Figure 9.3.1 shows the results of tensile tests on a bonded W / Cu as well as HIP treated OFHC-Cu and as-received OFHC-Cu. It is clear that the bonded specimens and HIP treated OFHC-Cu had almost the same strength at temperatures from 473K to 873K. The tensile strength of the bonded W / OFHC-Cu was almost equal to that of OFHC-Cu which was treated in the same HIP conditions.

Bonding tests of W and DS (Dispersion Strengthened)-Cu which was considered as heat sink material for ITER were also performed. Figure 9.3.2 shows SEM / EPMA observations around the bonding interface of W and DS-Cu. There are some cracks and a tungsten oxide layer at the interface. The cracks were produced by residual stresses. It is suggested that the tungsten oxide layer was caused by free oxygen in DS-Cu. The free oxygen might be introduced in the manufacturing process of DS-Cu. It was concluded that direct bonding of W and DS-Cu may be impossible and some insert materials will be necessary for bonding W and DS-Cu. As an insert material, OFHC-Cu was selected to decrease the residual stresses and to avoid tungsten oxide developing. The results of bonding tests of W and DS-Cu using OFHC-Cu inserts with various thickness are shown in Table 9.3.1. The specimens with a 0.1mm OFHC-Cu insert were not bonded but those with 0.3mm to 1.8mm OFHC-Cu inserts were successfully bonded. Figure 9.3.3 shows SEM photographs of bonding interfaces between W and DS-Cu with a 1.0mm OFHC-Cu insert. Neither cracks nor tungsten oxide layer were observed around the bonding interfaces. Figure 9.3.4 shows the results of tensile tests on the bonded W / DS-Cu with 0.3mm to 1.8mm OFHC-Cu inserts. At temperatures from R.T. to 473K the strength of 0.3mm insert was higher than those of 0.5mm to 1.8mm specimens, while it was lower At temperature from 673K to 873K. In the case of inserts from 0.5mm to 1.8mm, the tensile strength was independent of the thickness of insert metal, though the tensile strength was a little higher than that of HIP treated OFHC-Cu.

References

1) Saito, S., Fukaya, K., Ishiyama, S., Eto, M., Sato, K. and Akiba, M., Proceeding of 20th Symposium on Fusion Technology, Marseille, France,1998.

2) Saito, S., Fukaya, K., Ishiyama, S., Eto, M., and Akiba, JAERI Research 99-049.

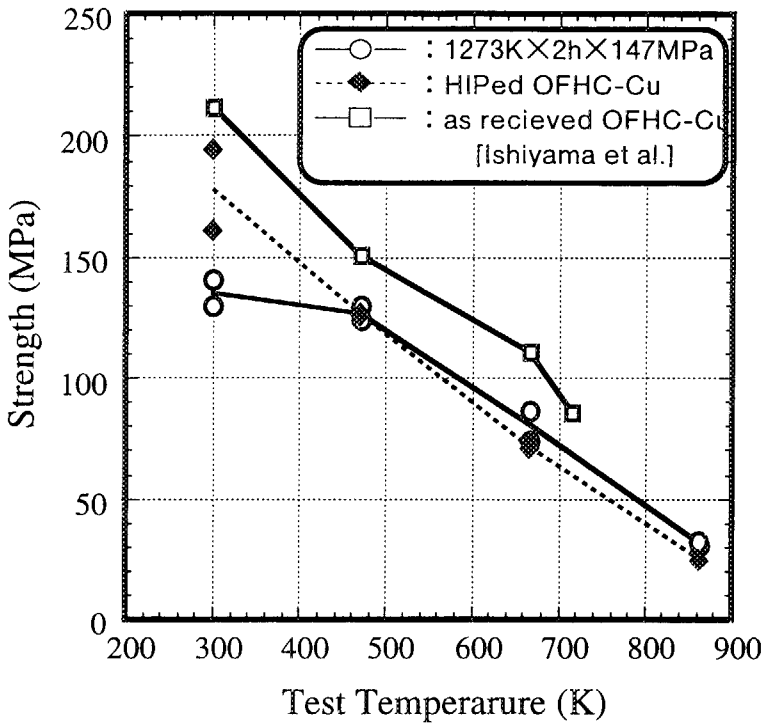

Fig.9.3.1 Results of tensile test on the bonded Wand OFHC-Cu at R.T. to 873K

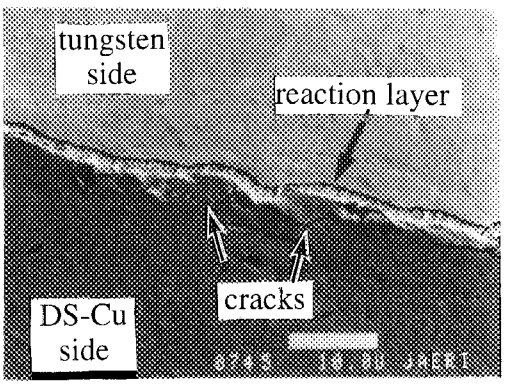

Fig.9.3.2 SEM photograph of bonding interface between W and DS-Cu

Table 9.3.1 Results of bonding test between W and DS-Cu with OFHC-Cu insert

Thickness of OFHC-Cu (mm)	0.1	0.3	0.5	1.0	1.4	1.8
Bonding	×	○	○	○	○	○

※ ×: not bonded, ○ : successfully bonded.

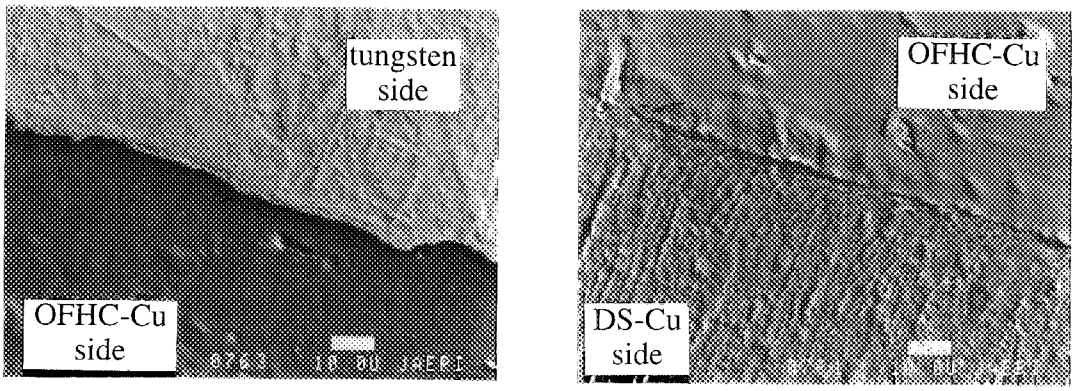

Fig.9.3.3 SEM photographs of bonding interface between W and DS-Cu with 1.0mm OFHC-Cu insert

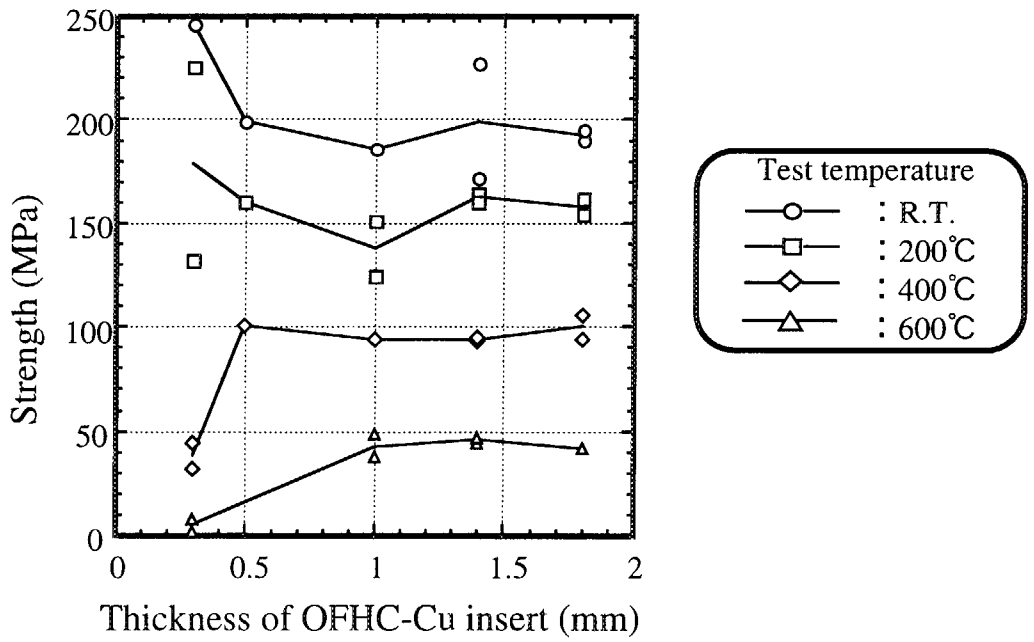

Fig.9.3.4 Results of tensile test onthe bonded W and DS-Cu with OFHC-Cu insert

9.4 Bonding Technique of Alumina Dispersion-Strengthened Copper to Stainless Steel and Evaluation of Interface Strength

H. Nishi, T. Araki* and M. Eto
(*E-mail*: nishi@popsvr.tokai.jaeri.go.jp)

The first wall of ITER is proposed to be made of austenitic stainless steel plate bonded to alumina dispersion-strengthened copper (DS Cu) plate. The DS Cu has excellent thermal conductivity, strength retention and microstructural stability at elevated temperatures. Therefore the development of a bonding technology for the DS Cu to stainless steel has been required for the first wall application.

Joints for DS Cu and Cu alloy to stainless steel have been investigated by brazing[1], friction welding and HIP. Diffusion bonding is a comparatively new technology, though its effectiveness has been successfully demonstrated in various similar and dissimilar metals. Since only limited data were available on the strength of the diffusion bonding joint between the DS Cu and stainless steel, the authors have carried out research on direct diffusion bonding joints between them[2]. As for the direct diffusion bonding joint in the previous investigation, recrystallization and intermetallic compounds consisted of B, Fe and Cr were developed in the DS Cu near the bonding interface, while the tensile strength was almost the same as that of DS Cu.

As for the joint, it is difficult to evaluate bonding strength near the interface by tensile test, because the deformation of DS Cu is constrained by 316 stainless steel[3]. Figure 9.4.1 shows the results of FEM analysis on the tensile test. The maximum stress and strain were generated at the DS Cu apart from the interface. The specimen may fracture at the DS Cu apart from the interface, even though some defect exist near the interface. The fracture strength on the tensile test does not always correspond to the bonding strength near the interface. However, as for the specimen with notch located at the interface such as Charpy specimen, strain concentrated near the interface as shown in Figure 9.4.2. The Charpy strength was sensitive to the strength near the bonding zone. Therefore, the Charpy test is superior to the tensile test to evaluate the bonding strength of joint.

Moreover, the solid state diffusion bonding of DS Cu to 316 stainless steel with

*Kawasaki Heavy Industries, Ltd

interlayer metals such as Au, Cu and Ni foil were carried out to avoid the intermetallic compounds forming and the DS Cu melting. The Charpy impact test on the joints were performed to evaluate their strength. Figure 9.4.3 is the results of the Charpy test making a comparison with the DS Cu and the direct diffusion bonding. The Charpy-absorbed energy of the joint with Au interlayer increased up to about 50% of the DS Cu and was superior to those with Cu and Ni interlayer and without interlayer metal. Optical micrographs near the interface of the joints are shown in Figure 9.4.4. The intermetallic compounds consisted of B, Fe and Cr were developed in the DS Cu near the bonding interface for the direct bonding joint. For the Cu interlayer joints, the same intermetallic compounds were formed at the Cu interlayer metal. In the case of the Ni interlayer joints, voids were generated in the DS Cu several tens micron meters from the interface between Ni layer and DS Cu. These voids were Kirkendall void caused by difference between the diffusion rates of the Ni and Cu elements.

References

1) Nishi, H., Muto, Y. and Sato, K.:" Solid-state Diffusion Bonding of Alumina Dispersion-strengthed Copper to 316 Stainless Steel" , J. Nucl. Mater., 212-215, p.1585-1589(1994)

2) Nishi, H. and Kikuchi, K.:" Influence of Brazing Conditions on the Strength of Brazed Joints of Alumina Dispersion-strengthed Copper to 316 Stainless Steel" , J. Nucl. Mater., 258-263, p.281-288(1998).

3) Nishi, H., Muto, Y. and Eto, M.:" Charpy Impact Properties of Diffusion Bonded Joints of Alumina Dispersion-strengthed Copper to 316 Stainless Steel" , SMiRT-14, 4, p.455-462(1997).

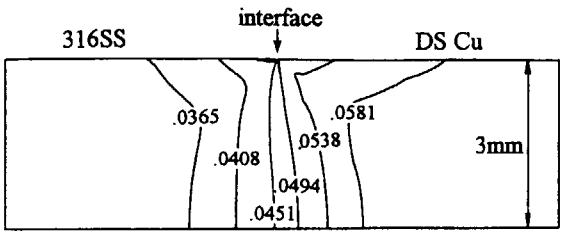

Fig.9.4.1 Contours of equivalent plastic strain at 5% of nominal strain for tensile specimen of joint

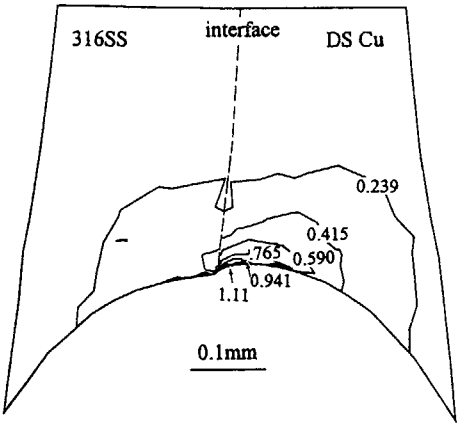

Fig.9.4.2 Contours of equivalent plastic strain near notch tip of joint Charpy specimen at 0.75mm deflection

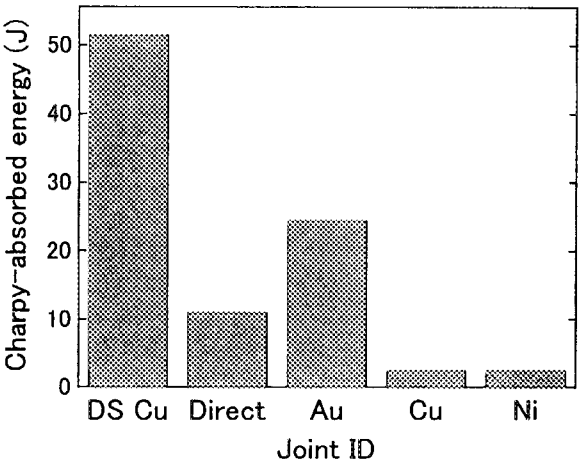

Fig.9.4.3 Charpy-absorbed energy of joints compared with DS Cu

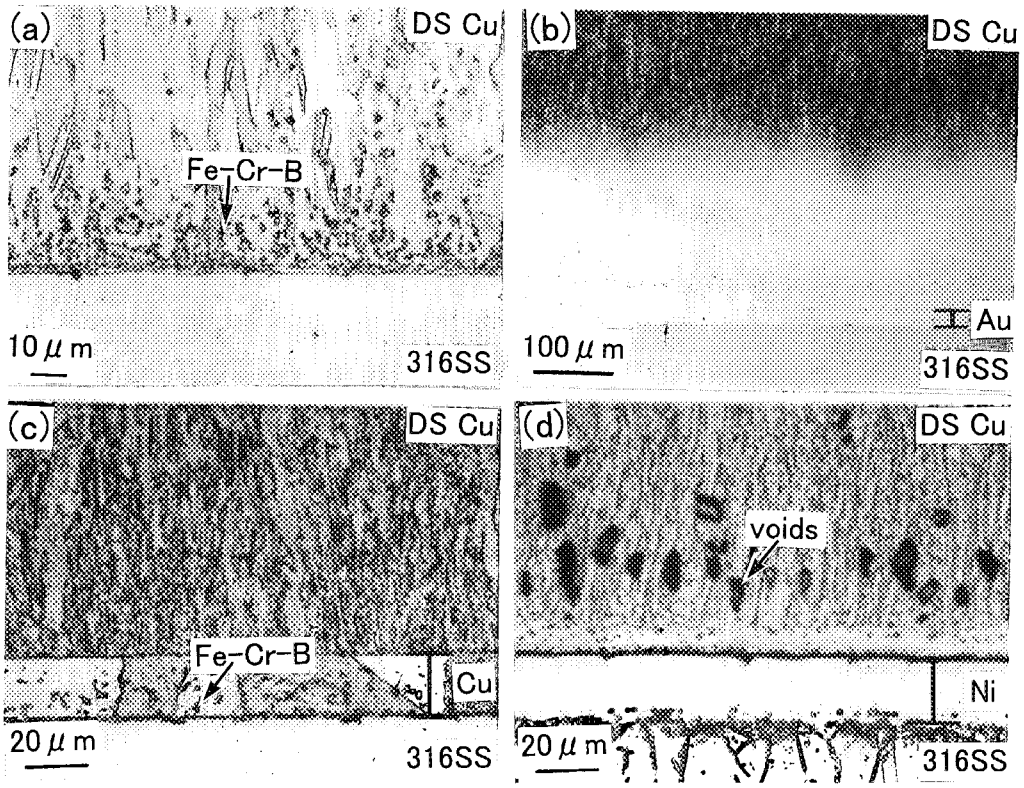

Fig.9.4.4 Optical micrographs near interface
(a) Direct Bonding (b) Au interlayer
(c) Cu interlayer (d) Ni interlayer

9.5 Weld Joint Strength of Vacuum Vessel for Fusion Reactor

H. Nishi, M. Eto, K. Kikuchi, K. Tachibana, S. Saito, E. Tada, K. Koizumi,
M. Nakahira and H. Takahashi
(*E-mail*: nishi@popsvr.tokai.jaeri.go.jp)

In a fusion reactor, deuterium and tritium are utilized to produce thermonuclear energy. Tritium is a radioactive material and must be contained securely. The high temperature plasma is confined and controlled inside a torus vacuum vessel(VV), which contains and supports in-vessel components such as the blankets and divertors. Pressure, thermal, electromagnetic, and seismic loads are expected to be imposed on the reactor components independently or simultaneously. Therefore, the VV is the most important component in view of the fact that it is the first barrier to prevent tritium release from the reactor. As for the VV, ductile fracture caused by the pressure, electromagnetic and seismic loads, low cycle fatigue caused by the cyclic electromagnetic and thermal stresses, and excessive plastic deformation due to the combination of such primary and cyclic thermal stresses are identified to be the dominant failure modes.[1)]

The VV of ITER is designed adopting 316LN stainless steel double-walled structure and composed of inner and outer shells, 40-60 mm in thickness, jointed by welded stiffening ribs as shown in Fig.9.5.1. The VV is divided toroidally into 20 sectors, which are jointed by field welding at the central plane of ports. Many kinds of welding are employed in the VV. However, some weld joints are not full penetration joints, which are not qualified in the conventional design standards for light water reactor. It is also crucial to develop the integrity evaluation method for the weld joints based on proper structural design code. Namely, weld joint efficiency for primary stresses, life reduction factor for fatigue and reduction of ductility for ratchet limit should be developed.

In this study, seven kinds of butt welding were carried out to investigate their tensile properties using tungsten inert gas welding, metal inert gas welding, electron beam welding and their combinations for 40 mm thick 316L stainless steel, which are candidate welding processes for the fabrication of VV. Table 9.5.1 shows their welding processes, ratio of incomplete penetration area and tensile properties of the weld metals using small round bar specimens. The maximum ratio of incomplete penetration area was 34% for the joint E.

As for the tensile properties, the tensile strength of weld metal were larger than that of 316L base metal except for EBW joints, while the elongation of weld metal were smaller than that of 316L base metal.

Figure 9.5.2 and 9.5.3 are tensile strength and elongation of the joints in the case of 40 mm thick as weld specimens. The tensile strength of the joints were larger than that of base metal irrespective of including the incomplete penetration, because the plastic deformation of the specimens was constrained near the incomplete penetration. When the joints included the incomplete penetration, however, the tensile specimens fractured from the incomplete penetration and showed lower rupture elongation than that of the base metal.

References

1) Miya, K., Kobayashi, A., Koizumi, K., Hada, K. and Shimakawa, T. :" Construction of Structural Design guidelines for Vacuum Vessels and Other Components" , Fusion Eng. and Design, 41, p.305-312(1998).

Table 9.5.1 Welding processes and properties of weld joints.

ID No.	Welding process	Configuration	Ratio of imcomplete penetration area(%)	Tensile strength of weld metal (MPa)	Elongation of weld metal (%)
316L	316L SS base metal	-	0.0	556	68
				557	68
A	Narrow-gap TIG welding (outer wall +outer wall)	Butt joint	8.1	608	45
				605	47
B	TIG+MAG welding (outer wall +outer wall)	Butt joint	7.8	564	44
				578	43
C	TIG+MAG welding (inner wall + rib)	T joint	0.0	542	50
				550	58
D	TIG+MAG welding (outer wall + port)	T joint	10.6	577	43
				580	47
E	TIG+MAG welding (outer wall + rib)	T joint	33.7	582	42
				597	45
F	EBW welding (inner wall + rib)	T joint	0.0	544	47
				544	48
G	EBW welding (outer wall + rib)	T joint	30.4	506	64
				514	77

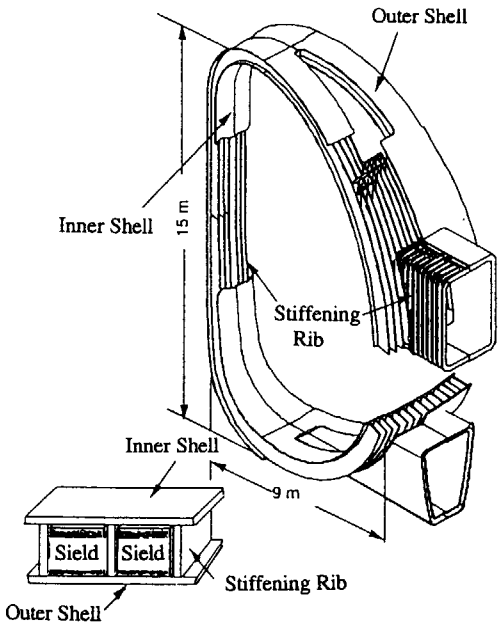

Fig.9.5.1 Schematic view of vacuum vessel.

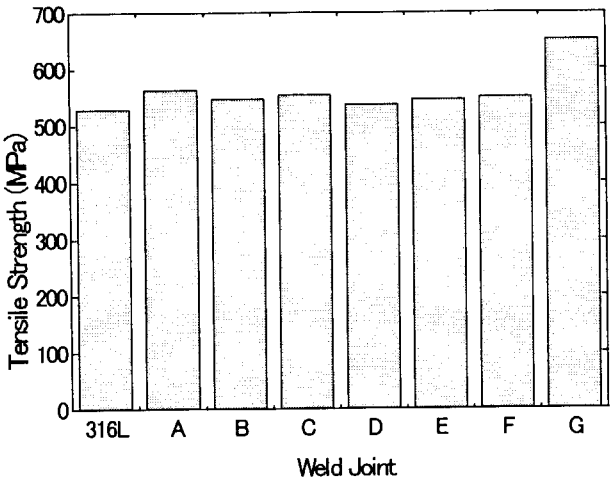

Fig.9.5.2 Tensile strength of weld joints by tensile tests

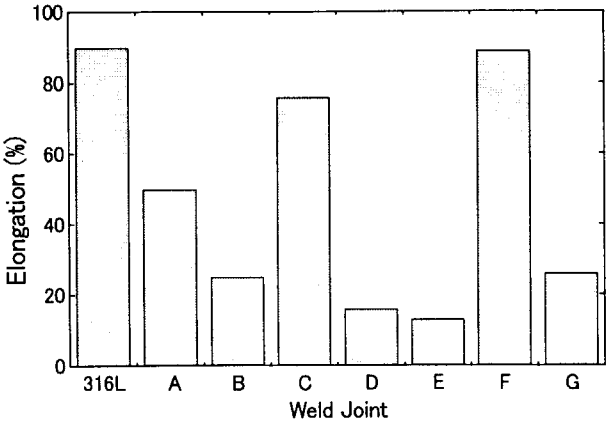

Fig.9.5.3 Elongation of weld joints by tensile test

9.6 Finite Element Modeling of Microindentation for Determining Mechanical Characterization of Ion Irradiated Layer

I.Ioka, M.Futakawa and T.Wakui*
(*E-mail:* ioka@popsvr.tokai.jaeri.go.jp)

A triple ion beam facility can be used to simulate the irradiation environment by producing displacement damage in the material while simultaneously implanting H and He, which is controlled to achieve the equivalent dpa to the expected irradiation. However, the ion-irradiated area is limited to the very shallow surface layer (<3μm depth) of the specimen so that the irradiation damage is distributed around the thin layer. Hence, a microindentation technique combined with an inverse analysis using a finite element method (FEM) was applied to examine the influence of ion irradiation on the mechanical properties of the thin layer and derive the constitutive equation of the damaged parts.

A material tested is 316 stainless steel. The configuration of specimen is a disk of 3mm diameter with 0.2mm thickness. The electrochemically polished disk specimens were irradiated in single (12MeV Ni^{3+}) ion beam mode at a temperature of 200°C. The SRIM97 code formerly known as TRIM[1] was used to compute the required ion fluence and the displacement dose as a function of depth beneath the specimen surface. The results of the SRIM97 calculation for the specified irradiation conditions are shown in Fig.1. This figure shows the displacement damage in dpa by Ni^{3+} ion and the distribution of the ions as a function of depth in the specimen. The displacement damage in the disk specimen is mainly attributed to Ni^{3+} ion irradiation. The peak dose is about 22dpa around 2μm. The peaks of Ni^{3+} ion is about 0.6at%.

The microindentation technique may be applicable to evaluate mechanical properties of the irradiated layer. The microindentation test was carried out on the surfaces of the irradiated and unirradiated (as received) disk specimens at room temperature using a Berkovich-shaped diamond indenter. A testing machine, DUH-200 (Shimadzu Co.), was used for the microindentation test. A load was applied with a loading speed of 2.6×10^{-3} N/s, held 1 second and then removed. During loading and unloading, the load was continuously monitored along with the displacement with a resolution of 2mN and 0.01μm, respectively.

The inverse analysis on the measured load/depth curve was performed using an explicit FEM code, DYNA, which permits us to do a large deformation analysis, to determine the mechanical properties of the irradiated-layer and give the interpretation on the behavior of the

* Department of Mechanical Engineering, Niigata University

load/depth relationship. The model is illustrated schematically in Fig.2. The indenter was perfectly rigid. The contacting interface between the specimen and the indenter tip is assumed to be frictionless. The mesh size was given to be sufficient fine to keep accuracy: the minimum element size is 0.05μm. The total number of the elements used in the specimen model is 5289. The loading rate in the calculation is sufficiently small to ignore an inertia effect as static condition.

In order to derive a constitutive equation of the irradiated layer of the specimen, we have carried out the inverse analysis based on FEM calculation. In the inverse analysis, firstly we assumed the form of constitutive equation for the irradiated layer and unirradiated part. And then, after iterating calculation on the load/depth-depth curve to be given the suitable fitting between experimental and analytical results, we determined the constants in the constitutive equation of the irradiated layer. The following constitutive equation was assumed :

$$\sigma=E\varepsilon, \qquad \sigma<\sigma_y \tag{1}$$

$$\sigma=C(\varepsilon_0+\varepsilon)^n,\ \varepsilon_0=(\sigma_y/C)^{1/n}-(\sigma_y/E), \qquad \sigma>\sigma_y \tag{2}$$

where E is Young's modulus and σ_y is yield stress, and C and n are material constants. It is generally believed that Young's modulus is not affected by irradiation. Hence, Young's modulus was determined to be 200GPa, regardless of the dpa value. Figure3(a) shows the analytical result giving a fairly good agreement with the experimental results on the unirradiated specimen. Based on this result we determined the constants in the Eq.(2), C=1380MPa, n=0.42.

The yield stress is very dependent on the amount of irradiation. The yield stress for the irradiated layer was calculated using the relationship between the dpa value on the depth and the yield stress dependency on the dose equivalent to the dpa[5] For the single ion(Ni^+) irradiated specimen, the yield stress change with depth in the irradiated thin layer was represented by dividing it into 6 layers. Finally, the analytical result represents the indentation behavior of the irradiated specimen described with the load/depth-depth curve very adequately, as shown in Fig.3(b). The curve is strongly dependent on the change of the mechanical properties.

References

1) Ziegler, J.F. et al. : "The Stopping and Range of Ion in Solids", vol.1, Pergamon Press, New York(1985).

2) Froehlich,F. et al. : Phys. Stat. Sol., 42, 79(1977).
3) Takahashi,H. et al. : "Development of evaluation techniques for small specimens", Atomic Energy Society of Japan, 84(1992).[in Japanese]
4) Cahoon,J.R. et al. : Metall. Trans. 2,1979(1971).
5) Robertson,J.P. et al. : ASTM1325, 671(1999).

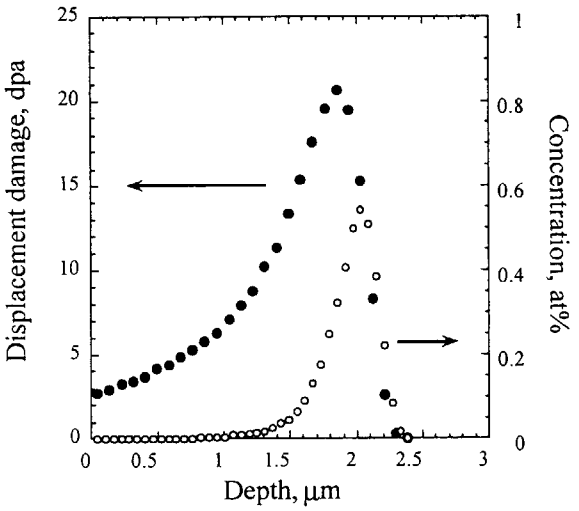

Fig.9.6.1 Displacement damage and implanted Ion profile for 316SS calculated by SRIM97

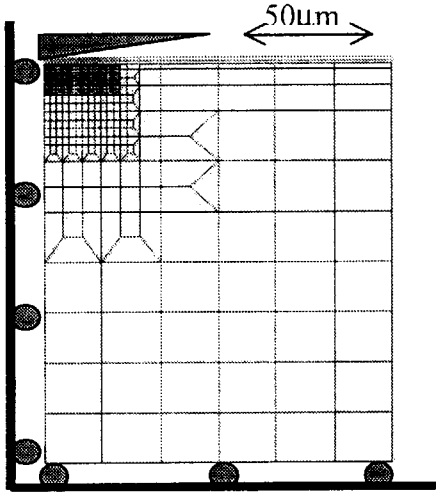

Fig.9.6.2 Axisymmetric two-dimensional mesh for simulating microindentation of the ion

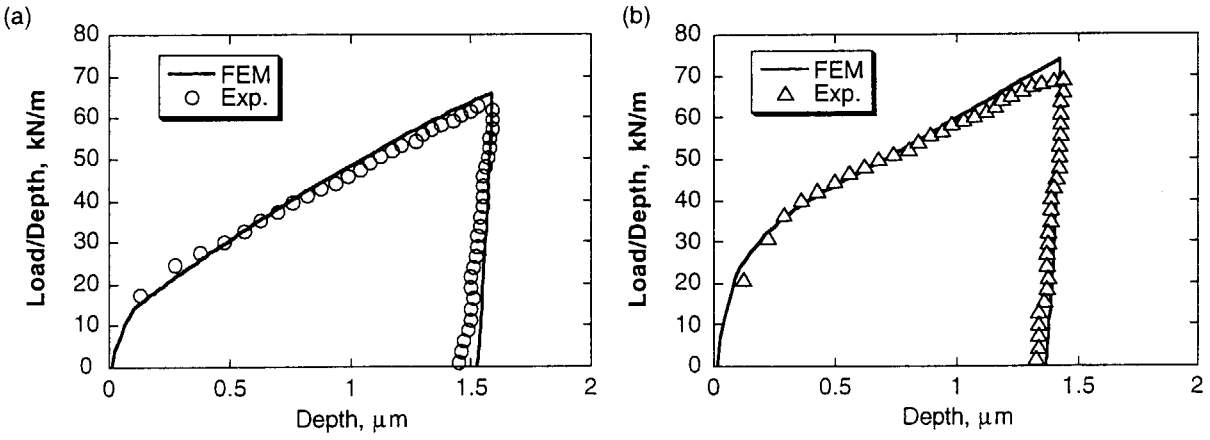

Fig.9.6.3 Experimental and calculated Load/Depth-Depth curves in (a)unirradiated and (b)single ion irradiated specimens

9.7 Development of Creep Constitutive Equations for Creep Curves under Constant Load

Y.Kurata and H.Utsumi*
(*E-mail:* ykurata@popsvr.tokai.jaeri.go.jp)

Development of the creep constitutive equation which can describe a total creep curve containing a tertiary creep stage is important to design high-temperature components and to predict their lives. The θ projection method[1,2] and Ω method[3,4] have been proposed for this purpose. In the θ projection method, creep strain, ε_c is described as a combination of the two exponential terms as

$$\varepsilon_c = \theta_1\{1 - \exp(-\theta_2 t)\} + \theta_3\{\exp(\theta_4 t) - 1\} \quad (1)$$

where t is time, θ_1, θ_2, θ_3 and θ_4 are parameter constants determined by fitting Eq.(1) to experimental data. In the Ω method, creep strain is expressed in terms of a logarithmic function as

$$\varepsilon_c = -\frac{1}{\Omega}\ln(1 - \dot{\varepsilon}_0 \Omega t) \quad (2)$$

where $\dot{\varepsilon}_0$ is initial creep rate after loading and Ω is a material constant. There is, however, a limit in applicability of these equations. Therefore, we studied improvement of the θ and Ω methods from the viewpoint of development of creep constitutive equations widely applicable.[5] Here, two new modified methods for constant-load creep curves are proposed: the modified θ method and modified Ω. The modified θ method represents creep strain as

$$\varepsilon_c = X(1)(1 - \exp(-X(2)t)) + \left(\frac{-1}{X(3)}\right)\ln(1 - X(4)t) \quad (3)$$

where X(1), X(2), X(3) and X(4) are parameter constants characterizing creep curve shapes. The modified Ω method represents creep strain as

$$\varepsilon_c = \left(\frac{1}{X(1)}\right)\ln(1 + X(2)t) + \left(\frac{-1}{X(3)}\right)\ln(1 - X(4)t) \quad (4)$$

Heat resistant alloys generally exhibit normal type creep curves consisting of primary,

* Graduate School of Engineering, Tohoku University (now Sumitomo Metal Industries, Ltd.)

secondary and tertiary creep stages or tertiary creep dominant curves. Therefore, we selected Ni-18.5Cr alloy exhibiting normal type creep curves and Ni-18.5Cr-16W alloy exhibiting tertiary creep dominant curves in this study. Creep data of Ni-18.5Cr and Ni-18.5Cr-16W alloys were analyzed using Eqs.(1), (3) and (4). Parameter constants of the each equation are optimized such that they provide the best fit to experimental data.

Applicability of the θ, modified θ, modified Ω methods are investigated for creep data obtained in creep tests of Ni-18.5Cr alloy at 700 and 800℃. Figure 9.7.1 shows an example of fitting for a creep curve at 800℃ using the modified θ method. The equation describes the creep curve until rupture precisely. From comparison of the fitting results using the θ, modified θ, modified Ω methods for the creep curve of Ni-18.5Cr alloy, it is found that the modified θ and modified Ω methods predict strains and life accurately and conservatively. Figure 9.7.2 shows comparison of rupture time calculated using the θ, modified θ, modified Ω methods. Although it is possible to predict rupture time using any method of the three methods, the θ projection method predicts a little longer rupture time at high temperatures and low stresses than modified θ and modified Ω methods. Figure 9.7.3 shows an example of fitting for a creep curve of Ni-18.5Cr-16W alloy at 800℃ using the modified θ method. The agreement between the fitted curve of Eq.(3) and experimental data is good. In comparison with the three methods, the θ projection method predicts smaller strains near rupture time than experimental data. As shown in Fig.9.7.4, the θ projection method predicts a little longer rupture time than the modified θ and modified Ω methods.

We conclude that applicability of the modified θ and modified Ω methods is superior for constant load creep curves because they can predict creep curves up to rupture and rupture life accurately and conservatively.

References

1) Evans R.W., Parker J.D. and Wilshire B.: "Recent Advances in Creep and Fracture of Engineering Materials and Structures", Pineridge Press, Swansea, 135 (1982).
2) Maruyama K., Harada C. and Oikawa H.: Trans. ISIJ, 26, 212 (1986).
3) Prager M.: ASME-PVP, 288, 401 (1994).
4) Endo T. and Shi J.: "Strength of Materials", Japan. Inst. Met., Sendai, 571 (1994).
5) Kurata Y. and Utsumi H.: Acta Metall. Sinica., 11, 397(1998).

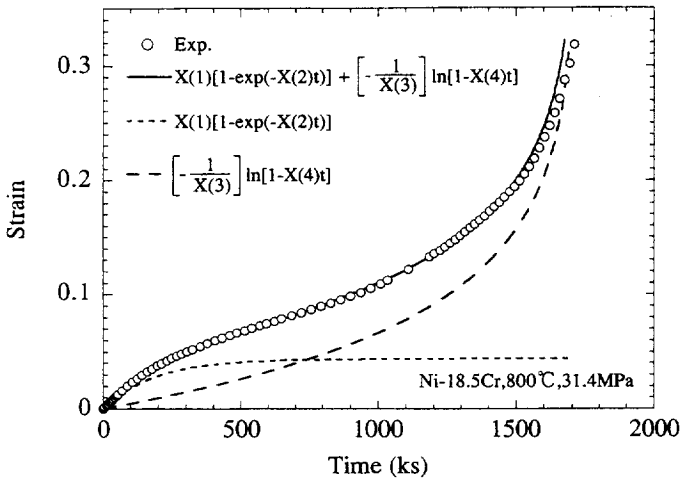

Fig. 9.7.1 Fitting to a creep curve of Ni-18.5Cr alloy at 800℃ using the modified θ method

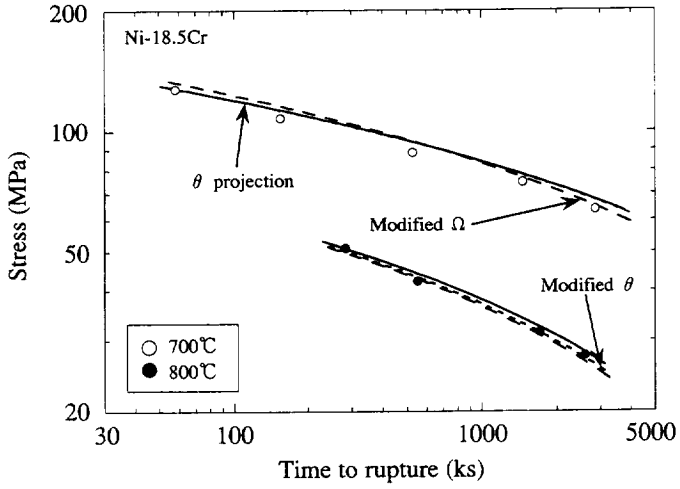

Fig. 9.7.2 Prediction of the rupture time using the θ, modified θ and modified Ω methods for Ni-18.5Cr alloy

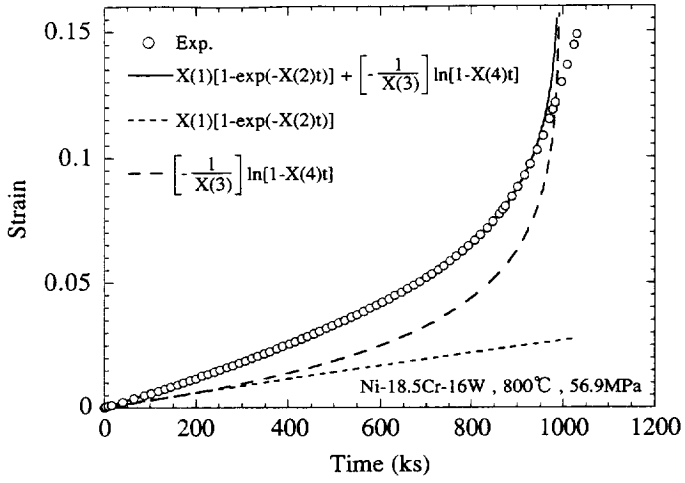

Fig. 9.7.3 Fitting to a creep curve of Ni-18.5Cr-16W alloy at 800℃ using the modified θ method

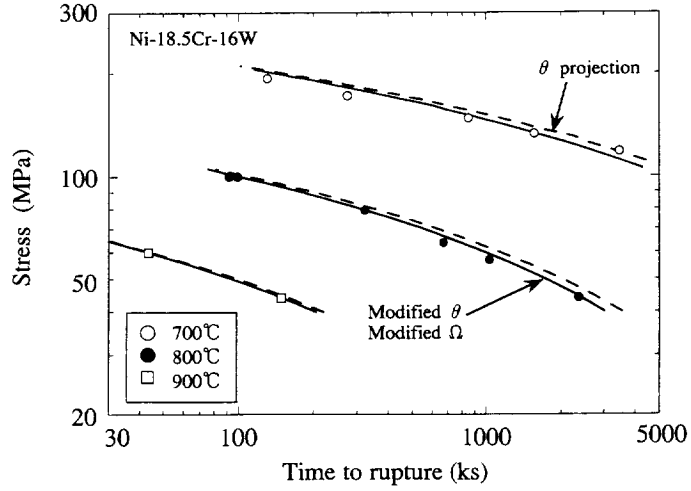

Fig. 9.7.4 Prediction of the rupture time using the θ, modified θ and modified Ω methods for Ni-18.5Cr-16W alloy

9.8 Development and Evaluation of Carbon and Graphite Materials for Nuclear Applications

M. Eto, S. Ishiyama, K. Fukaya, T. Saito H. Ugachi and S. Baba
(*E- mail:* etom@popsvr.tokai.jaeri.go.jp)

Introduction: Research activities on carbon and graphite materials include 1) R & D on C/C composites for HTTR control rod use, 2) Characterization of carbon fibers and irradiated C/C composites, and 3) Establishment of a database on irradiated nuclear graphites. The third subject has come into effect within the framework of an IAEA International Database. Here, the activities on C/C composites for control rod use are described.

The purpose of the development of C/C composite control rod for HTTR is primarily to increase the thermal resistance of the control rod so that the reactivity control is to be less-restricted in the process of shutdown. Moreover, the use of the material with the higher thermal resistance would make it possible to raise the operation temperature of future reactors. As for R & D on the C/C composite control rod, first, several C/C composites have been characterized as materials, including the effect of irradiation effect.[1] Then, some concepts of C/C composite control rod, together with the fabrication method for the rod components, have been investigated.[2,3] In this section, the possibility of use of C/C composite for the control rod is assessed on the basis of the results of strength tests on components such as tubes and bolts made of two kinds of materials.

Experimental: Two kinds of C/C composites were used in the present experiment; AC250(Across Ltd.) and CX- 270(Toyo Tanso Co.). First, two materials were characterized through measurements of mechanical and physical properties, the results of which are shown in Table9.8.1. It was considered that both materials had enough strength as candidates for the control rod use. A concept for the control rod shown in Fig.9.8.1 was employed here. Among the rod components, outer tubes (113mmOD x 105mmID x 300mmL), inner tubes (75mmOD x 60mmID x 300mmL), M16 and M8 bolts were fabricated using the materials above. For the tubes 2- dimensional precursor sheet was rolled up to a planned thickness, after which it was impregnated and sintered at about 2000 C. Bolts were machined from a layered precursor sheets which had been impregnated and sintered beforehand. Tubes and bolts were optically inspected to see if they were fabricated with enough precision. The

tubes were cut into ring- type specimens with thickness of 10 to 50 mm. These specimens were subject to ring compressive test or buckling test at a cross- head speed of 1 mm/min. For bolts tensile, bending, compressive and shear strength tests were carried out using a servohydraulic testing machine at a stroke speed of 1.25 mm/min.

Results and Discussion: The optical inspection indicated that the dimensions of the tubes and bolts could be deemed to be precise enough to assemble a control rod from them. Results of the ring compressive tests on tube specimens are shown in Fig.9.8.2. Here, one can see that the tube specimens showed the gradual decrease in stress after the maximum stress is reached. It was observed that at Stage 1 in Fig.9.8.2 several inner layers of the ring specimen were fractured and some layers were delaminated. At Stage 2 a large amount of delamination occurred and the crack propagated up to about a half of thickness of the specimen wall. At Stage 3, though the crack length was as large as that at the maximum stress, the larger deformation of specimen was observed. Buckling tests indicated that specimens fractured very abruptly at the maximum stress with no subsequent gradual decrease in stress. Results of the tensile or compressive test of M8 bolts are shown in Fig.9.8.3 for both materials. It is seen that the AC- 250 showed the larger strength and the more brittle nature. There was a good correlation found between the number of pitch and the tensile or compressive fracture strength, which means that the load was sustained uniformly with all the screw threads concerned. Fig.9.8.4 shows the ring compressive strength of the tube specimens plotted on the normal probability paper. Here, the dotted vertical line is a design strength determined temporarily by setting a safety factor as 5. All the tubes exceeded the design strength, although it seems that some improvement in strength is preferable.

References

1) Eto, M., Ishiyama, S., Ugachi, H., Fukaya, K. and Baba, S.: "Mechanical properties of neutron- irradiated C/C composites for plasma facing components", J. Nucl. Mater., 212-215, 1223(1994).

2) Eto, M., Ishiyama, S. and Ugachi, H.: "Development of C/C composite control rod for HTTR(I)", JAERI- Research 96- 043 (1996).

3) Eto, M., Ishiyama, S., Fukaya, K., Saito, T., Ishihara, M. and Hanawa, S.:"Development of C/C composite control rod for HTTR(II)", JAERI-Research 98-003 (1998).

Table 9.8.1 Characterization of 2D reinforced C/C composites

Characterization \ Materials	AC250-2D	CX270
Density(g/cm3)	1.7	1.59
Tensile strength(MPa)	131.9 (//)	227 (//)
Compressive strength(MPa)	194.8 (⊥)	88(//) 226 (⊥)
3 point bending strength(MPa)	171.3 (⊥)	169 (⊥)
Shear strength(MPa)	17.6 (⊥)	——
Young's modulus(GPa)	50.7	102
Thermal conductivity(W/mK)	68.6(//) 10.47(⊥)	35(//) 5(⊥)
Thermal expansion(10-6/K)	0.6(//) 8.2(⊥)	<1(//) 8(⊥)
Electrical resistivity(μΩm)	17(//)	17.1(//)

Loading or measuring direction; (//)Parallel to fiber, (⊥);Transverse to fiber

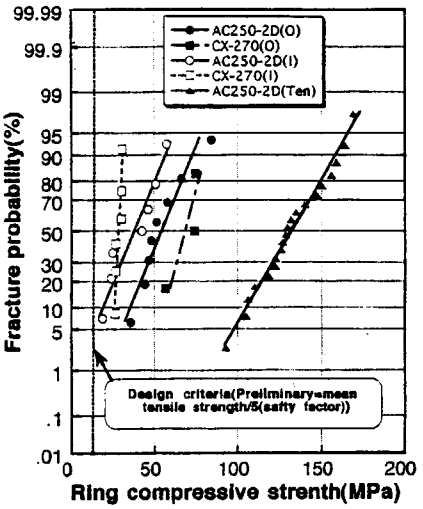

Fig. 9.8.4 Distribution of ring compressive strength of the tube specimens

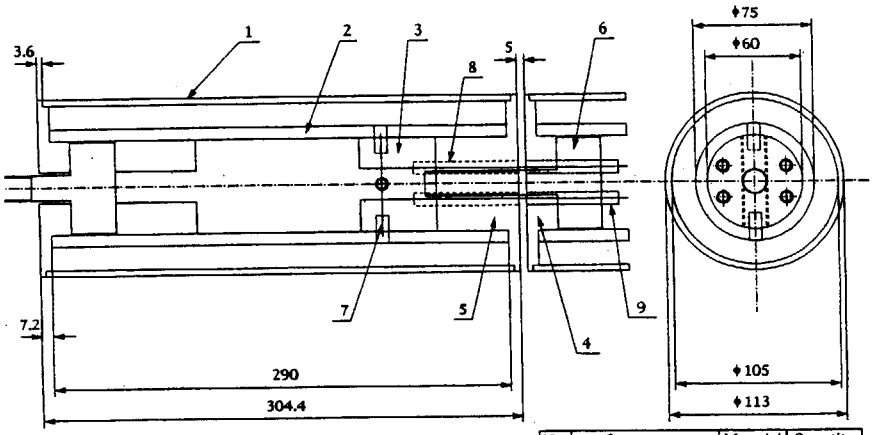

No.	Component	Material	Quantity
1	Outer tube	C/C	1
2	Inner tube	C/C	1
3	Lid supporting plug	C/C	1
4	Upper lid	C/C	1
5	Lower lid	C/C	1
6	M16 Bolt	C/C	1
7	M8 Bolt	C/C	8
8	M8 Bolt	C/C	4
9	M8 Bolt	C/C	4

Fig.9.8.1 A concept of C/C composite control rod

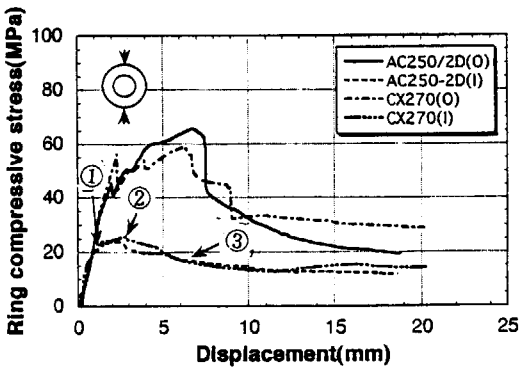

Fig.9.8.2 Ring compressive stress vs. displacement curves for the tube specimens

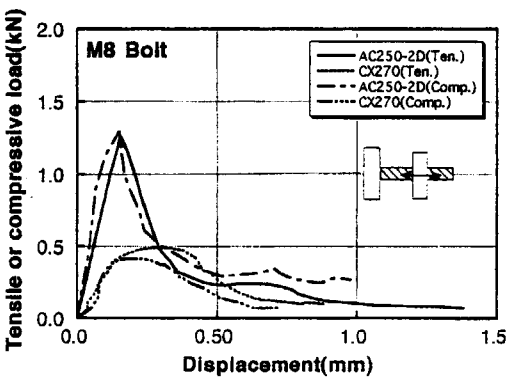

Fig.9.8.3 Tensile or compressive load vs. displacement curves for M8 bolt specimens

10. Compatible Materials Development for Advanced Nuclear Systems

The life prediction study of spent fuel reprocessing equipment materials and the development of alternative materials for the advanced purex process have been carried out in relation to the STA projects for the safety research on the RRP (Rokkasho Reprocessing Plant) and the Nuclear Cross-Over Research respectively. The mock-up of a thermo-siphon type evaporator for nitric acid recovery made of type 304ULC austenitic stainless steel was operated during one year from April in 1998 after the PSI. After operated for nearly 8,000hr, the first ISI was carried out. The wall thinning in this equipment was observed only in heat transfer tubes. The effectiveness for the practical application of alternative materials developed in our research was expected to show the high corrosion resistance at heat transfer conditions by suppressing the trans-passive corrosion. These are the modified stainless steel with immunity to intergranular attacks so-called the EB-SAR and a new Cr-W-Si nickel base superalloy enriched with passive film former elements. On the other hand, the mock-up of a dissolver made of zirconium was constructed and it operation was started at the end of March in 1999. The performance of this equipment is considered to be controlled by the resistance against SCC at heat transfer surfaces. This susceptibility and the corrosion fatigue crack growth rate in boiling nitric acid were examined for the TIG weldments made of reprocessing grade zirconium. The former was clearly dependent on the crystal texture of cph type structure, because it crack is easy to form along closely packed planes like (0001). The latter was accelerated independent with the crystal texture, because the rearrangement of crystal orientations is easy to occur by the low temperature creep in a crack front region stressed highly.

The development of new materials applied for water cooling reactor core components was carried out focusing on a new research project of fuel cladding for the advanced nuclear power plants. The major requirement of cladding materials for high burn-up was examined with respect to the nuclear characteristics and irradiation properties, by considering the practical experiences in the modified Zircaloy-2 and zirconium alloys. As for the high burn-up by using MOX fuels on the advanced reactors, the corrosion resistance against high temperature water and irradiation properties are considered to be the predominant requirements more important than nuclear properties like neutron absorption. A new surface reaction model was proposed by analyzing the low energy plasma driven permeation of hydrogen, for interpreting the accelerated corrosion behavior experienced in Zircaloy cladding. A new nickel base alloy strengthened by wolfram silicide dispersion was developed as an alternative material instead of cobalt base Stellite. The wear resistance of this alloy superior than it of Stellite was achieved by optimizing the chemical composition and the metallographic structures by strain aging.

10.1 The Life Prediction Study of Rokkasho Reprocessing Plant Materials

K .Kiuchi, M.Yano, M.Takizawa and S. Shibata

(*E-mail:* kkiuchi@popsvr.tokai.jaeri.go.jp)

The life prediction study of major equipment materials used in severe corrosive nitric acid solutions of RRP (Rokkasho Reprocessing Plant) was carried out. The nitric acid recovery made of type 304ULC austenitic steel and the dissolver made of type 702 metallic zirconium were selected for reliability testing. This study is composed of major three programs, namely, the mock-up tests by using the small-scaled equipment simulated to the practical design, laboratory tests for examining corrosion controlling factors by using small specimens and to establish the data base system for life prediction[1]. Important parameters on this study were extracted with analyzing the past data obtained from the life prediction study on the Tokai reprocessing equipments.

The design of mock-ups was made by considering the quantitative evaluation of the most important parts on objective equipments, namely, heat conducting tubes in an acid recovery evaporator and a thermal jacket in a dissolver. Table 10.1.1 shows the outline of life prediction study concerning the RRP equipments materials. The mock-up of thermo-siphon type acid recovery evaporator is consist of seven heat conducting tubes with the practical scale and it has been operated in the maximum corrosive condition expected in the steady state operation. From preexaminations, the effect of radioactive species, nitric acid solution chemistry, corrosion mechanisms were elucidated. Mock-up testing conditions and corrosion monitoring methods were selected from the plant operation planning and preexamination data. This mock-up was constructed as shown in Fig.10.1.1. After the PSI (pre-service inspection test), the operation started from April of 1997 with the operation condition (Table 10.1.2). The mock-up of a dissolver is designed for simulating a thermal jacket made of metallic zirconium by focusing on the oxide film stability at heat conducting surfaces (Fig.10.1.2). Laboratory testing methods were programed for obtaining reference data of the important corrosion parameters expected in stainless steels and metallic zirconium used in practical equipments, by considering the effect of radioactive elements like FP and TRU. The computer simulation is planned to develop the evaluation codes that is required for the life prediction from experimental data and to evaluate the simulation rate to the practical equipments. The thermo-fluid parameter that controls the corrosion rate of heat transfer tubes in a nitric acid evaporator, was evaluate as shown in Fig.10.1.3. This tendency was experimentally clarified by results of 1st ISI

---

* Sumitomo Chemical Eng. Co. Ltd.

** MRI Co.

Reference

1) K.Kiuchi, M.Yano, M.Takizawa and S.Shibata : RECOD'98,Vol.3(1998)859

Table 10.1.1 The outline of life prediction study concerning the RRP equipments materials

Fiscal year	1996	1997	1998	1999	2000	2001
Mock-up Tests Evaporator Dissolver	← Design & Construction →←			Operation (ISI; every year)		C&R →
			← Design & Construction → ←	Operation (ISI; every year)		→
Laboratory Tests Reference data Radioactive effect	← Apparatus →←		Tests under heat transfer, fretting and constant load			→
	← Basic evaluation	→← Apparatus → ←		Radioactive solution tests		→
Computer Simulation Evaluation code Data base system	← Thermo-fluid dynamics (Evaporator) & Thermal stress (dissolver)					→
	← Heating tubes, Major components, Mist separator, Mass transfer					→

Table 10.1.2 Major experimental parameters in the mock-up test simulated to an acid recovery evaporator of the RRP

Parameter	Test condition
Design of apparatus Heating conducting tubes	7
Nitric acid loop Chemical composition	9N HNO3 300ppm/Cr(3+) 1,200ppm/(Fe3+) 5ppm/Ru(3+) 50ppm/V(3+)
Boiling point	341K(at liquid surface)
Pressure	120torr(at mist-separator)
Operation Concentration ratio Heating steam	40 times 373K(saturation)

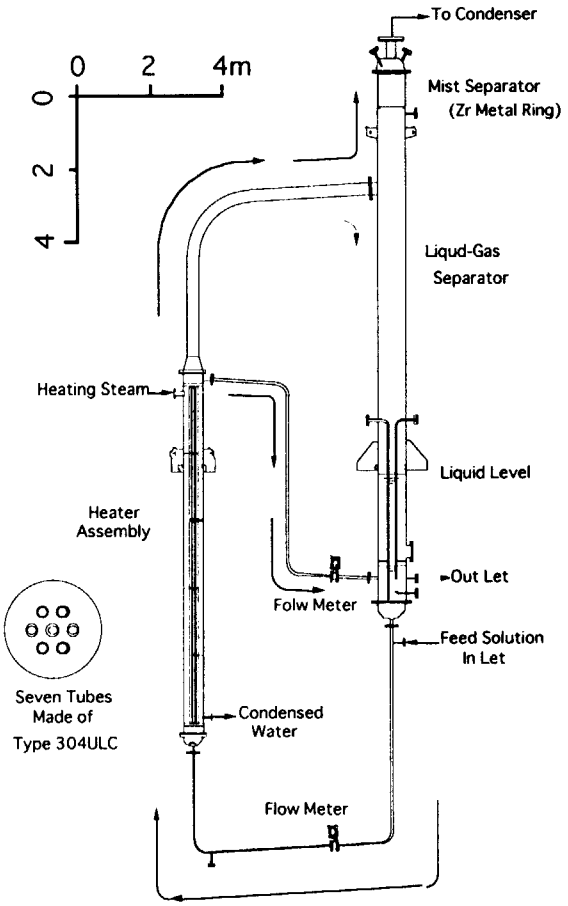

Fig.10.1.1 The small-sized mock-up equipment simulated to acid recovery evaporator made of type 304ULC steel of the RRP

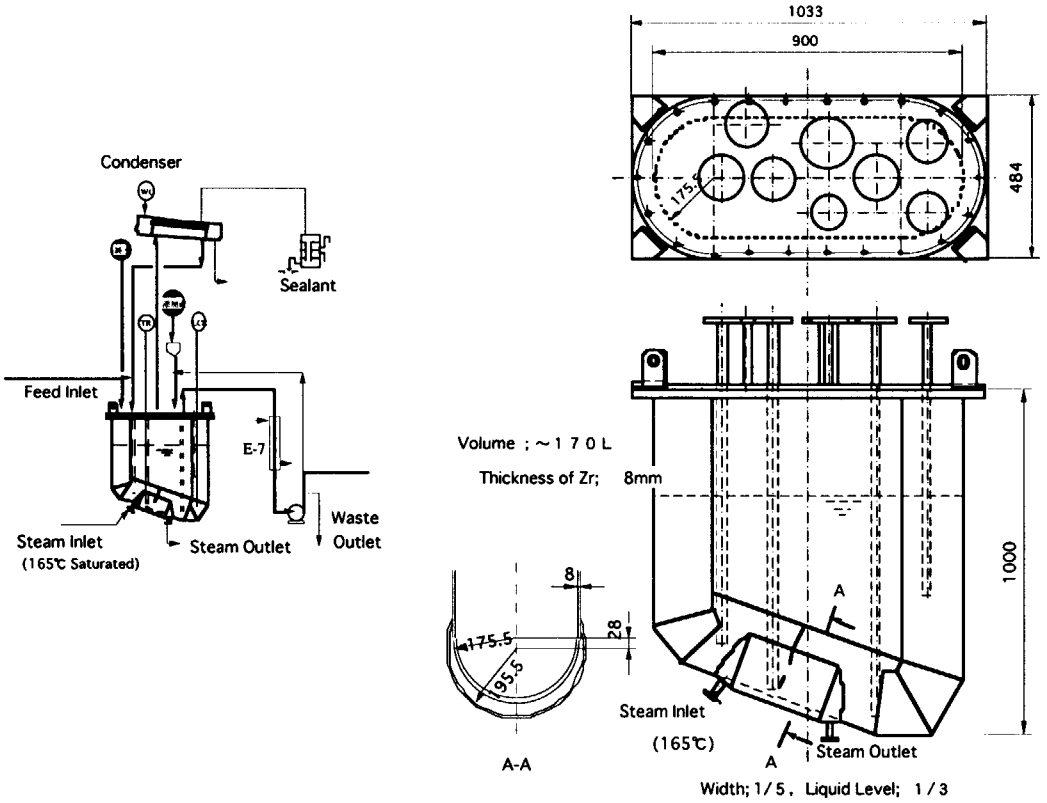

Fig.10.1.2 The mock-up apparatus of a dissolver used in the RRP equipments

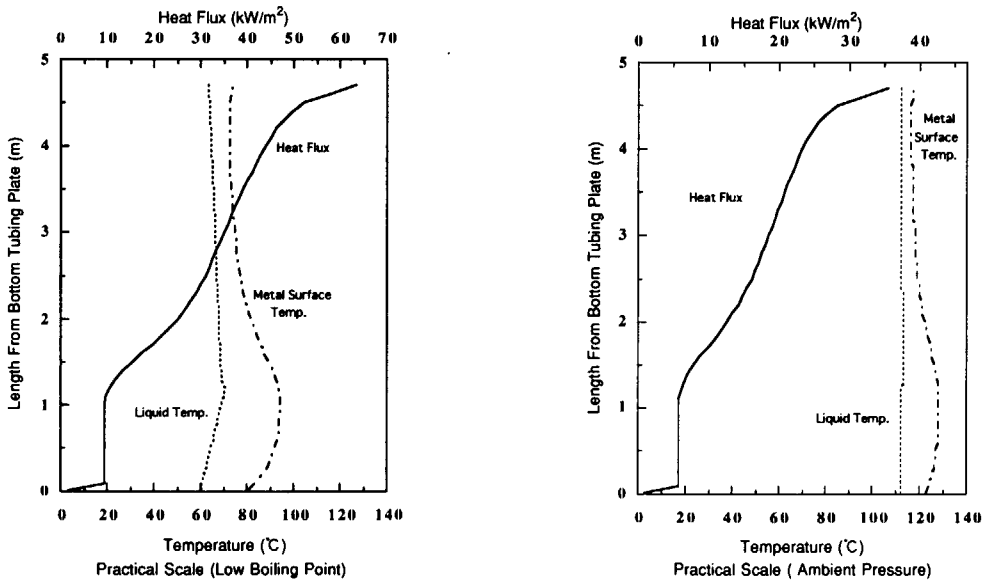

Fig.10.1.3 Change in thermo-fluid dynamics parameters of heat transfer tubes along longitudinal direction.
Left figure; ambient pressure control type. Right figure; low pressure control type

10.2 New Alloy Developments for Advanced Spent Fuel Reprocessing Using Nitric Acid Solutions

K. Kiuchi, H. Ide*, K. Hiratsuka* and A. Toyama**
(*E-mail:* kkiuchi@popsvr.tokai.jaeri.go.jp)

The developments of three types of corrosion resistant alloys have been carried out for application to the advanced purex reprocessing equipments used in several oxidizing grade of nitric acid environments[1]. The highest corrosion resistance is required to the heat transfer tubes exposed to the high oxidizing potential near 1.8V caused from the thermodynamic decomposition of boiling nitric acid. Type 304ULC steel treated by EB-SAR process with immunity to grain boundary attacks, and the high Cr-W-Si nickel base alloy so-called the RW designed for inhibiting the trans-passive corrosion by forming the stable oxide film have been developed as shown in Table 1 and 2. The corrosion resistance of above alloys were tested in Cr^{6+} added nitric acid solutions under the heat flux control for evaluating the applicability to heat transfer tubes in evaporators operated at boiling points lower than 343K as shown in Fig.10.2.1. The corrosion rate of the EB-SAR treated type 304ULC steel and RW alloy decreased up to 30% and less than 10% respectively, comparing with it of type 304ULC commercial heats. From viewpoint of the practical applicability for saving, the cladding of these alloys to commercial type 304L steels used at the steam heater side was examined. The diffusion bonding process was selected as the most promising practical technique from screening tests of representative techniques for making composite materials like HIP and multi layer melting so on. An appropriate region was examined by hot rolling as function of heating temperature and the reduction ratio as shown in Fig.10.2.2.

On the other hand, metallic grade 702 zirconium has been used in commercial reprocessing equipments operated in ambient pressure like a dissolver and a evaporator for concentrating Pu . However, this metal has the high susceptibility to SCC. In our study, Nb base binary alloy was selected by considering the corrosion mechanism in nitric acid solutions as shown in Fig.10.2.3. The corrosion rate of refractory metals in boiling nitric acid depends on the solubility of oxide film itself. And it depends on the periodic table of elements. Under heavy oxidizing nitric acid environments, the chemical stability of M_2O_5 formed on Ta and Nb is superior than it of MO_2 formed on Zr and Ti. Fig.10.2.4 shows the difference of the corrosion resistance among refractory metals in boiling nitric acid solutions added fluorine. Comparing with the corrosion resistance of Nb, it of Zr and Ti in nitric acid solutions decreased with increasing the concentration of fluorine which inhibits the formation of protective oxide films. The optimization of niobium base alloy was made for improving the mechanical strength and corrosion resistance as shown in Fig.10.2.5.

---

* Japan Energy Co.
** NKK Co.

Reference

1) K.Kiuchi, H.Ide, K.Hiratsuka and A.Toyama : RECOD'98,Vol.3(1998)867

Table 10.2.1 The outline of the development of corrosion resistant materials against oxidizing nitric acid solutions.

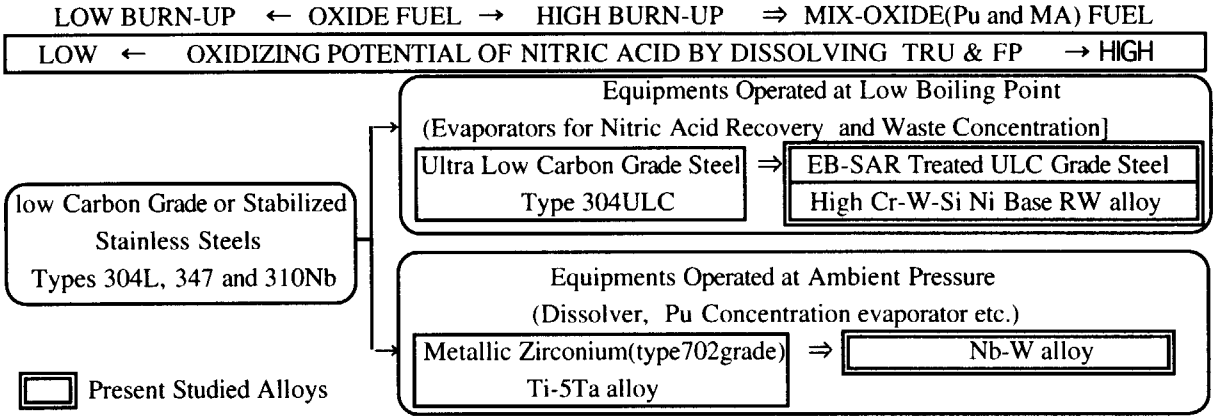

Table 10.2.2 The Chemical composition of major testing materials used in the present study

Commercial Grade Type 304ULC	0.008/C, 0.44/Si, 1.37/Mn, 0.021/P, 0.004/S, 10.3/Ni 18.7/Cr, 0.001/Al, 0.019/TN, 0.0002/B , Fe/Bal.
EB-SAR Treated Type 304ULC	<0.004/C, 0.2/Si, <0.1/Mn, <0.01/P, <0.002/S, 12.8/Ni 20.6/Cr, 0.02/Mo, <0.004/TN, <0.001/B, 0.2/Ti, Fe/Bal.
High Cr - W - Si Ni Base RW Alloy	<0.005/C, 2.72/Si, <0.1/Mn, <0.01/P, 0.002/S, 29.2/Cr 10.1/W, <0.001/TN, <0.001/B, Ni/Bal.

Unit; wt%

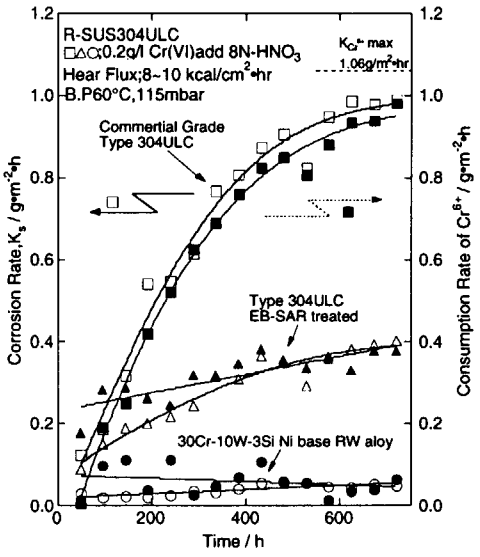

Fig.10.2.1 The corrosion rate of developed alloys under heat flux control in Cr6+ added nitric solutions compared with it of commercial heats of type 304ULC steels

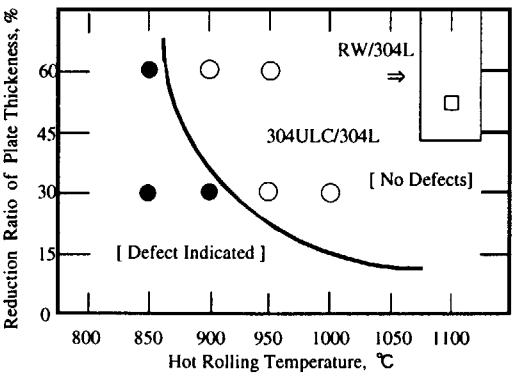

Fig.10.2.2 An appropriate diffusion bonding region without defects is selected by the metallographical observation after bending tests of cladding specimens made by hot rolling between commercial heats of 304L and new developed alloys, EB-SAR treated 304ULC and RW alloy

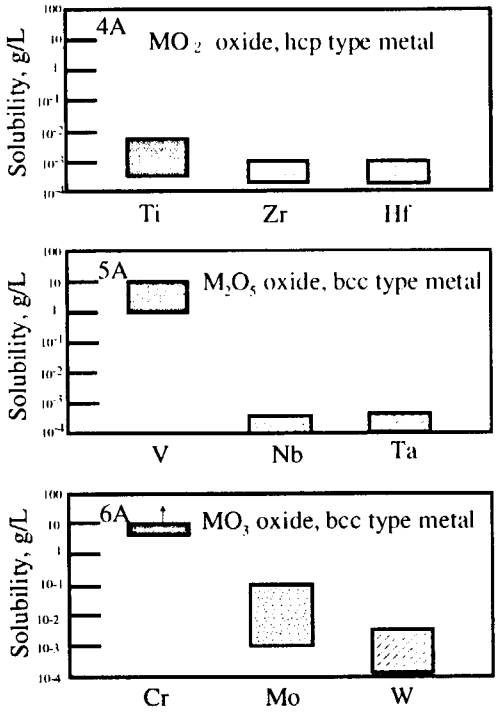

Fig.10.2.3 The comparison of the solubility in nitric acid solution up to 65% among high value oxide of major refractory metals

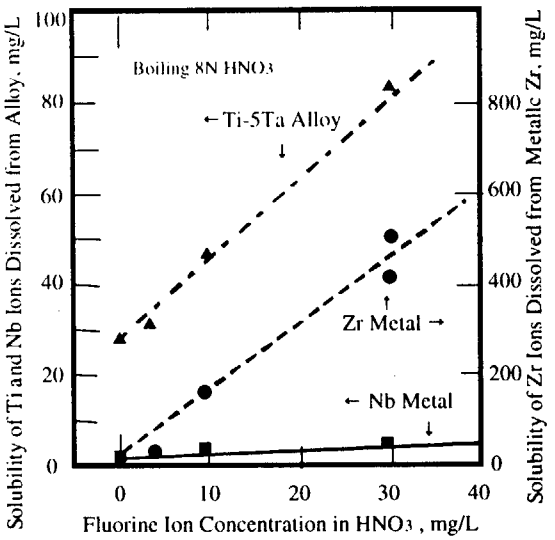

Fig.10.2.4 The effect of fluoride concentration in boiling nitric acid solutions on the corrosion rate of Zr, Nb and Ti-5Ta alloy

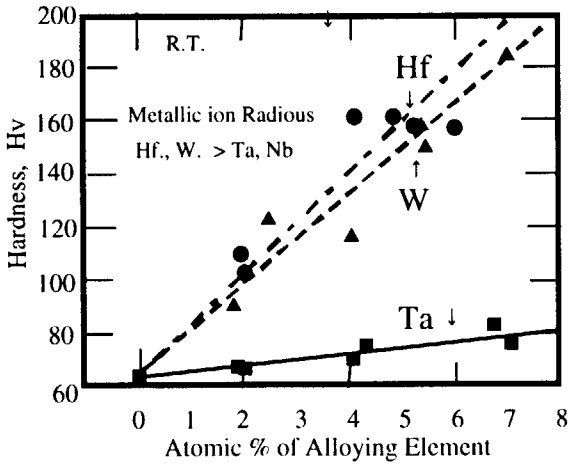

Hardness data measured as the concentration of alloying elements, Hf, W and Ta

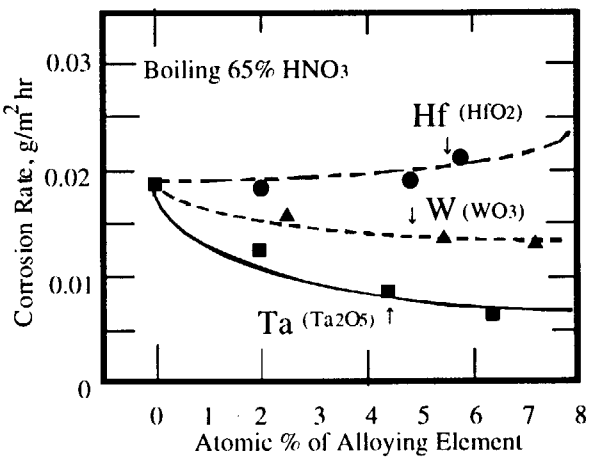

The corrosion rate examined by immersion tests in boiling 65% nitric acid

Fig.10.2.5 The effect of alloying elements of Hf, Ta and W on the micro-hardness and corrosion rate in boiling nitric acid

10.3 Evaluation of Susceptibility to SCC of Zirconium Weldments in Boiling Nitric Acid Solution by SSRT Method.

C.KATO and K.KIUCHI

(E-mail: multi@popsvr.tokai.jaeri.go.jp)

It is required that equipment materials used in the purex type nuclear fuel reprocessing plants have the excellent corrosion resistance in boiling nitric acid solutions with high corrosion potentials caused by oxidizing ions dissolved from spent nuclear fuels.[1] Zirconium has the excellent corrosion resistance in nitric acid solutions. So, zirconium has considered to be a most promising material for very corrosive condition in the nuclear fuel reprocessing plants recently. However, the susceptibility to stress corrosion cracking (SCC) of zirconium in nitric acid environments has been reported.[2] On the other hand, a problem of welding coupling is left furthermore when such crystal structure was provided temporarily. In particular, it was reported that weldments showed the high susceptibility to SCC by U-bend test in 65% boiling nitric acid.[3] From this view point, the susceptibility to SCC of zirconium TIG weldment in nitric acid solution was investigated.

Fig. 10.3.1 shows the decrease rate of life time in each weldment portions. The decrease rate of life time was calculated by the ratio of the time to failure in nitric acid environment to that in oil environment. As this result, the susceptibility to SCC is clearly observed in C-type specimens. On the other hand, it is low in L-type specimens. It is suggested that it occurred by crystal anisotropy in the hot rolling direction. In C-type specimen, the decrease rate of life time became lower at the boundary of HAZ1 and base material (HAZ2) than that of HAZ1. This has shown that the susceptibility to SCC become higher in HAZ2. However, the decrease rate of life time in L-type specimen wasn't clearly found in HAZ2. It is suppressed to be the effect of crystal anisotropy. Fig. 10.3.2 shows optical photographs of fracture surfaces after SSRT in notch type specimens. The SCC fractography shows the quasi-cleavage type fracture in circumference position of the fractured surface. In particular, the coarsened grain with acicular microstructure was observed in welding metal and HAZ1. The quasi-cleavage type fracture area is proportional to the decrease rate of life time.

Fig. 10.3.3 shows a relationship between the decrease rate of life time due to SCC and

relative ratio of the preferential orientation of cleavage plane (0002) in zirconium. It is understood that the decrease rate of life time has increased in proportional to the area of cleavage plane. It is suggested that the susceptibility to SCC caused by the preferential orientation of cleavage plane.

CONCLUSION

(1) The susceptibility to SCC of HAZ2 in boiling nitric acid solution is higher than that of HAZ1 and base metal.

(2) There is a relationship between the existance ratio of cleavage type fracture area by SCC and the decrease rate of life time.

References

1) K.Kiuchi; J.Atomic Energy Soc., **31**(1989), 229.

2) J.A.Beavers,J.C.Griess and W.K.Boyd, Corrosion, **36**(1981), 292.

3) P.Fauvet and G.Pinard Legry, EUROCORR' 92, Espoo, Finland.

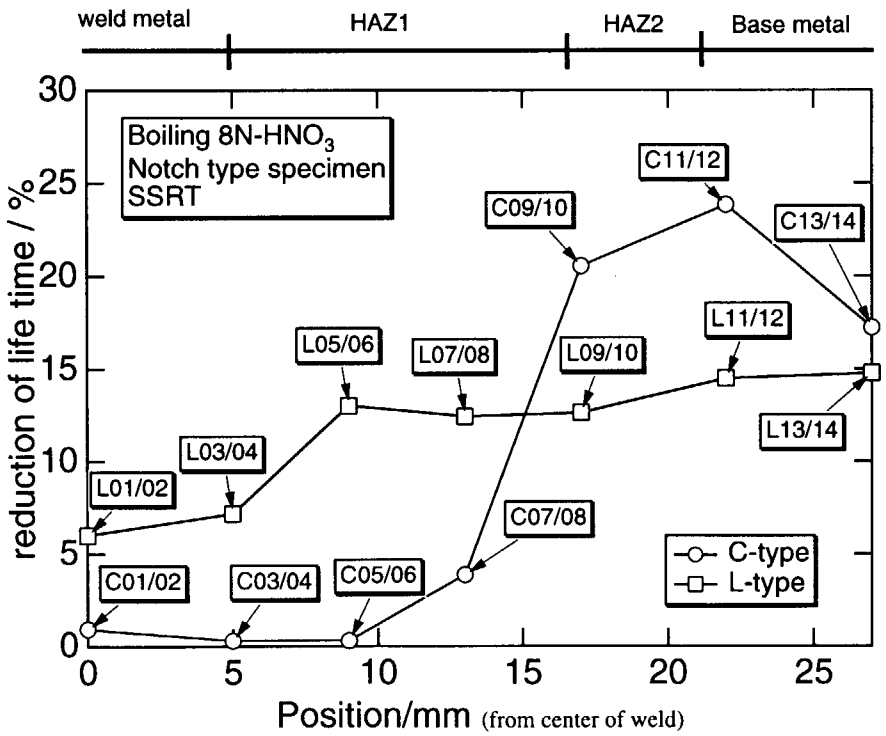

Fig. 10.3.1 Decrease rate of life time in zirconium weld each part by SSRT.

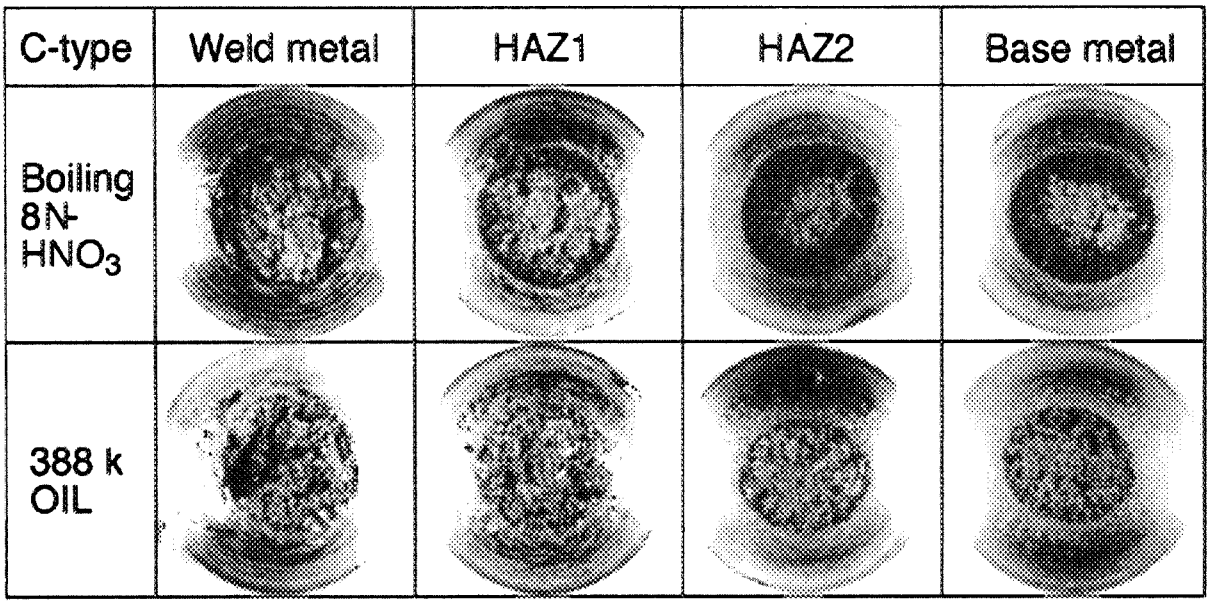

Fig. 10.3.2 Optical photographs of fracture surfaces after SSRT in notch type specimen.

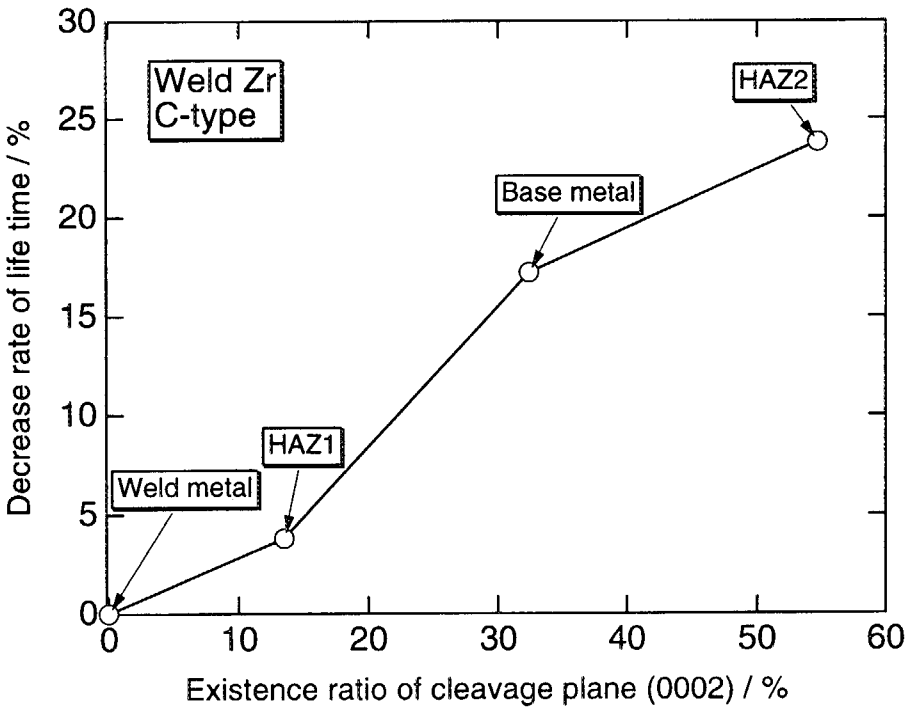

Fig. 10.3.3 Relationship between decrease rate of life time to SCC and existence ratio of cleavage plane (0002) in zirconium.

10.4 Fatigue Crack Propagation Behavior of Zirconium in Boiling Nitric Acid Solution

T. Motooka and K.Kiuchi
(E-mail : motooka@popsvr.tokai.jaeri.go.jp)

Long term durability is desired in the nuclear fuel reprocessing equipments. Zirconium (Zr) has been adopted as the equipment material. In order to evaluate the durability of the nuclear fuel reprocessing equipment made of Zr, we have been investigated the crack propagation behavior of Zr in boiling nitric acid solution by fatigue tests[1].

In this work, the fatigue crack propagation behavior of Zr in heat affected zone (HAZ), weld metal (DEPO), and base metal (BASE) was investigated. The fatigue crack of tapered-double-cantilever-beam specimen was propagated in air at room temperature and boiling 3 normal nitric acid solution. The crack propagation behavior of Zr was evaluated by the measurement of crack propagation rate and the fracture surface analysis.

Test specimens were machined out longitudinally (L-type) and transversely (T-type) to the rolling direction of plates. The crack of specimens was propagated with an electro-hydraulic servo-type fatigue testing machine under 0.1 Hz with a stress ratio (R), 0.1. Measurements of crack propagation rate were conducted by optical microscope observation.

Fig.10.4.1 shows the fatigue crack growth rate (da/dN) as a function of stress intensity factor range (ΔK) in air at room temperature and boiling 3 normal nitric acid solution. The da/dNs of BASE, HAZ and DEPO in boiling nitric acid solution are higher than those in air at room temperature. The crack growth of Zr is accelerated in boiling nitric acid environment. Fig.10.4.2 shows the comparison of crack propagation rates in boiling 3 normal nitric acid solution. There is no significant difference among da/dNs of BASE, HAZ and DEPO. Crack sensitivity in boiling nitric acid environment of welded joint (HAZ and DEPO) and BASE was almost the same.

Fig.10.4.3 shows fracture surfaces of Zr observed with scanning electron microscope. On the fracture surface of BASE tested in air, striation type fracture surface was observed. Ductile fracture surface was observed on the fracture surface of HAZ and DEPO. On the other hand, river pattern was observed on the surface of BASE tested in boiling nitric acid. Brittle striation and river pattern were observed on the fracture surface of HAZ and DEPO. It is known that river pattern was characteristic to cracking caused by stress corrosion cracking (SCC). It is guessed that an acceleration factor of the fatigue crack propagation was SCC.

Reference

1) T.Motooka and K.Kiuchi : JAERI-Research 99-031 (1999), in Japanese.

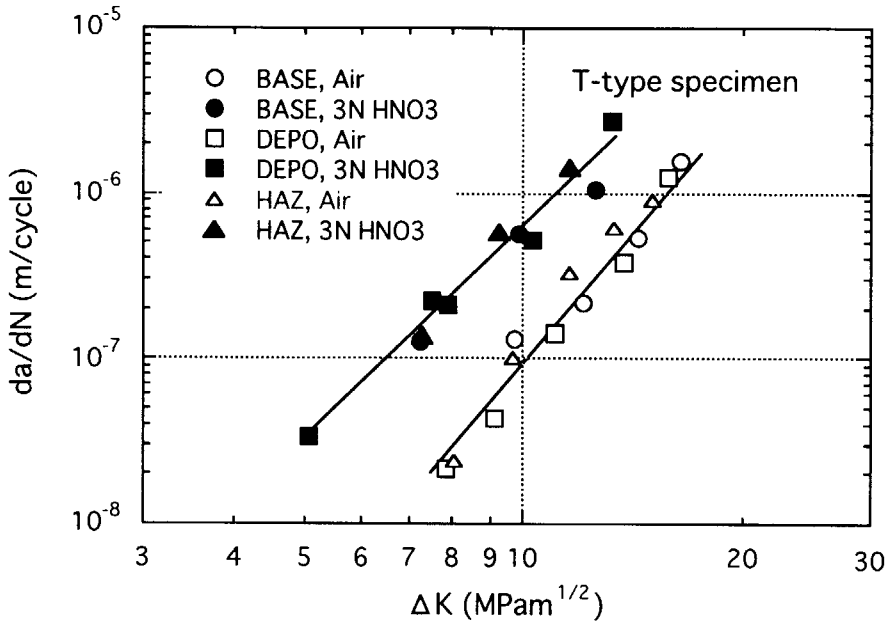

Fig.10.4.1 Crack propagation rates of Zr in air at room temperature and boiling 3 normal nitric acid solution.

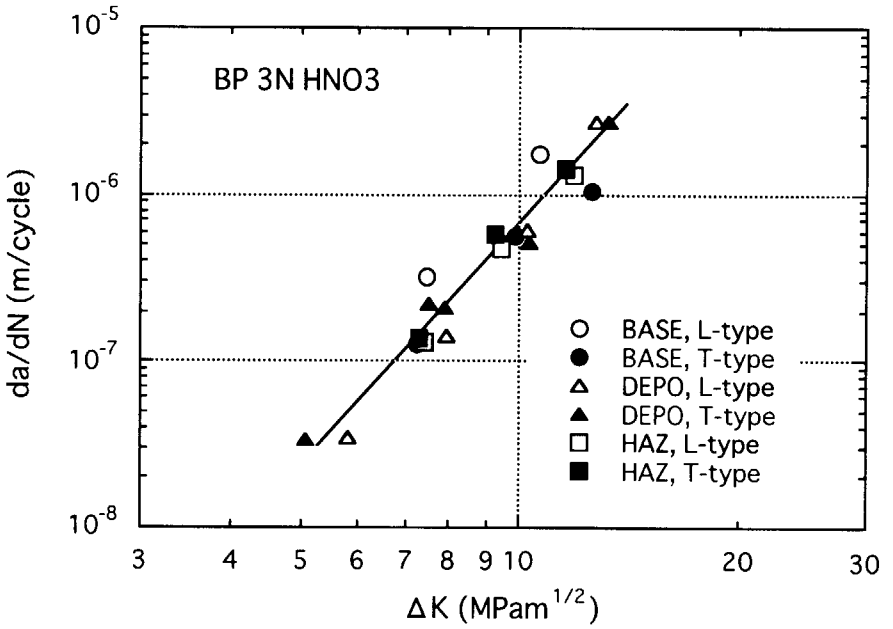

Fig.10.4.2 Comparison of crack propagation rates in boiling 3 normal nitric acid solution.

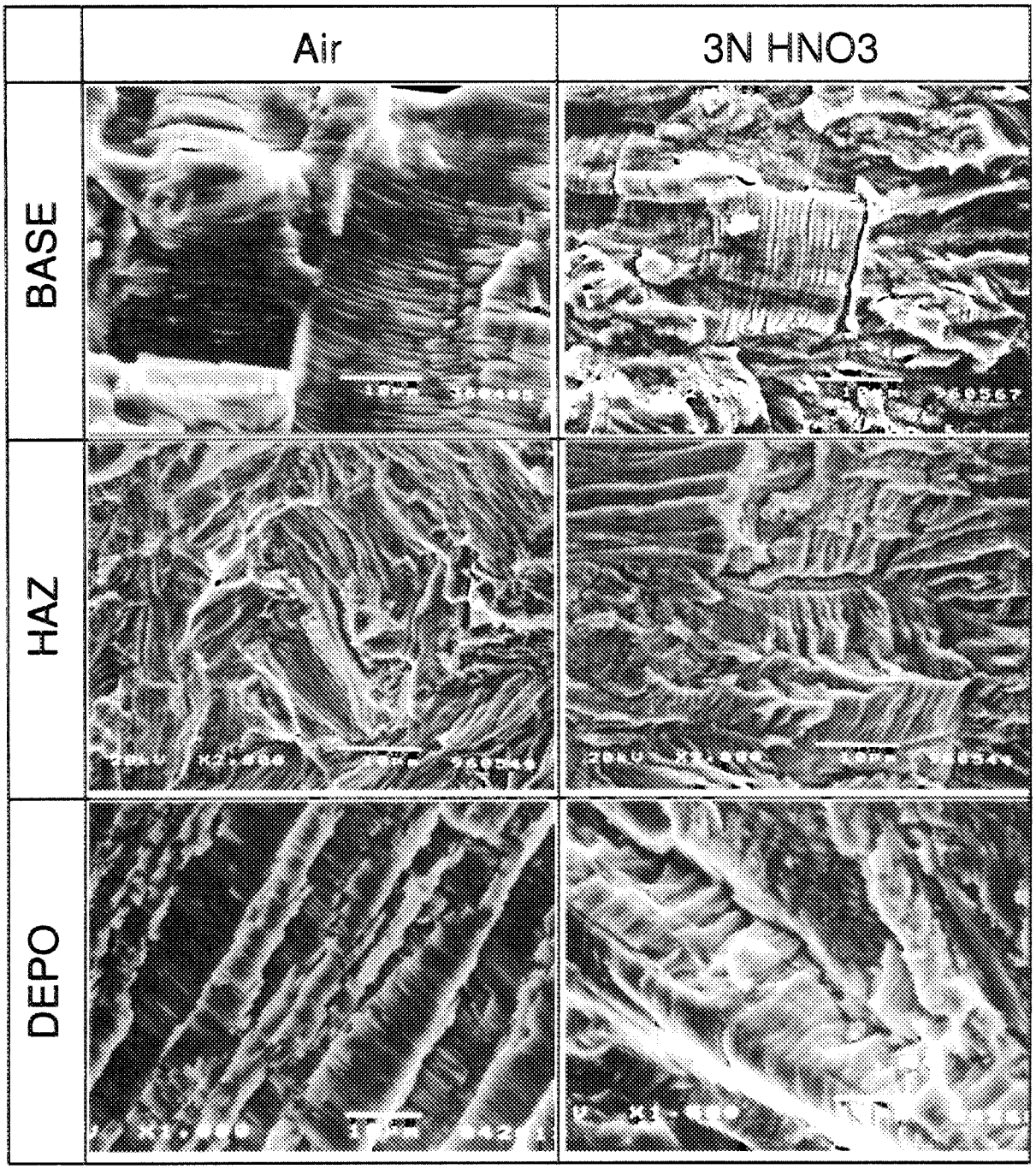

Fig.10.4.3 Fracture surfaces of zirconium tested in air at room temperature and boiling 3 normal nitric acid solution.

10.5 Mechanism of Low Energy Plasma Induced Permeation on Hydrogen Penetration Process.in Metallic Materials

M. Takizawa*, K. Kiuchi, H.Ishizuka** , M.Okamoto** and Y.Fujii;**
(*E-mail:* kkiuchi@popsvr.tokai.jaeri.go.jp)

The low energy plasma driven permeation (PDP) is considered to be played an important role on not only the plasma wall interaction, but also the gas - metal surface interactions under irradiation and thermal decomposition as shown in Fig.10.5.1. The permeation rate of hydrogen in metals at low temperature is enhanced by facing the low energy plasma, without the implantation by high energy ions. On the other hand, the degradation of Zircaloy cladding in water reactors is controlled by oxidation and hydrogen permeation. It would be accelerated by the exited ions in thin steam layer near metal surfaces under irradiation. Moreover, reprocessing materials like stainless steels and titanium alloys are suffering from severe corrosion by strong oxidizers of NOx decomposed from boiling nitric acid at heat transfer surfaces. These surface reactions by the exited gaseous species are considered to be controlled by PDP mechanism[1,2].

This study focuses on solving the fundamental mechanism of PDP. This experiment was employed by the low energy plasma testing devices for hydrogen permeation of various kinds of metal membranes. The acceleration mechanism by PDP on hydrogen permeation was examined by comparing PDP data with GDP data (gaseous hydrogen driven permeation). Arrhenius dependencies of deuterium permeation rate in Ni membrane were measured as shown in Fig.10.5.2. The permeation rate by PDP is nearly two order higher than it of GDP. It was controlled with the incident flux at temperature higher than 200℃ and the diffusion rate of hydrogen in metal at lower temperature respectively. Moreover, hydrogen permeation mechanism of PDP were analyzed with respect to the bias effect by adding minus and plus voltage on membrane surfaces. Although it is expected that the minus bias is effective to permeate hydrogen species with plus charge, the permeation rate decreased with adding minus bias. On the other hand, the PDP rate was enhanced with adding plus bias effect. This effect is proved by measuring D α spectrum in a sheath layer at a few mm far from the metal surface for evaluating the intensity of exited hydrogen atoms. The correlation ship was observed among the current density, electron flux captured and intensity of D α spectrum. The PDP rate of deuterium measured by adding 200mA plus bias current were measured in thin membranes made of Pd, Ti and Fe. As shown in Fig.10.5.3, the permeation rate is independent on testing temperature., because it is controlled with the formation of species exited by incident electrons and the recombination rate of it on plasma surfaces. The acceleration factor on PDP among above metals depended on the GDP rate and membrane thickness(Fig.10.5.4, 10.5.5).

---

* Mitsubishi Research Institute Inc. ** Tokyo Institute of Technology

The difference of rate determining step on hydrogen permeation rate by PDP is summarized in Fig.10.5.6 as several models expected from various metals and the thickness of specimens under adding plus charge.

References

1) M.Takizawa K.Kiuchi ,H.Ishizuka M.Okamoto and Y.Fujii; Fusion Eng. Des.39-40(1998)
2) M.Takizawa K.Kiuchi et.al.; J.Nuclear Materials 248.(1997)15, 258-263(1998)1066

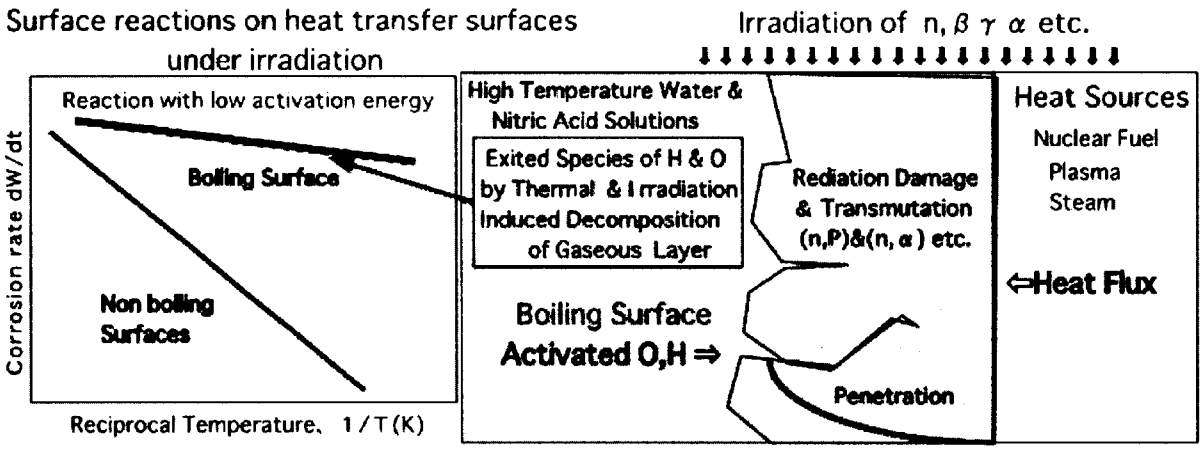

Fig.10.5.1 The PDP effects expected in surface reactions accelerated by the exited gaseous species

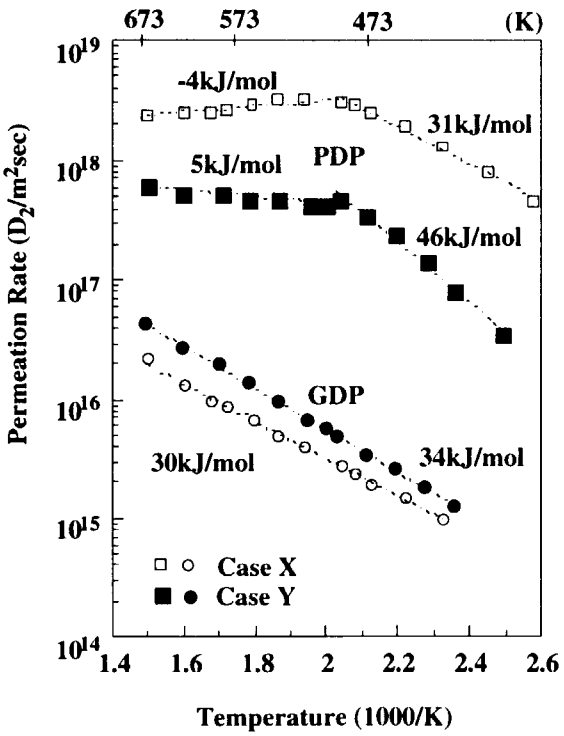

Fig.10.5.2 The permeation rate of deuterium in Ni membrane by PDP and GDP as function of testing temperature

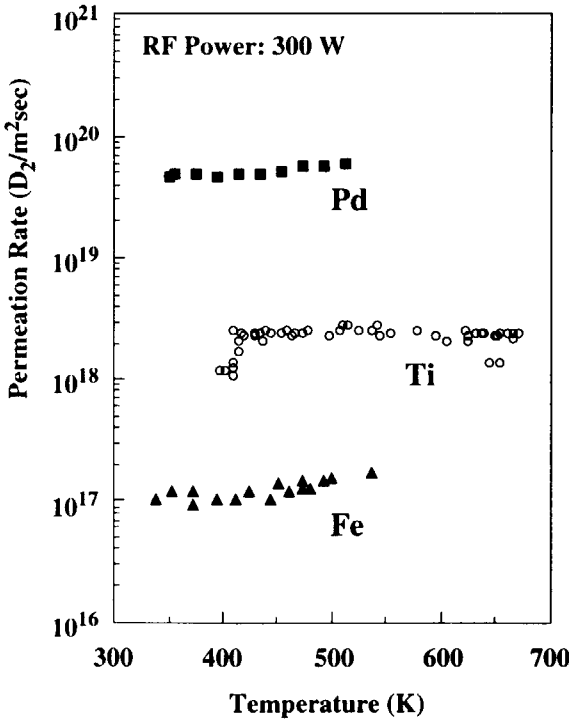

Fig.10.5.3 The permeation rate of deuterium in Cu and Ti membrane by PDP as function of plus bias current at 500K

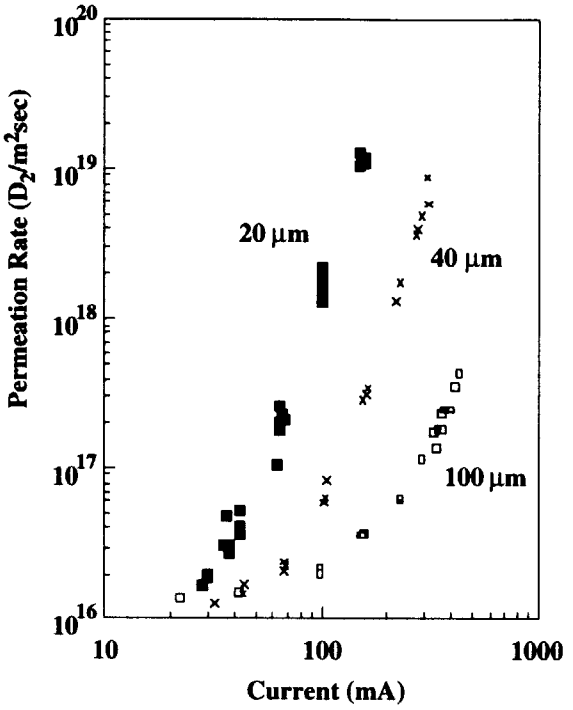

Fig.10.5.4 The permeation rate of deuterium in Ni membrane by PDP as function of plus bias current at 500K

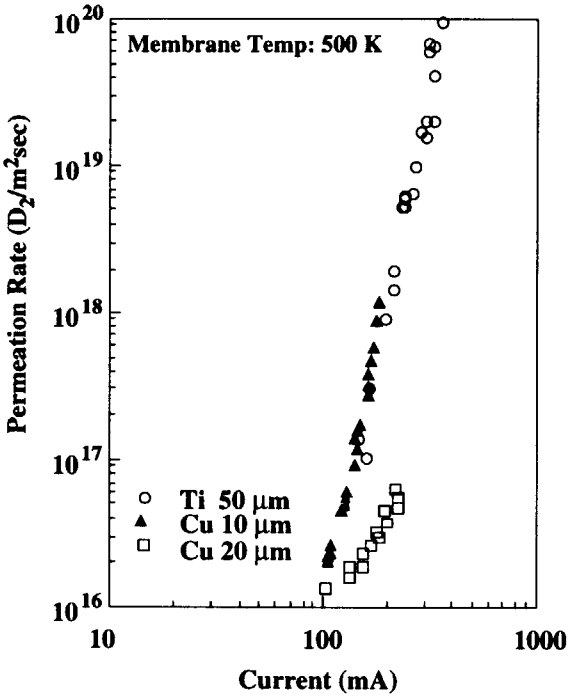

Fig.10.5.5 The permeation rate of deuterium in Cu and Ti membrane by PDP as function of plus bias current at 500K

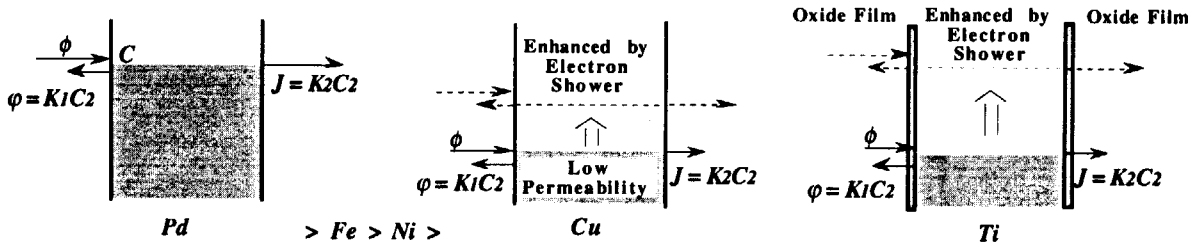

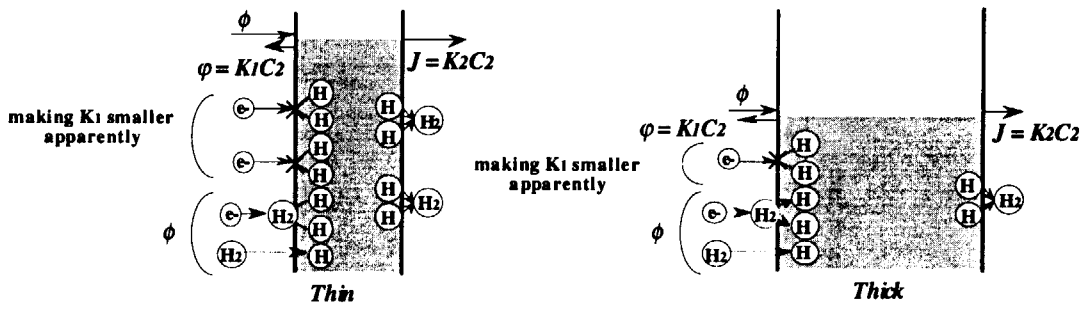

Fig.10.5.6 The schematic model of hydrogen permeation for PDP enhanced by electron shower that is analyzed by considering the rate determining step on surface reactions of various metals like Pd, Fe, Ni,Cu and Ti

10.6 Fundamental Research on Critical Issues Required on Cladding Materials Aiming at Burn-up Extension

K.Kiuchi, M.Takizawa*, I.Ioka, M.Suga, T.Yoshida and S.Hamada
(*E-mail:* kkiuchi@popsvr.tokai.jaeri.go.jp)

The burn-up extension for water reactor fuels of PWR and BWR is required with respect to both economical demands and spent fuel managements. This research is aiming at the development of new cladding materials for the advanced MOX fuels with burn-up twice higher than it of Zircaloys used in the present water reactors. The present study was planned to elucidate the fundamental properties required to cladding materials for high burn-up and to decide the primary testing matrix for selecting candidate materials[1].

The former was investigated with analyzing the practical experience data obtained from the modification of Zircaloys used in commercial plants. Technological problems of Zircaloys like nodular corrosion were overcome by adjusting the chemical composition and by modifying the metallographic structure with the fine dispersed intermetalic compounds. However, uniform corrosion at high burn-up more than 60GWd/TU and shadow corrosion are still remained. Major items and important issues are summarized in Fig.10.6.1. The corrosion rate of Zircaloy cladding in high temperature water showed the remarkable difference among testing conditions namely, cold loop tests, inpile loop tests and fuel assembly. It would be controlled by the irradiation effect at heat transfer surfaces as shown in Fig.10.6.2 and 10.6.3. Two types of acceleration effects on the water side corrosion were speculated. At thin oxide film range, the penetration of oxygen and hydrogen species exited by the low energy plasma driven permeation effect (PDP is described in this report) is considered to be playing an important role. At thick oxide film range, the oxidation rate depends on the metal surface temperature by decreasing the thermal diffusion coefficient. As seen in Fig.10.6.3, the oxide film growth rate[2] obtained in Zircaloy-4 cladding of PWR shows a linear Arrhenius relationship to the metal surface temperature calculated by thermo-fluid dynamics. The water side corrosion on high burn-up of PWR fuel cladding with high operation temperature would be more severe than it of BWR fuel cladding.

The fundamental properties were investigated with computer simulation methods for two types of reactor core with MOX fuels, namely , ABWR and HCPWR as shown in Table 10.6.1. The burn-up behavior of MOX fuels has superior than it of UO_2 fuels, because of the low displacement rate due to uniform burn-up rate. Comparing with 5% allowable enrichment rate in UO_2 fuels, 20% of MOX is also an advantage factor on high burn-up for alternative materials with the neutron absorption cross section lower than it of zirconium alloys. Even if ABWR, the practical limitation with respect to the neutron adsorptions would be not a predominant factor. The most important factor on selection of higher burn-up fuel cladding is

---

* Mitsubishi Research Institute Inc.

considered to be the water corrosion resistance and irradiation properties like ductility. Major structural materials were preexamined with respect to alternative materials to Zircaloys. Austenitic stainless steels is considered to be the most promising material with the intermediate neutron absorption rate, high corrosion resistance, high mechanical strength and practical experiences. In our study, the resistance to IGSCC of this steel was markedly improved by enhancing austenite stability and by minimizing the grain boundary segregation of impurities. It is achieved by adjusting the chemical composition, by making purified ingots through electron beam melting and by modifying the metallographic structure through the thermo-mechanical treatment so-called SAR process as already reported[3].

References

1) K.Kiuchi, M.Takizawa, I.Ioka, M.Suga, F.Nagase, M.Futakawa and S.Hamada ; JAERI-Research Report (in preparation)
2) G.R.Kilp et.al. ; Proc. ANS-ENS International Topical Meeting on LWR FuelPerformance, Avington, France Vol1(1991)284
3) K.Kiuchi et.al.; Journal of Nuclear Materials 212-215(1994)551

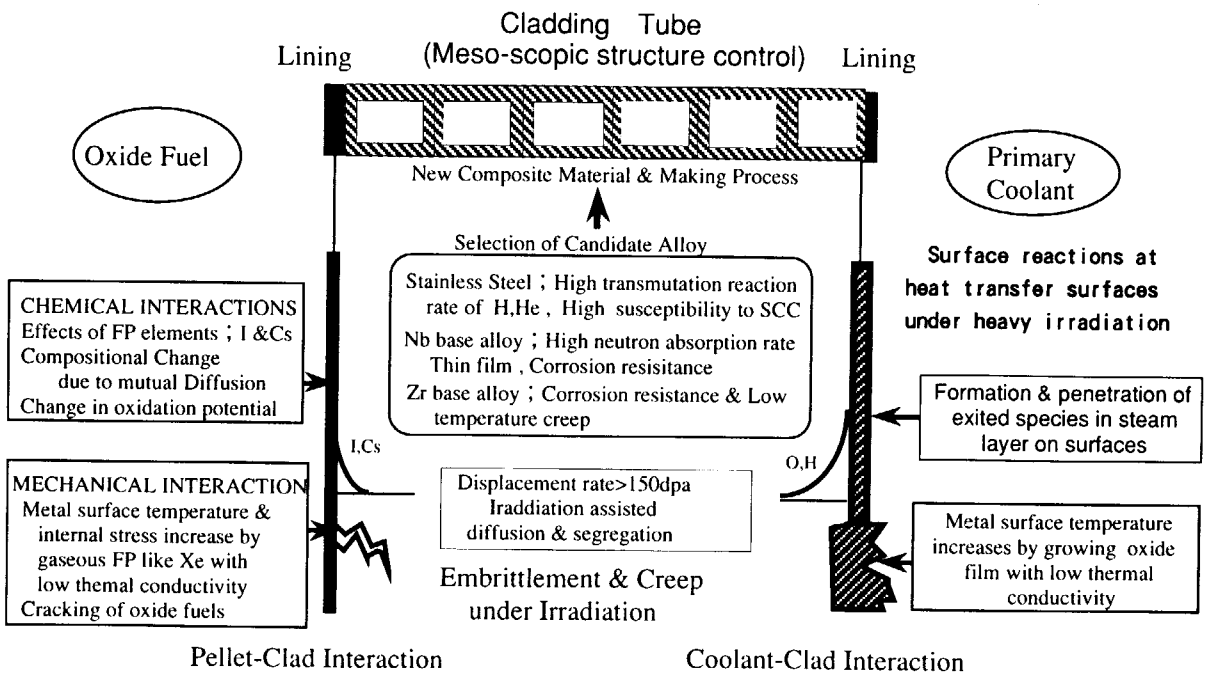

Fig.10.6.1 Major items required for developing candidate materials of cladding tubes aiming at ultra high burn-up

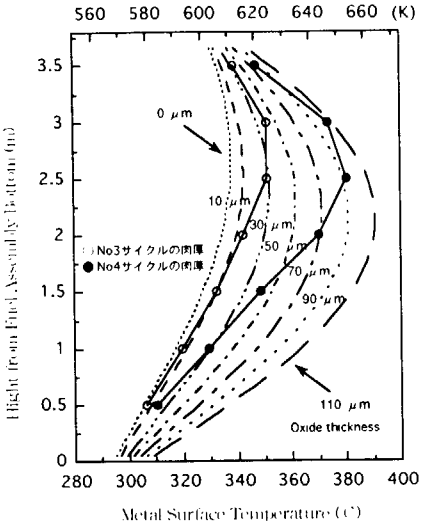

Fig.10.6.2 Change in the metal surface temperature as function of the oxide thickness at each position of PWR Zircaloy-4 cladding tubes

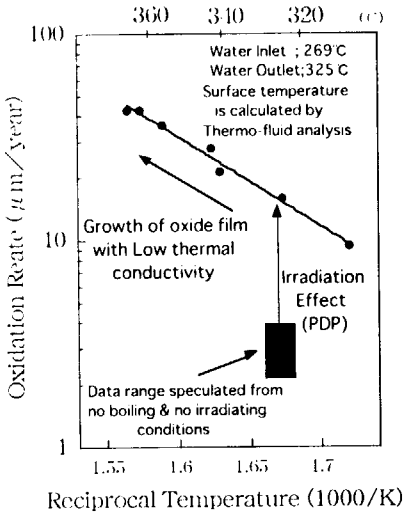

Fig.10.6.3 Arrhenius dependency of the oxidation rate of Zircaloy-4 cladding tubes plotted to the metal surface temperature

Table 10.6.1 Irradiation effects and limitations concerning neutron absorption evaluated by pin-cell model for cladding tube assembly of HB-BWR and HC-PWR

Materials	Irradiation Effect 100GWD/TU, Maximum enrichment of PuO2: 20% Void ratio : 0.40.70 %			Neutron absorption
	Displacement Rate dpa HB-ABWR (HC-PWR)	Trans-mutation He, appm HB-ABWR (HC-PWR)	Trans-mutation H, appm HB-ABWR (HC-PWR)	Relative thickness of cladding, mm HB-ABWR
Zircaloy-2	52.7(MOX) 81.6(UO2)	1.3(MOX) 1.5(UO2)	11(MOX 13(UO2)	0.7
Austenitic stainless steel (15-25Cr, 14-35Ni-2.5Mo)	48-50 (107-112)	59-128 (105-228)	593-1162 (1045-2022)	0.2
Niobium Alloy (0-10% Mo-Nb)	52-54 (120-123)	1.2-1.4 (2.0-2.3)	9-12 (16-19)	<0.1

This evaluation was done by using several calculation codes as follows.

Neutron spectra (LANL,MCNP) , Nuclear reaction (ANL,SPECTER),Thermo-fluid analysis(RELAP5/MOD2)

Irradiation effect; MOX(Uniform burn up rate) < UO2 (Initial burn up rate ; high)

Limitation to neutron absorption; MOX (Pu Enrichment 20%) < UO2(235U Enrichment 5%)

10.7 Characteristics of High Wear Resistant Ni-Base Materials Strengthened by Precipitation Hardening of Wolfram Silicide

K.Kiuchi, H.Ide* and T.Ishiyama
(*E-mail:* kkiuchi@popsvr.tokai,.jaeri.go.jp)

The practical application of Co-base Stellite and Ni-base Inconel for reactor core components with high allowable stress levels is considered to be limited by the formation of radioactive cruds and the susceptibility to IASCC respectively. For this view-point, W-silicide strengthened Cr-W-Si Ni-base alloy named as HWI alloy was newly developed as an alternative material. This alloy was designed for attaining the sufficient austenite phase stability at the practical temperature and for strengthening by precipitation hardening of silicides which are major precipitates observed in heavily neutron irradiated structural components[1]. The mechanical strength was improved by solid solution hardening and precipitation hardening. On this study, the chemical composition and alloy making process of HWI alloy were optimized by preexamination testing of experimental heats made by the electron beam melting process. Up to date, there is no workable Si enriched Ni base superalloys. Such alloys are only obtained as ingots like Stellite. However, the workable high Si superalloy was possible to make by minimizing harmful elements through the advanced electron beam melting process of EB-CHR.

Fig.10.7.1 shows the effect of Si on the workability of HWI heats obtained by compression tests at high temperature. The workable range corresponds to the stable austenitic region on 30Cr-10W-xSi diagram as shown in Fig.10.7.2. The strengthening factor of this alloy depends on the chemical composition of W and Si as seen in hardness data of Fig.10.7.3. The thermomechanical treatment is effective to strengthen by precipitation hardening of silicides (Fig.10.7.4). The hardness data of HWI heats as index for evaluating the wear resistance is shown in Fig.10.7.5. comparing with it of commercial alloys. The hardness of this alloy superior than it of Stellite is easy to obtain by means of both the chemical composition control and the thermomechanical treatment, because this alloy has the excellent cold and hot workabilities as described above. The strengthening mechanism by precipitating silicides was examined with the quantitative analyses of precipitates as shown in Table 10.7.1 and Fig.10.7.6. The irradiation resistance and the corrosion resistance superior than these of above commercial alloys were verified by several laboratory tests. As one of these examples, Fig.10.7.7 shows the excellent wear resistance in heavily corrosive nitric acid solutions .

Reference

1) K.Kiuchi, et al. ; Proc. of Inter. Conf. of Water Chemistry'98(1998)

* Japan Energy Co.

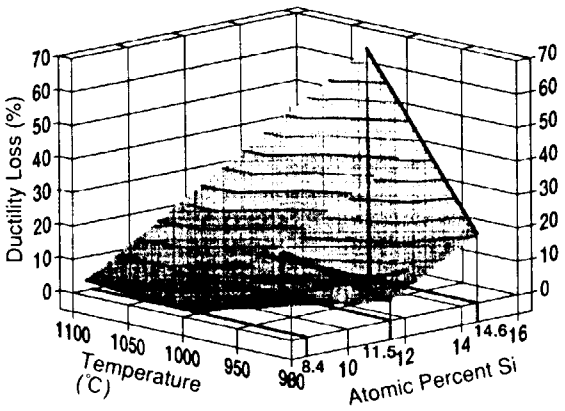

Fig.10.7.1 Effect of Si contents and compression testing temperature on the work-ability of HWI heats

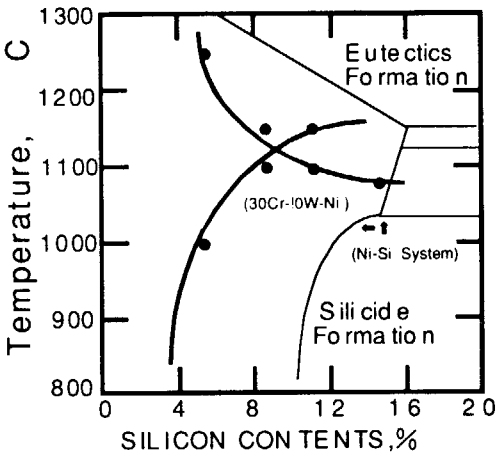

Fig.10.7.2 Effect of Si contents on γ phase stability in the 30Cr-10W-Si Ni-base alloy at high temperatures

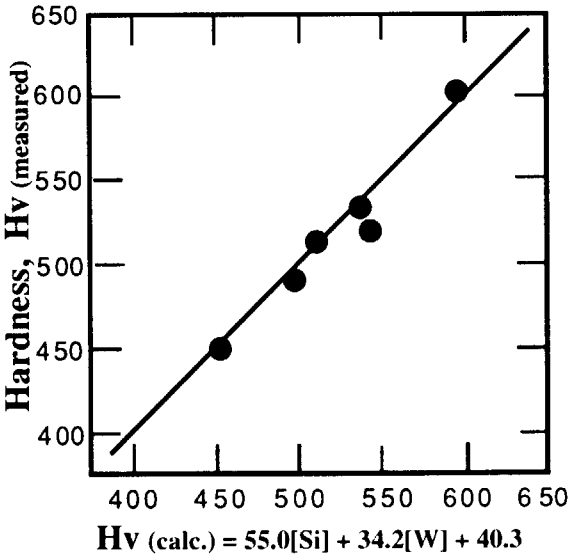

Fig.10.7.3 A relationship between the measured hardness and calculated one of HWI heats aged at 973K for 50hr

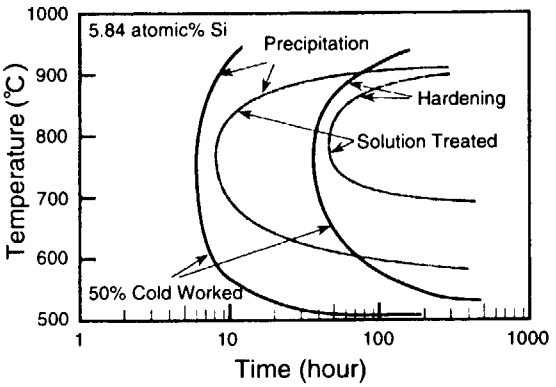

Fig.10.7.4 TTP diagram of experimental HWI heats with low Si contents

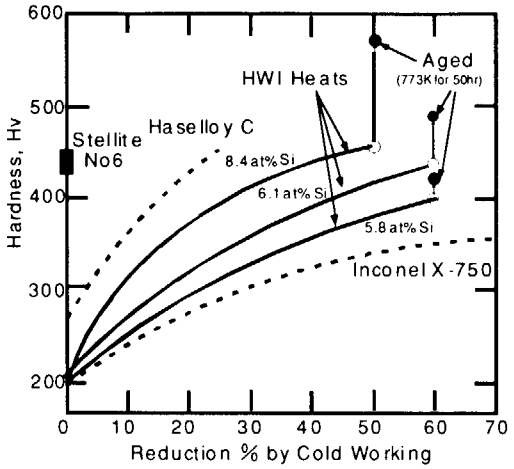

Fig.10.7.5 Comparison between hardness data of commercial wear resistant alloys and those of HWI heats as effects of cold working and strain aging

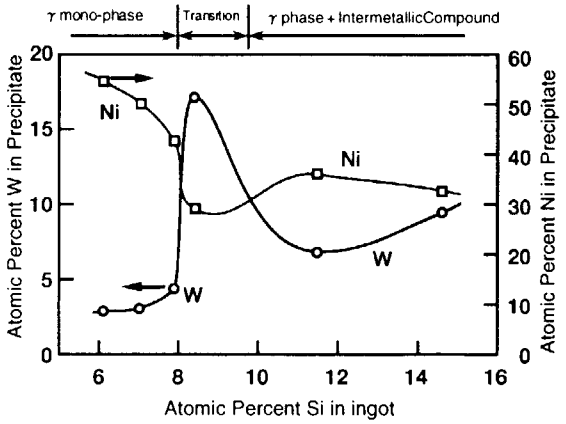

Fig.10.7.6 A relationship of W and Ni contents in precipitates as a function of Si contents of HWI heats aged at 973K for 50hr

Table 10.7.1 The chemical composition of major silicides observed in aged HWI alloy with two regions of Si contents

Experimental Heat		High Si HWI Alloy		Low Si HWI Alloy	
Si Contents		4.1 - 7.4 wt%		2.62 wt%	
Type of Silicide		A	B	β 1	β 2
Structure		M3Si	M4Si	M3Si	G-phase
Atomic % of Element	Ni	30.4	35.4	32.3	43.8
	Cr	27.5	36.6	33.3	30.7
	Si	22.9	18.0	27.3	19.0
	W	19.2	10.0	7.1	6.5
Classification Method		WDX/EPMA		EDX/ STEM	

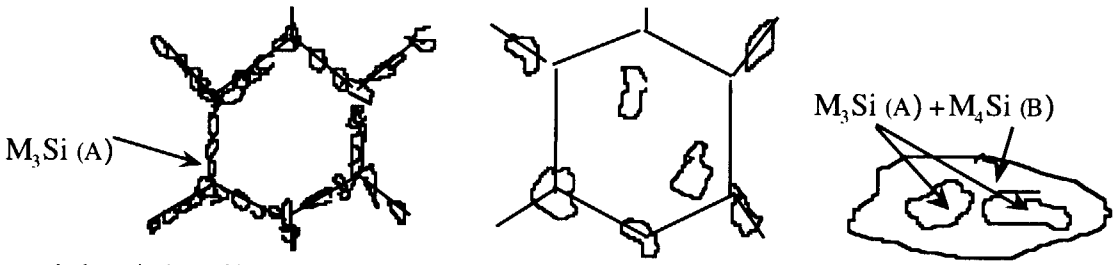

a) Silicides morphology in low Si HWI Heats

b) Silicides morphology in high Si HWI Heats

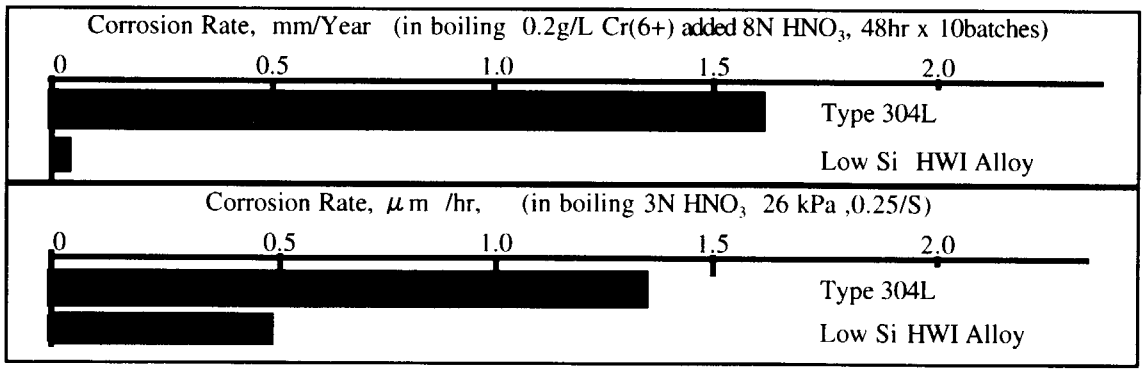

Fig.10.7.7 Examples of corrosion data of HWI heats compared with that of commercial stainless steels

11 Rock-Like Oxide Fuel for Plutonium Burning in LWRs

For the utilization of stockpiled plutonium, we have proposed plutonium rock-like oxide (ROX) fuels and their once-through burning in LWRs followed by direct disposal of spent fuels after cooling. The ROX fuel is a multi-phase mixture of mineral-like (or rock-like) compounds such as stabilized zirconia, corundum, spinel and so on. Plutonium is incorporated in one of these compounds. Direct disposal of spent ROX fuels requires that the spent fuels must have high chemical, physical and geological stabilities to reduce environmental hazards. Effective and almost complete burning of fissile plutonium is also essential from proliferation resistance, environmental safety and economic points of view.

In the materials science area, the ROX fuel concept was improved based on the findings obtained by the first ROX fuel disk irradiation test: the particle dispersed fuel with two phase mixture of YSZ and spinel phases. Some physico-chemical properties of this new ROX fuel were studied and fabrication technique of the particle dispersed fuel was also developed. As for the reactor physics area, inherent small reactivity coefficients of ROX fuel were improved by adding some resonant nuclides or by composing a heterogeneous $1/3ROX+2/3UO_2$ core. Fuel behavior was investigated in NSRR under RIA conditions, the results of which suggested that the limiting maximum fuel enthalpy was higher than that of the conventional UO_2 fuel. Burnup calculation, parametric survey of burnup characteristics and fuel temperature coefficients were also performed extensively by using the SRAC and MVP-BURN codes. Environmental safety analysis showed that the spent ROX fuel was superior to the spent MOX fuel from the viewpoint of public doses after direct disposal.

11.1 Post-Irradiation Examination of Pu-ROX Fuels with Ternary Mixture of Fluorite, Spinel and Corundum Phases

T. Yamashita, N. Nitani, H. Kanazawa, T. Ohmichi*, H. Takano and T. Muromura
E-mail: yamasita@analchem.tokai.jaeri.go.jp

Little is known about the in-pile irradiation behavior of inert matrices[1, 2]. No irradiation data are available for the composite ROX fuel. In order to obtain information on the in-pile irradiation behavior of Pu-ROX fuels with the ternary component system of yttria stabilized zirconia (YSZ) or thoria (ThO_2), spinel and corundum, we irradiated the fuels in the Japan Research Reactor No.3 (JRR-3) and performed post irradiation examinations. Phase equilibria, element distribution over the phases and microstructure changes in the irradiated fuels were studied using X-ray diffraction, metallography, scanning electron microscopy and electron probe microanalysis.

Chemical compositions and characteristics of fresh ROX fuel disks are summarized in Table 11.1.1. Fuel disks were sintered at 1670 K for 5 h in Ar/8%H_2 gas stream. The average size of sintered disks was 3.25 mm in diameter and 1 mm in thickness. Maximum neutron fluence was estimated to be 8.2×10^{24} m^{-2} (E<0.6 eV) and burnup was measured to be 21-28% of the initial plutonium atoms by destructive chemical analysis.

The axial profiles of main FPs in the platinum capsule were determined by measuring radio-activities through a thin slit placed in front of a Ge(Li) detector. Solid FPs such as ^{106}Rh and ^{144}Ce were observed only at the fuel disk region. Most of ^{134}Cs and ^{137}Cs, which is known as a semi-volatile FP, was observed at the fuel disk region and a part of them was also observed at the colder parts of the platinum capsule.

Few irradiated specimens kept their original circular disk shapes: some had large cracks and the others were broken into small pieces. The high linear heating rate of 40 kW/m, which was estimated by burnup calculation, may have caused the fragmentation of the disks. They also showed volume increases apparently and porous surface appearance. Rough measurements showed that the diameter of the disk irradiated at 980 K was about 3.6 mm and that of fresh fuel disks was about 3.25 mm; about 10% increase in diameter.

* Research Organization for Information Science and Technology

Table 11.1.1 Chemical compositions and characteristics of fresh ROX fuels disks

	Zr-type (mol%)	Th-type (mol%)
PuO_2	10	10
YSZ*	15	-
ThO_2	-	15
Al_2O_3	65	65
MgO	10	10
Phase	Lattice parameter/nm	Lattice parameter/nm
Fluorite	a=0.5180	a=0.5537
Corundum	a=0.4750 c=1.280	a=0.4760 c=1.280
Hibonite	a=0.5586 c=2.192	a=0.5588 c=2.191
Spinel	tr.	tr.
Average grain size/μm	8	5
Estimated porosity/%	18.4	17.4

* YSZ: 79.86mol%ZrO_2+19.78mol%$YO_{1.5}$+0.36mol%$GdO_{1.5}$

Phase relations, lattice parameters and Pu distribution in irradiated disks are shown in Table 11.1.2. All irradiated fuels consist of five-phase mixture of the fluorite-type phase, hibonite, corundum, spinel and alloy, which is consistent with the results of simulation experiments[3-6]. A new hibonite-like compound containing Pu, Mg and Al was found to be formed under very low oxygen potentials. Existence of Pu^{3+} and free Al_2O_3 was essential for the formation of this compound the possible formula of which is $PuMgAl_{11}O_{19}$. By irradiation

Table 11.1.2 Phase relations and distribution of plutonium in irradiated fuels.
Lattice parameters (L.P.) are given in nm. Plutonium distributions are given in relative amounts: +++: high; ++: medium; +: low; -: not observed.

	Fluorite		Corundum		Spinel		Hibonite		Alloy	
	L.P.	Pu	L.P.	Pu	L.P.	Pu	L.P.	Pu	L.P.	Pu
Zr-7	a=0.5180	++	a=0.475 c=1.29	-	tr.	-	a=0.5582 c=2.207	+++	ND	-
Zr-6	a=0.5153	+	tr.	-	a=0.807	-	a=0.5581 c=2.202	+++	ND	-
Th-3	a=0.5588	-	a=0.474 c=1.27	-	tr.	-	a=0.5579 c=2.199	+++	ND	-
Th-2	a=0.5600	-	tr.	-	tr.	-	a=0.5575 c=2.198	+++	ND	-

of the fuels almost all plutonium moved from the fluorite phase to the hibonite phase, especially at high irradiation temperature, as shown in Table 11.1.2.

SEM observation showed that in the fuel irradiated at 870 K some agglomerates of corundum were observed and that size and number of pores did not increase appreciably compared with the fresh fuel. On the other hand, large pores and grains of the fluorite phase were observed in the fuel irradiated at 1270 K. Porosity of the fuel disk was deduced to be 45.4% from the graphics treatment of the SEM image. The irradiated fuels showed considerable swelling, more than 30% in volume increase. Most of large swelling of the present fuels may be caused by gas bubble formation. The influence of irradiation damage and phase transformation from corundum to hibonite on the fuel volume increase were estimated to be small (about 5% each). However, repeated damage annealing processes and phase transformation from corundum to hibonite phase may enhance gas bubble movement, which might result in the large pore formation in this fuel.

The existence of excess Al_2O_3 was found to cause unfavorable effects on ROX fuel, such as large swelling, hibonite formation and lower melting point by forming ternary eutectic melts. So far, the best composition of ROX is considered to be a composite of fluorite and spinel phases.

References

1) Berman, R.M., Bleiberg, M.L. and Yeniscavich, W., J. Nucl. Mater. 2 (1960) 129.

2) Yanniscavin, W. and Bleiberg, M.L., WAPD-BT-20 (1960).

3) Akie, H., Muromura, T., Takano, H. and Matsuura, S., Nucl. Technol. 107 (1994) 182-192.

4) Akie, H., Takano, H., Muromura, T. and Nitani, N., Progress Nucl. Energy, 29 (Sup.) (1995) 345-352.

5) Nitani, N., Yamashita, T., Ohmichi, T. and Muromura, T., Proc. 10th Pacific Basin Nucl. Conf., Oct. 20-25, 1996, Kobe, Japan, vol.2, (1996) pp.1114-1121.

6) Nitani, N., Yokoi, H., Yamashita, T., Ohmichi, T., Matsui, T. and Muromura, T., J. Nucl. Mater. 247 (1997) 59-62.

11.2 Burnup Analysis of ROX Disks Irradiated in the JRR-3

Y. Nakano, H. Akie, M. Magara and H. Takano
(E-mail: nakano@jrr3fep2.tokai.jaeri.go.jp)

Burnup analysis of Rock-like Oxide (ROX) fuel[1] disks irradiated in the JRR-3 has been done and the results have been compared with measured values. The SRAC[2] code system and the MVP-BURN[3,4] code were used for the calculations. The cross section libraries for these codes are based on JENDL-3.2.

First step of the calculations, neutron spectrum of the irradiation hole was calculated by the SRAC. Using CITATION included in the SRAC system, two dimensional and 72 energy group diffusion calculation of the JRR-3 was performed and 72 group neutron energy spectrum of the irradiation hole was obtained. The spectrum was used as the fixed boundary source for the burnup calculation with the SRAC and the MVP-BURN codes.

For the burnup calculation with the SRAC, PIJ module was used. Fig. 11.2.1 shows the calculation model of the irradiation capsule. A fixed source problem was solved in 72 energy group. The neutron spectrum already obtained was used as the outer boundary neutron source into the capsule. Burnup calculations using the MVP-BURN have been performed with a 3-dimensional model that represents the effective part of the capsule structure as exactly as possible.

The results of burnup are shown in Table 11.2.1. SRAC gives slightly higher burnup than the measurement but shows good agreement in both cases of zirconia and thoria type ROX disks. MVP-BURN code overestimates the measurement by 10% or 11%. MVP-BURN gives higher burnup than SRAC. Table 11.2.2 shows ^{239}Pu microscopic fission reaction rates calculated by the two codes at the beginning of each burnup cycle. At all the cycles, reaction rates of MVP-BURN are larger than those of SRAC. Figure 11.2.2 shows the spectra calculated by MVP-BURN are softer than those by SRAC. In the MVP-BURN model, vertical void gaps are included as exactly as possible and energy dependent neutron leakage is included in the results. The real structure of the irradiation capsule has several vertical void gaps and fast neutron can easily escape from the capsule. On the other hand, in the SRAC model, neutron leakage on the vertical direction is not considered. It makes the MVP-BURN spectra softer than those of the SRAC.

Production ratios of americium and curium to initial plutonium atoms are listed in Table 11.2.3. All of calculations underestimate the measured values very much. Large discrepancy cannot be seen between the two codes, because the codes use the same burnup chain for minor actinides, depletion calculation methodology and base neutron cross section library.

Effect of burnup step number to calculated FIMA% is evaluated with SRAC. The irradiation experiment have been done through 4 operation cycles of the JRR-3. Burnup step

number was changed from 1 step per cycle to 4 steps per cycle. FIMA% going down according to the increase of the step number. It is found 4 steps per cycle is enough for the analysis of this time. Total number of burnup step becomes 20 including 3 interval steps and 1 cooling step. Absolute difference of FIMA% between 4 steps and 1 step per cycle is 0.9~1.2%. It is equivalent to 3~4% of the measured value. All of the calculations in the previous sections have been performed with 4 burnup steps per cycle.

References

1) Takano, H., Akie, H. and Muromura, T., Proc. 6th Int. Conf. on Nuclear Engineering. (ICONE-6), San Diego, CA, USA, May 10-14, 1998 (ASME, 1998).
2) Okumura, K., Kaneko, K. and Tsuchihashi, K., SRAC95; "General Purpose Neutronics Code System", Japan Atomic Energy Research Institute Report JAERI-Data/Code 96-015 (1996), (in Japanese).
3) Okumura, K., Nakagawa, M. and Kaneko, K., Proc. Joint Int. Conf. on Mathematical Methods and Supercomputing for Nuclear Applications, Saratoga Springs, NY, USA, Oct. 5-9, 1997 (ANS, 1997).
4) Mori, T. and Nakagawa, M., MVP/GMVP: "General Purpose Monte Carlo Codes for Neutron and Photon Transport Calculations based on Continuous Energy and Multigroup Methods", Japan Atomic Energy Research Institute Report JAERI-Data/Code 94-007, (1994), (in Japanese).

Table 11.2.1 Burnup of ROX disks / FIMA %

ROX Disk	Measurement	SRAC (Cal. / Meas.)	MVP-BURN (Cal. / Meas.)
Zirconia Type	27.90 ±0.087	28.85 (1.034)	30.64 (1.098)
Thoria Type	27.95 ±0.137	29.47 (1.054)	31.02 (1.110)

Table11.2. 2 Microscopic fission reaction rate of Pu-239

ROX Disk	Code	Cycle-1	Cycle-2	Cycle-3	Cycle-4
Zirconia Type	MVP-BURN 1σ error	4.524E+16 ±1.890%	4.533E+16 ±1.881%	4.800E+16 ±1.922%	4.949E+16 ±1.888%
	SRAC	4.078E+16	4.404E+16	4.554E+16	4.665E+16
Thoria Type	MVP-BURN 1σ error	4.800E+16 ±1.853%	4.831E+16 ±1.881%	4.747E+16 ±1.860%	4.980E+16 ±1.868%
	SRAC	4.386E+16	4.511E+16	4.656E+16	4.764E+16

Table 11.2.3 Production ratio of Am, Cm and U atoms to initial Pu atoms

ROX Disk	Isotope	Measurement	MVP-BURN (Cal. / Meas.)	SRAC (Cal. / Meas.)
Zirconia Type	Am-241	3.046E-3 ±0.16%	1.980E-3 (0.650)	1.819E-3 (0.597)
	Cm-242	2.985E-6 ±0.16%	1.300E-6 (0.436)	1.186E-6 (0.397)
	Cm-244	3.988E-6 ±0.80%	9.367E-7 (0.235)	9.062E-7 (0.227)
Thoria Type	Am-241	3.226E-3 ±0.16%	1.962E-3 (0.608)	1.877E-3 (0.582)
	Cm-242	3.124E-6 ±0.14%	1.378E-6 (0.441)	1.248E-6 (0.400)
	Cm-244	4.839E-6 ±0.66%	8.088E-7 (0.167)	9.520E-7 (0.197)

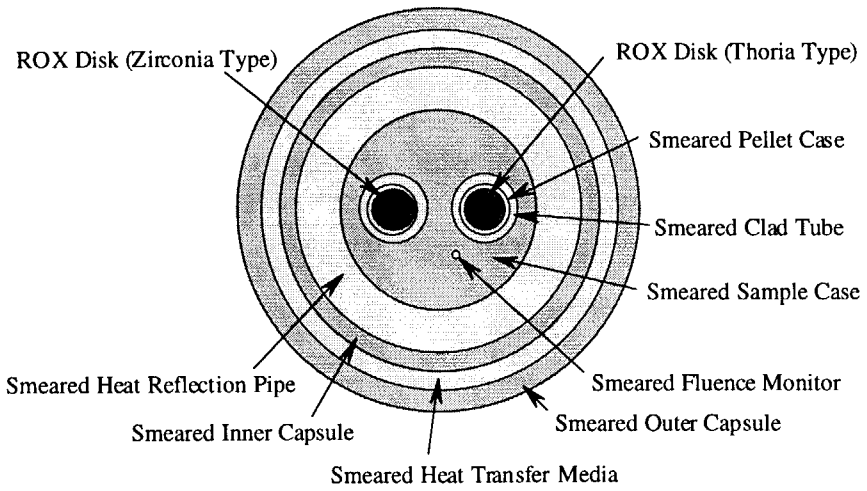

Fig. 11.2.1 SRAC calculation model of the irradiation capsule

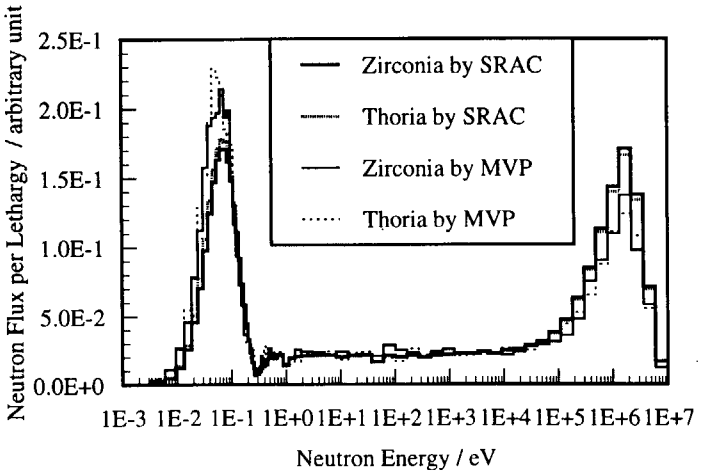

Fig. 11.2.2 Calculated neutron spectra of ROX disks before irradiation

11.3 Thermophysical Properties of ROX Fuel with YSZ-Spinel Composites

N. Nitani, T. Yamashita, T. Matsuda*, S. Kobayashi* and T. Ohmichi**
E-mail: nitani@analchem.tokai.jaeri.go.jp

In order to evaluate the fuel performance in the core, it is of important to know thermophysical properties of inert matrix candidates. However, little were known for thermophysical properties of inert matrices, because less attention was paid for such materials. Two-phase mixture of yttria stabilized zirconia (YSZ) and spinel ($MgAl_2O_4$) was a hopeful candidate of an inert matrix for the ROX fuel.[1] Thermal expansion, thermal diffusivity, melting temperature etc. were measured in the temperature range between room temperature and 1800 K. For the simulated ROX fuel, specimens containing UO_2 were also prepared and evaluated. Chemical composition of the composites is listed in Table 11.3.1.

Table 11.3.1 Composition of samples / mol%

sample No.	$MgAl_2O_4$	YSZ	UO_2
1	100.0	0.0	0.0
2	64.3	35.7	0.0
3	40.3	59.7	0.0
4	10.1	89.9	0.0
5	0.0	100.0	0.0
12	54.5	30.3	15.2
13	35.0	52.0	13.0

Thermal expansion was measured by a conventional dilatometric method in a reducing atmosphere. Sapphire was used as the standard. Values of linear thermal expansion of the composites were 1.3 to 1.6 % at 1800 K. Thermal expansion coefficients of $MgAl_2O_4$-YSZ composites increased with increasing YSZ content and the values were well represented by the Turner's equation[2] within 2% error. Addition of UO_2 to $MgAl_2O_4$-YSZ composite resulted in an increase of thermal expansion.

Thermal diffusivity was measured by the laser flash method with disk samples of approximately 2 mm in thickness. Thermal conductivity was calculated from data of thermal diffusivity, specific heat and density of the samples. The specific heat of each sample was

* Nuclear Fuel Industries Ltd.
** Research Organization for Information Science and Technology

calculated by the additive law, using data from literature on each oxide[3]. Fig.11.3.1 (a) and (b) show the thermal conductivities of samples No.1-5 and No.12-13, respectively, together with UO_2 data[4]. Thermal conductivity values of the $MgAl_2O_4$-YSZ composites decrease with increasing YSZ content. Addition of UO_2 also results in decrease of thermal conductivities, because the added UO_2 was dissolved in YSZ phase and made increase in volume fraction of YSZ phase. The observed thermal conductivities of the $MgAl_2O_4$-YSZ composites could be well represented by the Maxwell-Eucken equation[5] shown below.

$$\kappa = \kappa_1 \left(\frac{2\kappa_1 + \kappa_2 - 2\phi_2(\kappa_1 - \kappa_2)}{2\kappa_1 + \kappa_2 + \phi_2(\kappa_1 - \kappa_2)} \right)$$

where κ, κ_1 and κ_2 are thermal conductivity of the composite, phase 1 and phase 2, $\phi_1$and ϕ_2 are volume fraction of phase 1 and phase 2, respectively.

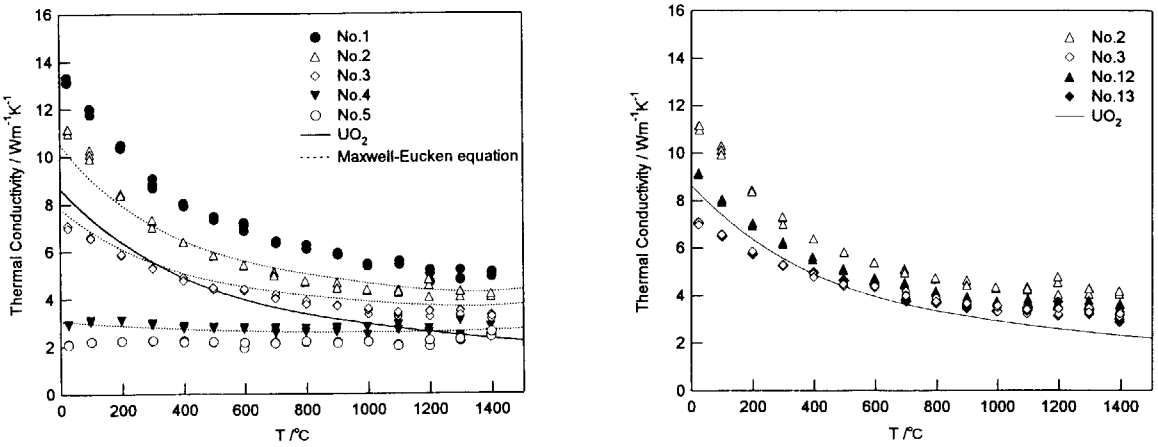

(a) (b)

Fig.11.3.1 Thermal conductivities of $YSZ(UO_2)$-$MgAl_2O_4$ composites. (a) Thermal conductivity of YSZ-$MgAl_2O_4$ system and calculated results by the Maxwell-Eucken equation. (b) Thermal conductivity of YSZ-$MgAl_2O_4$-UO_2 system. Solid line is data of UO_2[4].

The melting temperature was determined by the thermal arrest method. The sample of approximately 10 mg was heated on tungsten filament in an argon atmosphere. Al_2O_3, Y_2O_3 and HfO_2 standards were used for temperature calibration. The measured melting temperatures are summarized in Table 11.3.2. The melting temperature of the YSZ (No.5) is 2996 K which is very close to that of ZrO_2[3]. $MgAl_2O_4$ and YSZ form a eutectic melts and the

eutectic temperature (melting temperature) of the system is found to be 2200 K. Addition of UO_2 to the $MgAl_2O_4$-YSZ system does not affect the melting temperature very much.

Table 11.3.2 Melting temperature of samples

Sample No.	Melting temp. /K
1	2375.0
2	2203.7
3	2201.6
5	2996.6
12	2206.2
13	2205.6

Mechanical properties such as Vickers hardness and creep rate of the composites were also measured by conventional methods. The high temperature hardness of the composites was higher than that of the pure-phase components, YSZ or $MgAl_2O_4$. In the composite system, the hardness increased with increasing $MgAl_2O_4$ content. The hardness of ROX fuel seems to be considerably higher than that of UO_2 fuels. The creep rate of $MgAl_2O_4$-YSZ composite decreased with increasing $MgAl_2O_4$ content and was controlled by the lattice diffusion of YSZ.

References

1) Yamashita,T., Akie,H., Kimura,H., Takano,H. and Muromura,T., "ROX-LWR System for Almost Complete Burning of Plutonium", IAEA-TCM, Victoria, Canada, Apr. 28-May 1, 1998, to be published.

2) Kingery,W.D., Bowen,H.K. and Uhlmann,D.R., Introduction to Ceramics (John Wiley and Sons, New York, 1976).

3) Barin,I., Thermochemical Data of Pure Substance (VCH, Weinheim, 1989).

4) Hargman,D.L., MATPRO-Version11, A Handbook of Materials Properties for Use in the Analysis of Light Water Reactor Fuel Rod Behavior (Idaho National Eng. Lab., 1981).

5) Maxwell,J.C., A Treatise on Electricity and Magnetism vol.1 (1904) 441.

11.4 Preparation of ROX Fuels for the Irradiation Test in the JRR-3

T. Shiratori, T. Yamashita, T. Ohmichi*, A. Yasuda** and K. Watarumi**

E-mail: yamasita@analchem.tokai.jaeri.go.jp

The ROX fuel was originally composed of yttria-stabilized zirconia (YSZ), spinel ($MgAl_2O_4$) and corundum (Al_2O_3), although corundum could be excluded from the viewpoint of its irradiation behavior. Recently YSZ particle dispersed fuel concept has been studied in Japan Atomic Energy Research Institute (JAERI) to accommodate the swelling of the inert matrix materials[1]. To realize this new fuel concept, the fuel fabrication technology should be developed. Two main issues to be resolved are: 1) how to obtain sphere particles with a homogeneous YSZ solid solution and a well-defined size distribution. 2) how to obtain a particle dispersed pellet with homogeneous particle distribution and high density. The particle dispersed type ROX fuels were fabricated using enriched uranium (19.6% in ^{235}U) instead of plutonium and supplied for the irradiation test in the Japan Research Reactor No.3 (JRR-3).

The external sol-gel process was selected for the fabrication of YSZ particles, because the process was used to fabricate the coated particles for high-temperature gas cooled reactor fuels. Figure 11.4.1 shows the flow diagram for fabrication of YSZ particles. The starting materials were uranyl nitrate [$UO_2(NO_3)_2 \cdot 6H_2O$], zirconium nitrate [$ZrO(NO_3)_2 \cdot 2H_2O$] and yttrium nitrate [$Y(NO_3)_3 \cdot 6H_2O$]. Polyvinyl alcohol (PVA) and tetrahydrofurfuryl alcohol (THFA) were added into the solution for viscosity adjustment. The size of the gel spheres formed was controlled to be around 800 μm in diameter so that the size could become about 250 μm after sintering. Figure 11.4.2 shows the appearance and size distribution of the particles obtained by sintering at 2020 K for 4 h in a stream of 75%H_2/25%N_2 mixed gas. It is indicated that the particles have the average diameter of 250 μm and have a relatively narrow size distribution. The sphericity, which is defined as a ratio of any two orthogonal diameters, is a quality measure of sintered particles. The sphericity of the particles was between 1.00 and 1.10. X-ray diffraction analysis confirmed that the sintered spheres were a homogeneous solid solution of $(U,Zr,Y)O_2$.

---

* Research Organization for Information Science and Technology

** Nuclear Fuel Industries Ltd.

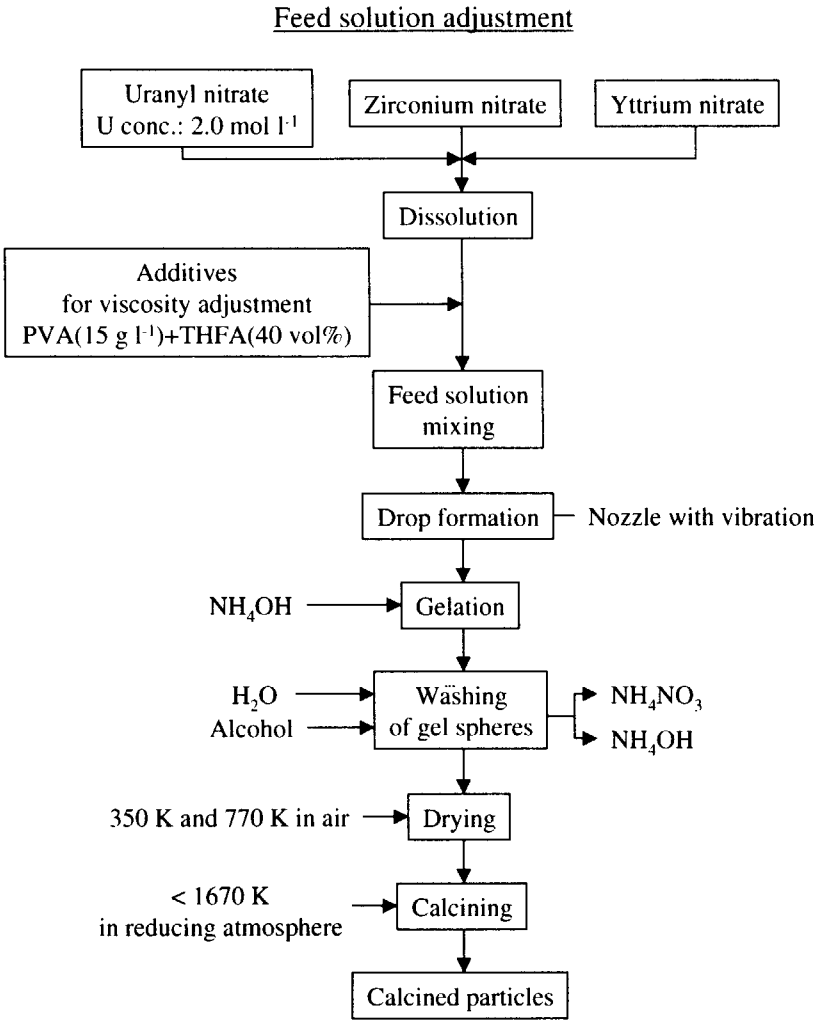

Fig. 11.4.1 Flow diagram for fabrication of YSZ particles with an external sol-gel process

Special attention was paid to keep homogeneous dispersion of particles in the matrix at the green pellet fabrication process. The calcined YSZ particles were put in slurry of spinel or corundum and were dispersed homogeneously by gentle stirring. Then the mixture was compacted into green pellets at about 200 MPa. Sintering was carried out at 2020 K for 4 h in a stream of 75%H_2/25%N_2 mixed gas. It is worthwhile to note here that adjustment of shrinkage rate of the calcined particles to that of matrix materials is of great importance to obtain high density pellets. The shrinkage rates of the calcined particles were measured as a function of calcining temperature prior to the fuel pellet fabrication. The calcining temperature of the pre-calcined particles was determined so as to meet the shrinkage rate of the matrix material determined separately. Figure 11.4.3 shows the appearance and microstructure of the particle dispersed pellet with spinel matrix. It can be seen that the white

$(U,Zr,Y)O_2$ particles are approximately 250 μm in diameter and are uniformly distributed in the spinel matrix. The gaps between the particles and the matrix are not so wide but further improvement is necessary because the gaps may have a tendency to increase the temperature of $(U,Zr,Y)O_2$ particles during irradiation.

The characterization tests showed that the pellets had a small void volume fraction (<9 %) and the homogeneous distribution of particles/grains of YSZ in the matrix. The X-ray diffraction analysis confirmed the formation of homogeneous $(U,Zr,Y)O_2$ solid solutions and no appreciable interactions between the $(U,Zr,Y)O_2$ phase and inert matrix materials (spinel or corundum).

References

1) Ohmichi,T., Japan Atomic Energy Research Institute report JAERI-Review 96-008 (1996). (in Japanese)

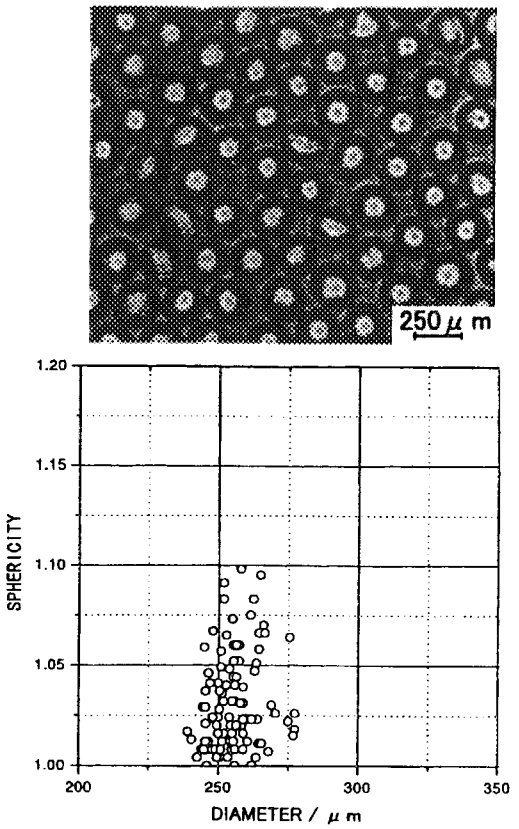

Fig. 11.4.2 Typical aspects of YSZ sintered particles and particle size distribution

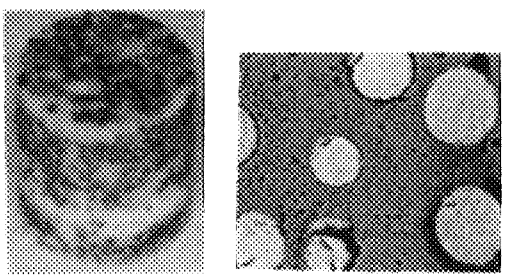

Fig. 11.4.3 Appearance and micro-structure of the particle dispersed pellet

11.5 Pulse Irradiation Tests of ROX Fuels with YSZ and Spinel Composites

K. Okonogi*, T. Nakamura, M. Yoshinaga, K. Ishijima, H. Akie and H. Takano
(E-mail : akie@mike.tokai.jaeri.go.jp)

Pulse irradiation tests of rock-like oxide(ROX) fuel were conducted in the Nuclear Safety Research Reactor (NSRR) to investigate transient behavior of ROX under reactivity initiated accidents (RIAs). Because of reactivity coefficients and fuel properties of ROX are different from UO_2, quite unique behavior of ROX fuel is expected under the RIA conditions. The test fuel rod contained in an experimental capsule is installed in the experimental cavity in the NSRR and exposed to a high pulsed neutron flux simulating RIA conditions. Specifications of ROX fuel used in the pulse tests are shown in Table 11.5.1. Here, U is used as Pu simulation in the tests. The primary specifications of the test rods are the current 17×17 PWR type rod of 135mm long pellet stack. Measured and estimated physical properties of the ROX fuel[1,2] are shown in Table 11.5.2. The ROX fuel has lower density, larger specific heat and lower melting temperature than UO_2. The test rod was irradiated by natural pulse operation at reactivity insertion of the peak fuel enthalpies of 240 cal/g, 390 cal/g and 530 cal/g.

Table 11.5.1 Specifications of ROX fuel rod used in the pulse irradiation tests

Pellet	
Material	UO_2 : YSZ : $MgAl_2O_4$
Composition =	25.4 : 26.8 : 47.8 (mol%)
	(YSZ = ZrO_2 : Y_2O_3 = 0.812 : 0.188)
Diameter	8.05 mm
Length	9 mm
Enrichment	20%-U235
Cladding	
Material	Zry-4
Outer Diameter	9.5mm
Wall Thickness	0.64mm
Element	
Over All Length	279mm
Fuel Stack Length	135mm
P/C – Gap	85 μ m
Filled Gas	He at 1.1MPa

Table 11.5.2 Primary thermo-physical properties of fresh ROX and UO_2 fuels

Items	ROX	Fresh UO_2
Pellet Density(g/cc)	6	10
Specific Heat (J/g/K)	0.7(500°C) 0.8(1000°C)	0.3 (500°C) 0.3(1000°C)
Melting Temp.(°C)	1940	2840
Thermal Conductivity (W/m/K)	4.3(500°C) 3.0(1000°C)	4.4(500°C) 3.0(1000°C)
Coefficient of Linear Thermal Expansion(1/K)	1.0E-5	1.2E-5

The tests irradiated at peak fuel enthalpies of 240 cal/g(Test 943-1) and 390cal/g(Test 943-2) did not cause the fuel rod failure. Cladding failure occurred in the third Test 943-3 at peak fuel enthalpy of 530 cal/g. Here, the cladding did not show the extended embrittlement due to heavy oxidation or thinning of molten cladding, which caused cladding failure of UO_2 fuel. Though considerable amount of the fragmented fuel(about 70%) was dispersed to the water, the pressure spike was not observed and the water column movement sensor indicated minor

* Toshiba Corp.

vibration, suggesting that the mechanical energy generation due to molten fuel/water interaction was negligible in this test.

The thermo-couple attached to the cladding at mid-height of the fuel stack in Test 943-1 showed temperature increase up to about 600°C. This thermo-couple data and the local oxidation of the post pulse cladding suggest that departure from nucleate boiling(DNB) occurred locally in this test. In the Test 943-3, the cladding temperature reached to 1500°C lower than its melting point(~1850°C) and rapidly dropped to about 800°C due to decrease of heat capacity by fuel dispersion.

The cross-sectional views of the three test rods are shown in Fig. 11.5.1. In Test 943-1, many small radial cracks are seen mostly in the outer region of the fuel, and micro-structure did not change. As the peak fuel enthalpy rises in Test 943-2, the fuel became so porous, central void was formed and micro-structure changed due to the fuel melting. In Test 943-3, at peak fuel enthalpy of 530cal/g, most of the fuel looks once molten and large amount of the pellet was ejected. The considerable pellet/cladding chemical interaction(PCCI) layer was observed, which likely contributed to the cladding burst.

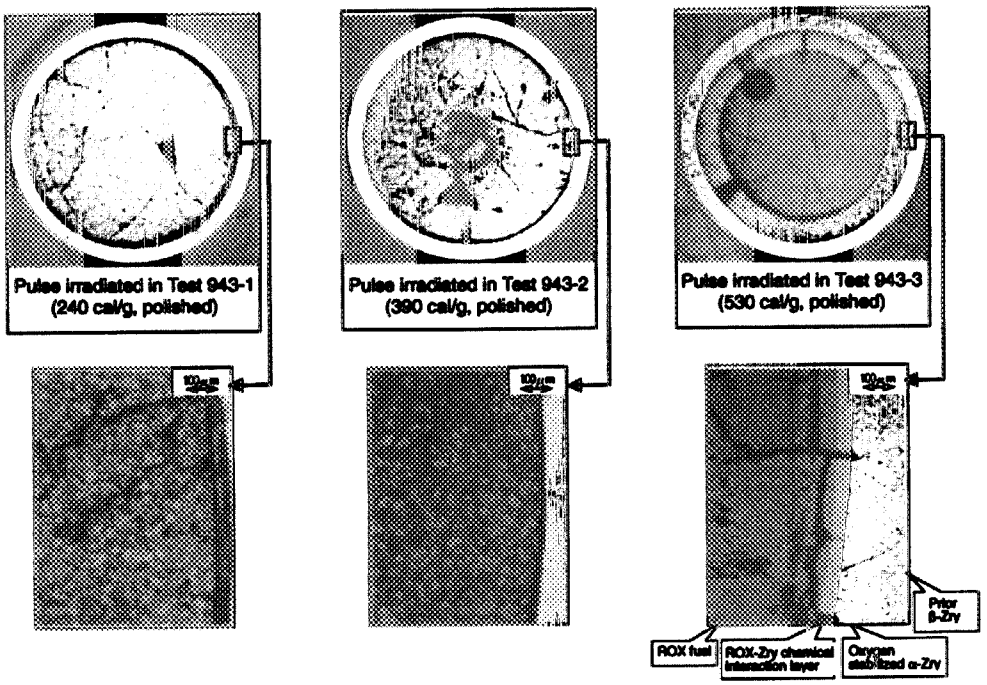

Fig. 11.5.1 Cross-sections of the ROX fuel for the pulse

The fuel rod behavior during the pulse irradiation in NSRR was simulated with the FRAP-T6 code[3]. In Test 943-1, peak fuel temperature is estimated to be 1600°C, which raise the

cladding temperature to be about 750°C at the peak. In Test 943-2, fuel temperature is expected to reach its melting point of 1940°C, while the cladding temperature remains about 1200°C, far below its melting point of 1850°C. In this simulation, about 15% of the ROX fuel is predicted to be in liquid phase. At the higher fuel enthalpy of 530 cal/g, about 55% of ROX fuel pellet is predicted to melt, and the cladding temperature is still lower than its melting point(~1850°C). In the fresh UO_2 fuel test at 240 cal/g, the cladding temperature is predicted to reach its melting point of 1850°C, which causes cladding failure of UO_2 fuel due to the extended oxidation embrittlement and the thinning by relocation of molten cladding.

From these results, it was found that the fuel and cladding temperature of ROX fuel rod is lower than those of UO_2 fuel rod at the same fuel enthalpy, due to larger specific heat of ROX fuel. Failure of UO_2 fuel occurs by cladding thermal failure at peak fuel enthalpy of 220 cal/g. On the other hand, ROX fuel rod did not fail at peak fuel enthalpy of 390 cal/g, even though partial fuel melting(~15%) was observed. Lower melting temperature of the ROX(~1940°C) than UO_2 (~2840°C) kept the cladding temperature lower than its melting point and prevented thermal failure of the cladding. ROX fuel failure occurred at peak fuel enthalpy of 530cal/g. In spite of the cladding rupture and fuel dispersion of about 70%, mechanical energy generation due to molten-fuel/water interaction was not observed. These tests indicated that the ROX fuel behavior and its rod failure mechanisms under the RIA conditions are quite different from those of UO_2. The failure could occur, however, at lower enthalpies for irradiated ROX fuel with certain amount of fission gas release which would cause higher rod pressure.

References

1) Nitani, N., et al. : "Phase Relations and Thermophysical Properties of Plutonium Rock-like Fuels for LWR Use", Proc. 10th Pacific Basin Nucl. Conf. (10-PBNC), Oct. 20-25, 1996, Kobe, Japan, Vol.2, p.1114.

2) Matsuda, T., et al. : JAERI-Research 97-083, "Thermal Expansion and Thermal Conductivity of Rock-like Fuel" (1997) [in Japanese].

3) Siefken, L.J., et al. : NUREG/CR-2148, EGG-2104, "FRAP-T6: A Computer Code for the Transient Analysis of Oxide Fuel Rods" (1981).

11.6 Core Design Study on ROX Fuels

H. Akie, H. Takano and Y. Anoda
(E-mail : akie@mike.tokai.jaeri.go.jp)

A zirconia based ROX (Zr-ROX) PWR core has problems such as a small negative Doppler coefficient and a large power peaking factor, which cause severe transients in accidents and high fuel temperature even under nominal condition. For the improvement of these characteristics, two approaches were considered: the additives UO_2, ThO_2 and Er_2O_3, or a heterogeneous core with Zr-ROX and UO_2 assemblies.

For the improvement of the Doppler coefficient, resonant isotopes ^{232}Th and ^{238}U were found to be very effective. The amount of the additives were decided to be 24 mol% of ThO_2 or 15 mol% of UO_2 in the weapons-grade plutonium (W-Pu) case, and 18 mol% ThO_2 or 8 mol% UO_2 in the reactor-grade plutonium (R-Pu) case. The Er additive was used to decrease burnup reactivity swing for power peaking reduction. The content of about 0.3 mol% Er_2O_3 was considered in both W-Pu and W-Pu Zr-ROX.

The physics characteristics of the original and the modified Zr-ROX PWR cores are compared in Table 11.6.1. These were evaluated with 2-dimensional core burnup calculations based on the diffusion method. As shown in the table, the small Doppler reactivity of the original Zr-ROX core is improved in all the modified cores. In the heterogeneous core with U and Pu fuel assemblies, it was difficult to reduce the power peaking to less than 2.8.

Table 11.6.1 Doppler reactivity (% Δk/k) and power peaking factor in a Zr-ROX PWR core (BOC)

	Doppler reactivity (900→1200 K)	Peaking factor
Weapons-Pu		
Zr-ROX	-0.098	2.7
Zr-ROX(Er)-15UO_2	-0.61	2.1
Zr-ROX-24ThO_2	-0.56	2.4
1/3Zr-ROX+2/3UO_2	-0.48	2.8
Reactor-Pu		
Zr-ROX(Er)-8UO_2	-0.59	2.2
Zr-ROX(Er)-18ThO_2	-0.64	-
UO_2	-0.75	2.0

The reactivity insertion accident (RIA) analysis results with the EUREKA-2 code[1] for improved Zr-ROX cores are compared with those for conventional UO_2 fuel PWR in Table 11.6.2. The additives UO_2 or ThO_2 are shown to be capable of reducing the maximum fuel enthalpy (H) to less than 230 kcal/kg, the limit value in the UO_2 PWR. The maximum fuel temperature (T_{FC}) also becomes less than the melting point of 2200 K. The fuel enthalpy is

still 2 times as large as that in the UO_2 PWR. Considering the smaller density of Zr-ROX fuel, the energy release per unit volume is also shown in the table. The value of Zr-ROX with UO_2 and Er additives is almost equivalent to that of the UO_2 fuel core. The actual enthalpy condition for Zr-ROX pin failure under RIA is now being studied in the NSRR by pulse irradiation experiments (Section 11.4). In the 1/3 ROX fuel heterogeneous core, further improvement is necessary.

Table 11.6.2 Maximum fuel enthalpy (H) and fuel temperature (T_{FC}) in Zr-ROX PWR RIA event

	H(cal/g)	H(cal/cm^3)	T_{FC}(K)
Weapons-Pu			
Zr-ROX	>>230		>>2200
Zr-ROX(Er)-15UO_2	193	1080	1700
Zr-ROX-24ThO_2	224	1250	1950
1/3Zr-ROX+2/3UO_2	244	1360	2100
Reactor-Pu			
Zr-ROX(Er)-8UO_2	192	1080	1700
UO_2	93	1020	2080

Table 11.6.3 Peak cladding temp. (T_{PC}) in LOCA of a Zr-ROX fuel PWR

	T_{PC}(K)
Weapons-Pu	
Zr-ROX	>1470
Zr-ROX(Er)-15UO_2	1090
Zr-ROX-24ThO_2	1240
1/3Zr-ROX+2/3UO_2	1240
Reactor-Pu	
Zr-ROX(Er)-8UO_2	1090
UO_2	1080

The loss of coolant accident (LOCA) in a Zr-ROX fueled PWR was analyzed by using the RETRAN2 code[2]. The analyzed event was a cold-leg large break LOCA event of 4-loop type 1100 MWe class PWR. The LOCA analysis results for the modified Zr-ROX fuel cores are shown in Table 11.6.3. In all of the modified Zr-ROX fuel cores, the peak cladding temperature T_{PC} is successfully reduced to less than the limit of 1470 K (1200 °C). By using UO_2 and Er_2O_3 additives, T_{PC} becomes as low as that of the UO_2 fuel case. Better LOCA behavior may be preferable in the other cores by further reducing the power peaking.

The fuel temperature within the Zr-ROX fuel pin was estimated by using the GAPCON-THERMAL2-HC code[3] for a single channel model. Figures 11.6.1 and 11.6.2 show the fuel temperature in the fuel pin at the peak power position. In Fig. 11.6.1, the temperature was calculated with the thermal conductivity measured for the Zr-ROX with 37mol% spinel ("SP-YSZ-UO_2"). As shown in the figure, the peaking factor of 2.1 gives a maximum fuel temperature less than the melting point. To obtain the lower fuel temperature, for example to be less than the melting point by 500°C, the peaking factor of about 1.7 is necessary. Such a peaking factor is difficult to realize in reactor core design. The fuel temperature can be also reduced by increasing the fuel thermal conductivity. Figure 11.6.2 compares the fuel

temperatures calculated with different ROX fuel thermal conductivities. When the conductivity of Zr-ROX with higher (56 mol%) spinel content ("SP-YSZ(calc.)") is used, the maximum fuel temperature becomes about 1700 K. On the other hand, with the lower conductivity of that of stabilized zirconia ("YSZ"), the temperature rises to about 2500 K. In this case, the melting point of stabilized zirconia is nearly 3000 K, and the fuel temperature is well below the melting point. To suppress the FP gas release, the fuel temperature is preferable to be still lower. From this point of view, further studies seem necessary.

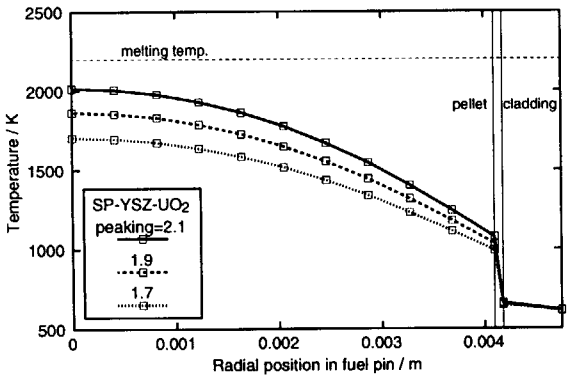

Fig. 11.6.1 Fuel temperature at peak power position calculated with different power peaking factors at BOL

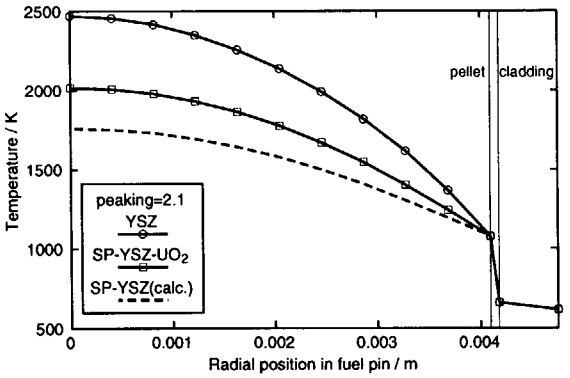

Fig. 11.6.2 Fuel temperature at peak power position calculated with different fuel thermal conductivities at BOL

In the 1/3 Zr-ROX core, the plutonium transmutation rate in Zr-ROX assembly is very high to be 86% of W-Pu or 74% of R-Pu. This is a very important factor for plutonium once-through disposal. By adding UO_2 or ThO_2 in the fuel, the transmutation rate is deteriorated slightly. The advantage of the full-ROX core with these additives is the larger amount of annual transmutation (0.7~0.9 t per GWe reactor power). For rapid annihilation of plutonium, full-ROX cores have an advantage.

References

1) Ohnishi, N. et al. : JAERI-M 84-074 "EUREKA-2 : A Computer Code for the Reactivity Accident Analysis in a Water Cooled Reactor" (1984) [in Japanese].

2) Peterson, C.E. et al. : EPRI NP-1850 CCM, 1, "RETRAN-02 - A Program for Transient Thermal-Hydraulic Analysis of Complex Fluid Flow Systems" (1981).

3) Mori, T., Nakagawa, M. and Fujii, S. : JAERI-M 88-224 "Parametric Study on Thermal-Hydraulic Characteristics of High Conversion Light Water Reactor" (1988) [in Japanese].

11.7 Power Distribution Flattening in Rock-like Fuel and UO_2 Fuel Assemblies Mixed System

H. Akie, Y. Sugo* and H. Takano
(E-mail : akie@mike.tokai.jaeri.go.jp)

As described in Section 11.8, for the improvement of reactivity coefficients of ZrO_2 based Pu ROX fuel LWR, two approaches are investigated in the ROX-PWR core design study in JAERI. In the ROX-UO_2 assemblies partial loading core, however, the power peaking becomes very large in comparison with the UO_2 core. This leads to another problem of the fuel temperature of ROX, whose melting point is much lower than that of UO_2.

Figure 11.7.1 compares the neutron spectra calculated for reactor-grade Pu (R-Pu) ROX and UO_2 fueled infinite lattices of 17×17 type PWR at BOL, and EOL after 1170 EFPD burnup. Here, 1170 EFPD corresponds to 45 GWd/t in UO_2 fuel cell. As shown in this figure, the spectrum in ROX is harder than that in UO_2 at BOL. As the thermal spectrum flows into ROX assembly from UO_2 assembly, it is expected a power peaking appears at the ROX fuel rods adjacent to UO_2 assembly. On the other hand at EOL, because of the extremely large thermal spectrum in ROX, a power peaking is expected at the UO_2 fuel rods adjacent to ROX assembly. In order to investigate the power distribution in ROX-UO_2 assemblies mixed system, assembly burnup calculations were performed on the 4 assembly geometry model shown in Fig. 11.7.2. The model is also based on the conventional 17×17 type PWR.

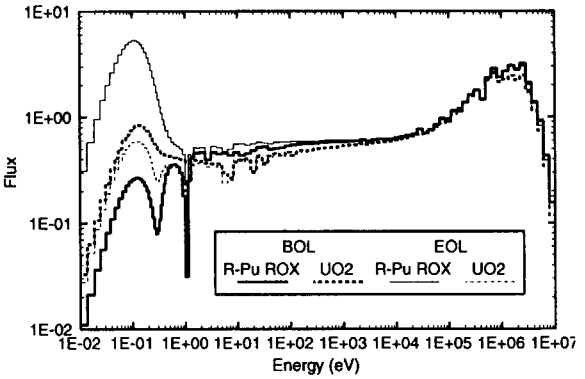

Fig. 11.7.1 Neutron spectrum in Zr-ROX (reactor-grade Pu) and UO_2 fuels (pin cell calculation)

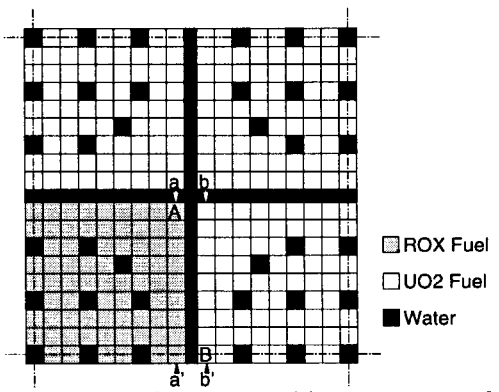

Fig. 11.7.2 Four assembly geometry of ROX and UO_2 fuels

* Information Technologies Japan Inc.

Figure 11.7.3 shows the power peaking factor of each ROX fuel rods on the row "a-a'" in Fig. 11.7.2 at BOL, and UO_2 fuel rods on the row "b-b'" at EOL. In this calculation for all ROX fuel rods, the uniform fuel compositions were assumed of 6.6 mol% PuO_2 and 0.12 mol% Er_2O_3 for R-Pu ROX, and 5.3 mol% PuO_2 and 0.24 mol% Er_2O_3 for weapons-grade Pu (W-Pu) ROX, respectively.

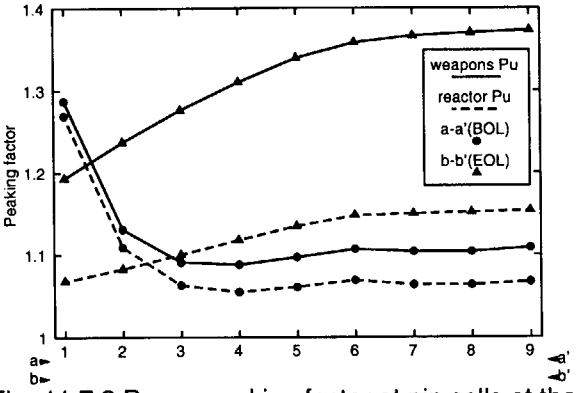

Fig. 11.7.3 Power peaking factor at pin cells at the border between ROX and UO_2 assemblies

At BOL the power peaking factor at the corner of ROX assembly (position "A" in Fig. 11.7.2) becomes as large as 1.3 both for R-Pu and W-Pu ROX cases. At EOL for the W-Pu ROX case, the peaking at the central rod on the side of UO_2 assembly (position "B" in Fig. 11.7.2) is still higher to be near 1.4.

The reduction of these large power peaking is next investigated by adjusting the fuel composition of ROX fuel rods. The composition of UO_2 is kept the same for all rods in the assembly. The results of Er_2O_3 content and PuO_2 enrichment adjustments are shown respectively in Figs. 11.7.4 and 11.7.5 for the W-Pu ROX case. In Fig. 11.7.4, the content of Er_2O_3 was increased from 0.24 mol% in the rods at the corner(point "A") and on the side (row "a-a'" but "A") of ROX assembly. The adjusted Er_2O_3 contents at (corner, side, others) are (0.94, 0.47, 0.24) and (2.4, 1.2, 0.24) mol%. The Er_2O_3 content adjustment is found to be effective for power peaking reduction in ROX assembly, and has only a slight effect on the power distribution in UO_2 assembly. In the same manner, the enrichment of PuO_2 was next

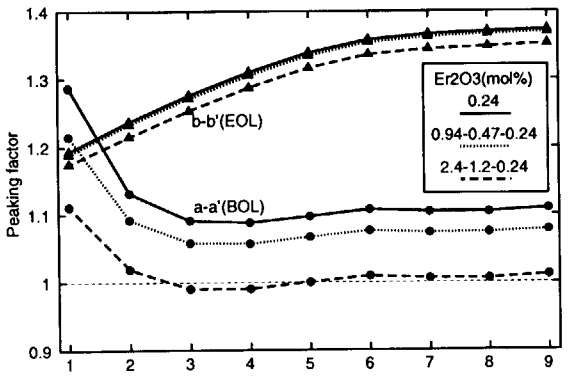

Fig. 11.7.4 Effect of Er_2O_3 content adjustment on power peaking (W-Pu ROX, 5.3 mol% PuO_2)

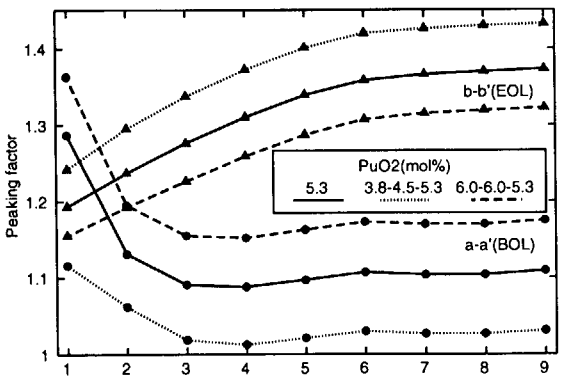

Fig. 11.7.5 Effect of PuO_2 enrichment adjustment on power peaking (W-Pu ROX, 0.24 mol% Er_2O_3)

decreased or increased in Fig. 11.7.5. The adjusted Pu enrichments are (3.8, 4.5, 5.3) and (6.0, 6.0, 5.3) mol%. The effect of PuO_2 enrichment is significant both in ROX and UO_2 assemblies, to the contrary directions. The reduction of the power peaking in ROX assembly at BOL results in the increase of the power peaking in UO_2 assembly at EOL.

Figure 11.7.6 shows the effect of UO_2 additive in ROX fuel. Here, 1.0 or 3.0 mol% UO_2 is added only in the ROX fuel rods on the side of ROX assembly. The PuO_2 enrichment is also reduced in the rod at "A", and the effect of UO_2 additive is clearly seen in the 2nd to 9th rods on "a-a'" and "b-b'" rows. It can be seen from the figure that the addition of UO_2 in ROX fuel have a influence only on the power distribution in UO_2 assembly.

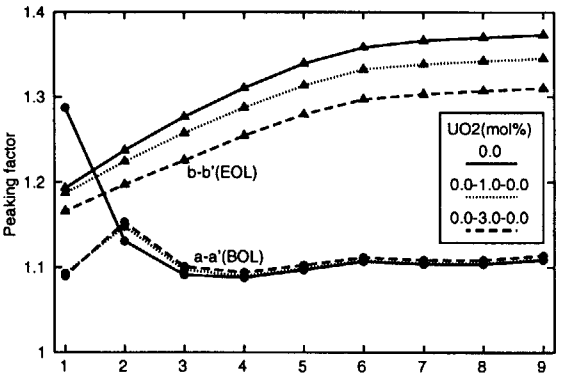

Fig. 11.7.6 Effect of UO_2 additive on power peaking (W-Pu ROX, 5.3 mol% PuO_2, 0.24mol% Er_2O_3)

By combining the use of Er_2O_3 and/or UO_2 additives with PuO_2 enrichment adjustment, it seems possible to effectively reduce the power peaking factor in the ROX-UO_2 assemblies heterogeneous system. It should be noted, however, all these three fuel composition adjustments have an effect on Pu transmutation capability of ROX fuel. In addition, the actual reactor core is usually composed of fuel assemblies at three different burnup stages. There can be a variety of combinations of ROX and UO_2 assemblies with different burnup. The power distribution flattening in such a heterogeneous core should further be studied by taking into account the fuel assemblies loading and shuffling patterns, paying attention to the Pu transmutation efficiency in the ROX fuel.

11.8 Comparison of Burnup Characteristics of PuO_2+ZrO_2 Fuel with PuO_2+ThO_2 Fuel in LWRs

A. Shelley*, H. Akie, H. Takano and H. Sekimoto*
(*E-mail:* shelley@popsvr.tokai.jaeri.go.jp)

Burnup characteristics of PuO_2+ZrO_2 (Rock-like oxide: ROX) fuel was compared with PuO_2+ThO_2 (Thorium oxide: TOX) fuel in LWRs for once-through use with soft to hard neutron spectrum core (a moderator to fuel volume ratio Vm/Vf was from 0.5 to 3.0). Furthermore, radiotoxicity hazards were studied by calculating minor actinides (MA) and long life fission product (LLFP) production buildup. Conventional MOX fuel was considered as a reference case. Reactor-grade Pu (R-Pu) and weapons-grade Pu (W-Pu) were considered separately. Cell burnup calculations were done by using SRAC95[1] based on JENDL-3.2[2] nuclear data library.

Figure 11.8.1 shows the percentage of net Pu transmutation in W-Pu fuels. ROX fuel can transmute 90% of initial loaded Pu and this transmutation percentage does not depend on Vm/Vf and discharge burnup. In TOX fuel, Pu transmutation percentage increases with increasing Vm/Vf, and discharge burnup. The net Pu transmutation percentage in TOX fuel varies from 40% to 80%. Production amount of ^{233}U in TOX fuel is approximately a half of fissile Pu transmutation amount. In MOX fuel, the transmutation percentage of Pu also increases with increasing Vm/Vf and discharge burnup. This percentage varies from about –5% to 60%. Net Pu transmutation percentages in R-Pu fuels are lower than W-Pu fuels.

Figure 11.8.2 shows the net MA production amount per year in ROX, MOX and TOX fuels for W-Pu. As MA we considered americium (Am), curium (Cm), and neptunium (Np) isotopes. MA production in ROX fuel is higher than that in TOX and MOX fuels especially when Vm/Vf is 0.5, because the flux level of ROX fuel is very high. Among MA ^{244}Cm production in ROX fuel is very high compared to TOX and MOX fuels. MA productions are 2.5% of initial loaded W-Pu in ROX fuel, 1.5% in TOX and 2.7% in MOX when Vm/Vf is 2.0 and discharge burnup is 33 GWd/t. At the same condition as W-Pu fuels, MA productions in R-Pu fuels are 6.7%, 4.0%, and 4.7% of initial loaded Pu in ROX, TOX and MOX fuels, respectively.

---

*Tokyo Institute of Technology

Figure 11.8.3 shows net LLFP production in W-Pu fuels. As for LLFP, we considered ^{79}Se, ^{93}Zr, ^{99}Tc, ^{107}Pd, ^{126}Sn, ^{129}I, and ^{135}Cs. The net LLFP production amount in ROX fuel is lower than that in MOX and TOX fuels especially when Vm/Vf is 0.5. The total number of fission is nearly the same for ROX, MOX, and TOX fuels of the same discharge burnup. Therefore, the FP production amounts in three fuels are assumed to be almost the same. From the yield of LLFP it was found that ^{135}Cs, ^{99}Tc ^{93}Zr and ^{107}Pd had higher yield than that the other LLFP nuclides. Capture cross-section of ^{135}Cs, ^{99}Tc ^{93}Zr and ^{107}Pd in ROX fuel is higher than in MOX and TOX fuels especially when Vm/Vf is 0.5. Net LLFP production amount of TOX and MOX fuels decreases very rapidly when the Vm/Vf increase from 0.5 to 3.0 and becomes nearly same as that of ROX fuel. The net productions of LLFP in R-Pu fuels are higher than that in W-Pu fuels.

Figure 11.8.4 shows the ingestion radiotoxicity hazard of MA+Pu+FP from W-Pu spent fuels without reprocessing for various Vm/Vf with 33 GWd/t discharge burnup. Net weight of heavy metal (HM) in ROX in the unit of metric ton is much less than that in TOX and MOX fuels. For this reason we considered the hazard in terms of one metric ton MOX equivalent fresh fuel volume for all type fuels. Radiotoxicity hazard of spent fuel nuclides is calculated by using the ingestion radioactivity concentration limit of nuclides that are approved by ICRP[3]. Radiotoxicity hazard of ROX spent fuel is low compared to TOX and MOX fuels when Vm/Vf is 2.0 or 3.0. For the first 18 years ^{244}Cm with half-life 18 years are dominant for hazard in ROX, TOX, and MOX spent fuels. After 18 years ^{241}Am increases from the β-decay of ^{241}Pu with half-life 14 years. Up to 10^3 cooling years ^{241}Am is the main contributor for hazard. In ROX fuel, Pu transmutation is very high and amount of ^{241}Pu at EOL is lower than TOX and MOX fuels. From 10^3 to 10^4 cooling years, ^{239}Pu and ^{242}Pu hazard are dominant, which is less in ROX spent fuel due to higher Pu transmutation percentage. After 10^4 cooling years, ^{237}Np mainly has hazard contribution, which is smaller in ROX spent fuel than that in TOX and MOX spent fuels, because ^{237}Np mainly comes from the α-decay of ^{241}Am, which production is less in ROX fuel. In consequence, after about 18 years of cooling time, the radiotoxicity hazard of the ROX spent fuel is always lower than that of the TOX and MOX fuels for all Vm/Vf.

In conclusion, ROX fuel has excellent performance as a once-through fuel compared to TOX and MOX fuel, because of higher Pu transmutation, lower LLFP production and radiotoxicity hazard for both W-Pu and R-Pu cases.

References

1) Okumura, K., Kaneko, K., and Tsuchihashi, K.: "SRAC95; General Purpose Neutronics Code system", JAERI-Data/Code 96-015, Japan Atomic Energy Research Institute (1996).

2) Nakagawa, T., et.al.: "Japanese Evaluated Nuclear Data Library Version 3 revision-2: JENDL-3.2", J. Nucl. Sci. Technology, vol. 32, pp. 1259 (1995).

3) ICRP Publication 30 Part 1 (1979); Part 2 (1980); Part 3 (1988).

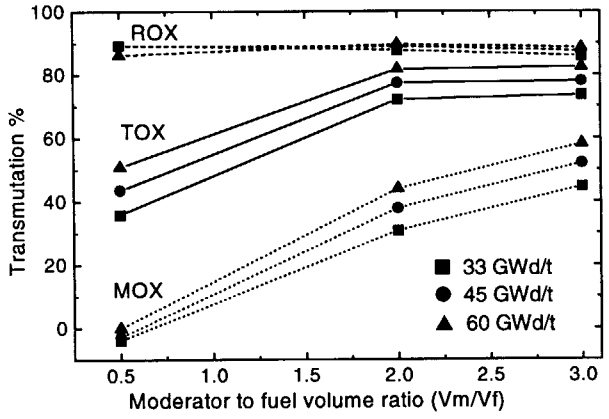

Fig. 11.8.1: Net Pu transmutation percentage in weapons-grade Pu fuel.

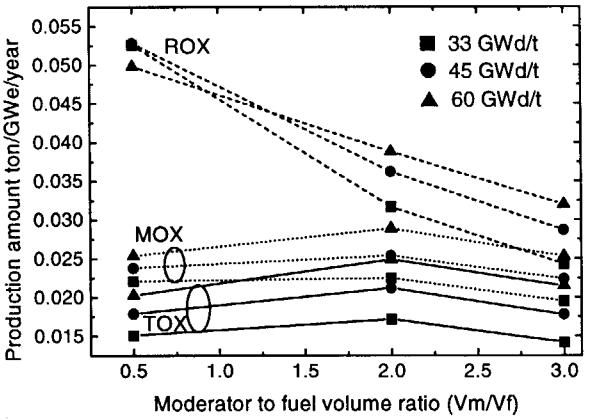

Fig. 11.8.2: Net produced amount of MA per year in weapons-grade Pu fuel.

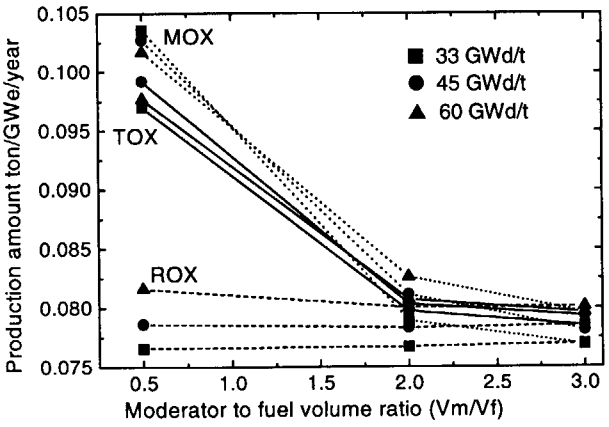

Fig. 11.8.3: Net amount of LLFP produced in W-Pu fuel.

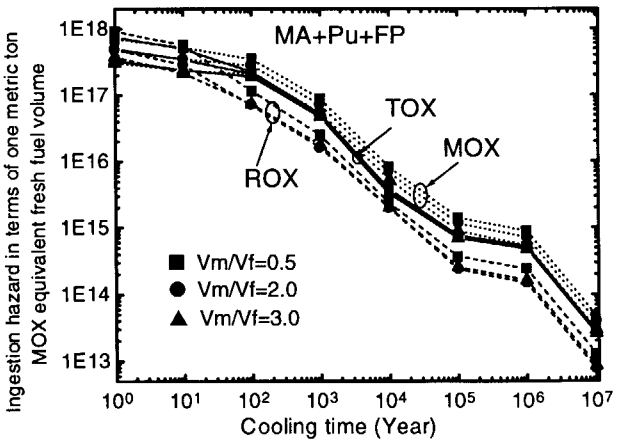

Fig. 11.8.4: Radiotoxicity hazard of W-Pu spent fuels for 33GWd/t-discharge burnup.

11.9 Neutronic Analyses of Fuel Temperature Coefficient of PuO_2+ZrO_2 Fuel in LWRs

A. Shelley*, H. Akie, H. Takano and H. Sekimoto*
(*E-mail:* shelley@popsvr.tokai.jaeri.go.jp)

Among inert matrix fuels, PuO_2+ZrO_2 (Rock-like oxide: ROX) fuel has excellent Pu transmutation capability, and low radiotoxicity hazard compared to those in PuO_2+ThO_2 (Thorium oxide: TOX) and MOX fuels [1]. The major drawback of ROX fuel is its fuel temperature coefficient (FTC) [2]. Detailed analyses have been made to explain physically the difference between the fuel temperature reactivity (FTR) behavior of nuclides in ROX fuel and the nuclides in TOX and MOX fuels. For FTC analyses, moderator to fuel volume ratio is 2.0 and discharge burnup is 33 GWd/t considered.

Figure 11.9.1 shows the burnup dependent FTC of ROX fuel with R-Pu and W-Pu in LWRs. TOX and conventional MOX fuels are shown as reference cases. As can be seen from this figure, the FTC of ROX fuel is a little negative at BOL and increases to positive direction with burnup both for W-Pu and R-Pu cases. ROX fuel has large positive FTC at EOL both for W-Pu and R-Pu fuels. TOX and MOX fuels have large negative FTC compared to ROX fuel at BOL and changes slightly with burnup. TOX fuel has much negative FTC value from BOL to EOL compared to MOX fuel both for W-Pu and R-Pu cases.

Figures 11.9.2 and 11.9.3 show the FTR contributor nuclides at BOL and EOL for W-Pu fuels. Fertile materials ^{238}U and ^{232}Th have a large resonance neutron absorption, which makes the fuel temperature coefficient largely negative at BOL and EOL in MOX and TOX fuels. On the contrary, ROX fuel contains only Pu; moreover the negative reactivity contribution of ^{239}Pu is less than that in TOX and MOX fuels at BOL. At EOL we can see from Fig. 11.9.3, ^{239}Pu and ^{241}Pu behaviors in ROX fuel are opposite to those in MOX and TOX fuels. The production reaction rate of ^{241}Pu in ROX fuel increases largely with increasing the temperature and makes the fuel temperature coefficient large positive value. The fission product (FP) also becomes an important contributor to the positive fuel temperature reactivity in the ROX fuel. The negative contribution of ^{239}Pu at BOL of ROX fuel becomes to positive contribution at EOL.

---

*Tokyo Institute of Technology

From the analysis of neutron production reaction rate of ^{241}Pu, it was found that neutron production reaction rate increases with temperature largely in the energy region from 0.1 to 0.4 eV in ROX fuel compared to that in TOX and MOX fuels.

Figure 11.9.4 shows the energy dependent neutron spectra (upper part) and its change with temperature (lower part) of W-Pu ROX, TOX and MOX fuels at EOL. Thermal neutron spectrum of ROX fuel is softer than that of MOX and TOX fuels. Because, the number density of Pu isotopes in ROX fuel is lower than that in MOX and TOX fuels. Moreover, resonance neutron absorption nuclides are absent in ROX fuel. When the fuel temperature is increased from 600°C to 900°C, thermal neutron spectrum of ROX fuel shifts largely than that in TOX and MOX fuels. This spectrum shift in ROX fuel is higher in the energy region from 0.1 to 1 eV. From the energy integration of neutron spectrum, ROX fuel spectrum change with temperature is positive, while in TOX and MOX fuels it is negative. As a result, we get positive FTR behaviors of ROX fuel nuclides whose resonance are in the energy region from 0.1eV to 1 eV.

Usually capture reaction rate of FP nuclide decreases with increasing the fuel temperature. In ROX fuel, capture reaction rate of ^{148m}Pm, ^{154}Eu, ^{155}Eu, ^{167}Er nuclides increases with temperature, while in TOX and MOX fuels decreases. From the energy dependent neutron cross-section it was found that these FP nuclides have resonance within the neutron energy.0.2 eV to 1.0 eV, where the neutron spectrum of ROX fuel has large shift (Fig. 11.9.4).

In conclusions, FTC of ROX fuel becomes positive at EOL, because of lack of resonance absorption nuclides and large shift of thermal neutron spectrum that result positive FTR contribution of ^{241}Pu and ^{239}Pu. Also FP has large positive FTR contribution in ROX fuel.

References:

1) Shelley, A., Akie, H., T., Takano, H., Sekimoto, H.: "Parametric studies on Plutonium Transmutation Using Uranium Free Fuels in LWRs", Nuclear Technology, (submitted).

2) Akie, H., Takano, H., Muromura, T. and Nitani, N.: "A New Idea of Excess Plutonium Once-Through Burning in Light Water Reactor", Progress in Nuclear Energy, vol. 29 (Supplement), pp. 345 (1995).

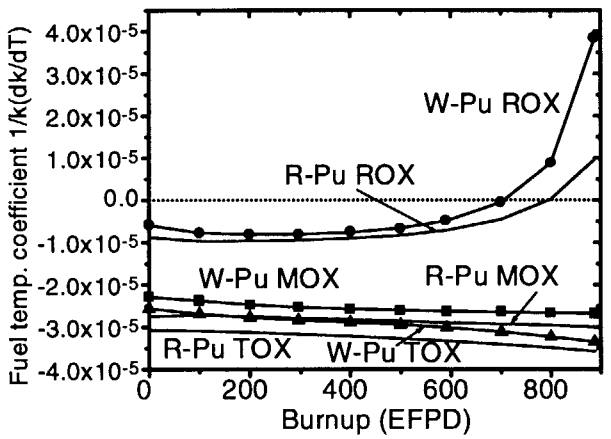

Fig. 11.9.1: Burnup dependent fuel temp. coefficient of W-Pu and R-Pu fuels.

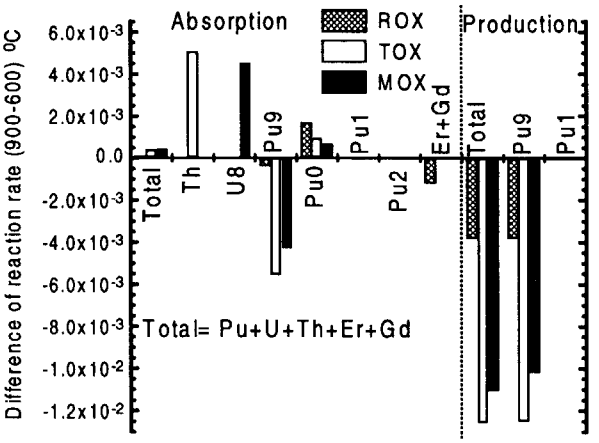

Fig. 11.9.2: Change of neutron reaction rate with temperature in W-Pu fuels at BOL.

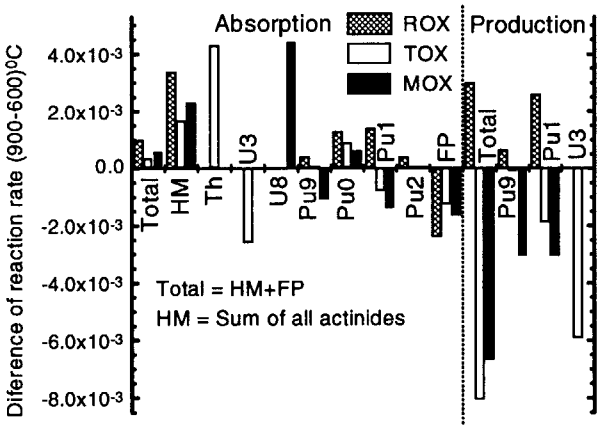

Fig. 11.9.3: Change of neutron reaction rate with temperature in W-Pu fuels at EOL.

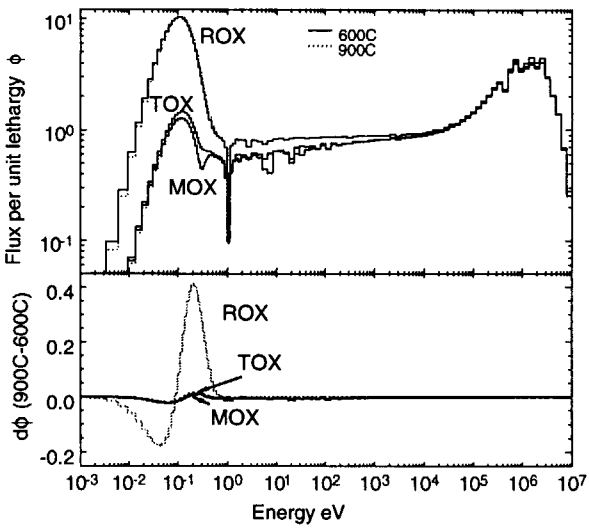

Fig. 11.9.4: Neutron spectra and its change with temperature in W-Pu fuels at EOL.

11.10 Environmental Safety of the Geologic Disposal of ROX and MOX Spent-fuels

H.Kimura, K.Kurmaoto, H.Matsuzuru, H.Takano and T.Muromura

(*E-mail*: kura1@nucef.tokai.jaeri.go.jp)

The plutonium ROX (Rock-like Oxide Fuel) spent fuels, as well as standard LWR spent fuels and high-level radioactive wastes from reprocessing plants, will be disposed into a deep geologic formation. In order to demonstrate the usefulness of ROX plutonium-burning system, a comparative study of environmental safety was carried out for the direct disposal of ROX and MOX spent fuels assuming the genetic geological condition of Japan. Safety analyses were performed on a case that 1 MTU of ROX and MOX spent fuels are disposed into a deep granite rock formation as shown in Fig. 11.10.1[1]. In the analyses, a computer code system GSRW[2] was used which was developed for a generic safety assessment of geologic disposal of HLW and which was composed of three interlinked models, a source term, a geosphere and a biosphere model. In the present study, two kinds of ROX fuels; PuO_2 [W or R]-stabilized ZrO_2-Al_2O_3 + 20 mol% ThO_2 (Zr/Th-W or -R) and PuO_2 [W or R]-stabilized ZrO_2-Al_2O_3 + 10 mol% UO_2 (Zr/U-W or -R) were analyzed, where "W" or "R" means weapons-grade or reactor-grade Pu, respectively. The committed effective dose equivalents due to the exposure pathway ingesting drinking water were calculated based on the groundwater migration scenario using the radionuclide inventory of the spent fuels discharged from PWR with burnup rate 0.18 MWd/cell and irradiation time 1000 days, and the conservative values of geochemical parameters. The radiological consequences of direct disposal of spent nuclear fuels were estimated only for actinides. Because crack data about spent nuclear fuel pellets of ROX and MOX are currently not available, and are very important to evaluate the quantities of gaseous radionuclides (I-129, Cl-36, etc.) which immediately releases to groundwater after failures of the container and fuel cladding material.

The results of committed effective dose equivalents obtained for actinides are as follows:

- **The committed dose equivalents for 4n+3 decay chain nuclides from ROX spent fuels are less than those from MOX spent fuels by 2 or more order of magnitude as shown in Fig. 11.10.2. The tendency is the same for the other decay chain of 4n+0, 4n+1 and 4n+2.**
- **Most important nuclide is Pa-231, and dose equivalents due to Pa-231 are 1.4 x 10^{-9} Sv/y at 1.8 x 10^{6} y (MOX-R) and 2.4 x 10^{-12} Sv/y (Zr/U-R) at 5 x 10^{6} y per 1 MTU. The peak value of 10^{-9} Sv/y per 1 MTU is not a negligible one, taking account of possible amount of disposed spent fuels which is order of 10^{4} MTU.**
- **The dose equivalents from R-Pu are larger than those from W-Pu, in any case, owing to the increase of amount of transuranic elements.**
- **Comparing the Zr/Th ROX with the Zr/U ROX, the dose equivalents from the Zr/U ROX fuels are slightly larger than those from Zr/Th ROX due to the increase of Pu-239 inventory.**

From the results, the ROX plutonium-burning system is superior to the plutonium recycle system using MOX fuels in the environmental safety for actinides.

1) SKB/KBS, Swedish Nuclear Fuel Supply Co.: KBS-3, "Final Storage of Spent Nuclear Fuel", (1983).

2) Kimura, H. et al., "A Generic Safety Assessment Code for Geologic Disposal of Radioactive Waste: GSRW Computer Code User's Manual", JAERI-M-92-161, (1992).

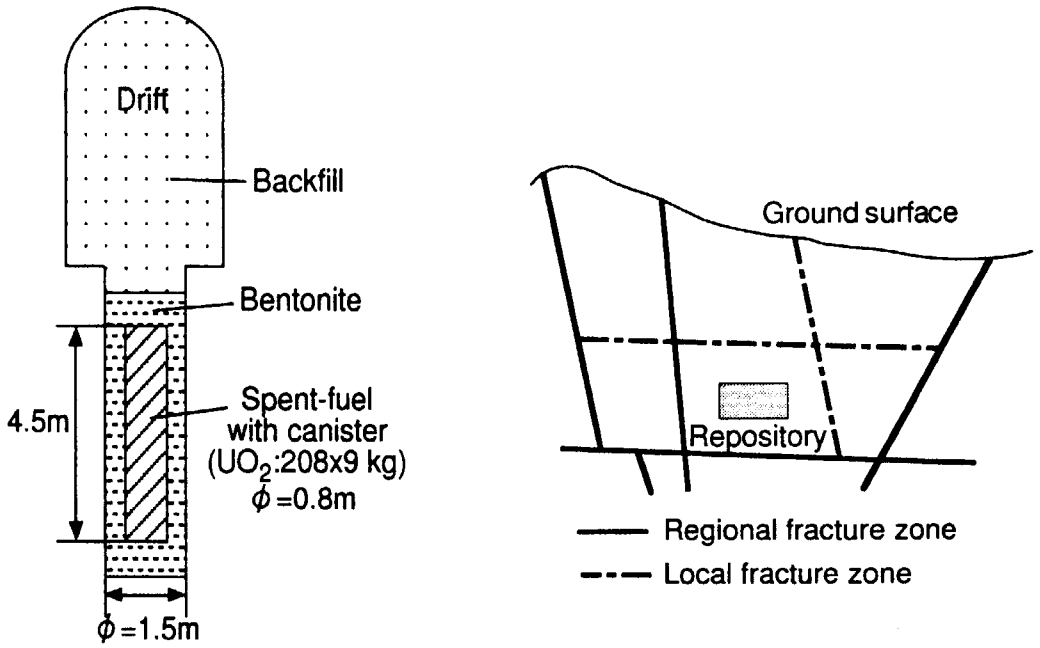

(a) Disposal concept (Sweden KBS-3)　(b) Location of a potential radioactive waste repository and fractured zones

Fig.11.10.1 Disposal and repository concept of this comparative study

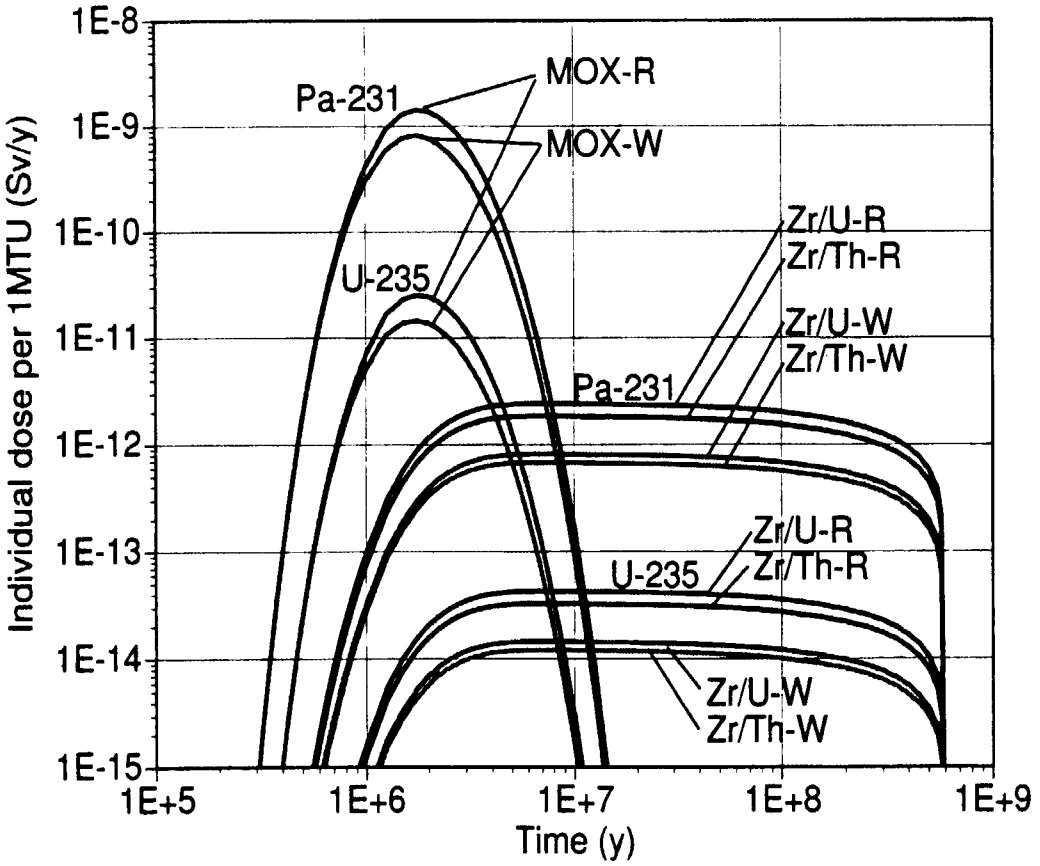

Fig.11.10.2 Individual dose from 4n+3 decay chain of disposed ROX and MOX spent fuels

12. Nitride Fuel and Related Pyrochemical Technology

The objective of this study is to develop nitride fuel cycle for advanced fast reactors and transmutation of long-lived minor actinides. The activity includes the fabrication and property measurements of nitride fuel, the irradiation tests of nitride fuel pins and the electrochemical study in LiCl-KCl eutectic melts in relation to pyrochemical reprocessing. In addition, some basic properties of actinide compounds are investigated in order to contribute to the preparation of database. In the fiscal year 1998, several experimental studies have been carried out as summarized below.

JAERI has proposed accelerator driven system (ADS) with sub-critical core with nitride fuel. Here plutonium-zirconium mixed nitride, (Pu,Zr)N, pellets were fabricated and characterized for the first time in order to evaluate the feasibility of nitride fuel for ADS. It was shown that the high-dense solid solution pellets were successfully fabricated with relative ease. On the other hand, vaporization behavior of neptunium mononitride, NpN, was investigated by Knudsen mass spectrometry where plutonium mononitride, PuN, was co-loaded in the same cell for controlling nitrogen partial pressure. From the temperature dependence of Np(g) pressure, Gibbs free energy of formation of NpN, ΔG_f(NpN(s)), was evaluated.

Several electrochemical measurements in LiCl-KCl eutectic melts were carried out in order to examine the dissolution and deposition behavior of actinides on a solid electrode. Information on the redox potential, the reduction mechanism, the effect of underpotential deposition and so on was obtained. Then several pieces of NpN and PuN pellets were anodically dissolved in LiCl-KCl eutectic melts and the recovery of the actinide metals on the solid cathode was demonstrated. Furthermore, the normal pulse voltammetry was applied to the determination of actinide concentration in the molten chlorides. It was shown that the method is a promising one for on-line monitoring of actinides in the region investigated.

Basic properties of actinide bearing oxides were also measured in this fiscal year. The temperature factor of ThO_2, NpO_2 and PuO_2 was determined by high-temperature X-ray diffractometry, from which Debye temperature and Grüneisen constant of these compounds were evaluated by analyzing the results. On the other hand, vaporization behavior of Pu and Np complex oxides with alkaline-earth metals was investigated. The perovskite-type oxides, $BaPuO_3$, $SrPuO_3$ and $BaNpO_3$, were prepared and subjected to the vapor pressure measurements. Principal vapor species identified were Ba(g) and BaO(g) for $BaPuO_3$ and $BaNpO_3$, while only Sr(g) for $SrPuO_3$. From their temperature dependences, standard enthalpy of formations, ΔH_f(298), were determined by thermodynamic treatments.

12.1 Fabrication and Characterization of (Pu,Zr)N Solid Solution Pellets

Y. Arai, K. Nakajima and Y. Suzuki
(*E-mail*: arai@popsvr.tokai.jaeri.go.jp)

JAERI has proposed the accelerator driven system (ADS) for transmutation of minor actinides (MAs) and long-lived fission products (LLFP). A sub-critical core of the ADS is to be constituted by nitride fuel containing MAs as a principal component[1]. A tentative fuel composition of Pb-Bi cooled ADS is (MAs,Pu,Zr)N in which Pu is added to control core efficient multiplication coefficient nearly constant at ~0.95 and ZrN serves as an inert matrix. The present study concerns fabrication and characterization of (Pu,Zr)N pellets and aims at providing basic information for evaluating feasibility of nitride fuel for the ADS.

Powder mechanical blending manner was adopted for the fabrication of (Pu,Zr)N pellets and plutonium concentration was chosen at 40 and 60 wt.%. Plutonium nitride was prepared by carbothermic reduction of PuO_2 and ZrN powder (purity; >99.5%) was obtained from CERAC Inc. The powders of PuN and ZrN were mixed at Pu/(Pu+Zr) ratios of 0.234 (Pu; 40 wt.%) and 0.420 (Pu; 60 wt.%), followed by compacting into thin disks and heating in N_2-H_2 mixed gas stream at 1673 K for homogenization. After repeating these procedures, mixing, compacting and heating, by three times, the disks were ground, compacted into green pellets and sintered in Ar gas stream at 2003 K. Finally, the pellets were heated in N_2-H_2 mixed gas stream at 1673 K again for the control of stoichiometry. A flowsheet for fabrication mentioned above is shown in Fig. 12.1.1. All the fabrication process was carried out in the gloveboxes with high purity inert gas atmosphere.

In order to clarify the characteristics of the products, X-ray diffraction analysis, chemical analysis for nitrogen, oxygen and carbon, and metallographic examination were carried out in addition to bulk density measurement. The results for PuN+ZrN and PuN pellets are summarized in Table 12.1.1.

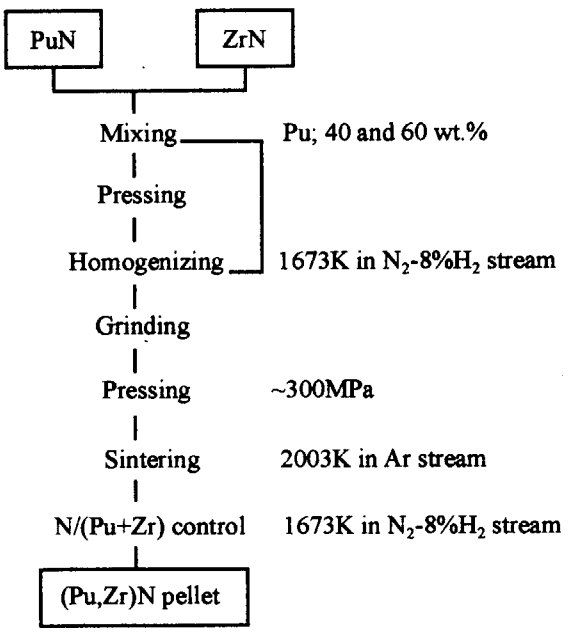

Fig. 12.1.1 Flowsheet for fabrication of the pellets

The formation of solid solution was confirmed from the X-ray diffraction pattern as shown in Fig. 12.1.2. Although a small amount of CaF_2-type oxide phase was identified as a second phase, it decreased with Pu content and was not identified in case of PuN. The lattice parameters of (Pu,Zr)N almost followed the Vegard's law between PuN and ZrN. There has been no experimental result for mutual solubility of PuN and ZrN, the present results supported the proposition of Benedict who predicted the solubility of solid fission product in actinide mononitride based on the relative lattice parameter difference[2].

Table 12.1.1 Typical characteristics of the PuN+ZrN and PuN pellets

Composition	Chemical analysis			X-ray diffraction		Density
	Nitrogen	Oxygen (wt.%)	Carbon	Phases	Lattice parameter (pm)	(%T.D.)
PuN+ZrN [1]	9.15	0.94	n.d. [3]	(Pu,Zr)N small $(Pu,Zr)O_2$	464.3	95
PuN+ZrN [2]	7.95	0.44	0.25	(Pu,Zr)N small $(Pu,Zr)O_2$	471.2	90
PuN	5.57	0.04	0.03	PuN	490.5	96

1) Pu content is 40 wt.% in nominal composition.
2) Pu content is 60 wt.% in nominal composition.
3) Not determined.

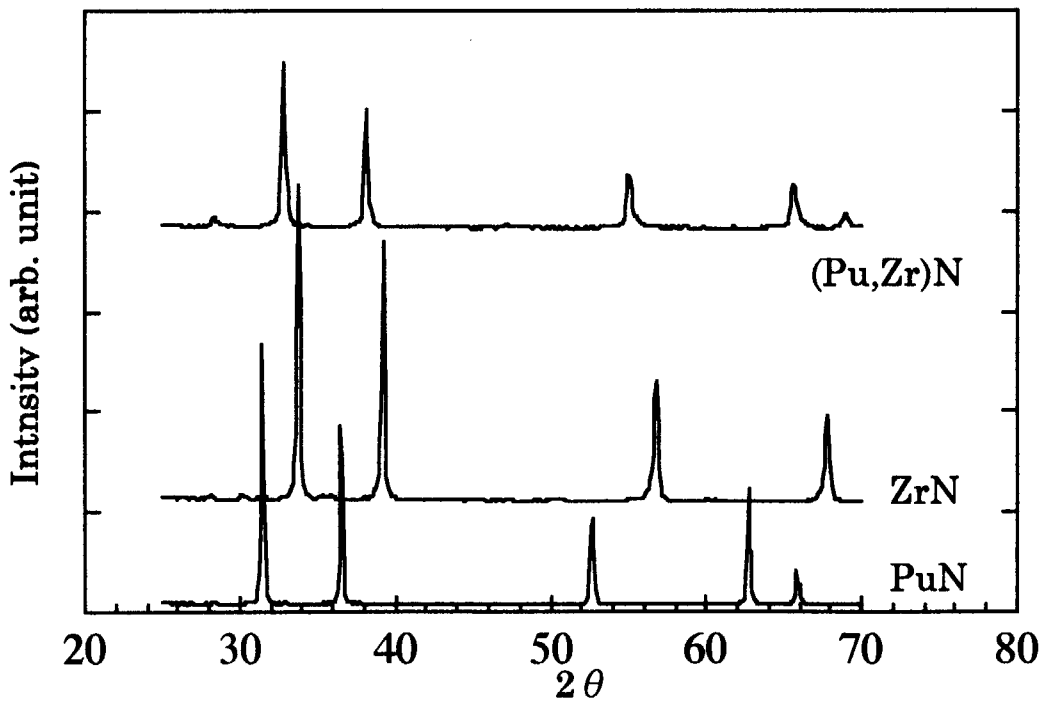

Fig. 12.1.2 X-ray diffraction pattern of (Pu,Zr)N pellet and those of PuN and ZrN

The results of chemical analysis showed that the impurity contents in the PuN+ZrN pellets were apparently higher than those in PuN. Especially the oxygen contents increased rapidly with ZrN content. So it was considered that most of oxygen impurity was derived from the ZrN powder. Namely, a large amount of oxygen might be included in the starting material or picked up during the preparation process. Some oxygen may be dissolved in nitride phase, but most of them are considered to be existing in oxide phase since the lattice parameters of (Pu,Zr)N almost followed the Vegard's law. Carbon impurity in the PuN+ZrN pellets was also considered to be derived from the ZrN powder. Assuming that oxygen is entirely included in the oxide phase and carbon dissolved in (Pu,Zr)N, and no segregation of Pu and Zr between the nitride and oxide phases, the composition of the PuN+ZrN pellet with 60 wt.% of Pu is calculated to be $0.98(Pu,Zr)N_{0.97}C_{0.03} + 0.02(Pu,Zr)O_2$, for example.

Bulk densities were obtained from the dimension and weight of the pellets. Theoretical densities were determined from the lattice parameters. High dense pellets could be prepared with relative ease in this case. Microstructures of the PuN+ZrN (Pu; 40 wt.%) and PuN pellets were shown in Fig. 12.1.3. It is seen that they have the similar grain size of 7-8 μm. In contrast to single-phase structure of PuN pellet, small "gray" oxide precipitates were observed among (Pu,Zr)N matrix in the PuN+ZrN pellet.

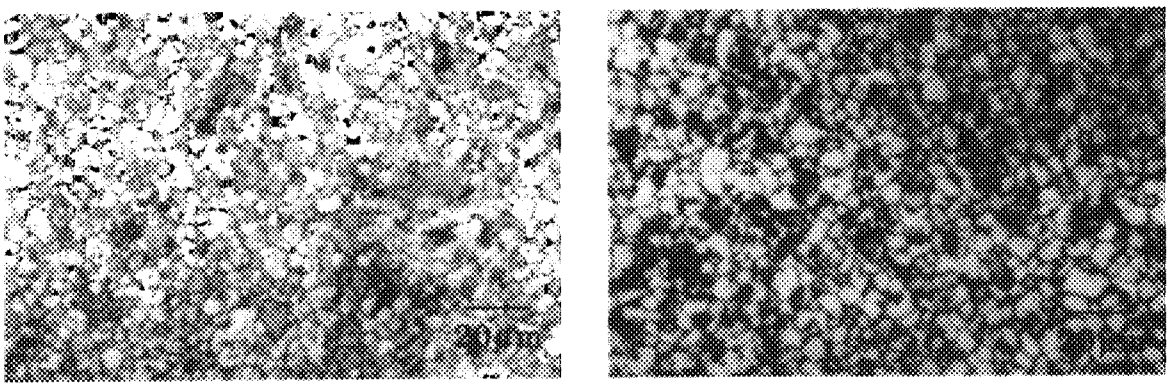

Fig. 12.1.3 Microstructures of PuN (left) and PuN+ZrN (right) pellets with 40 wt.% of Pu

In this study high dense (Pu,Zr)N solid solution pellets were fabricated and well characterized. Although many properties have to be examined hereafter, the present results gave some affirmative information for the use of nitride sub-critical core in ADS.

References

1) Mukaiyama, T., et al., 5th OECD/NEA Information Exchange Mtg. on P&T, Mol, Nov. 25-27, 1998.

2) Benedict, U., Euratom Report EUR-5766 EN (1977).

12.2 Vaporization Behavior of NpN Coloaded with PuN

K. Nakajima, Y. Arai and Y. Suzuki
(*E-mail*: kuni@popsvr.tokai.jaeri.go.jp)

Solid solution of actinide mononitrides is considered as one of the promising fuel materials for advanced fast reactors[1] and actinide burning reactors[2]. However, information on their thermophysical properties is scarce. Among them, the vaporization behavior is essential for understanding the irradiation behavior of such a material at elevated temperatures. The authors previously investigated the vaporization behavior of NpN(s) by means of a mass spectrometer equipped with a Knudsen-cell in the temperature range of 1690-2030K, where it was indicated that NpN(s) may decompose into liquid Np metal, Np(l), and N_2(g) as UN(s) does[3]. Further, the Gibbs energy of formation of NpN(s) was evaluated in this temperature range using the N_2(g) pressure over NpN(s)+Np(l) derived by extrapolating the experimental data given by Olson and Mulford[4]. But the temperature range where Olson and Mulford measured the N_2(g) pressure was much higher, from 2480 to 3100K. So we have carried out a mass-spectrometric study on NpN(s) accompanied by PuN(s) to confirm our previous results. It is well known that PuN(s) evaporates congruently[5]. In addition, the N_2(g) pressure over PuN(s) is expected to be about one order higher than that over NpN(s). When NpN(s) and PuN(s) coexist in a Knudsen-cell, the ambient nitrogen partial pressure could be governed by the nitrogen pressure derived from PuN (s). The purpose of this study is, therefore, to investigate the vaporization behavior of NpN(s)+PuN(s) and to ascertain that the free energy of formation of NpN(s) evaluated previously is reasonable.

The samples of NpN(s) and PuN(s) were prepared by carbothermic reduction of the dioxides, NpO_2 and PuO_2, respectively. The details of the preparation and characteristics of the starting materials were described in earlier papers[6,7]. The vapor pressures over the sample were measured in the temperature range from 1970 to 2070K by using a AGA-360 quadrupole mass spectrometer(ANELVA Co. Ltd.) equipped with a Knudsen-cell.

The determined partial pressures of Np(g) and Pu(g) are plotted in Fig. 12.2.1 as functions of the reciprocal absolute temperature. Figure 1 shows that the partial pressure of Pu(g) obtained in this study agrees well with that over PuN(s) given by Kent and Leary[8] and that the vapor pressure of Np(g) observed in this study is much lower than that of Np(g) over liquid Np metal given by Ackermann and Rauh[9], contrary to the case of mass-spectrometric measurement of NpN(s)[3]. Since the partial pressure of Pu(g) agrees well with that in the case of congruent vaporization of PuN(s) and the vapor pressure of Np(g) suggests that no liquid phase occurs, the vaporization mechanism could be expressed by the following reactions;

$$NpN(s)=Np(g)+1/2N_2(g), \quad (1)$$
$$PuN(s)=Pu(g)+1/2N_2(g). \quad (2)$$

The partial pressure of $N_2(g)$ over NpN(s) is needed for obtaining the Gibbs energy of formation of NpN(s) besides the partial pressure of Np(g). So the partial pressure of $N_2(g)$ over NpN(s)+PuN(s) was derived from the partial pressure of Pu(g) obtained in this study using the following relation based on the congruent vaporization of PuN(s)[5];

$$P_{N_2} = 0.5\sqrt{M_{N_2}/M_{Pu}}\,P_{Pu}. \quad (3)$$

The standard Gibbs energy of formation of NpN(s) was determined from the vapor pressure measured for Np(g), the pressure of $N_2(g)$ derived from eq.(3) and the Gibbs energy of formation of Np(g) obtained from the table given by Oetting et al.[10]. In Fig. 12.2.2 the Gibbs energy of formation of NpN(s) is plotted, together with the previously reported one[3] and those of UN(s) and PuN(s) given by Matsui and Ohse[5]. The least-squares treatment of the data gives the following equation:

$$\Delta_f G(T)(NpN,s)(J/mol)=-\ 269000\pm17000+74.0\pm8.4T. \quad (4)$$

The Gibbs energy of formation of NpN(s) obtained in this study agrees well with that reported previously[3]. Further it was reconfirmed that Gibbs energy of formation of NpN(s) is located between those of PuN(s) and UN(s).

References

1) Hj. Matzke, "Science of Advanced LMFBR Fuels", North-Hollands, Amsterdam(1986).

2) T. Mukaiyama, H. Yoshida and Y. Gunji, Proc. Int. Conf. on Fast Reactor and Related Fuel Cycles, Kyoto, 1991, Paper 19-6.

3) K. Nakajima, Y. Arai and Y. Suzuki, "Vaporization behavior of neptunium mononitride", J. Nucl. Mater., 247, 33 (1997).

4) W.M. Olson and R.N.R. Mulford, "The Melting point and Decomposition Pressure of Neptunium Mononitride", J. Phy. Chem., 70, 2932 (1966).

5) T. Matsui and R.W. Ohse, "Thermodynamic properties of uranium nitride, plutonium nitride and uranium-plutonium mixed nitride", High Temp. High Pressures, 19, 231 (1987).

6) Y.Suzuki, Y. Arai, T. Iwai and T. Ohmichi,"Lattice Parameter of UN-PuN Solid Solution", J. Nucl. Sci. Technol., 28, 689 (1991).

7) Y.Suzuki, Y. Arai, Y. Okamoto and T. Ohmichi, "Preparation of Neptunium Mononitride by Carbothermic Reduction", J. Nucl. Sci. Technol., 31, 677 (1994).

8) R.A. Kent and J.A. Leary, "Mass Spectrometric Studies of Plutonium Compounds at High Tempratures IV. The Vaporization of PuN", High Temp. Sci., 1, 176 (1969).

9) R.J. Ackermann and E.G. Rauh, "The thermodynamics of vaporization of neptunium and plutonium", J. Chem. Thermodynamics, 7, 211 (1975).

10) F.L. Oetting, M.H. Rand and R.J. Ackermann, The Chemical Thermodynamics of Actinide Elements and Compounds, part 1: The Actinide Elements (IAEA, Vienna, 1976) p.87.

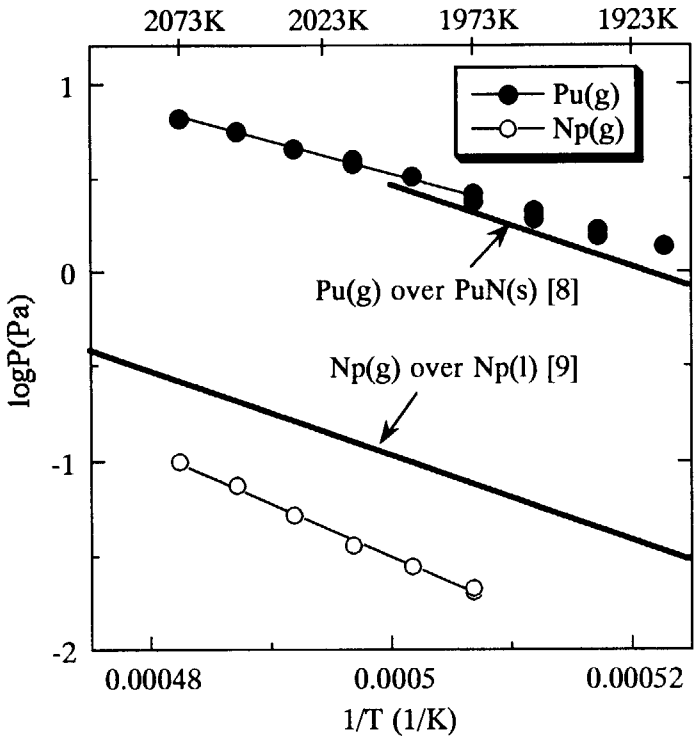

Fig. 12.2.1 Temperature dependence of the partial pressures of Np(g) and Pu(g) over NpN(s)+PuN(s)

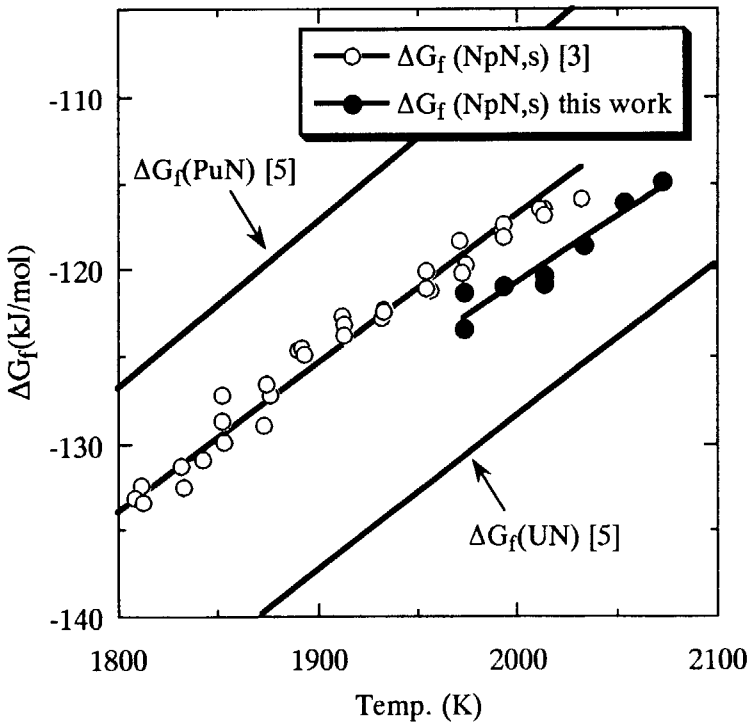

Fig. 12.2.2 The free energy of formation of NpN(s) compared with that of UN(s) and PuN(s)

12.3 Electrochemistry of U, Np and Pu in LiCl-KCl Eutectic Melts

O. Shirai, Y. Sakamura*, T. Iwai and Y. Suzuki
(*E-mail*: shirai@popsvr.tokai.jaeri.go.jp)

A pyrochemical method is proposed as an advanced reprocessing technique of nuclear fuels such as metal[1] and nitrides[2, 3]. In the electrorefining process, actinide elements are dissolved at an anode and deposited again at a cathode. There are some studies on the electrode reaction of U^{3+}/U in molten chloride but little information on those of Np^{3+}/Np and Pu^{3+}/Pu. In addition, a meaningful comparison of these reactions is difficult because of the variety of the experimental conditions including electrolyte composition, solute concentration, temperature, reference electrode and working electrode. In the present study, the electrode reactions of U, Np and Pu in the LiCl-KCl eutectic salt were investigated by cyclic voltammetry in the temperature range from 723 to 823 K[4].

In the voltammetric studies, Mo and W wires of 1.0 mm in diameter were used as working electrodes in the electrochemical cell. The wires were encased in alumina tubes in such a way that an apparent surface area of 0.479 cm^2 was exposed to the molten salt. A Ag/AgCl electrode with 1.0 wt % AgCl in the LiCl-KCl eutectic salt was used as a reference electrode. A glassy carbon rod was used as a counter electrode. The temperature of the molten salt was measured by using a calibrated Chromel-Alumel thermocouple. Actinide trichlorides were prepared by the chlorination of those metals or Pt alloys with $CdCl_2$ in Cd/LiCl-KCl system at 773 K. These salts were added into LiCl-KCl eutectic melt in order to obtain adequate concentrations of UCl_3, $NpCl_3$ and $PuCl_3$. The preparation and voltammetric measurements were carried out in a glovebox with high purity Ar gas atmosphere with the concentrations of moisture and O_2 of less than 2.0 ppm.

Figure 12. 3. 1 indicates a cyclic voltammogram obtained with 0.454 wt% UCl_3 in LiCl-KCl eutectic salt at the W working electrode at 773 K. Two cathodic (a1, a2) and two anodic (b1, b2) peaks were observed. The peaks of a1 and b1 correspond to a redox couple of U^{3+}/U. The potential differences between a1 and b1 were twice or three times larger than the theoretical values, and increased with the scan rate. These characteristics suggest that the redox of U^{3+}/U may be quasi-reversible. The potentials where the cathodic currents ascended in the voltammograms with 0.454 wt% UCl_3 were -1.430, -1.420 and -1.410 V at 723, 773 and 823 K, respectively, while those with 0.957 wt% UCl_3 were -1.425, -1.415 and -1.400 V, regardless of the scan rate. The peak heights were approximately proportional to the concentration of UCl_3, and there exists an approximately linear relationship between the peak current of a1 and the square root of the potential scan rate. This indicates that the reduction of

*Nuclear Fuel Cycle Department, Central Research Institute of Electric Power Industry

U^{3+} may be nearly diffusion-controlled. The cathodic current peaks at 823 K were about 1.3 times larger than those at 723 K. This temperature dependence might be compatible with the fact that this reaction is controlled by diffusion of U^{3+} in the LiCl-KCl eutectic melt, because the diffusion coefficient of U^{3+} in the melt at 823 K is 2.0 times larger than that at 723 K and the peak current is proportional to the square root of the diffusion coefficient. On the other hand, the peak heights of a2 and b2 were proportional to the scan rate. These peaks depended on the working electrode materials but not on the concentration of UCl_3. These peaks might be attributable to monolayer adsorption of U and its desorption, which is generally called as underpotential deposition. The potential can be correlated to the work functions of working electrode material and depositing metal. It is considered that the potential differences between b1 and b2 with the W were similar to that with the Mo working electrodes since the work function of W(4.55 eV) is approximately equal to that of Mo(4.6 eV).

As for the electrode reaction of Np, the cathodic and the anodic peaks (a and b) corresponding to a redox couple of Np^{3+}/Np were observed as shown in Fig. 12. 3. 2. There exists an approximately linear relationship between the peak currents of a and the square root of the potential scan rates. This indicates that the reduction may be nearly diffusion-controlled of Np^{3+} in the melt. But the peak currents of b did not increase linearly and the broad peak appeared in the positive potential range between -1.5V and -0.5V with the increase of the scan rate. These characteristics suggest that the rate of oxidation of Np to Np^{3+} may be slow and deposited Np should be stabilized in electrode materials by alloy formation.

A cyclic voltammogram with 0.544 wt% $PuCl_3$ in the LiCl-KCl eutectic salt at 773 K is indicated in Fig. 12. 3. 3. Two cathodic (a1, a2) and two anodic (b1, b2) peaks were observed. The peaks of a1 and b1 are attributed to a redox couple of Pu^{3+}/Pu. The reduction of Pu^{3+} is also nearly diffusion-controlled and quasi-reversible in analogy with the electrode reaction of U. The peak currents of a1 with 0.544 wt% $PuCl_3$ were about half of those with 1.00 wt% $PuCl_3$. The potentials where the cathodic currents ascended in the voltammograms were shifted by 0.025±0.005 V for each 50 K rise. The cathodic current peaks at 823 K were about 1.6 times larger than those at 723 K. This can be explained on the base of diffusion-controlled reaction since the diffusion coefficient of Pu^{3+} in LiCl-KCl eutectic at 823 K is 2.2 times larger than that at 723 K. The peaks of a2 and b2 which were attributable to the underpotential deposition of Pu were observed as well as those in the case of U.

References

1) J. P. Ackerman, Ind. Eng. Chem. Res., 30 (1991) 141.
2) Y. Arai, *et al.*, Proc. on Internat. Conf. on Evaluation of Emerging Nucl. Fuel Cycle Systems, Global '95, Versailles, Sept. 11-14, (1995) 538.
3) N. Kobayashi, *et al.*, J. Am. Ceram. Soc., 78 (1995) 2279.
4) O. Shirai, et al., J. Alloys Comp., 271-273 (1998) 685.

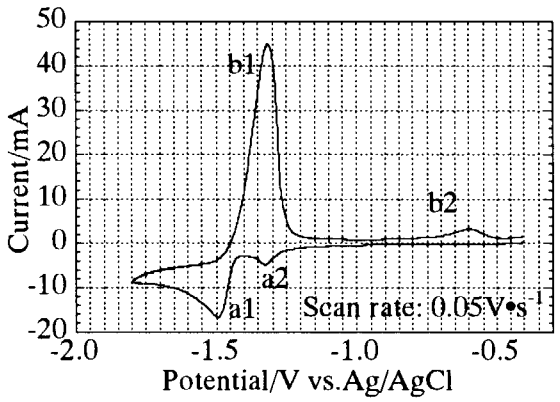

Fig. 12. 3. 1. Cyclic voltammogram of UCl_3 in the LiCl-KCl melt at 773 K.

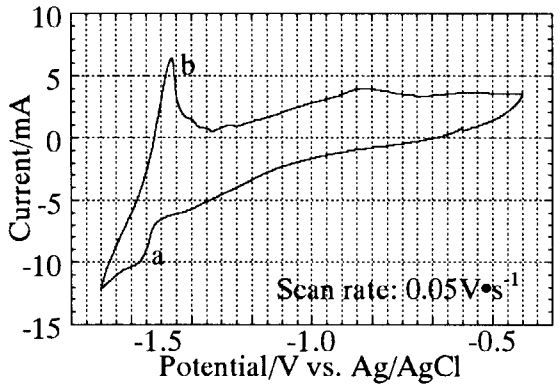

Fig. 12. 3. 2. Cyclic voltammogram of $NpCl_3$ in the LiCl-KCl melt at 773 K.

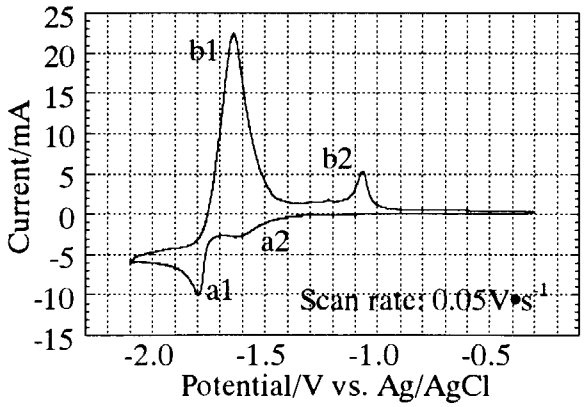

Fig. 12. 3. 3. C yclic voltammogram of $PuCl_3$ in the LiCl-KCl melt at 773 K.

12.4 Electrolysis of PuN and NpN in LiCl-KCl Eutectic Melts

O. Shirai, Y. Sakamura*, M. Iizuka*, T. Iwai, K. Shiozawa and Y. Suzuki
(*E-mail*: shirai@popsvr.tokai.jaeri.go.jp)

UN and PuN are potential advanced fuels having an advantage in Pu breeding or actinide burning because of its high thermal conductivity, high melting point and high metal density[1]. In JAERI, the application of the pyrochemical process to the nitride fuel cycle system has been studied[2]. In the pyrochemical reprocessing, actinide nitrides would be dissolved at an anode and actinide metals might be electrodeposited on a cathode at the same time. In the present work, the electrochemical behaviors of PuN and NpN in the melt and the results on the electrolysis were reported[3,4].

PuN and NpN were prepared by carbothermic reduction of PuO_2 and NpO_2, respectively[5]. $PuCl_3$ and $NpCl_3$ were prepared by the chlorination of $PuPt_3$ and $NpPt_3$ with $CdCl_2$ in the system of liquid Cd/LiCl-KCl eutectic melt at 773 K. The scheme of the electrochemical cell used is shown in Fig. 12. 4. 1. A cage made of W (99.95 %up) was served as a working electrode. A few pieces of PuN or NpN pellets were placed in the W cage. A counter electrode used was a wire made of Mo (99.95 %up). An Ag/AgCl electrode with 1.00 wt.% of AgCl in the LiCl-KCl eutectic salt was used as a reference electrode. The temperature of the molten salt was measured by a calibrated Chromel-Alumel thermocouple and controlled at 773 K. The electrolysis of PuN or NpN was performed under potential- or current-control by using a potentio/galvanostat. After the quantity of electricity reached 100-300 C, the Mo electrode was taken out from the salt. Since the electrodeposits were mixtures of Pu or Np metal and the salt, they were put in an alumina crucible and heated at 1073 K for 3.6 ks. The slag was separated from the mixture and the residue was analyzed by X-ray diffractometry. The preparation and electrochemical measurement were carried out in a glovebox with high quarity Ar gas atmosphere with the concentrations of moisture and O_2 of less than 2 ppm.

The redox potential of Pu^{3+}/Pu in the LiCl-KCl eutectic salt containing 0.54 wt.% $PuCl_3$ at 773K is -1.73±0.01 V *vs.* the Ag/AgCl reference electrode[6]. It means that the potential difference between the Mo and reference electrodes must be -1.8 V or lower in order to recover Pu metal on the Mo working electrode. Therefore, in the potential-controlled method, the constant potential of -2.00 V was applied between the Mo and reference electrodes. The current rose up to about -60 mA at the beginning of the electrolysis, but quickly fell down to -10±1 mA. It may be caused by the diffusion of Pu^{3+} in the salt. Then, the current increased gradually to -110±10 mA. Before the electrolysis, the anode potential showed a constant value, -0.880±0.005 V, which was the equilibrium potential. The anode potential was shifted more positively to facilitate the dissolution of PuN when -2.0 V was applied between the Mo and reference electrodes, and PuN started to be dissolved as Pu^{3+}. The change of the electric current during

*Nuclear Fuel Cycle Department, Central Research Institute of Electric Power Industry

the electrolysis might be caused by the increase of cathode area accompanied by the accumulated deposition of Pu. The anode potential shifted more positively with the increase of current, which can be understood from the relation between the current and the anode potential. Figs 12. 4. 2-a and -b show the deposits on the Mo electrodes in the potential-controlled method and those in the current-controlled method. In the current-controlled method, the cathode and anode potentials during the electrolysis were -1.73±0.02 V and -0.70±0.03 V, respectively. From the comparison of the results of voltammetric analysis, it was suggested that PuN was always dissolved at the anode and Pu was deposited at the cathode.

The electrolysis of NpN was carried out at constant current of –20 mA. The electrodeposits are shown in Fig. 12. 4. 3. The potential of the anode was gradually changed from -0.64±0.01 V to -0.32 ±0.01 V during the electrolysis. On the other hand, the potential of the cathode was changed from -2.15 ±0.05V to –1.64±0.01V immediately at the beginning of the electrolysis, and thereafter the cathode potential remained approximately constant. Because the standard redox potential of Np(III)/Np(0) at 773K is reported as -1.448V vs. the Ag/AgCl reference electrode with 0.487 mol% AgCl in the melt[7], the equilibrium potential of Np(III)/Np(0) at 773K could be assumed as -1.592V in the present system. In the electrolysis, Np metal was successfully recovered at the cathode while NpN was continuously dissolved at the anode.

After the separation process by heating the electrodeposits, Pu and Np metals were identified as a major phase in the product by X-ray diffraction analysis, but minor chloride phases were still observed. This indicates that gram-order of Pu and Np metals were successfully recovered on the solid cathode by the electrolysis of PuN and NpN, respectively, in the LiCl-KCl eutectic salt. These results suggest a possibility for practical use of pyrochemical reprocessing for nitride fuels.

References

1) H. Blank, in: Materials Science and Technology, Vol. 10A, Nuclear Materials, VCH, Weinheim, 1994, pp. 191-363.

2)Y. Arai, et al., in: Proc. Int. Conf. on Future Nuclear Systems (GLOBAL'97), Vol. 1, Yokohama, Japan, Oct. 5-10, 1997, pp.664-669.

3) O. Shirai, et al., J. Nucl. Mater. in press.

4) O. Shirai, et al., to be submitted to J. Nucl. Sci. Technol.

5) Y. Suzuki, et al., J. Nucl. Sci. Technol. **31**(1994) 677-680.

6) J. J. Roy, et al., J. Electrochem. Soc. **143** (1996) 2487-2492.

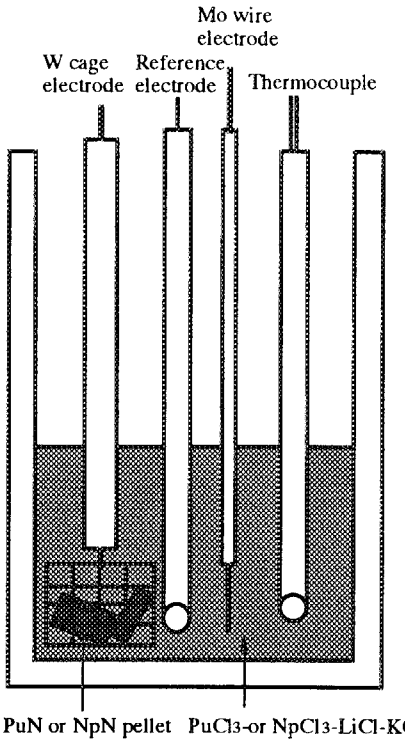

Fig. 1. Electrochemical cell for the electrolysis of PuN or NpN.

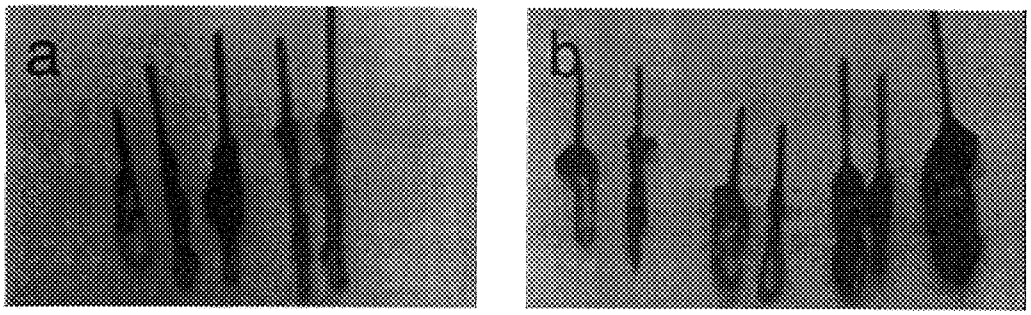

Fig. 2. Electrodeposits at Mo electrodes obtained by the electrolysis of PuN
a: potential-controlled electrolysis, b: current-controlled electrolysis.

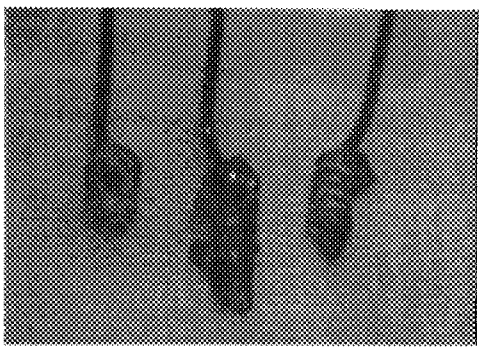

Fig. 3. Electrodeposits at Mo electrodes obtained by the electrolysis of NpN.

12.5 Determination of U/Pu Concentration in Molten Chlorides by Normal Pulse Voltammetry

M. Iizuka*, O. Shirai, T. Iwai and Y. Suzuki
(*E-mail :* iizuka@criepi.denken.or.jp)

In pyrometallurgical reprocessing of nuclear fuels, molten chlorides are to be used as solvent. In this study, applicability of two electroanalytical methods (SWV : Square Wave Voltammetry and NPV : Normal Pulse Voltammetry) to on-line monitoring of concentrations of actinide elements in molten lithium chloride-potassium chloride eutectic mixture was evaluated.

Fig. 12.5.1 shows the potential wave forms applied to the working electrode, current sampling programs and final output in SWV and NPV. The parameters in the potential wave forms shown in Fig. 12.5.1 were optimized in preliminary study with rare earth elements. All the experiments were carried out in high purity argon atmosphere and at 773 K. Uranium chloride was prepared by oxidation of uranium metal with cadmium chloride in LiCl-KCl. Plutonium chloride was prepared by (i) carbothermal reduction of PuO_2 to PuN, (ii) $PuPt_3$ formation by the reaction between PuN and Pt, and (iii) oxidation of $PuPt_3$ with cadmium chloride in LiCl-KCl/liquid cadmium system. The working electrode was a tungsten wire of 1 mm in diameter. The counter electrode was a tantalum wire of 1 mm in diameter which was coiled to increase the surface area. A silver wire immersed in LiCl-KCl-1 wt% AgCl which was contained in a thin Pyrex glass tube was used as the reference electrode. Actual concentrations of uranium and plutonium were determined by ICP-AES of the sampled salts.

Results from SWV for LiCl-KCl-PuCl3 are shown in Fig. 12.5.2. Very distinct and sharp current peaks were obtained in the wide range of plutonium concentration in the molten salt. But the relation between the peak height and the plutonium concentration was not linear as shown in Fig. 12.5.3. This non-linearity is at present considered to be due to the accumulation of cathodic product on the surface of the working electrode in the course of the measurement.

Fig. 12.5.4 shows the voltammograms by NPV measured in the molten salt containing both uranium and plutonium. It is known by cyclic votammetry and so on that reduction of uranium and plutonium occurs at about -1.4 V and -1.7 V vs. Ag/AgCl, respectively. In Fig. 12.5.4, it is clearly shown that the reduction current for uranium and plutonium rise up at those potentials and that the height of the current increases according to the increase of concentration of each element in the salt.

In order to separate the NPV data into the components which come from reduction of uranium and plutonium, the current value was differentiated to the working electrode potential. The increase of reduction current is transformed to the clear peaks by differentiation as shown in Fig. 12.5.5. The tails of the peaks were determined as shown also in Fig. 12.5.5, and the limiting current of each reaction was defined as the current increase within the peak width. The limiting current determined in this way are plotted to the actual concentration in Fig. 12.5.6. Good linearity seen in this plot tells that NPV is a promising method for quantitative on-line monitoring of actinide concentration in the molten salt.

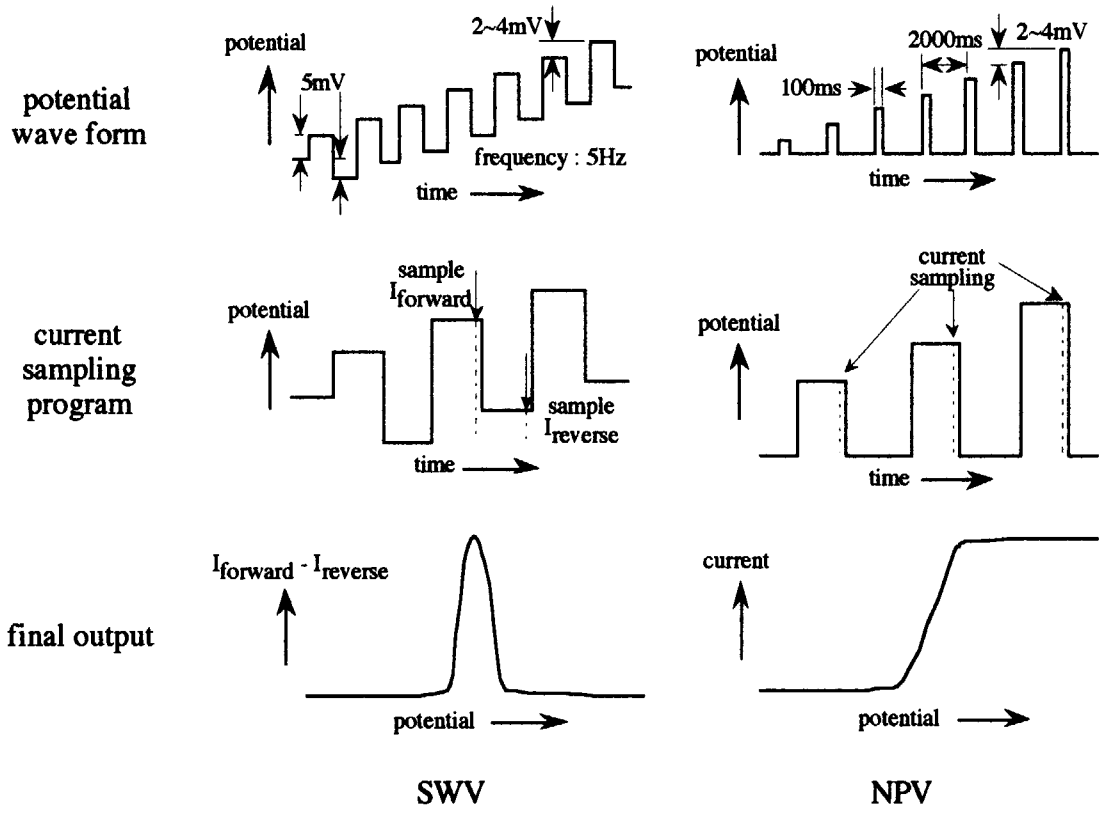

Fig. 12.5.1 potential wave form applied to workiing electrode, current sampling programs and final output in SWV and NPV.

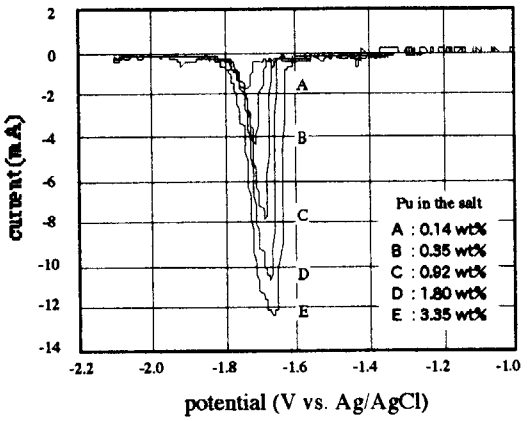

Fig. 12.5.2 SWVs for LiCl-KCl-PuCl3.

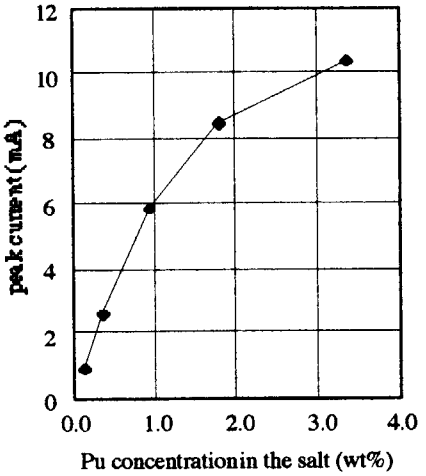

Fig. 12.5.3 relation between peak height in SWV and Pu concentration.

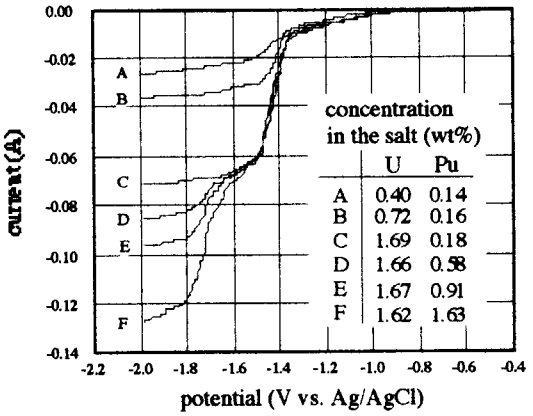

Fig. 12.5.4 NPVs for LiCl-KCl-UCl3-PuCl3.

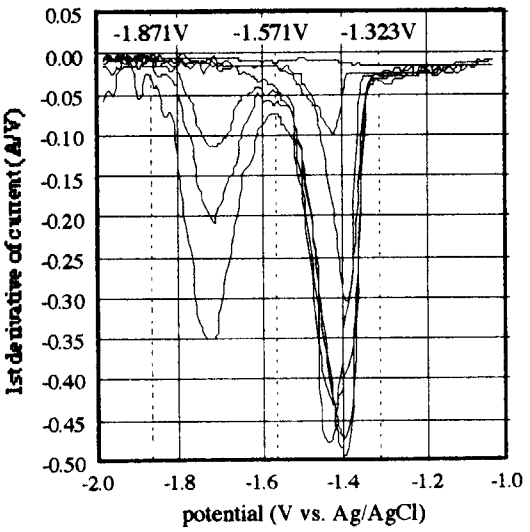

Fig. 12.5.5 differentiation of NPV data.

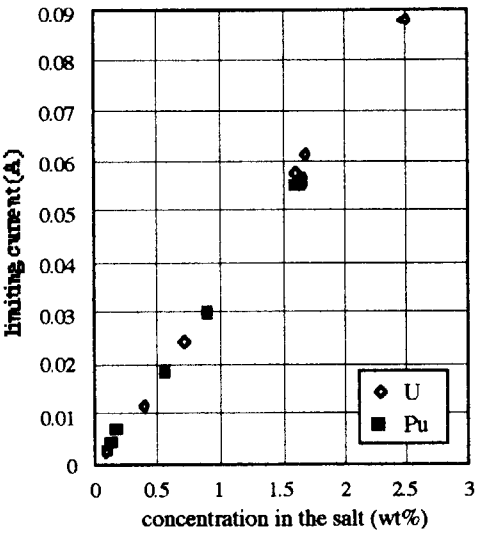

Fig. 12.5.6 relation between limiting current in SWV and U, Pu concentration.

12.6 Debye Temperature and Grüneisen Constant for Actinide Oxides

H. Serizawa, Y. Arai and Y. Suzuki
(*E-mail*: serizawa@popsvr.tokai.jaeri.go.jp)

The aim of the present study is to give the macroscopic factor for actinide oxides which is necessary to estimate thermal properties. We developed the simultaneous evaluation method of the Debye temperature, Θ_D, and Grüneisen constant, γ, using high temperature X-ray diffraction (XRD). XRD analysis has the advantage that the sample quantity is small (about 100 ~ 200 mg), which is well suited for the experimental treatment of the actinide compounds.

Evaluation of the temperature factor and Debye temperature

The XRD patterns of ThO_2, PuO_2 and NpO_2 have been measured at temperatures from room temperature up to 1174 K. The temperature factor of each component atom was calculated using Rietveld analysis code, "RIETAN", developed by Izumi [1]. Although we tried to refine the temperature factor for oxygen atom, B_o, it was difficult because of the small scattering factor. Thus, fixing the values of B_o to those reported for UO_2, we conducted the refinement only for the cation, B_M. The γ value was calculated from the temperature dependence of the non-corrected Θ_D with the contribution of anharmonic lattice vibrations. Θ_D was obtained through Paskin's correction [2] with the Grüneisen constant obtained in this work.

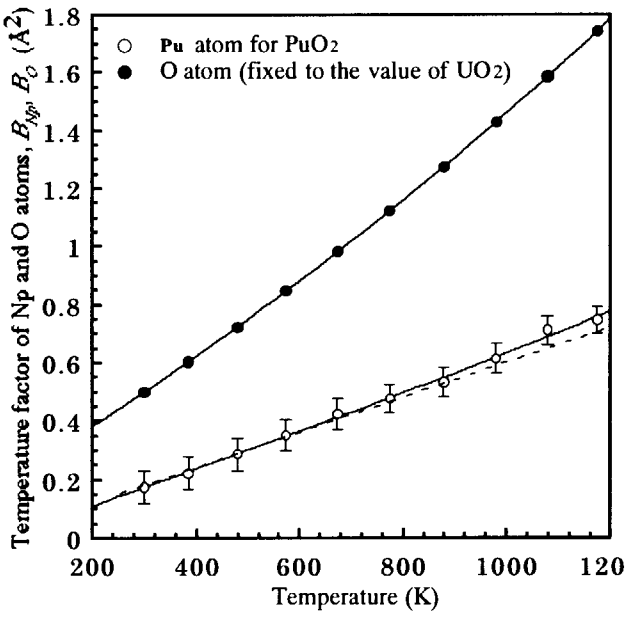

Fig. 12.6.1 Temperature factor for Pu and U atoms in PuO

Here, we show the outcome of the analysis for PuO_2 as a typical result. The values of the temperature factor for Pu, B_{Pu}, is plotted in Fig. 12.6.1 [3]. B_{Pu} increased with increasing temperature almost linearly in a low temperature region less than *ca.* 700 K. In a higher temperature region, however, the plotted data deviated from linearity in the upper direction. In a harmonic approximation, a frequency is independent of temperature, and so B_{Pu} should be almost proportional to T. This deviation indicates that the effect of the anharmonic vibration cannot be neglected especially at temperatures more than

ca. 700 K. Fig. 12.6.2 shows the temperature dependence of Θ_D calculated from B_{Pu} and B_o as a function of the temperature. Θ_D tends to decrease with increasing temperature. The reduction in Θ_D implies the contribution of thermal expansion arising from the anharmonic vibration that is not premised in the Debye theory. The temperature dependence of the Θ_D value for ThO_2 and NpO_2 is in analogy with that for PuO_2 [3, 4].

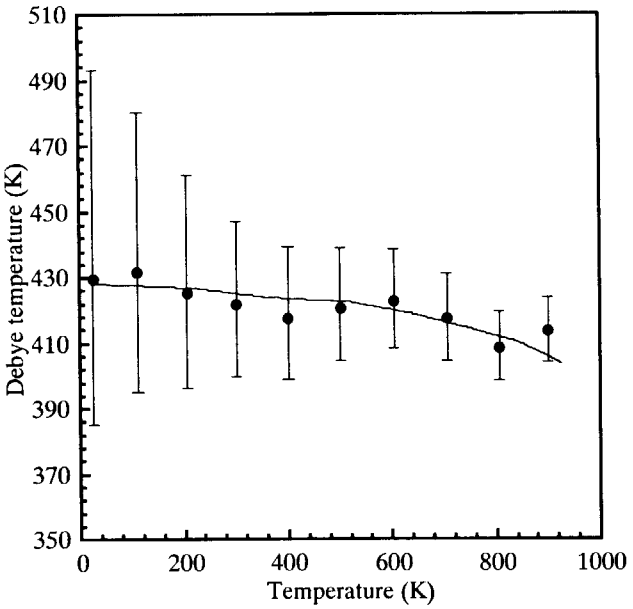

Fig. 12.6.2 Temperature dependence of the Debye temperature

Determination of the Grüneisen constant

The modification of the theory had been discussed by Paskin [2]. He indicated that the replacement of the absolute temperature T by the reduced temperature T' defined as $T'=T(V_T/V_{To})^{2\gamma}$, where V_T, V_{To} are the volume of the lattice at T and T_o, respectively. The Debye theory can be adjusted with his modification even at high temperature. Then, we tried to determine the γ value on the supposition that the value of Θ_D corrected by the Paskin's temperature modification was independent of the temperature [5]. If Θ_D is constant, Θ_D should be regarded as a function of γ. Fig. 12.6.3 shows the recalculated results of Θ_D for PuO_2 with correction by Paskin's modification. It can be seen that the value of the slope increases with elevating the value of γ; the differential coefficient of the fitted line changes from negative to positive in the vicinity of γ =2.0. The differential coefficient of the line increases linearly with increasing γ and becomes zero when the value of γ takes 1.62. The result means that if γ equals 1.62, the calculated Θ_D is nearly independent of the temperature.

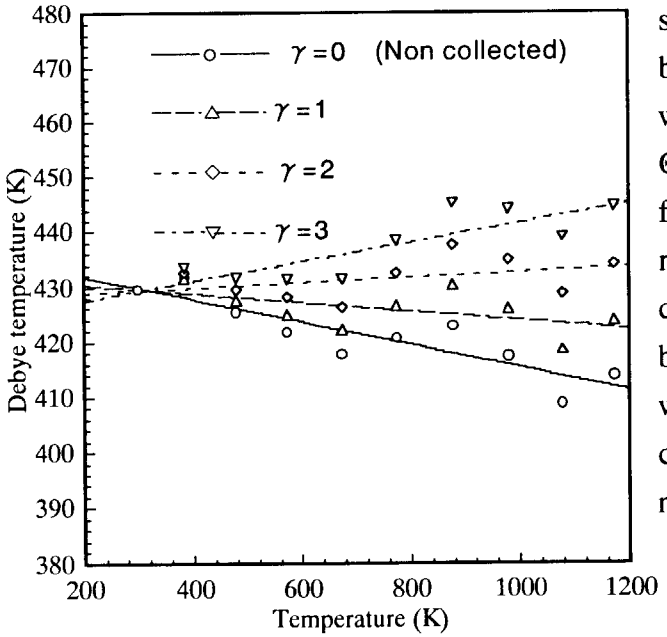

Fig. 12.6.3 Temperature dependence of the Debye temperature as a function of γ

Recalculation of the Debye temperature

The temperature dependence of Θ_D for PuO_2 corrected by the Paskin's modification with γ =1.62 is given in Fig. 12.6.4. The solid triangles in the figure show Θ_D calculated taking into account the inaccuracy in B_o. The estimated error in B_o was ± 15 %. It is evident that even though the inaccuracy in B_o must be taken into consideration, the change in the value of Θ_D obtained in this work is almost negligible. As is expected from Fig. 12.6.4, Θ_D for PuO_2 was almost constant and equals 426 K [4].

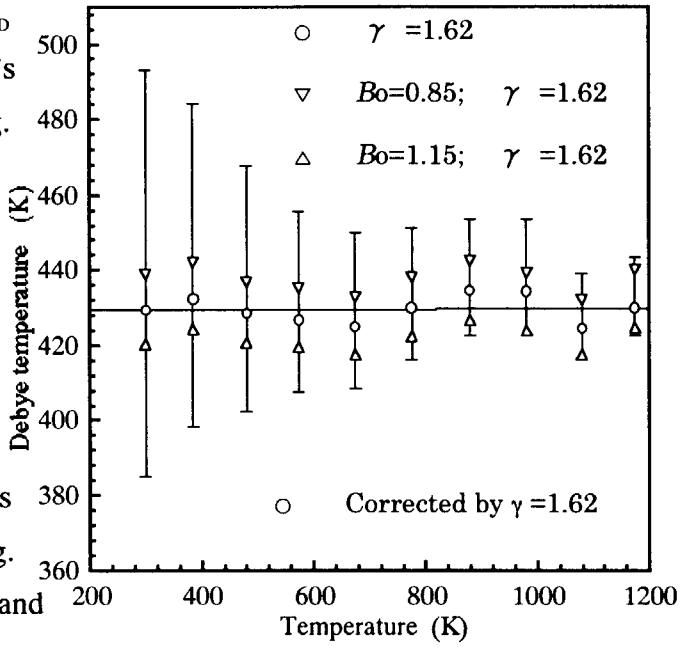

Fig. 12.6.4 Recalculated Debye temperatue with Grüneisen constant

The values of Θ_D and γ obtained in the present study are summarized in Table 12.6.1.

Table 12.6.1 Debye temperature and Grüneisen constant for a series of actinide oxides

Compounds	Debye temperature (K)	Grüneisen constant
ThO_2	463 [4]	1.51 [4]
PuO_2	426 [4]	1.62 [4]
NpO_2	435 [3]	1.93 [3]

References

1)F. Izumi, (R. A. Young, ed.), Vol. Chap. B. Oxford Univ. Press, Oxford, 1993.
2)A. Paskin, Acta. Cryst. 10(1957)667.
3)H. Serizawa, Y. Arai, M. Takano and Y. Suzuki, J. Alloys Comp. 282(1999)17.
4)H. Serizawa, Y. Arai and Y. Suzuki, submitted to J. Nucl. Mater. .
5)B. T. M. Willis, Proc. Roy. Soc. (London) A274(1963)134.

12.7 Vaporization Behavior of Pu and Np Complex Oxides with Alkaline-earth Metals

K. Nakajima, Y. Arai and Y. Suzuki
(*E-mail*: kuni@popsvr.tokai.jaeri.go.jp)

Multicomponent perovskite-type oxide phase with composition ABO_3(s) is generally found in irradiated oxide fuels[1]. Here A represents fission-produced elements such as barium, strontium and cerium, whereas B denotes zirconium, molybdenum and rare earth metals produced by fission and uranium and plutonium from the fuel. The composition of these phases depends largely on the fission yield, the temperature gradient in the fuel pin, the burnup and so on. The thermodynamic properties of fission-produced compounds are essential for the understanding of the fuel behavior in nuclear reactors. Few experimental data, however, have been reported for the relevant Pu compounds, especially high temperature. In the present study, the vapor pressures over $SrPuO_3$(s)[2], $BaPuO_3$(s)[3] and $BaNpO_3$(s) were measured by mass-spectrometry in order to identify the main vapor species and to obtain the thermodynamic data of these complex oxides.

These samples could be obtained by heating the mixed powders of PuO_2(s) or NpO_2(s) and $BaCO_3$(s) or $SrCO_3$(s) at 1660K for 75min in Ar. The vapor pressures were measured with a quadrupole mass-spectrometer equipped with a tantalum holder which contains a Knudsen-cell. The detail of the apparatus used in the present study were described in an earlier paper[4]. The platinum Knudsen-cell was used in order to avoid chemical interaction between samples and the Knudsen-cell.

As the predominant vapor species Ba(g) and BaO(g) were identified for the $BaPuO_3$(s) system. Temperature dependences of the vapor pressures of Ba(g) and BaO(g) over $BaPuO_3$(s)+PuO_2(s) are shown in Fig. 12.7.1. Since the partial pressures of BaO(g) was much higher than those of Pu-bearing vapor species, the decomposition of $BaPuO_3$(s) could be expressed with the following manner;

$$BaPuO_3(s)=PuO_2(s)+BaO(g) \qquad (1).$$

And the partial pressure of Ba(g) in Fig.1 was considered to be derived from the following equation(2);

$$2BaO(g)=2Ba(g)+O_2(g) \qquad (2).$$

The heat content and the free energy function of $BaPuO_3$(s) are necessary for the determination of the standard molar enthalpy of formation of $BaPuO_3$(s), $\Delta_f H_{298}(BaPuO_3,s)$ by second- and third-law treatments. So, the heat capacity and the entropy of $BaPuO_3$(s) were assumed to be the sum of those of BaO(s) and PuO_2(s) plus the difference between those of $BaZrO_3$(s) and the sum of those of BaO(s) and ZrO_2(s). The second- and third- law values obtained using the

estimated heat capacity and the entropy of $BaPuO_3$(s) are -1,661 kJmol^{-1} and -1,673 kJmol^{-1}, respectively. The agreement between these values is fairly good and these values agree with the estimated value, -1,666 kJmol^{-1} reported in the past[5].

On the other hand, Sr(g) and PuO(g) were identified for the $SrPuO_3$(s) system. The vapor pressures of Sr(g) and PuO(g) over $SrPuO_3$(s)+PuO_2(s) are shown in Fig 12.7.2. Since the partial pressure of Sr(g) was higher than that of PuO(g) as seen in the figure, the decomposition of $SrPuO_3$(s) was assumed to occur in the Pt cell as a following mechanism;

$$2SrPuO_3(s)=2PuO_2(s)+2Sr(g)+O_2(g), \quad (3)$$

$$2PuO_2(s)=2PuO(g)+O_2(g). \quad (4)$$

The heat content and the free energy function of $SrPuO_3$(s) are necessary for the determination of second- and third- law enthalpies of formation of $SrPuO_3$(s), $\Delta_fH_{298}(SrPuO_3,s)$. So the heat content and the free energy function of $SrPuO_3$(s) were estimated in the same manner as $BaPuO_3$(s) system using the data of $SrZrO_3$(s). The second- and third- law values obtained by using the estimated heat capacity and the entropy of $SrPuO_3$(s) are -1,752 kJmol^{-1} and -1,728 kJmol^{-1}, respectively. The agreement between these values is fairly good and these values also agree with the estimated value, -1,738 kJmol^{-1} reported in the past[6].

On the experiment of $BaNpO_3$(s) the main vapor species detected were Ba(g) and BaO(g) like the case of $BaPuO_3$(s). Since the partial pressures of Ba-bearing vapor species were much higher than that of Np-bearing vapor species, the decomposition of $BaNpO_3$(s) was assumed to occur in the Pt cell as a following mechanism;

$$BaNpO_3(s)=NpO_2(s)+BaO(g), \quad (5)$$

$$2BaO(g)=2Ba(g)+O_2(g). \quad (6)$$

The evaluation of the thermodynamic properties of $BaNpO_3$(s) is currently under way.

References

1) H. Kleykamp, "THE CHEMICAL STATE OF FISSION PRODUCTS IN OXIDE FUELS AT DIFFERENT STAGES OF THE NUCLEAR FUEL CYCLE", Nucl. Technol., 80, 412 (1988).

2) K. Nakajima, Y. Arai and Y. Suzuki, "Vaporization behavior of $SrPuO_3$", J. Nucl. Mater. 248, 233 (1997).

3) K. Nakajima, Y. Arai and Y. Suzuki, "Vaporization Behavior of $BaPuO_3$", J. Mass. Spectrom. Soc. Jpn., 47, 46 (1999).

4) T. Ohmichi, Y.Suzuki, Y. Arai, T. Sasayama and A. Maeda,"Mass spectrometric Study on the Carbothermic Reduction of Plutonium Dioxide", J. Nucl. Mater., 139, 253 (1986).

5) M. Yamawaki, J. Huang, K Yamaguchi, M. Yasumoto, H Sakurai and Y. Suzuki,"Investigation of the vaporization of $BaUO_3$ by means of mass spectromety", J. Nucl. Mater., 231, 199 (1996).

6) S. Aronson, "ESTIMATION OF THE HEAT OF FORMATION OF REFRACTORY MIXED OXIDES", J. Nucl. Mater., 107, 343 (1982).

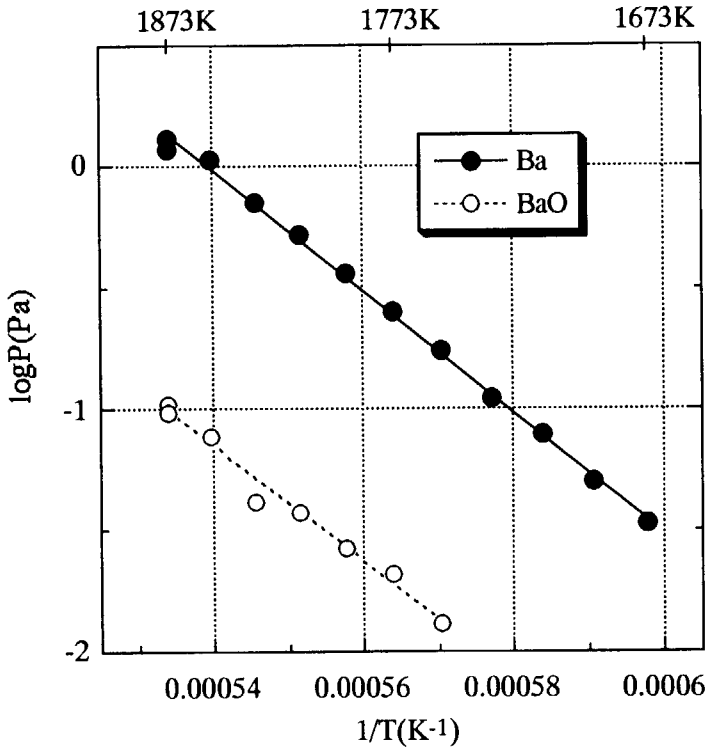

Fig. 12.7.1 Temperature dependence of the vapor pressures over $BaPuO_3$+PuO_2

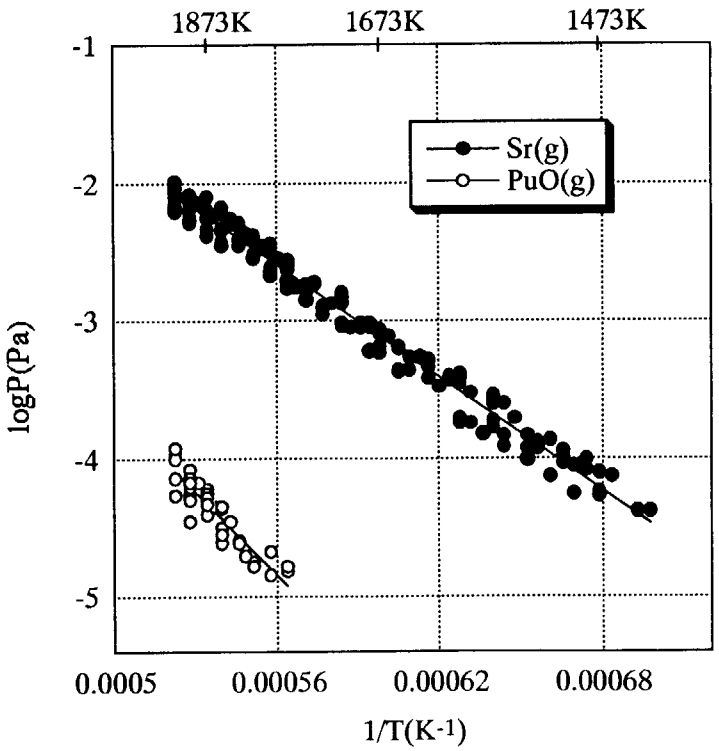

Fig. 12.7.2 Temperature dependence of the vapor pressures over $SrPuO_3$+PuO_2

13. Nuclear Ship Research and Development

Need for scientific research in under-sea with a nuclear submersible vessel was surveyed through discussions with experts such as physical oceanographers, geophysicists, etc. This survey revealed that the under-sea of the Arctic Ocean are the pressing research place from the view point of important data for study of mechanism of global environmental change and its anticipation, and a nuclear submersible vessel will promise a powerful activities at this research.

Design study on a very small-scale and highly compact marine reactor with thermal output of 1.25 MW aiming usage for a submersible scientific research vessel, named SCR, started in 1998 on the base of DRX design. The main parameters such as the core size, the operating pressure, temperature, flow rate, etc., were designed. Qualitative evaluation of build-up of active corrosion products in the SCR primary loop is necessary to check possibility of operation without the purification system. For the qualitative evaluation, the computer code was developed and confirmed by "Mutsu" experimental data. The SCR was evaluated to be operated without purification even for a year at least.

Experiment aiming to establish a simple procedure for DRX start-up was completed for the secondary loop. The experiment showed that the state of the secondary loop which was filled with water before the start-up could be transferred smoothly to that of the rated operation, through drainage of water by steam generated during the start-up.

Development of the in-vessel type control rod driving mechanisms was continued, and functioning tests of the latch and delatching (scram) were made in 1998. The development will be completed with endurance test of an integrated full scale in 1999 by schedule.

An advanced operating system has been developed for nuclear ship reactor operation based upon application of operator's knowledge of both normal and abnormal operations. Comparing plant behaviors from start-up to power level by the automatic operation with by "Mutsu" manual one, stable automatic operation was obtained almost same as manual one.

Nuclear engineering simulation system has been developed as a simulator of an integrated PWR ship reactor. In FY-1998, accident simulation programs and operation display system were added to the simulator. Nuclear ship database system was completed for both the experimental data and the document one of "Mutsu" project, and now open to use.

13.1 Evaluation of Radioactive Corrosion Products in Submersible Compact Marine Reactor without Purification System

N. Odano and T. Ishida

(*E-mail*: odano@koala.tokai.jaeri.go.jp)

A quantitative evaluation of buildup of activated corrosion products in a submersible compact marine reactor to be used for a scientific research vessel has been conducted. This evaluation is especially important from the viewpoint of radiation safety since the compact reactor plant being designed has no purification system to accomplish simplification of the plant. A computer program CTAM-II to estimate the accumulation of the activated corrosion products in the primary system has been developed on the base of CTAM, which was originally developed for the Oconee radiochemistry survey [1),2)] and modified for the shield modification project of the Japanese nuclear ship Mutsu[3)]. In the present study, validity and prediction accuracy of the CTAM-II code have been investigated by comparison with the experimental ones obtained from the radiochemistry tests of the Mutsu done during the start-up test and the experimental voyage [4)].

In the CTAM-II code, transport of corrosion products and buildup of the activities are mathematically modeled by the simultaneous ordinary differential equations as a model shown in Fig.13.1.1. It is assumed that the primary system consists of the five node: the fuel cladding, the steam generator, the decay heat removal

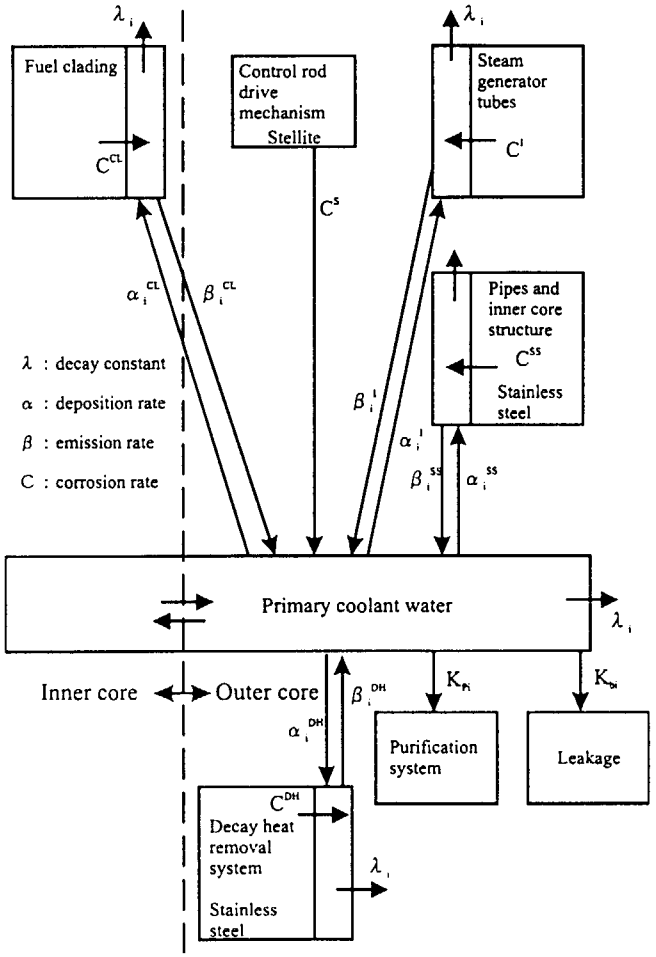

Fig.13.1.1 Mathematical model of CTAM-II

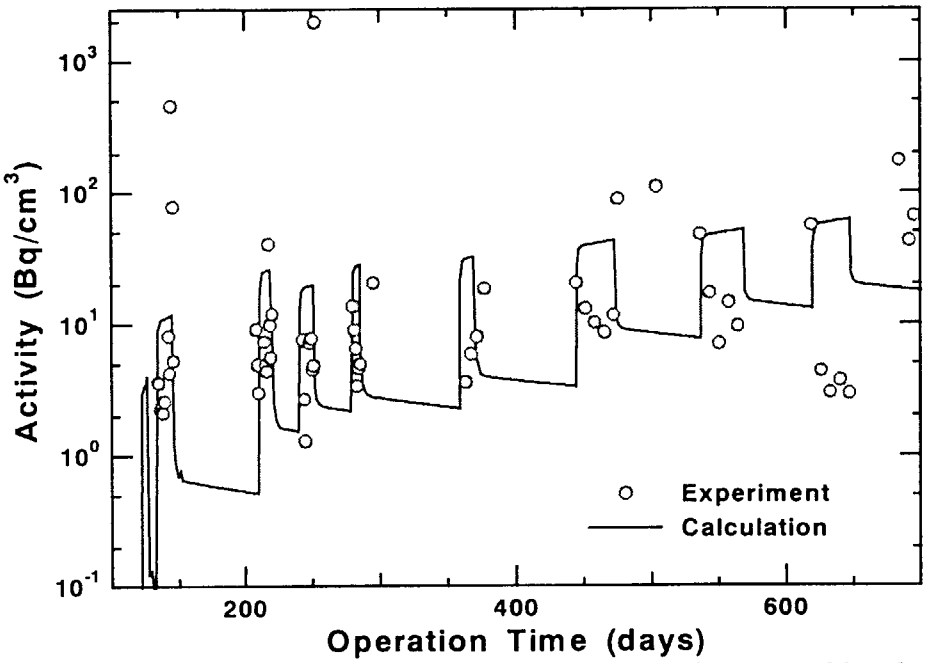

Fig.13.1.2 Comparison of activities in primary coolant of Mutsu with calculated results by CTAM-II

system, the stainless steel surface of the primary system and the primary coolant. The model includes empirical parameters such as the corrosion rate, emission rate and deposition rate. In the original CTAM code, these parameters were determined to represent the experimental data of the Oconne radiochemistry survey. To verify the parameters used in the CTAM code and investigate a prediction accuracy of the code for small reactor plants, the calculations of the activated corrosion products in the primary coolant water in the Mutsu were carried out. In Fig.13.1.2, a comparison of the calculated total activity, which is summation of activities of ^{58}Co, ^{60}Co, ^{54}Mn, ^{56}Mn and ^{187}W, with the experimental one is shown. Overall agreement between the calculated total activity and the experimental data is fairly good except a large discrepancy observed in early stage of the experiment mainly attributed to the short-lived nuclide ^{56}Mn. The comparison for the total activity indicates that calculated result is representing the experimental data within factor five and parameters used in CTAM-II is valid. Though the specific comparison for each nuclide are not shown, the calculated activities for the nuclei with relatively long half-life represent the qualitative tendency of the experimental data.

The CTAM-II code was applied to the submersible compact reactors DRX [5] and SCR250 [6] by modifying the mathematical model to take into account the effect of removal of the purification system. The calculated results assuming a certain operation model are shown

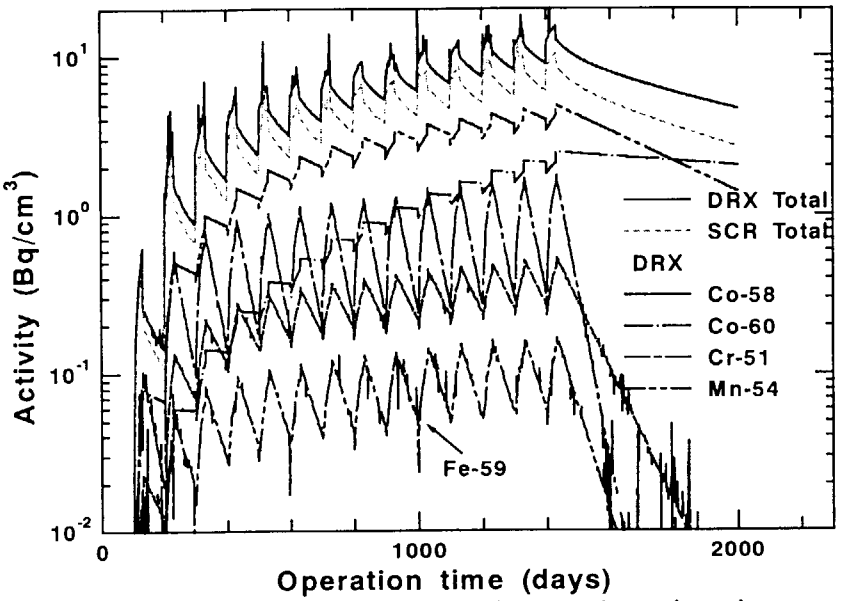

Fig.13.1.3 Calculated results of activated corrosion products in primary coolant of DRX and SCFR250

in Fig.13.1.3. For reference, the buildup of the corrosion products in their reactors was also calculated assuming the same performance of the purification system of the Mutsu plant is effective. It is found that the purification system has no significant influence on the buildup of the activated corrosion products for the DRX and the SCR250.

For assessment of radiation safety due to radiations from the activated corrosion products, shielding calculations by the point-kernel code QAD-CGGP2 [7] were carried out using source terms calculated from the CTAM-II code. The calculated results indicate that appropriate access control and additional shields are required for the maintenance operation since the dose rate equivalent near the steam generator is rather high immediately after the core life, 4 years. These results should be reflected on the detailed design of the reactors.

References

1) Grant, P. J., et al.: LRC 9053 (1976).

2) Kennedy, A.J.: LRC 9057 (1976).

3) Yamaji, A., et al.: JNS-T-report 1034 (1981), (in Japanese).

4) Yoshijima, T., et al.: JAERI-M 92-002 (1992).

5) Iida, H., et al.: Nucl. Technol,. 107, 38 (1994).

6) Kusunoki, T., et al.: to be published in this annual report (1999).

7) Sakamoto, Y. and Tanaka, S.: JAERI-M 90-110, (1990).

13.2 Development of the In-vessel Type Control Rod Driving Mechanism in 1998

H. Nunokawa, T.Yoritsune and T.Ishida
(*E-mail*: hnuno@koala.tokai.jaeri.go.jp)

The advanced marine reactors, MRX(Marine reactor X), DRX(Deep sea research reactor), and SCR(Submersible research reactor) are designed to adopt unique in-vessel type control rod driving mechanisms(CRDMs) for safety improvement of the reactor systems and compactness. Whole of the in-vessel type CRDM is installed inside the reactor vessel so as to eliminate the possibility of reactivity insertion accident due to control rod ejection, and use the space inside the reactor vessel effectively as well as to make a small containment possible. The in-vessel type CRDMs should operate in a very severe condition of high temperature and pressure water, the primary loop water, and be compact due to limited space. Since such CRDMs that can meet these requirements do not exist, the in-vessel type CRDM has been developed from the initial design in 1990 at the Advanced Marine Reactor laboratory.

The conceptual view of the in-vessel type CRDM is presented in Fig. 13.2.1 with the main parameters. It consists of a driving motor, a driving shaft, a latch magnet, separable ball-nuts, and so on. Mechanism to move the control rod by the CRDM is illustrated in Fig. 13.2.2. The driving shaft connecting with the control rods can move vertically up and down by rotation of the driving motor when the separable ball-nuts are closed to grasp the driving shaft by energizing the latch magnet. In reactor scram, the separable ball-nuts will open to separate the driving shaft by de-energizing the latch magnet, and the driving shaft will drop rapidly by the self-weight and a spring force. For normal operation, the latch magnet can be activated again and the separable ball-nuts can grasp the driving shaft. Each component has been developed by designing, fabricating, testing in a small scale and a full scale. The development will be completed by functioning test and endurance test of the integrated CRDM in the condition of high temperature and pressure water.

On functions of latching and delatching, the full scale tests were conducted firstly at the condition of the room temperature water to visualize motion of the separable ball-nuts and secondly at the condition of the high temperature water 310 ℃(of pressure 12Mpa). A subject to be settled in the latching motion was how to let the balls of the separable ball-nuts sit on the valley of the screw in the driving shaft independently of relation in both the positions.

Major Specifications	
Environmental Condition	
Temp.	320 ℃
Pressure	120 ata
Dimension of Drive Mechanism	
Outer	205 mm
Height	1735 mm
Drive Force	200 kgf
Scram Force	Weight+Spring

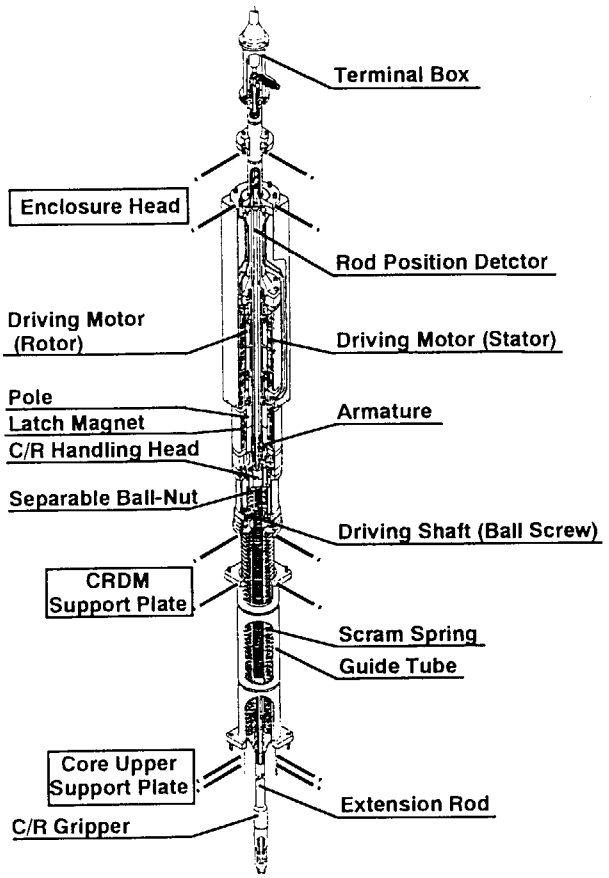

Fig.13.2.1 Conceptual View of In-Vessel Type CRDM

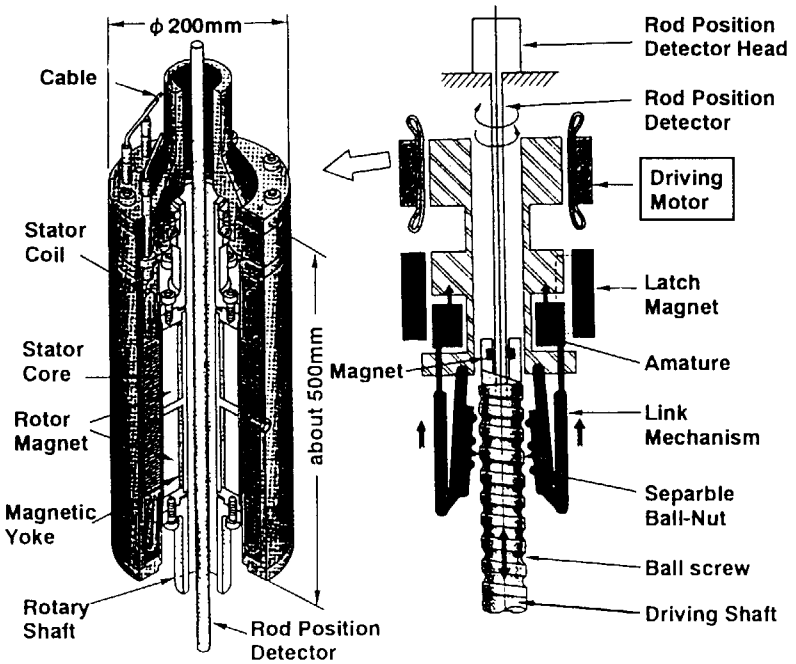

Fig.13.2.2 Driving Mechanism

Reliable latching motion, however, was confirmed in the full scale test. The minimum power input to the latch magnet was found to be 7.1A of the electric current. The complete latching can be obtained by rotating the separable ball-nuts in about 360 degrees peripherally with help of the driving motor after energizing the latch magnet, even if the balls sit on the top of screw at the beginning of latching motion.

In delatching motion, the time for complete release of the driving shaft from the latching device is very important since the total scram time should be within the design based value. The delay time from the cut-off of the latch magnet to the onset of driving shaft movement (called as delatch time) was measured in the delatching test with test parameters of a weight of driving shaft and the electric input power to the latch magnet. The target of an acceptable maximum delatch time was 0.2 seconds. Effect of the weight on the delatch time was small, 0.13 to 0.12 seconds for the weight of 50 to 220kgf. The delatch time increased with the electric input power to the latch magnet. The delatch time, however, was 0.13 seconds for the 10 A of the electric input power to the latch magnet with the weight of 220kgf. As the result, the functions of latching and delatching of the in-vessel type CRDM were revealed to be appropriate in the full scale test. These results can lead to the next endurance test.

13.3 Design Study of a Submersible Compact Reactor in 1999

T. Kusunoki, N. Odano, Y. Fukuhara and T. Ishida
(*E-mail*: tkusu@koala.tokai.jaeri.go.jp)

Advanced Marine Reactor Laboratory has been conducting design studies on a compact nuclear reactor aiming for use a submersible scientific research vessel navigating in 600 m of the water depth as one of nuclear energy utilization for ocean investigation.

This submersible scientific research vessel was selected by taking into account the pressing research needs through the activity of working group in the Research Committee on Marine Reactor. The research vessel is mainly utilized in the Arctic Ocean and the sea at low latitude where a normal ship hardly investigate due to thick ice or storm, but there exist important data affecting the earth's environmental change. A conceptual sketch of the research vessel and the major specifications are shown in Fig. 13.3.1 and Table 13.3.1, which are based on the requirement on the research mission. Electrical output of 500 kW and the total energy of 185,000 kWh are necessary for the research vessel to navigate in the Arctic Ocean. A nuclear energy source for the research vessel is more superior for more large and long operation in the undersea.

A conceptual design study of compact reactor for the research vessel was carried out. The research vessel employs two nuclear reactors with 250 kWe of each output for redundancy of power source taking account of navigation under ice in the Arctic Ocean. The concept of the Submersible Compact Reactor 250 kWe (SCR 250) is shown in Fig. 13.3.2. The major specifications are presented in Table 13.3.2. The reactor and all power system are contained in the pressure vessel of water pressure proof of 600 m. The size of core is 450 mm diameter and 420 mm height. The thermal rated output of the reactor is 1250 kW and the core life is approximately 470 days. The primary cooling system is designed to operate without the purification system.

The designed SCR 250 meets the requirements such as the electrical output, the plant size, but the total weight of SCR 250 may exceed the target by around 6 %, which will be reduced in the detailed design.

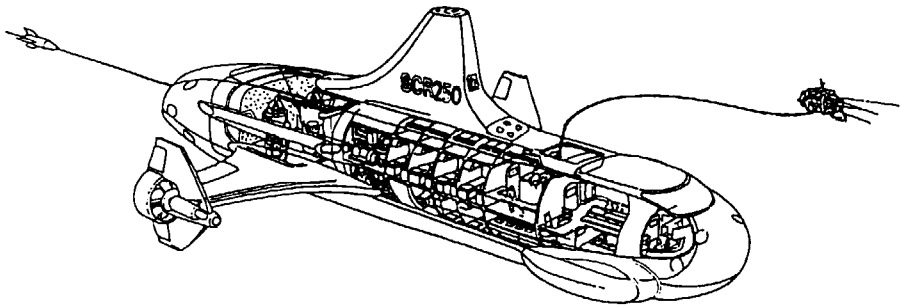

Figure 13.3.1 Submersible scientific research vessel with the SCR

Table 13.3.1 Major specification of submersible research vessel

Hull L×B×D	38m×5.5m×5.5m	Height	10m
Displacement	500 t	Power source	
Living vessel	4m ϕ ×22m	Reactor unit	250 kWe×2
Ship Speed		Battery	30 kWe
2 reactors operating	12 kn	Major equipment	Measuring instruments
1 reactor operating	8.5 kn	for investigation and observation	Sanling room, Sonar, etc.

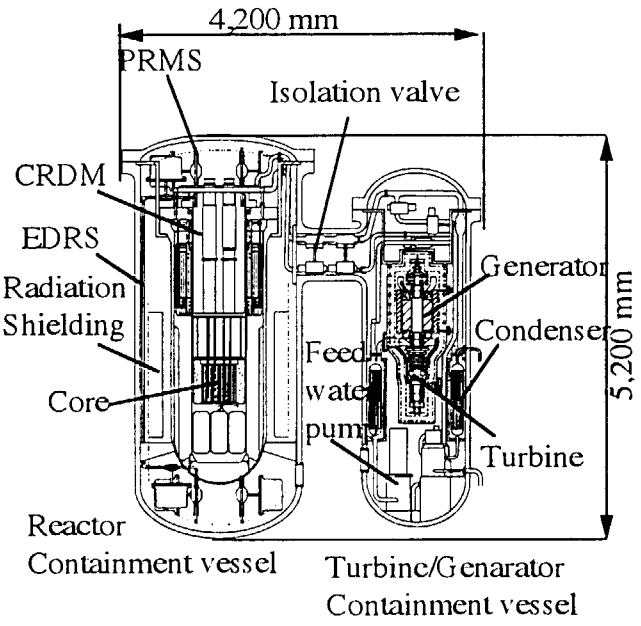

Figure 13.3.2 Concept of SCR plant

Table 13.3.2 Specification of SCR

Reactor power	1250kWt(250KWe)
Reactor type	INtegral type PWR
Primary cooling system	Natural circulation
Operating pressure	8.4 MPa
Core inlet/outlet temperature	282 / 298 ℃
Flow rate	46.8 t/h
Control rod drive Type	In-vesel type
Number of CRDM	4
Steam genarator Type	Once-through helical coil
Steam pressure	3 MPa
Steam temperature	242 ℃
Steam flow rate	1.8 t/h
Containment vessel Design pressure Outside/Inside	6MPa/10MPa

13.4 Experiment on Thermal Hydraulic Behavior of DRX Start-up

T. Yoritsune and T. Ishida

(*E-mail :* tyori@koala.tokai.jaeri.go.jp)

The deep sea research reactor DRX[1], one of the advanced marine reactor being studied at Advanced Marine Reactor Laboratory, is designed to adopt a water filled containment in which the secondary loop consisting of the turbine, steam pipe, etc., is submerged in the water. The secondary loop, therefore, will be filled with the water when the reactor is in the state of shut-down. The DRX needs a simple and reliable start-up procedure especially taking into account water drainage i.e., water replacement by the steam in the secondary loop, as well as stable heat-up in the primary loop by the nuclear heating. A conceivable start-up procedure for the secondary loop is a drainage of the water by the steam generated in the steam generator by feeding the water continuously during the start-up. In this procedure, it is important to survey experimentally the water drainage behavior and whether a pressure oscillation and impact force due to steam condensation at the surface of the steam and the water will occur or not.

The purpose of the experiment is to study the thermal hydraulics in the secondary loop for the start-up from the state of water filled and for load changes. The experimental loop simulating the basic configuration of the DRX secondary loop is shown in Fig. 13.4.1. It

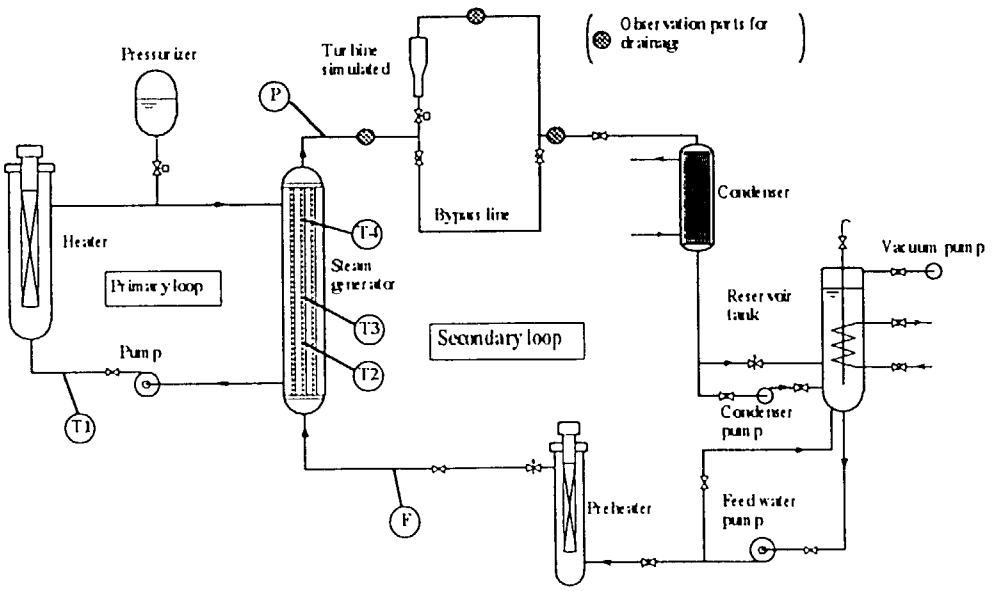

Fig. 13.4.1 Experimental loop for DRX start-up

consists of the primary loop and the secondary loop. The former has the heater, the pump, etc., and the latter does the one-through type steam generator, the steam pipe, the multi-stage orifice simulating the turbine, the condenser, the feed water pump, etc. Several procedure were studied for the secondary loop start-up with parameters of the feed water flow rate, timing of switching the valves, *i.e.*, opening the simulated turbine inlet valve and closing the bypass valve, and so forth. The water drainage was surveyed with a high-speed video camera at the sections of steam line shown in the figure. Pressure sensors were set for measuring the pressure pulse in the steam line.

The typical result is shown in Fig. 13.4.2. At the initial state of this case, the valve of the simulated turbine inlet was closed and that of the bypass was open. The feed water flow rate was initially 20 kg/h, 15 % of the rated flow rate. The evaporation and gradual pressure increase at the steam generator began at about 15 minutes. Heat input to the heater was increased from 10 kW to 40 kW per 50 minutes gradually. Switching of the valves was done at 42 minutes. The significant pressure oscillation or peak was not measured. Observation by the high-speed video camera indicated that the smooth water drainage by steam was done. The heat input and the heat transferred to the steam generator secondary balanced at 47 minutes and the steady state of the whole system was attained.

The recommended start-up procedure for the secondary loop from the water-filled

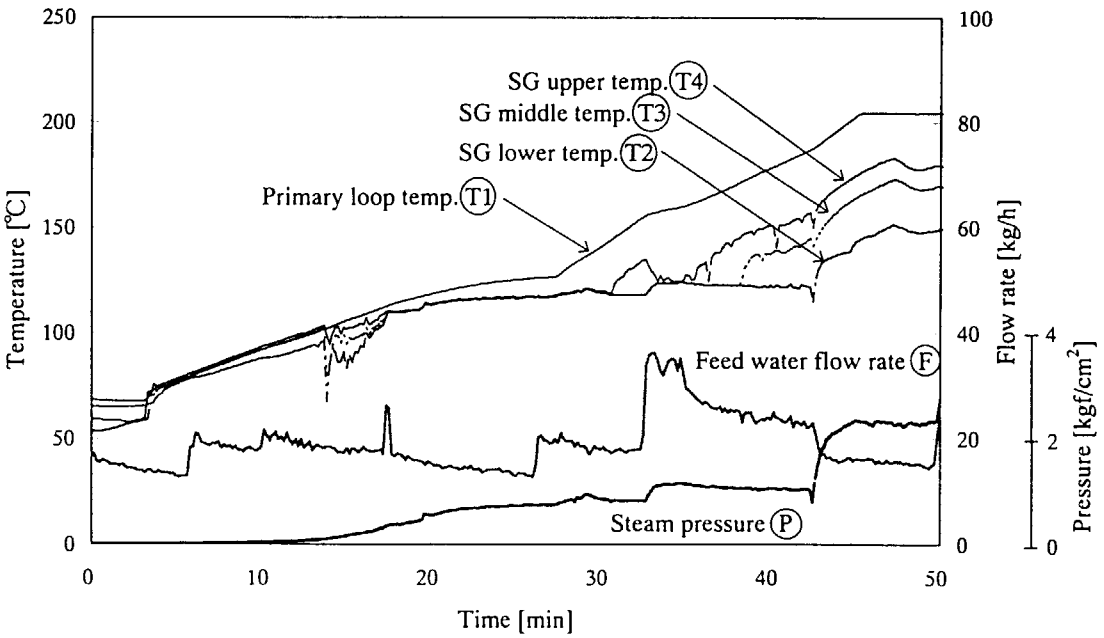

Fig. 13.4.2 Experimental results

state was as follows: From the beginning of the start-up, the feed water should be fed through the steam generator and the bypass of the turbine into the condenser. With heating-up, the steam will be generated and the steam pressure increase to the rated condition. The drainage of water in the turbine will be smoothly done if switching of the valves made after the steady state of the secondary loop having the steam flow into the condenser through the bypass line is attained. The experimental results will be used for verification of RETRAN-02/GRAV code to simulate the DRX start-up transient.

References

1) Iida, H., *et al.*: "Design Study of the Deep-sea Reactor X", Nuclear Technology, Vol.107, pp.38～45 (1994).

13.5 Knowledge-based Automatic Control for a PWR Plant

J.Shimazaki, T.Nakazawa and N.Yabuuchi
(*E-mail:* jshima@koala.tokai.jaeri.go.jp)

Plant operations aboard nuclear ships require quick judgements and actions due to changing marine conditions such as wind, waves and currents. Furthermore, additional human support is not available for nuclear ship operation at sea, so advanced automatic operations are necessary to reduce the number of operators required. Therefore, an advanced automatic operating system has been developed based on operational knowledge of nuclear ship "Mutsu" plant.

The advanced automatic operating system includes both the automatic operation system and the operator-support system which assists operators in completing actions during plant accidents, anomaly diagnosis and plant supervision[1]. These system are largely being developed using artificial intelligent techniques such as neural network, fuzzy logic and knowledge-based expert.

The automatic operation system is fundamentally based upon application of an operator's knowledge of both normal (start-up to rated power level) and abnormal (after scram) operations. The normal automatic system include manual actions at each operation modes: pre-check before start-up, temperature-raising, void generation during pressurization, temperature/pressure-raising, nuclear heating for temperature-raising, constant power related to temperature and pressure, reactor power change and so on. Comparing plant behaviors from start-up to power level by the automatic operation with by "Mutsu" manual operation, stable automatic operation was obtained almost same as manual operation within all operating limits in Fig.13.5.1. The abnormal automatic system was for hard work of manual operations after scram or LOCA accidents. An integrating system with the normal and the abnormal automatic systems are being developed for interacting smoothly both systems.

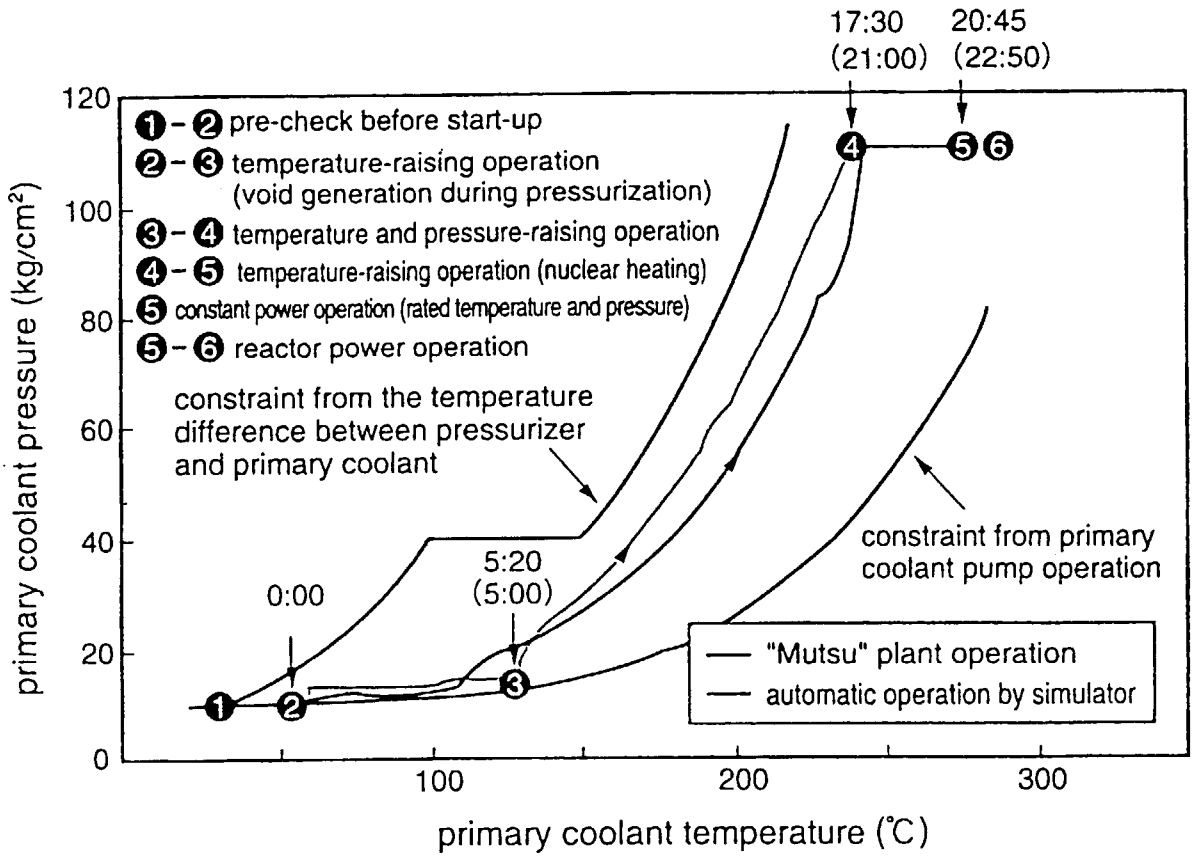

Figure 13.5.1 Comparison of the automatic operation system and "Mutsu" manual operation during reactor start-up

Reference

1) Shimazaki,J., et al.: "Integral-type Small Reactor MRX and its Applications",10th Pacific Basin Nucl.Conf.,Oct.20-25,Kobe,825(1996).

13.6 Simulation of Reactor Accidents in Integrated PWR Simulator

T.Takahashi and J.Shimazaki
(*E-mail*: ttaka@koala.tokai.jaeri.go.jp)

Nuclear engineering simulation system (NESSY) was initially developed as a simulator for "Mutsu", the first nuclear ship in Japan.[1),2)] The "Mutsu" simulator was totally verified by comparing simulation results with the experimental voyage data of "Mutsu".[3)]

After that, NESSY has been developed as a simulator of an integrated PWR for advanced marine reactor, using the same computing structure as "Mutsu" simulator. By the end of FY-1997, we built the integrated PWR simulator as to be able to simulate maneuvering condition from start to stoppage of plant.

In FY-1998, accident simulation programs and operational display systems were added to the integrated PWR simulator.

Accident simulation programs

The integrated PWR employs a water-filled containment vessel and a natural-convection-type decay heat removal system as a passive safety system. It is important to see plant behaviors and confirm the function of the passive safety system at accidents. [4)]

Accident simulation programs are consisted of LOCA, SGTR and steam lines break(SLB), which are main in accident phenomena in the reactor.

Simulation result of LOCA is shown in Fig.13.6.1. You can find the integrated PWR maintains passive safety during LOCA as follows.

-Pressure balanced in RV and CV is under 4MPa which is the allowable pressure in CV.
-Water level in RV keeps higher than the top of core (=23%).
-Average temperature in PCS gradually goes down by the function of emergency decay heat removal system (EDRS).

Also in accident simulation of both SGTR and SLB, the similar effects are obtained. From these results, we can verify the safety of the integrated PWR at accidents.

Simulation accuracy of accident programs is assured by comparing these simulation results with the computing results using safety analysis code RELAP5/MOD2.

Operational display systems of plant operating conditions

Most possible application of the integrated PWR is a power unit for a submersible research vessel, because of being able to continue long time voyage without usage of oxygen and supply of fuel. Room in a submersible type vessel is very small. Therefore it is necessary to make power and operating units compact, and to be easy operation by an operator of vessel so as to minimize a number of a crew.

A sample display packed important plant operating information for monitoring operating conditions is shown in Fig.13.6.2. This shows numerical values of main parameters, color-coded temperature, a pattern of void fraction, flow direction and the break point at accident on the display screen.

In addition to this kind of display systems, the integrated PWR plant will be operated by an operator of vessel with the assistance of alarm and diagnostic systems.

References

1) Kusunoki T.,et al.,:"Development of Nuclear Ship Engineering Simulation system",JAERI-M 93-079 (1993)
2) Kusunoki T.,et al.,: "Simulation of a marine nuclear reactor", Nuclear Technology vol.109, pp.275-285 (1995)
3) Kyouya M.,et al.,:"Performance Evaluation of Nuclear Ship Engineering Simulation system",JAERI-M 94-223 (1994)
4) Kusunoki T.,et al.,:"Analysis of Core Flooding Capability and Containment Vessel Pressure during LOCA on Advanced Marine Reactor MRX",JAERI-Tech 97-046 (1997)

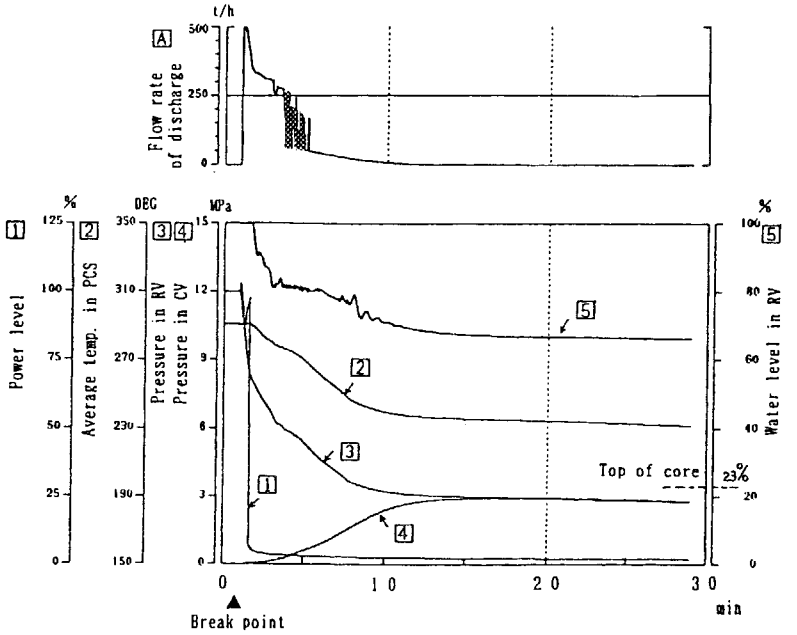

Simulation conditions

- Plant condition: ・100% Power level
- Break point: ・Inlet pipe of EDRS A-system
- Break dia.: ・50mm
- Operating condition of EDRS : ・EDRS C-system

Fig. 13.6.1 Simulation result of LOCA

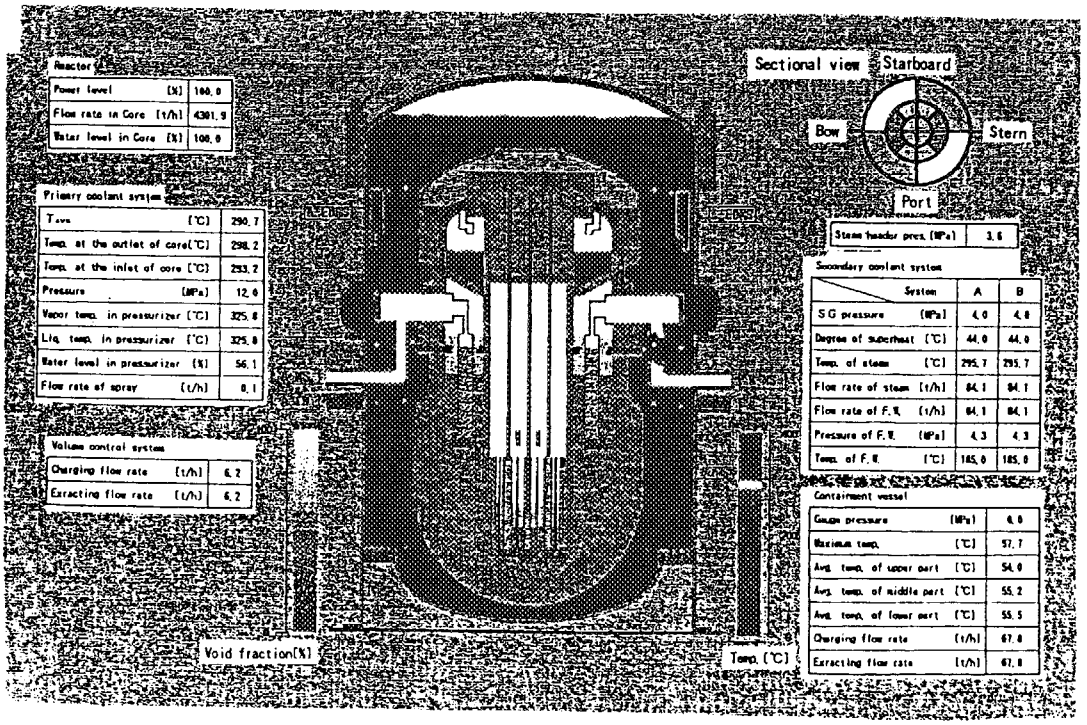

Fig. 13.6.2 Display for monitoring plant operating conditions

13.7 Development of Nuclear Ship Database System

M.Kyoya, T.Nakazawa, J.Shimazaki and M.Ochiai
(*E-mail*: mkyoya@koala.tokai.jaeri.go.jp)

Nuclear ship "Mutsu"was laid on keel in 1969 and completed for decommissioning in 1995. The radiation leakage occurred at low reactor power in the power-up tests in 1974 and shielding repair and safety checking were needed. Overall haul checking for the safety was done in 1980-1982 at Sasebo yard. According to the governmental agreement for "Mutsu" reoperation, inspection of the reactor vessel in 1988-1989, body check of a ship in 1989, the power-up tests in 1990, the sea trials for ship permission and finally the experimental voyages in 1990-1992. The decommissioning was carried out at the home port Sekinehama in 1992-1995.

We accumulated the techniques, the knowledge and others on the nuclear ship development at the each stage of the"Mutsu" research and development program, such as design, construction, operation and other stages[1].

In 1990-1992, we carried the power-up tests for reactor performance, sea trials for ship performance and experimental voyages of "Mutsu"for overall tests of a nuclear ship. We obtained the experimental data on the effects of the ship motions and the nuclear power plant behavior and the caused by change in load, the ship operations, the waves, the winds, etc..

It is important to keep and pigeonhole these data of the"Mutsu"program in order to utilize them effectively in the research and development of the advanced marine reactor[2]. From this point, A nuclear ship database system on the experimental data and the documental data has been developed, called nuclear ship experimental database and the documental database.

Experimental database has a single screen with a combination of experimental data and the documental data covering more detail information on reactor operation, navigating and environmental conditions (See Fig.13.7.1). The experimental date contains as follows.

- Nuclear and thermohydraulic calculations served in design and construction
- Records of nuclear reactor operation

- Records from the power-up tests, sea trials and experimental voyages at sea

  The documental data contains:

- Reference documentation served in the design
- Formal application documents submitted to regulatory authorities

  for permission to install nuclear reactor and the ship.

The experiment or test records over 600 magnetic tapes have been made covering power-up tests, sea trials, and experimental voyages at sea. The data can be searched and displayed specifying plant simultaneous conditions such as reactor power output and revolutional rates of main engine, navigating conditions such as ship speed, and environmental conditions such as wave height and seawater temperature. For instance, search is possible for reactor responses to changes in different sea conditions for maintaining the same ship speed. Documental data amounting to 25,000 items have been arranged and conserved in three groups according to its importance: A, as a text form, B, as a image form and C, other than A and B compacting information of 20,000 items on design drawings inputted through scanner, microfilms and original documents.

Users can have access to the nuclear ship database only at our laboratory and transfer the searched specific data to their site by FTP.

References

1) Ochiai, M., et al.:"Result of Power-up Test of The Nuclear Powered Ship Mutsu and Test Programs of Her Experimental Voyages", The lst JSME/ASME Joint Int. Conf. on Nucl. Eng., pp. 515-520 (1993).
2) Kyoya, M., Hasidate, K. and Ochiai, M.:"Development of the Nuclear Ship Database" (1995), JAERI-Data/Code 95-003 [in Japanese].

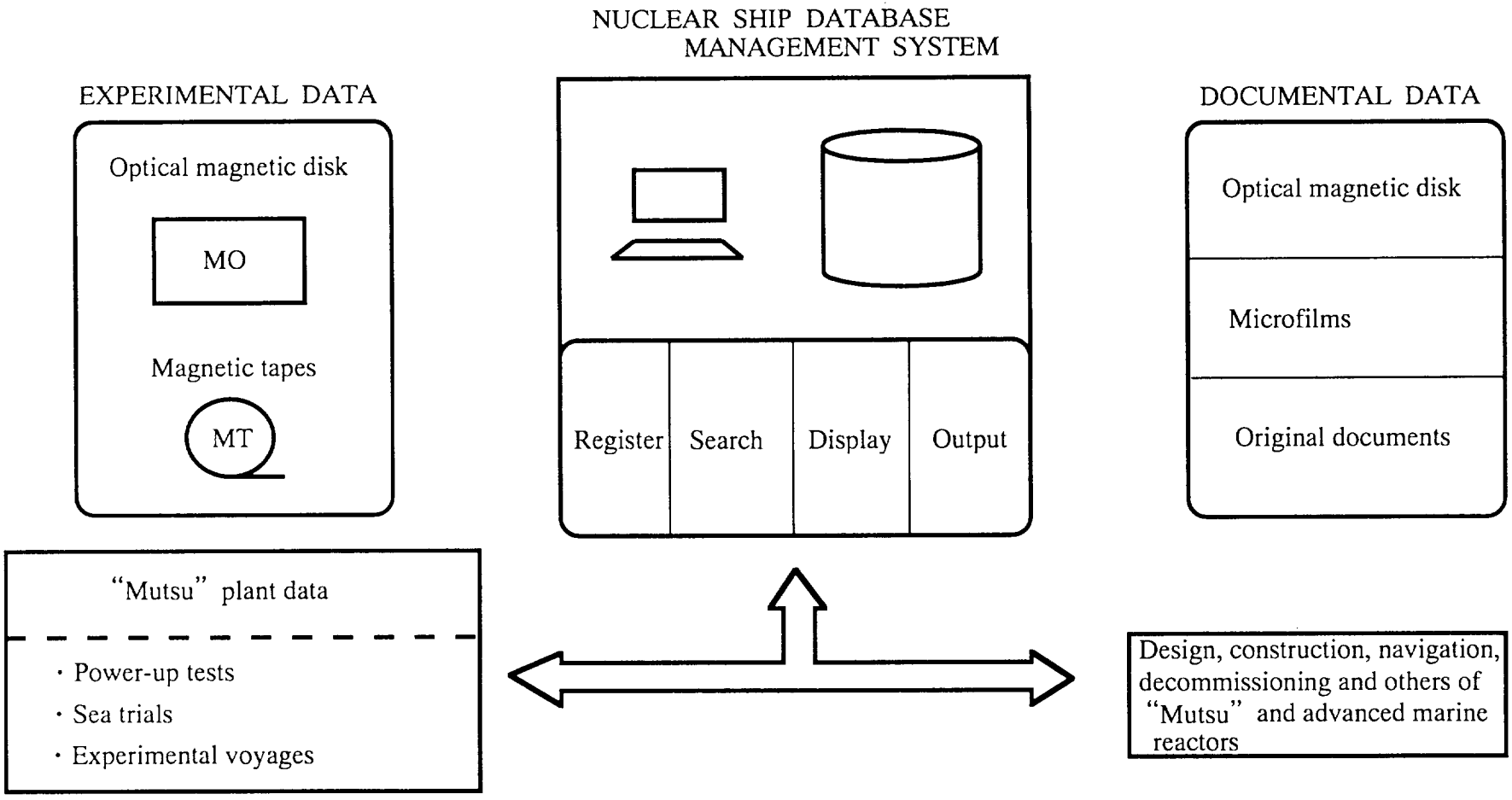

Fig. 13.7.1 Schema of Nuclear Ship Database System

13.8 Study on Safety Evaluation for an Offshore Floating Nuclear Power Plant

N.Yabuuchi, M.Takahashi and J.Shimazaki
(*E-mail*: yabuuchi@koala.tokai.jaeri.go.jp)

Technical feasibility studies of new siting such as Quaternary ground, offshore and underground are increasingly recognized as important to nuclear plant siting. Offshore siting have some advantages of (a) Expanding land supply, (b) Supplying electricity close to it's consumer, (c) Reducing enviromental impact on land, and (d) Providing excellent cooling water facilities.

The purpose of this study is to examine the safety and the technical requirements for offshore nuclear power plants and to discuss the engineering concepts and problems of design to evaluate the feasibility of the offshore siting. Main tasks contain three groups of technical requirements, setting of natural events and technical feasibility.

Survey on the technical requirements for the offshore siting

The offshore siting methods are classified three basic types: floating, settled and land reclamation types. In order to evaluate the early realization, survey on the technical requirements for three types such as safety, design philosophy and foundation stability were done.

Survey on setting of natural events

A natural event which should be specially considered on safety design of land based nuclear power plants is earthquake. Regarding to offshore floating nuclear power plants (OFFFNPP), natural events affecting the floating structure motion should be specially considered as winds, ocean waves, currents, earthquakes, seaquakes, tsunami and storm surges. The fundamental survey on the data of meteorological, oceanic and seaquake phenomena were done. Based on fundamental survey, magnitude of natural events which should be specially considered on safety design of OFFFNPP were discussed.

Study on technical feasibility for OFFFNPP

The reviews on the safety and the engineering concepts for OFFFNPP, and the survey on evaluation of the floating platform stability were performed. In conceptual design of OFFFNPP, the plant is located about 1 or 2km offshore with sea depth about 20m and is moored within protective breakwaters and has a 1,000 MWe PWR plant on a 80m X 300m

floating platform with displacement of about 300,000 tons.

The results of this study were summarized as follows.

(1) The floating types have the most technical requirements among the three types that should be considered for safety design. The land reclamation type such as offshore artificial island is similar to the conventional siting, and can be realized easily since the technical requirements and the engineering problems for safety assessment, design and construction technology are within bounds of present technology.

(2) OFFFNPP may have a couple of advantages over other types, such as seismic isolation, standardization of design and manufacturing, reduction of labor cost, etc.. However, OFFFNPP is required to establish the safety standards different from land based nuclear power plants.

(3) In safety design for OFFFNPP, magnitude of natural events affecting the floating structure motion should be fixed on the basis of the seismic design philosophy for land based nuclear power plants.

(4) The main results of the conceptual reviews for OFFFNPP are that it is technologically feasible and necessary to perform the basic studies required to the safety of the floating platform on the accidents possibly caused by collision, explosion, flooding, sinking, drafting, etc..

(5) The main results of survey on evaluation of the floating platform stability are that the methods for predicting the dynamical characteristic of large-sized floating structures has been established and that the floating platform with protection breakwaters is stable enough to build the nuclear power plant and its associated facilities on it through dynamic simulation analysis.

13.9 Design of JRR-4 Operation Support System

H. Takahashi, T. Yoritsune, N. Arai* and K.Yamamoto*
(*E-mail*: htaka@koala.tokai.jaeri.go.jp)

JRR-4 is a light water moderated, cooled and graphite reflected pool-type reactor with the thermal output of 3500kW. In February 1996, a work on core modification from high-enriched fuels to low-enriched ones was started and completed in May 1998. As a part of the work, Operation Support System (OSS) was adopted for. Hardware configuration of OSS is shown in Fig.13.9.1. OSS consists mainly of a workstation (WS) and two computers (μXL and Personal Computer : PC).

Cooling System Control and Monitoring

For the purpose of digital controlling and compacting the cooling control system, μXL is adopted in OSS. μXL has been used for a long time as an industrial process computer, and it is the equipment with the high reliability. So, it is suitable for control of the nuclear reactor. The data are processed in 1 or 0.2 second period. And the μXL data can be displayed on the screen (CRT2) with the meter type and the trend graphs. In addition, the μXL data are saved as a text file and then this data file is sent to WS by using FTP (File Transfer Protocol) in 4 seconds period. Beside signals of graphic panel and operation are output in 1 second period. And alarm signals are output in 0.2 second period in order to ensure the quick response for safety.

The μXL application programs are designed so that sub alarm is output with warning messages on CRT and warning sound before alarm signal occurs. So, the operator is able to deal early with abnormal state. Then, the sequence control is executed in some automatic controls of making the automatic formation of cooling circuit and setting the constant flow rate ($8m^3$/minute). And, using the test signals from μXL, checks for states before startup, alarms and scrams are effectively executed in the reactor operating system. The pre-startup check can be finished earlier than one in the past system.

---

* Department of Research Reactor

Data Collection and Processing

A data collection and processing system in WS with VXI bus is made for collection of fast-changing data (for example: from nuclear instrumentation) and for supply of data to the user. The VXI bus is on extended VME bus, which widely used in industrial data measurement, and excellent in high-speed measurement and noise-proof property. It is suitable for processing data of the nuclear instrumentation. Besides, the system is expansive to meet the number of process data increases in future.

The application program of WS is programmed in C language (ANSI) and SICL. Data are collected in 0.1 second period and saved as a binary file. This WS data and cooling control system data sent to WS from μXL are integrated and saved for a data file in 1 second period. These data files are utilized to the operation support or the data supply. Besides, when abnormality in the reactor is occurred, the data concerning to the abnormal state are referred in detail by the data files and are useful to early find the cause of the abnormality.

Data Display

A personal computer (PC) is adopted as a data display computer (CRT1) in OSS. PC is conventional computer and easy to upgrade. An operation data file is read from WS in the 0.1 second period for displaying the fast-changing parameters. Operator can select and observe the necessary data for all operation. The types for data display are round meter, bar graph and digital display. These data are renewed automatically in 0.2 second period. Some data are display trend graph in 1 second period.

Operating System of PC is Windows NT and application programs of PC are programmed in the Visual BASIC. Therefore, PC can be manipulated in a similar way of Windows95/98, training of the operator is not almost needed before using CRT1.

Operating record list is made automatically as an Excel file. The operating record list, which the operator has made once, can be made at the same format with MS Excel.

The numerical value of reactor power is displayed on reactor power indicator installed at the three places in JRR-4. This reactor power is calculated and given automatically at PC. It is sent to indicators by using RS-485.

Countermeasure in Abnormal State of OSS

At present, it is impossible to prove the verification of OSS hardware and software completely. Therefore, assuming the case when abnormality of OSS happens, OSS was

designed as follows.

(1) Control of the cooling control system can be changed by μXL control or by manual control by the selective switch, as shown in Fig.13.9.1. The μXL control is quitted in the abnormal case, and reactor operation can be done by manual control. μXL is designed so that it outputs not scram signal but alarm signal. So, dangerous state is avoided without relating to the condition of μXL.

(2) WS and PC are designed so that they do not completely control the reactor. So, there are no possibilities to cause the reactor malfunctions by WS or PC. The meters necessary to operate reactor are installed at the operation console. Therefore, it would be possible to operate the nuclear reactor when OSS could not be used.

(3) The alternative machine can always been prepared for immediate change of the hardware when machine became abnormal with its hardware.

Conclusion

JRR-4 Operation Support System realized reducing load of operator, data management and improvement of reliability for reactor operation. OSS has high reliability and flexibility. Now, JRR-4 Operation Support System has been using satisfactorily and will become more widely use in future.

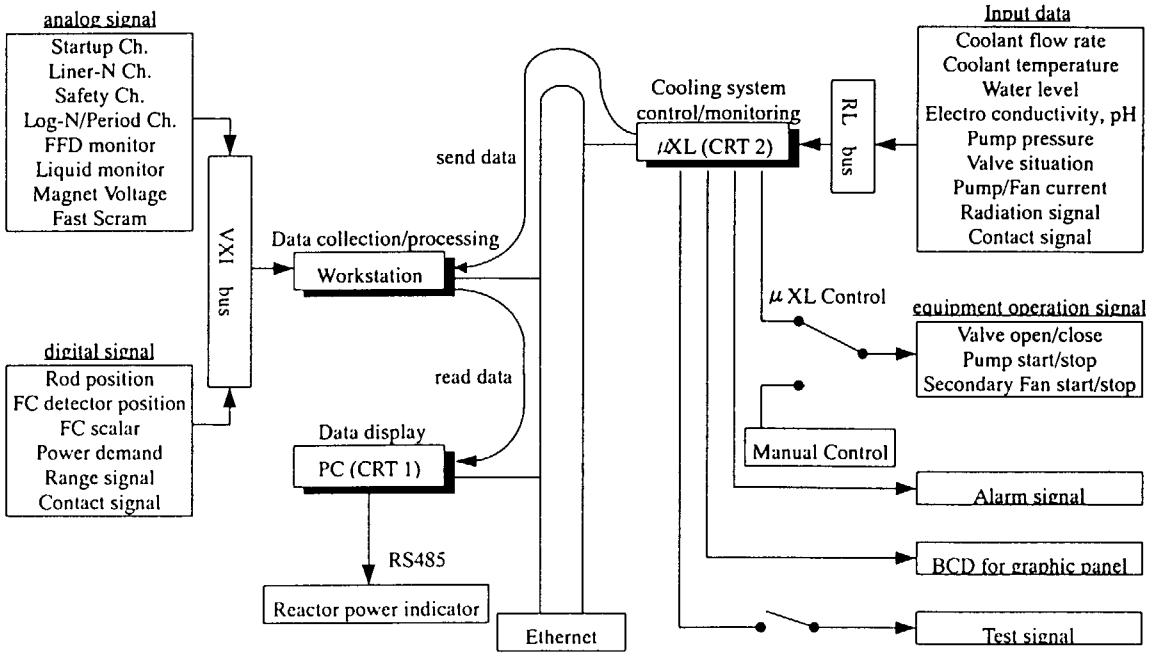

Fig.13.9.1 Configuration of JRR-4 Operation Support System

14. Facility Operation and Techniques Development

There are three reactor engineering facilities such as Heat Transfer Fluid Flow Test Facility, Fast Critical Assembly (FCA), Very High Temperature Reactor Critical Assembly (VHTRC). Maintenance work for VHTRC and operations of other facilities were carried out as scheduled. Major activities of each facility of this fiscal year are summarized briefly below.

(1) The Heat Transfer Fluid Flow Test Facility was operated for various experiments such as core thermal-hydraulic transient test for BWR, DNB Test for Advanced Reactor, Test with Two-Phase Flow Test Loop, etc. The designs and constructions of four test facilities for DNB Test Section were carried out. In addition, annual official inspections of the pressure vessels and the steam generator were carried out.

(2) The FCA was operated according to various purposes of experiments and recorded the operation time of 575.9 hours. Maintenance activities, fuel management and, physical protection were done, i.e., manufacturing the driving mechanism of Safety Control Rod, repair for defects of coating on fuels etc. And the PIV of nuclear fuel materials were carried out. The Year 2000 Problem was solved for the fuel management program as well.

(3) Maintenance works were done for VHTRC such as the monthly and annual inspections according to the safety regulation for operation. The PIT and PIV for VHTRC were also carried out as the fuel management. A report on the operating conditions and experimental items of VHTRC was published as a JAERI-memo. Also planning for decommissoning VHTRC was made.

14.1 Operation Report of Heat Transfer Fluid Flow Test Facility

T. Satoh, H. Watanabe, M. Shibata, K. Nakajima, and H. Watanabe

(*E-mail*: satou@kako32.tokai.jaeri.go.jp)

In FY-1998, operation and maintenance of Heat Transfer and Fluid Flow Test Facilities were carried out as scheduled.

As for the maintenance of test facilities, annual official inspections of the pressure vessels and the steam generator located at both of Large Scale Reflood Test Building and Chemical/Mechanical Engineering Building were carried out.

Core Thermal-Hydraulic Transient Tests for demonstrations of core safety during abnormal transient in BWR have carried out from 1998.

As for the operation of test facilities, the following six tests were performed.

1) DNB Test for Advanced Reactor
2) Core Thermal-Hydraulic Transient Test for LWRs[1)]
3) Test with Two-Phase Flow Test Loop
4) Ultra High Heat Flux Test by the NRG
5) Thermos Fluid Safety Test (ICE/LOVA) for Fusion Reactor[2)]
6) Steam Jet Test for Assessments of Multidimensional Two-Phase Flow

As for the design and construction of test facilities, the following four test facilities were newly constructed.

1) DNB Test Section for Advanced Reactor
2) Two-Phase Flow Test Facility with See Through Test Section
3) Basic Experimental Rig for Pool Water Cooling System
4) Coupled Nutronic Thermal-Hydraulic Test Section

As for the representative R&D, void fraction measurement system for Coupled Nutronic Thermal-Hydraulic Test were developed.

References

1) Watanabe, H., et al : Status of core thermal-hydraulic transient test at JAERI, Fall Meeting of the Atomic Energy Society of Japan G64 (1998)
2) Shibata, M., et al : Test results of suppression of pressure rise, Fall Meeting of the Atomic Energy Society of Japan D12 (1998)

14.2 Operation Report of FCA

K. Hayasaka, K. Satoh, H. Sodeyama, K. Kurosawa, M.Saitoh and H. Watanabe

Operation of Fast Critical Assembly (FCA) was carried out in accordance with the experimental schedule on the FCA XIX-3 and XX-1 assemblies. Operation of 118 times was carried out in 97 days. No scram was recorded during the operation. The total operation time was 575.9 hours and the integrated power was 0.64 kWh. A total number of 5372 criticality operation has been recorded at the end of this fiscal year since the first achievement of criticality on the 29th of April 1967. For the safety regulation of operation, two days were devoted to the monthly inspection and about 10 weeks from Octobre 1998 to the annual inspection. Routine maintenance activities were done during the inspections to provide maximum operation days for the experiments.

As for maintenance activities, The driving mechanisum of SCR (Safety Control Rod) were manufactured for decrepitude. And they were used for C/R (Control Rod).

As for fuel management , the defects of coating on Enrich uranium, Natural uranium and Decrepitude uranium metallic fuel were repaired for about 11,000 plates and about 2,400 blocks by spraying the surface with colloidal solution of fluorocarbon in oder to prevent the fuel from oxidation. Weights of the coating on the fuel plates were obtained from the difference of the weight between before and after coating.

As for the physical protection (P/P), the management of the entrance and exit was done restrictively and the system was maintained properly.

In connection with safeguard, IAEA and NSB* carried out monthly inspection under the international treaty. The Physical Inventory Taking (PIT) of the fuels was performed from the 21th to the 24th of July by means of item counting, weighing and non-destructive assay. IAEA and NSB made the Physical Inventory Verification (PIV) from the 27th to the 29th of July. And The Y2K (Year 2000 Problem) of the fuel management proguram (computer proguram), was solved by the improve.

---

* NSB: Nuclear Safety Bureau

14.3 Maintenance Work Report of VHTRC

M. Takeuchi, T. Ono, K. Nakajima and H. Watanabe

(*E-mail* : takeuchi@vhtrc01. tokai. jaeri. go. jp)

The critical experiments for the establishment of measurement technique of initial criticality of HTTR were finished on September, 1996 at VHTRC. Therefore, the HTTR achieved the first criticality on 10th Nov.1998.

Nowadays, the VHTRC is out of operation. Then, the VHTRC is doing maintenance work.

According to the safety regulation for operation, one day was devoted to the monthly inspection and two days to the semiannualy inspection.

Then, the operating report which summarized the operating conditions and experimental items of VHTRC was published JAERI-memo with records from the first critical day, May 13, 1985 to the end of 1997.

As for fuel management, Physical Inventory Taking (PIT) was carried out from May 12 to May 13 by means of item counting. IAEA and STA made the Physical Inventory Verification (PIV) under the international treaty on May 13. No anomaly was confirmed. The maintenance activity was also taken on the physical protection (p/p) system. The sensitivity and function of the system were examined and calibrated.

We are under consideration for decommission of VHTRC.

15. Activities of the Research Committee

The department of Nuclear Energy System serves as a secretariat of the following four research committees organized by JAERI; Japanese Nuclear Data Committee, Atomic and Molecular Data Research Committee, Research Committee on Reactor Physics and Research Committee on Marine Reactors. The purpose and the expected task of each committee are summarized here. The detailed activities of each committee are presented in the following sections.

Japanese Nuclear Data Committee

The Committee is organized to promote the evaluation of nuclear data and the production of group constants for application fields. There are three subcommittees, six standing groups and a steering committee under the Committees. The Committee also takes a task of compiling the activities of the International Nuclear Data Committee and the Working party on International Evaluation Cooperation under OECD/NEA/NSC.

Atomic and Molecular Data Research Committee

The Committee is organized to promote activities on atomic and molecular data for the research and development of controlled thermonuclear fusion. Three working groups are organized under the Committee.

Research Committee on Reactor Physics

The Committee reviews the research activities related to reactor physics in Japan and supports the activities of Nuclear Science Committee (NSC) of OECD/NEA. Two subcommittees on future nuclear energy system and high energy nucleonics are organized under the Committee.

Research Committee on Marine Reactors

The Committees is organized to review and discuss the research and development activities on marine reactors. Three subcommittees are organized under the Committee. The meeting of the Committee is normally held twice a year to discuss the present activities.

15.1 Activities of Japanese Nuclear Data Committee

A. Hasegawa

The Japanese Nuclear Data Committee (JNDC) consists of three subcommittees, six standing groups, a steering committee. Each subcommittee also consists of several working groups (WG). The Committee Meeting of JNDC was held in July 1998 to discuss the nuclear data activity in the previous fiscal year and plans for the fiscal year 1998. Furthermore, discussion was made on several topics including the planning of the 1998 Symposium on Nuclear Data and the international collaboration on nuclear data.

The 1998 Symposium on Nuclear Data, which is held every year, and a specialists' meeting on Delayed Neutron Nuclear Data, which is a topical meeting held every year on the selected hottest topics in the period, were held.

The activities of subcommittees and standing groups are briefly summarized below.

Subcommittee on Nuclear Data

1) High Energy Nuclear Data Evaluation WG :

WG structure of this group was changed drastically to perform the mission in high-energy data evaluation more efficiently. Two WGs relating to high-energy data evaluation, i.e., PKA Spectrum WG and Photonuclear Data WG, are merged into this WG. Under this WG, several sub-WGs (SWG) were reorganized. Finally all of the High Energy Files of JENDL are being made by this WG.

The evaluation is made in two phases. In the phase-I, the data up to 50 MeV for IFMIF(International Fusion Material Irradiation Facility) project is evaluated for neutron and proton induced reactions. In the phase-II, high-energy neutron/proton induced reactions up to 3GeV will be made. The maximum energy limit of 3GeV is extended from previous 2GeV specification to this value by the requests from the projects of JAERI Neutron Research Center and Japan Hadron Facility. Following is the status of each SWG.

- IFMIF Neutron File Compilation SWG: Neutron file compilation is the main task of this SWG. Up to now, evaluation of 62 nuclides in the phase-I for the neutron-induced reaction data has been finished and filed. The files are in the reviewing stage.
- MeV and GeV File compilation SWG: Compilation and evaluation of phase-II data is a main mission. This group is also responsible for proton-induced reaction data of structural materials in the Phase-I data. For Phase-II evaluation, the data of H, Al, Si, Cr, Ni, Cu, Pb and Bi have been evaluated up to 1GeV. The review of the evaluated results is in progress.

2) Covariance Data Evaluation WG : Methods of covariance matrix evaluation have been investigated. Full covariance matrices for Cr, Ni and fission spectra covariance matrices

for U-233,-235,-238 and Pu-239,-240 have been evaluated in ENDF/B-6 format. Evaluations were made by using a least-squares program GMA for the case of rich experimental data available. For the data evaluated by model calculations, covariances were obtained by using the KALMAN code system developed by Kyushu University. Processing system for the covariance files are also developed Group averaged data are generated by this system.

3)Evaluation and Calculation System WG : Scope of this WG was reviewed again by the WG members. Main missions were decided to supply evaluators recommended parameters required in the nuclear model calculations such as OMP, level density, gamma strength functions, as well as advanced methodologies like multi-modal fission, essence from the latest frontiers of theoretical calculations.

4) Fission Product Nuclear Data WG : This group has been making evaluations of JENDL FP nuclides and producing JEDL-FP data libraries. This group has the longest subgroup history about 35 years in JNDC. Closing of this sub group was decided due to the completion of the long standing missions at FY1997.

5) Activation-Cross-Section Data WG : The first version of Activation Cross Section File was completed and released in March 1996. Preparation for the evaluation report has been progressed. Due to the completion of the mission this sub group was closed at FY1997.

7) Charged Particle Nuclear Data WG : This WG is responsible for the JENDL (alpha,n) Reaction File. Calculation for C (alpha,n) angular distribution was made.

9) Delayed neutron data evaluation WG: This group was set up due to the follow up work of OECD/NEA/WPEC(Working Party on Evaluation Cooperation) subgroup 13 to investigate the delayed neutron data related problems. Evaluations of delayed neutron yields and spectra for main actinides of JENDL 3.3(U-235,-238,Pu-239) are also the mission of this group. 6 group time dependent scheme evaluation will be taken.

10) Evaluation WG on Intermediate Mass Elements: This WG was set up due to the revision fork for JENDL-3.3. Re-evaluation work has been progressed for Na-23, V-51, Co-59, Cr, Ti, Ni, W, Nb and Er.

11) Evaluation WG on Heavy Mass Elements: This WG was set up due to the revision fork for JENDL-3.3. Re-evaluation work has been progressed for U-233, -235,-236,-238 and Pu-236,-239,-240,-241,-242.

12) Fission Yields Evaluation WG: This group was organized so as to work with IAEA CRP. To give precise mass yields data for minor actinides as well as major actinides covering the wide range of incident neutron/proton energies is the main mission. This group was decided to move to Subcommittee on Nuclear Fuel Cycle considering the efficiencies and close affinities of the objects of the study.

Subcommittee of Reactor Constants

1) Reactor Integral Test WG : Benchmark test of JENDL-3.2 for fast and thermal reactors has been made. For thermal reactors, TCA and STACY benchmark problems are defined and analyzed(4 U lattices and 4 Mox lattices). For fast reactors, some benchmark models of metallic fueled cores of FCA XVI-1&2 , one Mox fueled core of FCA XVII-1 and three benchmark models of ZPPR-9 are defined and analyzed. Inert matrix benchmarks are also defined and analyzed.

2) Shielding Integral Test WG : This group was re-organized according to the mission of the group. The part of the missions for high energy data testing is moved to the high energy nuclear data WG in the subcommittee on Nuclear Data. Thus, the rest part, i.e. benchmark tests up to 20 MeV data of JENDL, is solely responsible to this group. Up to now, only preparation works for the benchmark tests of main shielding materials of JENDL-3.3 are scheduled because no new evaluations are available yet.

3) Dosimetry Integral Test WG : Reevaluation work has been progressed. Revision work for covariance data is a key item in this WG. A new version will be released in FY1999.

4) Fusion Neutronics Integral Test WG : This is a joint working group established between JNDC and the Committee of Reactor Physics of JAERI. Up to now all missions have been completed. Thus this group was closed last year. Revitalization is foreseen in the next version of JENDL-3.3 benchmarks.

5) Standard Group Constants WG : Revision work for JSSTDL library has been progressed.

Subcommittee on Nuclear Fuel Cycle

The subcommittee on nuclear fuel cycle consists of two WGs, Decay Heat Evaluation WG and WG on Evaluation of Nuclide Generation and Depletion. Generation of an ORIGEN-2/JNDC library based on JENDL-3.2 and JNDC FP Decay Data File has been made. A completely new entry for PWR-UO2, BWR-U2 and BWR-MOX has been added as a joint effort of the two WGs. Post irradiation experiment analysis using newly produced library was made to check the applicability. Re-evaluation work for the decay and fission yield data of the second version of JNDC FP Decay Data Library has been progressed to fix up the discrepancy in the decay heat calculation for the time interval from 300 to 3000sec existed as gamma-ray discrepancy.

Standing Groups

1) CINDA Group : Papers on neutron induced reaction data published in Japanese journals and reports are surveyed. Total of 127 entries were sent to the NEA Data Bank in the last one year to update the CINDA master database.

2) ENSDF Group : The evaluation of nuclear structure data is the duty of this group for

nuclei with mass numbers from 118 to 129. Re-evaluation were made for A= 125 and 119 .

3) Group on Atomic, Molecular and Nuclear Data for Medical Use : Survey work has been made for the radiopharmaceutical data needed in the field of nuclear medicine. Especially photo reaction data were discussed in details.

4) JENDL Compilation Group : Discussions were made about the strategic method for the production of JENDL-3.3 and preparation of review kits for actinides file have been made.

5) Editorial Group of "Nuclear Data News" : Three issues of "Nuclear Data News" (No.60-62) which is a periodic informal journal circulated in nuclear data communities of Japan (written in Japanese) were published in a year. Total of about 700 were distributed in the communities.

6) High Priority Request List Group: This group was newly established by the scrap and build of the former WRENDA group to supply Japanese requests cooperating with the relevant group of OECD/NEA/WPMA (Working Party on Measurement Activity).

The 1998 Symposium on Nuclear Data

The 1998 Symposium on Nuclear Data was held at Tokai Research Establishment of JAERI on 19th and 20th of November 1998. Japanese Nuclear Data Committee and Nuclear Data Center of JAERI organized this symposium. In the oral sessions, presented were 15 papers on accelerator facilities, astrophysics, international relations, radiation damage study and integral test of nuclear data. In the poster session, presented were 36 papers concerning experiments, evaluations, benchmark tests and on-line database on nuclear data. Total of 172 attendees including 14 foreigners, 102 outside JAERI were gathered.

Specialists' Meeting on Delayed Neutron Nuclear Data

The meeting was held on 28th and 29th January 1999 at JAERI TOKAI site. Total of 30 specialists were attended from all over Japan (research establishment (22), universities (5) and industries (3) : the number of the parenthesis is attendees.). Following topics were presented and discussed: Status of delayed neutron nuclear data, problems in the evaluations using aggregation method, integral measurements of β -eff in the typical critical assemblies (FCA, TCA, VHTRC), impacts of the delayed neutron data to the high level waste incineration applications in reactors and panel discussions for the future of this research.

15.2 Activities of Atomic and Molecular Data Research Committee

T. Shirai

The Atomic and Molecular (A&M) Data Research Committee is organized to promote activities on A&M data for the research and development of controlled thermonuclear fusion. The committee consists of members from JAERI, universities and other research institutions. Three working groups concerning particle-material interaction, atomic collision and atomic structure are organized under the Research Committee.

In collaboration with the A&M Data Research Committee, compilation and evaluation work is continued for making the 5th edition of Japanese Evaluated Atomic and Molecular Data Library (JEAMDL-5) as a five-year project from 1997. The activities of these three working groups are briefly summarized below.

Particle-material interactions data relevant to hydrogen-recycling in edge plasmas were surveyed and reviewed for retention and re-emission of hydrogen isotopes implanted into tungsten monocarbide and for dynamic behavior of hydrogen isotopes in tungsten-carbon composite materials. In conjunction with reduction of tritium inventory, data survey was made for exchange of deuterium implanted into oxide ceramics for protium. Irradiation effects of H^+on the crystal structure and band structure of silicon were surveyed to elucidate the release mechanism of excited hydrogen atoms and molecules from fusion structural materials.

Analytical least-squares fits were made to the recommended cross sections for many different collision processes of H_2O, CO, and CO_2 by electron impacts. Theoretical and experimental data production was made for the cross sections for state-selective electron capture in collisions of H, He, Be ions with He, and the electron capture cross sections of multiply charged Ne ions in collisions with hydrocarbons and of singly and doubly ionized Be ions with rare gases, respectively.

Data compilation has been finished of wavelengths, energy levels, ionization energies, line classifications, intensities and transition probabilities for argon in all stages of ionization. A similar data compilation is now in progress for tungsten.

15.3 Activities of the Research Committee on Reactor Physics

M. Nakagawa, T. Osugi and Y. Ikeda

The committee reviews research activities related to reactor physics in Japan and supports the activities of Nuclear Science Committee (NSC) of OECD/NEA. The committee consists of two sub-committees. The Reactor System Sub-committee discusses topics of future nuclear energy system, core analysis methods and reactor physics experiments. The Sub-committee on High Energy Nucleonics involves neutronics and diagnostics of fusion reactors, and various issues related to high energy neutrons, protons, etc., associated with high energy particle accelerators.

The 68th meeting of the Research Committee on Reactor Physics (RCRP) was held in July 1998. This meeting was joined with the 48th meeting of the Sub-committee on Reactor System. The following subjects were discussed: 1) International Benchmark Experiment on Effective Delayed Neutron Fraction in FCA Facility and 2) Status on Thorium Fuel Cycle Study. Documents discussed at the 9th meeting of NEA/NSC held at OECD Headquarters, Paris, June 3 - 5 1998 were distributed.

In the Sub-committee on Reactor System, the meetings were held twice in FY-1998: the 48th meeting held in July 1998 and the 49th one in February 1999. The former meeting was joined with the meeting of the RCRP, mentioned above. In the 49th meeting, the following subjects on topics of High Temperature Testing Reactor were discussed.

- The critical approach, the measured and calculated critical mass for the initial core and the measurements and analyses of core characteristics in the start-up program
- Application of the analyses of Mock-up Experiments in Critical Facility VHTRC to the estimation of critical mass for HTTR.

The 5th and the 6th sub-committee meetings of High Energy Nucleonics were held in October 1998 and March 1999, respectively. The following topics were focused on and were discussed.

- Experiments on Target of Spallation Source at AGS/BNL facility,
- Skyshine experiments at OKTAVIAN in Osaka university,
- Overview on SARE4 workshop on simulation codes for high energy radiation fields,
- A summary report of SATIF4 specialists meeting which was highlighted the international accelerator shielding benchmark endeavor,
- International Program on Irradiation Facility for Fusion Reactor Material,
- Status of ITER/EDA R&D program,
- Shielding Experiments in Spallation Neutron Source Facility ISIS,

- Progress in preparation for the ninth international conference on radiation shielding.

In FY-1998, all the meetings devoted to reconsider and to discuss the activities of the committee. Finally it was decided that the Sub-committee on High Energy Nucleonics was closed in FY-1998 and that several working parties relevant to the special tasks of reactor physics would be organized in the committee in the next fiscal year.

15.4 Activities of Research Committee on Marine Reactors

T. Ishida and J.Shimazaki

(*E-mail*: ishida@koala.tokai.jaeri.go.jp).

The committee is organized to review and discuss research and development (R&D) activities on marine reactor design and related technologies. The committee consists of three subcommittees : One is the subcommittee on concept design of a highly compact marine reactor for usage of submersible research vessel. The second is the subcommittee on feasibility study for stability evaluation of evolutional nuclear plant siting. The last one, which is at rest, is the subcommittee for review of Mutsu irradiated fuel and its forthcoming testing. The former two subcommittees have each working group respectively for detailed discussion on specific issues. The committee's members are from Japan Atomic Energy Research Institute (JAERI), universities, other research institutions and industries including reactor or ship manufactures and utilities.

The committee meeting is normally held twice a year. The R&D plan and activities of the subcommittees for the FY 1998 were reviewed and discussed in September 1998 and March 1999.

Subcommittee on concept design of a highly compact marine reactor

The subcommittee meetings were held twice in October 1998 and March 1999 respectively. The main topics were the reviews of plan on thermal-hydraulic experiment for the highly compact marine reactor, estimation of radioactive corrosion products in the highly compact marine reactor without purification system, and the report of working group activities of needs survey on utilization of the highly compact marine reactor.

The plan of thermal-hydraulic experiment for the highly compact marine reactor were reviewed on the purposes which are aiming to confirm the function of the passive safety system with a water filled containment vessel and a decay heat removal system by natural circulation and to study thermal hydraulics in the integral type reactor, the design of the experimental apparatus which will be build in three years, and the preliminary analysis of the experiment. On the estimation of radioactive corrosion products in the primary loop, a qualitative evaluation of the highly compact marine reactor by CTAM-Ⅱ code developed for the marine reactor was introduced, and the effect of the purification system on the amount of corrosion products which is very small in this reactor was reviewed.

The report from the working group of which members included the experts such as physical oceanographers, geophysicists, ocean-biologist etc., put together the needs-survey for scientific research

of under sea by using submersible vessel installed with the highly compact marine reactor. The pressing research needs is placed at the undersea of water depth below 600m in the Arctic Ocean and at low latitude sea where a normal observation ship hardly investigate due to thick ice or storm, although the possible important parameters dominating the earth environmental change such as the earth-warmness exist there. The concept of submersible research vessel for 16 persons with 500 tons of weight, 12 knots of speed, which requires a light-weighted, safe, and easy in operation power source generating for a long time with the maximum electric power of 250 kW, was made. To meet this requirement, the concept of highly compact marine reactor with 1250 kWt of thermal output called as SCR was presented and reviewed.

Subcommittee on feasibility study for stability evaluation of evolutional nuclear plant siting

The feasibility study for stability evaluation was four year survey project supported by the Science and Technology Agency. The purposes of this study are to examine the safety and the technical requirements for offshore nuclear power plants, and to discuss the engineering concepts and problems of design to evaluate the feasibility of offshore siting. The fourth year work was discussed and summarized in this year. The subcommittee meetings were held three times in June, November 1998, and March 1999. The working group meeting also held six times for discussing about natural event classification for safety design, data of meteorological, oceanic and seaquake phenomena, maximum magnitude of natural events, an engineering concept of offshore floating nuclear power plant and so on.

The results of this study were summarized as follows.

(1) The feasibility type nuclear plant siting has more technical requirements than in offshore artificial islands, but has a feasibility of construction by present technologies.

(2) The offshore floating nuclear power plant have a couple of advantages of seismic isolation, standardization of design and manufacturing, reduction of labor cost etc..

(3) The conceptual review of the offshore floating plant shows technically feasible, but additional design studies needed for the accidents.

(4) The survey on evaluation of the floating platform stability shows that the methods for predicting the motion of large-sized floating structure exist and an floating platform with protective break water has a sufficient stability by a simulation analysis.

Publication List

1. Nuclear Data and Atomic Molecular Data

1) Shibata, K., Nakajima, Y. and Murata, T.:"Estimation of Covariances of ^{10}B, ^{11}B, ^{55}Mn, ^{240}Pu and ^{241}Pu Neutron Nuclear Data", JAERI-Research 98-045 (1998)
2) Maslov, V.M., *et al.*:"Neutron Data Evaluation of ^{238}U", JAERI-Research 98-040 (1998)
3) Chiba, S., *et al.*:"Measurement and Theoretical Analysis of Neutron Elastic Scattering and Inelastic Reactions Leading to a Three-Body Final State for ^{6}Li at 10 to 20 MeV", Phys. Rev., C58, 2205 (1998)
4) Ibaraki, M., *et al.*:"Measurement and Theoretical Analysis of Neutron-Induced Neutron-Emission Reaction of ^{6}Li at 10 to 20 MeV Region", JAERI-Research 98-032 (1998)
5) Kawano, T., *et al.*:"Evaluation of Covariance for Fission Neutron Spectra", JAERI-Research 99-099 (1999) [in Japanese]
6) Sukhovitskii, E.Sh., *et al.*:"Programs OPTMAN and SHEMMAN Version 5 (1998) - Coupled Channels Optical Model and Collective Nuclear Structure Calculation-", JAERI-Data/Code 98-019 (1998)
7) Sukhovitskii, E.Sh., *et al.*:"New Options of Coupled Channels Optical Model Code OPTMAN Version 6 (1999)", JAERI-Data/Code 99-028 (1999)
8) Sukhovitskii, E.Sh., Chia, S. and Iwamoto, O.:"Coupled-Channels Optical Model Calculations with Account of Nuclear Volume Conservvation", Nucl. Phys., A646, 19 (1999)
9) Sukhovitskii, E.Sh., *et al.*:"Nucleon Interaction with ^{12}C Studied by the Soft-Rotator Model and a Limit on the Charge-Symmetry Breaking in the Nuclear Mean Field", Nucl. Phys., A640, 147 (1998)
10) Lee, Y., Fukahori, T. and Chang, J.:"Evaluation of Photonuclear Reaction Data on Tantalum-181 up to 140 MeV", J. Nucl. Sci. Technol., 35(10), 685 (1998)
11) Fukahori, T. and Japanese Nuclear Data Committee :"Status of Nuclear Data Evaluation for Photonuclear Data File", Proc. of the Third Specialists' Meeting on Shielding Aspects of Accelerators, Targets and Irradiation Facilities (SATIF-3), May 12-13, 1997, Tohoku University, Sendai, Japan, pp. 43 (OECD/NEA, 1998) ISBN 92-64-16071-X (1998)
12) Fukahori, T., *et al.*:"Status PKA, KERMA and DPA Files of JENDL", REACTOR DOSIMETRY, Proc. of the Ninth International Symposium on Reactor Dosimetry, September 2-6, 1996, Prague, Czech Republic, (Eds.) H.A. Abderrahim, P. D'hondt and B. Osmera, (World Scientific Publishing, Singapore, 1998) ISBN 981-02-3346-9, pp.449 (1998)
13) Uno, Y., *et al.*:"Measurement of Activation Cross Sections for Neutron Dosimetry at an Energy Range from 17.5 to 30 MeV by Using the $^{7}Li(p,n)$ Quasi-mono-energetic Neutron Source", REACTOR DOSIMETRY, Proc. of the Ninth International Symposium on Reactor Dosimetry, September 2-6, 1996, Prague, Czech Republic, (Eds.) H.A. Abderrahim, P. D'hondt and B. Osmera, (World Scientific Publishing, Singapore, 1998) ISBN 981-02-3346-9, pp.465 (1998)
14) Aruga, T., *et al.*:"Damage Energy Cross Sections of Charged Particles from Light Nuclides Irradiated with High Energy Neutrons", REACTOR DOSIMETRY, Proc. of the Ninth International Symposium on Reactor Dosimetry, September 2-6, 1996, Prague,

Czech Republic, (Eds.) H.A. Abderrahim, P. D'hondt and B. Osmera, (World Scientific Publishing, Singapore, 1998) ISBN 981-02-3346-9, pp.359 (1998)
15) Chiba, S., *et al.*:"Study of Intermediate-energy Total Reaction Cross Sections of Light- and Heavy-Ion Induced Reaction by an Improved QMD Framework", Proc. of Int. Conf. on Nuclear Data for Sci. and Technol., May 19-24, 1997, Trieste, Italy, p.320 (1998)
16) Watanabe, Y., *et al.*:"Continuum (p, p'x) Spectra at 14.1 and 26 MeV", Proc. of Int. Conf. on Nuclear Data for Sci. and Technol., May 19-24, 1997, Trieste, Italy, p.580 (1998)
17) Fukahori, T., *et al.*:"Status of JENDL Intermediate Energy Nuclear Data Files", Proc. of Int. Conf. on Nuclear Data for Sci. and Technol., May 19-24, 1997, Trieste, Italy, p.899 (1998)
18) Shibata, K., *et al.*:"JENDL-3.2 Covariance File for Fast Reactors", Proc. of Int. Conf. on Nuclear Data for Sci. and Technol., May 19-24, 1997, Trieste, Italy, p.904 (1998)
19) Kawai, M., *et al.*:"PKA, KERMA and DPA Files of JENDL", Proc. of Int. Conf. on Nuclear Data for Sci. and Technol., May 19-24, 1997, Trieste, Italy, p.1110 (1998)
20) Maekawa, H., Fukahori T. and Oyama Y.:"Status of Required Nuclear Data for Intense d-Li Neutron Source", Proc. of Int. Conf. on Nuclear Data for Sci. and Technol., May 19-24, 1997, Trieste, Italy, p.1473 (1998)
21) Nakamura, T., Fukahori, T., and Menapace, E.:"Relevant Nuclear Data Topics Related to Shielding Aspects for Accelerators and Irradiation Facilities", Proc. of Int. Conf. on Nuclear Data for Sci. and Technol., May 19-24, 1997, Trieste, Italy, p.1478 (1998)
22) Fukahori ,T.:"Status of JENDL High Energy File - Evaluation Method, Tools, Specification, Release Procedure, etc. -", Proc. of the Third Specialists' Meeting on High Energy Nuclear Data, Mar. 30-31, 1998, JAERI, Tokai, Japan, JAERI-Conf 98-016, pp.37 (1998)
23) Watanabe, Y., *et al.*:"Status of Experimental Data of Proton Induced Reactions for Intermediate Energy Nuclear Data Evaluation", Proc. of the Third Specialists' Meeting on High Energy Nuclear Data, Mar. 30-31, 1998, JAERI, Tokai, Japan, JAERI-Conf 98-016, pp.16 (1998)
24) Nakashima, H., *et al.*:"Review of Recent Benchmark Experiments on Integral Test for High Energy Nuclear Data Evaluation", Proc. of the Third Specialists' Meeting on High Energy Nuclear Data, Mar. 30-31, 1998, JAERI, Tokai, Japan, JAERI-Conf 98-016, pp.66 (1998)
25) Lee, Y. and Fukahori, T.:"Intercomparison of High Energy File [Neutron Induced, from 20 to 150 eV]", Proc. of the Third Specialists' Meeting on High Energy Nuclear Data, Mar. 30-31, 1998, JAERI, Tokai, Japan, JAERI-Conf 98-016, pp.97 (1998)
26) Lee ,Y.-O., *et al.*:"Evaluation of Neutron- and Proton-Induced Cross Sections of ^{27}Al up to 2 GeV", Proc. of the 1998 Symposium on Nuclear Data, Nov. 19-20, 1998, JAERI, Tokai, Japan, JAERI-Conf 99-002, pp.246 (1999)
27) Harada, M., *et al.*:"Study of Secondary Charged-particle Production by Proton-induced Reactions at Several Tens of MeV", Proc. of the 1998 Symposium on Nuclear Data, Nov. 19-20, 1998, JAERI, Tokai, Japan, JAERI-Conf 99-002, pp.268 (1999)
28) Bersillon, O., *et al.*:"Handbook for Calculations of Nuclear Reaction Data, Reference Input Parameter Library, Final Report of a Co-ordinated Research Project", IAEA-TECDOC-1034, IAEA (1998)
29) Oyama, Y., *et al.*:"A Study of Existing Experimental Data and Validation Process for

Evaluated High Energy Nuclear Data - Report of Task Force on Integral Test for JENDL High Energy File in Japanese Nuclear Data Committee -", JAERI-Review 98-020 (1998) [in Japanese]
30) Koning, A.J., Fukahori, T. and Hasegawa, A.:"International Evaluation Co-operation, Volume 13: Intermediate Energy Data", OECD/NEA/WPEC-13 (1998)
31) Fukahori, T.:"JAERI Progress Report of IAEA/CRP on Compilation and Evaluation of Photonuclear Data for Applications", Summary Report of the 2nd Research Coordination Meeting on Compilation and Evaluation of Photonuclear Data for Applications, Jun. 23-26, 1998, Los Alamos, USA, INDC(NDS)-384 (1998) pp.33 (1998)
32) Fukahori, T.:"Japanese Proposal and Contribution for IAEA/CRP on RIPL-II", Summary Report of the 1st Research Coordination Meeting on Nuclear Model Parameter Testing for Nuclear Data Evaluation (Reference Input Parameter Library: Phase II), Nov. 25-27, 1998, IAEA Headquarters, Vienna, Austria, INDC(NDS)-389 (1999) pp.39 (1999)
33) Fukahori, T.:"Present Status on the Evaluation of High Energy Neutron Cross Sections and the Transport Calculation Libraries", Monte Carlo Simulation on Nuclear Energy Study - Annual Report pf Nuclear Code Evaluation Committee -, (Eds.) Sakurai, K. and Yamamoto T., JAERI-Review 99-013, pp.3 (1999)
34) Fukahori, T. and Katakura, J.:"Report of the First Research Coordinate Meeting for IAEA/CRP on Fission Product Yield Data Required for Transmutation of Minor Actinide Nuclear Waste", J. Atom. Ener. Soc. of Japan, A40(5), 363 (1998) [in Japanese]
35) Katakura, J. and England, T.R.:"Introduction of Model Calculated Beta-Ray Spectrum to ENDF/B-VI Fission Products Decay Data File", Proc. Int. Conf. on the Physics of Nuclear Science and Technology, Brookhaven National Laboratory, pp438 (1998)
36) Suyama, K., *et al.*:"Libraries Based on JENDL-3.2 for ORIGEN2 Code : ORLIBJ32", JAERI-Data/Code 99-003 (1999) [in Japanese]
37) Suzuki, S., *et al.*:"Molecular-state Treatment of Electron Capture in Collisions with Be^{3+} Ions with Helium Atoms below 10 keV/amu", Phys. B 31, 1741 (1998)
38) Suzuki, S., *et al.*:"Attenuation of High-energy Neutral Hydrogen Beams in High-density Plasmas", Plasma Phys. Control. Fusion 40, 2097 (1998)
39) Ichihara, A., Iwamoto, O. and Yokoyama, K.:"Cross Sections for ion Production in Reactions of H^+ with D_2. Effects of Vibrational and Rotational Excited States of, D_2", JAERI-Research 98-056 (1998)
40) Eichler, J., Ichihara, A. and Shirai, T.:"Alignment Caused by Photoionization and in Radiative Electron Capture into Excited States of Hydrogenic High-Z Ions", Phys. Rev., C58, 2128 (1998)
41) Ichihara, A., Yokoyama ,K. and Iwamoto, O.:"Potential Energies for the Two Lowest 1A' Electronic States of H_3^+", JAERI-Data/Code 98-031 (1998)

2. Theoretical Method and Code Development

1) Kugo, T. and Nakagawa, M:"Application of Neural Network to Multi-Dimensional Design Window Search in Reactor Core Design", J. Nucl. Sci. Technol., 36, 332 (1999).
2) Ueki, K., Mori, T., Sakurai, K., Nakagawa, M., *et al.*:"Present Status of Monte Carlo Simulation for Neutron and Photon Transport Analysis", J. At. Energy Soc. Jpn, 41, 614

(1999) [in Japanese].
3) Kugo T. and Nakagawa M.:"Applicability of Design Window Search Procedure Using Neural Network to Neutronics", Proc. Int. Conf. Phy. Nucl. Sci. Tech., Long Island, 704 (1998).
4) Kugo, T. Shimada, S., Ohkubo, T. and Ochiai, M.:"Study on Nuclear Physics of High Burnup Full MOX PWR Core", JAERI-Research 98-059 (1998) [in Japanese].
5) Oigawa, H.:"Application of Anisotropic Neutron Streaming Effect in Plate Cell Geometry to Transport Theory", JAERI-Research 98-061 (1998) [in Japanese].
6) Okumura, K.:"MOSRA-Light ; High Speed Three-Dimensional Nodal Diffusion Code for Vector Computers", JAERI-DATA/Code 98-025 (1998) [in Japanese].
7) Ishiguro, M., Tsuboi, K. and Fujimura, T.:"Studies on the Technology of Parallel Numerical Processing", Annual Rep. Inter-University Joint Research Using the JAERI Facilities, Univ. Tokyo (1999). [in Japanese].

3. Reactor Physics Experiment and Analysis

1) Parish, T. A., Charlton, W. S. , Shinohara, N., Andoh, M., *et al.*:"Status of Six-Group Delayed Neutron Data and Relationships Between Delayed Neutron Parameters from the Macroscopic and Microscopic Approaches", Nucl. Sci. Eng., 131, 208 (1999).
2) Spriggs, G. D., Busch, R. D., Sakurai, T. and Okajima, S.:"The Equivalent Fundamental - Mode Source", Ann. Nucl. Energy, 26, 237 (1999).
3) Shinohara, N. ,Hatsukawa, Y. , Hata, K., Kohno, N. , Andoh, M. , *et al.*:"Measurements of Nuclear Data of Minor Actinides for Transmutation of High-level Waste", J. Radioanal. Nucl. Chem., 239, 631 (1999).
4) Oigawa, H., Iijima, S. and Andoh, M.:"Experiments and Analyses on Sodium Void Reactivity Worth in Mock-up Cores of M*et al.*lic Fueled and MOX Fueled Fast Reactors at FCA", J. Nucl. Sci. and Technol., 35, 264 (1998).
5) Okajima, S., Zuhair, Sakurai, T. and Song, H.:"Evaluation of Delayed Neutron Data Using FCA β_{eff} Benchmark Experiment", J. Nucl. Sci. and Technol., 35, 963 (1998).
6) Andoh, M. , Okajima, S., Oigawa, H., and Iijima, S.:"Measurement of ^{238}U Doppler Effect in A Nitride Fueled LMFBR at FCA", J. Nucl. Sci. Technol., 36, 386 (1999).
7) Osugi, T. and Okajima, S.:"The Present Active Status of Domestic Critical Assemblies and the Perspective for Their Future,- II-3. Fast Critical Assembly (FCA)-", J. At. Energy Soc. Jpn, 40, 259 (1998) [in Japanese].
8) Akino, F. and Yamane, T.:"The Present Active Status of Domestic Critical Assemblies and the Perspective for Their Future,-II-4. Very High Temperature Reactor Critical Assembly (VHTRC)-", J. At. Energy Soc. Jpn, 40, 262 (1998) [in Japanese].
9) Shiroya, S. and Okajima, S.:"Fortieth Anniversary Commemorative Issue, 2. Fission Energy Engineering, 2-1 Reactor Physics, 2. Reactor Physics Experiments and Analyses", J. At. Energy Soc. Jpn, 41, 318 (1999) [in Japanese].
10) Spriggs, G. D., Bunch, R. D., Sakurai, T. and Okajima, S.:"Measurement of the Equivalent Fundamental-Mode Source Strength", Trans. Am. Nucl. Soc., vol. 76, 374 (1997).
11) Sakurai, T., Okajima, S., Sodeyama, H , Osugi, T., *et al.*:"Benchmark Experiments of Effective Delayed Neutron Fraction β_{eff} in JAERI-FCA", Int. Conf. Nuclear Science and

Technology, Long Island, USA, 182 (1998).
12) Okajima, S., Oigawa, H., Andoh M., *et al.*:"Doppler Effect Measurement up to 2000 in the Fast Critical Facility FCA", Proc. 9-th Int. Symp. Reactor Dosimetry, Prague, Czech Republic, World Scientific Publishing, Singapore, ISBN981-02-3346-9, 172 (1998).
13) Sakurai, T., and Nemoto, T.:"Measurements and Analyses of Breeding Indices of ^{238}U Capture to ^{239}Pu Fission Rate Ratio and ^{238}U Capture to ^{235}U Fission Rate Ratio at Fast Critical Facility FCA", Proc. 9-th Int. Symp. Reactor Dosimetry, Prague, Czech Republic, World Scientific Publishing, Singapore, ISBN981-02-3346-9, 189 (1998).
14) Yamane, T., Yamashita, K. and Fujimoto, N.:"Weapons-Grade Plutonium Burning with HTRs", The first ISTC/SAC Seminar on New Approaches to the Nuclear Fuel Cycles and Related Disposal Schemes, Sarov, Russia, vol. 1, 267 (1998).
15) Yamashita, K., Andoh, H., Fujimoto, N., Nojiri, N., Nakano, M., Nagao, M., Nagaya, Y., Akino, F., *et al.*:"Benchmark Problems of Start-up Core Physics of High Temperature Engineering Test Reactor (HTTR)", Proc. IAEA-TCM on High Temperature Gas Cooled Reactor Applications and Future Projects, Holland, ECN-R--98-004, 185 (1998).
16) Okajima, S., Osugi, T., Nakajima, K., *et al.*:"Status and Future Program of Reactor Physics Experiments in JAERI Critical Facilities, FCA and TCA", Proc. 1998 Symp. Nuclear Data, JAERI-Conf 99-002, 92 (1999).
17) Kaneko, Y., Nagao, Y., Yamane, T. and Takeuchi, M.:"Two Proposals for Determination of Large Reactivity of Reactors", The Sixth Symposium on Research Reactors, Mito Japan, JAERI-Conf 99-006, 316 (1999).
18) Katoh, Y., Okajima, S. and Sakurai, T.:"BETA -A Code for β_{eff} Measurement and Analysis- ", JAERI-Data/Code 99-006 (1999) [in Japanese].
19) Yamane, T. and Tsuchihashi, K.:"A Fortran Code CVTRAN to Provide Cross-section File for TWODANT by Using Macroscopic File Written by SRAC", JAERI-Data/Code 99-011 (1999).
20) Osugi, T.:"Reactor Physics Experiment on High Conversion Light Water Reactor at FCA ", Text of 30-th Summer Seminar on Reactor Physics, At. Energy Soc. Jpn., 118 (1998) [in Japanese].
21) Haruyama, M.:"4.5 High Sensitive Detection of Fissionable Material by Active Neutron Method", JAERI Research Activities in FY 1998, JAERI, 60 (1998) [in Japanese].

4. Advanced Reactor System Design Studies

1) Shirakawa, T., *et al.*:"Study on Nuclear Physics of High Burn-up Full MOX-BWR Core", JAERI-Research 98-047 (1998) [In Japanese].
2) Okubo, T., *et al.*:"Steady-state and Transient DNB Analyses for JAERI Passive Safety Reactor (JPSR) using COBRA-IV- I and RETRAN-02/Mod3 Codes", JAERI-Research 98-042 (1998).
3) Kugo, T., *et al.*:"Study on Nuclear Physics of High Burnup Full MOX PWR Core",JAERI-Research 98-059 (1998) [In Japanese].
4) (Eds.) Nakajima, N. and Ochiai, M.:"The Study Meeting Report on the Undermoderated Spectrum Reactor: March4-5, 1998, JAERI, Tokai Japan", JAERI-Conf 98-013 (1998) [In Japanese].

5. Reactor Instrumentation, Control and Diagnostics

1) Kakuta, T., *et al.*:"Observation of Optical Signals using Optical Fibers in Operating Fission Reactor Core", VSJ-SPIE98, Yokohama, Japan, AB-054 (1998).
2) Kakuta, T., *et al.*:"Application of Silica Core Optical Fibers to Diagnostics in Heavy Irradiation Environment",VSJ-SPIE98, Yokohama, Japan, AB-053 (1998).
3) Nabeshima, K., *et al.*:"Nuclear Power Plant Monitoring with Recurrent Neural Network", EANN98, Gibraltar (1998).
4) *idem*: "Early Fault Detection for Nuclear Power Plant using Recurrent Neural Network", The 5th Int. Conf. on Neural Information Processing, Kitakyusyu, Japan (1998).
5) Suzudo, T., *et al.*:"Experimental Analysis of Coherent Neutron-Flux Fluctuation Observed in PWR", Nucl. Sci. Eng.,129, 203(1998).
6) Suzudo, T.:"Crystallisation of 2-dimesional Cellular Automata", Complex International vol. 6 (1999).
7) Kosaka, A. and Suzudo, T.:"OECD/NEA, SCORPIO-VVER Project", JAERI- Review 99-012 (1999).
8) Ishikawa, N., *et al.*:"A Method of Reactor Power Decrease by 2DOF Control System during BWR Power Oscillation", JAERI-Research 98-055 (1998) [In Japanese].
9) *idem*:"Development of Human Collaborative Mobile Robot System", The 4th Robotics Symposia, 22C3 (1999) [In Japanese].
10) Itoh, H., *et al.*:"Pulse Shape Measurement of Scintillation Emission", JAERI-Tech 98-043 (1998) [In Japanese].
11) Yamagishi, H., *et al.*:"Design of the Characteristic Impedance and Trial Manufacturing of the Solenoid Electrode Structure for a Position-sensitive Fission Counter", JAERI-Research 98-063 (1998)[In Japanese].
12) *idem*:"Pulse Propagation Characteristics of the Solenoid Electrode for a Position-sensitive Fission Counter", JAERI-Research 99-002 (1999) [In Japanese].
13) Sasaki, S.:"A Practical Computational Technique for Mobile Robot Navigation", 1998 IEEE Int. Conf. on Control Application, Italy (1998).
14) Fujii, Y. and Suzuki, K.:"Obstacle Avoidance Test using a Sensor-based Autonomous Robotic System", JAERI-Tech 98-054 (1998) [In Japanese].

6. Heat Transfer and Fluid Flow

1) Ohnuki, A. and Akimoto, H.:"Flow Characteristics of Air-Water Two-phase Flow in a Large Vertical Pipe", Proc. of 1st European-Japanese Two-phase Flow Group Meeting, Portoroz, Slovenia, June (1998).
2) Ohnuki, A. and Akimoto, H.:"Prediction of Phase Distribution under Bubbly Flow in a Large Vertical Pipe by Multidimensional Two-Fluid Model", Proc. of 3rd International Conference on Multiphase Flow (ICMF'98), Lyon, France, June (1998).
3) Ohnuki, A., Seimiya, M. and Akimoto, H.:"Experimental Study on Scale Effect of Flow Path against Phase Distribution of Bubbly Flow in a Vertical Pipe", Proc. of 17th National Symposium of Multiphase Flow, D17 (1998) [in Japanese].
4) Kureta, M. and Akimoto, H.:"Experimental Study on Critical Heat Flux along One-Side Heated Rectangular Channel under Subcooled Conditions", Proc. of the 6th International

Conference on Nuclear Engineering (ICONE-6), San Diego, U.S., ICONE-6226(1998).
5) Kureta, M. and Akimoto, H.:"Void Fraction Measurement with Neutron Radiography Method for Subcooled Boiling Two-Phase Flow in Rectangular Duct Heated from One-Side", Proc. of thermal Engineering Symposium '98, No.98-23, 73(1998) [In Japanese].
6) Kureta, M. and Akimoto, H.:"Burnout Behavior at the Super-High Heat Flux Condition", Proc. of the 76th JSME Fall Annual Meeting, No.98-3, 471(1998) [In Japanese].
7) Kureta, M., Matsubayashi, M. and Akimoto, H.:"Development of Measurement Method of Void Fraction Distribution on Subcooled Flow Boiling Using Neutron Radiography", JAERI-Research 99-023 (1999) [In Japanese].
8) Takase, K., Kunugi, T., Yamazaki, S. and Fujii, S.:"Possibility of Volume Reduction of Blowdown Tank in Fusion Reactor Safety System", Fusion Technology, 43, 640(1998).
9) Takase, K. and Kunugi, T.:"Quantitative Measurement of Dust Mobilization in a Vacuum Vessel of a Fusion Reactor During the Loss-of-Vacuum-Accident Event", Fusion Technology, 43, 645(1998).
10) Takase, K., Kunugi, T., Shibata, M. and Seki, Y.:"Temperature Distributions in a Tokamak Vacuum Vessel of a Fusion Reactor after the Loss-of-Vacuum Events Occurred", Fusion Engineering and Design, 42, 83(1998).
11) Kunugi, T., Takase, K., Shibata, M., Kurihara, R. and Seki, Y.:"Thermofluid Experiments on Ingress of Coolant Event", Fusion Engineering and Design, 42, 67(1998).
12) Takase, K., Akimoto, H. and Kunugi, T.:"Analysis of Pressure Transient During Ingress-of-Coolant Event in Fusion Reactor with TRAC-Code", Proc. of 6th International Conference of Nuclear Engineering (ICONE-6), San Diego, U.S., ICONE-6223(1998).
13) Takase, K., Kunugi, T., Seki, Y. and Akimoto, H.:"Thermal-Hydraulic Characteristics During Ingress-of-Coolant Event and Loss-of-Vacuum Events in Fusion Reactors", 17th IAEA International Conference on Fusion Energy, Yokohama, Japan, ITERP2-09(1998).
14) Takase, K. and Kunugi, T.:"Preliminary Numerical Analysis of Dust Transport Through Breaches of a Vacuum Vessel in a Fusion Reactor During the Loss-of-Vacuum Accident", 5th ASME-JSME Thermal Engineering Joint Conference, San Diego, U.S., AJTE99-6428(1999).
15) Takase, K., Kunugi, T., Akimoto, H. and Seki, Y.:"ICE/LOVA Experiments", ITER Safety Task Report, San Diego, U.S., June (1998).
16) Takase, K.,"Plan of Thermofluid Safety Experiments for Fusion Reactors", US/Japan Workshop on Fusion High Power Density Devices, Los Angeles, U. S., February (1998).
17) Takase, K., Kunugi, T. and Akimoto, H.:"Pressure Transients in Vacuum Vessel of Fusion Reactors due to Water Ingress", 75th JSME Spring Annual Meeting, No. 98-1, 349(1998) [in Japanese].
18) Takase, K., Kunugi, T., Ichimiya, K. and Watanabe, S.:"Heat Removal Characteristics of Helium-Cooling Porous Channels", JSME Thermal Engineering Conference '98, No.98-4, 281(1998) [in Japanese].
19) Takase, K.:"Fluid Flow Analysis in a vacuum Vessel After Loss-of-Vacuum Accident", JSME Fluids Engineering Conference '98, No.98-15, 367(1998) [in Japanese].
20) Takase, K., Kunugi, T., Yamaszaki, S. and Fujii, S.:"Behavior of Pressure Rise and Condensation Caused by Water Evaporation Under Vacuum at High Temperature", 35th National Heat Transfer Symposium, D342, 801(1998) [in Japanese].
21) Takase, K., Shibata, M. and Kunugi, T.:"Visualization on Mobilization Behavior of

Radioactivated Dust in a Vacuum Chamber", J. of the Visualization Society of Japan, 18 Supplement, 1, 27(1998) [in Japanese].
22) Takase, K. and Shibata, M.:"Mobilization Characteristics of Dust Conveyed by Buoyancy Flows during Loss-of-Vacuum Accident",J. of the Visualization Society of Japan, 18 Supplement, 2, 89(1998) [in Japanese].

7. Energy System Analysis and Assessment

1) Sato, O., *et al.*:"CO_2 Emission Reduction Strategy and Roles of Nuclear Energy in Japan", JAERI-Research 99-015 (1999).
2) Chen, H.:"Analysis on Long-term Strategy for Radwaste Management in China", JAERI-Research 98-044 (1998).

8. Material Performance and Testing Laboratory

1) Tsukada, T., Miwa, Y., Tsuji, H. and Nakajima, H.:"Effect of Irradiation Temperature on Irradiation Assisted Stress Corrosion Cracking of Model Austenitic Stainless Steels", J. Nucl. Mater., 258-263, 1669 (1998).
2) Matsui, Y., Niimi, M., Hoshiya, T., Tsukada, T. and Tsuji, H.:"Irradiation Techniques under High Pressurized Water Using Hybrid Type Saturated Temperature Capsule in the JMTR", J.Nucl. Mater., 258-263, 378 (1998).
3) Tsukada, T., Miwa, Y., Tsuji, H. and Nakajima, H.:"Post Irradiation Experiments on IASCC at JAERI", Proc. of the 3rd JAERI-KAERI Joint Seminar on PIE Technology, 319(1998).
4) Nakajima, R., Shimura, K., Fujita, M., Tsuji, H., Yokoyama, N., Tachi, Y.and Kano, S.: "A Distributed Material Database on the Internet - Recent Activity in Data-Free-Way", Proc. Society of Information Knowledge, 43 (1998) [in Japanese].
5) Tachi, Y., Kano, S., Fujita, M., Tsuji, H., Yokoyama, N., Shimura, K.,Nakajima, R. and Iwata, S.:"Utilization of Image Data in Data-Free-Way : A Fresh Attempt to Use Image Data inMaterial Database", Proc. 35th Information Science Technical Meeting, 97 (1998) [in Japanese].
6) Tsuji, H., Yokoyama, N., Fujita, M., Kano S., Tachi, Y., Shimura, K.,Nakajima, R. and Iwata, S.:"Distributed Database System for Mutual Usage of Material Information (Data-Free-Way)", Materials for Advanced Power Engineering 1998, Part III, Forschungs Zentrum Juelich, Juelich, Germany, 1739 (1998).
7) Tsuji, H., Yokoyama, N., Fujita, M., Kano S., Tachi, Y., Shimura, K., Nakajima, R. and Iwata, S.:"Distributed Database System for Advanced Nuclear Mutual Materials (Data-Free-Way)", Innovative Materials in Advanced Energy Technologies, TECHNA Srl, Faenza, Italy, 417 (1999).
8) Kaji, Y., Tsuji, H., Sakino, T., Fujita, M., Kinugawa, J., Tachi, Y., Saito, J., Kano, S., Shimura, K., Nakajima, R.and Iwata, S.:"Retrieval Results on Various Properties of Superalloy Using "Data-Free-Way" (Joint Research)", JAERI-Tech 99-007 (1999) [in Japanese].
9) Fujita, M., Kinugawa, J., Tsuji, H., Kaji, Y., Tachi, Y., Saito, J.,Shimura, K., Nakajima, R. and Iwata, S.:"Material Information of DFW Related Agencies on the Internet", Report of

the 10th Data-Free-Way Technical Meeting (1999) [in Japanese].
10) Tsuji, H., Kurata, Y., Miwa, Y., Itabashi, Y., Amezawa, H., Shimakawa, S., Mimura, H., Kita, S., Suzuki, T., Tsukada, T., Ioka, I., Sawai, T., Hoshiya, T., Shindo, M. and Nakajima, H.:"Post Irradiation Mechanical Properties of Type 304 Stainless Steel", Innovative Materials in Advanced Energy Technologies, TECHNA Srl, Faenza, Italy, 483 (1999).
11) Kurata, Y., Itabashi, Y., Mimura, H., Kikuchi, T., Amezawa, H., Shimakawa, S. and Tsuji, H.: "In-Pile and Post- Irradiation Creep of SUS304 with JMTR Thermal Neutron Spectrum", The Sixth Asian Symposium on Research Reactors, Mito, Japan, 175 (1998).
12) 1997 Annual Report on Demonstration Test on Lifetime Reliability of Structural Materials for Advanced Prototype Power Reactors(STA Commissioned Research) (1998).

9. Advanced Materials for Nuclear Applications

1) Tanabe, Y., *et al.*:"Dynamic Mechanical Behavior of SiCf/SiC",The Sixth International Conference on Nuclear Engineering (ICONE-6), San Diego, USA, ICONE6219 (1998).
2) Stockmann, Y., *et al.*:"Thermomechanical Properties of Silica Scales on SiSiC", Ceramic Trans. of Amer. Cer. Soc., 99, p.357(1998).
3) Kurata, Y. and Utsumi, H.:"Change in Creep Curve Shapes and Applicability of θ Projection Method of Ni-22Cr-18Fe-9Mo Alloy", JAERI-Research 98-027(1998) [in Japanese].
4) Kurata, Y. and Utsumi, H.:"Creep Curve Shapes of Ni-22Cr-18Fe-9Mo Alloy in Solution-Treated and Aged Conditions", J. of Japan Inst. Metals, 62(5), p.413 (1998) [in Japanese].
5) Kurata, Y. and Utsumi, H.:"Applicability of the θ Projection Method to Creep Curves of Ni-22Cr-18Fe-9Mo Alloy", J. of Japan Inst. Metals, 62, p.420(1998) [in Japanese].
6) Kikuchi, K., *et al.*:"Material Development for Spallation Target at JAERI", 14th International Collaboration on Advanced Neutron Sources(ICANS-14), Utica, USA (1998).
7) Futakawa, M., *et al.*:"Measurement of Pressure Wave in Mercury Target", 14th International Collaboration on Advanced Neutron Sources (ICANS-14), Utica, USA (1998).
8) Ishiyama, S., Fukaya, K. and Eto, M.:"Synthesis and Fabrication Technique of SiC/SiC Thermoelements", Key Engineering Materials, 159-160, p.423(1998).
9) Futakawa, M. and Steinbrech, R., W.:"Viscosity of Amorphous Oxide Scales on SiSiC at Elevated Temperatures", J. American Cer. Soc., 81, p1819(1998).
10) Saito, S., *et al.*:"Development of Bonding Techniques of W and Cu Alloys for Plasma Facing Components of Fusion Reactor with HIP Method", Proc. 20th Symposium on Fusion Technology, Marseille, France(1998).
11) Futakawa, M., *et al.*:"Dynamic Effect on Strength in SiCf/SiC Composite" ,Proc. International Symposium on Impact Engineering (ISIE) , Singapore, p.363 (1998).
12) Futakawa, M., Steinbrech, R., W., Wakui, T. and Kurabe, M.:"Heat Treatment Effect on Bilayer Silica Scale Formed on Si-SiC", J. of Surface Finishing Soc. Japan, 50(1), p.58(1999) [in Japanese].
13) Eto, M. and Konishi, T.:"Change in Electrical Resistivity of Nuclear Graphite and Carbon

Materials during Low Cycle Fatigue", Tanso, 186, p.30(1999).
14) Ishiyama, S., Fukaya, K. and Eto, M.:"R&D of C/C Composite Control Rod for HTTR", International Symposium on Carbon Science & Technology for New Carbon, Tokyo, Japan(1998).
15) Kikuchi, K.:"Transient Thermal Stress in the Mercury Target Window at the Beam Trip of High Intensity Pulsed Proton Accelerator", OECD/NEA Workshop on Utilization and Reliability of High Power Proton Accelerators, Mito, Japan, p.381(1998).
16) Nishi, H., Araki, T. and Eto, M.:"Diffusion Bonding of Alumina Dispersion-Strengthened Copper to 316 Stainless Steel with Interlayer Metals", Fusion Eng. Design, 39-40, p.505(1998).
17) Eto, M and Ishiyama, S.:"Biaxial Fatigue Strength of a Fine-Grained Isotropic Graphite for HTTR", J. Nucl. Sci. & Technology, 35, p.808(1998).
18) Takahashi, H., *et al.*:"Mechnical Properties and Damage Behavior of Non-Magnetic High Manganese Austenitic Steels", J. Nucl. Mater., 258-263, p.1664(1998).
19) Nishiyama, Y., Fukaya, K., Suzuki, M. and Eto, M.:"Irradiation Embrittlement of 21/4Cr-1Mo Steel at 400℃ and Its Electrochemical Evaluation" , J. Nucl. Mater., 258-263, p.1187(1998).
20) Ishii, T., Fukaya, K., Nishiyama, Y., Suzuki, M. and Eto, M.:"Low Cycle Fatigue of 8Cr-2W-V-Ta Ferritic Steel at Elevated Temperatures", J. Nucl. Mater., 258-263, p.1183 (1998).
21) Kaji, Y., Roedig, M. and Kikuchi, K.:"Comparison and Evaluation of Creep Crack Growth Rate and Fracture Time for Alloy 800 by the Q* Parameter", Int. J. Pressure Vessel and Piping, 75, p.1065(1998).
22) Nishi, H. and Kikuchi, K.:"Influence of Brazing Conditions on the Strength of Brazed Joints of Alumina Dispersion-Strengthened Copper to 316 Stainless Steel", J. Nucl. Mater., 258-263, p.281(1998).
23) Eto, M., Baba, S., Ishihara, M. and Ugachi, H.:"High Energy Neutron and Changed Particle Irradiation Effects on Thermomechanical Properties of Carbon-Carbon Composites for Divertor Applications", J. Nucl. Mater., 258-263, p.843(1998).
24) Kikuchi, K., *et al.*:"Analysis of Intergranular Cracking for Incoloy 908 during a Heat Treatment", J. Soc. Mater. Sci. Japan, 48(2),p.152(1999)[in Japanese].
25) Tachibana, K., Nishi, H., Eto, M. and Muto, Y.:"Creep Strength of Hastelloy XR Welded Joints", JAERI-Tech 99-024(1999)[in Japanese].

10. Compatible Materials Development for Advanced Nuclear Systems

1) Kiuchi, K., *et al.*:"Characteristics of High Wear Resistant Ni-base Materials Strengthened by precipitation Hardening of Wolfram Silicide",Proc. Inter. Conf. of Water Chemistry'98, Japan(1998)
2) Kiuchi, K., *et al.*:"New Alloy Developments for Advanced Spent Fuel Reprocessing Using Nitric Acid Solutions", RECOD'98/REC'98, Vol.3,867(1998)
3) Kiuchi, K., *et al.*:"The Life Prediction Study of Rokkasho Reprocessing Plant Materials", RECOD'98/REC'98, Vol.3, 859(1998)
4) Kato, C., *et al.*:"Evaluation of Resistance against Environmental Cracking of Reprocessing Grade Zr in Nitric Acid Solution", RECOD'98/REC'98,1998.10.25-28,

France
5) Kato, C. and Kiuchi, K.:"Corrosion Behavior of Heating Zirconium in Nitric Acid", Proc. 1999 Annual Meeting of the Atomic Energy Society of Japan,669(1999) [In Japanese]
6) Motooka,T. and Kiuchi, K.:"Fatigue Crack Propagation Behavior of Heat Affected Zone of Zirconium Weldment in Boiling Nitric Acid Solution", JAERI-Research 99-031(1999)[In Japanese]
7) Motooka, T. and Kiuchi, K.:"Fatigue Crack Propagation Behavior of Zirconium in Boiling Nitric Acid Solution", Proc. 1999 Annual Meeting of the Atomic Energy Society of Japan, 609(1999) [In Japanese]

11. Rock-Like Oxide Fuel for Plutonium Burning in LWRs

1) Takano, H.,*et al.*:"Plutonium Annihilation and Disposition by Rock-like Fuel in Light-water Reactors", Proc. 6th Int. Conf. Nuclear Engineering (ICONE-6), May 10-14, 1998, San Diego, USA, ICONE-6065 (1998) (CD-ROM)
2) Takano, H., *et al.*:"Reactor Benchmark Testing for JENDL-3.2, JEF-2.2 and ENDF/B-VI.2", Proc. Int. Conf. Physics of Nuclear Science and Technology, October 5-8, 1998, Long Island, USA, Vol. 1, (1998)58
3) Nakano, Y., *et al.*:"Neutronics Characteristics of JRR-4 Low Enriched Uranium Core", Proc. 21st Int. Mtg. Reduced Enrichment for Research and Test Reactors (RERTR), October 18-23, 1998, Sao Paulo, Brazil (1998)
4) Nitani, N., *et al.*:"Thermophysical Properties of Rock-like Oxide Fuel with Spinel-yttria Stabilized Zirconia System", Proc. 4th Inert Matrix Fuel Workshop, October 19-20, 1998, PSI, Villigen, Switzerland, J. Nucl. Matr., 274 (1999)15
5) Shiratori, T. , *et al.*:"Preparation of Rock-like Oxide Fuels for the Irradiation Test in the Japan Research Reactor No.3", ibid., (1999)40
6) Yamashita, T. , *et al.*:"In-pile Irradiation of Plutonium Rock-like Oxide Fuels with Yttria Stabilized Zirconia or Thoria, Spinel and Corundum", ibid., (1999)98
7) Nakano, Y. , *et al.*:"Burnup analysis of Rock-like Oxide Fuel Disks Irradiated in the Japan Research Reactor No. 3", ibid., (1999)127
8) Akie, H., , *et al.*:"Core Design Study on Rock-like Oxide Fuel Light Water Reactor and Improvements of Core Characteristics", ibid., (1999)139
9) Okonogi, K. , *et al.*:"Pulse Irradiation Tests of Rock-like Oxide Fuel", ibid., (1999)167
10) Kimura, H. , *et al.*:"A Study of Actinide Decay Chains on the Environmental Effect of A Geologic Disposal of 'Rock-like Oxide' Fuels and Uranium-plutonium Oxide Fuels", ibid., (1999)197
11) Yanagisawa, K. , *et al.*:"A Study on Density, Melting Point, Thermal Expansion, Creep, Thermal Diffusivity and Thermal Conductivity of the Simulated Rock-like Oxide (ROX) Fuels", JAERI-Tech 99-032 (1999)
12) K. Yanagisawa, T., *et al.*:"Out-of-pile Tests of Simulated Rock-like Oxide (ROX) Fuels", J. Nucl. Sci.,Technol., 36 [2](1999)160.

12. Nitride Fuel and related Pyrochemical Technology

1) Suzuki, Y. and Arai, Y.:"Plutonium and Actinides Fuels, 4.4 Nitride and carbide fuels",

Plutonium Fuel Technology, (1998)260
2) Arai, Y:"Plutonium and Actinides Fuels, Fuels for Transmutation", Plutonium Fuel Technology, (1998)330
3) Arai, Y. *et al.*:"Design and Installation of High-temperature X-ray Diffractometer for Transuranium Elements and Its Performance", JAERI-Tech 98-022 (1998)
4) Suzuki, Y. and Arai, Y.:"Thermophysical and Thermodynamic Properties of Actinide Mononitrides and their Solid Solutions", J. Alloys and Compounds, 271-273(1998) 577
5) Arai, Y. *et al.*:"Thermal Concuctivity of Actinide Mononitrid Solid Solutions", J. Alloys and Compounds, 271-273 (1998) 602
6) Nakajima, K. *et al.*:"Vaporization Behavior of (Np,Pu)N", J. Alloys and Compounds, 271-273 (1998) 666
7) Shirai, O. *et al.*:"Electrochemical Behavior of Actinide Ions in LiCl-KCl Eutectic Melts", J. Alloys and Compounds, 271-273 (1998) 685
8) Shirai, O. *et al.*:"Ion Transport across a Bilayer Lipid Membrane: An Interpretation Based on Ion Transfer Voltammetry", Rev. Polarog., 44 (2) (1998) 76
9) Serizawa, H. *et al.*:"X-ray Debye Temperature and Gruneisen Constant of NpO_2", J. Alloys and Compounds, 282 (1999) 17
10) Nakajima, K. *et al.*:" Vaporization Behavior of $BaPuO_3$", J. Mass Spectrum. Soc. Jpn., 47 (1) (1999) 46

13. Nuclear Ship Research and Development

1) Kusunoki, T. *et al.*:"Application of a Compact Nuclear Reactor to a Submersible Research Vessel", The 14th Ocean Engineering Symposium, Tokyo, Japan (1998)
2) Miura, T., Ishida, T. and Hirao, Y.: "Shielding Analysis of Neutron Detector Guide Tubes of Advanced Marine Reactor MRX", JAERI-Tech 98-030 (1998) [In Japanese]
3) Takahashi, H., *et al.*:"JRR-4 Operation Supporting System", The 6th Asian Symposium on Research Reactor, Mito, Japan (1999)
4) Nakazawa, T., Yabuuchi, N., Takahashi, H. and Shimazaki, J.:"Development of Advanced Automatic Operation System for Nuclear Ship (1) - Perfect Automatic Normal Operation", JAERI-Tech 99-008 (1999) [In Japanese]
5) Nakazawa, T., Watahiki, M., Takahashi, H. and Kyoya, M.:"Operational Data of Nuclear Ship MUTSU", JAERI-Data/Code 99-010 (1999) [In Japanese]
6) Takahashi, H., Yamamoto, K., Yoritsune, T., Arai, N. and Birumachi, T.:"Development of JRR-4 Operation Support System",JAERI-Tech 99-037 (1999) [In Japanese]

Appendix I

Department of Nuclear Energy System Organization Chart

March 1999

Department of Nuclear Energy System
Director : M. Nakagawa
Deputy Director : H. Nakajima

K. Fukuda
K. Ara

Administrative Service
T. Kimura (Administrative Manager)
T. Nogami T.Takada T.Ohno T. Tomita

Reactor Engineering Facility Operation Division
H. Watanabe (Head)
K. Nakajima H. Watanabe K. Kurosawa M. Takeuchi
K. Satoh T. Satoh T. Ono M. Shibata
Y. Hakamazuka H. Sodeyama M. Saitoh S. Fujisaki(1)

Nuclear Data Center
A.Hasegawa (Head)
T. Shirai Y. Nakagawa J. Katakura K. Shibata
T. Fukahori A. Ichihara O. Iwamoto S. Chiba(2)
H. Naramoto(2) H. Takano(3) M. Mizumoto(3) M. Sataka(4)
H. Iimura(4)

Energy System Assessment Laboratory
O. Sato (Head)
Y. Tadokoro S. Goto K.Kunii K. Tatematsu

Advanced Reactor Systems Laboratory
M. Ochiai (Head)
T. Okubo N. Nakajima F. Araya T. Shirakawa
S. Usui H. Yoshida

Reactor Analysis Laboratory
T. Osugi (Head)
T. Mori T. Fujimura K. Okumura T. Kugo
Y. Nagaya T. Hasegawa H. Takano(3)

Rector Physics Laboratory
T. Osugi (Head)
S. Iijima S. Okajima M. Haruyama T. Yamane
H. Oigawa T. Sakurai M. Takase M. Andoh
Y. Sugimoto H. Yasuda(3) T. Ogawa(4)

Control & AI Laboratory
K. Suzuki (Head)
S. Sasaki K. Watanabe T. Kakuta H. Yamagishi
H. Itoh T. Suzudo K. Nabeshima N. Ishikawa
M. Katagiri(2) Y. Fujii(3) M. Kishimoto(2) J. Kaneko(4)
N. Ebine(5)

Heat Transfer & Fluid Flow Laboratory
H. Akimoto (Head)
A. Ohnuki K. Takase M. Kureta Y. Ose

Material Performance and Testing Laboratory
H. Tsuji (Head)
T. Tsukada Y. Kaji M. Kikuchi Y. Miwa
S. Kita Y. Sawai(4)

Material Strength Laboratory
M. Eto (Head) K. Kikuchi Y. Kurata M. Futakawa
T. Saito I. Ioka H. Nishi T. Suzuki
K. Tachibana H. Ugachi S. Saito S. Ishiyama(6)
S. Baba(6) H. Nishiyama(5) T. Ishii(7)

Interfacial Studies Laboratory
K. Kiuchi (Head) S. Hamada K. Fukaya M. Suga
T. Motooka S. Shibata C. Kato Y. Sekiyama
T. Fujimoto T. Ishiyama(4)

Advanced Fuel Laboratory
Y. Suzuki (Head) Y. Arai T. Yamashita K. Yanagisawa
T. Sasayama T. Shiratori K. Shiozawa A. Inoue
T. Iwai H. Akie Y. Nakano H. Serizawa
K. Kikuchi O. Shirai K. Nakajima K. Ishijima(5)
K. Hojou(4) T. Baba(8) Y. Anoda(5) T. Yamada(9)
H. Amano(10) H. Kanazawa(10) H. Mitamura(8) N. Shirasu(4)
H. Kimura(8) T. Muromura(8) H. Takano(3) T. Nakamura(5)

Nuclear Ship Research and Development Division
M. Ochiai (Head) T. Nakazawa T. Takahashi T. Maruyama(11)

Advanced Marine Reactor Laboratory
T. Ishida (Head) Y. Fukuyara H. Nunokawa K. Saitoh
T. Kusunoki N. Odano T. Yoritsune

Nuclear Ship System Laboratory
J. Shimazaki (Head) N. Yabuuchi M. Kyoya M. Takahashi
H. Takahashi

Research Committee
Japanese Nuclear Data Committee
Atomic and Molecular Data Committee
Research Committee on Reactor Physics
Research Committee on Marine Reactors

(No.) Original Organization of the Shared-Time Members
(1) Dept. HTTR Project
(2) Advanced Science Research Center
(3) Center for Neutron Science
(4) Dept. of Materials Science
(5) Dept. of Reactor Safety Research
(6) Dept of Advanced Nuclear Heat Technology
(7) Dept. of JMTR
(8) Dept. of Environmental Safety Research
(9) Dept. of Research Reactor
(10) Dept. of Hot Laboratories
(11) Dept. of Facilities (Mutsu Establishment)

Appendix Ⅱ Engineering Facilities Related to the Department

FCA : Fast Critical Assembly

The FCA is a split-table type facility of horizontal matrix structure designed for studying nuclear characteristics of fast reactor. The construction of the FCA was started in 1965 and the first core went critical on 29th April,1967. The main features of facility are summarized as follows:

Type:	Split-table type of horizontal matrix structure
Size:	2.8m × 2.8m × 1.3m (each half assembly)
Fuel:	Enriched uranium and plutonium (Plate type)
Other material:	Sodium, stainless steel, aluminum oxide, polystyrene etc. (Plate type)
Maximum power:	2kW
Assembly name:	FCA-I～FCA-XIX

Critical experiment using enriched uranium cores were made in 1960s investing basic characteristics of fast reactor cores. Mock-up experiments were extensively made in 1970s for the Fast Experimental Reactor JOYO and the Prototype Fast Breeder Reactor MONJU. In 1980s, the main subjects of experiments were the investigation of the core characteristics of an axially heterogeneous large fast breeder reactor and the core physics study on a high conversion light water reactor. In early 1990s, the reactor physics experiment of metallic-fueled LMFBR was carried out. Since 1995, international benchmark experiments for β_{eff} have been carried out by using FCA XIX core.

VHTRC : Very High Temperature Reactor Critical Assembly

The VHTRC is a low-enriched uranium fueled and graphite moderated / reflected critical assembly. At VHTRC, reactor physics experiments have been carried out mainly for the verification of the neutronics design of the HTTR.

Main features of VHTRC

Type:	Split table of hexagonal prism (prismatic block structure)
Size:	2.4m across the flats and 2.4m long
Fuel:	2,4 and 6wt% enriched UO_2
	Coated particle fuel compact, Pin-in-block type
Moderator/reflector:	Graphite
Core temperature:	Room temperature to 210℃ by electric heaters
Maximum power:	10W
Auxiliary equipments:	① Sample heating device (up to 800℃)
	② Pulsed neutron source

国際単位系 (SI) と換算表

表 1　SI基本単位および補助単位

量	名称	記号
長さ	メートル	m
質量	キログラム	kg
時間	秒	s
電流	アンペア	A
熱力学温度	ケルビン	K
物質量	モル	mol
光度	カンデラ	cd
平面角	ラジアン	rad
立体角	ステラジアン	sr

表 2　SIと併用される単位

名称	記号
分，時，日	min，h，d
度，分，秒	°，′，″
リットル	l，L
トン	t
電子ボルト	eV
原子質量単位	u

1 eV = 1.60218 × 10^{-19} J

1 u = 1.66054 × 10^{-27} kg

表 5　SI接頭語

倍数	接頭語	記号
10^{18}	エクサ	E
10^{15}	ペタ	P
10^{12}	テラ	T
10^{9}	ギガ	G
10^{6}	メガ	M
10^{3}	キロ	k
10^{2}	ヘクト	h
10^{1}	デカ	da
10^{-1}	デシ	d
10^{-2}	センチ	c
10^{-3}	ミリ	m
10^{-6}	マイクロ	μ
10^{-9}	ナノ	n
10^{-12}	ピコ	p
10^{-15}	フェムト	f
10^{-18}	アト	a

表 3　固有の名称をもつSI組立単位

量	名称	記号	他のSI単位による表現
周波数	ヘルツ	Hz	s^{-1}
力	ニュートン	N	m·kg/s^2
圧力，応力	パスカル	Pa	N/m^2
エネルギー，仕事，熱量	ジュール	J	N·m
工率，放射束	ワット	W	J/s
電気量，電荷	クーロン	C	A·s
電位，電圧，起電力	ボルト	V	W/A
静電容量	ファラド	F	C/V
電気抵抗	オーム	Ω	V/A
コンダクタンス	ジーメンス	S	A/V
磁束	ウェーバ	Wb	V·s
磁束密度	テスラ	T	Wb/m^2
インダクタンス	ヘンリー	H	Wb/A
セルシウス温度	セルシウス度	℃	
光束	ルーメン	lm	cd·sr
照度	ルクス	lx	lm/m^2
放射能	ベクレル	Bq	s^{-1}
吸収線量	グレイ	Gy	J/kg
線量当量	シーベルト	Sv	J/kg

表 4　SIと共に暫定的に維持される単位

名称	記号
オングストローム	Å
バーン	b
バール	bar
ガル	Gal
キュリー	Ci
レントゲン	R
ラド	rad
レム	rem

1 Å = 0.1 nm = 10^{-10} m

1 b = 100 fm^2 = 10^{-28} m^2

1 bar = 0.1 MPa = 10^5 Pa

1 Gal = 1 cm/s^2 = 10^{-2} m/s^2

1 Ci = 3.7 × 10^{10} Bq

1 R = 2.58 × 10^{-4} C/kg

1 rad = 1 cGy = 10^{-2} Gy

1 rem = 1 cSv = 10^{-2} Sv

（注）

1. 表1－5は「国際単位系」第5版，国際度量衡局 1985年刊行による。ただし，1 eVおよび1 uの値はCODATAの1986年推奨値によった。
2. 表4には海里，ノット，アール，ヘクタールも含まれているが日常の単位なのでここでは省略した。
3. barは，JISでは流体の圧力を表わす場合に限り表2のカテゴリーに分類されている。
4. EC閣僚理事会指令ではbar，barnおよび「血圧の単位」mmHgを表2のカテゴリーに入れている。

換算表

力	N(=10^5 dyn)	kgf	lbf
	1	0.101972	0.224809
	9.80665	1	2.20462
	4.44822	0.453592	1

粘度　1 Pa·s(N·s/m^2) = 10 P(ポアズ)(g/(cm·s))

動粘度　1 m^2/s = 10^4 St(ストークス)(cm^2/s)

圧力	MPa(=10 bar)	kgf/cm^2	atm	mmHg(Torr)	lbf/in^2(psi)
	1	10.1972	9.86923	7.50062 × 10^3	145.038
	0.0980665	1	0.967841	735.559	14.2233
	0.101325	1.03323	1	760	14.6959
	1.33322 × 10^{-4}	1.35951 × 10^{-3}	1.31579 × 10^{-3}	1	1.93368 × 10^{-2}
	6.89476 × 10^{-3}	7.03070 × 10^{-2}	6.80460 × 10^{-2}	51.7149	1

エネルギー・仕事・熱量	J(=10^7 erg)	kgf·m	kW·h	cal(計量法)	Btu	ft·lbf	eV
	1	0.101972	2.77778 × 10^{-7}	0.238889	9.47813 × 10^{-4}	0.737562	6.24150 × 10^{18}
	9.80665	1	2.72407 × 10^{-6}	2.34270	9.29487 × 10^{-3}	7.23301	6.12082 × 10^{19}
	3.6 × 10^6	3.67098 × 10^5	1	8.59999 × 10^5	3412.13	2.65522 × 10^6	2.24694 × 10^{25}
	4.18605	0.426858	1.16279 × 10^{-6}	1	3.96759 × 10^{-3}	3.08747	2.61272 × 10^{19}
	1055.06	107.586	2.93072 × 10^{-4}	252.042	1	778.172	6.58515 × 10^{21}
	1.35582	0.138255	3.76616 × 10^{-7}	0.323890	1.28506 × 10^{-3}	1	8.46233 × 10^{18}
	1.60218 × 10^{-19}	1.63377 × 10^{-20}	4.45050 × 10^{-26}	3.82743 × 10^{-20}	1.51857 × 10^{-22}	1.18171 × 10^{-19}	1

1 cal = 4.18605 J(計量法)
= 4.184 J (熱化学)
= 4.1855 J (15 °C)
= 4.1868 J(国際蒸気表)

仕事率　1 PS(仏馬力)
= 75 kgf·m/s
= 735.499 W

放射能	Bq	Ci
	1	2.70270 × 10^{-11}
	3.7 × 10^{10}	1

吸収線量	Gy	rad
	1	100
	0.01	1

照射線量	C/kg	R
	1	3876
	2.58 × 10^{-4}	1

線量当量	Sv	rem
	1	100
	0.01	1

（86年12月26日現在）